

Special Issue Reprint

Electric, Magnetic, and Electromagnetic Fields in Biology and Medicine

From Mechanisms to Biomedical Applications:
2nd Edition

Edited by
Stefania Romeo and Anna Sannino

mdpi.com/journal/bioengineering

**Electric, Magnetic, and Electromagnetic
Fields in Biology and Medicine: From
Mechanisms to Biomedical
Applications: 2nd Edition**

Electric, Magnetic, and Electromagnetic Fields in Biology and Medicine: From Mechanisms to Biomedical Applications: 2nd Edition

Guest Editors

Stefania Romeo

Anna Sannino



Basel • Beijing • Wuhan • Barcelona • Belgrade • Novi Sad • Cluj • Manchester

Guest Editors

Stefania Romeo

Institute for Electromagnetic
Sensing of the Environment
(IREA)

National Research Council
(CNR)

Napoli

Italy

Anna Sannino

Institute for Electromagnetic
Sensing of the Environment
(IREA)

National Research Council
(CNR)

Napoli

Italy

Editorial Office

MDPI AG

Grosspeteranlage 5

4052 Basel, Switzerland

This is a reprint of the Special Issue, published open access by the journal *Bioengineering* (ISSN 2306-5354), freely accessible at: https://www.mdpi.com/journal/bioengineering/special_issues/15ALND0PQM.

For citation purposes, cite each article independently as indicated on the article page online and as indicated below:

Lastname, A.A.; Lastname, B.B. Article Title. <i>Journal Name</i> Year , <i>Volume Number</i> , Page Range.

ISBN 978-3-7258-4699-3 (Hbk)

ISBN 978-3-7258-4700-6 (PDF)

<https://doi.org/10.3390/books978-3-7258-4700-6>

© 2025 by the authors. Articles in this book are Open Access and distributed under the Creative Commons Attribution (CC BY) license. The book as a whole is distributed by MDPI under the terms and conditions of the Creative Commons Attribution-NonCommercial-NoDerivs (CC BY-NC-ND) license (<https://creativecommons.org/licenses/by-nc-nd/4.0/>).

Contents

About the Editors	vii
Stefania Romeo and Anna Sannino Special Issue “Electric, Magnetic, and Electromagnetic Fields in Biology and Medicine: From Mechanisms to Biomedical Applications: 2nd Edition” Reprinted from: <i>Bioengineering</i> 2025, 12, 739, https://doi.org/10.3390/bioengineering12070739	1
Milan Pantovic, Daniel E. Lidstone, Lidio Lima de Albuquerque, Erik W. Wilkins, Irwin A. Munoz, Daniel G. Aynlender, et al. Cerebellar Transcranial Direct Current Stimulation Applied over Multiple Days Does Not Enhance Motor Learning of a Complex Overhand Throwing Task in Young Adults Reprinted from: <i>Bioengineering</i> 2023, 10, 1265, https://doi.org/10.3390/bioengineering10111265	8
Milan Pantovic, Rhett Boss, Kevin J. Noorda, Mario I. Premyanov, Daniel G. Aynlender, Erik W. Wilkins, et al. The Influence of Different Inter-Trial Intervals on the Quantification of Intracortical Facilitation in the Primary Motor Cortex Reprinted from: <i>Bioengineering</i> 2023, 10, 1278, https://doi.org/10.3390/bioengineering10111278	26
Lidio Lima de Albuquerque, Milan Pantovic, Erik W. Wilkins, Desiree Morris, Mitchell Clingo, Sage Boss, et al. Exploring the Influence of Inter-Trial Interval on the Assessment of Short-Interval Intracortical Inhibition Reprinted from: <i>Bioengineering</i> 2024, 11, 645, https://doi.org/10.3390/bioengineering11070645	46
Pei L. Robins, Sergey N. Makaroff, Michael Dib, Sarah H. Lisanby and Zhi-De Deng Electric Field Characteristics of Rotating Permanent Magnet Stimulation Reprinted from: <i>Bioengineering</i> 2024, 11, 258, https://doi.org/10.3390/bioengineering11030258	65
Francesca Camera, Caterina Merla and Valerio De Santis Comparison of Transcranial Magnetic Stimulation Dosimetry between Structured and Unstructured Grids Using Different Solvers Reprinted from: <i>Bioengineering</i> 2024, 11, 712, https://doi.org/10.3390/bioengineering11070712	85
Erica Costantini, Lisa Aielli, Giulio Gualdi, Manuela Baronio, Paola Monari, Paolo Amerio and Marcella Reale Pulsed Radiofrequency Electromagnetic Fields as Modulators of Inflammation and Wound Healing in Primary Dermal Fibroblasts of Ulcers Reprinted from: <i>Bioengineering</i> 2024, 11, 357, https://doi.org/10.3390/bioengineering11040357	99
Zhengwu Sun, Payel Sen, Jules Hamers, Thomas Seidel, Andreas Dendorfer and Petra Kameritsch Optimized Conditions for Electrical Tissue Stimulation with Biphasic, Charge-Balanced Impulses Reprinted from: <i>Bioengineering</i> 2025, 12, 234, https://doi.org/10.3390/bioengineering12030234	113

Kamal Asadipour, Carol Zhou, Vincent Yi, Stephen J. Beebe and Shu Xiao Ultra-Low Intensity Post-Pulse Affects Cellular Responses Caused by Nanosecond Pulsed Electric Fields Reprinted from: <i>Bioengineering</i> 2023, 10, 1069, https://doi.org/10.3390/bioengineering10091069	129
Andras Szasz Pulsing Addition to Modulated Electro-Hyperthermia Reprinted from: <i>Bioengineering</i> 2024, 11, 725, https://doi.org/10.3390/bioengineering11070725	147
Amr Kaadan, Simona Salati, Stefania Setti and Roy Aaron Augmentation of Deficient Bone Healing by Pulsed Electromagnetic Fields—From Mechanisms to Clinical Outcomes Reprinted from: <i>Bioengineering</i> 2024, 11, 1223, https://doi.org/10.3390/bioengineering11121223	175
Tan Guo, Dina Moazamian, Arya A. Suprana, Saeed Jerban, Eric Y. Chang, Yajun Ma, et al. Are Collagen Protons Visible with the Zero Echo Time (ZTE) Magnetic Resonance Imaging Sequence: A D ₂ O Exchange and Freeze-Drying Study Reprinted from: <i>Bioengineering</i> 2025, 12, 16, https://doi.org/10.3390/bioengineering12010016	193
Xi Wang, Shao Ying Huang and Abdulkadir C. Yucel Uncertainty Quantification in SAR Induced by Ultra-High-Field MRI RF Coil via High-Dimensional Model Representation Reprinted from: <i>Bioengineering</i> 2024, 11, 730, https://doi.org/10.3390/bioengineering11070730	205
Matteo B. Lodi, Eleonora M. A. Corda, Francesco Desogus, Alessandro Fanti and Giuseppe Mazzarella Modeling of Magnetic Scaffolds as Drug Delivery Platforms for Tissue Engineering and Cancer Therapy Reprinted from: <i>Bioengineering</i> 2024, 11, 573, https://doi.org/10.3390/bioengineering11060573	225
Lovleen Tina Joshi, Emmanuel Brousseau, Trefor Morris, Jonathan Lees, Adrian Porch and Les Baillie Rapid, Point-of-Care Microwave Lysis and Electrochemical Detection of <i>Clostridioides difficile</i> Directly from Stool Samples Reprinted from: <i>Bioengineering</i> 2024, 11, 632, https://doi.org/10.3390/bioengineering11060632	243

About the Editors

Stefania Romeo

Stefania Romeo has earned an MSc in Biomedical Engineering (2008) (University of Naples Federico II) and a PhD in Electronic Engineering (2012) (formerly the Second University of Naples, which is now referred to as the University of Campania "Luigi Vanvitelli"). She currently holds a Senior Researcher position at the Institute for Electromagnetic Sensing of the Environment (IREA), Italian National Research Council (CNR). Her work in the field of bioelectromagnetics has resulted in more than 100 publications in peer-reviewed journals, book chapters, conference proceedings, and abstracts. Her research interests include electromagnetic dosimetry, the design and set-up of high-voltage, ns pulse generators and RF electromagnetic field exposure systems, the assessment of biological effects of electromagnetic fields, the assessment of electroporation in vitro, the modeling of the interactions between cells and pulsed electric fields, and the systematic review of the scientific literature regarding the interactions between electromagnetic fields and living systems.

Anna Sannino

Anna Sannino has earned an MSc in Biological Sciences (2002) (University of Naples Federico II) and a PhD in Biochemistry and the pathology of drug action (2013) (University of Salerno). She currently holds a Researcher position at the Institute for Electromagnetic Sensing of the Environment (IREA), Italian National Research Council (CNR). Her work in the field of bioelectromagnetics has resulted in more than 80 publications in peer-reviewed journals, book chapters, conference proceedings and abstracts. Her research interests include the evaluation of effects related to genotoxic (DNA damage) and non-genotoxic (apoptosis, oxidative stress, proliferation, and cell cycle) carcinogenesis in mammalian cells exposed to signals in use in the third, fourth, and fifth generation of mobile technologies (RF), ELF, and high voltage, ns electric pulses; the study of the interaction between biological systems and electromagnetic fields using experimental approaches; the evaluation of occupational exposure to electromagnetic fields; and the systematic review of the literature on biological effects of electromagnetic fields.

Editorial

Special Issue “Electric, Magnetic, and Electromagnetic Fields in Biology and Medicine: From Mechanisms to Biomedical Applications: 2nd Edition”

Stefania Romeo * and Anna Sannino *

CNR—Institute for Electromagnetic Sensing of the Environment (IREA), 80124 Napoli, Italy

* Correspondence: romeo.s@irea.cnr.it (S.R.); sannino.a@irea.cnr.it (A.S.)

1. Introduction

Electric, magnetic, and electromagnetic fields (EMFs) are widely used in everyday life, as well as in specific occupational environments and clinical settings. EMF-based technologies employ different parts of the spectrum, from static fields to low- and high-frequency EMFs encompassing millimeter waves and THz [1].

Exposure to these fields raises concerns about the possible effects on human health. On the other hand, biomedical applications of non-ionizing radiation are successfully employed for diagnosis and therapy (e.g., electroporation-based treatments, microwave hyperthermia, transcranial magnetic stimulation, etc.). There is great interest in evaluating the associated interaction mechanisms, which are also relevant in fostering the development of new biomedical applications and the optimization of the existing ones.

This Special Issue, entitled “Electric, Magnetic, and Electromagnetic Fields in Biology and Medicine: From Mechanisms to Biomedical Applications: 2nd Edition”, includes contributions focusing primarily on the therapeutic and diagnostic applications of EMFs. *In vitro*, *in silico*, and human studies are presented where the aim was either to optimize technical aspects of the applications, or to provide insight into biological, biophysical, electrical, or electrochemical mechanisms. Overall, these contributions present an overview of the broad spectrum of established and potential applications of electromagnetics in the biomedical field.

2. Contributions to the Special Issue

The call for articles on “Electric, Magnetic, and Electromagnetic Fields in Biology and Medicine: From Mechanisms to Biomedical Applications: 2nd Edition” resulted in a total of 14 accepted manuscripts: 12 regular papers, and 2 review papers. A brief description of each contribution is reported in the following passages, with the papers organized based on the topics addressed.

2.1. Transcranial Magnetic and Direct Current Stimulation

Transcranial Magnetic and Direct Current Stimulation (TMS, tDCS) are non-invasive brain stimulation techniques that have gained increased interest in recent decades not only for their potential application in the treatment of mental health conditions (addiction, depression, anxiety, etc.), but also for other neurological conditions as well as for rehabilitation purposes. TMS uses coil-generated magnetic fields to induce an electrical current in the brain and stimulate specific cortical regions, whereas tDCS applies low-intensity direct currents by means of suitable electrodes to modulate brain excitability through changes in the resting membrane potentials [2].

In this Special Issue, five full papers addressed TMS or tDCS, considering different aspects of the techniques and their applications.

Pantovic and co-workers performed a double-blind, randomized, between-subject, sham-controlled, experimental study to analyze whether cerebellar tDCS could improve motor learning in a complex overhand throwing task in thirty young adults. The subjects were able to improve accuracy in performing the task, but there were no significant differences between those subjected to tDCS and sham controls. The authors concluded that tDCS failed to improve motor learning in this complex motor task to a greater degree than practice alone (sham) in the experimental conditions tested in the study, and that future studies are needed to fully determine the efficacy of cerebellar tDCS for potentially enhancing motor skill acquisition and learning in healthy young adults [3].

Pantovic and co-workers addressed the optimization of Intracortical Facilitation (ICF), which is a paired-pulse TMS measurement used to quantify interneuron activity in the primary motor cortex in healthy populations and motor disorders. Specifically, they considered the role of time between ICF trials (inter-trial interval; ITI). In a within-subject experimental design, twenty young adults participated in an experimental session involving voluntary muscle contraction under four separate ICF trial blocks, with each utilizing different ITIs (4, 6, 8, and 10 s). The outcome was assessed by analyzing the electromyographic response. The main finding of the study was that ICF values were similar for all four ITIs tested and did not significantly change over the course of time for any of the ICF blocks considered [4].

In a similar study, de Albuquerque and co-authors assessed the role of ITIs on Short-Interval Intracortical Inhibition (SICI), which is a common paired-pulse TMS measure of the primary motor cortex interneuron activity in healthy subjects and neurological disorders. The experiments were performed on the right-hand of twenty-three healthy, young participants, and involved voluntary muscle contraction under four SICI trial blocks, each utilizing different ITIs (4, 6, 8, and 10 s). The outcome was assessed by analyzing the electromyographic response. The main findings indicated that measurements of SICI neither differed between ITIs (ranging between 4 and 10 s) nor demonstrated significant time-dependent amplitude changes within blocks of trials [5].

In another paper, Robins and co-workers addressed an alternative approach to magnetic neurostimulation in which the time-varying magnetic field (and the resultant, induced electric field) is generated not by current-carrying coils, but by using rotating permanent magnets. The authors assessed the electric field characteristics of various rotating magnet configurations through computational modeling and validated the results via experimental measurements of field strengths on a head phantom. The results of the analysis showed that the maximum induced E-field strength on the head surface was around 0.1% of the field strength induced by conventional TMS, and that electric field strength depended on rotational frequency. Further research is needed to conduct simulations of rotating magnetic stimulation on anatomically accurate head models, as well as to optimize treatment parameters such as stimulation frequency and magnet placement [6].

In the paper by Camera and co-authors, low-frequency numerical dosimetry approaches used for TMS studies were compared across simplified and realistic anatomical models to assess their accuracy in evaluating induced electric fields. For the study, a typical figure-of-8 coil was used as the TMS source, and the performance levels of two simulation platforms, SimNIBS v4.0.0 [7] and Sim4Life v7.2.4 (ZMT, Zurich MedTech, Zurich, Switzerland), were compared based on three different exposure scenarios: a homogeneous sphere, a sphere with an internal discontinuity, and a head model derived from Magnetic Resonance Imaging (MRI) data. The results indicated that the differences between the obtained

results were larger upon increasing the geometric complexity of the model. However, the differences remained contained overall [8].

2.2. Mechanisms and Clinical Applications of Pulsed Electromagnetic and Electric Fields

Pulsed Electromagnetic (PEMFs) and Electric Fields (PEFs) are successfully employed within numerous medical applications, including the treatment of musculoskeletal disorders, like non-union fractures, osteoarthritis and osteoporosis, and also the stimulation of bone healing, promotion of wound healing, electrical stimulation of tissues, and can even be used in adjuvant cancer treatments. Nevertheless, a clear understanding of the underlying molecular mechanisms and associated robust clinical outcomes remains elusive because of their diverse use [1,9].

In this Special Issue, three full papers and two reviews addressed the biological mechanisms and clinical applications of PEMFs and PEFs.

Costantini and co-authors assessed the inflammatory, antioxidant, cell proliferation, and wound healing response of human primary dermal fibroblasts (HDFs) isolated from normal and ulcerated areas of venous leg ulcer patients and then exposed to PEMFs in the radiofrequency range by means of a commercial medical device. The exposure to RF PEMFs induced an earlier reduction in the scratch-induced cell-free area displayed by exposed ulcer-HDFs compared to the unexposed ones and even to normal-HDFs. This trend persisted after 24 h, suggesting an increase in the repair ability in PRF-EMF-exposed ulcer-derived HDFs. The results of the study show that a PEMF may affect ulcer-HDF cell proliferation and modulate the expression and production of cytokines, leading to an improvement in wound healing by activating the robust migration of fibroblasts and by further stimulating the inflammatory response [10].

Sun and co-workers analyzed whether biphasic, charge-balanced electric impulses, generated with either manual calibration, capacitive electrode coupling, or feedback regulation of electrode polarization, could reduce the electrochemical reactions at the interface of graphite electrodes used for the continuous stimulation of myocardial tissue. Faradaic reactions at the electrode surface were quantified using phenol red as a redox-sensitive tracer. The study demonstrated that charge control is an effective measure to improve the electrochemical compatibility of biphasic electrical impulses, whereas the capacitive coupling approach gave less satisfactory results. Further studies are thus warranted to understand the biological implications of this technique [11].

In Asadipour et al., the authors analyzed the effects of post-pulse waveform nanosecond (ns) PEFs, i.e., low-intensity, spurious pulses occurring after the main one due to an incomplete discharge, that have been demonstrated to affect the biological effects of nsPEFs. Two commonly used pulse generator designs, both featuring identical main pulse characteristics but different post-pulse shapes, were used to compare the effects on various cellular endpoints. The thresholds for the dissipation of the mitochondrial membrane potential, loss of viability, and increase in plasma membrane permeability all occurred at different pulsing numbers for the two generators, and biphasic effects were detected in only one case. The paper demonstrated that conditions resulting from low post-pulse intensity charging have a significant impact on cell responses and should be considered when comparing the results from similar pulse waveforms [12].

The first review, presented by A. Szasz, reports on modulated electro-hyperthermia (mEHT), a variation of the conventional hyperthermia treatment, which selectively heats malignant tissues and makes them more sensitive to oncological treatments. Specifically, the author discusses pulsed mEHT, in which heat is applied to tumor tissue in short, controlled bursts rather than continuously. This approach can potentially enhance the

effectiveness of cancer treatments while minimizing the damage to healthy surrounding tissues [13].

In the second review, presented by Kaadan and co-workers, scientific literature regarding the use of PEMFs for the treatment of fresh fractures, delayed union, and non-union, and possible underlying mechanisms, was discussed. The review describes biological pathways behind the bone-repair effect of PEMFs, starting from the cellular scale, and continuing up to the tissue and organismal scale. Overall, the use of PEMFs in orthopedic applications could potentially become a standard adjunctive therapy in the management of fractures and non-union thanks to the safety profile, absence of adverse effects reported, and non-invasive nature, provided that a better understanding of the mechanisms is unlocked [14].

2.3. Magnetic Resonance Imaging

MRI is a non-invasive imaging modality that uses intense, static magnetic fields and RF pulses to generate detailed images of internal body structures. MRI has become a cornerstone in medical diagnostics due to its high spatial resolution and excellent contrast resolution, especially for soft tissue. MRI is widely used in neurology, cardiology, musculoskeletal imaging, and oncology, among other fields, providing detailed information that can aid in diagnosis, treatment planning, and monitoring. Its advantages include high-contrast resolution, non-ionizing radiation, and the ability to acquire multiplanar images. On the other hand, limitations include long scan times, high costs, contraindications in patients with certain implants or devices, and sensitivity to patient motion, although the MRI technology continues to expand in clinical applications [15].

This Special Issue includes two full articles addressing this topic.

Guo et al. focused on advanced diagnostic techniques to improve the visualization of biological tissues with specific proton relaxation characteristics. They investigated whether the use of imaging techniques such as Zero Echo Time (ZTE) and the Ultrashort Echo Time (UTE) sequence can directly detect collagen protons in bone and tendons in comparison to water protons. Their main conclusions are that the ZTE sequence, like the UTE one, cannot directly detect collagen protons in bone and tendons, as the MRI signal originates from water protons and not via the collagen matrix. These results underscore the limits of current MRI techniques for direct collagen imaging, and the need for alternative imaging techniques or biochemical markers to study collagen integrity in bone and tendons [16].

Wang and co-workers addressed the study of electromagnetic fields and the dielectric properties of human tissues in the context of Ultra-High-Field Magnetic Resonance Imaging (UHF MRI), such as 7 T systems, with a focus on managing safety related to the Specific Absorption Rate (SAR). Their research proposes a computational framework based on High-Dimensional Model Representation (HDMR) as an effective alternative to traditional methods, and the proposed modeling framework provides an accurate, computationally efficient method for SAR estimation while reducing computational costs [17].

2.4. Other Topics

The use of magnetic scaffolds (MagSs) represents a fascinating and rapidly evolving area in biomedical engineering, holding significant promise for both tissue repair and cancer treatment. The integration of magnetic nanoparticles (MNPs) into biocompatible scaffold materials is expected to facilitate remote manipulation and localized effects using external magnetic fields. Overcoming these challenges will require new interdisciplinary efforts and technological advances, including the development of mathematical tools and additional elaborations to ensure the biocompatibility of MNPs [18]. From this perspective, Lodi et al. assessed the performance of MagSs, which are biomaterials combined with

MNPs for drug delivery (DD) in tissue engineering (TE) and cancer therapy (CT). The use of MagSs is discussed as an innovative system for controlled drug release and tissue repair, using static or dynamic magnetic stimuli. The authors analyzed MagS drug release literature data and fitted them to mathematical and computational models. The study establishes a strong quantitative foundation for MagS-based DD, aiding future research in TE and CT applications. Future work should focus on improving MagS formulations, optimizing magnetic properties, and integrating advanced modeling techniques for better predictability and efficiency [19].

A further contribution to this Special Issue discussed the use of microwaves in biomedical applications. In recent years, microwave energy has been successfully exploited within medicine to treat diseases such as cancer and microbial infections via ablation therapy and for rapid cell lysis. [20]. Moreover, microwaves can be used to enhance electrochemical biosensor performance; for example, they can help modify electrode surfaces or facilitate rapid chemical reactions, increasing the sensitivity and response speed of the biosensor. In some cases, microwaves are also used to activate or boost electrochemical reactions, making biosensors more efficient and suitable for quickly detecting small amounts of biomolecules or pathogens [21].

In this framework, Joshi et al. presented a novel method for the rapid detection of *Clostridioides difficile* (*C. difficile*) spores in stool samples. The study introduces a microwave-enhanced lysis approach for DNA extraction combined with electrochemical biosensing to identify *C. difficile* toxin genes. A custom-built microwave cavity operating at 2.45 GHz was used to lyse *C. difficile* spores within 5 s. The microwave-enhanced method significantly reduces the time needed for *C. difficile* detection (<10 min) compared to traditional methods. The study introduces a diagnostic tool for quickly and accurately detecting *C. difficile* infections as an alternative to existing diagnostic tests [22].

3. Conclusions

In the first edition of the Special Issue on “Electric, Magnetic, and Electromagnetic Fields in Biology and Medicine: From Mechanisms to Biomedical Applications”, the included contributions mainly addressed EMF exposure assessment, the biological effects of EMF exposure, and health risk evaluation [23].

In the second edition, the included contributions mainly address the biomedical applications of non-ionizing radiation, with different approaches spanning from in vitro and human studies, to numerical modeling for the optimization of diagnostic or therapeutic techniques, as well as to improve specific, technical aspects related to the development of EMF-based technologies.

Overall, the papers presented in this Special Issue represent a diverse account of EMF-based application complexity, guiding the reader through explanations of general problems related to the use of EMFs and the basic results obtained from experimental and in silico studies. We hope readers will find these articles useful and informative and inspire further ground-breaking research in this area.

Author Contributions: Both authors contributed equally to the conception, drafting, and editing of the manuscript. All authors have read and agreed to the published version of the manuscript.

Funding: This research received no external funding.

Acknowledgments: We sincerely thank the Editor-in-Chief of the journal, Anthony Guiseppi-Elie and the Managing Editors for their support and encouragement in setting up this Special Issue. We also wish to thank the researchers who submitted their contributions, and the reviewers who helped in the evaluation of the manuscripts and made very valuable suggestions to improve the quality

of the contributions. We wish to thank Maria Rosaria Scarfi and Olga Zeni (CNR—Institute for Electromagnetic Sensing of the Environment) for their invaluable support and suggestions.

Conflicts of Interest: The authors declare no conflicts of interest.

Abbreviations

The following abbreviations are used in this manuscript:

<i>C. difficile</i>	<i>Clostridioides difficile</i>
CT	Cancer Therapy
DD	Drug Delivery
HDF	Human Dermal Fibroblasts
HDMR	High-Dimensional Model Representation
ICF	Intracortical Facilitation
ITI	Inter-Trial Interval
MagS	Magnetic scaffold
mEHT	Modulated Electro-HyperThermia
MNP	Magnetic Nanoparticle
MRI	Magnetic Resonance Imaging
ns	Nanosecond
PEF	Pulsed Electric Field
PEMF	Pulsed ElectroMagnetic Field
RF	Radiofrequency
SAR	Specific Absorption Rate
SICI	Short-Interval Intracortical Inhibition
tDCS	Transcranial Direct Current Stimulation
TE	Tissue Engineering
TMS	Transcranial Magnetic Stimulation
UHF	Ultra-High-Field
UTE	Ultrashort Echo Time
ZTE	Zero Echo Time

References

1. Mattsson, M.O.; Simko, M. Emerging medical applications based on non-ionizing electromagnetic fields from 0 Hz to 10 THz. *Med. Devices* **2019**, *12*, 347–368. [CrossRef]
2. Hyde, J.; Carr, H.; Kelley, N.; Seneviratne, R.; Reed, C.; Parlatini, V.; Garner, M.; Solmi, M.; Rosson, S.; Cortese, S.; et al. Efficacy of neurostimulation across mental disorders: Systematic review and meta-analysis of 208 randomized controlled trials. *Mol. Psychiatry* **2022**, *27*, 2709–2719. [CrossRef] [PubMed]
3. Pantovic, M.; Lidstone, D.E.; de Albuquerque, L.L.; Wilkins, E.W.; Munoz, I.A.; Aynlender, D.G.; Morris, D.; Dufek, J.S.; Poston, B. Cerebellar Transcranial Direct Current Stimulation Applied over Multiple Days Does Not Enhance Motor Learning of a Complex Overhand Throwing Task in Young Adults. *Bioengineering* **2023**, *10*, 1265. [CrossRef] [PubMed]
4. Pantovic, M.; Boss, R.; Noorda, K.J.; Premyanov, M.I.; Aynlender, D.G.; Wilkins, E.W.; Boss, S.; Riley, Z.A.; Poston, B. The Influence of Different Inter-Trial Intervals on the Quantification of Intracortical Facilitation in the Primary Motor Cortex. *Bioengineering* **2023**, *10*, 1278. [CrossRef]
5. de Albuquerque, L.L.; Pantovic, M.; Wilkins, E.W.; Morris, D.; Clingo, M.; Boss, S.; Riley, Z.A.; Poston, B. Exploring the Influence of Inter-Trial Interval on the Assessment of Short-Interval Intracortical Inhibition. *Bioengineering* **2024**, *11*, 645. [CrossRef] [PubMed]
6. Robins, P.L.; Makaroff, S.N.; Dib, M.; Lisanby, S.H.; Deng, Z.D. Electric Field Characteristics of Rotating Permanent Magnet Stimulation. *Bioengineering* **2024**, *11*, 258. [CrossRef]
7. Saturnino, G.B.; Puonti, O.; Nielsen, J.D.; Antonenko, D.; Madsen, K.H.; Thielscher, A. SimNIBS 2.1: A Comprehensive Pipeline for Individualized Electric Field Modelling for Transcranial Brain Stimulation. In *Brain and Human Body Modeling: Computational Human Modeling at EMBC 2018*; Makarov, S., Horner, M., Noetscher, G., Eds.; Springer International Publishing: Cham, Switzerland, 2019; pp. 3–25.
8. Camera, F.; Merla, C.; De Santis, V. Comparison of Transcranial Magnetic Stimulation Dosimetry between Structured and Unstructured Grids Using Different Solvers. *Bioengineering* **2024**, *11*, 712. [CrossRef]

9. Flatscher, J.; Pavez Lorie, E.; Mittermayr, R.; Meznik, P.; Slezak, P.; Redl, H.; Slezak, C. Pulsed Electromagnetic Fields (PEMF)-Physiological Response and Its Potential in Trauma Treatment. *Int. J. Mol. Sci.* **2023**, *24*, 11239. [CrossRef]
10. Costantini, E.; Aielli, L.; Gualdi, G.; Baronio, M.; Monari, P.; Amerio, P.; Reale, M. Pulsed Radiofrequency Electromagnetic Fields as Modulators of Inflammation and Wound Healing in Primary Dermal Fibroblasts of Ulcers. *Bioengineering* **2024**, *11*, 357. [CrossRef]
11. Sun, Z.; Sen, P.; Hamers, J.; Seidel, T.; Dendorfer, A.; Kameritsch, P. Optimized Conditions for Electrical Tissue Stimulation with Biphasic, Charge-Balanced Impulses. *Bioengineering* **2025**, *12*, 234. [CrossRef]
12. Asadipour, K.; Zhou, C.; Yi, V.; Beebe, S.J.; Xiao, S. Ultra-Low Intensity Post-Pulse Affects Cellular Responses Caused by Nanosecond Pulsed Electric Fields. *Bioengineering* **2023**, *10*, 1069. [CrossRef] [PubMed]
13. Szasz, A. Pulsing Addition to Modulated Electro-Hyperthermia. *Bioengineering* **2024**, *11*, 725. [CrossRef]
14. Kaadan, A.; Salati, S.; Setti, S.; Aaron, R. Augmentation of Deficient Bone Healing by Pulsed Electromagnetic Fields-From Mechanisms to Clinical Outcomes. *Bioengineering* **2024**, *11*, 1223. [CrossRef] [PubMed]
15. Tofts, P.S. *Quantitative MRI of the Brain: Principles of Physical Measurement*; CRC Press: Boca Raton, FL, USA, 2009; Volume 2.
16. Guo, T.; Moazamian, D.; Suprana, A.A.; Jerban, S.; Chang, E.Y.; Ma, Y.; Carl, M.; Chen, M.; Du, J. Are Collagen Protons Visible with the Zero Echo Time (ZTE) Magnetic Resonance Imaging Sequence: A D₂O Exchange and Freeze-Drying Study. *Bioengineering* **2024**, *12*, 16. [CrossRef] [PubMed]
17. Wang, X.; Huang, S.Y.; Yucel, A.C. Uncertainty Quantification in SAR Induced by Ultra-High-Field MRI RF Coil via High-Dimensional Model Representation. *Bioengineering* **2024**, *11*, 730. [CrossRef] [PubMed]
18. Goranov, V. Biomaterials functionalized with magnetic nanoparticles for tissue engineering: Between advantages and challenges. *Biomater. Biosyst.* **2024**, *15*, 100100. [CrossRef]
19. Lodi, M.B.; Corda, E.M.A.; Desogus, F.; Fanti, A.; Mazzarella, G. Modeling of Magnetic Scaffolds as Drug Delivery Platforms for Tissue Engineering and Cancer Therapy. *Bioengineering* **2024**, *11*, 573. [CrossRef]
20. Gartshore, A.; Kidd, M.; Joshi, L.T. Applications of Microwave Energy in Medicine. *Biosensors* **2021**, *11*, 96. [CrossRef]
21. Wang, J.; Wang, R.; Shen, Z.; Liu, B.; Sun, C.; Xue, Q. Microwave biosensors utilizing metamaterial enhancement: Design and application. *Nanotechnol. Precis. Eng.* **2025**, *8*, 015001. [CrossRef]
22. Joshi, L.T.; Brousseau, E.; Morris, T.; Lees, J.; Porch, A.; Baillie, L. Rapid, Point-of-Care Microwave Lysis and Electrochemical Detection of *Clostridioides difficile* Directly from Stool Samples. *Bioengineering* **2024**, *11*, 632. [CrossRef]
23. Scarfi, M.R.; Mattsson, M.O.; Simko, M.; Zeni, O. Special Issue: "Electric, Magnetic, and Electromagnetic Fields in Biology and Medicine: From Mechanisms to Biomedical Applications". *Int. J. Environ. Res. Public Health* **2019**, *16*, 4548. [CrossRef] [PubMed]

Disclaimer/Publisher's Note: The statements, opinions and data contained in all publications are solely those of the individual author(s) and contributor(s) and not of MDPI and/or the editor(s). MDPI and/or the editor(s) disclaim responsibility for any injury to people or property resulting from any ideas, methods, instructions or products referred to in the content.

Article

Cerebellar Transcranial Direct Current Stimulation Applied over Multiple Days Does Not Enhance Motor Learning of a Complex Overhand Throwing Task in Young Adults

Milan Pantovic ¹, Daniel E. Lidstone ², Lidio Lima de Albuquerque ³, Erik W. Wilkins ⁴, Irwin A. Munoz ⁵, Daniel G. Aynlender ⁵, Desiree Morris ⁵, Janet S. Dufek ⁴ and Brach Poston ^{4,*}

¹ Health and Human Performance Department, Utah Tech University, St. George, UT 84770, USA; milan.pantovic@utahtech.edu

² Center for Neurodevelopment and Imaging Research, Kennedy Krieger Institute, Department of Neurology, Johns Hopkins University School of Medicine, Baltimore, MD 21205, USA; lidstone@kennedykrieger.org

³ School of Health and Applied Human Sciences, University of North Carolina Wilmington, Wilmington, NC 28403, USA; limadeal@uncw.edu

⁴ Department of Kinesiology and Nutrition Sciences, University of Nevada Las Vegas, Las Vegas, NV 89154, USA; wilkie1@unlv.nevada.edu (E.W.W.); janet.dufek@unlv.edu (J.S.D.)

⁵ School of Medicine, University of Nevada-Las Vegas, Las Vegas, NV 89154, USA; munoz2@unlv.nevada.edu (I.A.M.); aynlende@unlv.nevada.edu (D.G.A.); morrid3@unlv.nevada.edu (D.M.)

* Correspondence: brach.poston@unlv.edu; Tel.: +1-702-895-5329

Abstract: Cerebellar transcranial direct current stimulation (tDCS) enhances motor skill and learning in relatively simple motor tasks, but it is unclear if c-tDCS can improve motor performance in complex motor tasks. The purpose of this study was to determine the influence of c-tDCS applied over multiple days on motor learning in a complex overhand throwing task. In a double-blind, randomized, between-subjects, SHAM-controlled, experimental design, 30 young adults were assigned to either a c-tDCS or a SHAM group. Participants completed three identical experiments on consecutive days that involved overhand throwing in a pre-test block, five practice blocks with concurrent c-tDCS, and a post-test block. Overhand throwing endpoint accuracy was quantified as the endpoint error. The first dorsal interosseous muscle motor evoked potential (MEP) amplitude elicited by transcranial magnetic stimulation was used to quantify primary motor cortex (M1) excitability modulations via c-tDCS. Endpoint error significantly decreased over the 3 days of practice, but the magnitude of decrease was not significantly different between the c-tDCS and SHAM group. Similarly, MEP amplitude slightly increased from the pre-tests to the post-tests, but these increases did not differ between groups. These results indicate that multi-day c-tDCS does not improve motor learning in an overhand throwing task or increase M1 excitability.

Keywords: motor skill; transcranial magnetic stimulation; transcranial direct current stimulation

1. Introduction

Transcranial direct current stimulation (tDCS) delivered to the cerebellum (c-tDCS) has shown the ability to induce acute enhancements in skill acquisition in a variety of motor tasks [1–5]. Specifically, most studies have observed motor skill increases on the order of 10–15% when c-tDCS is applied before or during motor practice compared with task practice alone [6–11]. These improvements can approach the results obtained when tDCS is applied to the primary motor cortex (M1) [8,12]. M1 has been the brain area most commonly targeted by tDCS and stimulation of this area has generally been found to confer the greatest performance benefits [1,13–16]. However, c-tDCS may be able to elicit similar or greater effects when compared with M1-tDCS in specific experimental conditions such as adaptation-learning paradigms [4,8]. In addition, c-tDCS may be more effective for specific

motor tasks where execution is highly dependent on the specialized contributions of the cerebellum in motor control [2–5].

The vast majority of motor skill studies that have applied tDCS to any brain area have involved a single stimulation session, usually lasting between 10 and 25 min. However, a few studies [13,14] that applied M1-tDCS for 3–5 consecutive days reported cumulative effects that produced 20–40% enhancements in total motor learning compared to SHAM stimulation in a sequential visual isometric pinch force task (SVIPT) of the thumb and index fingers. In addition, Cantarero et al. (2015) [12] delivered c-tDCS over 3 consecutive days simultaneous with the same SVIPT and found substantial increases in motor learning in an anodal c-tDCS group compared to both a cathodal c-tDCS and a SHAM stimulation group. Interestingly, the phase of learning in which the gains in motor performance were predominantly realized differed between M1-tDCS and c-tDCS in these studies. M1-tDCS led to performance enhancements that were primarily mediated between the daily stimulation sessions, whereas c-tDCS motor skill gains were achieved within the stimulation sessions. This was quantified via a method developed [12–14] to mathematically determine the unique contributions of within-session effects (online) and between-session effects (offline) to the overall total motor learning. Taken together, these single- and multi-session c-tDCS studies have important implications for enhancing performance in various motor tasks and in numerous populations.

Despite the promising results in single-day and multi-day c-tDCS studies, all but one of them [11] have involved relatively simple motor tasks such as two-dimensional arm reaching, split-belt walking, eye movements, and unilateral pinch tasks of the hand. In addition, almost all previous c-tDCS studies either involved adaptation-learning paradigms or only a single stimulation session, with the exception of Cantarero et al. (2015) [12]. The motor tasks were also usually laboratory tasks that were novel to the participants and performed in contexts very different from those encountered in everyday life. Therefore, it is unclear at the present time if c-tDCS can improve motor learning in a complex, multi-joint task involving coordination of the whole body with concomitant strict endpoint accuracy requirements. This is an important limitation because while simple motor tasks allow for simpler experiments [17] and more rigorous experimental controls, and facilitate concurrent physiological measurements, the study of complex motor tasks is needed to fully understand movement [18,19]. Complex motor tasks are also more applicable to real world activities performed in settings such as the workplace, military applications, sports, and in activities of daily living.

The primary purpose was to determine the influence of c-tDCS applied over multiple days on motor learning in a complex overhand throwing task in young adults. This was accomplished by requiring two groups of participants to complete three practice sessions on consecutive days concurrent with either tDCS or SHAM stimulation. Based on a single-day c-tDCS overhand throwing study performed in our laboratory as well as a multi-day c-tDCS study [12] and several previous multi-day M1-tDCS studies involving simple motor tasks, it was hypothesized that c-tDCS would enhance overhand throwing accuracy. Accordingly, it was predicted that c-tDCS would lead to greater improvements in online learning, offline learning, and total motor learning compared to practice alone (SHAM stimulation) over 3 days of practice. The secondary purpose was to determine if c-tDCS could increase M1 excitability and whether any potential increases in M1 excitability would be positively correlated with the amount of motor learning induced by c-tDCS. Although previous studies have been mixed regarding the ability of c-tDCS to increase M1 excitability [20], it was hypothesized that if an enhancement of motor evoked potential (MEP) amplitudes obtained from M1 would be observed, the increase would be positively correlated with the magnitude of motor learning displayed by the participants in the c-tDCS group.

A three-dimensional overhand ball throwing task (similar to a baseball throw) was selected as the motor task due to the involvement of the cerebellum in several specific interrelated features of the movement: (1) unconstrained, multi-joint skill that involves the regulation of joint interaction torques [21–25]; (2) the modulation of the finger forces

to precisely time the opening of the fingers on a timescale of a few milliseconds [26–30]; (3) the timing and coordination of agonist and antagonist muscle activations [21,28]; and (4) the detection and gradual correction of errors across multiple trials of goal-directed movements [31].

2. Materials and Methods

2.1. Participants

Thirty young adults participated in the study (16 males and 14 females; mean age: 24.7 ± 3.1 ; range: 20–31 years; 8 men and 7 women in each group). All participants threw with their right arm and were strongly right-handed based on the Edinburgh Handedness Inventory [32] laterality quotient values. Participants were free of any neurological or psychiatric disorder, had no uncontrolled medical conditions, and did not meet international non-invasive brain stimulation exclusion criteria [33]. In addition, participants were excluded from participating in the study if they were currently competing in a throwing sport at the recreational, collegiate, or professional level. Subjects provided written, informed consent before participating in the study. The experimental procedures were conducted in accordance with the Declaration of Helsinki and were approved by the Institutional Review Board at the University of Nevada, Las Vegas.

2.2. Experimental Design

The study employed a double-blind, SHAM-controlled randomized, between-subjects, experimental design. Participants were assigned to either a c-tDCS or a SHAM stimulation group using Research Randomizer (www.randomizer.org, accessed 8-1-2018) by an investigator who did not participate in data collection. Thus, the SHAM condition served as the control or placebo condition, which was implemented using a standard set of procedures from previous tDCS studies that have been shown to not elicit physiological effects (see Section 2.4). In addition, research using this methodology for SHAM stimulation has found that participants cannot distinguish between the active (c-tDCS) condition and the inactive (SHAM) condition. All participants completed 3 experimental sessions on 3 consecutive days at the same time each day. The experimental sessions were identical except that a familiarization involving a short didactic video and an overhand throwing demonstration by one of the investigators was completed at the beginning of the first experimental session. Each session lasted about 1.5–2 h and the following major experimental steps were performed in the order prescribed: (1) pre-test block of overhand throwing trials without stimulation; (2) TMS testing of c-tDCS effects on M1 excitability that collectively involved a TMS pre-test, 5 min of either c-tDCS or SHAM stimulation, and a TMS post-test; (3) practice blocks of overhand throwing trials performed concurrently with 20 min of either c-tDCS or SHAM stimulation; and (4) post-test block of overhand throwing trials (without stimulation). A schematic of these major experimental steps that comprised the experimental protocol is depicted in Figure 1A, whereas the finer methodological details of each step are provided in the subsequent sections. In all the experimental conditions described below, the investigators who conducted the experiments were blind to the group assignment of the subjects. Accordingly, the investigator who was responsible for operating the c-tDCS device and applying stimulation did not participate in any of the other experimental procedures.

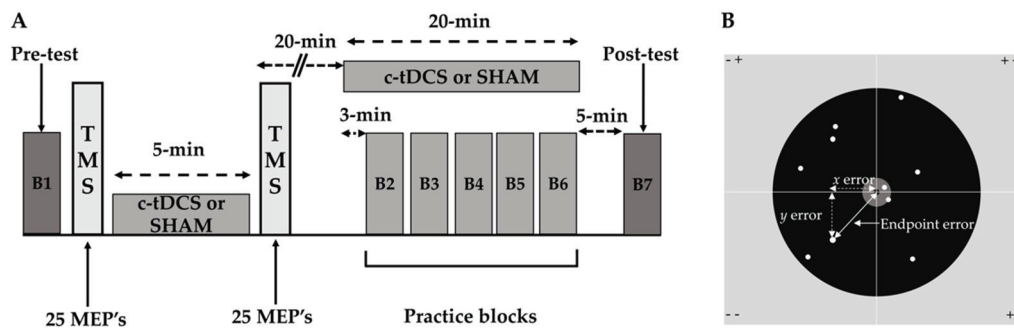


Figure 1. Schematic representation of the major components of the experimental protocol. (A) One of the 3 consecutive identical experimental sessions is depicted for illustration purposes. The experimental protocol comprised a pre-test block of overhand throws, a TMS testing paradigm testing the effects of c-tDCS on M1 excitability, 5 practice blocks of overhand throws performed concurrent with 20 min of c-tDCS or SHAM stimulation, and a post-test block of overhand throws; (B) the target and the quantification of endpoint error. The entire target area was 1.27 m in length, 1 m in width, the center of the target was 1.71 m from the floor, and the target circle had a diameter of 1 cm. An example data cloud of the endpoints of the ball is depicted for a block of 10 trials along with the x and y errors for a single trial shown that were used to calculate the trial's endpoint error.

2.3. Experimental Procedures

2.3.1. Pre-Test Blocks

A pre-test block consisting of 10 overhand throwing trials was performed without concurrent c-tDCS to determine the baseline performance levels for the two groups on Day 1 before any stimulation was applied. Similarly, the pre-test blocks on Days 2–3 were performed in an identical manner and provided a baseline not influenced by stimulation on those days, but possibly influenced by consolidation effects from the previous day. Ten trials per block were chosen for all pre-test blocks as this number was previously determined to be sufficient [11] for baseline data without eliciting an excessive influence on the overhand throwing performance curves during the subsequent practice blocks. In addition, this allowed the number of trials per block to be the same as in the practice and post-test blocks. Finally, the performance of the pre-test blocks without concurrent c-tDCS allowed for the quantification of the contribution of online and offline learning effects to total motor learning (see Section 2.7 Statistical Analysis).

2.3.2. TMS Testing of c-tDCS Effects on M1 Excitability

Single-pulse TMS was performed with a Magstim 200² connected to a double 70 mm remote control figure-of-eight coil. The coil was orientated tangential to the scalp with the handle pointed backwards and laterally at an angle of 45 degrees from the midline. The coil was positioned by an investigator over the “motor hot spot” of the first dorsal interosseous (FDI) muscle of the left M1 to evoke MEPs in the FDI of the right contralateral hand [34]. The electromyographic (EMG) activity of the FDI muscle was recorded with surface electrodes that were arranged in a belly tendon montage. EMG signals were acquired and recorded using Cambridge Electronic Design (CED; Cambridge, UK) hardware (1902 amplifiers, micro 1401 data acquisition interface) and software (Signal 5.04). All MEPs were evoked at rest while subjects sat in a chair with the forearm on a table, the wrist in neutral with the hand prone, the elbow flexed to ~90 degrees, and the shoulder abducted to ~45 degrees. The subjects were provided FDI EMG feedback on a computer screen and continually monitored by one investigator to assure the FDI was at rest during all recordings.

The TMS aspect of the study proceeded in the following steps: (1) FDI hot spot identification. Participants received suprathreshold TMS pulses as the coil position was optimized so that the scalp area that corresponded to the FDI motor hot spot could be identified; this coil position was marked on a scalp cap, and the scalp cap position on the head was outlined with a mark on the forehead. (2) 1 mV MEP determination. Suprathreshold

TMS pulses starting at ~55% of maximum stimulator output (MSO) were applied and the stimulation intensity adjusted while MEPs were monitored and quantified online until the MEPs evoked were as close as possible to a 1 mV peak-to-peak amplitude on average. The software program was then reset to collect the pre-test TMS block. (3) Pre-test TMS block. A total of 25 MEPs were collected using the previously established 1 mV stimulation intensity. (4) Five minutes of c-tDCS or SHAM stimulation. After the previous step, the TMS cap was taken off, the c-tDCS electrode montage was placed on the head, and 5 min of c-tDCS or SHAM stimulation was applied. (5) Post-test TMS block. Immediately after the stimulation time was completed in the previous step, readied investigators acted in coordination as quickly and as accurately as possible to remove the c-tDCS montage, reposition the scalp cap and TMS coil arrangement, and start collection of the post-test TMS block (25 MEPs) immediately using the same 1 mV stimulation intensity as before. During this time, the subject was instructed to remain still and to continue relaxing the hand. (6) Twenty-minute inter-stimulation period. A 20 min time clock was set by one investigator (at the end of the fourth step) who enforced a 20 min time delay between the end of the 5 min c-tDCS application and the subsequent start of the 20 min c-tDCS period associated with the overhand throwing practice blocks (see Figure 1 and below).

This rather complicated and novel paradigm involving a 5 min c-tDCS application followed by a 20 min break was developed to address methodological issues related to MEP measurement before and after tDCS. It was based on research findings by other research groups (described below) in studies that were entirely focused on the influence of different tDCS duration protocols on M1 excitability. The paradigm developed for our study purposes was then extensively piloted in our laboratory for the current study and an identical study that used M1-tDCS (manuscript in press) as opposed to c-tDCS. This was done to assure as much as possible that the paradigm worked as originally intended.

Accordingly, the paradigm was developed relative to three interrelated methodological considerations based on the following: (1) tDCS applied for 3–5 min increase MEPs for 3–5 min after stimulation ends [35–37]; (2) if a 20–30 min break is employed before a second tDCS application, the same pattern of MEP increases is observed, whereas inhibition occurs if the break is only 3–10 min [35,36]; and (3) tDCS-induced MEP increases can be obliterated after muscle contractions (task performance), the subject moving, e.g., walking, and other related activities [38–41], which may render MEP measurement after practice meaningless (for a review of these issues, see Horvath et al. (2014) [39]). Therefore, the paradigm was designed to overcome this limitation while keeping the ability to measure the possible correlations between the increases and the degree of motor learning [42–44], but assumes that the second application of tDCS had the same M1 excitability effects as the first [35,36].

2.3.3. Practice Blocks

The practice blocks were performed concurrent with either c-tDCS or SHAM stimulation for a total practice and stimulation period of 20 min (Figure 1A). The practice blocks aspect of the study proceeded in the following steps: (1) the stimulator was turned on for 3 min while subjects stood quietly before performing the first block of overhand throwing trials [11]; (2) a total of 5 blocks of overhand throwing trials were performed with each block comprising 10 overhand throws. These blocks were completed within the remaining 17 min of stimulation as each block took ~1 to 1.5 min to perform and a 2 min rest interval was employed between blocks; (3) the stimulator was kept on after the last block of overhand throws was completed, which was usually 1–2 min to complete the 20 min stimulation period.

2.3.4. Post-Test Blocks

After the practice blocks and the 20 min stimulation period ended, participants stood in place quietly while the inert electrode montage remained on the head, and observed a 5 min rest period before performing the post-test block of 10 trials. The performance of the post-test blocks without concurrent c-tDCS allowed for the quantification of the

contribution of online and offline learning effects to total motor learning when incorporated into calculations involving the pre-tests that were performed without stimulation (see Section 2.7 Statistical Analysis).

2.4. *c-tDCS*

A NeuroConn DC Stimulator Plus/MR was utilized to deliver anodal *c-tDCS* at a current strength of 2 mA via a pair of 5×5 cm rubber electrodes that were enclosed in saline soaked sponges. Accordingly, the anode was placed 3 cm lateral to theinion over the right cerebellum (ipsilateral to the right arm), whereas the cathode was placed over the ipsilateral buccinator muscle. The anode and cathode were held in place by separate rubber elastic straps. As mentioned previously, *c-tDCS* was applied for 5 min between the TMS pre-test and post-test blocks and for 20 min during the practice blocks of overhand throws using the same stimulation parameters. During the overhand throwing trials, the stimulation device was placed in the small backpack [11], whereas the stimulator was placed behind the participant on a table in association with MEP testing protocol. Although other *c-tDCS* parameters are possible and some have yielded positive effects [5], the aforementioned combination set of *c-tDCS* polarity, montage, current strength, and duration was chosen as it had the most previous studies that have demonstrated positive effects [6–10,12]. Most importantly, this included our previous single-session overhand throwing *c-tDCS* study conducted in the same laboratory [11]. SHAM stimulation was applied according to standard procedures [45,46]. Accordingly, current was ramped up to over 10 s, held constant at 2 mA for 30 s, and ramped back down over 10 s, which has been shown to induce the same scalp skin sensations as real *c-tDCS* without exerting any physiological effects.

2.5. *Overhand Throwing Task*

The overhand throwing task was identical to a previous study [11] and performed using very similar experimental procedures. Participants stood behind a line on the floor located at a distance of 6 m from a cement wall. A wooden board was tightly screwed into the wall and a laminated poster that was further encased in clear tape was mounted on the board. The poster depicted a large target area with a very small (1 cm diameter) “bull’s-eye” center (Figure 1B).

Participants threw a tennis ball with their dominant right arm in a manner consistent with a baseball throw and were instructed to execute each throw as accurately as possible by attempting to hit the center of the target. Participants used their visual feedback of the ball’s endpoint relative to the center of the target after each trial and were told to use that information to minimize the error distance between the ball’s endpoint and the target center on subsequent trials. An investigator who stood near the participant covered the ball with red chalk before and midway through each block of 10 trials so that marks were made denoting final endpoint position of the ball upon hitting the target area. The same investigator retrieved the ball after it had rebounded back off of the target area on the wall and handed it to the participant after each trial. Each mark was recorded with a small trial-numbered circular sticker after each trial by a second investigator who stood near the target area. After each trial block (participants’ inter-block rest interval), the sticker endpoint *x*, *y* coordinates were measured, recorded, and entered directly into a file on a laptop computer by 2–3 investigators. Finally, the stickers were removed from the target area between trial blocks and the process repeated for the next trial block.

The overhand throwing task was executed identically in all trial blocks and always conducted while wearing a small, tightly fitting backpack with the *tDCS* device placed inside. Importantly, the *tDCS* device was only turned on during the practice blocks (Figure 1), but was not on during the test-blocks though the inert electrode montage remained on the head of the participant. The configuration of the backpack, stimulator, and associated *tDCS* electrode montage did not restrict task performance [11]. Thus, overhand throws were always conducted in the same experimental conditions and in an

unconstrained manner in 3-dimensional space. Taken together, the overhand throwing task, small target size, and long throwing distance were all task details that were specifically selected within the laboratory space limits to assure that the motor task would represent a very difficult motor skill.

2.6. Data Analysis

The primary dependent measure of interest was the endpoint error, whereas the secondary dependent measure of interest was the MEP amplitude obtained from TMS applied to M1. The dependent measures of age, laterality quotient, and 1 mV MEP intensity were also quantified and viewed as control measures. The endpoint error was quantified in the same manner as in previous studies [11,47–49]. The Pythagorean Theorem was utilized to determine the shortest absolute distance between the x, y coordinates of the target center and the final endpoint x, y coordinates of the ball (Figure 1B). For a detailed description of endpoint error calculation in goal-directed tasks, see Poston et al. (2013) [50]. The ball's endpoint coordinates were entered into a custom-written program in Microsoft Excel, which calculated the endpoint error for each trial. The average endpoint error of the 10 overhand throwing trials performed in each trial block was taken as the final endpoint error value for analysis. MEP data were analyzed offline using a customized script written in Signal software (Cambridge Electronic Design, Cambridge, UK). The MEP size was calculated as the peak-to-peak amplitude for each MEP and the average of the 25 MEPS in each TMS test block was taken for analysis. For the control measures, the average age and laterality quotient was calculated for each group, whereas the average 1 mV MEP intensity for each subject across the 3 days was calculated and then these values were averaged for the two groups.

2.7. Statistical Analysis

Endpoint error was analyzed using a methodology that was mainly similar to the previous 3-day c-tDCS study by Cantarero et al. (2015) [12], but also shared some features similar to our previous single- and multiple-day studies [11,47,48]. The endpoint error analysis proceeded in three steps: (1) endpoint error obtained from only the test blocks was analyzed with a 2 Group (c-tDCS, SHAM) \times 3 Day (1, 2, 3) \times 2 Test (pre-test, post-test) three-way mixed ANOVA. This analysis was conducted using only endpoint error data from the test blocks as stimulation was not applied during these blocks. This also allowed for the results to be able to be compared to the results of Cantarero et al. (2015) [12]; (2) each endpoint error from each day (test blocks and practice blocks) was analyzed with a two-way mixed ANOVA: 2 Group (c-tDCS, SHAM) \times 3 Day (1, 2, 3). Thus, this second analysis used the average endpoint error value of all 7 blocks combined (2 test and 5 practice blocks) performed for each day. This was done to complement the first analysis because pilot data, a previous single-day study [11], and the current study all had many individual participant instances where performance in the test block could differ rather substantially from some of the practice blocks. This was almost certainly due to the difficulty of this motor task. Thus, this analysis could, at least potentially, better represent the overall average performance for each day; and (3) the online, offline, and total learning effects were compared between the two groups using unpaired two-tailed *t*-tests.

The MEP amplitude data were analyzed with a three-way mixed ANOVA: 2 Group (c-tDCS, SHAM) \times 3 Day (1, 2, 3) \times 2 Test (pre-test, post-test). In addition, bivariate linear regression analyses were used to examine the association between the change in MEP amplitudes between the TMS pre-tests and post-tests and the change in endpoint error (endpoint accuracy) between the pre-test and post-test blocks for the two groups. These correlations were repeated for each of the days. For the control measures, the age, laterality quotient, and 1 mV MEP intensity differences between groups were analyzed with separate unpaired two-tailed *t*-tests. For all the ANOVAs described above, post hoc comparisons using Bonferroni adjustment for multiple comparisons were performed when appropriate to locate where significant differences occurred between pairs of means. The significance

level was set at $\alpha < 0.05$ for all above analyses and data are depicted as means \pm standard errors in the figures.

3. Results

3.1. Endpoint Error

Motor learning differences between groups were compared across practice days and test blocks with a 2 Group (c-tDCS, SHAM) \times 3 Day (1, 2, 3) \times 2 Test (pre-test, post-test) ANOVA and are depicted in Figure 2A. There was a significant Day \times Test interaction ($p = 0.050$, $\eta^2 = 0.102$) and post hoc analyses of the interaction indicated that endpoint error when collapsed across Group was significantly lower in the post-test compared to the pre-test on Day 1 ($p < 0.001$) and Day 3 ($p = 0.002$), but not Day 2 ($p = 0.491$). There was also a significant main effect for Day ($p = 0.02$, $\eta^2 = 0.131$) and post hoc analysis indicated that endpoint error when collapsed across Group and Test was lower on Day 3 compared to Day 1 ($p = 0.048$). However, the pairwise mean comparison between Day 2 and Day 3 along with the pairwise mean comparison between Day 1 and Day 2 were both non-statistically significant ($p = 0.433$ and $p = 0.35$, respectively). There was also a significant main effect for Test ($p < 0.001$, $\eta^2 = 0.45$), which indicated that endpoint error was lower in the post-tests compared to the pre-tests. The main effects for Group ($p = 0.332$, $\eta^2 = 0.034$), Group \times Test interaction ($p = 0.404$, $\eta^2 = 0.025$), Group \times Day interaction ($p = 0.359$, $\eta^2 = 0.036$), and Group \times Day \times Test interaction ($p = 0.268$, $\eta^2 = 0.046$) were all non-statistically significant.

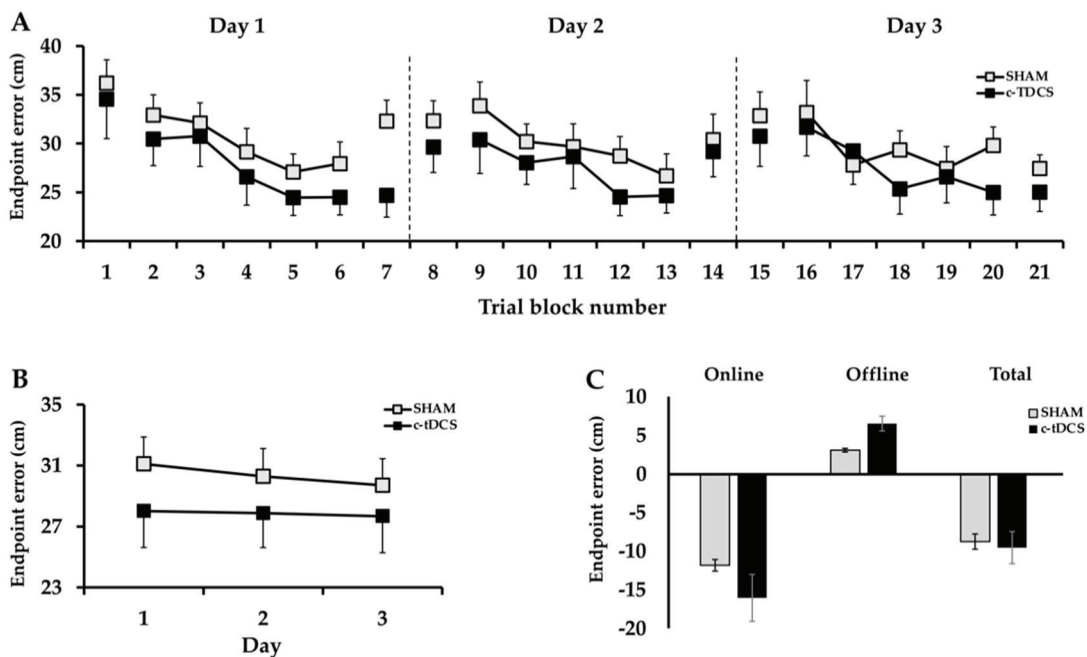


Figure 2. Endpoint error in the overhand throwing task averaged over all 7 daily trial blocks for the c-tDCS and SHAM groups. (A) Endpoint error declined across the test blocks for the 3 days of practice ($p = 0.02$), but the decline was similar for the c-tDCS and SHAM groups ($p = 0.332$); (B) endpoint error was similar for the two groups ($p = 0.381$) and across the 3 days ($p = 0.507$); (C) the online ($p = 0.325$), offline ($p = 0.188$), and total learning ($p = 0.843$) were similar for the c-tDCS and the SHAM groups.

Motor learning differences between groups were also compared across practice days using average endpoint error data collapsed across all the practice and test blocks with a 2 Group (c-tDCS, SHAM) \times 3 Day (1, 2, 3) mixed ANOVA. The analysis revealed that the Group \times Day interaction ($p = 0.773$, $\eta^2 = 0.009$; Figure 2B), the main effect for Day ($p = 0.507$, $\eta^2 = 0.024$), and the main effect for Group ($p = 0.381$, $\eta^2 = 0.028$) were all non-statistically significant.

To determine differences between groups in online, offline, and total motor learning, a series of separate unpaired two-tailed *t*-tests were used to compare online, offline, and total learning effects between groups. The analyses revealed that the online ($p = 0.404$), offline ($p = 0.353$), and total learning effect ($p = 0.818$) were all non-statistically significant between the c-tDCS and SHAM groups (Figure 2C).

3.2. MEP Amplitude

MEP amplitude differences were compared between groups across practice days and test blocks with a 2 Group (tDCS, SHAM) \times 3 Day (1, 2, 3) \times 2 Test (pre-test, post-test) ANOVA. There was a significant main effect for Test ($p = 0.011$, $\eta^2 = 0.211$, Figure 3), which indicated that when collapsed across group MEP amplitude was higher in the post-tests compared to the pre-tests. However, the main effect for Group ($p = 0.677$, $\eta^2 = 0.006$), main effect for Day ($p = 0.479$, $\eta^2 = 0.026$), Group \times Test interaction ($p = 0.835$, $\eta^2 = 0.002$), Group \times Day interaction ($p = 0.629$, $\eta^2 = 0.016$), Test \times Day interaction ($p = 0.213$, $\eta^2 = 0.054$), and Group \times Day \times Test interaction ($p = 0.192$, $\eta^2 = 0.057$) were all non-statistically significant.

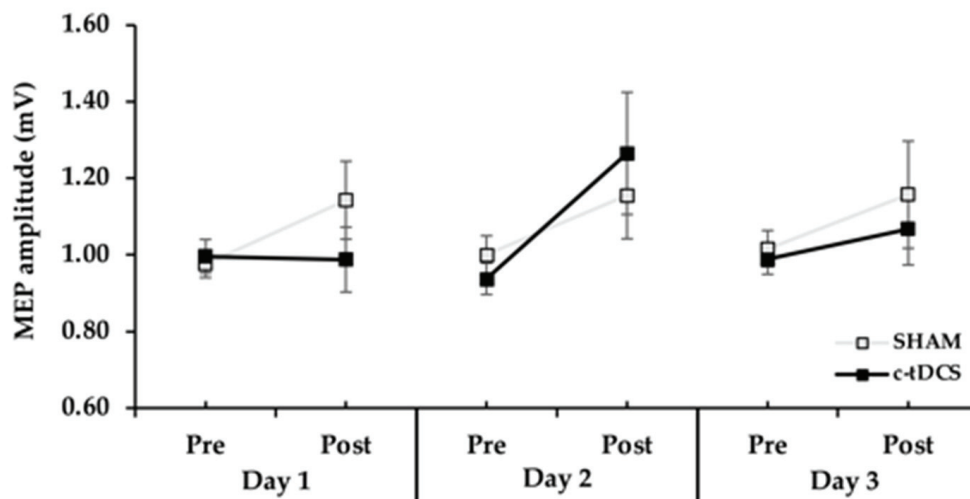


Figure 3. MEP amplitude in the TMS pre-tests and post-tests for the 3 days in the c-tDCS and SHAM groups. MEP amplitude was significantly increased between the pre-test and post-test on all 3 days (Test main effect, $p < 0.011$), but the increase was not statistically significant between the c-tDCS and the SHAM groups ($p = 0.677$).

3.3. Associations between Increases in MEPs and Increases in Endpoint Accuracy

Separate bivariate linear regressions were performed for each day and only using participants who displayed an increase in both MEP amplitude and endpoint accuracy were included in the analyses. The analyses revealed that the associations between the change in MEP amplitudes between the TMS pre-tests and post-tests and the change in endpoint error (endpoint accuracy) between the pre-test and post-test blocks for the two groups were all non-statistically significant (p value range: 0.087–0.758) and characterized by very low r^2 values (range: 0.026–0.72) as indicated in Figure 4A–C.

3.4. Control Measures

Separate unpaired *t*-tests revealed that differences between groups for age ($p = 1.00$), laterality quotient ($p = 0.602$), and the 1 mV MEP intensity ($p = 0.754$) were all non-statistically significant.

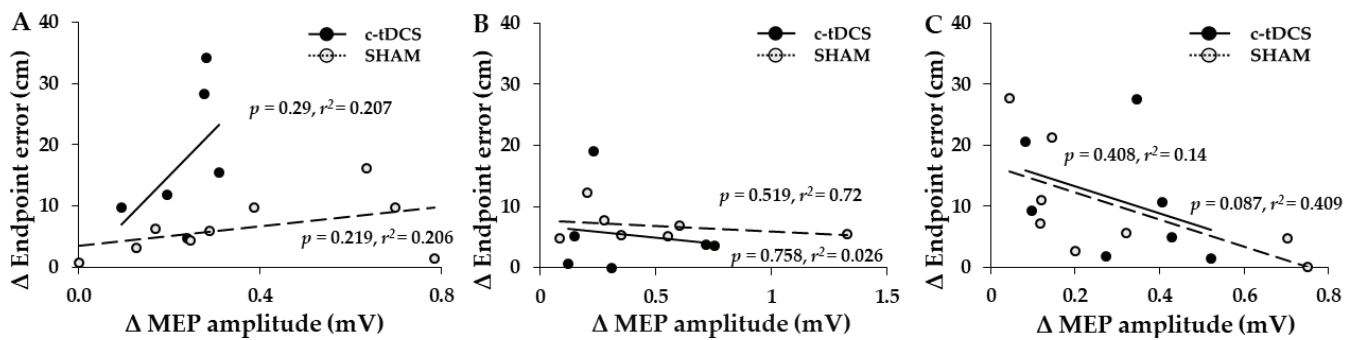


Figure 4. Associations between increases in MEP amplitude and increases in endpoint accuracy. (A–C) The absolute change (increase) in endpoint accuracy (decrease in endpoint error) was not associated with the absolute change (increase) in MEP amplitude for the participants in either group that displayed both increases in endpoint accuracy and MEP amplitude.

4. Discussion

The primary purpose was to determine the influence of c-tDCS applied over multiple days on motor learning in a complex overhand throwing task in young adults. The secondary purpose was to determine if c-tDCS could increase M1 excitability and if any potential increases in M1 excitability would be positively correlated with the amount of motor learning induced by c-tDCS. There were four main findings: (1) overhand throwing accuracy improved over the 3 days of practice, but the magnitude of reduction in endpoint error achieved at the end of practice was not significantly different between the c-tDCS and SHAM stimulation groups; (2) the relative influences of online and offline learning on the total motor learning were also similar between the two groups; (3) M1 excitability was increased for both the c-tDCS and SHAM groups, but the increases in M1 excitability were similar for the two groups; and (4) increases in endpoint accuracy were not associated with increases in MEP amplitude even when comparisons were restricted to participants in either group that displayed both increases in endpoint accuracy and MEP amplitude. Collectively, these results indicate that three consecutive daily applications of c-tDCS does not improve motor learning in a very complex motor task in young adults or significantly increase M1 excitability to a greater degree than practice alone.

4.1. Effects of c-tDCS on Motor Learning

Motor learning is defined as a relatively permanent improvement in motor performance due to practice. The physiological mechanisms and adaptations underlying the motor learning process are complex and occur in numerous brain regions [51,52], over different time scales [51,53], and vary depending on the details of the motor task [54]. Nonetheless, classic research over many years has shown that M1 and the cerebellum are brain areas that play the predominate roles in motor skill learning [52,54]. Accordingly, this is one major reason that non-invasive brain stimulation methods such as tDCS have targeted these brain areas the most frequently when attempting to enhance motor performance [1,2,4]. However, the vast majority of these studies have investigated relatively simple motor tasks (see tables in these reviews [1,2]) that were rather novel to the participants.

The present study was the first to investigate the influence of c-tDCS on motor learning over multiple days in a complex motor task involving whole body coordination with strict endpoint accuracy requirements. The original hypotheses were that the c-tDCS group would exhibit significantly greater motor learning at the end of the 3 days of practice compared to the SHAM group. Furthermore, it was expected that most of the improvements in total motor learning in the c-tDCS group would be realized through online effects while offline effects would play a much smaller role. Contrary to this set of predictions, the reductions in endpoint error across the three practice sessions were nearly identical for the c-tDCS and SHAM groups. In fact, all aspects of the entire performance curve were

comparable as the between-group differences were only 1.6 cm in the pre-test on Day 1 (baseline), modulated similarly across the 3 days, and only 2.4 cm difference in the post-test on Day 3 (Figure 2A). Accordingly, there were also no differences between groups in the relative contributions of online and offline learning to the total motor learning (Figure 2C).

The findings of the current study are not consistent with the findings of the majority of the initial previous single-session c-tDCS studies by other research groups [6–10], although most of these studies used adaptation-learning paradigms. Furthermore, the findings differ from a very recent study that reported that c-tDCS improved strength and coordination in full-body motor tasks in gymnasts [55]. However, this study used a novel bilateral electrode montage. Most notably, the results are also in contrast to an earlier study performed in our lab [11] that used the same overhand throwing task, the same c-tDCS parameters, and a very similar experimental paradigm, except the prior study only had one day of c-tDCS application. In that study, the decline in endpoint error was greater for the c-tDCS group compared with the SHAM group at the end of the practice session and this difference was maintained in a retention test completed a day later (no stimulation on the retention day). The present outcomes are also in contrast to the one available 3-day c-tDCS and motor skill study [12], where extremely large enhancements in motor skill were observed for the c-tDCS group compared to the SHAM group in the SVIPT. This is the most comparable study as we intentionally chose to have three practice sessions, use the same c-tDCS parameters, and employ similar statistical analysis, but with an overhand throwing task as opposed to the SVIPT. This was also done to simultaneously try to extend our previous single-session overhand throwing c-tDCS study [11]. Other than the obvious possible differences due to the motor task utilized, the reasons for these disparate findings between the two studies are not clear.

However, the present results are similar to a series of more recent studies performed in a range of contexts, which have found little to no positive effects of c-tDCS on motor performance [3]. Interestingly, two separate research groups each failed to replicate a previous c-tDCS study performed either in the same lab [56,57] or by some of the same researchers [8,58]. This was despite the motor tasks being quite different to each other as one set of studies involved conditioned eyeblink responses and the other set involved arm reaching movements with a pen held in the hand. Similarly, the current study also failed to replicate most, but not all, aspects of our prior single-session c-tDCS study using the same motor task. As mentioned before, that study showed improved throwing scores at the end of practice on Day 1 and in a retention test the next day. Thus, the overall results of the current study and that previous study are not compatible. However, in the current study, the endpoint error on Day 1 was substantially lower in the post-test block in the c-tDCS group just as in Day 1 of the previous study. However, the lack of a Group \times Day interaction precluded this from being evaluated statistically in the current study. Furthermore, although comparisons of those two data points look similar to the previous study, a close examination of the performance curves reveals other differences. For example, the current study had neither adjacent practice blocks before the post-test on Day 1 nor the pre-test on Day 2 with endpoint errors that were substantially lower for the c-tDCS group, as in the previous study. Thus, it is very difficult to know if the post-test performance on Day 1 was due to c-tDCS as opposed to random variation in the data. Thus, it cannot be ruled out completely that c-tDCS had a small, but non-statistically significant effect of slightly accelerating the rate of motor learning on Day 1. Nonetheless, any possible advantage of c-tDCS by the end of Day 1 was transient and not evident on Days 2 and 3. Therefore, it appears that the current results represent a third set of c-tDCS studies in the literature performed by the same research groups that could not replicate their own previous results. In addition, other recent studies have reported that c-tDCS failed to enhance performance in a whole-body balance task [59] and an adaptation task involving moving a joystick with the hand and wrist [60]. Taken together, all these results provide support for the current findings and strongly suggest that c-tDCS effects on motor performance may not be as strong or consistent as initial studies indicated.

4.2. Effects of c-tDCS on M1 Excitability

The application of anodal tDCS to M1 usually results in both increases in motor skill and increases in M1 excitability as measured via MEPs evoked by TMS. Furthermore, these increases in motor skill and MEPs were positively correlated in some initial studies [43,44]. Therefore, it was initially assumed that the increases in M1 excitability were at least partially responsible for the improvements in motor skill. Accordingly, a handful of c-tDCS studies have measured changes in MEPs obtained from M1 following c-tDCS, ostensibly with the rationale that c-tDCS-mediated increases in M1 excitability could also be a mechanism underlying motor skill improvements with c-tDCS. However, a review and meta-analysis of previous studies on the topic found mixed results. Increases and decreases as well as no changes in M1 excitability were all reported after c-tDCS application [20]. Therefore, the secondary purpose of the current study was to examine if increases in M1 excitability occur with c-tDCS, and if these increases would be positively associated with improvements in endpoint accuracy.

The major finding was that MEP amplitude was significantly increased in both the SHAM and c-tDCS from the pre-tests to the post-tests when the results were averaged across the 3 days (Figure 3). Thus, the significant MEP increase in the SHAM group was unexpected, although small increases in MEP have been observed in many M1-tDCS studies following SHAM stimulation [61]. Thus, this type of result is not a rare occurrence when measuring MEPs in tDCS studies. However, the absolute increases were very small for both groups (13.9–15.5%) and only approximately 40% of subjects in each group displayed an increase in MEPs on a given day. This magnitude of increase is well below the range of MEP increases (~20–50%) typically observed in M1-tDCS studies [39,61,62]. In addition, another recent study in our lab (manuscript in press) used the exact same experimental paradigm, with the exception that M1-tDCS was used. This study found significant MEP increases of 47% in the M1-tDCS group and only a non-significant 5% increase in the SHAM group. Based on these collective lines of reasoning, the daily increases in MEP in the SHAM group were most likely due to the large inherent variability involved in MEP measurements and random variation in the MEP data [61], which are issues that have been described and analyzed extensively (see [39,62] for reviews). However, the possible contributions of small c-tDCS or placebo effects cannot be completely ruled out. Nonetheless, the lack of significant positive associations in MEP amplitude changes and endpoint accuracy changes and very small r^2 values (Figure 4A–C) indicate that the MEP increases likely had little functional significance relevant to motor learning. The absence of significant positive associations between changes in MEPs and changes in endpoint accuracy is consistent with a previous comprehensive study, which found that MEP increases elicited by M1-tDCS were not associated with the amount of motor learning achieved by subjects across a range of motor tasks [42].

4.3. Possible Reasons for the Failure of c-tDCS to Improve Overhand Throwing Accuracy

The lack of statistically significant results of the current study, the failure of c-tDCS replication studies, and other recent negative studies suggest that it should not be presumed that application of c-tDCS almost always elicits improvements in motor skill in young adults. Nonetheless, there are a few possible factors that could have been responsible for the lack of an ability of c-tDCS to enhance motor learning in the present study. First, it could be argued that the c-tDCS parameters were suboptimal. This view is supported by the fact that various combinations of electrode montage, polarity, current strength, timing relative to task performance, and stimulation duration have also shown efficacy [5]. Although the issue of other optimal stimulation parameters cannot be ruled out, this possibility is unlikely as the current set of c-tDCS parameters was selected specifically because it had the highest number of total positive study outcomes relative to other sets of parameters [6–12]. Most importantly, the identical parameters were successful in improving the same overhand throwing task in our laboratory even though this study involved only a one-time c-tDCS application [11]. Second, it is conceivable the group of participants randomly assigned

to the c-tDCS group may have contained a relatively high number of non-responders as some studies have shown that a moderate number of people may be non-responders to M1-tDCS [63]. However, it should be pointed out that these studies defined non-responders based solely on TMS cortical excitability measures taken from M1 (resting motor threshold, 1 mV MEP) in response to tDCS. Thus, they did not measure motor performance at all. Accordingly, the most comprehensive study on the topic found that MEP increases elicited by M1-tDCS (and two other forms of non-invasive brain stimulation) were not associated with the amount of motor learning achieved by subjects in several motor tasks [42]. Thus, no direct studies have been conducted in an attempt to discriminate between responders and non-responders to c-tDCS based on a combination of TMS and motor learning outcomes, which renders this explanation plausible, but extremely speculative. Nevertheless, there could be variations across individuals in the amount of current delivered to cerebellar neurons due to dissimilarities in many physiological, biological, and anatomical factors. For example, differences in the nerve fiber orientation are thought to be one major factor responsible for the effective amount of current reaching cerebellar neurons [3,64]. These possibilities will have to be examined in subsequent studies that combine behavioral and several physiological measures. Finally, a combination of the above factors could be responsible for the lack of c-tDCS effects on motor learning in the current study.

Although the aforementioned factors could potentially have contributed to the current findings, other possible factors such as the baseline skill level, age of the participants, TMS stimulation intensity to evoke a 1 mV MEP [65], and degree of right-handedness do not apply to the current findings, as these factors were almost exactly the same between groups. Furthermore, other common criticisms of tDCS studies that observe negative effects, such as only one day of stimulation or the use of a motor task that is not amenable to tDCS, are also not relevant. This is because the current study involved 3 days of stimulation using the same motor task that was improved with c-tDCS in our single-day study [11]. Collectively, these lines of reasoning imply that the present study design should have been able to find performance enhancements induced by c-tDCS if they existed.

4.4. Limitations and Future Directions

Although the findings were clear in regard to the absence of positive effects of c-tDCS on motor learning, the study had several limitations that should be addressed in future research. These are mainly related to the interrelated issues of choice of stimulation parameters, the population studied, and individual differences in response to c-tDCS. The parameters of c-tDCS (e.g., electrode montage, current strength) were chosen because they had increased motor skill in the greatest number of previous studies by another research group [6–10,12] and in our previous single-session study [11]. Nonetheless, it is possible that another set of c-tDCS parameters could be more effective. For example, a recent study used bilateral anodal c-tDCS and demonstrated improvements in complex whole-body tasks in gymnasts [55]. Another study found that a bilateral electrode montage (anode over the right cerebellar hemisphere, cathode over the left cerebellar hemisphere) and a 4 mA current strength outperformed several other unilateral montage and lower-current-strength combinations. However, this study involved gait and balance performance in Parkinson's disease patients. Nevertheless, it is possible that bilateral montages or increasing the total dose of c-tDCS through greater current strengths could be superior to the stimulation parameter used here. Other related types of non-invasive brain stimulation such as transcranial alternating current (tACS) applied to cerebellum alone [66,67] or to cerebellum and M1 simultaneously [68–70] have also elicited significant improvements in motor skill in healthy adults. Therefore, future research is warranted to further examine these other sets of cerebellar-stimulation parameters.

The other notable limitations of the study were that the application of c-tDCS was not individualized for each participant and the only population studied were healthy young adults in a tight age range. Recently, initial research has attempted to optimize cerebellar-stimulation parameters based on participant anatomy [71] by using neuronavigation to

focus stimulation on cerebellar lobule VIII in an individualized manner. This strategy along with modulating current strength could be particularly important when applying c-tDCS to healthy young adults or children with movement impairments that involve cerebellar contributions [72–74] compared with healthy [75] or diseased older populations with cerebellar dysfunction [76]. This is because the cerebellum cortex is highly convoluted in nature, has a high variation in nerve fiber orientation [3], and shrinks with advanced age [77], which strongly implies that individualization of cerebellar stimulation could further enhance performance outcomes. In summary, further research could explore the synergies between unilateral and bilateral electrode montages as well as varying c-tDCS dose parameters such as current strength, duration, and days of stimulation. Based on the available research, these strategies have significant potential to enhance motor skill acquisition and motor learning across different populations and motor tasks.

5. Conclusions

Participants were able to progressively decrease endpoint error across the three consecutive days of practice, but these improvements in endpoint accuracy were similar between the c-tDCS and SHAM stimulation groups. Therefore, c-tDCS failed to improve motor learning in this complex motor task to a greater degree than practice alone in the current experimental conditions. In addition, c-tDCS did not significantly increase M1 excitability to a greater extent than SHAM stimulation. Furthermore, when increases in M1 excitability occurred, they were not positively associated with improvements in endpoint accuracy for either group. When these results are considered in the context of the overall c-tDCS and motor skill literature, they are consistent with recent replication studies [56,57] that have suggested that the effects of c-tDCS may not be as robust as initial studies indicated [8,58]. Therefore, future studies are needed to fully determine the efficacy of c-tDCS for potentially enhancing motor skill acquisition and learning in healthy young adults. Finally, interindividual differences in the motor performance responses elicited by c-tDCS and the physiological mechanisms underlying these will be especially important, but challenging issues that should be addressed in future work.

Author Contributions: Conceptualization, B.P., M.P., D.E.L. and L.L.d.A.; methodology, M.P., D.E.L., L.L.d.A. and B.P.; software, M.P. and B.P.; validation, D.E.L., L.L.d.A. and B.P.; formal analysis, M.P., D.E.L., L.L.d.A. and B.P.; investigation, D.E.L., L.L.d.A., I.A.M., E.W.W., D.G.A., D.M. and M.P.; resources, J.S.D. and B.P.; data curation, M.P. and B.P.; writing—original draft preparation, M.P. and B.P.; writing—review and editing, D.E.L., L.L.d.A., J.S.D., I.A.M., E.W.W., D.G.A., D.M., M.P. and B.P.; visualization, M.P. and B.P.; supervision, J.S.D. and B.P.; project administration, M.P., D.E.L., L.L.d.A. and B.P. All authors have read and agreed to the published version of the manuscript.

Funding: This research received no external funding.

Institutional Review Board Statement: The study was conducted in accordance with the Declaration of Helsinki, and approved by the Institutional Review Board of University of Nevada, Las Vegas (protocol number: 1249171, and original date of approval: 19 July 2018).

Informed Consent Statement: Informed consent was obtained from all subjects involved in the study.

Data Availability Statement: The data presented in the study are available on request from the corresponding author.

Conflicts of Interest: The authors declare no conflict of interest.

References

1. Buch, E.R.; Santarnecchi, E.; Antal, A.; Born, J.; Celnik, P.A.; Classen, J.; Gerloff, C.; Hallett, M.; Hummel, F.C.; Nitsche, M.A.; et al. Effects of tDCS on motor learning and memory formation: A consensus and critical position paper. *Clin. Neurophysiol. Off. J. Int. Fed. Clin. Neurophysiol.* **2017**, *128*, 589–603. [CrossRef] [PubMed]
2. van Dun, K.; Bodranghien, F.; Manto, M.; Marien, P. Targeting the Cerebellum by Noninvasive Neurostimulation: A Review. *Cerebellum* **2017**, *16*, 695–741. [CrossRef] [PubMed]

3. Miterko, L.N.; Baker, K.B.; Beckinghausen, J.; Bradnam, L.V.; Cheng, M.Y.; Cooperrider, J.; DeLong, M.R.; Gornati, S.V.; Hallett, M.; Heck, D.H.; et al. Consensus Paper: Experimental Neurostimulation of the Cerebellum. *Cerebellum* **2019**, *18*, 1064–1097. [CrossRef] [PubMed]
4. Celnik, P. Understanding and modulating motor learning with cerebellar stimulation. *Cerebellum* **2015**, *14*, 171–174. [CrossRef] [PubMed]
5. Oldrati, V.; Schutter, D. Targeting the Human Cerebellum with Transcranial Direct Current Stimulation to Modulate Behavior: A Meta-Analysis. *Cerebellum* **2018**, *17*, 228–236. [CrossRef] [PubMed]
6. Block, H.; Celnik, P. Stimulating the cerebellum affects visuomotor adaptation but not intermanual transfer of learning. *Cerebellum* **2013**, *12*, 781–793. [CrossRef] [PubMed]
7. Galea, J.M.; Jayaram, G.; Ajagbe, L.; Celnik, P. Modulation of cerebellar excitability by polarity-specific noninvasive direct current stimulation. *J. Neurosci. Off. J. Soc. Neurosci.* **2009**, *29*, 9115–9122. [CrossRef] [PubMed]
8. Galea, J.M.; Vazquez, A.; Pasricha, N.; de Xivry, J.J.; Celnik, P. Dissociating the roles of the cerebellum and motor cortex during adaptive learning: The motor cortex retains what the cerebellum learns. *Cereb. Cortex* **2011**, *21*, 1761–1770. [CrossRef]
9. Hardwick, R.M.; Celnik, P.A. Cerebellar direct current stimulation enhances motor learning in older adults. *Neurobiol. Aging* **2014**, *35*, 2217–2221. [CrossRef]
10. Jayaram, G.; Tang, B.; Pallegadda, R.; Vasudevan, E.V.; Celnik, P.; Bastian, A. Modulating locomotor adaptation with cerebellar stimulation. *J. Neurophysiol.* **2012**, *107*, 2950–2957. [CrossRef]
11. Jackson, A.K.; de Albuquerque, L.L.; Pantovic, M.; Fischer, K.M.; Guadagnoli, M.A.; Riley, Z.A.; Poston, B. Cerebellar Transcranial Direct Current Stimulation Enhances Motor Learning in a Complex Overhand Throwing Task. *Cerebellum* **2019**, *18*, 813–816. [CrossRef] [PubMed]
12. Cantarero, G.; Spampinato, D.; Reis, J.; Ajagbe, L.; Thompson, T.; Kulkarni, K.; Celnik, P. Cerebellar direct current stimulation enhances on-line motor skill acquisition through an effect on accuracy. *J. Neurosci. Off. J. Soc. Neurosci.* **2015**, *35*, 3285–3290. [CrossRef] [PubMed]
13. Reis, J.; Fischer, J.T.; Prichard, G.; Weiller, C.; Cohen, L.G.; Fritsch, B. Time-but Not Sleep-Dependent Consolidation of tDCS-Enhanced Visuomotor Skills. *Cereb. Cortex* **2013**, *25*, 109–117. [CrossRef] [PubMed]
14. Reis, J.; Schambra, H.M.; Cohen, L.G.; Buch, E.R.; Fritsch, B.; Zarah, E.; Celnik, P.A.; Krakauer, J.W. Noninvasive cortical stimulation enhances motor skill acquisition over multiple days through an effect on consolidation. *Proc. Natl. Acad. Sci. USA* **2009**, *106*, 1590–1595. [CrossRef] [PubMed]
15. Meek, A.W.; Greenwell, D.; Poston, B.; Riley, Z.A. Anodal tDCS accelerates on-line learning of dart throwing. *Neurosci. Lett.* **2021**, *764*, 136211. [CrossRef] [PubMed]
16. Wilson, M.A.; Greenwell, D.; Meek, A.W.; Poston, B.; Riley, Z.A. Neuroenhancement of a dexterous motor task with anodal tDCS. *Brain Res.* **2022**, *1790*, 147993. [CrossRef] [PubMed]
17. Lemon, R.N. Neural control of dexterity: What has been achieved? *Exp. Brain Res.* **1999**, *128*, 6–12. [CrossRef]
18. Cordo, P.J.; Gurfinkel, V.S. Motor coordination can be fully understood only by studying complex movements. *Prog. Brain Res.* **2004**, *143*, 29–38. [CrossRef]
19. Wulf, G.; Shea, C.H. Principles derived from the study of simple skills do not generalize to complex skill learning. *Psychon. Bull. Rev.* **2002**, *9*, 185–211. [CrossRef]
20. Behrangrad, S.; Zoghi, M.; Kidgell, D.; Jaberzadeh, S. Does cerebellar non-invasive brain stimulation affect corticospinal excitability in healthy individuals? A systematic review of literature and meta-analysis. *Neurosci. Lett.* **2019**, *706*, 128–139. [CrossRef]
21. Timmann, D.; Lee, P.; Watts, S.; Hore, J. Kinematics of arm joint rotations in cerebellar and unskilled subjects associated with the inability to throw fast. *Cerebellum* **2008**, *7*, 366–378. [CrossRef] [PubMed]
22. Hirashima, M.; Kudo, K.; Ohtsuki, T. Utilization and compensation of interaction torques during ball-throwing movements. *J. Neurophysiol.* **2003**, *89*, 1784–1796. [CrossRef] [PubMed]
23. Hirashima, M.; Kudo, K.; Watarai, K.; Ohtsuki, T. Control of 3D limb dynamics in unconstrained overarm throws of different speeds performed by skilled baseball players. *J. Neurophysiol.* **2007**, *97*, 680–691. [CrossRef] [PubMed]
24. Hirashima, M.; Ohtsuki, T. Exploring the mechanism of skilled overarm throwing. *Exerc. Sport. Sci. Rev.* **2008**, *36*, 205–211. [CrossRef] [PubMed]
25. Debicki, D.B.; Gribble, P.L.; Watts, S.; Hore, J. Kinematics of wrist joint flexion in overarm throws made by skilled subjects. *Exp. Brain Res.* **2004**, *154*, 382–394. [CrossRef] [PubMed]
26. Hore, J.; Timmann, D.; Watts, S. Disorders in timing and force of finger opening in overarm throws made by cerebellar subjects. *Ann. N. Y. Acad. Sci.* **2002**, *978*, 1–15. [CrossRef]
27. Hore, J.; Watts, S. Skilled throwers use physics to time ball release to the nearest millisecond. *J. Neurophysiol.* **2011**, *106*, 2024–2033. [CrossRef]
28. Flament, D.; Hore, J. Movement and electromyographic disorders associated with cerebellar dysmetria. *J. Neurophysiol.* **1986**, *55*, 1221–1233. [CrossRef]

29. Timmann, D.; Citron, R.; Watts, S.; Hore, J. Increased variability in finger position occurs throughout overarm throws made by cerebellar and unskilled subjects. *J. Neurophysiol.* **2001**, *86*, 2690–2702. [CrossRef]
30. Timmann, D.; Watts, S.; Hore, J. Failure of cerebellar patients to time finger opening precisely causes ball high-low inaccuracy in overarm throws. *J. Neurophysiol.* **1999**, *82*, 103–114. [CrossRef]
31. Tseng, Y.W.; Diedrichsen, J.; Krakauer, J.W.; Shadmehr, R.; Bastian, A.J. Sensory prediction errors drive cerebellum-dependent adaptation of reaching. *J. Neurophysiol.* **2007**, *98*, 54–62. [CrossRef] [PubMed]
32. Oldfield, R.C. The assessment and analysis of handedness: The Edinburgh inventory. *Neuropsychologia* **1971**, *9*, 97–113. [CrossRef] [PubMed]
33. Groppa, S.; Oliviero, A.; Eisen, A.; Quartarone, A.; Cohen, L.G.; Mall, V.; Kaelin-Lang, A.; Mima, T.; Rossi, S.; Thickbroom, G.W.; et al. A practical guide to diagnostic transcranial magnetic stimulation: Report of an IFCN committee. *Clin. Neurophysiol. Off. J. Int. Fed. Clin. Neurophysiol.* **2012**, *123*, 858–882. [CrossRef] [PubMed]
34. Poston, B.; Kukke, S.N.; Paine, R.W.; Francis, S.; Hallett, M. Cortical silent period duration and its implications for surround inhibition of a hand muscle. *Eur. J. Neurosci.* **2012**, *36*, 2964–2971. [CrossRef] [PubMed]
35. Fricke, K.; Seeber, A.A.; Thirugnanasambandam, N.; Paulus, W.; Nitsche, M.A.; Rothwell, J.C. Time course of the induction of homeostatic plasticity generated by repeated transcranial direct current stimulation of the human motor cortex. *J. Neurophysiol.* **2011**, *105*, 1141–1149. [CrossRef] [PubMed]
36. Monte-Silva, K.; Kuo, M.F.; Hessenthaler, S.; Fresnoza, S.; Liebetanz, D.; Paulus, W.; Nitsche, M.A. Induction of late LTP-like plasticity in the human motor cortex by repeated non-invasive brain stimulation. *Brain Stimul.* **2012**, *6*, 424–432. [CrossRef] [PubMed]
37. Nitsche, M.A.; Paulus, W. Excitability changes induced in the human motor cortex by weak transcranial direct current stimulation. *J. Physiol.* **2000**, *527 Pt 3*, 633–639. [CrossRef] [PubMed]
38. Thirugnanasambandam, N.; Sparing, R.; Dafotakis, M.; Meister, I.G.; Paulus, W.; Nitsche, M.A.; Fink, G.R. Isometric contraction interferes with transcranial direct current stimulation (tDCS) induced plasticity: Evidence of state-dependent neuromodulation in human motor cortex. *Restor. Neurol. Neurosci.* **2011**, *29*, 311–320. [CrossRef]
39. Horvath, J.C.; Carter, O.; Forte, J.D. Transcranial direct current stimulation: Five important issues we aren't discussing (but probably should be). *Front. Syst. Neurosci.* **2014**, *8*, 2. [CrossRef]
40. Quartarone, A.; Morgante, F.; Bagnato, S.; Rizzo, V.; Sant'Angelo, A.; Aiello, E.; Reggio, E.; Battaglia, F.; Messina, C.; Girlanda, P. Long lasting effects of transcranial direct current stimulation on motor imagery. *Neuroreport* **2004**, *15*, 1287–1291. [CrossRef]
41. Antal, A.; Terney, D.; Poreisz, C.; Paulus, W. Towards unravelling task-related modulations of neuroplastic changes induced in the human motor cortex. *Eur. J. Neurosci.* **2007**, *26*, 2687–2691. [CrossRef] [PubMed]
42. Lopez-Alonso, V.; Cheeran, B.; Fernandez-del-Olmo, M. Relationship Between Non-invasive Brain Stimulation-induced Plasticity and Capacity for Motor Learning. *Brain Stimul.* **2015**, *8*, 1209–1219. [CrossRef] [PubMed]
43. Hummel, F.; Celnik, P.; Giraux, P.; Floel, A.; Wu, W.H.; Gerloff, C.; Cohen, L.G. Effects of non-invasive cortical stimulation on skilled motor function in chronic stroke. *Brain A J. Neurol.* **2005**, *128*, 490–499. [CrossRef] [PubMed]
44. Fregni, F.; Boggio, P.S.; Santos, M.C.; Lima, M.; Vieira, A.L.; Rigonatti, S.P.; Silva, M.T.; Barbosa, E.R.; Nitsche, M.A.; Pascual-Leone, A. Noninvasive cortical stimulation with transcranial direct current stimulation in Parkinson's disease. *Mov. Disord. Off. J. Mov. Disord. Soc.* **2006**, *21*, 1693–1702. [CrossRef] [PubMed]
45. Nitsche, M.A.; Cohen, L.G.; Wassermann, E.M.; Priori, A.; Lang, N.; Antal, A.; Paulus, W.; Hummel, F.; Boggio, P.S.; Fregni, F.; et al. Transcranial direct current stimulation: State of the art 2008. *Brain Stimul.* **2008**, *1*, 206–223. [CrossRef] [PubMed]
46. de Albuquerque, L.L.; Pantovic, M.; Clingo, M.; Fischer, K.; Jalene, S.; Landers, M.; Mari, Z.; Poston, B. A Single Application of Cerebellar Transcranial Direct Current Stimulation Fails to Enhance Motor Skill Acquisition in Parkinson's Disease: A Pilot Study. *Biomedicines* **2023**, *11*, 2219. [CrossRef] [PubMed]
47. Albuquerque, L.L.; Fischer, K.M.; Pauls, A.L.; Pantovic, M.; Guadagnoli, M.A.; Riley, Z.A.; Poston, B. An acute application of transcranial random noise stimulation does not enhance motor skill acquisition or retention in a golf putting task. *Hum. Mov. Sci.* **2019**, *66*, 241–248. [CrossRef]
48. de Albuquerque, L.L.; Pantovic, M.; Clingo, M.G.; Fischer, K.M.; Jalene, S.; Landers, M.R.; Mari, Z.; Poston, B. Long-Term Application of Cerebellar Transcranial Direct Current Stimulation Does Not Improve Motor Learning in Parkinson's Disease. *Cerebellum* **2021**, *21*, 333–349. [CrossRef]
49. de Albuquerque, L.L.; Pantovic, M.; Clingo, M.; Fischer, K.; Jalene, S.; Landers, M.; Mari, Z.; Poston, B. An Acute Application of Cerebellar Transcranial Direct Current Stimulation Does Not Improve Motor Performance in Parkinson's Disease. *Brain Sci.* **2020**, *10*, 735. [CrossRef]
50. Poston, B.; Van Gemmert, A.W.; Sharma, S.; Chakrabarti, S.; Zavaremi, S.H.; Stelmach, G. Movement trajectory smoothness is not associated with the endpoint accuracy of rapid multi-joint arm movements in young and older adults. *Acta Psychol.* **2013**, *143*, 157–167. [CrossRef]
51. Doyon, J.; Penhune, V.; Ungerleider, L.G. Distinct contribution of the cortico-striatal and cortico-cerebellar systems to motor skill learning. *Neuropsychologia* **2003**, *41*, 252–262. [CrossRef]

52. Spampinato, D.; Celnik, P. Multiple Motor Learning Processes in Humans: Defining Their Neurophysiological Bases. *Neurosci. Rev. J. Bringing Neurobiol. Neurol. Psychiatry* **2021**, *27*, 246–267. [CrossRef] [PubMed]
53. Spampinato, D.; Celnik, P. Temporal dynamics of cerebellar and motor cortex physiological processes during motor skill learning. *Sci. Rep.* **2017**, *7*, 40715. [CrossRef] [PubMed]
54. Krakauer, J.W.; Mazzoni, P. Human sensorimotor learning: Adaptation, skill, and beyond. *Curr. Opin. Neurobiol.* **2011**, *21*, 636–644. [CrossRef] [PubMed]
55. Anoushiravani, S.; Alizadehgoradel, J.; Iranpour, A.; Yousefi Bilehsavar, O.; Pouresmali, A.; Nitsche, M.A.; Salehinejad, M.A.; Mosayebi-Samani, M.; Zoghi, M. The impact of bilateral anodal transcranial direct current stimulation of the premotor and cerebellar cortices on physiological and performance parameters of gymnastic athletes: A randomized, cross-over, sham-controlled study. *Sci. Rep.* **2023**, *13*, 10611. [CrossRef] [PubMed]
56. Beyer, L.; Batsikadze, G.; Timmann, D.; Gerwig, M. Cerebellar tDCS Effects on Conditioned Eyeblinks using Different Electrode Placements and Stimulation Protocols. *Front. Hum. Neurosci.* **2017**, *11*, 23. [CrossRef] [PubMed]
57. Jalali, R.; Miall, R.C.; Galea, J.M. No consistent effect of cerebellar transcranial direct current stimulation on visuomotor adaptation. *J. Neurophysiol.* **2017**, *118*, 655–665. [CrossRef] [PubMed]
58. Zuchowski, M.L.; Timmann, D.; Gerwig, M. Acquisition of conditioned eyeblink responses is modulated by cerebellar tDCS. *Brain Stimul.* **2014**, *7*, 525–531. [CrossRef]
59. Steiner, K.M.; Enders, A.; Thier, W.; Batsikadze, G.; Ludolph, N.; Ilg, W.; Timmann, D. Cerebellar tDCS Does Not Improve Learning in a Complex Whole Body Dynamic Balance Task in Young Healthy Subjects. *PLoS ONE* **2016**, *11*, e0163598. [CrossRef]
60. Panouilleres, M.T.; Joundi, R.A.; Brittain, J.S.; Jenkinson, N. Reversing motor adaptation deficits in the ageing brain using non-invasive stimulation. *J. Physiol.* **2015**, *593*, 3645–3655. [CrossRef]
61. Dissanayaka, T.; Zoghi, M.; Farrell, M.; Egan, G.F.; Jaberzadeh, S. Does transcranial electrical stimulation enhance corticospinal excitability of the motor cortex in healthy individuals? A systematic review and meta-analysis. *Eur. J. Neurosci.* **2017**, *46*, 1968–1990. [CrossRef] [PubMed]
62. Horvath, J.C.; Forte, J.D.; Carter, O. Evidence that transcranial direct current stimulation (tDCS) generates little-to-no reliable neurophysiologic effect beyond MEP amplitude modulation in healthy human subjects: A systematic review. *Neuropsychologia* **2015**, *66*, 213–236. [CrossRef]
63. Wiethoff, S.; Hamada, M.; Rothwell, J.C. Variability in response to transcranial direct current stimulation of the motor cortex. *Brain Stimul.* **2014**, *7*, 468–475. [CrossRef] [PubMed]
64. Rahman, A.; Toshev, P.K.; Bikson, M. Polarizing cerebellar neurons with transcranial Direct Current Stimulation. *Clin. Neurophysiol. Off. J. Int. Fed. Clin. Neurophysiol.* **2014**, *125*, 435–438. [CrossRef] [PubMed]
65. Labruna, L.; Jamil, A.; Fresnoza, S.; Batsikadze, G.; Kuo, M.F.; Vanderschelden, B.; Ivry, R.B.; Nitsche, M.A. Efficacy of Anodal Transcranial Direct Current Stimulation is Related to Sensitivity to Transcranial Magnetic Stimulation. *Brain Stimul.* **2016**, *9*, 8–15. [CrossRef] [PubMed]
66. Naro, A.; Bramanti, A.; Leo, A.; Manuli, A.; Sciarrone, F.; Russo, M.; Bramanti, P.; Calabro, R.S. Effects of cerebellar transcranial alternating current stimulation on motor cortex excitability and motor function. *Brain Struct. Funct.* **2017**, *222*, 2891–2906. [CrossRef] [PubMed]
67. Sugata, H.; Yagi, K.; Yazawa, S.; Nagase, Y.; Tsuruta, K.; Ikeda, T.; Matsushita, K.; Hara, M.; Kawakami, K.; Kawakami, K. Modulation of Motor Learning Capacity by Transcranial Alternating Current Stimulation. *Neuroscience* **2018**, *391*, 131–139. [CrossRef]
68. Miyaguchi, S.; Inukai, Y.; Matsumoto, Y.; Miyashita, M.; Takahashi, R.; Otsuru, N.; Onishi, H. Effects on motor learning of transcranial alternating current stimulation applied over the primary motor cortex and cerebellar hemisphere. *J. Clin. Neurosci. Off. J. Neurosurg. Soc. Australas.* **2020**, *78*, 296–300. [CrossRef]
69. Miyaguchi, S.; Otsuru, N.; Kojima, S.; Saito, K.; Inukai, Y.; Masaki, M.; Onishi, H. Transcranial Alternating Current Stimulation With Gamma Oscillations Over the Primary Motor Cortex and Cerebellar Hemisphere Improved Visuomotor Performance. *Front. Behav. Neurosci.* **2018**, *12*, 132. [CrossRef]
70. Miyaguchi, S.; Otsuru, N.; Kojima, S.; Yokota, H.; Saito, K.; Inukai, Y.; Onishi, H. Gamma tACS over M1 and cerebellar hemisphere improves motor performance in a phase-specific manner. *Neurosci. Lett.* **2019**, *694*, 64–68. [CrossRef]
71. Herzog, R.; Bolte, C.; Radecke, J.O.; von Moller, K.; Lencer, R.; Tzvi, E.; Munchau, A.; Baumer, T.; Weissbach, A. Neuronavigated Cerebellar 50 Hz tACS: Attenuation of Stimulation Effects by Motor Sequence Learning. *Biomedicines* **2023**, *11*, 2218. [CrossRef] [PubMed]
72. Lidstone, D.E.; Miah, F.Z.; Poston, B.; Beasley, J.F.; Dufek, J.S. Manual dexterity in children with autism spectrum disorder: A cross-syndrome approach. *Res. Autism Spect. Dis.* **2020**, *73*, 101546. [CrossRef]
73. Lidstone, D.E.; Miah, F.Z.; Poston, B.; Beasley, J.F.; Mostofsky, S.H.; Dufek, J.S. Children with Autism Spectrum Disorder Show Impairments During Dynamic Versus Static Grip-force Tracking. *Autism Res.* **2020**, *13*, 2177–2189. [CrossRef] [PubMed]
74. D’Mello, A.M.; Stoodley, C.J. Cerebro-cerebellar circuits in autism spectrum disorder. *Front. Neurosci.* **2015**, *9*, 408. [CrossRef] [PubMed]
75. Boisgontier, M.P. Motor aging results from cerebellar neuron death. *Trends Neurosci.* **2015**, *38*, 127–128. [CrossRef] [PubMed]

76. Wu, T.; Hallett, M. The cerebellum in Parkinson's disease. *Brain A J. Neurol.* **2013**, *136*, 696–709. [CrossRef]
77. Rezaee, Z.; Dutta, A. Lobule-Specific Dosage Considerations for Cerebellar Transcranial Direct Current Stimulation During Healthy Aging: A Computational Modeling Study Using Age-Specific Magnetic Resonance Imaging Templates. *Neuromodulation J. Int. Neuromodulation Soc.* **2020**, *23*, 341–365. [CrossRef]

Disclaimer/Publisher's Note: The statements, opinions and data contained in all publications are solely those of the individual author(s) and contributor(s) and not of MDPI and/or the editor(s). MDPI and/or the editor(s) disclaim responsibility for any injury to people or property resulting from any ideas, methods, instructions or products referred to in the content.

Article

The Influence of Different Inter-Trial Intervals on the Quantification of Intracortical Facilitation in the Primary Motor Cortex

Milan Pantovic ¹, Rhett Boss ², Kevin J. Noorda ², Mario I. Premyanov ², Daniel G. Aynlender ², Erik W. Wilkins ³, Sage Boss ⁴, Zachary A. Riley ⁵ and Brach Poston ^{3,*}

¹ Health and Human Performance Department, Utah Tech University, St. George, UT 84770, USA; milan.pantovic@utahtech.edu

² School of Medicine, University of Nevada-Las Vegas, Las Vegas, NV 89154, USA; bossr1@unlv.nevada.edu (R.B.); noordk1@unlv.nevada.edu (K.J.N.); premayno@unlv.nevada.edu (M.I.P.); aynlende@unlv.nevada.edu (D.G.A.)

³ Department of Kinesiology and Nutrition Sciences, University of Nevada-Las Vegas, Las Vegas, NV 89154, USA; wilkie1@unlv.nevada.edu

⁴ School of Life Sciences, University of Nevada-Las Vegas, Las Vegas, NV 89154, USA; boss1@unlv.nevada.edu

⁵ Department of Kinesiology, Indiana University Purdue University Indianapolis, Indianapolis, IN 46202, USA; zariley@iupui.edu

* Correspondence: brach.poston@unlv.edu; Tel.: +1-702-895-5329

Abstract: Intracortical facilitation (ICF) is a paired-pulse transcranial magnetic stimulation (TMS) measurement used to quantify interneuron activity in the primary motor cortex (M1) in healthy populations and motor disorders. Due to the prevalence of the technique, most of the stimulation parameters to optimize ICF quantification have been established. However, the underappreciated methodological issue of the time between ICF trials (inter-trial interval; ITI) has been unstandardized, and different ITIs have never been compared in a paired-pulse TMS study. This is important because single-pulse TMS studies have found motor evoked potential (MEP) amplitude reductions over time during TMS trial blocks for short, but not long ITIs. The primary purpose was to determine the influence of different ITIs on the measurement of ICF. Twenty adults completed one experimental session that involved 4 separate ICF trial blocks with each utilizing a different ITI (4, 6, 8, and 10 s). Two-way ANOVAs indicated no significant ITI main effects for test MEP amplitudes, condition-test MEP amplitudes, and therefore ICF. Accordingly, all ITIs studied provided nearly identical ICF values when averaged over entire trial blocks. Therefore, it is recommended that ITIs of 4–6 s be utilized for ICF quantification to optimize participant comfort and experiment time efficiency.

Keywords: transcranial magnetic stimulation; motor evoked potential; intracortical facilitation; short-interval intracortical inhibition; electromyography

1. Introduction

Transcranial magnetic stimulation (TMS) is a non-invasive technique that allows the assessment of corticospinal excitability at rest and during muscle activation [1–4]. Accordingly, a single suprathreshold TMS pulse applied to the primary motor cortex (M1) elicits an electromyographic (EMG) response termed the motor evoked potential (MEP), which is used as an index of corticospinal excitability [5]. In addition, a test MEP can be paired with a subthreshold conditioning TMS pulse (paired-pulse TMS) in condition-test paradigms at various inter-stimulus intervals (ISIs) and stimulation intensities to measure several inhibitory and excitatory intracortical interneuronal pathways in M1 [6–8]. Short-interval intracortical inhibition (SICI) and intracortical facilitation (ICF) are the most studied and described of these pathways [6,9–11].

ICF is examined by applying a subthreshold conditioning TMS pulse briefly followed by a suprathreshold TMS test pulse at ISIs of 6–25 milliseconds with 10 milliseconds being the most common. This leads to facilitation of the condition-test MEP amplitudes compared to single-pulse test MEP amplitudes that are randomly intermixed in the same block of TMS testing. Although findings have been somewhat mixed, the balance of evidence suggests that ICF is most likely mediated by populations of intracortical interneurons in M1 and not due to subcortical or spinal mechanisms [6,10,12,13]. Accordingly, ICF is thought to be mainly mediated by excitatory glutamatergic neurons in M1 and has been shown to be altered (either increased or decreased) in several motor disorders [6,10,13]. For this reason, along with the fact that ICF is often quantified with several other measures of intracortical inhibition and facilitation, accurate quantification of ICF is important in the study of movement control.

Due to the significance and prevalence of single and paired-pulse TMS techniques, extensive research has endeavored to determine optimal methodological procedures [14] and consensus guidelines for TMS studies involving these methods [10]. For example, an international panel of 42 experts identified 21 methodological items that should be reported or controlled in TMS studies [15]. One of the items was the time between MEP trials (hereafter termed inter-trial interval; ITI) and 82% of the expert panel respondents reported that this item was important or very important to control, whereas 87% reported that ITI should be reported always or most of the time [15]. Despite these recommendations and the observations that ITI can influence other evoked responses such as the Hoffman reflex [16,17] and auditory evoked potentials [18], there currently appears to be no consensus guidelines and little research available regarding the appropriate ITI to utilize between single-pulse MEPs, but especially paired-pulse MEPs. Thus, ITI has been underemphasized and underappreciated relative to many of the other stimulation parameters that are involved in paired-pulse TMS such as stimulation intensities and ISIs to name a few. Accordingly, both a wide range of ITIs and several methods of varying the ITI on a trial-to-trial basis have been used in the literature on single-pulse TMS. For instance, protocols such as “an interval of 7 s (10% variance) [19]”, “less than every 5 s [11]”, “the intervals between the stimuli usually ranged between 20 and 30 s [20]”, “pseudo randomly at intervals ranging between 3.5 and 7 s [21]”, “every 15 s [22]”, “varied between 1.5 and 2.5 s [23]”, and many others have been used. Furthermore, observation suggests that the most common ITIs used in the literature are between 4 and 6 s, although the vast majority of TMS studies do not even report the ITI at all.

It is difficult to determine why ITI has received considerably less attention compared to other TMS parameters of stimulation. Perhaps ITI has simply been overlooked or this is due to the widespread view that only repetitive TMS techniques involving high stimulation rates and extended stimulation periods lead to effects that persist for a significant time after the stimulation [24–26]. Accordingly, the commonly held belief that each MEP is an independent event [27] was supported by the observation that a single TMS pulse given to M1 increased cortico-muscular coherence for only 300–800 milliseconds before values returned to baseline [28]. However, a few single-pulse TMS studies do exist that have shown that the amplitudes of successive MEPs evoked in a block of trials may not be as time-invariant as commonly thought [29]. For example, one extensive study found that single-pulse MEP amplitudes elicited at a constant stimulation intensity were significantly lower at short ITIs (1, 2, 3, and 5 s) compared with a long ITI of 10 s. This effect was most prominent in the first 1–10 MEP trials of a 30 MEP trial block. Furthermore, MEP recruitment curves obtained at rest using both increasing and decreasing TMS stimulation intensities exhibited hysteresis when the average ITI was 5 s, but not when the average ITI was 20 s [27]. Although recruitment curve construction involves the usage of a wide range of stimulation intensities versus the constant stimulation intensities used in other types of single and paired-pulse TMS measures, these findings lend some further support to the idea that MEP measurements may be influenced by ITI. Accordingly, another single-pulse TMS

study reported similar results as a 5 second ITI resulted in lower average MEP amplitudes in a block of 25 MEP trials compared to ITIs of 10, 15, and 20 s [30].

However, no studies have examined the influence of different ITIs on paired-pulse TMS measurements. Accordingly, the ICF values attained during a typical block of TMS trials involving intermingled condition-test trials and test MEP trials using different ITIs have never been investigated. This is surprising given the aforementioned single-pulse ITI studies and the fact that single-TMS pulses serve as the test MEP in paired-pulse TMS paradigms as well as the test MEP being a component of the condition-test MEP. Taken together, these lines of reasoning raise the possibility that different ITIs, including those that have been used in many paired-pulse TMS studies, could have resulted in skewed, different, or even erroneous ICF values. Therefore, the primary purpose was to examine the influence of different ITIs on measurements of ICF at rest. This was accomplished by quantifying ICF during 4 blocks of trials at ITIs of 4, 6, 8, and 10 s. Based on the limited number of single-pulse TMS studies [27,29], it was hypothesized that ICF amplitude would differ for the short (4 s) compared with long (6, 8, and 10 s) ITI blocks. Furthermore, it was predicted that this would be due to an initial suppression (lower facilitation) in the first few trials and not a serial reduction in ICF amplitude over the entire trial block. The secondary purpose was to examine the influence of different ITIs on measurements of single-pulse MEPs at rest. This was accomplished by quantifying single-pulse MEPs at rest during 2 blocks of trials at ITIs of 4 and 10 s. These separate single-pulse blocks had the dual purpose of serving as control blocks for the ICF blocks and as comparisons to previous TMS studies that assessed the effect of ITI on single-pulse MEP amplitudes [27,29,30]. Based on these previous studies, it was hypothesized that MEP amplitude would be lower for the 4-second ITI block compared to the 10-second ITI block. Finally, it was expected that this would be due to an initial MEP suppression in the first few trials of the 4-second ITI block and not a serial reduction in MEP amplitude over the entire trial block.

2. Materials and Methods

2.1. Participants

Twenty young adults participated in the study (10 males and 10 females; mean age: 25.0 ± 2.3). All participants were determined to be right-handed based on the Edinburgh Handedness Inventory [31]. Participants reported that they were free of any psychiatric or neurological disorders and had no uncontrolled medical conditions. In addition, none of the participants met the exclusion criteria for non-invasive brain stimulation studies [14]. Finally, all experimental procedures were conducted in accord with the Declaration of Helsinki and the Institutional Review Board at the University of Nevada, Las Vegas approved the study (protocol number: 1445199).

2.2. Experimental Design

The study utilized a within-subjects experimental design and all participants completed one experimental session that lasted about 2 h. The size of the sample of participants ($n = 20$) was based on the available previous studies on ITI that involved single-pulse TMS [27,29,30,32–34]. Collectively, these studies had a sample size range of 8–17; participants and an average sample size of 12.5. Thus, it was decided that 20 participants should be more than enough to demonstrate the influence of ITI on ICF if this phenomenon were to exist. Each experimental session proceeded in the following set of 7 steps: (1) baseline maximum voluntary contraction (pre-MVC) measurements; (2) motor hotspot localization; (3) resting motor threshold quantification; (4) determination of the stimulation intensity as a percentage of maximum stimulator output (% MSO) required to elicit a MEP of approximately 1 mV with a 10-second ITI; (5) 2 control blocks that involved single-pulse MEPs evoked with either a 4-second ITI or a 10-second ITI (hereafter referred to as the 1 mV_4 and 1 mV_10 conditions); (6) 4 separate trial blocks that involved paired-pulse TMS measurement of ICF at 4 ITIs of 4, 6, 8, and 10 s (hereafter referred to as ICF_4, ICF_6, ICF_8, and ICF_10 conditions), and (7) post-MVCs. Figure 1 depicts the major experimental steps

of the experimental protocol while the methodological details of each step are provided below in subsequent sections.

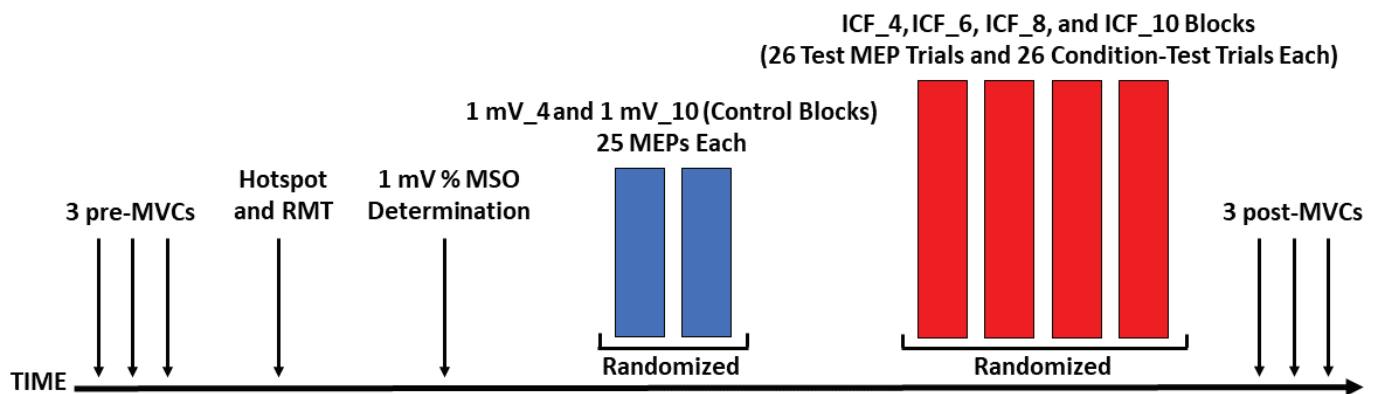


Figure 1. Schematic of the experimental protocol. Each experiment comprised 7 steps that included: 3 MVCs (pre), motor hotspot localization, RMT quantification, 1 mV stimulation intensity determination, the 1 mV₄ and 1 mV₁₀ control blocks, the ICF₄, ICF₆, ICF₈, and ICF₁₀ blocks, and 3 MVCs (post).

2.3. Experimental Arrangement

The experimental arrangement (equipment setup and participant posture) was similar to previous studies [35,36]. Briefly, participants were seated comfortably in a chair next to a small table such that their shoulder was abducted to about 45 degrees, the elbow was flexed to approximately 90 degrees, the forearm rested on a flat block that was placed on the table, and the wrist was placed in a neutral position with the hand prone. Most importantly, participants were required to keep this same posture during all TMS testing as changes in upper limb and shoulder posture can influence MEPs in hand muscles [37,38]. A computer monitor was located at eye level about a meter in front of the participants to provide feedback of the EMG activity of the right FDI muscle, which served as the target muscle for all TMS and experimental testing. Participants were given detailed and strict instructions on how to use this visual feedback to ensure that the FDI muscle remained at rest during all of the TMS recordings. In addition, this computer screen was also constantly monitored by one of the investigators to further ensure that participants were keeping the FDI at rest throughout the TMS testing blocks.

TMS was performed using two Magstim 200² stimulators connected by a Bistim module and delivered through a standard double 70 mm remote control figure-of-eight coil. All single-pulse and paired-pulse TMS measurements were completed with the TMS unit in Bistim Mode [39]. The TMS coil was held in such a way that it was kept tangential to the scalp with the handle orientated backward and laterally at a 45-degree angle relative to the midline. An investigator placed the TMS coil over the location corresponding to the “motor hot spot” of the FDI muscle of the left M1 to evoke MEPs in the FDI of the right hand [40]. The EMG activity of the FDI muscle was recorded with prewired disposable surface electrodes arranged in a belly tendon montage. All EMG signals were acquired using Cambridge Electronic Design (CED; Cambridge, UK) hardware (1902 amplifiers, micro 1401 data acquisition interface) and software (Signal 5.04).

2.4. Experimental Procedures

2.4.1. MVCs

MVCs were conducted using standard methodology and similar to previous studies [35,41,42]. Since the FDI was the muscle of interest, MVCs were performed using index finger abduction as almost all of the index finger abduction force is produced by the FDI. A manipulandum instrumented with a force transducer was situated on the table very near the end of the block where their hand was placed. Thus, participants could exert force on

the force transducer at the level of the proximal interphalangeal joint with the index finger. For all MVC trials, participants were instructed to generate their maximum force in the shortest time possible and to hold this maximum for ~5 s [42]. Visual feedback of the FDI abduction force was given in the form of a red force trace that scrolled across the computer monitor. Three MVC trials were completed at the beginning (pre-MVCs) and at the end of the experimental session (post-MVCs) immediately after the ICF blocks. A rest period of one minute was enforced between all MVC trials.

The rationale for performing MVCs was to provide some confirmation that the ability to voluntarily activate the FDI muscle and by extension factors such as alertness or arousal [5] that can influence MEPs had not substantially declined over the course of the experiment due to central fatigue. Although the chances of significant central fatigue in the current study were likely extremely remote as all procedures were obtained at rest, the concentration required to complete the experiment could theoretically lead to mental fatigue. It has been known for a long time that mental fatigue even in the absence of physical exercise can reduce voluntary activation [43] and therefore potentially even resting MEP measurements in a long experimental session.

2.4.2. Motor Hotspot Localization

Suprathreshold TMS pulses were delivered as the coil position was optimized so that the point on the scalp where the largest MEPs could be evoked. This location was denoted as the FDI motor hot spot, the coil position was marked on a scalp cap, and the scalp cap position on the head was outlined with a mark on the forehead [40]. Accordingly, all MEPs in the experiment were evoked using this location.

2.4.3. RMT

The RMT was measured for each participant and was defined as the lowest stimulation intensity required to induce a 50-microvolt peak-to-peak MEP in at least 5 out of 10 consecutive TMS trials. Subsequently, the RMT value was used to determine the stimulation intensity for the conditioning pulses of the ICF measurements for each participant.

2.4.4. mV Stimulation Intensity (% MSO) Determination

Suprathreshold TMS pulses were applied and the stimulation intensity was adjusted while MEPs were monitored and quantified online until the MEPs evoked were as close as possible on average to a 1 mV peak-to-peak amplitude [44]. This initial testing was completed to determine the stimulation intensity as a percentage of maximum stimulator output (% MSO) to elicit an average MEP of approximately 1 mV. This stimulation intensity was then used for all subsequent experimental blocks (the single-pulse MEPs in the control blocks and all the test MEPs in the ICF blocks). This testing was completed using an ITI of 10 s so as to get the 1 mV MEP stimulation intensity at the longest ITI used in the study. This was based on previous studies [27,29,30] that this should be the true 1 mV MEP value as an ITI of 10 s should not be influenced by time-dependent effects. Most importantly, great attention and time were devoted to identifying the % MSO value that elicited MEPs as close to 1 mV as possible. Briefly, this was completed by monitoring and estimating the MEP amplitudes online using a software script in Signal and resetting the program as needed and changing the stimulation intensity until the investigators were confident the best possible value had been identified. Finally, this value was used for all of the subsequent single-pulse and ICF trial blocks that were used for analysis.

2.4.5. Control Blocks

Two separate control blocks using ITIs of 4 and 10 s (hereafter referred to as the 1 mV_4 and 1 mV_10) consisting only of single-pulse MEPs were performed in randomized order (Figure 1). These blocks were included to serve the dual purpose of controls for the single-pulse test MEPs elicited in the ICF blocks and to compare the results to previous ITI studies that involved only single-pulse TMS [27,29,30]. Accordingly, only the shortest

and longest ITIs of 4 and 10 s used in the subsequent ICF blocks were investigated in the control blocks. This was decided upon because any ITI differences were most likely to be observed between the shortest and longest ITIs and in the interest of time as it was already a long experiment with the primary focus being on the ICF blocks. A total of 25 MEPs was collected in both blocks using the 1 mV stimulation intensity (% MSO) for each participant that was established in the previous step. This stimulation intensity to evoke an MEP of 1 mV was used in the control blocks as it is the typical number used to measure MEP changes before and after numerous types of interventions (e.g., transcranial direct current stimulation, exercise, various behavioral state changes, etc) in TMS studies. Most importantly, the 1 mV MEP is almost always used as the test pulse stimulation intensity in paired-pulse TMS. The number of 25 MEP trials per block was selected for the following interrelated reasons: (1) the most comprehensive study on the topic [45] found that 20–30 MEPs generally provide the best trade-off between the minimum number of trials to provide valid results for average MEP amplitude of a block of trials at both the individual and group level; (2) this is also the range of MEPs that the same authors determined is broadly applicable and practical to accomplish due to time and other constraints inherent in most TMS studies; and (3) the two most relevant prior single-pulse TMS studies involving ITI used 25 and 30 trials per block [29,30].

2.4.6. ICF Blocks

ICF was quantified in 4 separate trial blocks using ITIs of 4, 6, 8, and 10 s (hereafter referred to as ICF_4, ICF_6, ICF_8, and ICF_10) with the blocks performed in a randomized order (Figure 1). The ITI employed was the only difference across the four ICF trial blocks. Accordingly, the ICF protocol was always administered using the same coil to deliver the subthreshold conditioning pulse followed by a suprathreshold test pulse separated by an interstimulus interval (ISI) of 10 milliseconds. The conditioning pulse stimulation intensity was set to 90% of RMT, whereas the test pulse stimulation intensity was set to the previously determined 1 mV stimulation intensity as is almost always completed in paired-pulse TMS studies. This combination of ICF parameter values for ISI, conditioning pulse intensity, and test pulse intensity were chosen as they are generally the most common in the literature and found to be the most optimal for observing ICF in the most systematic study on the topic [11].

All ICF blocks involved a total of 52 TMS trials with 26 trials involving single-pulse TMS (test MEPs alone) and 26 trials involving paired-pulse TMS (condition-test MEPs) that collectively were used to calculate ICF. Within each ICF trial block, these two types of trials (termed “states” in Signal software) were presented in a semi-randomized order, which in this case means that every two TMS trials were randomized between the trial types (states). The number of 26 trials per each type of trial was selected for reasons similar to those mentioned for the 25 MEP number in the previous section. In addition, this allowed at least 25 trials for each trial type in the event that the first 2 trials would have to be discarded (see Section 4.4 of the Discussion), although this turned out to not be the case. Accordingly, each ICF block consisted of 26 test MEP trials, 26 condition-test MEP trials, and therefore 26 ICF measurements. Accordingly, ICF was calculated as the condition-test MEP amplitude divided by the test MEP amplitude and expressed as a percentage.

The 4 ITIs used for investigation were selected for the following interrelated reasons: (1) although some previous single-pulse TMS studies examined ITIs below 4 s [29,33], it was determined in extensive pilot testing that any ITI below 4 s for ICF testing was not practical. This was because the TMS device could easily skip trials due to the capacitors not charging quickly enough if a participant required relatively high stimulation intensities for the test and/or condition-test MEPs. Relatedly, ITIs shorter than 4 also were found to be prone to coil overheating in a small number of instances during piloting. Obviously, any skipped trials would render the results of this particular study uninterpretable; (2) an ITI of 4 s should still have been able to detect time-varying changes in MEP amplitudes due to ITI if they were present, based on previous single-pulse studies [27,29,30]. Similarly, an

ITI of 10 should be adequate to reveal valid MEP amplitude according to the same studies; (3) ITIs over 10 are essentially impractical for the vast majority of TMS experiments as these conditions lead to experiment times that are too long and uncomfortable for both the experimenter and the participant. This was readily apparent in pilot testing and would also reduce the total number of TMS blocks or conditions that could be completed in typical TMS experiments.

2.5. Data Analysis

All MEP and MVC data were analyzed using customized scripts written in Signal 5.04 software (Cambridge Electronic Design, Cambridge, UK). The investigators who performed the data collection experiments did not participate in the data reduction or data analysis aspects of the study [46].

2.5.1. MVC Force, MVC EMG, RMT, and 1 mV (% MSO) Stimulation Intensity Analyses

MVC force was calculated as the average force produced over the 3–5 s plateau period for each trial and the highest MVC among each set of pre and post-MVCs was used for analysis [36]. The maximum MVC EMG was calculated over this same time period and the highest MVC EMG among each set of pre and post-MVCs were used for analysis. MEP size was always calculated as the peak-to-peak amplitude for each individual MEP in all the analyses below. The RMT and 1 mV stimulation intensity (% MSO) are reported as the group averages to provide information on the participant characteristics and the numbers used to determine the ICF test and condition pulse stimulation intensities.

2.5.2. Control Block Analyses

The MEP amplitudes in the control blocks were averaged in three different ways for analysis and illustration purposes. First, possible changes in MEP amplitude over the time course of the control blocks were analyzed by dividing the 25 MEP trials in each block into 3 separate time epochs of consecutive MEP trials (Epoch 1: trials 1–8; Epoch 2: trials 9–16; and Epoch 3 trials 17–25; Figure 2A). Thus, Epochs 1 and 2 consisted of 8 trials, whereas Epoch 3 consisted of 9 trials. This was similar to a previous single-pulse study that divided 30 MEP trial blocks into 3 sub-blocks of 10 for analysis [29]. The reason for Epochs 1 and 2 ultimately consisting of 8 trials instead of 9 such as Epoch 3 (or some similar arrangement of exactly equal trials per epoch) was in the event that the first trial of each block would have to be discarded (see Section 4.4 of the Discussion), although this turned out to not be the case. Second, MEP amplitude was also quantified as the average of all 25 MEP trials in each control block (Figure 2B). This was mainly completed to illustrate the overall average MEP amplitude for the control blocks as the same information is contained in the prior step and associated figure, but the overall averages are not as easy to ascertain. Third, to further evaluate possible changes in MEP amplitude over the time course of the control blocks, the average MEP amplitudes of all 20 participants were quantified for each of the 25 trials and plotted. This was completed primarily for visual assessment and illustrative purposes of the series of 25 trials in each control block (Figure 3).

2.5.3. ICF Block Analyses

Similar to the control blocks, the MEP amplitudes in the ICF blocks were processed in three different ways for analysis and illustration purposes. First, groups of MEP trials were also divided into epochs with the exception that the corresponding Epochs 1, 2, and 3 consisted of 16, 16, and 18 trials, respectively. In addition to the obvious reasons for these trial blocks involving paired-pulse TMS and more total trials, the major reason for the slightly different number of trials per epoch was similar to the previous explanation regarding the possibility of discarding the first two trials, which also that did not materialize (see Section 4.4 of the Discussion). Accordingly, the average MEP amplitudes of the test MEP trials, condition-test MEP trials, and therefore ICF calculation were quantified as the average 8, 8, and 9 trials for each of these measures in the ICF blocks and used for analysis

(Figure 4A–C). Thus, ICF was calculated as the condition-test MEP amplitude divided by the test MEP amplitude and expressed as a percentage according to standard practice [6,9–11]. Second, the average MEP amplitudes for each of the 26 test MEP trials, 26 condition-test MEP trials, and therefore 26 ICF measurements were taken for analysis and plotted (Figure 5). This was mainly completed to illustrate the overall average MEP amplitude for these measures as the same information is contained in the prior step and associated figure, but the overall averages are not as easy to visualize. Third, to further visualize changes in test and condition-test MEP trials individually over the time course of the ICF blocks, the average test MEP and condition-test MEP amplitudes of all 20 participants were quantified for each of their respective 26 trials and plotted. This was completed primarily for visual assessment and illustrative purposes. This was completed primarily for visual assessment and illustrative purposes of the series of trials that comprised each ICF block (Figure 6).

2.6. Statistical Analysis

2.6.1. MVCs

The pre-MVC and post-MVC conditions were compared with a paired *t*-test. Similarly, the pre-MVC EMG and post-MVC EMG were also compared with a paired *t*-test.

2.6.2. Control Blocks

To analyze possible differences in MEP amplitude over the time course of the control blocks a 2 *Control Block* (1 mV_4, 1 mV_10) \times 3 *Epoch* (1, 2, 3) within-subjects ANOVA was utilized. Post hoc comparisons using Bonferroni adjustment for multiple comparisons were performed to locate where significant differences occurred between pairs of means if appropriate.

2.6.3. ICF Blocks

The possible differences in test MEP amplitudes, condition-test MEP amplitudes, and ICF values over the time course of the ICF blocks were analyzed by 3 separate 4 *ICF Block* (ICF_4, ICF_6, ICF_8, ICF_10) \times 3 *Epoch* (1,2,3) within-subjects ANOVAs. Post hoc comparisons using Bonferroni adjustment for multiple comparisons were performed to locate where significant differences occurred between pairs of means if appropriate.

The significance level for all statistical tests was set to $p < 0.05$, except when modified by Bonferroni corrections. All data are expressed as means \pm standard error in the figures and mean \pm standard deviation within the text.

3. Results

The group average RMT and 1 mV stimulation intensity (% MSO) were 48.3 ± 7.2 and 55.3 ± 10.1 , respectively.

3.1. MVCs

The paired *t*-test indicated that there was no significant difference ($p = 0.06$) between the pre-MVC (40.4 ± 13.2 N) and post-MVC force (43.7 ± 13.4 N). Similarly, another paired *t*-test indicated that there was no significant difference ($p = 0.441$) between the pre-MVC EMG (0.89 ± 0.2 mV) and post-MVC EMG (0.84 ± 0.2 mV).

3.2. Control Blocks

For MEP amplitudes in the control blocks, the 2 *Control Block* (1 mV_4, 1 mV_10) \times 3 *Epoch* (1, 2, 3) within-subjects ANOVA revealed that the main effect for *Control Block* ($p = 0.721$), main effect for *Epoch* ($p = 0.610$), and *Control Block* \times 3 *Epoch* interaction ($p = 0.480$) were all non-statistically significant (Figure 2A,B). MEP amplitudes as a function of trial number for the control blocks are depicted for illustration in Figure 3A,B.

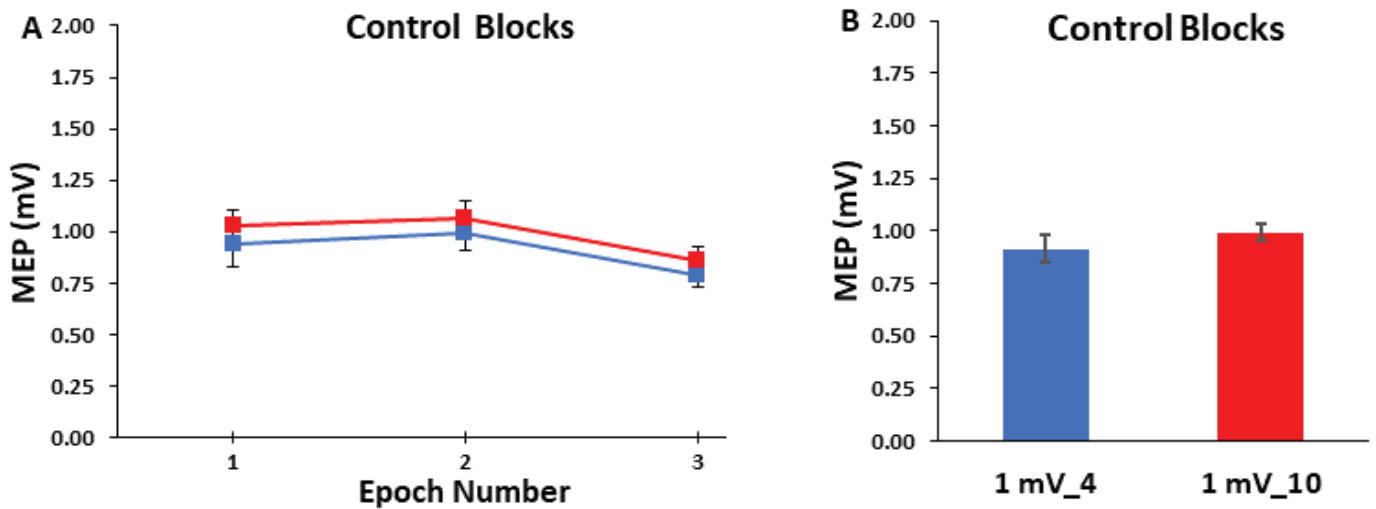


Figure 2. MEP amplitude in the control blocks. (A) The MEP amplitude as a function of Epoch number. MEP amplitude was similar for the 1 mV_4 condition and 1 mV_10 conditions and across the three epochs; (B) The MEP amplitude was similar for the 1 mV_4 and 1 mV_10 control blocks when averaged over the whole block.

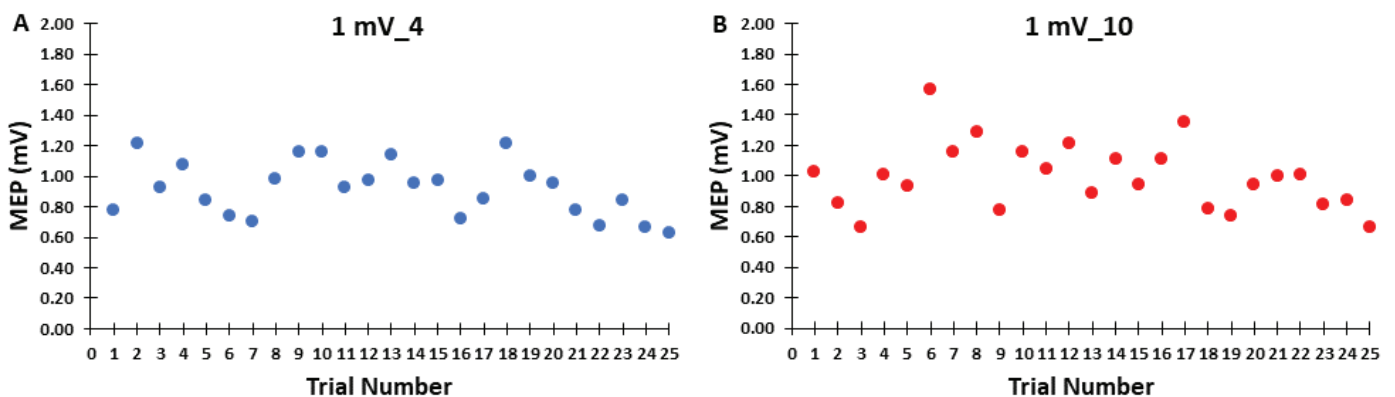


Figure 3. MEP amplitude as a function of trial number for the control blocks. Each point represents the average of all twenty participants for a given trial in each of the two blocks. (A) MEP amplitude as a function of trial number for the 1 mV_4 condition; (B) MEP amplitude as a function of trial number for the 1 mV_10 condition.

3.3. ICF Blocks

For test MEP amplitude, the 4 ICF Block (TEST_4, TEST_6, TEST_8, TEST_10) × 3 Epoch (1,2,3) within-subjects ANOVA revealed that the main effect for ICF Block ($p = 0.893$) and main effect for Epoch ($p = 0.976$) were both non-statistically significant (Figures 4A and 5A). However, there was a significant ICF Block × 3 Epoch interaction ($p = 0.017$). Nonetheless, post-hoc analysis of the interaction using Bonferroni adjustment for multiple comparisons indicated that all of the differences between pairs of means were non-significant (all p -values > 0.137).

For condition-test MEP amplitude, the 4 ICF Block (C-T_4, C-T_6, C-T_8, C-T_10) × 3 Epoch (1,2,3) within-subjects ANOVA revealed that the main effect for ICF Block ($p = 0.688$), main effect for Epoch ($p = 0.593$), and ICF Block × 3 Epoch interaction ($p = 0.635$) were all non-statistically significant (Figures 4B and 5B). Test MEP and condition-test MEP amplitudes as a function of trial number for the ICF blocks for the four ITIs are depicted for illustration in Figure 6A–D.

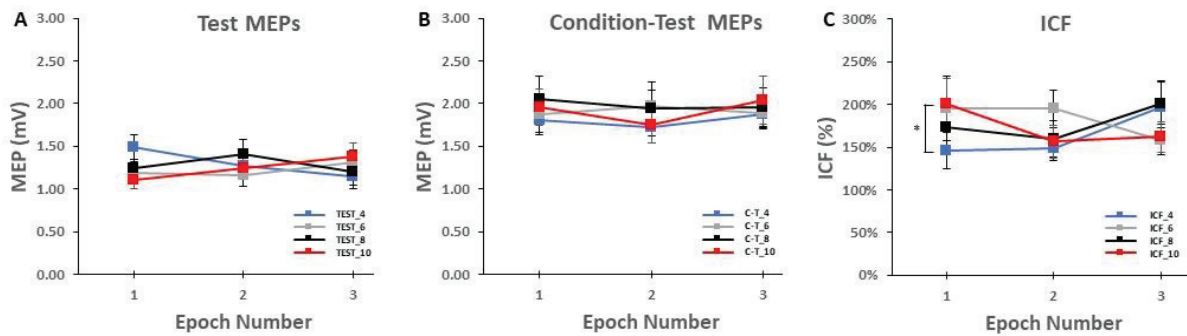


Figure 4. Test MEPs, condition-test MEPs, and ICF values in the ICF blocks. (A) The MEP amplitude as a function of Epoch number for the test MEP trials only. MEP amplitude was similar for the four test MEP ITI conditions across the three epochs; (B) The MEP amplitude as a function of Epoch number for the condition-test MEP trials only. MEP amplitude was similar for the four condition-test ITI conditions across the three epochs; (C) ICF values as a function of Epoch number. ICF was lower for the ICF_4 condition compared with the ICF_10 condition, but only in the first epoch ($p = 0.015$). All other ICF values were similar for the four ICF ITI conditions across the 3 epochs. * indicates the significant pairwise comparison between ICF_4 and ICF_10 in Epoch 1.

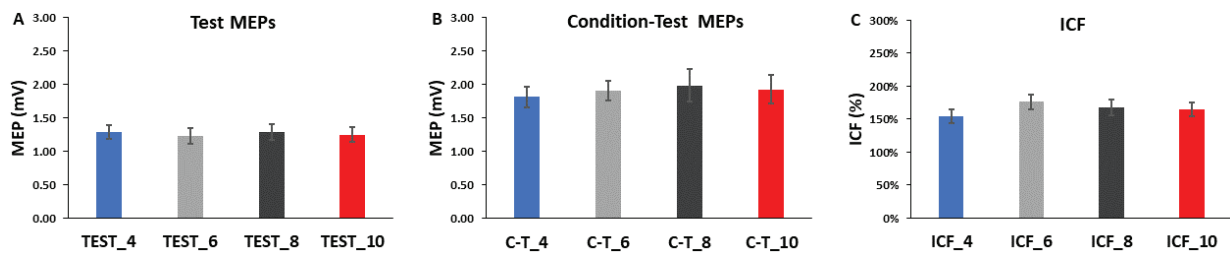


Figure 5. The overall block averages for test MEPs, condition-test MEPs, and ICF values in the ICF blocks. (A) There were no differences in average MEP values for the test MEPs for any of the ITIs. (B) There were no differences in average MEP values for the condition-test MEPs for any of the ITIs. (C) Thus, there was no difference in ICF for the four ITIs when comparing the overall block averages.

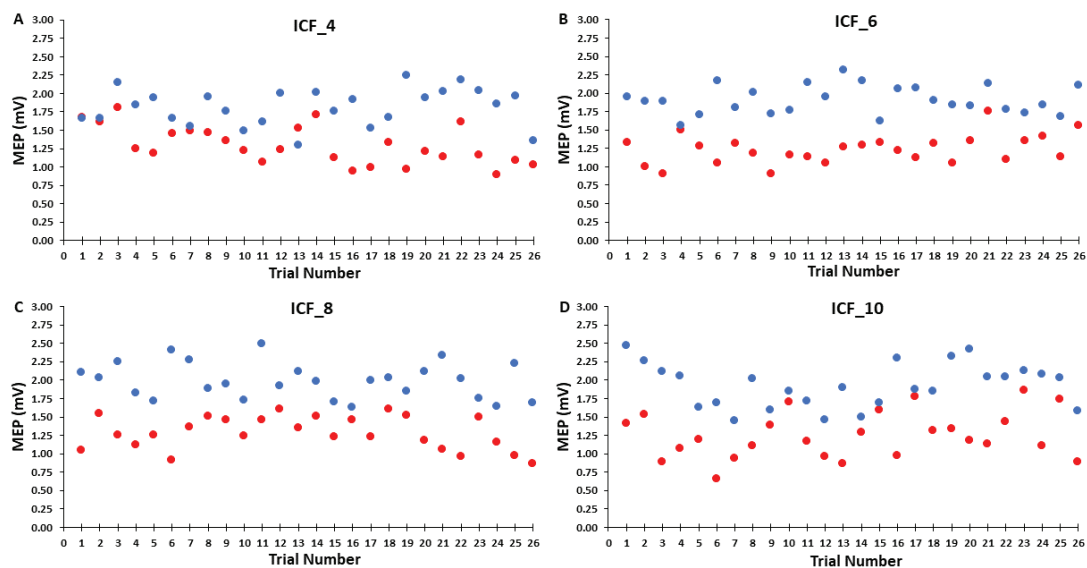


Figure 6. Test MEP and condition-test MEP amplitudes as a function of trial number for the ICF blocks for the four ITIs are depicted for illustration (A–D). Test MEP trials are indicated in red and condition-test MEP trials are indicated in blue. Each data point represents the average MEP amplitudes of all 20 subjects for a given trial.

For ICF values, the 4 ICF Block (ICF_4, ICF_6, ICF_8, ICF_10) × 3 Epoch (1,2,3) within-subjects ANOVA revealed that the main effect for ICF Block ($p = 0.397$) and main effect for Epoch ($p = 0.534$) were both non-statistically significant (Figure 4C). However, there was a significant ICF Block × 3 Epoch interaction ($p = 0.04$). Post-hoc analysis of the interaction using Bonferroni adjustment for multiple comparisons indicated that ICF_4 was less than ICF_10 in Epoch 1 ($p = 0.015$; Figure 4C). ICF as a function of trial number for the ICF blocks for the four ITIs are depicted for illustration in Figure 7A–D.

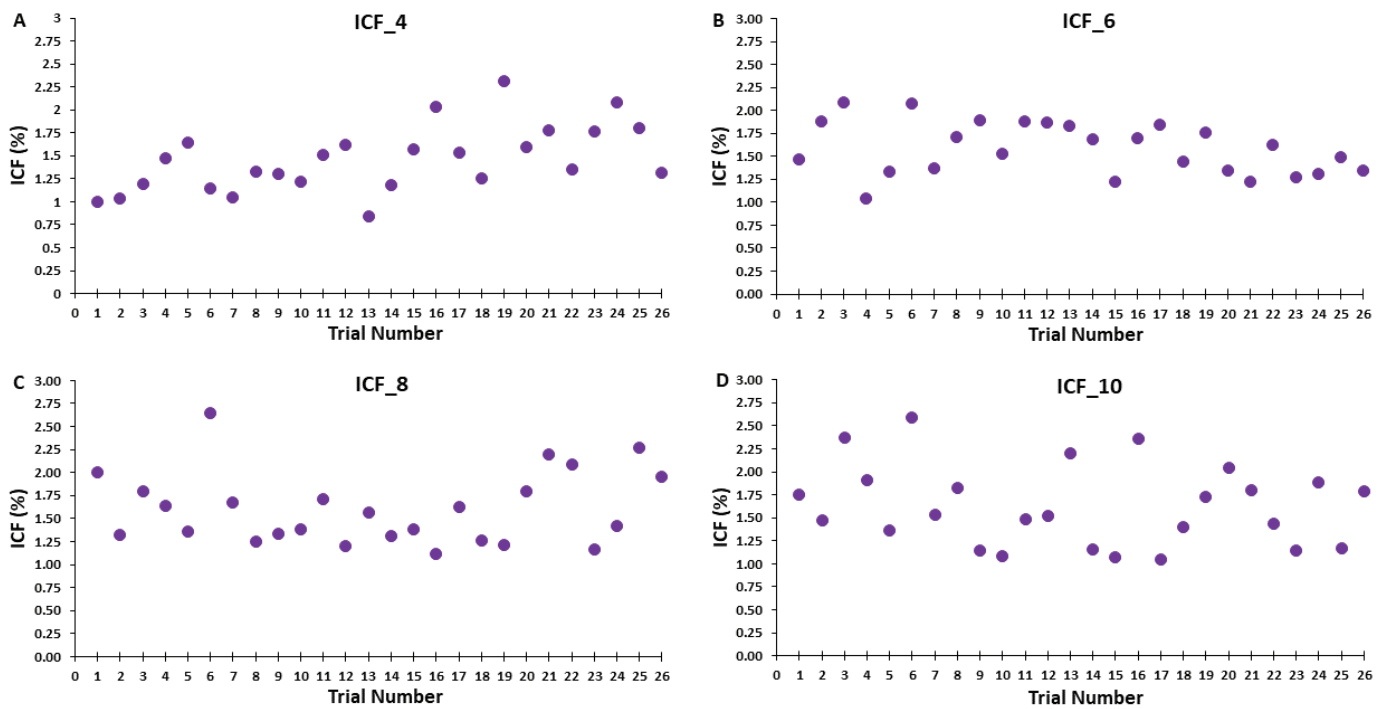


Figure 7. ICF as a function of trial number for the ICF blocks for the four ITIs are depicted for illustration (A–D). Each data point represents the average ICF values of all 20 subjects for a given trial.

4. Discussion

The primary purpose was to examine the influence of different ITIs on ICF measurements at rest, whereas the secondary purpose was to examine the influence of different ITIs on single-pulse MEP measurements at rest. The study produced two sets of main findings: (1) single-pulse MEPs elicited in the short 4-second ITI condition (1 mV_4) and the long 10-second ITI condition (1 mV_10) did not significantly change over the time course of the trial blocks and had similar average amplitudes; (2) ICF values were similar for the four ITIs and did not significantly change over the course of time for any of the ICF blocks. However, the details of the overall ICF results were somewhat nuanced due to a random, non-physiological covariation of data. Taken together, the current findings indicate that ITIs of 4, 6, 8, and 10 s provide nearly identical single-pulse MEP and ICF values.

4.1. Effects of ITI on MEP Amplitude in the Control Blocks

MEP amplitude is one of the most common and useful measurements in human motor control studies and provides a global measure of net corticospinal excitability. However, a number of TMS parameters must be considered to ensure proper interpretation of MEP measurements. The possible relevance of ITI on MEP amplitude has been recognized since the early days of TMS research methodology, at least in specific task conditions [21,47,48]. Accordingly, a little over a decade ago the vast majority of an international panel of TMS experts stated that ITI was important to control and should always be reported in TMS studies [15], although there was little if any direct systematic research available on the topic at that time. Despite these recommendations, common observation suggests that very

few single-pulse TMS studies report ITI when describing the TMS parameters selected in the research design. This assertion is supported by a systematic review that focused on the related topic of single-pulse TMS reliability measurement, which was reported in an analysis of 16 included studies that only 1 reported the ITI utilized [49]. Therefore, it appears that ITI has been underreported and underappreciated relative to other TMS stimulation parameters with no consensus on the topic as a wide range of constant ITIs and methods of varying the ITI within TMS trial blocks have been used in the literature.

The current study investigated the influence of different ITIs on single-pulse MEPs at rest in 2 control blocks using 4 and 10-second ITIs (1 mV_4 and 1 mV_10 conditions). Although the primary focus of the study was the examination of the effect of ITI on ICF, these blocks served as control measurements for the ICF blocks, especially for the test MEPs elicited in an intermingled fashion with the condition-test MEPs. In addition, the control blocks allowed for comparisons with prior single-pulse TMS studies involving ITI [27,29,30,32,34] in an attempt to confirm or extend previous findings. These studies collectively found that MEP amplitudes were generally decreased at ITIs of 5 s and below compared to longer ITIs. This effect was most prominent in approximately the first 10 trials of a block [27,29,30]. Thus, these results suggest that this phenomenon could lead to inaccurate quantification of the average MEP amplitude over a typical block of MEPs collected in most studies if an ITI of 5 and below is used.

Based on the most relevant previous studies, it was originally hypothesized that MEP amplitude would be lower for the 1 mV_4 block compared to the 1 mV_10 block. This could result from either the initial MEP trials being depressed, a serial reduction in MEP amplitude over the entire block, or a combination of both factors in the 1 mV_4 block compared to the 1 mV_10 block. However, the major findings obtained in the control blocks were contrary to the original hypothesis. First, the first 8 trials that comprised Epoch 1 were not significantly different than the subsequent Epochs 2–3 which contained 8 and 9 trials each in either control block (Figure 2A). Second, MEP amplitudes did not exhibit a serial decrement over the course of either of the control blocks. Third, the overall average MEP amplitudes (25 trials) reflected the previous two findings and were not significantly different between the 1 mV_4 block and the 1 mV_10 block (Figure 2A,B). Fourth, there was no indication of the first trial being substantially different compared to the average MEPs in the same trial block and relative to the normal inherent variability of all of these trials. Fifth, the previous findings and observations are supported by visual inspection of the group average MEP amplitudes plotted as a function of trial number (Figure 3A,B). In summary, single-pulse MEP amplitudes did not display time-varying characteristics within either of the control blocks of 25 trials but rather fluctuated about the average value observed over the entirety of the blocks.

The findings appear to be inconsistent with the results of the majority of previous single-pulse TMS studies. However, many of these dissimilarities are likely due to methodological differences, although a few discrepancies are difficult to resolve. For example, one study [27] found that MEP amplitudes obtained while measuring recruitment curves at rest were significantly lower with an ITI of 5 s compared to an ITI of 20 s. However, recruitment curve construction involves the application of a wide range of stimulus intensities versus constant stimulation intensities used here and in other ITI studies. Furthermore, only 5 MEP trials per condition were averaged in that study, which is common for recruitment curves, but well below the approximate 25 MEPs recommended in most experimental circumstances [45]. Another study reported that MEPs evoked at a constant stimulation intensity were significantly lower at short ITIs (1, 2, 3, and 5 s) compared with a long ITI of 10 s. This was mainly evident in the first 1–10 MEPs of a 30-trial block, which contrasts with the current control block results. However, this study had a number of differences relative to the present study, three of which could be considered major: (1) the sample size consisted of only 8 participants. This is important as the sample size is a large contributor to the estimator error for MEP amplitude quantification [45]; (2) a TMS device that delivered biphasic pulses was used, which can give different results compared with the most common

single and paired-pulse TMS devices that give monophasic pulses [50]; and (3) participants watched television (TV) during the experiment as opposed to concentrating on a relatively constant experimental screen where EMG feedback was given. Since MEPs are modulated during the up and down states of neuronal oscillations as measured by EEG and by changes in attention [5], it is uncertain what differential effect TV viewing could have had on results. In another study, Matilainen et al. (2022) found that MEPs were suppressed at a 2-second ITI compared to 5 and 10-second ITIs, although this study also had a low sample size of 9 participants. [32]. In addition, Schmidt et al., (2009) [33] employed a 3-second ITI and observed a transient initial state (~first 20 trials) of MEP amplitudes that differed from subsequent trials, consistent with the other previous studies. However, this study did not compare the 3-second ITI to longer ITIs. In contrast, another report clearly indicated that MEP amplitudes were lower using a 4-second versus a 10-second ITI [34]. These findings were supported by a second study by the same research group that found lower MEP amplitudes at an ITI of 5 seconds compared to 10, 15, and 20-second ITIs. Since these studies used methodology very similar to the current control blocks, the reasons for the different findings are unknown and difficult to reconcile.

In contrast, the present findings are consistent with a few other studies that involved ITI examination as well as physiological studies that provide evidence of why relatively short ITIs are unlikely to cause serial decrements in MEP amplitude. In a classic repetitive TMS study [26], Pascual-Leone and colleagues found that an ITI of 1 second did not influence subsequent MEP amplitudes, and ITIs lower than 1 second were needed to induce time-dependent effects. These direct results are supported by indirect physiological results that demonstrated that a single TMS pulse given to M1 increased cortico-muscular coherence for only 300–800 milliseconds before values returned to baseline [28]. Furthermore, experiments that have evoked single-pulse MEPs in FDI and simultaneously recorded the sequence of descending volleys (direct wave and indirect waves) via an electrode in the cervical epidural space [51,52] have shown that the latest of these waves reach the spinal cord in 10 milliseconds. Thus, it has been argued that single MEPs elicited in hand muscles should theoretically not be influenced by a suprathreshold test MEP stimulus after this time period [53], which is much shorter than the ITIs of 1–5 s in the aforementioned studies. However, this would not necessarily preclude that a series of successive MEPs (e.g., 5–10) at short ITIs of 1–5 s could result in an initial transient suppression of MEP amplitudes. In summary, research is mixed on the impact of short ITIs on MEP amplitude with the balance of studies being in contrast to the current findings, although differences in methodology and interindividual differences in the response to single-pulse TMS across participants in these studies may explain some of these discrepancies.

4.2. Effects of ITI on Test MEPs. Condition-Test MEPs, and ICF

The application of a subthreshold conditioning TMS pulse followed by a suprathreshold TMS test pulse at ISIs of between 6–25 milliseconds through the same TMS coil leads to the facilitation of the condition-test MEP amplitudes compared to single-pulse test MEP amplitudes. This phenomenon is termed ICF [6,9,10] and is one of the most common paired-pulse TMS measures of intracortical excitability. The present study was the first to investigate the influence of different ITIs on the quantification of ICF. Based on the limited available data on the influence of ITI on single-pulse TMS measurements, it was originally hypothesized that ICF would be lower in the ICF_4 block compared with the ICF_6, ICF_8, and ICF_10 blocks. This could be due to either the initial ICF trials being depressed, a serial reduction in ICF values over the entire block, or a combination of both factors in the ICF_4 block compared to the longer ITI ICF blocks. Therefore, this could cause the overall average of the ICF_4 block to be lower compared to longer ITIs, which would suggest that ICF measured in previous studies at relatively short ITIs could have yielded inaccurate results. Taken together, the aforementioned hypotheses were not confirmed as ICF values were similar for the four ITIs and did not significantly change over the course of time for

any of the ICF blocks. However, the details of the overall results were somewhat nuanced due to a random, non-physiological-based covariation of data as described below.

4.2.1. Effects of ITI on Test MEP Trials Alone

A total of 26 test MEP trials were semi-randomly intermingled with 26 condition-test MEP trials, divided into time epochs, and collectively used to calculate ICF. The test MEP trials were also analyzed alone to determine their specific contribution to ICF. The first 8 test MEP trials that comprised Epoch 1 of the ICF_4 block were technically not statistically different compared with the test MEP trials of Epochs 2 and 3 of ICF_4 and across all the epochs of the other three ICF blocks (ICF_6, ICF_8, and ICF_10). Although there was an *ICF Block* \times *Epoch* interaction (Figure 4A), Bonferroni's post-hoc analyses failed statistical significance ($p = 0.137$) between the ICF_4 and ICF_10 mean pairs in Epoch 1. Based on previous single-pulse ITI studies and this result, one would immediately think that this difference was due to low test MEPs in ICF_4 due to suppression at the short ITI. Crucially, the opposite was true as test MEP amplitudes in ICF_4 were actually much larger than in ICF_10. Thus, there are likely two interrelated reasons for this apparent difference between the two mean pairs: (1) random covariation between the two pairs of means due to the inherent high variability in MEP measurements; and (2) the fact that each epoch only consisted of the average of 8 MEPs makes random occurrences more likely compared to averages across greater numbers of trials (e.g., a whole block). These relationships are clearly reflected in the equations of an extensive review that showed that MEP amplitude estimation error depends on the number of MEP trials and the MEP variability [45]. This topic is covered below when the influence of the test MEP amplitudes in these two epochs on ICF values is discussed.

There was also no evidence of a serial reduction in MEP amplitude over any of the epochs of test MEP trials in any of the ICF blocks (Figure 4A). Test MEP amplitudes did appear to decline slightly over the time course of the ICF_4 trial block, but this small decrease did not reach statistical significance (Figures 5A and 6A). The other ICF blocks displayed even smaller, non-significant serial increases or decreases in test MEP amplitudes over their time courses (Figures 5A and 6B–D). Accordingly, the overall average MEP amplitudes (25 trials) reflected the previous findings and were not significantly different between the four ICF blocks (Figures 4A and 5A). These statistical results are supported by visual inspection of the group average test MEP amplitudes plotted as a function of trial number (Figure 6A–D). In summary, test MEP amplitudes alone displayed no differences across epochs or between ICF blocks. The possible exception was a lower technically non-significant MEP amplitude in Epoch 1 for the ICF_4 compared with the ICF_10 block; however, this was likely due to a random covariation of MEP amplitudes between the two conditions in Epoch 1.

4.2.2. Effects of ITI on Condition-Test MEP Trials Alone

The results of the analysis of the condition-test MEP trials alone were more straightforward compared to the test MEP trial results. Overall, the general findings were similar to those attained in the control blocks. The condition-test MEP amplitudes did not display time-varying characteristics over any of the epochs that comprised a total of 26 condition trials in any of the four ICF blocks (Figure 4B). Thus, condition-test MEP amplitudes fluctuated about the average value observed over the entirety of the ICF blocks (Figure 5B). These statistical findings are supported by visual inspection of the group average condition-test MEP amplitudes plotted as a function of trial number (Figure 6A–D). In summary, condition-test MEP amplitudes neither displayed significant time-varying behavior nor different overall average values across any of the four ICF blocks. Thus, these findings would indicate that the condition-test trials alone should provide only small contributions to any differences observed in the quantification of ICF.

4.2.3. Effects of ITI on ICF

All ICF blocks involved 52 TMS trials that included 26 test MEP trials and 26 condition-test MEP trials that were semi-randomly intermingled, divided into time epochs, and collectively used to calculate ICF. Similar to the analysis of the test MEP trial results alone, there was an *ICF Block × Epoch* interaction (Figure 4C). However, in this case, Bonferroni’s post-hoc analyses were statistically significant and indicated that ICF was lower in the ICF_4 condition compared with the ICF_10 condition in Epoch 1 ($p = 0.015$). Based on previous single-pulse ITI studies and this result, one would immediately think that this difference could be due to the suppression of test MEPs in ICF_4 or some related problem due to the influence of the short ITI of 4 s. However, a detailed analysis of the test MEP and condition-test MEP amplitudes that caused this difference in ICF values indicated random covariation in a similar manner to that described above in the test MEP results (See Figure 8 for a description and theoretical mathematical example using created round numbers). In summary, the seemingly random covariation of the 4 elements is likely responsible for the difference between the 2 elements of ICF in ICF_4 and ICF_10.

Combination #	Test MEP	Condition-Test MEP	Criteria Averages			delta (20%) Resultant ICF Relative to Criteria
			Test MEP (mV) 1	Condition-Test MEP (mV) 1.5	ICF (%) 150%	
1	Higher	Higher	1.2	1.8	150%	SAME
2	Higher	Lower	1.2	1.2	100%	LOWER
3	Higher	Same	1.2	1.5	125%	LOWER
4	Lower	Higher	0.8	1.8	225%	HIGHER
5	Lower	Lower	0.8	1.2	150%	SAME
6	Lower	Same	0.8	1.5	188%	HIGHER
7	Same	Higher	1	1.8	180%	HIGHER
8	Same	Lower	1	1.2	120%	LOWER
9	Same	Same	1	1.5	150%	SAME

Figure 8. Theoretical mathematical example using created round numbers to illustrate the general concept of how random covariation between the 2 elements of ICF (test MEP, condition-test MEP) for 2 separate epochs (blue and red rows) could influence ICF values and therefore the paired *t*-test between the ICF values for the 2 epochs. This analysis is best explained through the six following steps: (1) ICF is calculated as the ratio of the condition-test MEP amplitude to the test MEP amplitude and then expressed as a percentage; (2) this means that for the ICF value of a specified epoch (blue or red rows) to be higher or lower relative to the average ICF value of other epochs (black row criteria average values, a few mathematical conditions must be met; (3) relative to the average condition-test/test MEP = ICF value (150%), there are 3 possible outcomes (higher, lower, the same) for each of the 2 ICF inputs (test MEP, condition-test MEP). Thus, there are 3 (test MEP) × 3 (condition-test MEP) = 9 combinations that can uniquely influence the value of ICF; (4) 3 leads to a lower ICF vs. the average, 3 leads to a higher ICF vs. the average, and 3 lead to the same ICF vs. the average. Note criteria average test MEP and condition-test MEP absolute values (columns 4–5 from left) were multiplied by 20% (delta 20%) to give a lower or higher change; (5) Epoch 1 of the ICF_4 condition (blue) had a higher test MEP and a lower condition-test MEP than average and therefore lower ICF than average; (6) Epoch 1 of the ICF_10 condition had a lower test MEP and a higher condition-test MEP than average and therefore higher ICF than average; and (7) the low ICF in ICF_4 and high ICF in ICF_10 combined to cause the significant difference in ICF in Epoch 1 between ICF_4 and ICF_10.

There was also no evidence of a serial reduction in ICF over the remaining time course of the ICF_4 block. In fact, ICF actually increased in Epoch 2 and especially in Epoch 3 in ICF_4 (Figure 4C). The ICF blocks with the longer ITIs also did not display any significant time-varying behavior (Figure 4C). As a result, the overall average ICF values reflected the previous findings and were not significantly different between the four ICF blocks (Figures 4C and 5C). These statistical findings are supported by visual inspection of the

group average test MEP and condition-test MEP amplitudes plotted as a function of trial number (Figure 6A–D). Finally, a visual inspection of the resulting ICF values plotted as a function of trial number (Figure 7A–D) shows that ICF randomly fluctuated around the average value for all four ITIs utilized in the ICF blocks. In conclusion, ICF displayed no differences across epochs or between ICF blocks, with the exception of a transient significantly lower ICF value in Epoch 1 for the ICF_4 compared with the ICF_10 block. Notably, this difference quickly disappeared by Epoch 2 between these two conditions. As explained above, this exception was likely due to random covariation of the test MEP and condition-test MEP amplitudes in Epoch 1 for both the ICF_4 and ICF_10 conditions (Figures 4 and 8).

4.3. Overall Interpretation of the Combined Control Blocks and ICF Blocks Results

The majority of the current findings were relatively clear. There were negligible, non-significant effects of ITI on the overall single-pulse MEP amplitudes in the control blocks. Similarly, there were negligible, non-significant effects of ITI on single-pulse test MEP and paired-pulse condition-test MEP amplitudes and resulting ICF values. The notable exception was the interrelated outcomes of the test MEP trials and overall ICF values in Epoch 1 of the ICF_4 and ICF_10 blocks. Collectively, several lines of reasoning argue against this one statistical difference being due to an inherent physiological process: (1) the single-pulse MEP amplitudes in both control blocks (1 mV_4 and 1 mV_10) were similar and did not show time-varying characteristics; (2) the test MEP amplitude results in the ICF blocks followed this same pattern. The one exception was the differences in Epoch 1 between ICF_4 and ICF_10. Most importantly, ICF_4 actually had a higher MEP amplitude than ICF_10 in Epoch 1, which would be the opposite finding expected if a physiological mechanism had caused a transient initial suppression of MEP amplitude at the short ITI. Thus, aforementioned exception was almost certainly due to random covariation and the small number of MEP trials per epoch; (3) the condition-test MEP amplitudes were similar across epochs in all four ICF blocks; and (4) ICF also showed no differences across epochs or between ICF blocks, with the exception of a transient significantly lower ICF value in Epoch 1 for the ICF_4 compared with the ICF_10 block. This was also almost certainly a random covariation of the 4 elements (test MEPs and condition-test MEPs in ICF_4 and ICF_10) and not due to physiological suppression of MEPs in the short ITI condition (ICF_4).

4.4. Possible Impact of Methodological Issues on the Results

Methodological details are important in TMS studies as a variety of different experimental and biological factors can influence MEP amplitude and likely collectively lead to the well-known high variability of MEPs. Therefore, numerous experimental controls and the most common and standard methods were employed to minimize any confounding influences. The study utilized almost all of the components of methodological quality listed in recent TMS review articles [5,15,49] and similar methods to many of the existing single-pulse ITI studies [27,29,30,32–34]. Other notable aspects of the study were that the participants were young adults (equal numbers of men and women) in a tight age range and strongly right-handed. Finally, pre and post-MVCs were performed and provided confirmation that the ability to voluntarily activate the FDI muscle and by extension factors such as alertness or arousal [5] that could influence MEPs had not substantially declined over the course of the experiment due to central fatigue.

The methodological issue most relevant to the current study was the relatively common practice of excluding the first 1 or first 3–5 MEPs of a trial block from analysis. It can be clearly seen from the results and visual inspection of the figures that such practices are largely unwarranted for ITIs of 4 s and above. This practice originates from the results of two early TMS studies. Flament et al., (1993) [21] reported that the first MEP trial of a block was commonly deleted from analysis due to the tendency for this trial to be larger than all subsequent responses. Since the ISI varied between 3.5 and 7 s in this study, this would seem to imply that ISIs in this range could lead to a small short-term reduction in MEP

amplitude beginning after the first trial. Unfortunately, these authors did not provide any data to substantiate deleting the first MEP trial and it seems that this practice was adopted based on subjective observations. In another study, Brasil-Neto et al., (1994) [47] observed a progressive decrement in the first 4 MEPs of a series. However, this was after a fatiguing contraction and therefore not relevant to resting conditions, despite its implied relevance when this topic is mentioned [33]. Finally, an extensive study on MEP reliability found no advantage to deleting the first 3–5 trials of a block of MEPS [54].

4.5. Implications and Practical Application of the Findings for ICF Studies

The findings have a least five implications for the practical execution of studies involving both single-pulse TMS and especially ICF measurement: (1) there are no strong reasons to discard the first 3–5 MEP trials of a block for both single-pulse TMS and ICF measurement, especially when ITIs of over 5 s are used; (2) it is probably best practice to be conservative and not combine short ITIs (less than 5 s) and longer ITIs in the same trial block if using randomized ITIs for reasons such as to reduce participant anticipation; (3) based on our pilot work with ITIs over 10 s and the experience with 10 second ITIs in the current study, ITIs above 10 s are not comfortable for the investigators or the participants and are too time consuming in most experimental situations. Most importantly, a prior single-pulse TMS study found no further benefits in MEP measurements for ITIs above 10 s [30]; (4) the common practice of setting the test MEP stimulus intensity to 1 to 1.5 mV seems to allow for relatively accurate MEP measurement for any ITI between 4–10 s. Similarly, previous studies that have used stimulation intensities of 110–120% of RMT support this practice as these result in 1 to 1.5 mV MEPs for most participants [45]; and (5) based on previous studies and the current results, the major point researchers should keep in mind is that there should be no difference in ICF values between ITIs ranging from 4–10 s. Thus, investigators can choose a relatively short ITI if it is more convenient in a given study or a longer one to be conservative and it should not influence the final ICF results. Our overall general recommendation would be to utilize 4–6 second ITIs for both single-pulse TMS and ICF measurements to optimize the trade-off between investigator and participant comfort as well as experimental time efficiency. This would be even more important in clinical studies where patients may be less able to tolerate or maintain concentration in long experiments compared to healthy young adults. Accordingly, we believe the equations and explanations in an extensive review [45] offer an excellent basis for researchers to consider the trade-offs between the number of participants, the number of MEP trials per TMS block, the expected MEP variability, the time available and the number of total TMS blocks needed to answer the research question, and the estimation error deemed acceptable by the investigators.

4.6. Limitations

The study had several limitations that should be acknowledged: (1) ITIs of less than four seconds were not tested in either the single-pulse control blocks or ICF blocks, although this was not possible in the ICF blocks due to technical limitations (see Methods). Nonetheless, based on the combined results of several single-pulse studies [27,29,30,32–34] any ITI below 4 s should have been sufficient to see ITI-related differences if they existed; (2) single-pulse MEPs or ICF were not tested during active muscle contraction conditions. However, it would be highly unlikely that there would be any effect of ITI on MEP amplitude in these conditions based on previous studies [27,32] and the fact that muscle activation at a set background level provides a much more constant state of corticospinal excitability compared to rest; (3) experimental conditions were not included that varied the ITI trial randomly (within a certain range) as some studies have completed (see Introduction). On the other hand, it is highly doubtful in light of the current results and previous studies [27,29,30,32–34] that such an approach would lead to different results, but could be directly tested in future studies as a non-trivial number of TMS studies utilize random ITIs; (4) only ICF was tested and other paired-pulse TMS measures were not investigated. It is

possible that other intracortical pathways, especially perhaps inhibitory ones such as SICI, that are mediated by different neurotransmitter and receptor systems, could yield different results. Accordingly, this possibility will have to be investigated in a future study; (5) it could be argued that the sample size of the current study was somewhat small. However, the sample size of 20 was substantially larger than all of the most relevant single-pulse ITI studies (range 8–17; average 12.5 participants) [27,29,30,32–34]. The sample sizes typically used in most neuroscience studies could almost always be viewed as a limitation [55,56]; and (6) only one combination of the possible parameters for stimulation (e.g., stimulation intensities of the conditioning and test stimuli, different ISIs) was employed. Although this study used the most common and optimal set of parameters to evoke ICF [11], it can't be ruled out that different results could emerge. There is evidence that some methods of eliciting ICF could be dependent on different intracortical neuronal populations [12] so further studies could be warranted.

5. Conclusions

In summary, the primary findings of the study were that ICF values were similar for all four ITIs (4, 6, 8, 10 s) and did not significantly change over the course of time for any of the ICF blocks. The secondary findings were that single-pulse MEP amplitudes were similar for the 4 and 10-second ITIs and did not significantly change over the time course of the trial blocks. Based on these results, it is recommended that ITIs of 4–6 s be utilized for ICF quantification in TMS studies to optimize participant comfort and experiment time efficiency.

Author Contributions: Conceptualization, B.P., M.P. and Z.A.R.; methodology, M.P., B.P. and Z.A.R.; software, M.P. and B.P.; validation, M.P., R.B., K.J.N., M.I.P., D.G.A., E.W.W., S.B. and B.P.; formal analysis, M.P., E.W.W. and B.P.; investigation, R.B., K.J.N., M.I.P., D.G.A., E.W.W., S.B. and M.P.; resources, B.P.; data curation, M.P., E.W.W. and B.P.; writing—original draft preparation, M.P. and B.P.; writing—review and editing, M.P., R.B., K.J.N., M.I.P., D.G.A., E.W.W., S.B., Z.A.R. and B.P.; supervision, B.P.; project administration, M.P., E.W.W. and B.P. All authors have read and agreed to the published version of the manuscript.

Funding: This research received no external funding.

Institutional Review Board Statement: The study was conducted in accordance with the Declaration of Helsinki, and approved by the Institutional Review Board of University of Nevada, Las Vegas (protocol number: 1445199, and original date of approval: 31 July 2019).

Informed Consent Statement: Informed consent was obtained from all subjects involved in the study.

Data Availability Statement: The data presented in the study are available on request from the corresponding author.

Conflicts of Interest: The authors declare no conflict of interest.

References

1. Rothwell, J.C. Techniques and mechanisms of action of transcranial stimulation of the human motor cortex. *J. Neurosci. Methods* **1997**, *74*, 113–122. [CrossRef] [PubMed]
2. Hallett, M. Transcranial magnetic stimulation and the human brain. *Nature* **2000**, *406*, 147–150. [CrossRef] [PubMed]
3. Bestmann, S.; Krakauer, J.W. The uses and interpretations of the motor-evoked potential for understanding behaviour. *Exp. Brain Res.* **2015**, *233*, 679–689. [CrossRef] [PubMed]
4. Nielsen, J.B.; Pyndt, H.S.; Petersen, N.T. Investigating human motor control by transcranial magnetic stimulation. *Exp. Brain Res.* **2003**, *152*, 1–16. [CrossRef] [PubMed]
5. Spampinato, D.A.; Ibanez, J.; Rocchi, L.; Rothwell, J. Motor potentials evoked by transcranial magnetic stimulation: Interpreting a simple measure of a complex system. *J. Physiol.* **2023**, *601*, 2827–2851. [CrossRef] [PubMed]
6. Chen, R. Interactions between inhibitory and excitatory circuits in the human motor cortex. *Exp. Brain Res.* **2004**, *154*, 1–10. [CrossRef]
7. Vucic, S.; Chen, K.-H.S.; Kiernan, M.C.; Hallett, M.; Benninger, D.H.; Di Lazzaro, V.; Rossini, P.M.; Benussi, A.; Berardelli, A.; Currà, A.; et al. Clinical Diagnostic Utility of Transcranial Magnetic Stimulation in Neurological Disorders. Updated Report of an IFCN Committee. *Clin. Neurophysiol.* **2023**, *150*, 131–175. [CrossRef]

8. Siebner, H.R.; Funke, K.; Aberra, A.S.; Antal, A.; Bestmann, S.; Chen, R.; Classen, J.; Davare, M.; Di Lazzaro, V.; Fox, P.T.; et al. Transcranial magnetic stimulation of the brain: What is stimulated?—A consensus and critical position paper. *Clin. Neurophysiol.* **2022**, *140*, 59–97. [CrossRef]
9. Kujirai, T.; Caramia, M.D.; Rothwell, J.C.; Day, B.L.; Thompson, P.D.; Ferbert, A.; Wroe, S.; Asselman, P.; Marsden, C.D. Corticocortical inhibition in human motor cortex. *J. Physiol.* **1993**, *471*, 501–519. [CrossRef]
10. Berardelli, A.; Abbruzzese, G.; Chen, R.; Orth, M.; Ridding, M.C.; Stinear, C.; Suppa, A.; Trompetto, C.; Thompson, P.D. Consensus paper on short-interval intracortical inhibition and other transcranial magnetic stimulation intracortical paradigms in movement disorders. *Brain Stimul.* **2008**, *1*, 183–191. [CrossRef]
11. Ortu, E.; Deriu, F.; Suppa, A.; Tolu, E.; Rothwell, J.C. Effects of volitional contraction on intracortical inhibition and facilitation in the human motor cortex. *J. Physiol.* **2008**, *586*, 5147–5159. [CrossRef] [PubMed]
12. Reis, J.; Swayne, O.B.; Vandermeeren, Y.; Camus, M.; Dimyan, M.A.; Harris-Love, M.; Perez, M.A.; Ragert, P.; Rothwell, J.C.; Cohen, L.G. Contribution of transcranial magnetic stimulation to the understanding of cortical mechanisms involved in motor control. *J. Physiol.* **2008**, *586*, 325–351. [CrossRef] [PubMed]
13. Ni, Z.; Chen, R. Transcranial magnetic stimulation to understand pathophysiology and as potential treatment for neurodegenerative diseases. *Transl. Neurodegener.* **2015**, *4*, 22. [CrossRef] [PubMed]
14. Groppa, S.; Oliviero, A.; Eisen, A.; Quartarone, A.; Cohen, L.; Mall, V.; Kaelin-Lang, A.; Mima, T.; Rossi, S.; Thickbroom, G.; et al. A practical guide to diagnostic transcranial magnetic stimulation: Report of an IFCN committee. *Clin. Neurophysiol.* **2012**, *123*, 858–882. [CrossRef] [PubMed]
15. Chipchase, L.; Schabrun, S.; Cohen, L.; Hodges, P.; Ridding, M.; Rothwell, J.; Taylor, J.; Ziemann, U. A checklist for assessing the methodological quality of studies using transcranial magnetic stimulation to study the motor system: An international consensus study. *Clin. Neurophysiol.* **2012**, *123*, 1698–1704. [CrossRef]
16. Zehr, E.P. Considerations for use of the Hoffmann reflex in exercise studies. *Eur. J. Appl. Physiol.* **2002**, *86*, 455–468. [CrossRef]
17. Stein, R.B.; Estabrooks, K.L.; McGie, S.; Roth, M.J.; Jones, K.E. Quantifying the effects of voluntary contraction and inter-stimulus interval on the human soleus H-reflex. *Exp. Brain Res.* **2007**, *182*, 309–319. [CrossRef]
18. Rosburg, T.; Zimmerer, K.; Huonker, R. Short-term habituation of auditory evoked potential and neuromagnetic field components in dependence of the interstimulus interval. *Exp. Brain Res.* **2010**, *205*, 559–570. [CrossRef]
19. Doeltgen, S.H.; McAllister, S.M.; Ridding, M.C. Simultaneous application of slow-oscillation transcranial direct current stimulation and theta burst stimulation prolongs continuous theta burst stimulation-induced suppression of corticomotor excitability in humans. *Eur. J. Neurosci.* **2012**, *36*, 2661–2668. [CrossRef]
20. Tinazzi, M.; Farina, S.; Tamburin, S.; Facchini, S.; Fiaschi, A.; Restivo, D.; Berardelli, A. Task-dependent modulation of excitatory and inhibitory functions within the human primary motor cortex. *Exp. Brain Res.* **2003**, *150*, 222–229. [CrossRef]
21. Flament, D.; Goldsmith, P.; Buckley, C.J.; Lemon, R.N. Task dependence of responses in first dorsal interosseous muscle to magnetic brain stimulation in man. *J. Physiol.* **1993**, *464*, 361–378. [CrossRef]
22. Kimiskidis, V.K.; Papagiannopoulos, S.; Sotirakoglou, K.; Kazis, D.A.; Kazis, A.; Mills, K.R. Silent period to transcranial magnetic stimulation: Construction and properties of stimulus–response curves in healthy volunteers. *Exp. Brain Res.* **2005**, *163*, 21–31. [CrossRef]
23. Devanne, H.; Lavoie, B.A.; Capaday, C. Input-output properties and gain changes in the human corticospinal pathway. *Exp. Brain Res.* **1997**, *114*, 329–338. [CrossRef]
24. Hoogendam, J.M.; Ramakers, G.M.J.; Di Lazzaro, V. Physiology of repetitive transcranial magnetic stimulation of the human brain. *Brain Stimul.* **2010**, *3*, 95–118. [CrossRef]
25. Ridding, M.C.; Rothwell, J.C. Is There a Future for Therapeutic Use of Transcranial Magnetic Stimulation? *Nat. Rev. Neurosci.* **2007**, *8*, 559–567. [CrossRef]
26. Pascual-Leone, A.; Valls-Solé, J.; Wassermann, E.M.; Hallett, M. Responses to rapid-rate transcranial magnetic stimulation of the human motor cortex. *Brain* **1994**, *117 Pt 4*, 847–858. [CrossRef]
27. Möller, C.; Arai, N.; Lücke, J.; Ziemann, U. Hysteresis effects on the input–output curve of motor evoked potentials. *Clin. Neurophysiol.* **2009**, *120*, 1003–1008. [CrossRef]
28. Hansen, N.L.; Nielsen, J.B. The effect of transcranial magnetic stimulation and peripheral nerve stimulation on corticomuscular coherence in humans. *J. Physiol.* **2004**, *561*, 295–306. [CrossRef]
29. Julkunen, P.; Saisanen, L.; Hukkanen, T.; Danner, N.; Kononen, M. Does Second-Scale Intertrial Interval Affect Motor Evoked Potentials Induced by Single-Pulse Transcranial Magnetic Stimulation? *Brain Stimul.* **2012**, *5*, 526–532. [CrossRef]
30. Hassanzahraee, M.; Zoghi, M.; Jaberzadeh, S. Longer Transcranial Magnetic Stimulation Intertrial Interval Increases Size, Reduces Variability, and Improves the Reliability of Motor Evoked Potentials. *Brain Connect.* **2019**, *9*, 770–776. [CrossRef]
31. Oldfield, R.C. The assessment and analysis of handedness: The Edinburgh inventory. *Neuropsychologia* **1971**, *9*, 97–113. [CrossRef]
32. Matilainen, N.; Soldati, M.; Laakso, I. The Effect of Inter-pulse Interval on TMS Motor Evoked Potentials in Active Muscles. *Front. Hum. Neurosci.* **2022**, *16*, 845476. [CrossRef]
33. Schmidt, S.; Cichy, R.; Kraft, A.; Brocke, J.; Irlbacher, K.; Brandt, S. An initial transient-state and reliable measures of corticospinal excitability in TMS studies. *Clin. Neurophysiol.* **2009**, *120*, 987–993. [CrossRef]
34. Vaseghi, B.; Zoghi, M.; Jaberzadeh, S. Inter-pulse Interval Affects the Size of Single-pulse TMS-induced Motor Evoked Potentials: A Reliability Study. *Basic Clin. Neurosci.* **2015**, *6*, 44–51.

35. Poston, B.; Kukke, S.N.; Paine, R.W.; Francis, S.; Hallett, M. Cortical silent period duration and its implications for surround inhibition of a hand muscle. *Eur. J. Neurosci.* **2012**, *36*, 2964–2971. [CrossRef]
36. de Albuquerque, L.L.; Pantovic, M.; Clingo, M.; Fischer, K.; Jalene, S.; Landers, M.; Mari, Z.; Poston, B. A Single Application of Cerebellar Transcranial Direct Current Stimulation Fails to Enhance Motor Skill Acquisition in Parkinson's Disease: A Pilot Study. *Biomedicines* **2023**, *11*, 2219. [CrossRef]
37. Dominici, F.; Popa, T.; Ginanneschi, F.; Mazzocchio, R.; Rossi, A. Cortico-motoneuronal output to intrinsic hand muscles is differentially influenced by static changes in shoulder positions. *Exp. Brain Res.* **2005**, *164*, 500–504. [CrossRef]
38. Ginanneschi, F.; Del Santo, F.; Dominici, F.; Gelli, F.; Mazzocchio, R.; Rossi, A. Changes in corticomotor excitability of hand muscles in relation to static shoulder positions. *Exp. Brain Res.* **2005**, *161*, 374–382. [CrossRef]
39. Do, M.; Clark, G.M.; Fuelscher, I.; Kirkovski, M.; Cerins, A.; Corp, D.T.; Bereznicki, H.G.; Albein-Urios, N.; Enticott, P.G. Magstim 2002 and Bistim Mode maximum stimulus output values are not equivalent: Configuration selection is critical. *Brain Stimul.* **2020**, *13*, 444–446. [CrossRef]
40. de Albuquerque, L.L.; Fischer, K.M.; Pauls, A.L.; Pantovic, M.; Guadagnoli, M.A.; Riley, Z.A.; Poston, B. An acute application of transcranial random noise stimulation does not enhance motor skill acquisition or retention in a golf putting task. *Hum. Mov. Sci.* **2019**, *66*, 241–248. [CrossRef]
41. Lidstone, D.E.; Miah, F.Z.; Poston, B.; Beasley, J.F.; Mostofsky, S.H.; Dufek, J.S. Children with Autism Spectrum Disorder Show Impairments During Dynamic Versus Static Grip-force Tracking. *Autism Res.* **2020**, *13*, 2177–2189. [CrossRef]
42. De Albuquerque, L.L.; Pantovic, M.; Clingo, M.; Fischer, K.; Jalene, S.; Landers, M.; Mari, Z.; Poston, B. An Acute Application of Cerebellar Transcranial Direct Current Stimulation Does Not Improve Motor Performance in Parkinson's Disease. *Brain Sci.* **2020**, *10*, 735. [CrossRef]
43. Gandevia, S.C. Spinal and Supraspinal Factors in Human Muscle Fatigue. *Physiol. Rev.* **2001**, *81*, 1725–1789. [CrossRef]
44. Pantovic, M.; de Albuquerque, L.L.; Mastrantonio, S.; Pomerantz, A.S.; Wilkins, E.W.; Riley, Z.A.; Guadagnoli, M.A.; Poston, B. Transcranial Direct Current Stimulation of Primary Motor Cortex over Multiple Days Improves Motor Learning of a Complex Overhand Throwing Task. *Brain Sci.* **2023**, *13*, 1441. [CrossRef]
45. Ammann, C.; Guida, P.; Caballero-Insaurriaga, J.; Pineda-Pardo, J.A.; Oliviero, A.; Foffani, G. A framework to assess the impact of number of trials on the amplitude of motor evoked potentials. *Sci. Rep.* **2020**, *10*, 21422. [CrossRef]
46. de Albuquerque, L.L.; Pantovic, M.; Clingo, M.G.; Fischer, K.M.; Jalene, S.; Landers, M.R.; Mari, Z.; Poston, B. Long-Term Application of Cerebellar Transcranial Direct Current Stimulation Does Not Improve Motor Learning in Parkinson's Disease. *Cerebellum* **2022**, *21*, 333–349. [CrossRef]
47. Brasil-Neto, J.P.; Cohen, L.G.; Hallett, M. Central fatigue as revealed by postexercise decrement of motor evoked potentials. *Muscle Nerve* **1994**, *17*, 713–719. [CrossRef]
48. Brasil-Neto, J.P.; Pascual-Leone, A.; Cammarota, A.; Cohen, L.G.; Hallett, M.; Valls-Solé, J. Postexercise depression of motor evoked potentials: A measure of central nervous system fatigue. *Exp. Brain Res.* **1993**, *93*, 181–184. [CrossRef]
49. Cavaleri, R.; Schabrun, S.M.; Chipchase, L.S. The number of stimuli required to reliably assess corticomotor excitability and primary motor cortical representations using transcranial magnetic stimulation (TMS): A systematic review and meta-analysis. *Syst. Rev.* **2017**, *6*, 48. [CrossRef]
50. Corp, D.T.; Bereznicki, H.G.; Clark, G.M.; Youssef, G.J.; Fried, P.J.; Jannati, A.; Davies, C.B.; Gomes-Osman, J.; Kirkovski, M.; Albein-Urios, N.; et al. Large-scale analysis of interindividual variability in single and paired-pulse TMS data. *Clin. Neurophysiol.* **2021**, *132*, 2639–2653. [CrossRef]
51. Di Lazzaro, V.; Oliviero, A.; Saturno, E.; Pilato, F.; Insola, A.; Mazzone, P.; Profice, P.; Tonali, P.; Rothwell, J. The effect on corticospinal volleys of reversing the direction of current induced in the motor cortex by transcranial magnetic stimulation. *Exp. Brain Res.* **2001**, *138*, 268–273. [CrossRef]
52. Di Lazzaro, V.; Restuccia, D.; Oliviero, A.; Profice, P.; Ferrara, L.; Insola, A.; Mazzone, P.; Tonali, P.; Rothwell, J.C. Effects of voluntary contraction on descending volleys evoked by transcranial stimulation in conscious humans. *J. Physiol.* **1998**, *508 Pt 2*, 625–633. [CrossRef]
53. Corp, D.T.; He, J.; Cooke, D.; Perellón-Alfonso, R.; Joutsa, J.; Pascual-Leone, A.; Fox, M.D.; Hyde, C. 'Expedited Interhemispheric Inhibition': A Simple Method to Collect Additional IHI Data in the Same Amount of Time. *Brain Topogr.* **2021**, *34*, 1–5. [CrossRef]
54. Hashemirad, F.; Zoghi, M.; Fitzgerald, P.B.; Jaberzadeh, S. Reliability of Motor Evoked Potentials Induced by Transcranial Magnetic Stimulation: The Effects of Initial Motor Evoked Potentials Removal. *Basic Clin. Neurosci. J.* **2017**, *8*, 43–50. [CrossRef]
55. Szucs, D.; Ioannidis, J.P. Sample size evolution in neuroimaging research: An evaluation of highly-cited studies (1990–2012) and of latest practices (2017–2018) in high-impact journals. *NeuroImage* **2020**, *221*, 117164. [CrossRef]
56. Consideration of Sample Size in Neuroscience Studies. *J. Neurosci.* **2020**, *40*, 4076–4077. [CrossRef]

Disclaimer/Publisher's Note: The statements, opinions and data contained in all publications are solely those of the individual author(s) and contributor(s) and not of MDPI and/or the editor(s). MDPI and/or the editor(s) disclaim responsibility for any injury to people or property resulting from any ideas, methods, instructions or products referred to in the content.

Article

Exploring the Influence of Inter-Trial Interval on the Assessment of Short-Interval Intracortical Inhibition

Lidio Lima de Albuquerque¹, Milan Pantovic², Erik W. Wilkins³, Desiree Morris⁴, Mitchell Clingo⁴, Sage Boss⁵, Zachary A. Riley⁶ and Brach Poston^{3,*}

¹ School of Health and Applied Human Sciences, University of North Carolina Wilmington, Wilmington, NC 28403, USA; limadeal@uncw.edu

² Health and Human Performance Department, Utah Tech University, St. George, UT 84770, USA; milan.pantovic@utahtech.edu

³ Department of Kinesiology and Nutrition Sciences, University of Nevada Las Vegas, Las Vegas, NV 89154, USA; wilkie1@unlv.nevada.edu

⁴ School of Medicine, University of Nevada-Las Vegas, Las Vegas, NV 89154, USA; morrid3@unlv.nevada.edu (D.M.); clingom@unlv.nevada.edu (M.C.)

⁵ School of Life Sciences, University of Nevada-Las Vegas, Las Vegas, NV 89154, USA; bosss1@unlv.nevada.edu

⁶ Department of Kinesiology, Indiana University Purdue University Indianapolis, Indianapolis, IN 46202, USA; zariley@iupui.edu

* Correspondence: brach.poston@unlv.edu; Tel.: +1-702-895-5329

Abstract: Short-interval intracortical inhibition (SICI) is a common paired-pulse transcranial magnetic stimulation (TMS) measure used to assess primary motor cortex (M1) interneuron activity in healthy populations and in neurological disorders. Many of the parameters of TMS stimulation to most accurately measure SICI have been determined. However, one TMS parameter that has not been investigated is the time between SICI trials (termed inter-trial interval; ITI). This is despite a series of single-pulse TMS studies which have reported that motor evoked potential (MEP) amplitude were suppressed for short, but not long ITIs in approximately the initial ten trials of a TMS block of 20–30 trials. The primary purpose was to examine the effects of ITI on the quantification of SICI at rest. A total of 23 healthy adults completed an experimental session that included four SICI trial blocks. Each block utilized a different ITI (4, 6, 8, and 10 s) and was comprised of a total of 26 SICI trials divided into three epochs. ANOVA revealed that the main effects for ITI and epoch as well as their interaction were all non-statistically significant for SICI. We conclude that the shorter (4–6 s) ITIs used in studies investigating SICI should not alter the interpretation of M1 activity, while having the advantages of being more comfortable to participants and reducing the experimental time needed to evaluate perform single and paired-pulse TMS experiments.

Keywords: short-interval intracortical inhibition; transcranial magnetic stimulation; motor evoked potential; intracortical facilitation; short-interval intracortical facilitation; electromyography

1. Introduction

Transcranial magnetic stimulation (TMS) is an established noninvasive brain stimulation technique that is frequently used to evaluate net corticospinal excitability in neurophysiology and motor control studies [1–5]. This is accomplished through the measurement of the motor evoked potential, which is the brief response generated in the electromyography (EMG) recording about 21–23 ms after a single TMS pulse above motor threshold is delivered to the primary motor cortex (M1) [3,6]. Moreover, two separate MEPs can be combined in short succession in paired-pulse TMS protocols. This involves the application of a below-threshold conditioning TMS pulse that is followed by an above-threshold test TMS pulse using various timespans (inter-stimulus intervals; ISIs) between the conditioning and test pulses. In addition, the exact stimulation intensities of the pulses can also be modulated. Accordingly, a number of condition–test protocols have been developed

to quantify different intracortical interneuronal inhibitory and excitatory pathways in M1 [7–9]. These primarily include short-interval intracortical inhibition (SICI), intracortical facilitation (ICF), long-interval intracortical inhibition, and short-interval intracortical facilitation (SICF). Importantly, extensive prior combined physiological and pharmacological studies have determined that the function of these pathways are mediated by different neurotransmitter and receptor systems. However, SICI is the most extensively investigated of these intracortical neuron systems [7,10–12], and seems to have the most direct relevance to certain aspects of motor behavior, such as movement initiation [13], force relaxation [14], and motor learning [15–17].

The phenomenon of SICI was first identified in a classic study [10] by Kujirai and colleagues (1993). The research methodology was based on older animal studies that utilized cortical electrical stimulation and involved interhemispheric inhibition [18]. The main findings were that short ISIs of 1–6 ms resulted in pronounced inhibition of the condition–test MEP compared to the test MEP alone. In contrast, longer ISIs of 10 and 15 ms resulted in pronounced facilitation of the condition–test MEP compared to the test MEP alone. These measurements later became to be known as SICI and ICF, respectively. Subsequently, research focused on the best stimulation intensities and ISIs to employ to optimize the measurement of SICI with a study by Ortu and colleagues probably representing the most comprehensive SICI parameter assessment [12]. Extensive work has also been performed to uncover the physiological mechanisms underlying SICI and the roles that it may play in movement. SICI results from the activation of an inhibitory population of small inhibitory neurons that modulate the activity of pyramidal cells. Specifically, accumulated evidence from concurrent cortical physiology and spinal reflex measurements as well as studies involving descending spinal cord volleys determined that SICI originates at the cortical and at the levels of the brainstem or spinal cord [7,11,13,19]. In addition, SICI has been determined to be primarily mediated via chandelier cell activity through inputs onto M1 pyramid cells at their axonal hillock. Furthermore, pharmacological studies have pointed to the involvement of the alpha-2-subunit-bearing subtype and not the alpha-1-subunit-bearing subtype of the GABA_A receptor in these connections. The interneuronal populations responsible for SICI also receive inputs from other intercortical and intracortical pathways (for visual depictions and review, see Reis et al., 2008 [13]). The functional significance of these pathways to and from SICI has been demonstrated by a observations that SICI is not only involved in the initiation of movements, force modulation, and motor skill acquisition in healthy adults, but is also impaired in a number of movement disorders [7,11,19] that exhibit deficits in these and other facets of movement control.

Based on the widespread application and critical role TMS plays in many neurophysiology and motor control studies, considerable efforts have been dedicated to establishing optimal methodological frameworks [20] and formulating guidelines published in review articles for conducting TMS research utilizing these approaches [11]. An example of such an effort was the convening of a large international expert panel where the relative importance of over 20 critical methodological aspects were surveyed [21]. The time between MEP trials, henceforth referred to as the inter-trial interval (ITI), and not to be confused with ISI, was included as one of these critical TMS parameters. The results revealed that over 80% of the panelists voted that ITI was important or very important to experimentally control and that it's chosen value should be explicitly stated always or most of the time. This is notable, as this relatively early paper is perhaps the only review that has dedicated any attention to ITI. In spite of this consensus viewpoint and other strong evidence from other types of stimulation such as the H-reflex [22,23] and auditory evoked potentials [24], there seem to be no specific standards concerning ITI to implement between single-pulse and especially paired-pulse MEPs. This is in stark contrast to numerous studies and reviews concerning almost all of the other 20 aforementioned methodological items involved in TMS studies. It is therefore not surprising that a large and varied assortment of ITI approaches are present in the literature. For example, some studies have used exceedingly long ITIs ranging from 15 to 30 s [25,26], whereas others have used exceptionally short ones of between 1.5 and

5 s [12,27]. Another practice is to vary the ITI between trials randomly within range around a set average ITI [28,29]. Additionally, it appears that the most frequently employed ITIs span between 4 or 6 s, though a significant portion of studies either use ambiguous wording or neglect to report the ITI altogether [30].

The limited focus on ITI in comparison to other TMS stimulation parameters is not easily explained, but likely stems from the prevailing assumption that only repetitive TMS techniques involving high-frequency stimulation over extended periods result in lasting post-stimulation effects [31–33]. Accordingly, ITIs of one second or more would be expected to not induce time-dependent changes in MEP amplitudes across successive trials. This view is supported by findings suggesting that single TMS pulses to M1 transiently enhance cortico-muscular coherence for only a brief period of less than a second before returning to pre-stimulation levels [34]. However, certain studies contradict this notion, showing variations in MEP amplitudes within a series of trials, indicating potential influences of ITI on single-pulse TMS MEP measurement [35]. Another more comprehensive study demonstrated statistically significant differences in MEPs evoked at short ITIs (5 s and below) versus a long (10 s) ITI using a set TMS stimulation intensity. Most importantly, this phenomenon mainly occurred in the first 10 of the 30 MEPs constituting a block of trials. These studies and others [36,37] suggest that ITI may indeed play a non-trivial role in the variability of MEP measurements, which would warrant further investigation and potential reevaluation of ITI practices in TMS research to ensure valid and reliable findings.

A recent study performed in our laboratory was the first to determine the influence of ITI on any measure of paired-pulse TMS [38] and found no effect of ITI on ICF. However, no studies have explored how different ITIs might affect quantification of SICI. This is despite the prevalence of SICI research, the importance of SICI in movement control, and that SICI is mediated by different neurotransmitter and receptor systems than other paired-pulse TMS measures such as ICF. Furthermore, single-pulse TMS seems to be subject to the influence of ITI [35–37,39–41] and SICI quantification involves the pseudorandom interleaving of condition–test MEP trials and single-pulse test MEP trials within a TMS block. In addition, a test MEP is also obviously a constituent of the condition–test MEP. These lines of rationale form the basis for the possibility that short ITIs of approximately 6 s and below that have been used in the majority of SICI studies may have negatively affected the SICI values obtained in studies involving healthy adults and in patients with movement disorders. This possibility would be more likely the many studies that have involved small sample sizes or a relatively small number of MEP trials [42], which have also been the case in many SICI studies. Thus, the primary purpose was to examine the effects of ITI on the quantification of SICI at rest. This was accomplished by quantifying SICI in four separate trial blocks that utilized ITIs of 4, 6, 8, and 10 s. Based on a number of previous single-pulse TMS studies [35,36], it was predicted that the magnitude of SICI in the short (4 s ITI) SICI block would be increased (greater inhibition) compared with the 6, 8, and 10 s ITI SICI blocks. In addition, it was hypothesized that these differences would be manifested through an initial suppression (greater inhibition) over approximately the first 8–10 MEP trials and would not be due to a serial increase (more inhibition) in SICI over the entire trial block. The secondary purpose was to determine the effects of ITI on the quantification of single-pulse MEP amplitudes at rest. This was achieved by measuring single-pulse MEP amplitudes in two control blocks using ITIs of 4 and 10 s, respectively. It was predicted based on prior single-pulse TMS studies [35–37] that the 4 s ITI control block would exhibit a lower average MEP amplitude compared with the 10 s ITI control block. Finally, it was expected that this would be due to significantly lower MEP amplitudes over approximately the first 8–10 MEP trials and not a gradual decrease in MEP amplitude over the entire duration of the 4 s ITI control block.

2. Materials and Methods

2.1. Participants

The experiments were performed on the right hand of a total of 23 (12 males and 11 females; average age: 26.7 ± 6.0 years) healthy young participants. Participants were recruited using flyers posted in several buildings throughout the university. Inclusion criteria included (1) ability to provide informed consent; (2) being free from any known neurological or psychiatric condition; (3) age between 18 and 45 years old; and (4) being right-handed. Accordingly, all participants were right-handed as evidenced by the Edinburgh Handedness Inventory [43]. Exclusion criteria included (1) an uncontrolled medical condition; (2) metal in the skull or eye such as a cardiac pacemaker, brain stimulator, shrapnel, surgical metal, clips in the brain, cochlear implants, and metal fragments in the eye; (3) diagnosed hearing loss; (4) having had a brain tumor, a stroke, head trauma, epilepsy, or a history of seizures, having a neurological disorder or a movement disorder, or having a head injury that involved being passed out for more than a few seconds; and (5) being pregnant or thought to be pregnant. Finally, participants were screened to confirm that they did not meet the exclusion criteria for noninvasive brain stimulation [20]. The study was approved by the Institutional Review Board at the University of Nevada, Las Vegas and performed in accordance with the Declaration of Helsinki.

2.2. Experimental Design

Participants completed a single experimental session (~2 h), and the experimental steps were completed in the following order: (1) maximum voluntary contractions (MVCs); (2) identification of the motor hotspot location; (3) resting motor threshold (RMT) determination; (4) 1 mV stimulation intensity quantification; (5) two control blocks of single-pulse MEPs that were evoked with ITIs of 4 and 10 s (hereafter referred to as the 1 mV_4 and 1 mV_10 conditions); (6) four SICI trial blocks that involved ITIs of 4, 6, 8, and 10 s (hereafter referred to as the SICI_4, SICI_6, SICI_8, and SICI_10 conditions), and (7) MVCs. These experimental steps are depicted in Figure 1 and the methodology of each of the steps is described in the sections below.

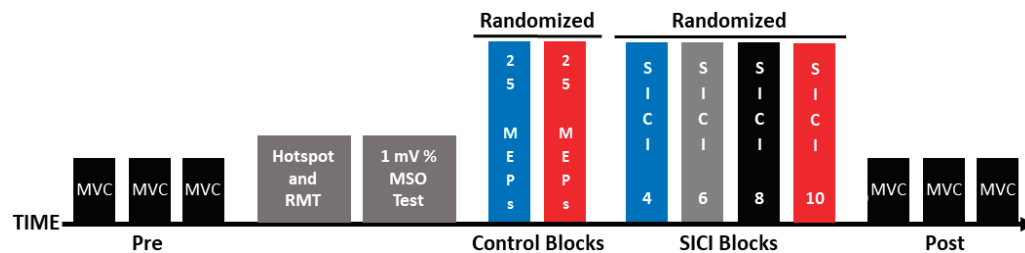


Figure 1. Experimental protocol. Each experiment involved the following set of procedures: pre-MVCs, identification of the motor hotspot location, RMT determination, 1 mV stimulation intensity quantification, control blocks (1 mV_4 and 1 mV_10), SICI blocks (SICI_4, SICI_6, SICI_8, and SICI_10), and post-MVCs.

2.3. Experimental Arrangement

The first dorsal interosseus (FDI) muscle of the right hand was the target muscle for all experimental testing. Participants sat in a chair beside a table with the forearm resting on the table surface. The upper limb posture was set so that the shoulder was abducted (~45 degrees), the elbow was flexed (~90 degrees), the wrist was in neutral, and the right hand was prone [44]. This posture was strictly maintained during all TMS procedures as it has been clearly shown that MEPs evoked in hand muscles can be significantly altered when the configuration of the upper limb is changed [45,46]. The right FDI muscle EMG activity was provided as feedback on a computer monitor that was situated in front of the participants. The participants were given stringent and detailed directions before the TMS testing blocks began on how to utilize the visual EMG feedback to make sure that the FDI was deactivated and at rest for all of the TMS testing procedures. In all TMS testing, the

participants could see the baseline EMG noise level on the screen at a high gain [47]. A black horizontal cursor line was placed at a level of 25 microvolts above the top of the baseline noise. Participants were told not to let the EMG level go above this line for a sustained period of time as it would represent a light muscle contraction. To further ensure that the FDI was relaxed, the same computer display was continually monitored by one of the three to four investigators present in the data collection of each experiment. This investigator had the sole responsibility of incessantly scrutinizing the EMG level and the participant's body and hand posture. Accordingly, this investigator provided verbal feedback to participants as needed if the EMG signal indicated that the FDI was contracting at any time point during the TMS testing blocks. Finally, the data analysis programs checked for any MEP trials that had an FDI EMG level greater than an average of 25 microvolts in the 50 ms before the MEP was evoked in each trial. This was carried out to identify trials for further inspection and rejection if this criterion were met, which is a common process in TMS experiments [48]. However, no trials had to be rejected in the study.

TMS was applied via two Magstim 200² stimulators linked by a Bistim module and through a double 70 mm remote control figure-of-eight coil. The TMS unit was put in the Bistim Mode [49] configuration for all of the single and paired-pulse TMS measurements. The coil was positioned tangential to the scalp and the coil handle was positioned laterally and backwards at an angle of 45 degrees with respect to the midline. The TMS coil was placed over the scalp site corresponding to the FDI muscle's "motor hot spot" of the left M1 to elicit MEPs in the FDI of the right hand [50]. The right FDI EMG activity was recorded with surface electrodes placed in a belly tendon montage. The EMG signals were collected utilizing Cambridge Electronic Design (CED); Cambridge, UK software (Signal 5.04) and hardware (micro 1401 data acquisition interface and 1902 amplifiers).

2.4. Experimental Procedures

2.4.1. MVCs

The MVCs were performed using index finger abduction as the FDI was the target muscle for the TMS procedures and almost all index finger abduction force is generated by the FDI muscle [51]. A custom manipulandum mounting a force transducer was located on the table close to the block where the hand was placed. This allowed participants to produce force on that transducer at the proximal interphalangeal joint of the right index finger. The MVCs were collected using methodology similar to prior studies [52–54]. Participants were required to exert their maximum force in the shortest possible time and to maintain the maximum for approximately 5 s [53]. The FDI force was provided to participants by a red force trace on a computer monitor. A total of three MVC trials were performed at both the start (pre-MVCs) and end of the experimental session (post-MVCs) with a minute of rest between all trials.

These pre- and post-MVCs were completed to give some assurance that the voluntary activation capacity of the right FDI muscle had not considerably decreased during the experimental session due to some manifestation of central or mental fatigue. For example, MEP amplitude can be affected by changes in attention, arousal, and alertness [6]. Since the experiments in this study lasted approximately two hours, the levels of concentration needed during the experiment could potentially have led to mental fatigue and influenced MEP measurements. Accordingly, it has been established since the beginning of fatigue research that voluntary muscle activation can be reduced following mental fatigue alone [55]. While the probability of meaningful levels of mental and central fatigue were likely very low due to all of the experimental procedures being completed with the FDI muscle at rest, the MVCs nonetheless served as a relevant, simple, and time-efficient experimental control.

2.4.2. Motor Hotspot Identification

The TMS coil was moved over the scalp while suprathreshold TMS pulses were applied until the point where the highest MEPs in the right FDI was identified. This site was designated as the FDI motor hot spot, and all MEPs were evoked from this location.

Finally, the associated TMS coil position was outlined on a scalp cap to ensure a constant coil position throughout the experiment and the position of the scalp cap on the forehead was marked using an erasable marker [50].

2.4.3. RMT

RMT was quantified according to standard practice and was defined as the lowest TMS stimulation intensity needed to elicit a MEP with a 50-microvolt peak-to-peak amplitude in a minimum of 5 out of 10 consecutive TMS trials [56]. The RMT obtained from each participant was taken to calculate the individual TMS conditioning pulse stimulation intensity needed for the SICI measurements.

2.4.4. The 1 mV Stimulation Intensity Quantification

The 1 mV stimulation intensity as a percentage of maximum stimulator output (%MSO) was determined according to the procedures of previous studies [57,58]. Briefly, the stimulation intensity started at 55% of MSO and adjusted while MEPs were monitored and quantified online until the average MEP amplitudes were as close as possible to 1 mV. Subsequently, this stimulation intensity was utilized for all of the single-pulse TMS MEPs obtained in the control blocks and for the test MEPs in the SICI blocks. Importantly, the 1 mV stimulation intensity quantification was completed using an ITI of 10 s as this corresponded to the longest ITI in the present study. In addition, this choice was based on prior single-pulse TMS ITI studies [35–37] whose results had collectively indicated that ITIs of 10 s and above should definitely be sufficient to reflect the best estimate for 1 mV stimulation intensity value and should not be subject to time-dependent effects.

2.4.5. Control Blocks

Two separate control blocks involving single-pulse TMS trials were completed in randomized order. These blocks were included in the study so that the findings could be compared to a series of prior ITI studies [35–37] that only involved single-pulse TMS. In addition, these blocks also provided a control comparison to the single-pulse test MEPs evoked in the SICI blocks. One control block utilized an ITI of 4 s, whereas the other control block utilized an ITI of 10 s (herein referred to as the 1 mV_4 and 1 mV_10 control blocks, respectively). Therefore, the control blocks comprised the shortest (4 s) and longest (10 s) ITIs that were later employed in the SICI blocks. Since differences across ITIs were most likely to be seen between the 4 and 10 s ITIs, the 6 and 8 s ITIs used in the SICI blocks were not included in the control blocks to keep the total experiment time from exceeding two hours.

Both control blocks consisted of 25 MEPs evoked utilizing the previously determined 1 mV stimulation intensity for each individual participant. The 1 mV stimulation intensity is the most common value used to quantify changes in MEP amplitude before and after various experimental interventions in TMS studies. Furthermore, the stimulation intensity to evoke a 1 mV MEP also serves as the test MEP stimulation intensity in virtually all paired pulse TMS studies. The total of 25 MEP trials per block was chosen based on the following rationale. First, a detailed quantitative study [42] reported that a total of 20–30 MEPs per trial block strikes the best balance between the requisite number of trials to minimize estimation error for average MEP. Second, this was also the range of MEPs that the same authors determined is most appropriate and realistic to accomplish due to time and other constraints inherent in most TMS studies; and third, the most comparable previous ITI studies involving single-pulse TMS utilized 25 and 30 MEP trials per block [35,37].

2.4.6. SICI Blocks

SICI was measured at ITIs of 4, 6, 8, and 10 s (herein referred to as SICI_4, SICI_6, SICI_8, and SICI_10) in four separate blocks of trials that were completed in randomized order. Thus, the only difference between the SICI blocks was the ITI that was utilized. SICI was evoked using constant parameters that were selected because they have been the

most common in the literature and determined to be the optimal to detect SICI at rest [12]. Specifically, the conditioning pulse stimulation intensity was 90% of RMT, the test pulse stimulation was the 1 mV stimulation intensity as a % MSO, and the ISI was 3 ms.

Each of the four SICI blocks consisted of 52 total trials that included 26 test MEP trials evoked with single-pulse TMS and 26 condition-test MEP trials evoked with paired-pulse TMS. These two types of TMS trials were delivered in a semi-randomized order, which involved each consecutive set of two TMS trials being randomized between the two types of trials. Therefore, a total of 26 SICI measurements were taken in each block. SICI was calculated by dividing the condition–test MEP amplitude by the test MEP amplitude and expressed in percentage terms, which corresponds to the percent inhibition. Twenty-six trials per block were chosen for reasons analogous to those stated above for the number of 25 total MEPs in each of the control blocks. Furthermore, this would have permitted a minimum of 25 SICI measurements in case the first test MEP and condition–test MEP would have had to be deleted from the analyzes. However, this deletion ultimately was not necessary as the first 1–2 MEP trials were similar in amplitude to the average of all the other trials within each trial block (see Section 4.3 of the Discussion).

The specific ITIs of 4, 6, 8, and 10 s utilized for the SICI blocks were selected according to the following rationale: (1) While a few of the prior studies that investigated the influence of ITI on single-pulse MEP amplitude used ITIs of less than four seconds [35,40], extensive pilot testing revealed that ITIs of less than four seconds was not always feasible for SICI testing. In these conditions, the TMS unit would sometimes skip trials as a result of the capacitors not recharging fast enough if a given participant had a high RMT and 1 mV MEP, which would correspond to the need for relatively high stimulation intensities for the test MEPs and condition–test MEPs. Similarly, evoking SICI with ITIs of less than four seconds also resulted in coil overheating for a nontrivial number of participants. In the current study, these issues would have rendered the results meaningless since the change SICI on a trial-by-trial basis as a function of time was a primary interest. (2) Based on prior single-pulse TMS studies involving ITI, the shortest 4 s ITI should be brief enough to be able to identify any time-dependent modulations in MEP amplitudes due to ITI, if they were to exist [35–37]. Specifically, these studies demonstrated that ITIs of 5 s and below influenced MEP amplitudes. Relatedly, these studies clearly indicated that a 10 s ITI would be sufficient to provide valid and reliable MEP amplitude measurements given that ITIs as low as approximately 6–8 s and especially 10–20 s were not subject to time-dependent effects; (3) it quickly became evident that ITIs of greater than 10 s would not be practical for almost all TMS experiments. The total time required to conduct TMS experiments would be far too great, the experiments would be too unpleasant for the participants and investigators, and the number of blocks, conditions, and total trials would have to be reduced compared to what is usually desired in most TMS experiments. In summary, both prior research and extensive piloting deemed that the shortest ITI of 4 s should be adequate to find time-dependent effects and the longest ITI of 10 s should be more than long enough to provide valid and reliable measures of MEP amplitudes to compare to the shorter ITIs.

2.5. Data Analysis

The MVC and MEP data were reduced and analyzed using custom Signal software scripts by members of the research team who were not present during data collection. Accordingly, the investigators who collected the data during the experimental sessions did not perform the data analysis [59].

2.5.1. MVC Force, MVC EMG, RMT, and 1 mV Stimulation Intensity Analyses

The MVC force was quantified as the average force generated over the plateau portion (usually about three to five seconds) of the MVC trials. The MVC trial with the greatest force for each group of three pre- and post-MVC trials was denoted as the MVC force and used for analysis [44,60]. Similarly, the average FDI EMG was quantified over the same plateau period and the greatest FDI EMG for group of three pre- and post-MVC trials was

denoted as the maximum FDI EMG. For all MEP analyses, the MEP size was quantified as the peak-to-peak amplitude value for each MEP. The RMT and 1 mV stimulation intensity (% MSO) are expressed as the averages of the entire sample of participants.

2.5.2. Control Block Analyses

MEP amplitudes were evaluated in three different ways in the control blocks: (1) to assess potential variations in MEP amplitude throughout the control blocks, the 25 MEP trials within each block were divided into three distinct time periods consisting of consecutive MEP trials (epoch 1: trials 1–8; epoch 2: trials 9–16; epoch 3: trials 17–25). As a result, epochs 1–2 included 8 trials each, whereas epoch 3 consisted of 9 trials. This mirrors the approach in our previous investigation on the influence of ITI on ICF [38]. In addition, a similar strategy was used in a single-pulse TMS study, which segmented 30 MEP trials into three equal sub-blocks of 10 MEPs [35]. The decision to allocate 8 trials to epochs 1 and 2 with 9 in epoch 3, as opposed to distributing an equal number of trials across all epochs, accounted for the possibility of excluding the initial trial in each block, a contingency discussed further in Section 4.3 of the Discussion. Nevertheless, this deletion ultimately was not necessary as the first 1–2 MEP trials were similar in amplitude to the average of all the other trials within each trial block. (2) MEP amplitude was also calculated as the average of all 25 MEP trials in each control block to provide a comprehensive view of the average MEP amplitude during control blocks. (3) To examine changes in MEP amplitude across the control blocks in more detail, the average MEP amplitudes for all participants were determined for each of the 25 trials, serving primarily to graphically depict the time series of MEP trials within each control block.

2.5.3. SICI Block Analyses

MEP amplitudes in the SICI blocks were also analyzed in three ways: (1) MEP trials were segmented into epochs, with epochs 1, 2, and 3 comprising 16, 16, and 20 trials, respectively. Beyond the evident rationale that these blocks having more total trials due to them involving paired-pulse TMS, the primary justification for the variation in the number of trials across epochs aligns with the previously mentioned rationale concerning the potential exclusion of the initial two trials, which ultimately was not implemented (refer to Section 4.3 of the Discussion). Consequently, the average MEP amplitudes for test MEP trials, condition-test MEP trials, and thus SICI quantification were determined based on the average of 8, 8, and 10 trials for each metric (test MEPs, condition-test MEPs) within the SICI segments and utilized for subsequent analysis. Hence, SICI was determined by division of the condition-test MEP amplitude block average by the test MEP amplitude block average and reporting the as a percentage [7,10–12]. (2) The average MEP amplitudes across all 26 test MEP trials, 26 condition-test MEP trials, and thus 26 SICI assessments were compiled for analysis. This was carried out to provide a comprehensive view of the average MEP amplitude during the SICI blocks; (3) to more effectively depict variations in test and condition-test MEP trials across the duration of the SICI blocks, the average test MEP and average condition-test MEP amplitudes for each of the respective trials of all participants was quantified and depicted. This approach was employed for the purposes of illustration and depict the time series of MEP trials within each SICI block.

2.6. Statistical Analysis

2.6.1. MVCs

A paired *t*-test was used to compare the pre-MVC and post-MVC force values. Similarly, the pre-MVC EMG and post-MVC EMG values were also compared with a paired *t*-test.

2.6.2. Control Blocks

A 2 *ITI* (1 mV_4, 1 mV_10) \times 3 *Epoch* (1, 2, 3) within-subjects ANOVA was used to analyze differences in MEP amplitudes over the time course of the control blocks. To locate where significant differences occurred between pairs of means, post hoc analyses using Bonferroni adjustment for multiple comparisons were performed if appropriate.

2.6.3. SICI Blocks

Three separate 4 *ITI* (SICI_4, SICI_6, SICI_8, SICI_10) \times 3 *Epoch* (1, 2, 3) within-subjects ANOVAs were used to analyze the dependent variables of test MEP amplitude, condition-test MEP amplitude, and SICI.

Significance level for all statistical tests was $p < 0.05$, unless modified by Bonferroni corrections. Data are expressed as mean \pm standard deviation within the text and mean \pm standard error in the figures.

3. Results

The mean RMT for the participants was 46.0 ± 9.0 (% MSO), whereas the mean 1 mV stimulation intensity was 59.5 ± 14.1 (% MSO).

3.1. MVCs

The paired *t*-test revealed that the difference between the pre-MVC (44.2 ± 10.0 N) and post-MVC force (46.8 ± 12.8 N) values was non-statistically significant ($p = 0.107$, $d = 0.351$). In addition, another paired *t*-test revealed that the difference between the pre-MVC EMG (0.88 ± 0.3 mV) and post-MVC EMG (0.89 ± 0.4 mV) values was non-statistically significant ($p = 0.753$, $d = 0.066$).

3.2. Control Blocks

The differences in MEP amplitudes were compared across ITIs and epochs in the control blocks with a 2 *ITI* (1 mV_4, 1 mV_10) \times 3 *Epoch* (1, 2, 3) within-subjects ANOVA. The main effect for *ITI* ($p = 0.103$, $\eta_p^2 = 0.116$), the main effect for *Epoch* ($p = 0.727$, $\eta_p^2 = 0.014$), and the *ITI* \times *Epoch* interaction ($p = 0.444$, $\eta_p^2 = 0.036$) were all non-statistically significant (Figure 2A,B). Accordingly, Figure 3A,B illustrate that the MEP amplitudes did not show a trend for an increase or decrease as a function of trial number, but rather fluctuated around the mean value for both the 1 mV_4 and 1 mV_10 control blocks.

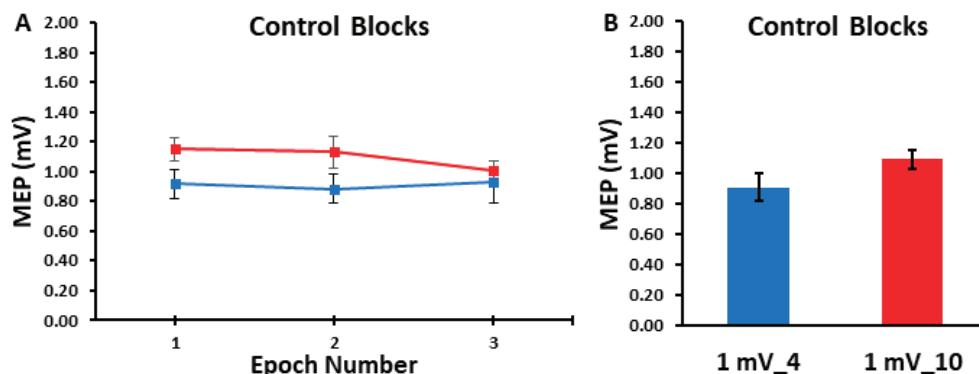


Figure 2. The MEP amplitudes obtained in the control blocks are shown across epoch number (A) and as the overall control block averages (B). The 1 mV_4 control block (blue) and the 1 mV_10 (red) control blocks displayed statistically similar MEP amplitudes across the three epochs and therefore over each entire trial block.

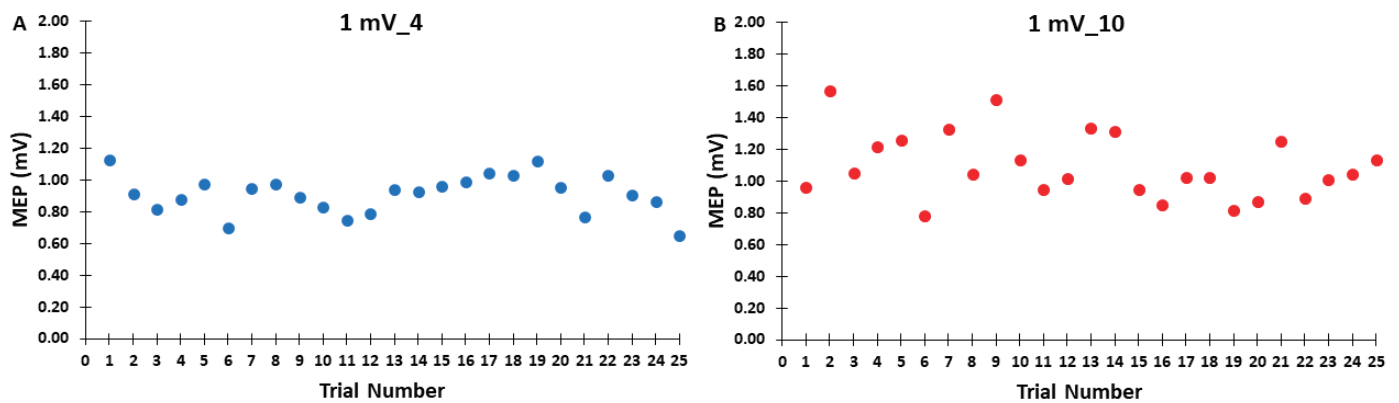


Figure 3. The MEP amplitudes across trials for the 1 mV_4 (A) and 1 mV_10 (B) control blocks are shown for illustrative purposes, with each data point corresponding to the average MEP amplitude of all participants for each trial in a given control block.

3.3. SICI Blocks

The differences in test MEP amplitudes were compared across ITIs and epochs in the SICI blocks with a 4 ITI (TEST_4, TEST_6, TEST_8, TEST_10) × 3 Epoch (1, 2, 3) within-subjects ANOVA. The main effect for ITI ($p = 0.861, \eta_p^2 = 0.011$), the main effect for Epoch ($p = 0.293, \eta_p^2 = 0.053$), and the ITI × Epoch interaction ($p = 0.477, \eta_p^2 = 0.039$) were all non-statistically significant (Figures 4A and 5A).

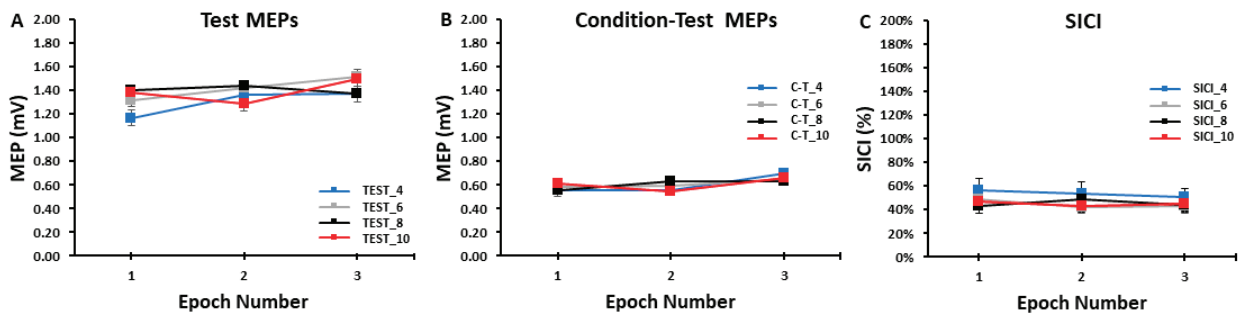


Figure 4. The test MEP, condition–test MEP, and SICI values obtained in the SICI trial blocks. There were no significant differences between the 4, 6, 8, and 10 s ITIs and across the three epochs for the test MEPs (A), the condition–test MEPs (B), or SICI (C).

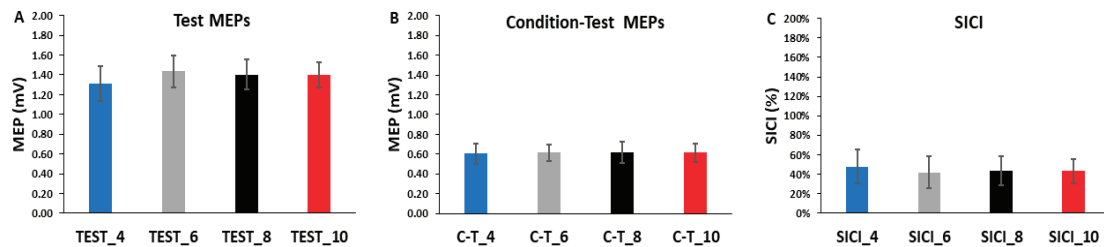


Figure 5. The test MEPs, condition–test MEPs, and SICI magnitudes for the 4, 6, 8, and 10 s ITIs (A–C) are shown as the overall averages for each SICI trial block. There were no significant differences between ITIs for the test MEPs, the condition–test MEPs, or SICI.

The differences in condition–test MEP amplitudes were compared across ITIs and epochs in the SICI blocks with a 4 ITI (C-T_4, C-T_6, C-T_8, C-T_10) × 3 Epoch (1, 2, 3) within-subjects ANOVA. The main effect for ITI ($p = 0.999, \eta = 0.000$), the main effect for Epoch ($p = 0.194, \eta = 0.075$), and the ITI × Epoch interaction ($p = 0.683, \eta = 0.024$) were all non-statistically significant (Figures 4B and 5B).

The differences in SICI values were compared across ITI and epochs in the SICI blocks with a 4 ITI (SICI_4, SICI_6, SICI_8, SICI_10) × 3 Epoch (1, 2, 3) within-subjects ANOVA. The main effect for ITI ($p = 0.127$, $\eta_p^2 = 0.082$), the main effect for Epoch ($p = 0.568$, $\eta_p^2 = 0.022$), and the ITI × Epoch interaction ($p = 0.836$, $\eta_p^2 = 0.013$) were all non-statistically significant (Figures 4C and 5C).

Accordingly, Figure 6A–D illustrates that the test MEP amplitudes and condition-test MEP amplitudes did not show a trend for an increase or decrease as a function of trial number, but rather fluctuated around the mean value for the SICI_4, SICI_6, SICI_8, and SICI_10 blocks. Similarly, Figure 7A–D illustrates that the SICI values did not show a trend for an increase or decrease as a function of trial number, but rather fluctuated around the mean value for the SICI_4, SICI_6, SICI_8, and SICI_10 blocks.

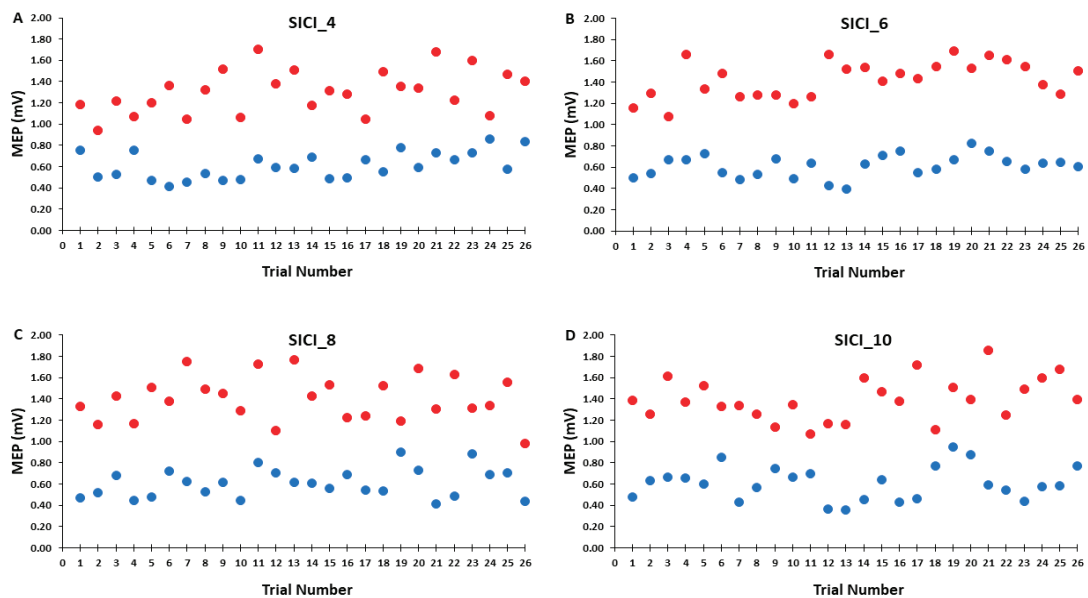


Figure 6. The test MEP (red) and condition-test MEP (blue) magnitudes across trials for the 4, 6, 8, and 10 s ITIs (A–D) in the SICI trial blocks are shown for illustrative purposes. Each data point corresponds to the average MEP amplitudes of all participants for each trial.

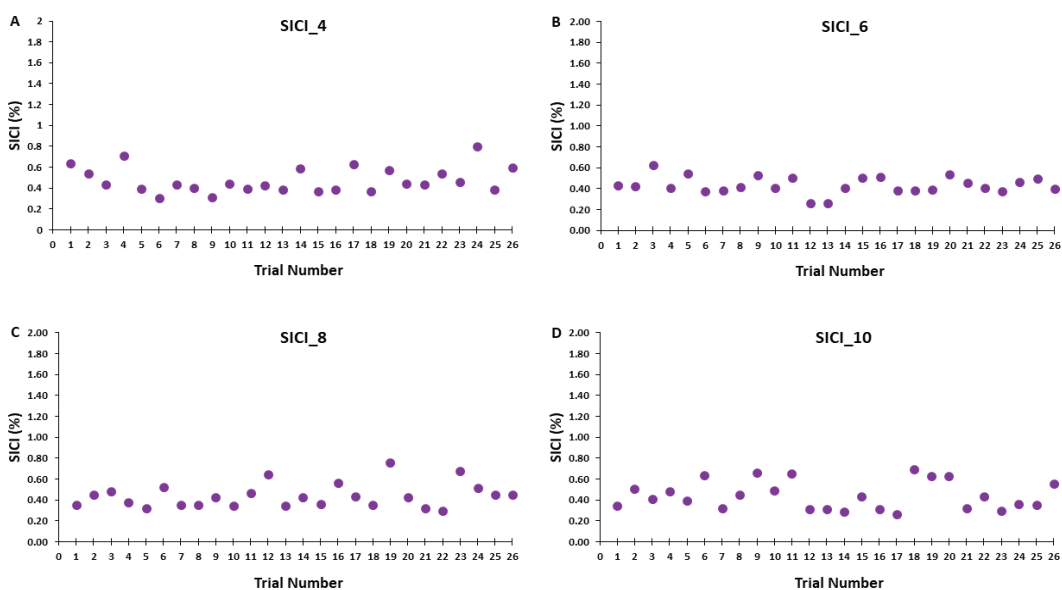


Figure 7. SICI magnitude across trials for the 4, 6, 8, and 10 s ITIs (A–D) are shown for illustrative purposes. Each data point corresponds to the average SICI of all participants for each trial in a SICI trial block.

4. Discussion

The primary purpose was to examine the effects of ITI on the quantification of SICI at rest. The secondary purpose was to determine the effects of ITI on the quantification of single-pulse MEP amplitudes at rest. The main findings were as follows: (1) The single-pulse MEP amplitudes in the 1 mV_4 and 1 mV_10 conditions did not display serial reductions with time in either of these control blocks. Accordingly, the overall average MEP amplitudes did not differ for the 1 mV_4 and 1 mV_10 blocks. (2) The magnitude of SICI did not exhibit a serial increase (greater inhibition) with time for any of the four ITIs (4, 6, 8, and 10 s) that were investigated in the SICI blocks. Similarly, the overall average SICI values were also not different between the four SICI blocks. Collectively, these results indicate that 4 and 10 s ITIs give similar overall single-pulse MEP values and 4, 6, 8, and 10 s ITIs give similar SICI values. Therefore, ITI had no meaningful influence on single-pulse MEP amplitude in the control blocks or on the test MEP, condition–test MEP, and therefore SICI values obtained under the current experimental conditions.

4.1. The Influence of ITI on MEP Amplitudes in the Control Blocks

The MEP elicited by TMS applied over M1 provides a simple measure of corticospinal excitability at the time of arrival of the TMS pulse. MEPs are widely used to understand the physiological mechanisms responsible for producing and controlling movements. Although MEPs can be evoked and recorded relatively easily, numerous methodological issues and experimental controls are needed to obtain valid MEP measurements in specific experimental circumstances. Accordingly, numerous review articles have focused on the optimal TMS parameters to use when obtaining single and paired-pulse MEPs [29,61, 62]. However, ITI has received much less little attention in comparison to other TMS parameters involved in single-pulse TMS, but especially in regard to paired-pulse TMS. It could be that ITI has been inadvertently neglected or perhaps this can be attributed to the prevailing notion that there are no post-stimulation effects at the most commonly used ITIs. Nonetheless, well over a decade ago, a significant majority of an international assembly of TMS experts emphasized the importance of controlling and reporting ITI in TMS experiments, despite the paucity of direct systematic investigations available at that point in time [21]. Contrary to these suggestions, the vast majority of TMS studies rarely mention or explicitly report ITI information in their methods sections. This observation is substantiated by a TMS review where, among 16 the reviewed studies, only 1 (~6%) disclosed the ITI employed [30]. This underscores that ITI lacks a unified approach, which is further evidenced by the varied ITI ranges and methods for adjusting ITI across trial blocks documented in existing literature.

The present study included two control blocks performed under resting conditions to examine the effects of short (4 s) and long (10 s) ITIs on single-pulse TMS MEP amplitudes (1 mV_4 and 1 mV_10 conditions, respectively). These blocks were performed to provide control measures for both the test MEPs completed in the SICI blocks and for the overall measurement of SICI. The control blocks served the dual purpose of being a control comparison to the single-pulse test MEPs evoked in the SICI blocks and enabling the findings to be compared to previous single-pulse ITI studies [35–37,39,41]. In general, the main findings of these studies were similar and reported MEP amplitude suppression of approximately the first 10 MEPs of a block of 20–30 trials when ITIs of less than or equal to 5 s were administered. This issue could therefore be a potential confound in any previous or future studies involving MEPs evoked with ITIs in this range.

Consequently, the a priori hypothesis of the current study was that the 1 mV_4 control block would exhibit a lower overall MEP amplitude than the 1 mV_10 block due to MEP suppression in approximately the first 8–10 trials. However, the results were not consistent with this hypothesis as there were no differences in overall block average between the two control blocks. Furthermore, MEP amplitudes in epoch 1 were also nearly identical compared with epochs 2 and 3 for both control blocks, which provides no evidence of a serial reduction in MEP amplitude with time in these conditions (Figure 2A,B). In addition,

visual inspection of Figure 3A,B not only reflects these statistical outcomes, but also clearly shows no discernable pattern in regard to the first MEP trial being larger in amplitude than subsequent MEPs later in the block. Accordingly, the first 1–5 MEPs were squarely in the middle of the range of variation of MEP amplitude observed across the entirety of the control blocks.

Taken together, the current results are in contrast to the majority of the findings in prior ITI single-pulse TMS studies. At first glance, these inconsistencies appear rather difficult to explain, but a detailed examination of the details and nuances of each study points to sample size and methodological disparities as the most likely explanations. In regard to sample size, the maximum number of participants was 17 and the average was 12.5 across these investigations [35–37,39–41]. This is important as sample size is the factor that provides the largest mathematical contribution to the estimator error for MEP amplitude quantification [42].

A good example of a methodological difference is a study by Moller and colleagues [36], which reported that recruitment curves determined with a 5 s ITI were significantly different compared to an ITI of 20 s. A key issue, however, was that a wide range of TMS intensities are used when obtaining recruitment curves compared to the constant stimulation intensities employed in this study, previous ITI studies, and in the majority of TMS blocks in most experimental conditions. Additionally, that study only collected five MEPs per block, a number far under the 20–30 recommended to minimize MEP error estimation [42]. In another study that involved only nine participants, a 2 s ITI resulted in significant lower MEPs compared with ITIs of 5 and 10 s [39], which is only partially consistent with the current results. In a much more comprehensive study, MEPs were lower at short ITIs of 1, 2, 3, and 5 s when compared to a long 10 s ITI. This finding was mainly due to the first 10 MEPs collected in blocks consisting of 30 total trials. Importantly, this study was characterized by several structural and procedural differences in comparison to the current study. First, the sample size comprised eight total participants. Second, biphasic TMS pulses were utilized compared with the much more common monophasic pulses used in most single pulse TMS studies, a difference that is well-known to yield different MEP results [63]. Third, the participants were allowed to watch television during the experiments versus the common practice of monitoring visual EMG feedback of muscle activity or having no significant external stimuli. Because MEP amplitude can be different within the up and down phases of neuronal oscillations as quantified by EEG and by attention level [6], this experimental issue could have significantly influenced results. A study by Schmidt and colleagues [40] has also provided results in opposition to the current ones. These authors reported that an ITI of 3 s produced a temporary initial state where MEP amplitudes in the first 20 trials were significantly lower compared with subsequent trials. One major difference in this study versus other ITI studies was that ITIs of over 3 s were not investigated, which makes meaningful comparisons with our study difficult. On the other hand, another report with very similar methodology to the many aspects of the single-pulse portion of the present study indicated that MEPs were significantly reduced in a 4 s as opposed to a 10 s ITI condition [41]. A second study by the same authors using similar methods indicated that MEP amplitudes at an ITI of 5 s were lower compared with 10, 15, and 20 s ITIs. In these two cases, the possible explanations for divergent findings compared to the current are somewhat difficult to reconcile.

In contrast, the current results align with a seminal repetitive TMS study [33], which discovered that an ITI of one second did not affect successive MEPs, indicating that ITIs shorter than one second were needed to induce significant after-effects on MEP amplitude. This conclusion is bolstered by physiological findings showing that a solitary TMS pulse applied to M1 only elevates cortico-muscular coherence for a duration of 300–800 ms before returning to baseline levels [34]. Furthermore, our recent study that involved the influence of ITI on ICF was conducted in nearly identical experimental conditions as the current study and also found no evidence of time-dependent effects in the single-pulse TMS control blocks [38]. To conclude, the overall literature displays mixed findings on the effect of brief

ITIs of 5 s or less on MEP amplitude measurement with the preponderance of the available studies being in opposition to the present results. However, differences in methodology and the much lower sample sizes in previous studies likely account for most of these discrepancies.

4.2. The Influence of ITI on the Measurement of SICI

SICI is the most common and extensively studied paired-pulse TMS protocol [7,10,11]. Although a series of previous studies by different research groups have investigated the effect of short and long ITIs on single-pulse TMS amplitudes, this was the first study to examine the effects of ITI on the measurement of SICI. Based on these prior single-pulse studies [35–37,39–41], the a priori hypothesis of the current study was that the magnitude of SICI in the short (4 s ITI) SICI block would be increased (greater inhibition) compared with the 6, 8, and 10 s ITI SICI blocks. In addition, it was hypothesized that these differences would be manifested through an initial suppression (greater inhibition) over approximately the first 8–10 MEP trials and would not be due to a serial increase (more inhibition) in SICI over the entire trial block. Theoretically, some weighted contribution of both of these elements within SICI_4 block relative to the three SICI blocks with longer ITIs could also occur. Any of these results would imply that prior SICI studies that utilized ITIs of 4–5 s or less may have provided imprecise or even partially inaccurate results.

A total of 52 MEP trials were attained in each of the four SICI blocks. Each block comprised 26 test MEP trials and 26 condition–test MEP trials presented in a semi-random fashion. For analysis, these sets of responses were divided into three epochs and were collectively utilized to calculate SICI. Separate analyses were also performed on the test MEP trials and condition–test MEP trials alone to examine their individual role in determining the magnitude of SICI induced in each of the four SICI blocks. For the test MEP trials alone, the results mirrored those of the control blocks as there was no indication of a serial reduction in MEP amplitude over any of the epochs of test MEP trials in any of the SICI blocks (Figure 4A). Therefore, the overall average test MEP was also not different between the four SICI blocks (Figure 5A). All of these statistical findings are clearly corroborated by the graphical representation of the group average test MEP amplitudes plotted by trial number (Figure 6A–D). In conclusion, the test MEP amplitudes when analyzed alone displayed no differences across epochs or between SICI blocks.

Similarly, the condition–test trial MEP amplitudes when analyzed alone displayed the exact pattern of findings and therefore overall results as the test MEP trials. They failed to exhibit time-varying characteristics over any of the epochs that comprised the total of 26 condition–test MEP trials in any of the four SICI blocks (Figure 4B). Accordingly, the overall average condition–test MEP was also not different between the four SICI blocks (Figure 5B). Thus, condition–test MEP amplitudes randomly varied around the average value obtained over the entire duration of the SICI blocks. All of these statistical findings are clearly supported by the graphical representation of the group average condition–test MEP amplitudes plotted by trial number (Figure 6A–D). In conclusion, the condition–test MEP amplitudes when analyzed alone displayed no differences across epochs or between SICI blocks.

Since the test MEP and condition–test MEP are the two components that comprise the measurement and mathematical calculation of SICI, the same overall pattern of results had to manifest for SICI. Therefore, there was neither a serial increase (greater inhibition) in SICI over the course of any of the SICI blocks (Figure 4C) nor a difference in the overall SICI block average values (Figure 5C). These findings were reflected in the graphical representations of the group average SICI values plotted as a function of trial number (Figure 7A–D). Thus, there were no significant differences in the magnitude of SICI obtained across epochs or between SICI blocks. In summary, the present findings were relatively straightforward as ITI had no meaningful influence on single-pulse MEP amplitude in the control blocks or on the test MEP, condition–test MEP, and therefore SICI values obtained under the current experimental conditions.

4.3. Methodological Considerations

There are numerous methodological issues that can potentially impact the quantification of single- and paired-pulse MEPs. Thus, this study implemented nearly all the elements of methodological quality that have been proposed for single- and paired-pulse TMS studies [6,21,30]. In addition, the study employed similar procedures to most previous single-pulse TMS studies that explicitly studied the influence of ITI on MEP amplitude [35–37,39–41]. The study was also limited to healthy young adults and had nearly equivalent numbers of women and men. Therefore, any differences that could have occurred due to any disorder, a wide age range, or an unequal distribution of participants by gender was greatly minimized. The possible influence of handedness or degree of laterality was also likely very low as all participants were strongly right-handed. Lastly, MVCs were also performed before and after the main aspect of the experiment to verify that the target FDI muscle's voluntary activation levels did not significantly change over the entire course of the experiment. Although the experiments were performed completely at rest it may have been possible that concentration, arousal, or alertness [6] could have decreased during that rather long experiment and impacted MEP amplitude.

The data analysis aspect most pertinent to the interpretation of results of the present study could be argued to be the somewhat common procedure to exclude the first few (e.g., 1–5) MEPs from the analysis of each trial block. However, close scrutiny of Figures 3, 6 and 7 all unambiguously show that this procedure would not have influenced any of the current findings. It appears that the first mention of this method of MEP data reduction was in a study dating back to the earliest days of TMS [29]. The authors stated that they usually excluded the first MEP because it displayed a greater amplitude compared with all the successive MEPs of the trial block. In that study, the ITI employed in that study was randomly given within a range of 3.5 and 7 s. However, this appeared to be based solely on subjective examination and no objective calculations were provided. Another possible origin to the idea of deleting the first several MEPs was a fatigue study [61] that reported a serial decline in the initial four MEPs of trial block. Nevertheless, the condition of the motor system and corticospinal excitability subsequent to the completion of a fatiguing contraction is not comparable to rest and the evolution of the after-effects of fatigue obviously contributed to those results. Accordingly, a comprehensive study that focused only on the effects of initial MEP removal concluded as long as an adequate number of total MEPs were collected the deletion of the first 3–5 MEPs did not significantly influence results [64].

4.4. Practical Applications for SICI Studies

The current results have a number of practical implications for single-pulse TMS studies and the quantification of SICI. First, the tactic of removing the first MEP or initial several MEPs of a trial block from analysis seems to be an unwarranted loss of data and not necessary. Second, the widespread approach of adjusting the SICI test MEP amplitude to 1 mV or slightly higher was further supported in the current study for ITIs ranging between 4 and 10 s and appears to be the best practice. By extension, the less frequent method of setting the test MEP stimulation intensity to 110–120% of the RMT is also viable as this almost always elicits MEPs of 1 mV or slightly [42]. Third, it probably does not matter if short and long ITIs are employed in a randomized fashion within the same block of trials as long as they are in the range of 4 to 10 s. Therefore, some researchers may want to do this in experimental circumstances where they do not want the participants to anticipate the TMS pulses that would occur at constant fixed intervals. Fourth, the administration of the 10 s ITI condition clearly indicated to the experimenters and participants that ITIs of that length or longer are uncomfortable, time-inefficient, and not necessary [37] to obtain the same results as shorter ITIs. In summary, it is recommended based on the current findings that ITIs of between 4–6 s represent the optimal balance between reasonable MEP amplitude estimation, participant comfort, and the use of the time of investigators. Obviously, this approach may be especially relevant to older adult or patient populations who may find it more difficult to undergo prolonged experiments relative to younger adults. These

recommendations seem to be congruent with the calculations of a recent review article [42], which gave mathematically derived guidelines for determining the trade-offs involved when considering the interrelated experimental variables of sample size, MEP variability and error estimation, experiment time, MEP trials per block, and the total number of blocks.

4.5. Limitations

The study had a few potential limitations that warrant discussion. First, the study only used a single constant ITI in all trial blocks. Many studies have chosen to randomly present MEP trials of different ITIs with a range of several seconds within blocks. However, it is pretty unlikely that varying ITI over a span of several seconds would have resulted in different overall results based on the current findings and prior studies [35–37,39–41]. Nonetheless, a comparison between constant and varied ITIs could be warranted in subsequent studies. Second, only one set of stimulation parameters were used to evoke SICI. This set was carefully chosen to reflect not only the most frequent in the literature, but also the best to produce the greatest SICI [12]. Despite these considerations, it cannot be completely discounted that a different set of stimulation intensities and ISI could deliver dissimilar findings as modification of some of these parameters provide measurements of SICI that are due to different populations of intracortical neurons [13]. Third, the single-pulse control blocks and the SICI blocks did not investigate ITIs below four seconds. However, as mentioned previously this was often not possible due to the TMS device's limitations for SICI. Although this could have been carried out for the single-pulse blocks [35–37,39–41], this approach would have not fit well into our research design for comparisons to the SICI measurements and would have been a repetition of several of the aforementioned previous studies. Fourth, none of the TMS measures in the current study were conducted under experimental conditions involving FDI muscle contraction. On the other hand, former studies have clearly shown that ITI has influence on MEP quantification during active muscle contraction [36,39] due to the fact that the values of background cortical excitability and therefore EMG levels are relatively stable compared with the fluctuating levels of cortical excitability over small time scales at rest. Fifth, the other possible pathways measured with paired-pulse TMS such as ICF, LICI, and SICF were assessed in the current study. However, based on our previous similar ITI study involving ICF [38], which yielded a similar lack of influence of ITI on results, it is highly improbable that ITI would differentially influence these other paired pulse measures. Sixth, the number of participants in the study could be viewed as low as in many neurophysiology studies in general [65,66]. As mentioned above, however, the current sample size of was substantially greater than all former single-pulse ITI studies by a wide margin (grand average of 12.5 and maximum of 17 participants) in these investigations [35–37,39–41]. Finally, the effect sizes were exceedingly low in the current study and provided objective evidence that further increasing the sample size would be unlikely to change the results and to have been a worth the additional time and resources to accomplish.

5. Conclusions

The major findings indicated that measurements of SICI neither differed between ITIs ranging between 4 and 10 s nor demonstrated significant time-dependent amplitude changes within blocks of trials. MEPs elicited with single-pulse TMS exhibited analogous overall results between the ITIs and during trial blocks. Based on these two sets of findings, it appears that ITIs of 4–6 s provides comparable results for SICI relative to longer ITIs, while having the advantages of being more comfortable to participants and reducing the experimental time needed to evaluate perform single- and paired-pulse TMS experiments.

Author Contributions: Conceptualization, B.P., L.L.d.A., M.P. and Z.A.R.; methodology, L.L.d.A., B.P., M.P. and Z.A.R.; software, L.L.d.A., M.P. and B.P.; validation, L.L.d.A., M.P., E.W.W., S.B. and B.P.; formal analysis, M.P., E.W.W. and B.P.; investigation, L.L.d.A., E.W.W., D.M., M.C. and S.B.; resources, B.P.; data curation, M.P., D.M., M.C. and B.P.; writing—original draft preparation, L.L.d.A., M.P., E.W.W., Z.A.R. and B.P.; writing—review and editing, L.L.d.A., M.P., E.W.W., D.M., M.C., S.B., Z.A.R.

and B.P.; supervision, B.P.; project administration, L.L.d.A., M.P., E.W.W. and B.P. All authors have read and agreed to the published version of the manuscript.

Funding: This research received no external funding.

Institutional Review Board Statement: The study was conducted in accordance with the Declaration of Helsinki, and approved by the Institutional Review Board of University of Nevada, Las Vegas (protocol number: 1445199, and date of approval: 31 July 2019).

Informed Consent Statement: Informed consent was obtained from all subjects involved in the study.

Data Availability Statement: The data presented in the study are available on request from the corresponding author.

Conflicts of Interest: The authors declare no conflicts of interest.

References

1. Rothwell, J.C. Techniques and Mechanisms of Action of Transcranial Stimulation of the Human Motor Cortex. *J. Neurosci. Methods* **1997**, *74*, 113–122. [CrossRef] [PubMed]
2. Hallett, M. Transcranial Magnetic Stimulation and the Human Brain. *Nature* **2000**, *406*, 147–150. [CrossRef]
3. Bestmann, S.; Krakauer, J.W. The Uses and Interpretations of the Motor-Evoked Potential for Understanding Behaviour. *Exp. Brain Res.* **2015**, *233*, 679–689. [CrossRef] [PubMed]
4. Petersen, N.T.; Pyndt, H.S.; Nielsen, J.B. Investigating Human Motor Control by Transcranial Magnetic Stimulation. *Exp. Brain Res.* **2003**, *152*, 1–16. [PubMed]
5. Hallett, M. Transcranial Magnetic Stimulation: A Primer. *Neuron* **2007**, *55*, 187–199. [CrossRef] [PubMed]
6. Spampinato, D.A.; Ibanez, J.; Rocchi, L.; Rothwell, J. Motor Potentials Evoked by Transcranial Magnetic Stimulation: Interpreting a Simple Measure of a Complex System. *J. Physiol.* **2023**, *601*, 2827–2851. [CrossRef]
7. Chen, R. Interactions between Inhibitory and Excitatory Circuits in the Human Motor Cortex. *Exp. Brain Res.* **2004**, *154*, 1–10. [CrossRef]
8. Vucic, S.; Chen, K.H.S.; Kiernan, M.C.; Hallett, M.; Benninger, D.H.; Di Lazzaro, V.; Rossini, P.M.; Benussi, A.; Berardelli, A.; Curra, A.; et al. Clinical Diagnostic Utility of Transcranial Magnetic Stimulation in Neurological Disorders. Updated Report of an Ifcn Committee. *Clin. Neurophysiol.* **2023**, *150*, 131–175. [PubMed]
9. Siebner, H.R.; Funke, K.; Aberra, A.S.; Antal, A.; Bestmann, S.; Chen, R.; Classen, J.; Davare, M.; Di Lazzaro, V.; Fox, P.T.; et al. Transcranial Magnetic Stimulation of the Brain: What Is Stimulated?—A Consensus and Critical Position Paper. *Clin. Neurophysiol.* **2022**, *140*, 59–97. [CrossRef]
10. Kujirai, T.; Caramia, M.D.; Rothwell, J.C.; Day, B.L.; Thompson, P.D.; Ferbert, A.; Wroe, S.; Asselman, P.; Marsden, C.D. Corticocortical Inhibition in Human Motor Cortex. *J. Physiol.* **1993**, *471*, 501–519. [CrossRef]
11. Berardelli, A.; Abbruzzese, G.; Chen, R.; Orth, M.; Ridding, M.C.; Stinear, C.; Suppa, A.; Trompetto, C.; Thompson, P.D. Consensus Paper on Short-Interval Intracortical Inhibition and Other Transcranial Magnetic Stimulation Intracortical Paradigms in Movement Disorders. *Brain Stimul.* **2008**, *1*, 183–191. [CrossRef] [PubMed]
12. Ortu, E.; Deriu, F.; Suppa, A.; Tolu, E.; Rothwell, J.C. Effects of Volitional Contraction on Intracortical Inhibition and Facilitation in the Human Motor Cortex. *J. Physiol.* **2008**, *586 Pt 21*, 5147–5159. [CrossRef] [PubMed]
13. Reis, J.; Swayne, O.B.; Vandermeeren, Y.; Camus, M.; Dimyan, M.A.; Harris-Love, M.; Perez, M.A.; Ragert, P.; Rothwell, J.C.; Cohen, L.G. Contribution of Transcranial Magnetic Stimulation to the Understanding of Cortical Mechanisms Involved in Motor Control. *J. Physiol.* **2008**, *586*, 325–351. [CrossRef] [PubMed]
14. Buccolieri, A.; Abbruzzese, G.; Rothwell, J.C. Relaxation from a Voluntary Contraction Is Preceded by Increased Excitability of Motor Cortical Inhibitory Circuits. *J. Physiol.* **2004**, *558 Pt 2*, 685–695. [CrossRef] [PubMed]
15. Liepert, J.; Classen, J.; Cohen, L.G.; Hallett, M. Task-Dependent Changes of Intracortical Inhibition. *Exp. Brain Res.* **1998**, *118*, 421–426. [CrossRef] [PubMed]
16. Coxon, J.P.; Stinear, C.M.; Byblow, W.D. Intracortical Inhibition During Volitional Inhibition of Prepared Action. *J. Neurophysiol.* **2006**, *95*, 3371–3383. [CrossRef] [PubMed]
17. Mooney, R.A.; Cirillo, J.; Byblow, W.D. Neurophysiological Mechanisms Underlying Motor Skill Learning in Young and Older Adults. *Exp. Brain Res.* **2019**, *237*, 2331–2344. [CrossRef] [PubMed]
18. Ferbert, A.; Priori, A.; Rothwell, J.C.; Day, B.L.; Colebatch, J.G.; Marsden, C.D. Interhemispheric Inhibition of the Human Motor Cortex. *J. Physiol.* **1992**, *453*, 525–546. [CrossRef] [PubMed]
19. Ni, Z.; Chen, R. Transcranial Magnetic Stimulation to Understand Pathophysiology and as Potential Treatment for Neurodegenerative Diseases. *Transl. Neurodegener.* **2015**, *4*, 22. [CrossRef]
20. Groppa, S.; Oliviero, A.; Eisen, A.; Quartarone, A.; Cohen, L.G.; Mall, V.; Kaelin-Lang, A.; Mima, T.; Rossi, S.; Thickbroom, G.W.; et al. A Practical Guide to Diagnostic Transcranial Magnetic Stimulation: Report of an Ifcn Committee. *Clin. Neurophysiol.* **2012**, *123*, 858–882. [CrossRef]

21. Chipchase, L.; Schabrun, S.; Cohen, L.; Hodges, P.; Ridding, M.; Rothwell, J.; Taylor, J.; Ziemann, U. A Checklist for Assessing the Methodological Quality of Studies Using Transcranial Magnetic Stimulation to Study the Motor System: An International Consensus Study. *Clin. Neurophysiol.* **2012**, *123*, 1698–1704. [CrossRef] [PubMed]
22. Zehr, E.P. Considerations for Use of the Hoffmann Reflex in Exercise Studies. *Eur. J. Appl. Physiol.* **2002**, *86*, 455–468. [CrossRef]
23. Stein, R.B.; Estabrooks, K.L.; McGie, S.; Roth, M.J.; Jones, K.E. Quantifying the Effects of Voluntary Contraction and Inter-Stimulus Interval on the Human Soleus H-Reflex. *Exp. Brain Res.* **2007**, *182*, 309–319. [CrossRef]
24. Rosburg, T.; Zimmerer, K.; Huonker, R. Short-Term Habituation of Auditory Evoked Potential and Neuromagnetic Field Components in Dependence of the Interstimulus Interval. *Exp. Brain Res.* **2010**, *205*, 559–570. [CrossRef] [PubMed]
25. Kimiskidis, V.K.; Papagiannopoulos, S.; Sotirakoglou, K.; Kazis, D.A.; Kazis, A.; Mills, K.R. Silent Period to Transcranial Magnetic Stimulation: Construction and Properties of Stimulus-Response Curves in Healthy Volunteers. *Exp. Brain Res.* **2005**, *163*, 21–31. [CrossRef]
26. Tinazzi, M.; Farina, S.; Tamburin, S.; Facchini, S.; Fiaschi, A.; Restivo, D.; Berardelli, A. Task-Dependent Modulation of Excitatory and Inhibitory Functions within the Human Primary Motor Cortex. *Exp. Brain Res.* **2003**, *150*, 222–229. [CrossRef]
27. Devanne, H.; Lavoie, B.A.; Capaday, C. Input-Output Properties and Gain Changes in the Human Corticospinal Pathway. *Exp. Brain Res.* **1997**, *114*, 329–338. [CrossRef] [PubMed]
28. Doeltgen, S.H.; McAllister, S.M.; Ridding, M.C. Simultaneous Application of Slow-Oscillation Transcranial Direct Current Stimulation and Theta Burst Stimulation Prolongs Continuous Theta Burst Stimulation-Induced Suppression of Corticomotor Excitability in Humans. *Eur. J. Neurosci.* **2012**, *36*, 2661–2668. [CrossRef] [PubMed]
29. Flament, D.; Goldsmith, P.; Buckley, C.J.; Lemon, R.N. Task Dependence of Responses in First Dorsal Interosseous Muscle to Magnetic Brain Stimulation in Man. *J. Physiol.* **1993**, *464*, 361–378. [CrossRef] [PubMed]
30. Cavaleri, R.; Schabrun, S.M.; Chipchase, L.S. The Number of Stimuli Required to Reliably Assess Corticomotor Excitability and Primary Motor Cortical Representations Using Transcranial Magnetic Stimulation (Tms): A Systematic Review and Meta-Analysis. *Syst. Rev.* **2017**, *6*, 48. [CrossRef]
31. Hoogendam, J.M.; Ramakers, G.M.; Di Lazzaro, V. Physiology of Repetitive Transcranial Magnetic Stimulation of the Human Brain. *Brain Stimul.* **2010**, *3*, 95–118. [CrossRef]
32. Ridding, M.C.; Rothwell, J.C. Is There a Future for Therapeutic Use of Transcranial Magnetic Stimulation? *Nat. Rev. Neurosci.* **2007**, *8*, 559–567. [CrossRef]
33. Pascual-Leone, A.; Valls-Sole, J.; Wassermann, E.M.; Hallett, M. Responses to Rapid-Rate Transcranial Magnetic Stimulation of the Human Motor Cortex. *Brain* **1994**, *117 Pt 4*, 847–858. [CrossRef]
34. Hansen, N.L.; Nielsen, J.B. The Effect of Transcranial Magnetic Stimulation and Peripheral Nerve Stimulation on Corticomuscular Coherence in Humans. *J. Physiol.* **2004**, *561 Pt 1*, 295–306.
35. Julkunen, P.; Saisanen, L.; Hukkanen, T.; Danner, N.; Kononen, M. Does Second-Scale Intertrial Interval Affect Motor Evoked Potentials Induced by Single-Pulse Transcranial Magnetic Stimulation? *Brain Stimul.* **2012**, *5*, 526–532. [CrossRef]
36. Moller, C.; Arai, N.; Lucke, J.; Ziemann, U. Hysteresis Effects on the Input-Output Curve of Motor Evoked Potentials. *Clin. Neurophysiol.* **2009**, *120*, 1003–1008. [CrossRef]
37. Hassanzahraee, M.; Zoghi, M.; Jaberzadeh, S. Longer Transcranial Magnetic Stimulation Intertrial Interval Increases Size, Reduces Variability, and Improves the Reliability of Motor Evoked Potentials. *Brain Connect.* **2019**, *9*, 770–776. [CrossRef]
38. Pantovic, M.; Boss, R.; Noorda, K.J.; Premyanov, M.I.; Aynlender, D.G.; Wilkins, E.W.; Boss, S.; Riley, Z.A.; Poston, B. The Influence of Different Inter-Trial Intervals on the Quantification of Intracortical Facilitation in the Primary Motor Cortex. *Bioengineering* **2023**, *10*, 1278. [CrossRef]
39. Matilainen, N.; Soldati, M.; Laakso, I. The Effect of Inter-Pulse Interval on Tms Motor Evoked Potentials in Active Muscles. *Front. Hum. Neurosci.* **2022**, *16*, 845476. [CrossRef]
40. Schmidt, S.; Cichy, R.M.; Kraft, A.; Brocke, J.; Irlbacher, K.; Brandt, S.A. An Initial Transient-State and Reliable Measures of Corticospinal Excitability in Tms Studies. *Clin. Neurophysiol.* **2009**, *120*, 987–993. [CrossRef]
41. Vaseghi, B.; Zoghi, M.; Jaberzadeh, S. Inter-Pulse Interval Affects the Size of Single-Pulse Tms-Induced Motor Evoked Potentials: A Reliability Study. *Basic Clin. Neurosci.* **2015**, *6*, 44–51.
42. Ammann, C.; Guida, P.; Caballero-Insaurriaga, J.; Pineda-Pardo, J.A.; Oliviero, A.; Foffani, G. A Framework to Assess the Impact of Number of Trials on the Amplitude of Motor Evoked Potentials. *Sci. Rep.* **2020**, *10*, 21422. [CrossRef]
43. Oldfield, R.C. The Assessment and Analysis of Handedness: The Edinburgh Inventory. *Neuropsychologia* **1971**, *9*, 97–113. [CrossRef]
44. de Albuquerque, L.L.; Pantovic, M.; Clingo, M.; Fischer, K.; Jalene, S.; Landers, M.; Mari, Z.; Poston, B. A Single Application of Cerebellar Transcranial Direct Current Stimulation Fails to Enhance Motor Skill Acquisition in Parkinson’s Disease: A Pilot Study. *Biomedicines* **2023**, *11*, 2219. [CrossRef]
45. Dominici, F.; Popa, T.; Ginanneschi, F.; Mazzocchio, R.; Rossi, A. Cortico-Motoneuronal Output to Intrinsic Hand Muscles Is Differentially Influenced by Static Changes in Shoulder Positions. *Exp. Brain Res.* **2005**, *164*, 500–504. [CrossRef]
46. Ginanneschi, F.; Del Santo, F.; Dominici, F.; Gelli, F.; Mazzocchio, R.; Rossi, A. Changes in Corticomotor Excitability of Hand Muscles in Relation to Static Shoulder Positions. *Exp. Brain Res.* **2005**, *161*, 374–382. [CrossRef]
47. Eckert, N.R.; Poston, B.; Riley, Z.A. Modulation of the Cutaneous Silent Period in the Upper-Limb with Whole-Body Instability. *PLoS ONE* **2016**, *11*, e0151520. [CrossRef] [PubMed]

48. Wessel, M.J.; Draaisma, L.R.; de Boer, A.F.W.; Park, C.H.; Maceira-Elvira, P.; Durand-Ruel, M.; Koch, P.J.; Morishita, T.; Hummel, F.C. Cerebellar Transcranial Alternating Current Stimulation in the Gamma Range Applied During the Acquisition of a Novel Motor Skill. *Sci. Rep.* **2020**, *10*, 11217. [CrossRef]
49. Do, M.; Clark, G.M.; Fuelscher, I.; Kirkovski, M.; Cerins, A.; Corp, D.T.; Bereznicki, H.G.K.; Albein-Urios, N.; Enticott, P.G. Magstim 200(2) and Bistim Mode Maximum Stimulus Output Values Are Not Equivalent: Configuration Selection Is Critical. *Brain Stimul.* **2020**, *13*, 444–446. [CrossRef] [PubMed]
50. Albuquerque, L.L.; Fischer, K.M.; Pauls, A.L.; Pantovic, M.; Guadagnoli, M.A.; Riley, Z.A.; Poston, B. An Acute Application of Transcranial Random Noise Stimulation Does Not Enhance Motor Skill Acquisition or Retention in a Golf Putting Task. *Hum. Mov. Sci.* **2019**, *66*, 241–248. [CrossRef]
51. Poston, B.; Christou, E.A.; Enoka, J.A.; Enoka, R.M. Timing Variability and Not Force Variability Predicts the Endpoint Accuracy of Fast and Slow Isometric Contractions. *Exp. Brain Res.* **2010**, *202*, 189–202. [CrossRef]
52. Lidstone, D.E.; Miah, F.Z.; Poston, B.; Beasley, J.F.; Mostofsky, S.H.; Dufek, J.S. Children with Autism Spectrum Disorder Show Impairments During Dynamic Versus Static Grip-Force Tracking. *Autism. Res.* **2020**, *13*, 2177–2189. [CrossRef]
53. Lima de Albuquerque, L.; Pantovic, M.; Clingo, M.; Fischer, K.; Jalene, S.; Landers, M.; Mari, Z.; Poston, B. An Acute Application of Cerebellar Transcranial Direct Current Stimulation Does Not Improve Motor Performance in Parkinson’s Disease. *Brain Sci.* **2020**, *10*, 735. [CrossRef] [PubMed]
54. De Guzman, K.A.; Young, R.J.; Contini, V.; Clinton, E.; Hitchcock, A.; Riley, Z.A.; Poston, B. The Influence of Transcranial Alternating Current Stimulation on Fatigue Resistance. *Brain Sci.* **2023**, *13*, 1225. [CrossRef] [PubMed]
55. Gandevia, S.C. Spinal and Supraspinal Factors in Human Muscle Fatigue. *Physiol. Rev.* **2001**, *81*, 1725–1789. [CrossRef]
56. Rossini, P.M.; Barker, A.T.; Berardelli, A.; Caramia, M.D.; Caruso, G.; Cracco, R.Q.; Dimitrijevic, M.R.; Hallett, M.; Katayama, Y.; Lucking, C.H.; et al. Non-Invasive Electrical and Magnetic Stimulation of the Brain, Spinal Cord and Roots: Basic Principles and Procedures for Routine Clinical Application. Report of an Ifcn Committee. *Electroencephalogr. Clin. Neurophysiol.* **1994**, *91*, 79–92. [CrossRef]
57. Pantovic, M.; Albuquerque, L.L.; Mastrantonio, S.; Pomerantz, A.S.; Wilkins, E.W.; Riley, Z.A.; Guadagnoli, M.A.; Poston, B. Transcranial Direct Current Stimulation of Primary Motor Cortex over Multiple Days Improves Motor Learning of a Complex Overhand Throwing Task. *Brain Sci.* **2023**, *13*, 1441. [CrossRef]
58. Pantovic, M.; Lidstone, D.E.; de Albuquerque, L.L.; Wilkins, E.W.; Munoz, I.A.; Aynlender, D.G.; Morris, D.; Dufek, J.S.; Poston, B. Cerebellar Transcranial Direct Current Stimulation Applied over Multiple Days Does Not Enhance Motor Learning of a Complex Overhand Throwing Task in Young Adults. *Bioengineering* **2023**, *10*, 1265. [CrossRef]
59. de Albuquerque, L.L.; Pantovic, M.; Clingo, M.G.; Fischer, K.M.; Jalene, S.; Landers, M.R.; Mari, Z.; Poston, B. Long-Term Application of Cerebellar Transcranial Direct Current Stimulation Does Not Improve Motor Learning in Parkinson’s Disease. *Cerebellum* **2022**, *21*, 333–349. [CrossRef]
60. Chattopadhyay, R.; Jesunathadas, M.; Poston, B.; Santello, M.; Ye, J.; Panchanathan, S. A Subject-Independent Method for Automatically Grading Electromyographic Features During a Fatiguing Contraction. *IEEE Trans. Biomed. Eng.* **2012**, *59*, 1749–1757. [CrossRef]
61. Brasil-Neto, J.P.; Cohen, L.G.; Hallett, M. Central Fatigue as Revealed by Postexercise Decrement of Motor Evoked Potentials. *Muscle Nerve* **1994**, *17*, 713–719. [CrossRef] [PubMed]
62. Brasil-Neto, J.P.; Pascual-Leone, A.; Valls-Sole, J.; Cammarota, A.; Cohen, L.G.; Hallett, M. Postexercise Depression of Motor Evoked Potentials: A Measure of Central Nervous System Fatigue. *Exp. Brain Res.* **1993**, *93*, 181–184. [CrossRef]
63. Corp, D.T.; Bereznicki, H.G.K.; Clark, G.M.; Youssef, G.J.; Fried, P.J.; Jannati, A.; Davies, C.B.; Gomes-Osman, J.; Kirkovski, M.; Albein-Urios, N.; et al. Large-Scale Analysis of Interindividual Variability in Single and Paired-Pulse Tms Data. *Clin. Neurophysiol.* **2021**, *132*, 2639–2653. [CrossRef]
64. Hashemirad, F.; Zoghi, M.; Fitzgerald, P.B.; Jaberzadeh, S. Reliability of Motor Evoked Potentials Induced by Transcranial Magnetic Stimulation: The Effects of Initial Motor Evoked Potentials Removal. *Basic Clin. Neurosci.* **2017**, *8*, 43–50. [CrossRef]
65. Szucs, D.; Ioannidis, J.P. Sample Size Evolution in Neuroimaging Research: An Evaluation of Highly-Cited Studies (1990–2012) and of Latest Practices (2017–2018) in High-Impact Journals. *Neuroimage* **2020**, *221*, 117164. [CrossRef] [PubMed]
66. Consideration of Sample Size in Neuroscience Studies. *J. Neurosci.* **2020**, *40*, 4076–4077. [CrossRef]

Disclaimer/Publisher’s Note: The statements, opinions and data contained in all publications are solely those of the individual author(s) and contributor(s) and not of MDPI and/or the editor(s). MDPI and/or the editor(s) disclaim responsibility for any injury to people or property resulting from any ideas, methods, instructions or products referred to in the content.

Article

Electric Field Characteristics of Rotating Permanent Magnet Stimulation

Pei L. Robins¹, Sergey N. Makaroff², Michael Dib³, Sarah H. Lisanby¹ and Zhi-De Deng^{1,*}

¹ Computational Neurostimulation Research Program, Noninvasive Neuromodulation Unit, Experimental Therapeutics and Pathophysiology Branch, National Institute of Mental Health, Bethesda, MD 20892, USA; pei.robins@nih.gov (P.L.R.); sarah.lisanby@nih.gov (S.H.L.)

² Department of Electrical and Computer Engineering, Worcester Polytechnic Institute, Worcester, MA 01609, USA; snmakaroff@wpi.edu

³ Fischell Department of Bioengineering, University of Maryland, College Park, MD 20742, USA; msdib98@gmail.com

* Correspondence: zhi-de.deng@nih.gov

Abstract: Neurostimulation devices that use rotating permanent magnets are being explored for their potential therapeutic benefits in patients with psychiatric and neurological disorders. This study aims to characterize the electric field (E-field) for ten configurations of rotating magnets using finite element analysis and phantom measurements. Various configurations were modeled, including single or multiple magnets, and bipolar or multipolar magnets, rotated at 10, 13.3, and 350 revolutions per second (rps). E-field strengths were also measured using a hollow sphere ($r = 9.2$ cm) filled with a 0.9% sodium chloride solution and with a dipole probe. The E-field spatial distribution is determined by the magnets' dimensions, number of poles, direction of the magnetization, and axis of rotation, while the E-field strength is determined by the magnets' rotational frequency and magnetic field strength. The induced E-field strength on the surface of the head ranged between 0.0092 and 0.52 V/m. In the range of rotational frequencies applied, the induced E-field strengths were approximately an order or two of magnitude lower than those delivered by conventional transcranial magnetic stimulation. The impact of rotational frequency on E-field strength represents a confound in clinical trials that seek to tailor rotational frequency to individual neural oscillations. This factor could explain some of the variability observed in clinical trial outcomes.

Keywords: electric field; finite element method; permanent magnets; head phantom measurement; rotating magnets; magnetic stimulation; neuromodulation; depression

1. Introduction

Conventional magnetic stimulation systems, such as transcranial magnetic stimulation (TMS), utilize a current-carrying coil to generate a time-varying magnetic field pulse. This process produces a spatially varying electric field (E-field)—via electromagnetic induction—in the central or peripheral nervous system. TMS is cleared by the United States Food and Drug Administration (FDA) for major depression, anxious depression, obsessive-compulsive disorder, smoking cessation, and migraines [1,2]. An alternative approach to generating a time-varying magnetic field involves mechanically rotating permanent magnets. Several rotating magnet devices have been proposed [3–5], using rotating high-strength neodymium magnets to induce an E-field in nearby nerve tissue. The strength, efficiency, and precision of these rotating magnets in inducing E-fields for use in neuromodulation have yet to be established.

One such system, known as synchronized transcranial magnetic stimulation (sTMS) or Neuro-EEG Synchronization Therapy (NEST), has been investigated as an innovative approach to personalize the treatment of major depressive disorder (MDD) [6–10]. The sTMS device consists of three cylindrical N52 grade neodymium magnets (Figure 1; Model

I), which are diametrically magnetized with a surface field of 0.64 T [3,7,9,11]. The magnets rotate along the cylindrical axis and are positioned over the midline frontal polar brain region, the superior frontal gyrus, and the parietal region. The rotation speed of the magnets is customized to match the patient's individual alpha frequency (IAF) of neural oscillations, as determined by pre-treatment electroencephalography (EEG) recorded from a fronto-occipital montage while the patient is in an eyes-closed resting state [9]. The hypothesized mechanism of action involves the entrainment of alpha oscillations through exogenous subthreshold sinusoidal stimulation produced by sTMS. This aims to reset the neural oscillators, enhance cortical plasticity, normalize cerebral blood flow, and thereby ameliorate depressive symptoms [6]. In contrast to conventional TMS, the sTMS device delivers a sinusoidal and subthreshold intensity stimulus.

In a multicenter, double-blinded, sham-controlled clinical trial evaluating the efficacy of sTMS for the treatment of depression, no significant difference was observed between the active and sham in the intent-to-treat (ITT) analysis [7]. However, among patients who completed the treatment per-protocol, there was a significant treatment response after six weeks. The authors also showed that patients in the per-protocol treatment group with a history of poor response or failed medication trials had a better improvement compared to those who received no prior treatment, suggesting that more severely depressed patients may benefit more from sTMS treatment. Additionally, secondary analysis showed that a lower IAF correlated with a lower treatment response [8]. In addition to MDD, sTMS has also been explored as a therapeutic intervention for post-traumatic stress disorder (PTSD) [12]. In a small prospective, sham-controlled, multisite pilot of sTMS treatment for patients experiencing moderate-to-severe symptoms of PTSD, there was a greater reduction in the PTSD threshold symptoms [12]. However, there was no significant difference between the active and sham groups. Furthermore, ongoing research is assessing the safety and feasibility of sTMS in individuals with cocaine, opioid, and alcohol use disorders (ClinicalTrials.gov Identifier: NCT04336293).

Another device that employs similar mechanics is the transcranial rotating permanent magnet stimulator (TRPMS) [5,13,14]. This portable, battery-operated device consists of an array of small cylindrical N52-grade neodymium magnets mounted on high-speed motors, which are in turn mounted on a helmet. Compared to the sTMS device, the TRPMS device uses smaller magnets, measuring 0.9525 cm in height and 0.635 cm in diameter, but has a stronger remanent magnetic flux density ($B_r = 1.48$ T). In addition, the TRPMS magnets are axially magnetized, whereas the sTMS magnets are diametrically magnetized. However, the axis of rotation for the TRPMS magnets is perpendicular to the cylindrical axis of the magnet, whereas in the sTMS system, the axis of rotation is parallel to the cylindrical axis of the magnet. The motor operates at a no-load speed of 24,000 revolutions per minute (rpm) or 400 revolutions per second (rps), achieving a rotational speed of 20,000 rpm (approximately 333 rps) under load. The induced E-field strength is directly proportional to the rotational frequency of the magnet, a higher rotational speed of the TRPMS magnets results in a higher E-field strength compared to the sTMS system. Voltage measurements conducted by Helekar and colleagues used an inductor search coil to estimate the maximum intensity of the TRPMS device to be approximately 7% of that produced by the maximum conventional TMS output [14]. At a distance of 21.2 to 26.2 mm from the TRPMS and inductor, representing the depth of the cerebral cortex, the intensity reduces by approximately half.

Recent studies have shown the safety and potential effectiveness of the TRPMS device in treating voiding dysfunction in patients with multiple sclerosis (MS) [15–18]. In a feasibility and safety study, the microstimulators from the TRPMS device were individually placed over predetermined regions of interest (ROI) during voiding initiation [15,17,18]. These predetermined ROIs were identified from the individual blood-oxygen-level-dependent (BOLD) activation at voiding initiation. Applying the TRPMS device to brain regions that modulate voiding initiation significantly improved bladder emptying symptoms [15,17,18].

Additionally, a proof-of-concept pilot study suggests that the TRPMS device may offer potential benefits for muscle function in individuals with type 1 myotonic dystrophy [16].

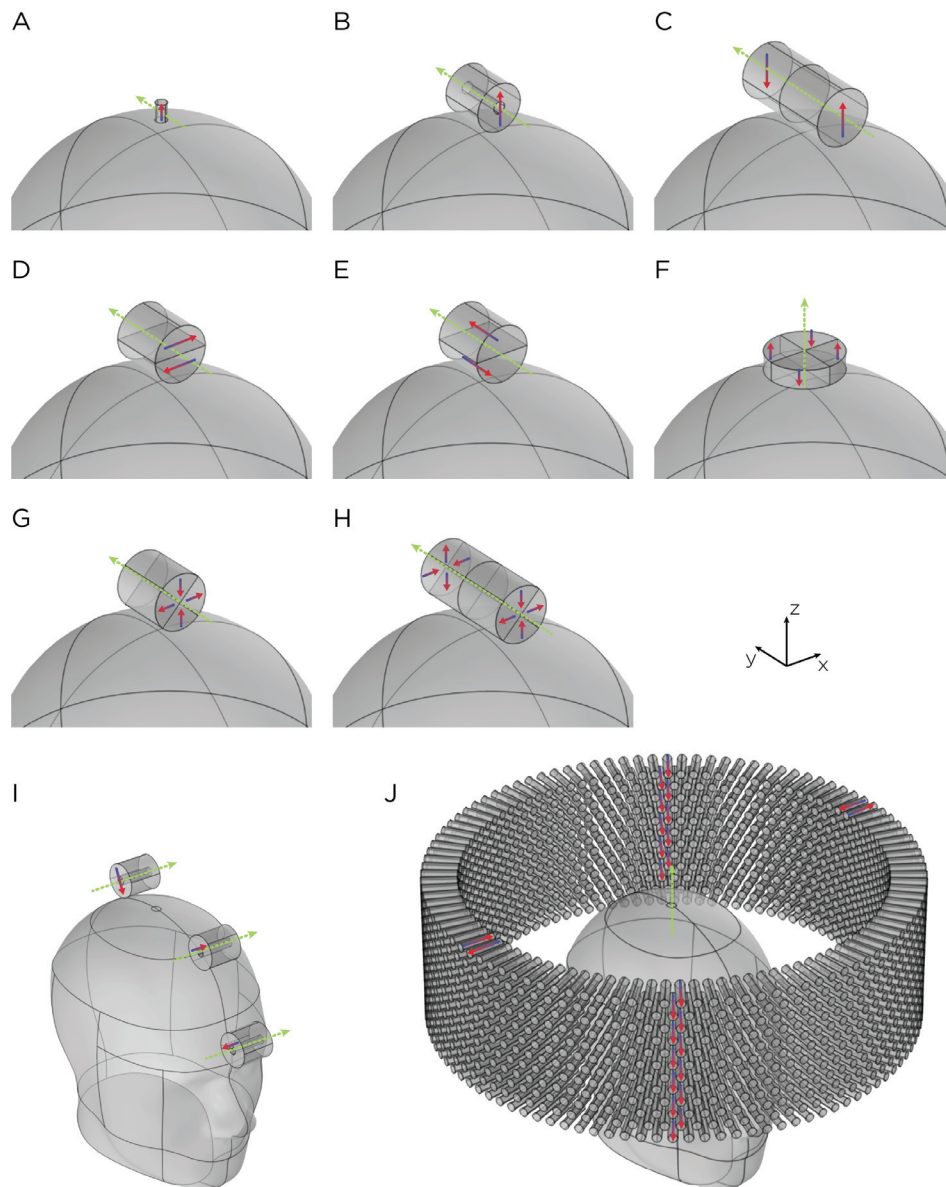


Figure 1. Dimensions, placement, and magnetization directions for ten configurations of rotating magnets (A–J). Model of single magnets in the (A) TRPMS and (B) sTMS systems. (C–H) Model of single magnets with multiple segments of different magnetization directions. (I) Model of the full sTMS system. (J) Model of the wide-bore, low-frequency magnetic spinner. The green arrows show the rotation axes, with the rotation direction determined by the right-hand rule. The red/blue arrows show the direction of the magnetization.

Yet another system that uses a magnet array is a wide-bore, low-frequency magnetic spinner comprising approximately 1300 Alnico permanent magnets [19]. These magnets are arranged radially within a 30 cm diameter ring (Figure 1; Model J). The resulting rotating magnetic field is perpendicular to the ring axis, in which the measured magnetic field strength at the center of the bore is approximately 32 mT. The device reaches a rotational speed up to 15 rps. This wide-bore magnetic spinner was originally designed to induce alternating electric currents in biological tissues, particularly in bones. Its application for brain stimulation has yet to be evaluated.

The utilization of rotating magnets has also been proposed for the stimulation of peripheral nerves and muscles [20]. Recognizing that long, straight nerves are more responsive to E-field gradients, Watterson proposed the use of multipole magnets with different magnetization directions and different axes of rotation to achieve a higher field gradient [4,20]. In a series of in vitro experiments, Watterson employed a bipole configuration, featuring two diametrically magnetized cylindrical segments (N52 grade neodymium magnets with a surface field ranging from 1.43 T to 1.48 T), positioned adjacent to one another with opposite magnetization directions, to activate the cane toad sciatic nerve and the attached gastrocnemius muscle [20]. It was demonstrated that muscle and nerve activation could be achieved with rotational frequencies of 180 rps and 230 rps, respectively.

In this work, we assess the E-field characteristics of various rotating magnet configurations through computational modeling. Complementary to numerical simulations, experimental measurements of field strengths are performed on a head phantom, validating the computational results. Our objective is to provide a comprehensive and comparative understanding of the E-field profiles generated by different rotating magnet setups. We further compare their E-field characteristics to those generated by conventional TMS. Via a combination of computational simulations and experimental validation, this comparative analysis aims to elucidate a comprehensive understanding of the potential advantages and limitations offered by rotating magnets for noninvasive brain stimulation applications.

2. Methods

2.1. Simulations and Solver

The finite element models were implemented in COMSOL Multiphysics (COMSOL, Burlington, MA, USA). Two different head models were used: a spherical head with a radius of 8.5 cm (Model A–H) and the Institute of Electrical and Electronics Engineers’ (IEEEs) Specific Anthropomorphic Mannequin (SAM) phantom head (Model I–J), as illustrated in Figure 1. Both the sphere and SAM phantom head were characterized by uniform, isotropic electrical conductivity, $\sigma = 0.33 \text{ S/m}$, and relative permeability, $\mu_r = 1$. In a homogeneous, symmetric conductor head model, the E-field induced by magnetic stimulation is tangential to the surface of the head model. The E-field is insensitive to radial variations of conductivity. This has been shown mathematically for low frequencies that are generally used for transcranial stimulation of the brain [21]. Therefore, the exact conductivity value used in our head model is not expected to affect the E-field. The tissue relative permittivity at low frequencies is approximately 1×10^7 [22,23], although this parameter does not affect our quantity of interest. The magnets are cylindrical; they have recoil permeability, $\mu_{\text{rec}} = 1.05$, which is typical of neodymium magnets [24]. The recoil permeability is the slope of the linear portion of the B - H curve, where B is the magnetic flux density and H is the magnetic field strength (see neodymium magnet demagnetization curves in [24]). The rotor—the moving components of the system—includes the magnet(s); the stator—the stationary part of the system—includes the head model and the surrounding air sphere.

Under the magnetic vector potential (\mathbf{A} - V) formulation and the induced solenoidal E-field, Ampère’s law was applied to all domains:

$$\sigma \frac{\partial \mathbf{A}}{\partial t} + \nabla \times \left(\frac{1}{\mu} \nabla \times \mathbf{A} \right) = 0. \quad (1)$$

This equation signifies the relationship between the time-varying component of the magnetic vector potential (\mathbf{A}), the material’s conductivity (σ), and its permeability (μ). Additionally, for the sections of both the rotor and stator that were devoid of current, a magnetic flux conservation equation pertinent to the scalar magnetic potential was applied. This equation is represented as:

$$-\nabla \cdot (\mu \nabla V_m - \mathbf{B}_r) = 0. \quad (2)$$

Here, V_m denotes the magnetic scalar potential, while \mathbf{B}_r represents the remanent magnetic flux density, as detailed in [25]. Furthermore, to maintain consistency, the continuity of the scalar magnetic potential was ensured at the interface between the rotor and stator.

The stator and rotor were meshed, and then the stationary solution was obtained using the multifrontal massively parallel sparse direct solver (MUMPS). The time-dependent problem was then solved in 10° rotation steps, using a relative tolerance of 1.0×10^{-8} . This approach is based on the assumption that the transient effects originating from the initiation of the rotating magnets have diminished. Consequently, the obtained final solution is indicative of the system's steady-state behavior.

2.2. Magnet Configuration

The magnets in each model are cylindrically shaped (Figure 1). Models A and B represent single magnets from the TRPMS and sTMS systems, respectively. Model A, which measures 0.9525 cm in height and 0.635 cm in diameter, has an axial magnetization and a residual flux density of 1.48 T. This magnet is rotated around its diameter axis and tangentially to the spherical head at 350 rps. Model B measures 2.54 cm in height and diameter, with an inner diameter of 0.635 cm. The magnet is diametrically magnetized with a residual flux density of 1.32 T and rotates about its central axis at 10 rps. To confirm that the E-field strength is linearly proportional to the rotational frequency of the magnet, we performed a parametric simulation using Model A, varying the rotational frequency from 10 rps to 400 rps.

Models C–H represent multipole configurations [4]. Model C is a bipolar magnet configuration, consisting of two diametrically magnetized cylindrical segments, each segment measures 3 cm in height and diameter, placed adjacent to each other with opposite magnetization. Model D is another bipolar configuration (3 cm in height and diameter), consisting of two diametrically magnetized, half-cylindrical segments with opposite magnetization directions. Model E (3 cm in height and diameter), similar to Model D, consists of two axially magnetized, half-cylindrical segments with opposite magnetization directions. Model F is a quadrupolar configuration (1 cm in height and 5 cm in diameter), consisting of four quadrants axially magnetized with each quadrant alternating and opposite magnetization around the central axis. The configuration is positioned on the base of the cylindrical configuration and rotates around its central axis. Model G is a quadrupolar configuration (3 cm in height and diameter), consisting of four quadrants radially magnetized with each quadrant alternating and opposite magnetization around the central axis. Model H's configuration utilizes eight segments (6 cm in height and 3 cm in diameter), in which two Model G-like configurations are placed adjacent to each other, ensuring all eight quadrants have opposite magnetization. Configuration C–H has a residual flux density of 1.48 T and rotates around its central axis at 10 rps.

Model I depicts the complete sTMS system, which includes three cylindrical magnets aligned along the sagittal midline of the head. The positioning of these magnets is as follows: The frontmost magnet is situated above the frontal pole, above the eyebrows; the middle magnet, positioned 7.1 cm from the frontmost magnet, aligns approximately with the superior frontal gyrus; and the most posterior magnet, located 9.2 cm from the middle magnet, corresponds roughly to the parietal cortex area. Each magnet measures 2.54 cm in both diameter and height, with an inner diameter of 0.635 cm. They are diametrically magnetized and possess a residual flux density of 1.32 T. The rotation axes are oriented perpendicular to the sagittal plane, and the rotational frequency is 10 rps, mirroring the center frequency of the alpha band oscillation. Model J, on the other hand, represents a wide-bore, low-frequency magnetic spinner. This spinner is composed of 1224 cylindrical magnets, each 2.54 cm tall and 0.3175 cm in diameter. These magnets are axially magnetized and arranged radially within a ring with a 30 cm diameter. The magnets are uniformly distributed across 12 layers in a staggered stacking formation, with each layer being 1.905 cm apart. The spinner operates at a rotational frequency of 13.3 rps.

2.3. E-Field Measurements

The E-field was characterized experimentally using a hollow sphere mold with a radius of 9.2 cm (Ibili, Bergara, Spain) as the head phantom, along with a custom-made

silver–chloride (AgCl) twisted pair dipole probe [26]. The probe was constructed from 99.99% pure silver, 21 gauge wire, with a bare diameter of 0.635 mm, and coated with a 0.762 mm perfluoroalkoxy (PFA) layer. For insulation, the probe was coated in epoxy resin with a thickness of approximately 0.2 cm. The tips of probes are separated by a distance of 9.40 mm. The exposed tips of the probe were immersed in Clorox bleach until a light gray color was observed. The two hemispheres of the sphere mold were sealed with vacuum grease and were filled with approximately 3 L of 0.9% sodium chloride (NaCl) in deionized water to emulate the conductivity of the brain (3.33 mS/cm at 20 °C) [27]; previous research has shown that 0.9% NaCl has a conductivity of 12 mS/cm at 20 °C [28]. Figure 2 illustrates the measurement apparatus.

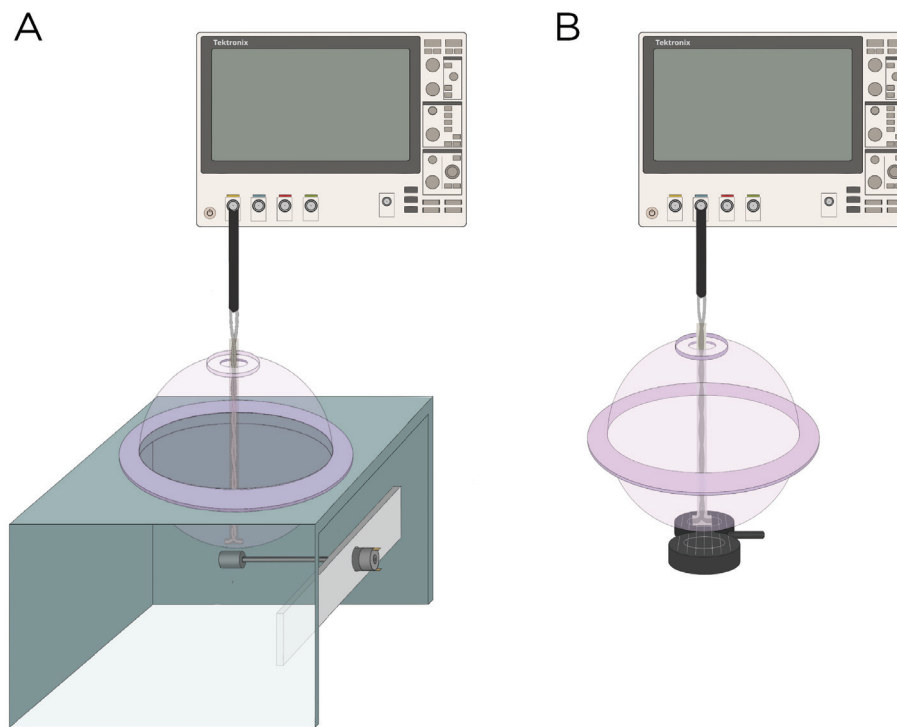


Figure 2. Experimental setup to measure the induced E-field strength using (A) rotating magnets Models A and B and (B) the MagVenture TMS coil.

Model A and B were experimentally measured using magnets from K & J Magnets Inc (Pipersville, USA). (Figure 2A). The magnet in Model A was mounted perpendicular inside a cylinder-shaped polyetheretherketone (PEEK) material and attached to a 24 V motor (model RS550, Shengle Electronic, Quanzhou, China), enabling the magnet to rotate around its central axis and tangentially to the spherical head. The magnet in Model B had an aluminum rod attached to its inner diameter and positioned approximately 5.08 cm away from the motor to minimize interference between the magnet and the motor. Rotation of the magnet occurred along the axial direction of the cylinder. The revolution (period = T) of the magnets was measured using a digital hand tachometer (PH-200LC, Mitutoyo, Kawasaki, Japan) and a piece of reflective tape (0.64 cm × 1.27 cm). In addition to the rotating magnets, the E-field was measured with the MagVenture TMS coil (figure-8, cooled B65 coil). The probe was oriented to measure the maximum E-field at 100% maximum output of a MagPro X100 stimulator (MagVenture A/S, Farum, Denmark) (Figure 2B).

3. Results

3.1. Simulations

The computational parameters and the maximum induced E-field strength for Model A–J are found in Table 1. Figure 3A illustrates the E-field distribution for Model A, representing the single rotating magnet in the TRPMS system. As the magnet rotates, the E-field

distribution transitions from a figure-8 pattern (when the magnetic dipole is perpendicular to the spherical head at multiples of $T/2$) to a circular pattern (when the magnetic dipole aligns parallel to the head at multiples of $T/4$). The peak induced E-field strength at the surface of the head is approximately 0.52 V/m, in the direction parallel to the rotation axis of the magnet. In addition, the induced E-field strengths are linearly proportional to the rotational frequencies in the range of 10 rps to 400 rps (Figure 3B). Figure 4, representing the single magnet in the sTMS system (Model B), presents a similar E-field distribution to Figure 3 at a lower E-field strength. The peak induced E-field strength at the head’s surface for this magnet configuration measures approximately 0.098 V/m in the direction perpendicular to the direction magnetization.

Table 1. Magnet specifications (magnet dimensions, magnetization directions, magnetic flux densities, rotational frequency) and the maximum induced B- and E-field strength for Models A–J.

Model	Dimensions (cm)	Magnetization Direction	B_r (T)	Rotational Frequency (rps)	Maximum B (mT)	Maximum E (V/m)
A	Cylinder × 1 od = 0.635 h = 0.9525	Axial	1.48	350	94.1	0.52
B	Ring × 1 od = 2.54 id = 0.635 h = 2.54	Diametrical	1.32	10	334.8	0.098
C	Cylinder × 1 2 segments od = 3, h = 6	Diametrical, multipole	1.48	10	462.8	0.13
D	Cylinder × 1 2 segments od = 3, h = 3	Diametrical, multipole	1.48	10	209.8	0.13
E	Cylinder × 1 2 segments od = 3, h = 3	Axial, multipole	1.48	10	134.1	0.025
F	Cylinder × 1 4 segments od = 5, h = 1	Axial, multipole	1.48	10	2	0.13
G	Cylinder × 1 4 segments od = 3, h = 3	Radial, multipole	1.48	10	353.7	0.23
H	Cylinder × 1 8 segments od = 3, h = 6	Radial, multipole	1.48	10	350.6	0.14
I	Ring × 3 od = 2.54 id = 0.635 h = 2.54	Diametrical	1.32	10	354.7	0.11
J	Cylinder × 1224 od = 0.3175 h = 2.54 Array id = 30 12 layers s = 1.905	Axial	1.48	13.3	2.5	0.0092

od: outer diameter; id: inner diameter; h: height; s: layer separation.

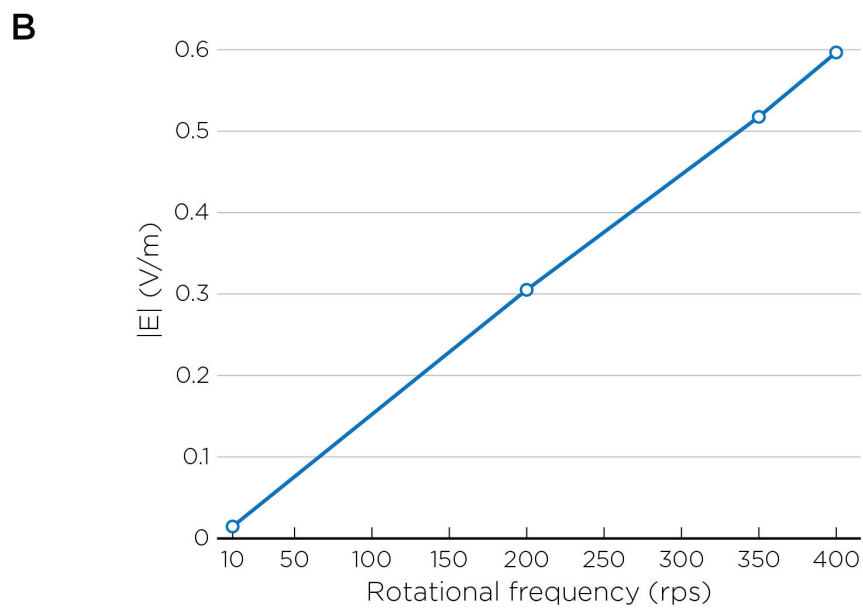
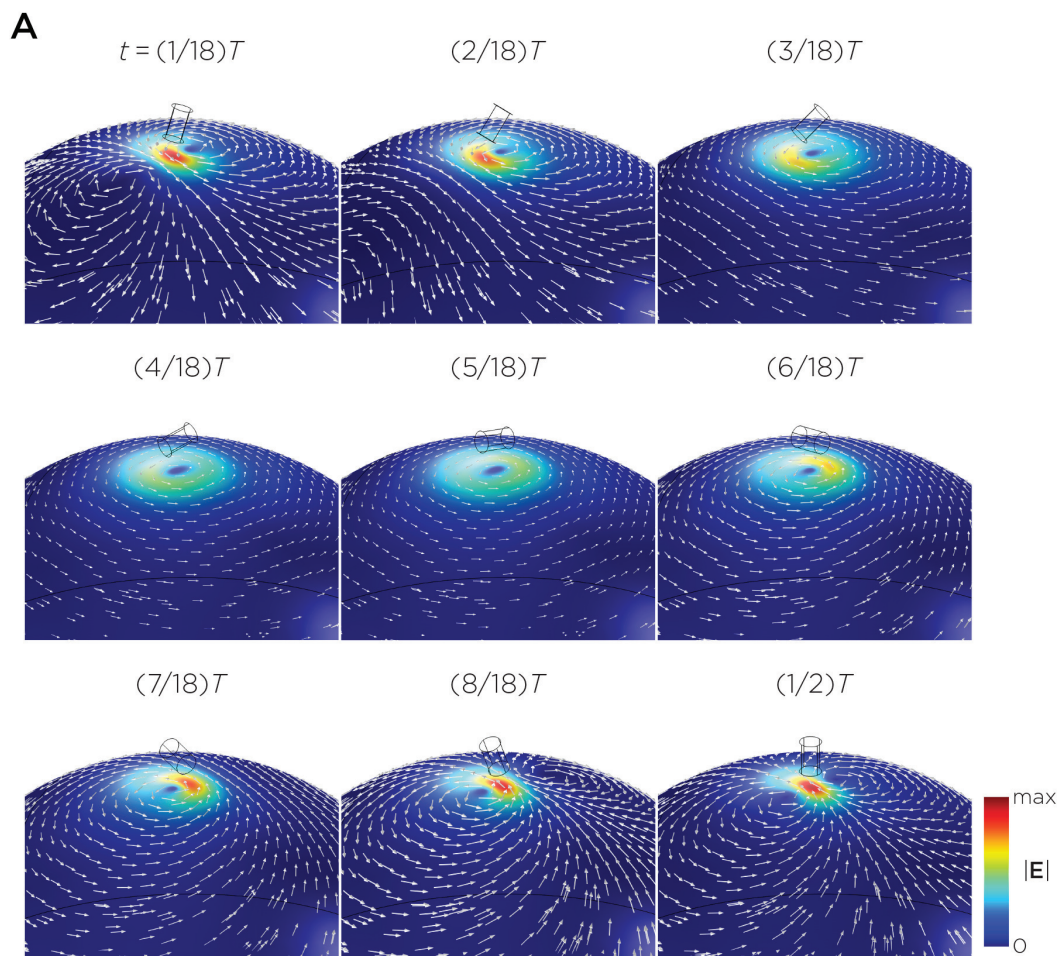


Figure 3. (A) Half revolution of configuration A in steady state. The cylinder represents the magnet. (B) The induced E-field strengths as a function of rotational frequencies.

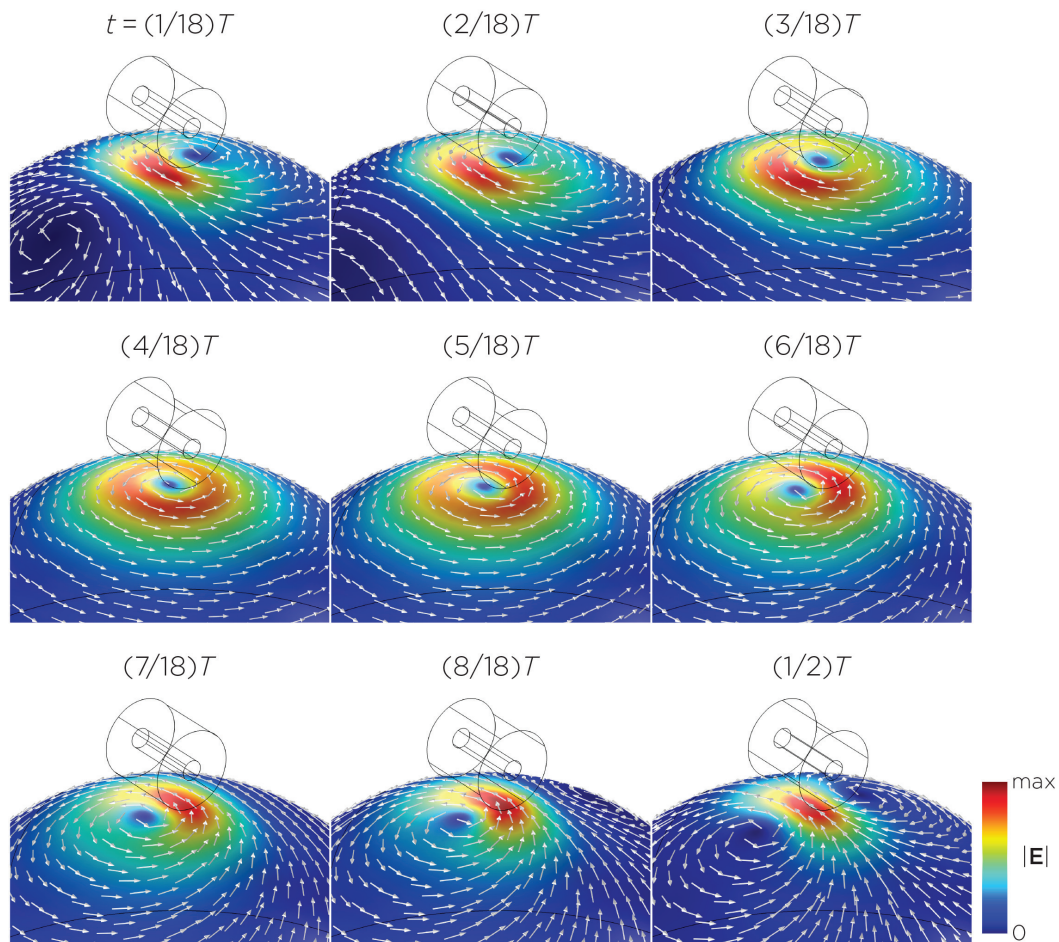


Figure 4. Half revolution of configuration B in steady state. The cylinder represents the magnet.

Figure 5 displays a bipolar E-field distribution in Model C. As the magnet rotates, the E-field distribution shifts from a four-leaf-clover pattern (when the magnetization direction is perpendicular to the spherical head at multiples of $T/2$) to a figure-8 pattern (at multiples of $T/4$). The peak induced E-field strength at the head's surface measures approximately 0.13 V/m. Figure 6 (Model D) showcases another bipolar E-field distribution similar to Models A and B. Similarly, the circular pattern occurs when the magnetization directions are parallel to the spherical head. In this configuration, the peak induced E-field strength measures approximately 0.13 V/m. Additionally, Figure 7 (Model E) shows a bipolar E-field distribution with a similar pattern to Figure 5 (Model C), with a lower peak induced E-field strength of approximately 0.025 V/m. Figure 8 (Model F) demonstrates a quadrupolar E-field distribution. As the magnet rotates, the E-field distribution has the shape of a four-leaf clover that rotates. The peak induced E-field strength measures approximately 0.13 V/m. Figure 9 is another quadrupole E-field distribution, with similar E-field patterns to Models A, B, and D. In this configuration, the peak induced E-field strength is approximately 0.23 V/m. Figure 10 shows an eight-pole E-field distribution with a similar E-field distribution as Model C. The peak induced E-field strength measures approximately 0.14 V/m.

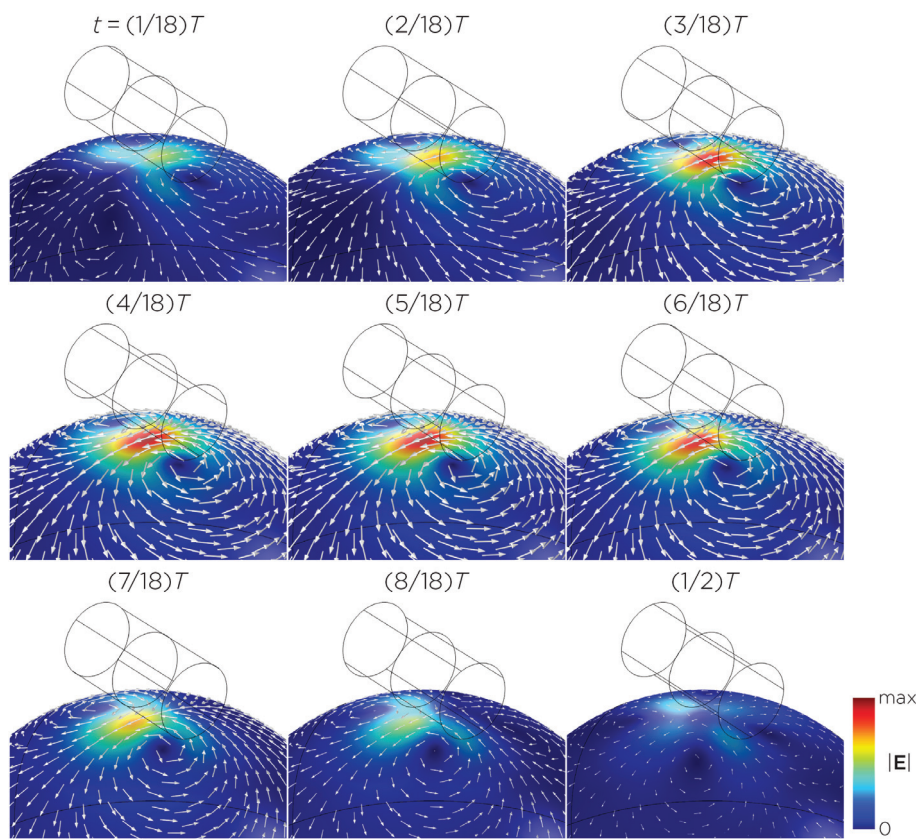


Figure 5. Half revolution of configuration C in steady state. The cylinder represents the magnet.

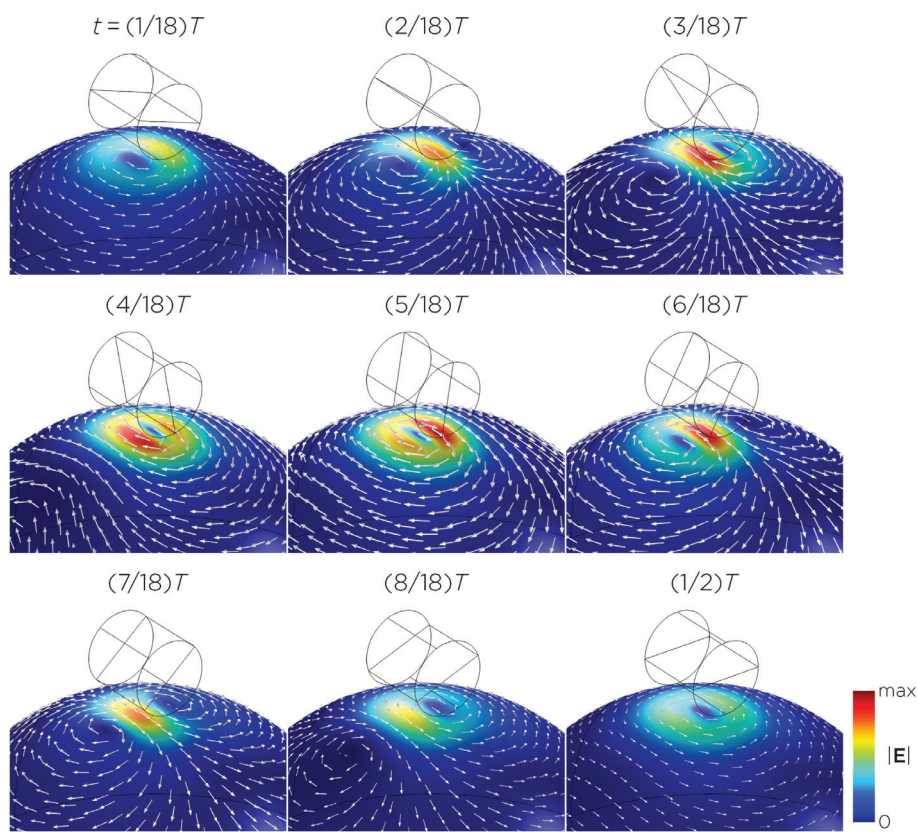


Figure 6. Half revolution of configuration D in steady state. The cylinder represents the magnet.

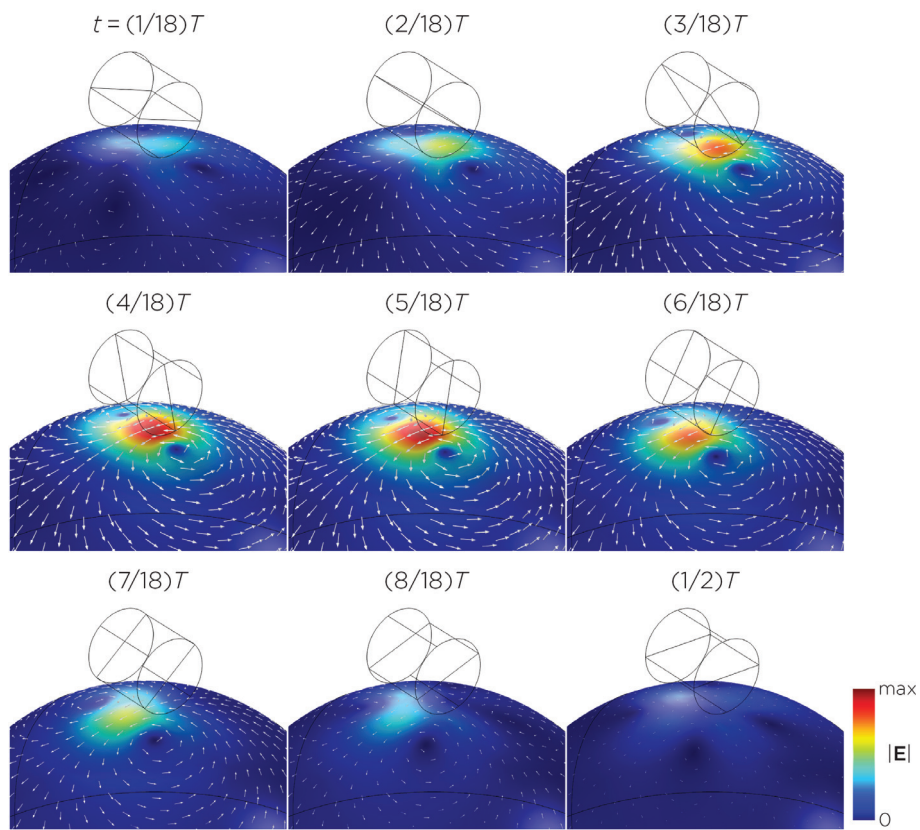


Figure 7. Half revolution of configuration E in steady state. The cylinder represents the magnet.

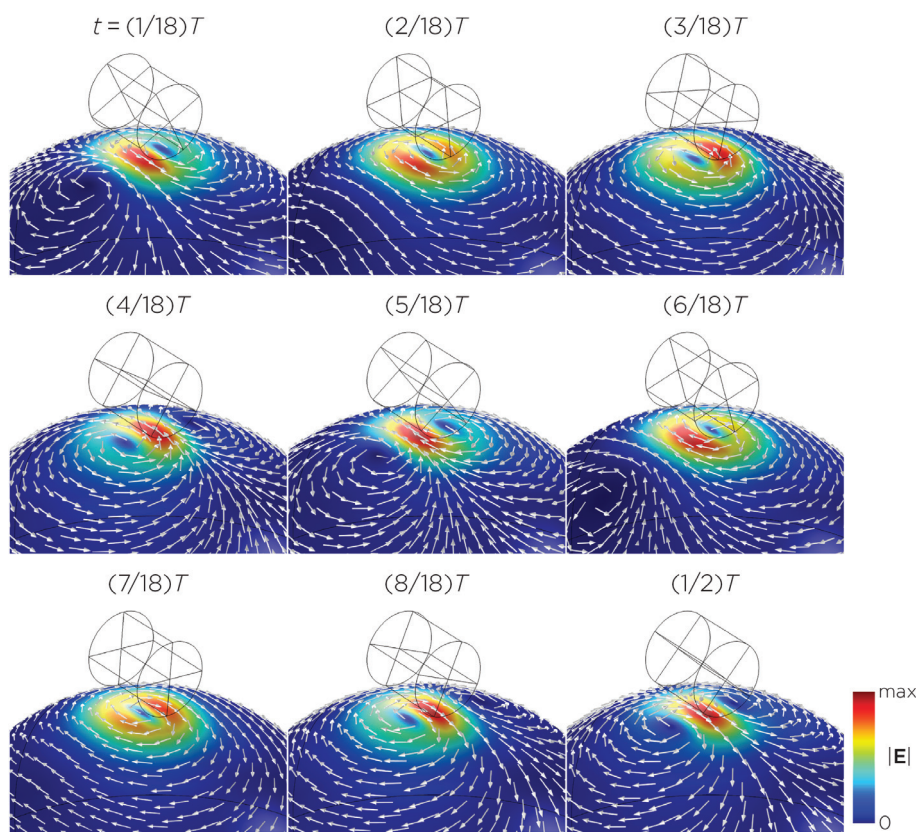


Figure 8. Half revolution of configuration F in steady state. The cylinder represents the magnet.

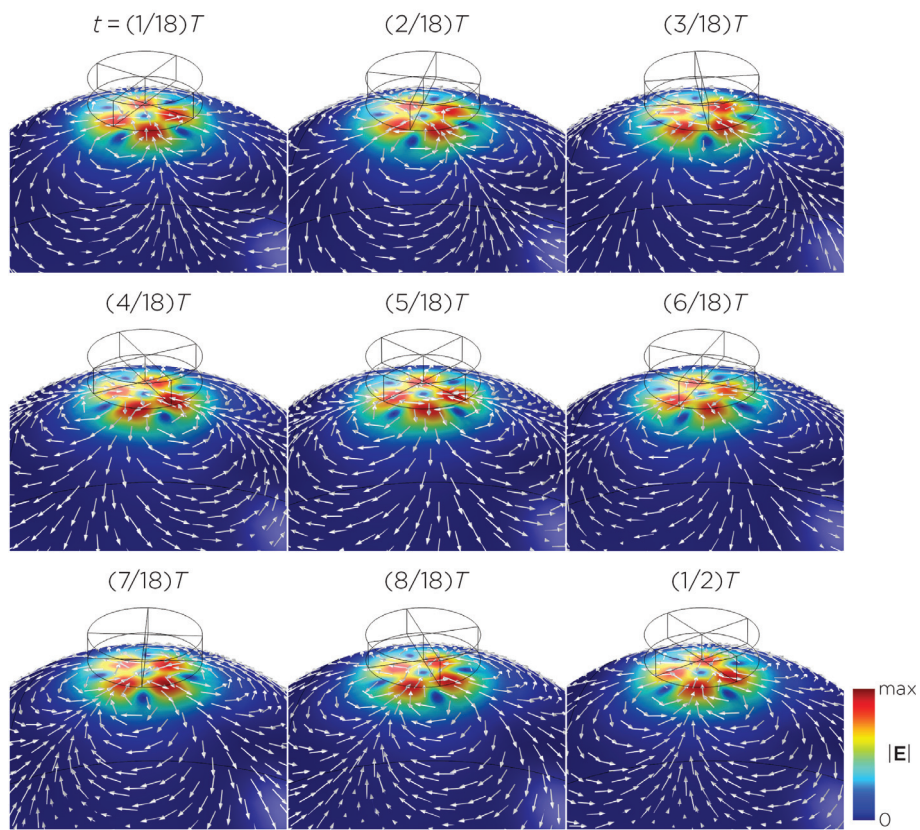


Figure 9. Half revolution of configuration G in steady state. The cylinder represents the magnet.

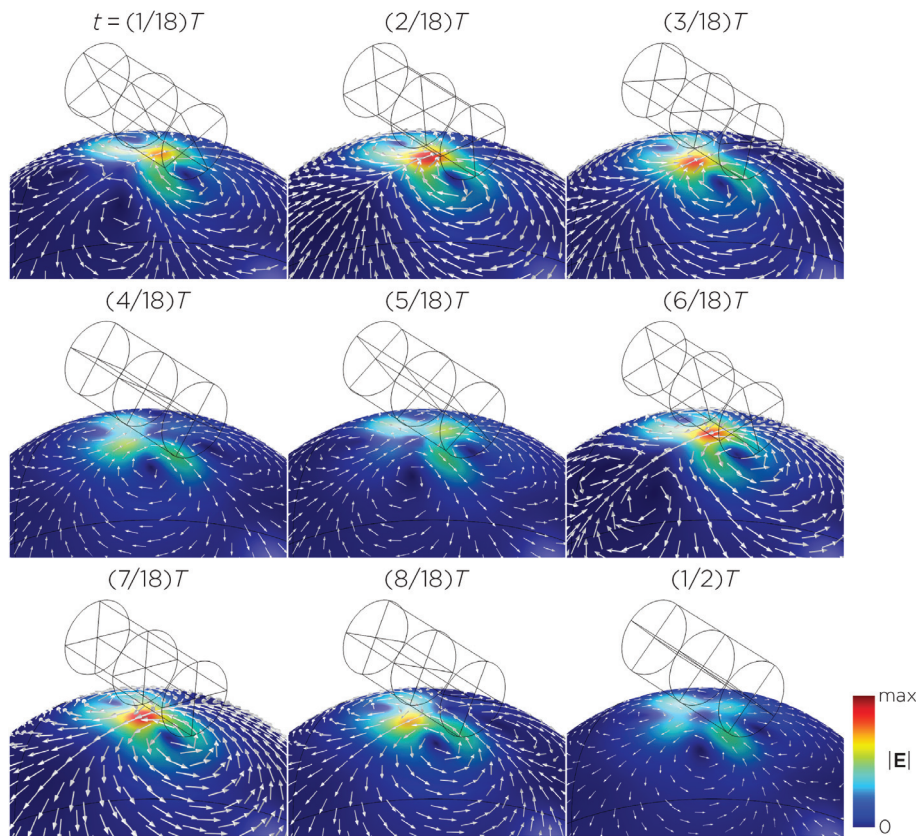


Figure 10. Half revolution of configuration H in steady state. The cylinder represents the magnet.

Figure 11 shows the E-field distribution of the full sTMS configuration in the SAM head model. The stimulation is broadly distributed over the midline frontal polar, medial frontal, and parietal regions. The peak induced E-field strength at the surface of the head is approximately 0.11 V/m. At a depth of 1.5 cm from the head surface, corresponding to the depth of the cortex, the E-field strength attenuates by approximately half. Figure 12 shows the E-field distribution of the wide-bore, low-frequency magnetic spinner. The stimulation is broadly distributed vertically of the head and rotates around the head as the device spins. The peak induced E-field strength at the surface of the head is approximately 0.0092 V/m.

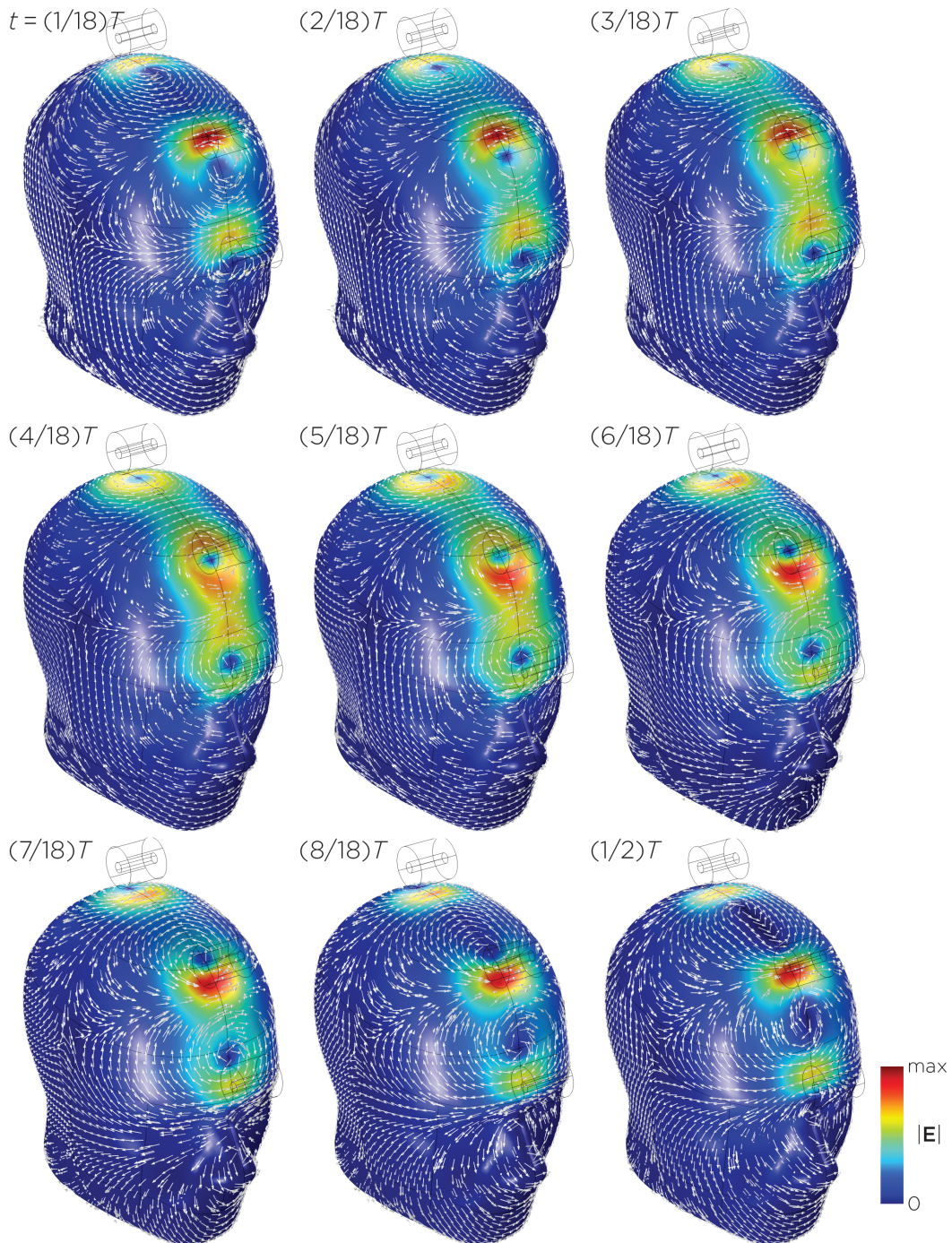


Figure 11. Half revolution of configuration I in steady state. The cylinders represent the magnets.

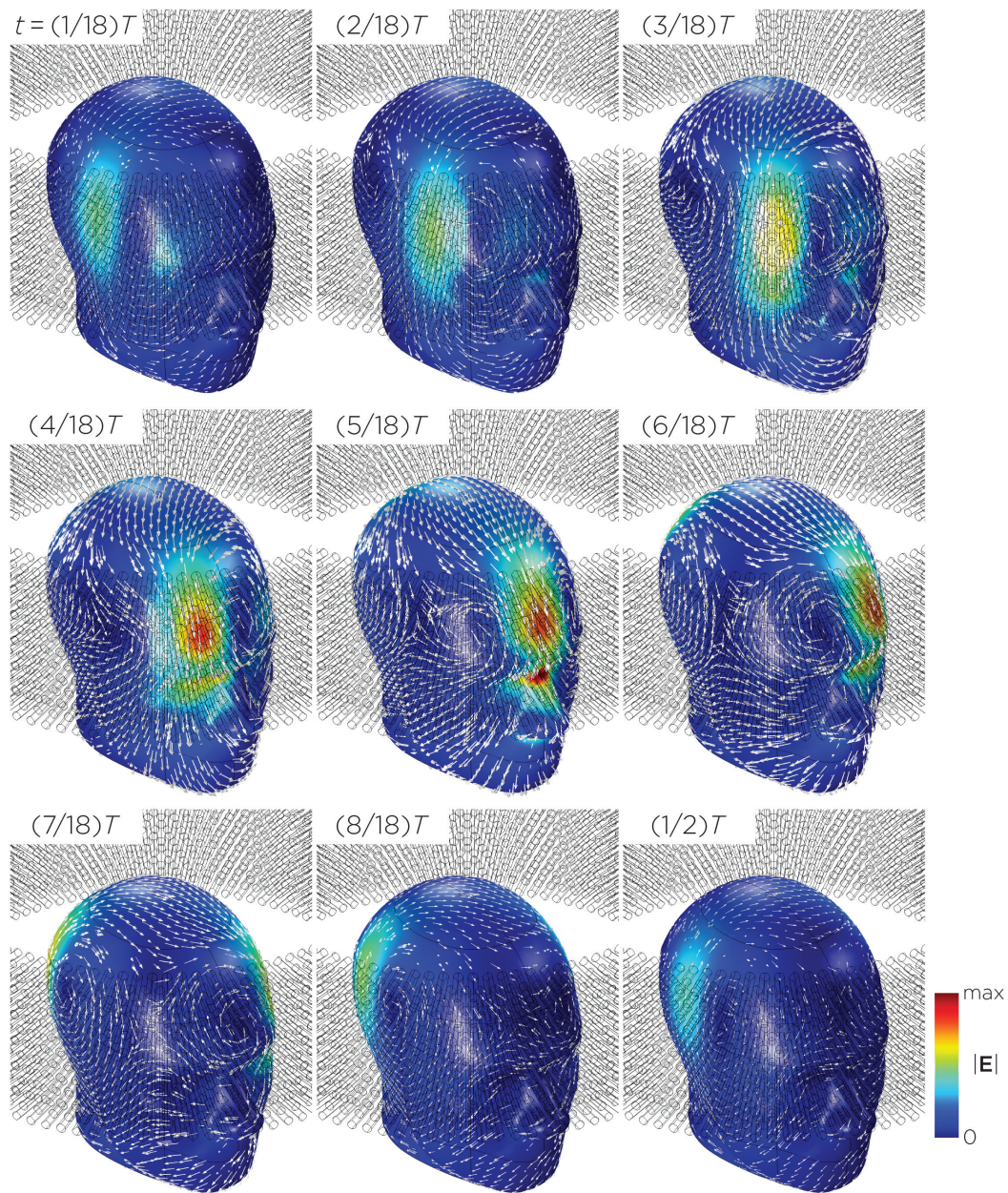


Figure 12. Half revolution of configuration J in steady state. The cylinders represent the magnets.

3.2. Experimental Measurements

When comparing the E-field measurements to the computational results for Models A and B, similar values are reported in Table 2. Specifically, the maximum E-field strength for Models A and B was found to be approximately 0.39 V/m and 0.082 V/m when the magnets were spun at 349.9 rps and 10.1 rps, respectively. Model B, representing one single magnet in the sTMS system, induces a maximum E-field strength (0.082 V/m) which is lower than the maximum induced E-field strength of the sTMS system (0.11 V/m). The maximum induced E-field for the MagVenture TMS coil was measured to be approximately 401.5 V/m at a pulse frequency of 3448 Hz, corresponding to a pulse width of 290 μ s. The measured induced E-field has a similar order of magnitude to previous simulations (370 V/m) [29].

Table 2. E-field measurements compared to the computational measurements.

Configuration	Measured Rotational/Pulse Frequency (rps, Hz)	Measured Maximum E (V/m)	Simulated Maximum E (V/m)
Model A	349.9	0.39	0.52
Model B	10.1	0.082	0.098
TMS	3448	401.5	370 [29]

4. Discussion

The distribution of the E-field induced by a single rotating magnet is influenced by several factors, including the dimensions and placement of the magnet(s), the number of poles, the direction of the magnetization, and the axis of rotation. Furthermore, the E-field strength is dependent on the rotational frequency and the surface field strength of the magnets. Our simulations revealed that the induced E-field strength on the head surface ranged from 0.0092 V/m to 0.52 V/m. The spatial pattern of the E-field varied between circular, figure-8, or four-leaf-clover shapes, depending on the relative orientation of the magnetization vector to the head model. For instance, in Model A, the E-field exhibits a circular pattern when the magnetization vector is parallel to the head and morphs into a figure-8 pattern when the magnetization vector is rotated perpendicular to the head. With more than one magnet, the E-fields from each magnet are summated according to the principle of superposition, resulting in more complex patterns and strengths depending on the arrangement and characteristics of the magnets (e.g., the distance between the magnets and their initial polarizations). Similarly, single-magnet configurations with multiple poles illustrated complex patterns and strengths, depending on the summated magnetization directions. In general, configurations with a figure-8 or a more localized E-field distribution resulted in a higher peak surface E-field strength, while those with a circular or more spread-out pattern induced lower peak surface E-field strength. This phenomenon mirrors the depth–focality trade-off observed in TMS coils, where the E-field strength in a more focal distribution decays more rapidly with distance compared to a more spread-out E-field distribution [30].

In the full sTMS model (Model I), the magnets were set to rotate at a fixed frequency of 10 rps. Since the induced E-field strength is linearly proportional to the rotational frequency, the field strengths at other frequencies can be easily calculated (Figure 3B). In practice, the sTMS system synchronizes the rotational frequency of the magnets to the IAF measured from EEG, which typically ranges between 8 and 13 Hz [9]. Jin and Phillips estimated the intensity of sTMS to be less than 1% that of conventional TMS [9]. This estimate was based on the ratio of the maximum rate of change in the magnetic field over time, dB/dt , between the sinusoidal waveform of sTMS and pulsed waveform of conventional TMS. However, this comparison did not account for the magnetic fields' spatial characteristics and the head's boundary conditions, which are crucial factors that affect the distribution and intensity of the induced E-field. Our simulation and measurement of the single magnet (Model B), as well as simulation of the full three-magnet array (Model I), yielded a peak E-field strength of approximately 0.11 V/m. This strength represents only 0.025% of conventional TMS at the surface of the head.

Synchronizing the exogenous subthreshold sinusoidal stimulation to the intrinsic alpha EEG rhythm was thought to be an important feature that underlies the mechanism of sTMS treatment for depression [6]. In the sTMS depression study, some participants did not receive stimulation at the correct IAF, which led to inferior outcomes compared to those treated at the correct IAF [7]. Secondary analysis showed that participants with a lower IAF exhibited the least clinical improvement [8]. It is important to note that since the induced E-field strength is directly proportional to the rotational frequency of the magnets, customizing the rotational frequency could introduce variability in the induced E-field strength across individuals. Consequently, a lower IAF would determine a

lower rotational frequency of the magnets, leading to decreased E-field strength, thereby potentially confounding the interpretation of this finding. One potential solution to mitigate this confound is to employ electromagnets, such as those used in n-phase motors. In a three-phase motor, for example, three coil windings in the motor stator receive power from three alternating currents that are out of phase with each other by one-third of their cycle, creating a magnetic field that rotates, similar to that in a mechanically rotating permanent magnet system. The advantage of using electromagnets is that they independently control frequency and amplitude, as opposed to the fixed coupling of these variables in mechanical rotating systems.

Compared to the sTMS system, the TRPMS system produces an E-field strength which is approximately five times higher, achieved through the use of a stronger magnet and a higher rotational frequency. Both the sTMS and TRPMS systems fall within similar order of magnitude, which are significantly lower compared to conventional TMS. Inductive measurements by Helekar and colleagues estimated the maximum TRPMS stimulation intensity to be approximately 7% of the maximum conventional TMS output at a distance of 6.2 mm from the magnet or TMS coil [14]. First, these estimates are based on measurements made in the air and do not account for head boundary conditions, potentially overestimating the E-field strength. Second, the TMS waveform reported in Helekar et al. [14] does not resemble the conventional biphasic cosine waveform generated by the Magstim Rapid² stimulator. This is possibly due to a lower sampling rate in their measurements, causing a distortion in the waveform, thus underestimating the peak value. Third, since smaller magnets have faster field attenuation with distance compared to larger magnets [30], the E-field strength of the TRPMS system at the depth of the cortex would be further overestimated. Our simulation and measurement for a single magnet in the TRPMS system showed that the peak E-field strength is approximately 0.1% of conventional TMS.

In the simulations of multipole magnets rotating at 10 rps (Model C–H), the E-field strengths are similar to that of the sTMS system, except for Model E, which exhibits an E-field strength of 0.025 V/m, which was approximately an order of magnitude lower. The E-field distribution from Watterson's configurations demonstrated characteristics of multiple magnets. For example, Model C, representing the bipole configuration used in Watterson's nerve stimulation experiments, exhibits a four-clover and a figure-8-shaped field pattern. The four-clover pattern emerges when the magnetization direction is perpendicular and shifts to a figure-8 pattern when the magnetization direction is parallel to the head model. Using this bipole configuration, Watterson and colleagues demonstrated the ability to achieve nerve activation at a rotational frequency of 230 rps [20]. According to their measurements, this resulted in an E-field strength of approximately 1 V/m, equivalent to 0.4% of the conventional TMS maximum output. In our finite element models, we use a rotational frequency of 10 rps to simulate the effect of multipolar magnet stimulation for brain stimulation. The 10 Hz frequency matches that of the sTMS model. Our simulation shows that this configuration induces an E-field strength of 0.13 V/m, approximately 0.032% of conventional TMS at the surface of the head. The multipolar magnets could be as effective as sTMS when used as part of a brain stimulation device.

In comparison to other proposed rotating magnetic systems, the wide-bore, low-frequency magnetic spinner (Model J), designed to induce alternating electric currents in biological tissues, induced the lowest and most nonfocal E-fields. This device generates a maximum magnetic field of 2.5 mT, resulting in a maximum induced E-field of 0.0092 V/m in the head model. With the installation of a magnetic yoke, which concentrates the magnetic flux to the inside of the bore, the measured magnetic field reaches 32 mT, bringing the induced E-field strength close to that of other devices. In terms of the spatial distribution, there are two E-field peaks located where the column of magnets reverses magnetization, e.g., where the magnetic field gradient is the highest. Since the induced field is more diffused, the field penetration is deeper compared to other smaller rotating magnetic configurations.

One potential advantage of utilizing rotating permanent magnets is the ability to create portable, cost-effective devices compared to conventional TMS [20]. Depending on the magnet strength and rotational frequency, the E-field strengths in the sTMS, TRPMS, and Watterson multipolar systems are comparable to other forms of low field stimulation, including low field magnetic stimulation (LFMS) [31], transcranial current stimulation (tCS) [32,33], and low-intensity repetitive magnetic stimulation (LI-rMS) [34,35]. Low field stimulation has been shown to induce changes at the cellular and molecular levels. For example, in an *in vitro* model, LI-rMS has been shown to alter cellular activation and gene expression in an organotypic hindbrain explant and in a stimulation frequency-specific manner [34]. Dufor and colleagues reported the induced E-field strengths of this device to be between 0.05 and 0.075 V/m [36]. Similarly, LI-rMS delivered during visually evoked activity increased the densities of parvalbumin-expressing GABAergic interneurons in an adult mouse visual cortex [37]. These findings suggest that the low field strengths produced by rotating permanent magnets might be biologically active, warranting further investigation to evaluate their potential therapeutic value.

Achieving higher field strengths through increased rotational speeds of the magnets is feasible. However, it is important to consider the low-pass filtering property of the neuronal membrane, rapid changes in voltage are not transmitted as efficiently across the membrane, diminishing the effect of high frequency stimulation [38]. Additionally, the interaction between field strength and excitation frequency could be nonlinear, as demonstrated in a transcranial alternating current stimulation (tACS) study [39,40]. For example, when 140 rps tACS is applied to the motor cortex, a low current amplitude of 0.4 mA results in a reduction in motor evoked potential (MEP) amplitudes; intermediate amplitudes of 0.6 mA and 0.8 mA showed no effect on MEP, and a high amplitude of 1 mA resulted in the enhancement of MEP amplitudes [39].

Several limitations should be acknowledged when interpreting this work. First, the simulations were not performed on realistic head models. Our models assume a simplified geometry with homogeneous, isotropic conductivity to better illustrate the spatial field distribution. Realistic head models consist of several tissue types with varying conductivities, the values of which are frequency dependent [22,23]. However, at the low frequency range that we are operating in (<1 kHz), tissue conductivity values remain relatively stable [22,23]. In addition, cortical folding in realistic head models can increase the maximum E-field strength compared to spherical head models [32,41]. It has been shown, for example, that skin conductivities' variation can result in minor changes in E-field strength induced by TMS [42]. Future work could consider integrating realistic head models to better represent accurate head anatomy and the variations in E-field strengths across individuals. The second limitation of our work is that we did not perform a high-resolution spatial sampling of the E-field in the phantom to characterize the full spatial distribution, which varies over time. Our focus was simply on measuring the peak E-field strength to validate the simulation magnitudes and compare them to previously conducted measurements and to conventional TMS.

5. Conclusions

In this study, we evaluated the E-field characteristics of the sTMS system, TRPMS system, and other configurations of rotating magnets using finite element modeling and phantom head measurements. Our findings indicate that the maximum induced E-field strength on the head surface ranged from 0.0092 V/m to 0.52 V/m, which is on the order of 0.1% of the field strength induced by conventional TMS. Furthermore, we demonstrate that E-field strength depends on rotational frequency, which represents a previously unappreciated confound in clinical trials that seek to synchronize rotational frequency to individual endogenous oscillatory activity. Future research directions include conducting simulations of rotating magnetic stimulation on anatomically accurate head models, which would be based on individual brain imaging data, as well as optimizing treatment parameters such as stimulation frequency and magnet placement. Additionally, it is essential to gather direct

electrophysiological data to corroborate the hypothesized mechanism of action of these stimulation systems.

Author Contributions: Conceptualization, Z.-D.D. and P.L.R.; methodology, P.L.R., S.N.M. and Z.-D.D.; validation, P.L.R. and Z.-D.D.; formal analysis, P.L.R. and Z.-D.D.; data curation, P.L.R. and Z.-D.D.; writing—original draft preparation, P.L.R. and Z.-D.D.; writing—review and editing, P.L.R., S.N.M., M.D., S.H.L. and Z.-D.D.; visualization, P.L.R. and Z.-D.D.; supervision, Z.-D.D. All authors have read and agreed to the published version of the manuscript.

Funding: P.L.R., S.H.L., and Z.-D.D. are supported by the National Institute of Mental Health (NIMH) Intramural Research Program (ZIAMH002955), National Institutes of Health (NIH). S.N.M. is supported by NIH/NIMH grant R01 MH130490.

Institutional Review Board Statement: Not applicable.

Informed Consent Statement: Not applicable.

Data Availability Statement: The raw data supporting the conclusions of this article will be made available by the authors on request.

Acknowledgments: This work utilized the computational resources of the NIH HPC Biowulf cluster (<http://hpc.nih.gov>, accessed 6 December 2023) The authors also thank the NIMH Section on Instrumentation for helping to build the measurement apparatus. The opinions expressed in this article are the author's own and do not reflect the views of the National Institutes of Health, the Department of Health and Human Services, or the United States government.

Conflicts of Interest: Z.-D.D. is an inventor of patents and patent applications on electrical and magnetic brain stimulation therapy systems held by the NIH, Columbia University, and University of New Mexico. S.H.L. is an inventor of patents and patent applications on electrical and magnetic brain stimulation therapy systems held by the NIH and Columbia University.

References

1. Cohen, S.L.; Bikson, M.; Badran, B.W.; George, M.S. A visual and narrative timeline of US FDA milestones for Transcranial Magnetic Stimulation (TMS) devices. *Brain Stimul.* **2022**, *15*, 73–75. [CrossRef]
2. Rizvi, S.; Khan, A.M. Use of transcranial magnetic stimulation for depression. *Cureus* **2019**, *11*, e4736. [CrossRef]
3. Phillips, J.W.; Jin, Y. Systems and Methods for Neuro-EEG Synchronization Therapy. U.S. Patent 8961386B2, 24 February 2015.
4. Watterson, P.A. Device Including Moving Magnet Configurations. U.S. Patent 20140163305A1, 12 June 2014.
5. Helekar, S.A.; Voss, H.U. Method and apparatus for providing transcranial magnetic stimulation (TMS) to a individual. U.S. Patent 10398907B2, 3 September 2019.
6. Leuchter, A.F.; Cook, I.A.; Jin, Y.; Phillips, B. The relationship between brain oscillatory activity and therapeutic effectiveness of transcranial magnetic stimulation in the treatment of major depressive disorder. *Front. Hum. Neurosci.* **2013**, *7*, 37. [CrossRef]
7. Leuchter, A.F.; Cook, I.A.; Feifel, D.; Goethe, J.W.; Husain, M.; Carpenter, L.L.; Thase, M.E.; Krystal, A.D.; Philip, N.S.; Bhati, M.T.; et al. Efficacy and safety of low-field synchronized transcranial magnetic stimulation (sTMS) for treatment of major depression. *Brain Stimul.* **2015**, *8*, 787–794. [CrossRef]
8. Philip, N.S.; Leuchter, A.F.; Cook, I.A.; Massaro, J.; Goethe, J.W.; Carpenter, L.L. Predictors of response to synchronized transcranial magnetic stimulation for major depressive disorder. *Depress. Anxiety* **2019**, *36*, 278–285. [CrossRef]
9. Jin, Y.; Phillips, B. A pilot study of the use of EEG-based synchronized transcranial magnetic stimulation (sTMS) for treatment of major depression. *BMC Psychiatry* **2014**, *14*, 13. [CrossRef]
10. Cook, I.A.; Wilson, A.C.; Corlier, J.; Leuchter, A.F. Brain activity and clinical outcomes in adults with depression treated with synchronized transcranial magnetic stimulation: An exploratory study. *Neuromodulation* **2019**, *22*, 894–897. [CrossRef]
11. Phillips, J.W.; Jin, Y. Devices and Methods of Low Frequency Magnetic Stimulation Therapy. U.S. Patent 9649502B2, 16 May 2017.
12. Philip, N.S.; Aiken, E.E.; Kelley, M.E.; Burch, W.; Waterman, L.; Holtzheimer, P.E. Synchronized transcranial magnetic stimulation for posttraumatic stress disorder and comorbid major depression. *Brain Stimul.* **2019**, *12*, 1335–1337. [CrossRef] [PubMed]
13. Helekar, S.A.; Voss, H.U. Transcranial brain stimulation with rapidly spinning high-field permanent magnets. *IEEE Access* **2016**, *4*, 2520–2528. [CrossRef]
14. Helekar, S.A.; Convento, S.; Nguyen, L.; John, B.S.; Patel, A.; Yau, J.M.; Voss, H.U. The strength and spread of the electric field induced by transcranial rotating permanent magnet stimulation in comparison with conventional transcranial magnetic stimulation. *J. Neurosci. Methods* **2018**, *309*, 153–160. [CrossRef] [PubMed]

15. Khavari, R.; Tran, K.; Helekar, S.A.; Shi, Z.; Karmonik, C.; Rajab, H.; John, B.; Jalali, A.; Boone, T. Noninvasive, individualized cortical modulation using transcranial rotating permanent magnet stimulator for voiding dysfunction in women with multiple sclerosis: A pilot trial. *J. Urol.* **2022**, *207*, 657–668. [CrossRef]
16. Greene, E.; Thonhoff, J.; John, B.S.; Rosenfield, D.B.; Helekar, S.A. Multifocal noninvasive magnetic stimulation of the primary motor cortex in type 1 myotonic dystrophy - a proof of concept pilot study. *J. Neuromuscul. Dis.* **2021**, *8*, 963–972. [CrossRef]
17. Jang, Y.; Tran, K.; Shi, Z.; Christof, K.; Choksi, D.; Salazar, B.H.; Lincoln, J.A.; Khavari, R. Predictors for outcomes of noninvasive, individualized transcranial magnetic neuromodulation in multiple sclerosis women with neurogenic voiding dysfunction. *Continence* **2022**, *4*, 100517. [CrossRef]
18. Tran, K.; Shi, Z.; Karmonik, C.; John, B.; Rajab, H.; Helekar, S.A.; Boone, T.; Khavari, R. Therapeutic effects of non-invasive, individualized, transcranial neuromodulation treatment for voiding dysfunction in multiple sclerosis patients: Study protocol for a pilot clinical trial. *Pilot Feasibility Stud.* **2021**, *7*, 83. [CrossRef]
19. Wide-Bore Low-Frequency Magnetic Spinner for Non-Contact E-Field Generation in a Tissue via Faraday's Law of Induction. Available online: <https://www.nevaelectromagnetics.com/wide-bore-low-freq-generator-type1> (accessed on 24 December 2023).
20. Watterson, P.A.; Nicholson, G.M. Nerve-muscle activation by rotating permanent magnet configurations. *J. Physiol.* **2016**, *594*, 1799–1819. [CrossRef]
21. Heller, L.; van Hulsteyn, D.B. Brain stimulation using electromagnetic sources: Theoretical aspects. *Biophys. J.* **1992**, *63*, 129–138. [CrossRef] [PubMed]
22. Gabriel, S.; Lau, R.; Gabriel, C. The dielectric properties of biological tissues: II. Measurements in the frequency range 10 Hz to 20 GHz. *Phys. Med. Biol.* **1996**, *41*, 2251–2269. [CrossRef] [PubMed]
23. Gabriel, S.; Lau, R.; Gabriel, C. The dielectric properties of biological tissues: III. Parametric models for the dielectric spectrum of tissues. *Phys. Med. Biol.* **1996**, *41*, 2271–2293. [CrossRef] [PubMed]
24. Temperature and Neodymium Magnets. Available online: <https://www.kjmagnetics.com/blog.asp?p=temperature-and-neodymium-magnets> (accessed on 10 January 2023).
25. Rotating Machinery 3D Tutorial. Available online: https://doc.comsol.com/6.0/doc/com.comsol.help.models.acdc.rotating_machinery_3d_tutorial/models.acdc.rotating_machinery_3d_tutorial.pdf (accessed on 15 February 2022).
26. Glover, P.M.; Bowtell, R. Measurement of electric fields due to time-varying magnetic field gradients using dipole probes. *Phys. Med. Biol.* **2007**, *52*, 5119–5130. [CrossRef] [PubMed]
27. Ramon, C.; Garguilo, P.; Fridgeirsson, E.A.; Hauelsen, J. Changes in scalp potentials and spatial smoothing effects of inclusion of dura layer in human head models for EEG simulations. *Front. Neuroeng.* **2014**, *7*, 32. [CrossRef] [PubMed]
28. Sauerheber, R.; Heinz, B. Temperature effects on conductivity of seawater and physiologic saline, mechanism and significance. *Chem. Sci. J.* **2015**, *6*, 1000109. [CrossRef]
29. Smith, J.E.; Peterchev, A.V. Electric field measurement of two commercial active/sham coils for transcranial magnetic stimulation. *J. Neural. Eng.* **2018**, *15*, 054001. [CrossRef]
30. Deng, Z.D.; Lisanby, S.H.; Peterchev, A.V. Electric field depth–focality tradeoff in transcranial magnetic stimulation: Simulation comparison of 50 coil designs. *Brain Stimul.* **2013**, *6*, 1–13. [CrossRef]
31. Rohan, M.L.; Yamamoto, R.T.; Ravichandran, C.T.; Cayetano, K.R.; Morales, O.G.; Olson, D.P.; Vitaliano, G.; Paul, S.M.; Cohen, B.M. Rapid mood-elevating effects to low field magnetic stimulation in depression. *Biol. Psychiatry* **2014**, *76*, 186–193. [CrossRef] [PubMed]
32. Miranda, P.C.; Mekonnen, A.; Salvador, R.; Ruffini, G. The electric field in the cortex during transcranial current stimulation. *Neuroimage* **2013**, *70*, 48–58. [CrossRef] [PubMed]
33. Guidetti, M.; Arlotti, M.; Bocci, T.; Bianchi, A.M.; Parazzini, M.; Ferrucci, R.; Priori, A. Electric fields induced in the brain by transcranial electric stimulation: A review of in vivo recordings. *Biomedicines* **2022**, *10*, 2333. [CrossRef]
34. Grehl, S.; Martina, D.; Goyenvalle, C.; Deng, Z.D.; Rodger, J.; Sherrard, R.M. In vitro magnetic stimulation: A simple stimulation device to deliver defined low intensity electromagnetic fields. *Front. Neural. Circuits* **2016**, *10*, 85. [CrossRef] [PubMed]
35. Moretti, J.; Terstege, D.J.; Poh, E.Z.; Epp, J.R.; Rodger, J. Low intensity repetitive transcranial magnetic stimulation modulates brain-wide functional connectivity to promote anti-correlated c-Fos expression. *Sci. Rep.* **2022**, *12*, 20571. [CrossRef] [PubMed]
36. Dufor, T.; Grehl, S.; Tang, A.D.; Doulazmi, M.; Traoré, M.; Debray, N.; Dubacq, C.; Deng, Z.D.; Mariani, J.; Lohof, A.M.; et al. Neural circuit repair by low-intensity magnetic stimulation requires cellular magnetoreceptors and specific stimulation patterns. *Sci. Adv.* **2019**, *5*, eaav9847. [CrossRef] [PubMed]
37. Makowiecki, K.; Garrett, A.; Harvey, A.R.; Rodger, J. Low-intensity repetitive transcranial magnetic stimulation requires concurrent visual system activity to modulate visual evoked potentials in adult mice. *Sci. Rep.* **2018**, *8*, 5792. [CrossRef] [PubMed]
38. Brunel, N.; van Rossum, M.C.W. Quantitative investigations of electrical nerve excitation treated as polarization. *Biol. Cybern.* **2007**, *97*, 341–349. [CrossRef] [PubMed]
39. Moliadze, V.; Atalay, D.; Antal, A.; Paulus, W. Close to threshold transcranial electrical stimulation preferentially activates inhibitory networks before switching to excitation with higher intensities. *Brain Stimul.* **2012**, *5*, 505–511. [CrossRef] [PubMed]
40. Numssen, O.; Zier, A.L.; Thielscher, A.; Hartwigsen, G.; Knösche, T.R.; Weise, K. Efficient high-resolution TMS mapping of the human motor cortex by nonlinear regression. *Neuroimage* **2021**, *245*, 118654. [CrossRef] [PubMed]

41. Thielscher, A.; Opitz, A.; Windhoff, M. Impact of the gyral geometry on the electric field induced by transcranial magnetic stimulation. *Neuroimage* **2011**, *54*, 234–243. [CrossRef]
42. Colella, M.; Paffi, A.; De Santis, V.; Apollonio, F.; Liberti, M. Effect of skin conductivity on the electric field induced by transcranial stimulation techniques in different head models. *Phys. Med. Biol.* **2021**, *66*, 035010. [CrossRef]

Disclaimer/Publisher’s Note: The statements, opinions and data contained in all publications are solely those of the individual author(s) and contributor(s) and not of MDPI and/or the editor(s). MDPI and/or the editor(s) disclaim responsibility for any injury to people or property resulting from any ideas, methods, instructions or products referred to in the content.

Article

Comparison of Transcranial Magnetic Stimulation Dosimetry between Structured and Unstructured Grids Using Different Solvers

Francesca Camera ^{1,*}, Caterina Merla ¹ and Valerio De Santis ²

¹ Division of Biotechnologies, Italian National Agency for Energy, New Technologies and Sustainable Economic Development (ENEA), 00123 Rome, Italy; caterina.merla@enea.it

² Department of Industrial and Information Engineering and Economics, University of L'Aquila, 67100 L'Aquila, Italy; valerio.desantis@univaq.it

* Correspondence: francesca.camera@enea.it; Tel.: +39-0630486741

Abstract: In recent years, the interest in transcranial magnetic stimulation (TMS) has surged, necessitating deeper understanding, development, and use of low-frequency (LF) numerical dosimetry for TMS studies. While various ad hoc dosimetric models exist, commercial software tools like SimNIBS and Sim4Life are preferred for their user-friendliness and versatility. SimNIBS utilizes unstructured tetrahedral mesh models, while Sim4Life employs voxel-based models on a structured grid, both evaluating induced electric fields using the finite element method (FEM) with different numerical solvers. Past studies primarily focused on uniform exposures and voxelized models, lacking realism. Our study compares these LF solvers across simplified and realistic anatomical models to assess their accuracy in evaluating induced electric fields. We examined three scenarios: a single-shell sphere, a sphere with an orthogonal slab, and a MRI-derived head model. The comparison revealed small discrepancies in induced electric fields, mainly in regions of low field intensity. Overall, the differences were contained (below 2% for spherical models and below 12% for the head model), showcasing the potential of computational tools in advancing exposure assessment required for TMS protocols in different bio-medical applications.

Keywords: conformal mesh; solvers comparison; structured and unstructured grids; transcranial magnetic stimulation (TMS) dosimetry

1. Introduction

Lately, transcranial magnetic stimulation (TMS) is undergoing significant interest due to its non-invasive approach and lower side effects than its counterparts [1–6]. TMS can be successfully used for diagnostic purposes (e.g., myelopathy, amyotrophic lateral sclerosis, and multiple sclerosis) or the treatment of several mental disorders. Recently, it received significant attention for its application in the treatment of Alzheimer's disease in patients at the early stage of the pathology, as proposed by [7], thanks to its ability to modulate the synaptic plasticity of specific brain areas devoted to memory and cognition. In all cases, a changing magnetic field is applied to induce an electric field at a specific area of the brain through Faraday's law of induction.

During the design stage, the use of numerical tools for predicting this induced electric field is paramount. Low frequency (LF) numerical dosimetry for TMS studies is therefore more and more relevant [8–11]. Several ad hoc (or in-house) models have been developed [12–18], but commercial software tools are more user-friendly and general-purpose. Among these, SimNIBS [19] and Sim4Life (ZMT, Zurich MedTech, Zürich, Switzerland) are the most widely used. The former uses a pipeline that interpolates data from a Neuroimaging Informatics Technology Initiative (NifTI) format image to obtain a model with an unstructured tetrahedral mesh, whereas the latter employs voxel-based models in a

structured or rectilinear grid. The computational techniques to evaluate the induced electric fields are based on the finite element method (FEM) for both software, but with different numerical solvers. The results of these two software packages have been compared in simplified geometries consisting of a homogeneous and non-homogeneous sphere or in a realistic anatomical model of the head and brain.

In the past, several inter-comparison studies have examined LF numerical issues [20–23]. These studies employed various anatomical models, but primarily focused on uniform exposures and voxelized models prone to staircasing errors, using methods like the scalar potential finite difference (SPFD) or the scalar potential finite element (SPFE). In a study by Poljak et al. [15], different computational models and/or solvers (i.e., surface integral Equation (SIE)-based Method of Moments (SIE/MoM) [14,24], the FEM with cubical elements [12], the BEM and the hybrid FEM/BEM [25,26], and the FEM with rectilinear elements using Sim4Life software [15]) have been used for a non-uniform exposure (i.e., TMS application), but only for a homogeneous sphere or head. The only works where more realistic anatomical models for a TMS application were applied for both voxelized grids and tetrahedral mesh are found in [16,18,27]. However, the comparison in the induced electric field (E-field) was made only for a simplified homogeneous sphere in [16], or a multi-layered sphere with E-field looping tangentially on it [18,27], while for the realistic head, it was evaluated on a plane situated in the middle between the surfaces of the white and gray matter [16] to avoid evaluating the field on the boundary of tissues having different conductivities. In [27], the excitation source was also a simple circular coil far from realistic TMS applications, while in [18], the head was made of four tissues only.

In this paper, the comparison between the two solvers adopting different grids (structured and unstructured) is, instead, performed in the overall domain consisting of both homogeneous and moreover non-homogeneous spheres intentionally created to enhance the induced E-field at these discontinuities that have been poorly investigated so far. A more realistic non-homogeneous anatomical model is also considered for TMS applications (with a realistic figure-of-8 coil) to validate both commercial software. These results could sign an important advancement in exposure assessment, which is based more and more on computational tools.

2. Materials and Methods

2.1. Source Model

For this study, a typical figure-of-8 coil, the Deymed 70BF (Deymed Diagnostic, Payette, ID, USA), has been chosen as a TMS source. This coil, consisting of two adjacent circular loops with current flowing in opposite directions, produces a magnetic field with pulses waveforms approximable to a sinus at 3200 Hz. Due to the time-varying nature of the field, the E-field is induced in the underlying area of the head via the induction Faraday's law. The focality of the induced E-field is given by the particular shape and path of the coil current, and reaches its maximum at the point of intersection between the two loops [1].

2.2. Computational Methods

The simulation environments chosen for this comparison are two widely available software packages: SimNIBS v.4.0.0 [19], which is based on tetrahedral mesh, and Sim4Life v7.2.4 (ZMT, Zurich MedTech, Zürich, Switzerland), which is based on a voxelized model or structured grids. All of the simulations have been run on a Workstation with a 32-Core processor at 3.69 GHz and with 256 GB RAM.

2.2.1. SimNIBS

SimNIBS is an open-source pipeline for simulating the E-fields induced by TMS based on FEM and individualized head models generated from magnetic resonance images (MRIs). The pipeline automatically makes FEM tetrahedral mesh starting both from T1 + T2 MRI-scans and from only T1 MRI-scans. We used the default solver option, which consists of an algebraic multigrid preconditioned conjugate gradient solver (CG-AMG).

SimNIBS provides a built-in range of TMS coil models [28], including the Deymed 70BF. The coil shape is obtained from geometric models of the coil turns, and it is represented as a set of magnetic dipoles, from which it is possible to calculate, in a user-defined voxelized volume, the normalized magnetic induction (B-field) and the normalized magnetic vector potential (A-field) obtained when the coil is fed by a current of 1 A, using a simple formula [29]. These fields will also be used in Sim4Life to model the TMS source (see Section 2.2.2). However, SimNIBS does not allow the user to directly choose the current intensity feeding the coil (I), but the input for the simulations is in terms of dI/dt . Therefore, a comparison with the analytical solution using a single-shell sphere with a uniform B-field is needed to correlate the normalized B-field and the normalized A-field used as input in Sim4Life and the output of SimNIBS simulations (see Appendix A). Based on this comparison, it is obtained that the results of the simulations carried out with SimNIBS with $dI/dt = 1 \text{ A}/\mu\text{s}$ must be divided by 50 to be compared to the ones carried out with Sim4Life (see Figure A1).

TMS simulations start by calculating the change in the A-field in the elements of the volume conductor mesh for the appropriate coil model, position and current. The time-varying A-field (dA/dt) is used as source terms to solve a linear system and obtain the electric potentials (ϕ) at the nodes of the mesh, considering the following equation:

$$\mathbf{E} = -\frac{d\mathbf{A}}{dt} - \nabla\phi \quad (1)$$

2.2.2. Sim4Life

Sim4Life is a simulation platform developed by the IT'IS Foundation and ZMT (Switzerland, CH) to model the interactions between physical stimuli and the human body. Similar to SimNIBS, this software can even deal with medical image data obtained from MRI. The simulation platform includes many physical solvers. Among these, the Magneto Quasi-Static (M-QS) module included in the LF Solvers (EM-LF-MQS) has been selected. This solver evaluates the induced E-field by applying the SPFE method on graded voxel grids and solving (1) in the frequency domain by setting the operation frequency to 3200 Hz.

In the EM-LF-QS solver, it is possible to add a magnetic source in two principal ways: (1) modeling the current path with dimensionless wires that replicate the coil's windings in the desired position, or (2) importing an external source file with a user-defined discretized volume on a 3-D grid where the values of B-field and A-field are known. It should be noted that a cubic (tri-linear) interpolation is performed on the magnetic field source values from this grid (which is usually coarse) to the one used in the induced E-field evaluation (which is usually finer). Also note that if the A-field is unknown, it can be derived starting from the only knowledge of the B-field by means of the procedure described in [30], implemented in Sim4Life. In order to have a fair comparison of the field generated by the two software, the second way has been chosen, since the B-field and A-field are easily calculated in the SimNIBS coil database and exported to Sim4Life in a *.txt* file in the desired discretized volume.

Under the QS approximation, the conduction currents are at least one order of magnitude higher than the displacement currents for most of the tissues [31,32], and therefore only tissue conductivity can be considered.

2.3. Exposure Scenarios

Three different scenarios have been considered for the numerical comparison, as shown in Figure 1.

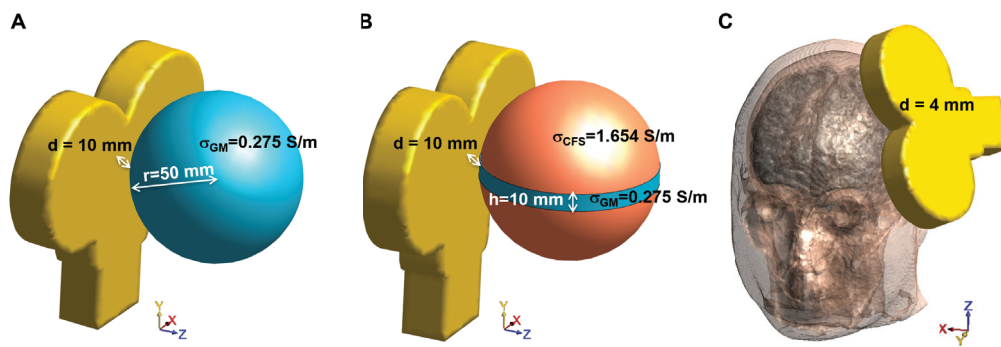


Figure 1. Considered exposure scenarios for the numerical comparison: (A) single-shell sphere, (B) single-shell sphere with orthogonal slab, and (C) MRI-derived human head model.

2.3.1. Single-Shell Sphere

The first scenario is a homogeneous sphere model comprised a single-shell sphere with a radius of 50 mm and conductivity of 0.275 S/m (like the gray matter GM, [33]). Preliminary simulations have been carried out varying both the voxels side of the grid (0.25, 0.5, 1 and 2 mm) and the side of tetrahedrons (see Appendix B), both for the single-shell sphere and for the single-shell sphere with slab (see Section 2.3.2). These simulations showed that the differences between the results of the two solvers are minimized when the voxels side in Sim4Life is 0.25 mm only in the homogeneous case (Table A3). This means that when a discontinuity is introduced in the model, like in Section 2.3.2 and in Section 2.3.3, the accuracy of the results is not guaranteed by shrinking the grid (Table A5).

For this reason, and also because the MRI-derived human head models are generally discretized at 1 mm, for the sake of uniformity in the comparison, in all the simulations in Sim4Life, a regular grid constituted of 1 mm side cubic voxels has been set, and the SimNIBS mesh has been chosen to have a comparable number of tetrahedrons (632,765 tetrahedrons vs. 520,613 voxels). For each simulation environment, the sphere is centered about the origin and the bottom of the coil windings is at a distance (d) of 10 mm above its apex at location (50, 0, 0) mm (Figure 1A).

2.3.2. Single-Shell Sphere with Orthogonal Slab

The second scenario is a sphere model of the same size as the previous one, but with a conductivity of 1.654 S/m (like the cerebrospinal fluid, CSF, [33]) in which a rounded slab with 10 mm height and conductivity of 0.275 S/m (like GM) is included. As in the previous case, both the sphere and the slab are centered about the origin and the bottom of the coil windings is at a distance (d) of 10 mm above its apex at location (50, 0, 0) mm, as shown in Figure 1B. Once again, we handled the discretization parameters in order to obtain a number of tetrahedrons in SimNIBS comparable with that of voxels in Sim4Life with a fixed 1 mm grid (637,816 tetrahedrons vs. 520,613 voxels).

2.3.3. MRI-Derived Head Model

The head model was the one provided in the SimNIBS v4.0 package Ernie, which is a human head model obtained by the segmentation *headreco* tool that segments, cleans-up the tissue maps and meshes the surfaces into triangles and volumes into tetrahedrons. The mesh consisted of nine homogeneous tissues in which the tissue conductivities were considered constant and were set as follows: σ (white matter, WM) = 0.126 S/m, σ (GM) = 0.275 S/m, σ (CSF) = 1.654 S/m, σ (scalp) = 0.465 S/m, σ (compact bone) = 0.008 S/m, σ (spongy bone) = 0.025 S/m, σ (eyeball) = 0.500 S/m, σ (blood) = 0.600 S/m, σ (muscle) = 0.160 S/m [33,34]. The coil was placed in order to mimic the dorsolateral prefrontal cortex (DLPFC) stimulation, 4 mm away from the scalp (Figure 1C). The resulting number of tetrahedrons in SimNIBS and voxels in Sim4Life (fixed 1 mm grid resolution) were 4066640 tetrahedrons vs. 5077706 voxels.

2.4. Metrics for Comparison

To facilitate a direct comparison of the results from the two simulation environments, the E-field calculated in SimNIBS has been interpolated for each model to derive values corresponding to the Sim4Life grid.

First, of all, a comparison of the maximum E-field obtained from each simulation (E_{Max} and $E_{99,9th}$) has been made. $E_{99,9th}$ was obtained by taking the 99.9th percentile of each GM E-field distribution, and it is, as some authors suggested [8,35–39], a good trade-off for localized exposures that reduces hot spots of E-field due to numerical artifacts. All of the E-field values higher than $E_{99,9th}$ were considered equal to the maximum.

To further quantify the comparison, different metrics have been used. The first local metric, i.e., voxel-by-voxel, is the symmetric mean absolute percentage error (SMAPE), and it is defined as:

$$SMAPE_{loc} \% = 100 \cdot \frac{|E_{sim4} - E_{simN}|}{(|E_{sim4}| + |E_{simN}|)/2} \quad (2)$$

where E_{sim4} is the calculated module of the E-field with Sim4Life, while E_{simN} is the one calculated with SimNIBS. Note that the above expression is evaluated in each voxel, so it is possible to obtain the spatial distribution of the differences between the two solutions. If this quantity (2) is averaged on the entire domain, a global metric is obtained, i.e.,

$$SMAPE\% = \frac{100}{n} \sum_n \frac{|E_{sim4} - E_{simN}|}{(|E_{sim4}| + |E_{simN}|)/2} \quad (3)$$

where n is the number of voxels of the domain in which the E-field is calculated. Other global metrics can be defined as:

$$\epsilon_1 = 100 \cdot \frac{\sum_n |E_{sim4} - E_{simN}|}{\sum_n |E_{sim4}|} \quad (4)$$

and

$$\epsilon_2 = 100 \cdot \frac{\sqrt{\sum_n |E_{sim4} - E_{simN}|^2}}{\sqrt{\sum_n |E_{sim4}|^2}} \quad (5)$$

These metrics consider the differences (in a global sense) between the results of SimNIBS with respect to the ones obtained in Sim4Life. Since the exposure that has been simulated in all three scenarios (Section 2.3) is a localized one, it becomes interesting to analyze the errors in the Stimulating Volume X (SV_X), which is the volume exposed to an E-field equal to or greater than $X\%$ of $E_{99,9th}$.

Therefore, it is possible to define the $SMAPE\%_X$, the ϵ_{1X} and the ϵ_{2X} , which are the global metrics of Equations (2)–(4) in which only the voxels where the E-field is equal to or greater than $X\%$ of $E_{99,9th}$ are considered.

3. Results

Table 1 summarizes the maximum values of the E-field for all exposure scenarios considering an input current for the coil of 1 A. Looking at the $E_{99,9th}$, the two software packages yield very close results, while the E_{Max} exhibits a higher discrepancy. For both software packages, E_{Max} overestimates the expected maximum induced field, so tetrahedral meshes are not capable of suppressing numerical errors caused by stair-casing in voxelized models when curved boundaries are approximated with voxels. However, nothing can be said about the actual maximum induced field, because, in such localized exposure with the figure-eight coil, no direct comparison with the analytic solution can be made. The contrast of conductivities between tissues and low-quality tetrahedral mesh cause numerical artifacts as well, but $E_{99,9th}$ calculated for both software return stable and comparable values.

Table 1. Maximum value of E-field for the three exposure scenarios calculated by both software with an input current of 1 A. (E_{Max}) is the maximum E-field obtained from each simulation and $E_{99.9th}$ was obtained by taking the 99.9th percentile of each GM E-field distribution.

	Sim4Life		SimNIBS	
	Max (mV/m)	99.9th (mV/m)	Max (mV/m)	99.9th (mV/m)
Single-shell sphere	38.3	29.1	34.0	29.1
Single-shell sphere with slab	82.6	79.0	100.1	78.3
MRI-derived head model	43.0	27.9	38.0	27.2

An example of E-field distribution induced in a single-shell sphere model calculated in Sim4Life (panel A) and in SimNIBS (panel B) for an input current of 1 A is reported in Figure 2. The selected slice is perpendicular to the coil, and passes through the center of the sphere, i.e., also through the maximum of the localized induced E-field. By visual inspection, meshes and grids produce similar field distributions, meaning physically reasonable results. Panel C shows the $SMAP E_{loc}$ calculated in the sphere. To enhance visibility, the results have been saturated to 40%. As can be observed, the error becomes significant only in the volume in which the calculated E-field is very low, so it can be given to numerical errors.

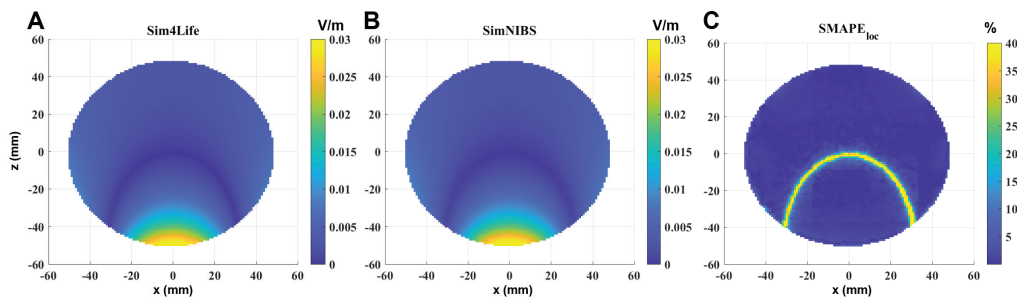


Figure 2. E-field induced in the sphere model on a section perpendicular to the coil and passing through the center of the sphere, calculated by (A) Sim4Life and (B) SimNIBS, and the $SMAP E_{loc}$ between the two software results (C). Input current: 1 A. Computing time: 6 s (SimNIBS) and 9 s (Sim4Life).

Similar considerations can be performed in the single-shell sphere with the orthogonal slab (Figure 3). In this case, to better visualize what happens near the discontinuity between the two materials, the selected slice is parallel to the coil, perpendicular to the slab and passing through the center of the sphere. It is also possible to see that, in this case, the error is significant and exceeds 40% only where the calculated E-field is very low, i.e., in the inner part of the sphere (due to Faraday’s law); however, the error also slightly increases near the interface between the two materials (Figure 3C).

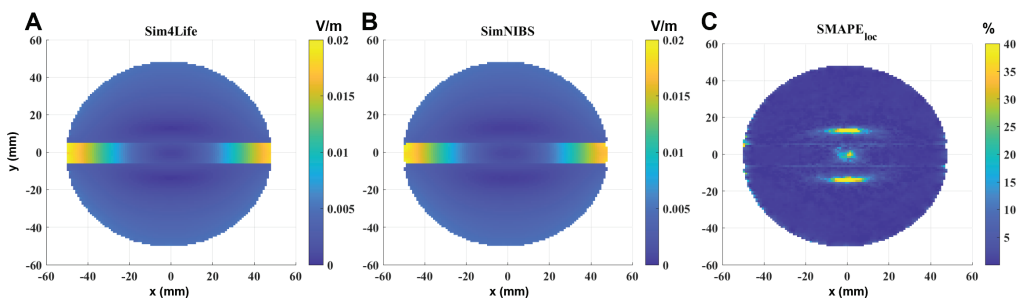


Figure 3. E-field induced in the sphere with orthogonal slab model on a section parallel to the coil, perpendicular to the slab and passing through the center of the sphere, calculated by (A) Sim4Life and (B) SimNIBS and the $SMAP E_{loc}$ between the two software results (C). Input current: 1 A. Computing time: 6 s (SimNIBS) and 9 s (Sim4Life).

Figure 4 shows the same comparison on a transverse section passing through the maximum of the localized induced E-field of the MRI-derived head model. Results on materials not belonging to the brain are neglected, so the calculated E-field is shown only on the GM and WM. In this case, the geometrical and electrical discontinuities are more pronounced than in the other two models, and the difference between the two solvers becomes more evident at the interface between GM and WM and between GM and materials outside the brain.

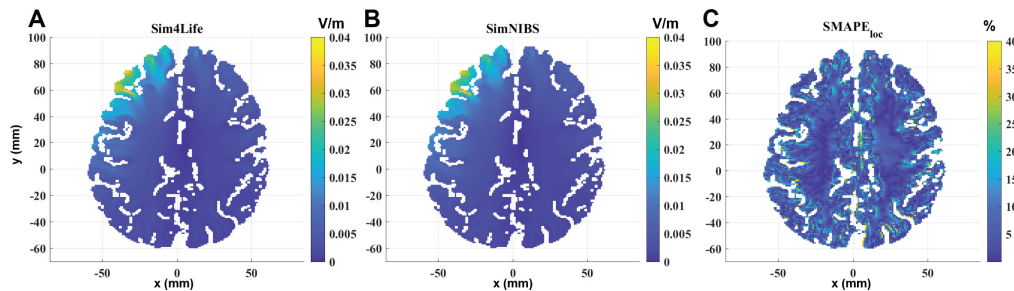


Figure 4. E-field induced in the MRI-derived head model in the GM and WM on a transverse section passing through the $E_{99,9th}$, calculated by (A) Sim4Life and (B) SimNIBS and the $SMAPE_{loc}$ between the two software results (C). Input current: 1 A. Computing time: 205 s (SimNIBS) and 122 s (Sim4Life).

Table 2 summarizes all of the global error metrics between the two software for the three models. As the model becomes more complex, the computational differences between the two software packages increase, albeit remaining within acceptable bounds (below 5% for the spherical models and below 12% for the realistic head model).

Table 2. Global error metrics between the results of the two software for the three dosimetric models.

	$SMAPE\%$	ϵ_1	ϵ_2
Single-shell sphere	1.1	1.2	3.0
Single-shell sphere with slab	1.6	1.4	4.4
MRI-derived head model	9.4	8.6	11.5

An analysis of the Stimulating Volume X (SV_X), i.e., the volume exposed to E-field equal to or greater than X% of $E_{99,9th}$, varying X% has been conducted for the head model (as shown in Figure 5). This metric is interesting when a localized exposure is considered, because it is an estimation of the focality of the stimulation. In particular, many authors [10] take the SV_{50} to quantify the focality. Figure 5 shows that the focality (SV_{50}) slightly differs (of about 5%) between the two software.

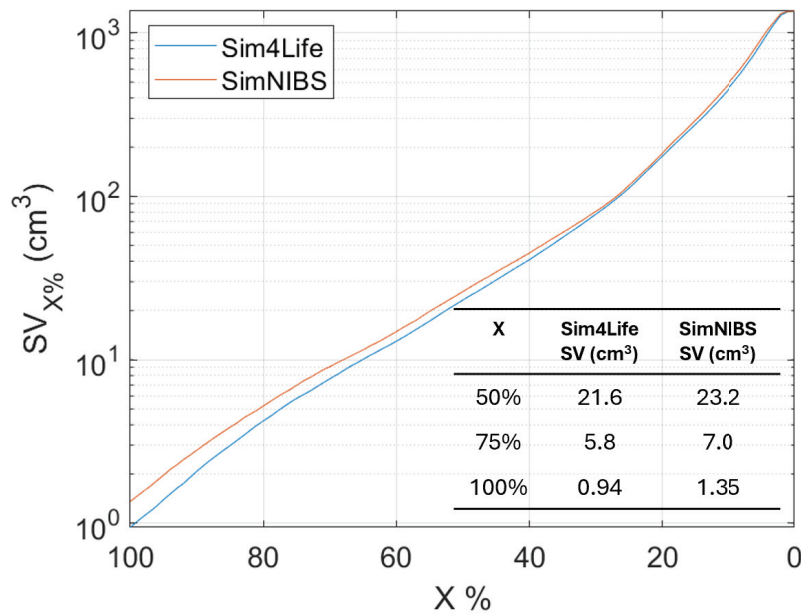


Figure 5. Stimulating Volume X (SV_X), i.e., the volume exposed to E-field equal to or greater than X% of $E_{99,9th}$ in MRI-derived human head model varying X%.

Finally, an analysis of the errors varying X% is shown in Figure 6. As X% decreases, the comparison is conducted over an increasingly larger volume (Figure 5). Indeed, when $X = 100\%$, it means that the comparison is made in the volume in which the E-field is equal or higher than the $E_{99,9th}$, whereas when $X = 0\%$, the comparison is made in the entire volume.

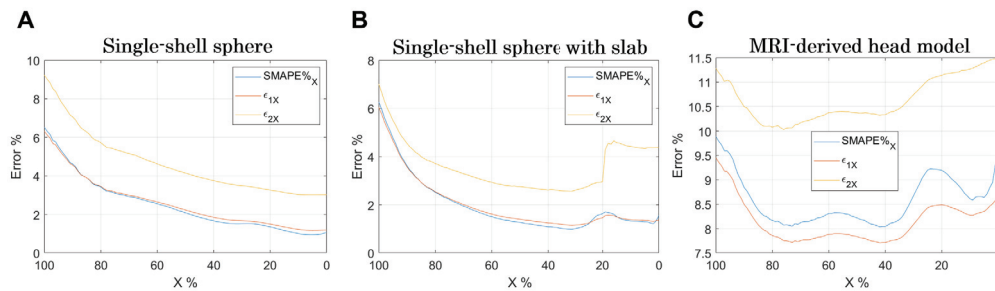


Figure 6. Errors in the Stimulating Volume X (SV_X), i.e., the volume exposed to E-field equal to or greater than X% of $E_{99,9th}$. (A) Single-shell sphere, (B) single-shell sphere with orthogonal slab, and (C) MRI-derived human head model.

Certainly, the stair-casing error, which, as already described, results in an overestimation of the E-field at certain points, and maximizes the error when the analysis focuses on that volume. However, by widening the analysis volume, the error reduces and increases again when considering volumes where the E-field is very low (Figure 6B,C).

4. Discussion

The comparison of LF numerical dosimetry results between conformal and non-conformal discretization of the human bodies, specifically the head and brain, has been deeply investigated [15,16,18,27]. Usually, conformal meshes are employed in solvers adopting the FEM or BEM/MoM or hybrid combinations of them for solving the induced electric field. This generally yields more accurate results, at the expense however of computationally heavier simulations. On the other hand, non-conformal solvers (e.g.,

SPFD or SPFE) using rectilinear grids are easier and faster to implement but suffer from staircasing errors.

When doing this discretization comparison, particular attention must therefore be paid to aligning or “matching” the nodes of the meshes with those of the grids. More precisely, the barycenter of tetrahedra should coincide with that of the voxel, in order to have a fair comparison of the dielectric properties of the material and hence of the obtained results. This is what has been made in [27,40], where special focus has been given to the parameters used to generate the meshes.

Such attention has been paid also in this study, where some parameters have been settled in SimNIBS to obtain a desired mesh. The rationale behind a fair comparison is to have a number of tetrahedral nodes similar to that of voxel numbers. This has been shown to be a good approach, as demonstrated in the supporting material with the analytic solution.

Besides paying attention to mesh generation, a lot of efforts have been made in the past to “remove” or quantify the staircasing error [8,35–39], finding, for instance, some smoothing techniques with fixed artifact removal (e.g., 99.9th or 99.99th [35,37,38], rather than 99th percentiles (as suggested by ICNIRP-2010 [41]) or flexible/variable removal artifact (depending on the grid resolution employed) [36,39]. However, among these suggested approaches, no one can be perfect in removing 100% of the numerical artifacts, as no analytic or experimental solution exists for realistic anatomical models. This is erroneously stated in [16], even though we can draw the same conclusions that choosing a grid resolution of 1 mm (or below) is retained to be good enough for structured or rectilinear grids. Once again, this is confirmed by the results shown in our and their supporting materials when comparing the induced E-field in a homogeneous sphere with the analytic solution. Further, looking at the errors reported in Figure 6, it emerges that their minimization is for X% between 40% and 60% for both software. This result indicates this volume % range as the optimal one for dosimetric assessment.

The comparison between structured and unstructured numerical solvers revealed that errors become more pronounced with increasing geometric complexity, this finding has several practical implications for TMS applications.

This comparison could be helpful when it is required to target small and specific brain regions. This is of interest for TMS applications in treating conditions such as Alzheimer’s disease [7]. Their approach focuses on stimulating specific areas of the brain, which requires precise modeling to ensure effectiveness of the treatment. The increased error in complex geometries indicates the need for advanced solvers to accurately define exposure also in interconnected brain areas. This is important for TMS applications that aim to target networks of brain regions. Accurate modeling can help in understanding the effects of TMS on these interconnected areas, leading to more effective treatments. Understanding the limitations and potential errors of different numerical solvers can aid in optimizing TMS protocols. Clinicians and researchers can choose the most appropriate solver based on the complexity of the target geometry, improving the precision of TMS treatments and potentially enhancing clinical outcomes. In summary, the results underscore the importance of selecting the right numerical solver for accurate TMS application, particularly when dealing with complex brain geometries. This has direct implications for the treatment of neurological conditions like Alzheimer’s disease [7], as well as for the broader use of TMS in targeting specific and interconnected brain areas.

Finally, regarding the comparison between the two commercial software packages, no preferences or endorsements are made. The computation time for the two software packages is comparable (below 10 s for the two spherical model, and about 2–3 min for the head model, cfr. Figures 2–4). The choice between the software packages should be based on practical considerations, such as the type of sources available. SimNIBS, for example, offers more specific commercial coils built into the software, while the other software may require the realization of specific geometries. Sim4Life, for instance, includes permittivity

values for tissues, which are not included by default in the other software, and could be relevant in specific applications.

The flexibility in terms of GUI and computing interface varies, and the operator may prefer one over the other based on their skill set. Both software packages are user-friendly for standard cases and deliver computational results quickly.

Overall, these tools have the potential to open numerous doors in the treatment of various mental disorders using TMS applications. They allow for rigorous assessment of E-field values for different protocols in real-time patient scenarios.

5. Conclusions

In this study, a comparison of TMS dosimetry between structured and unstructured grids using different solvers was performed with the two most commonly used software packages for TMS dosimetry: Sim4Life and SimNIBS. The comparison was conducted on three different geometrical models of increasing complexity: a homogeneous sphere, a sphere with an internal discontinuity, and a head model derived from MRI data.

The results demonstrate that differences between the obtained results are larger as geometric complexity increases. However, these differences remain on overall contained (below 5% for spherical geometric models and below 12% for the head model) and locally significant only in areas of tissues where the electric field value is very low (and therefore much more susceptible to numerical errors) or, as expected, near the tissues discontinuities. These results could sign an important advancement in exposure assessment protocols, which are based more and more on computational tools.

Author Contributions: Conceptualization, F.C., C.M. and V.D.S.; methodology, F.C., C.M. and V.D.S.; software, F.C. and V.D.S.; validation, F.C.; formal analysis, F.C.; resources, C.M.; data curation, F.C. and V.D.S.; writing—original draft preparation, F.C. and V.D.S.; writing—review and editing, C.M.; visualization F.C. All authors have read and agreed to the published version of the manuscript.

Funding: This research was funded by ECS 0000024 Project RomeTechnopole, CUP. B83C22002820006, PNRR Mission 4 Component 2 Investment 1.5, funded by the European Union–NextGenerationEU.

Institutional Review Board Statement: Not applicable.

Informed Consent Statement: Not applicable.

Data Availability Statement: Data are available from the corresponding author upon reasonable request.

Conflicts of Interest: The authors declare no conflicts of interest.

Appendix A

Since in SimNIBS the magnetic source can be generated only in the form of magnetic dipoles, in the case of the spatially uniform exposure, the magnetic vector potential A was given by a strong point-wise magnetic dipole placed very far away from the head, in order to obtain a spatially uniform B-field at 3200 Hz of 0.2 mT, directed along the x -axis. The spatial distribution of the induced E-field in a homogeneous conductive sphere is well-known, i.e., the analytic solution exists and is given by:

$$E = \frac{\omega B r}{2} = \pi f B r \quad (\text{A1})$$

where $f = 3200$ Hz, $B = 0.2$ mT and r is the radial direction.

Figure A1 shows the magnitude of the E-field along this radial direction. This quantity is calculated with Equation (A1) (blue line) and with Sim4Life (red line). The yellow line is the E-field derived by multiplying SimNIBS results by a multiplicative factor k , which was determined through fitting the results to the analytical values (found to be equal to 0.02).

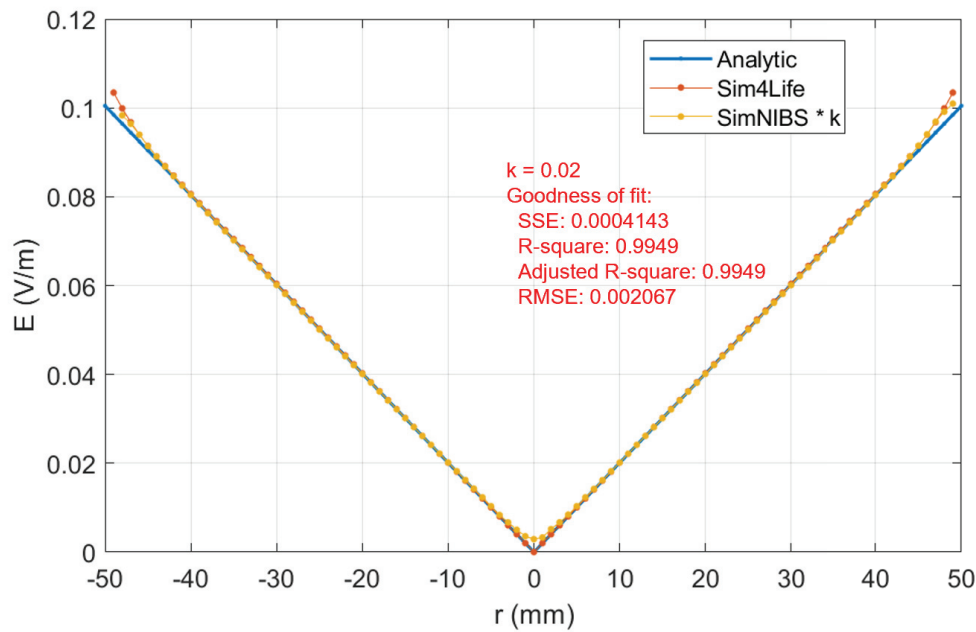


Figure A1. Comparison between the E-field obtained with analytical calculation (A1) and the two software packages, calculated on y -axis (perpendicular to B-field and passing through the center of the sphere). Blue line: E-field obtained with analytical solution (A1); red line: E-field calculated with Sim4Life; yellow line: E-field derived by multiplying SimNIBS results by a multiplicative factor k , which was determined through fitting the results to the analytical values ($k = 0.02$).

Appendix B

In this appendix, a comparison between several meshes and grid discretizations will be provided in order to compare the results obtained in SimNIBS and Sim4Life.

Five different tetrahedral single-shell sphere models were generated with different resolutions in SimNIBS, as reported in Table A1, whereas four different voxels side of the grid have been chosen for simulations in Sim4Life (see Table A2).

Table A1. Tetrahedral meshes for single-shell sphere models (SimNIBS).

	Mean Edge Length (mm)	Tetrahedra ($\times 10^6$)	Nodes ($\times 10^6$)
Mesh 1	2.64	0.30	0.05
Mesh 2	2.03	0.63	0.11
Mesh 3	1.20	3.07	0.52
Mesh 4	0.80	9.46	1.56
Mesh 5	0.54	30.90	5.07

Table A2. Number of voxels in different grids for single-shell sphere models (Sim4Life).

	Voxels Side (mm)	Voxels ($\times 10^6$)
Grid 1	2.00	0.07
Grid 2	1.00	0.52
Grid 3	0.50	4.17
Grid 4	0.25	33.32

In Table A3, the *SMAPE%* obtained by comparing all the combinations between different meshes and different voxel sizes is reported. Decreasing the mean tetrahedral edge length from Mesh 3 to Mesh 4 and Mesh 5 does not significantly reduce the errors with Sim4Life. On the contrary, decreasing the grid size in Sim4Life always reduces the

errors with SimNIBS. However, a convergence trend is almost found at around (or less) 1 mm grid size.

Table A3. SMAPE% between the results of different meshes/grid sizes for single-shell sphere.

	Grid 1	Grid 2	Grid 3	Grid 4
Mesh 1	1.54	1.17	1.00	0.93
Mesh 2	1.44	1.08	0.90	0.83
Mesh 3	1.38	0.97	0.76	0.67
Mesh 4	1.37	0.95	0.75	0.66
Mesh 5	1.38	0.95	0.75	0.66

For the single-shell sphere with slab, only two different tetrahedral meshes have been tested in SimNIBS (Mesh 6 and Mesh 7, which have similar characteristics to Mesh 2 and Mesh 3; see Tables A3 and A4). In Table A5, the SMAPE% obtained comparing all the combinations between different meshes and different voxel sizes is reported. It is possible to notice that minimizing the grid size to 0.25 mm does not guarantee the error minimization. This is probably due to the local enhancement of the induced E-field around the low-lossy slide.

Table A4. Tetrahedral meshes for single-shell sphere model with slab (SimNIBS).

	Mean Edge Length (mm)	Tetrahedra ($\times 10^6$)	Nodes ($\times 10^6$)
Mesh 6	2.03	0.64	0.11
Mesh 7	1.20	3.08	0.52

Table A5. SMAPE% between the results of different meshes/grid sizes for single-shell sphere with slab.

	Grid 1	Grid 2	Grid 3	Grid 4
Mesh 6	2.30	1.56	2.33	2.45
Mesh 7	1.89	1.00	1.98	2.11

References

1. Ueno, S.; Tashiro, T.; Harada, K. Localized Stimulation of Nerves and Muscles by Means of a Pair of Pulsed Magnetic Fields. *IEEE Transl. J. Magn. Jpn.* **1988**, *3*, 500–501. [CrossRef]
2. Koponen, L.M.; Peterchev, A.V. Transcranial magnetic stimulation: Principles and applications. *Neural Eng.* **2020**, *245–270*.
3. Siebner, H.R.; Funke, K.; Aberra, A.S.; Antal, A.; Bestmann, S.; Chen, R.; Classen, J.; Davare, M.; Lazzaro, V.D.; Fox, P.T.; et al. Transcranial magnetic stimulation of the brain: What is stimulated?—a consensus and critical position paper. *Clin. Neurophysiol.* **2022**, *140*, 59–97. [CrossRef] [PubMed]
4. Pateraki, G.; Anargyros, K.; Aloizou, A.M.; Siokas, V.; Bakirtzis, C.; Liampas, I.; Tsouris, Z.; Ziogka, P.; Sgantzios, M.; Folia, V.; et al. Therapeutic application of rTMS in neurodegenerative and movement disorders: A review. *J. Electromyogr. Kinesiol.* **2022**, *62*, 102622. [CrossRef] [PubMed]
5. Somaa, F.A.; de Graaf, T.A.; Sack, A.T. Transcranial Magnetic Stimulation in the Treatment of Neurological Diseases. *Front. Neurol.* **2022**, *13*, 793253. [CrossRef] [PubMed]
6. Grano, I.; Mutanen, T.; Tervo, A.; Nieminen, J.; Souza, V.; Fecchio, M.; Rosanova, M.; Lioumis, P.; Ilmoniemi, R. Local brain-state dependency of effective connectivity: A pilot TMS-EEG study. *Open Res. Eur.* **2022**, *2*, 45. [CrossRef] [PubMed]
7. Koch, G.; Bonni, S.; Pellicciari, M.C.; Casula, E.P.; Mancini, M.; Esposito, R.; Ponzo, V.; Picazio, S.; Di Lorenzo, F.; Serra, L.; et al. Transcranial magnetic stimulation of the precuneus enhances memory and neural activity in prodromal Alzheimer’s disease. *Neuroimage* **2018**, *169*, 302–311. [CrossRef] [PubMed]
8. Chen, X.; Benkler, S.; Chavannes, N.; De Santis, V.; Bakker, J.; Van Rhoon, G.; Mosig, J.; Kuster, N. Analysis of human brain exposure to low-frequency magnetic fields: A numerical assessment of spatially averaged electric fields and exposure limits. *Bioelectromagnetics* **2013**, *34*, 375–384. [CrossRef] [PubMed]
9. Colella, M.; Camera, F.; Capone, F.; Setti, S.; Cadossi, R.; Di Lazzaro, V.; Apollonio, F.; Liberti, M. Patient Semi-specific Computational Modeling of Electromagnetic Stimulation Applied to Neuroprotective Treatments in Acute Ischemic Stroke. *Sci. Rep.* **2020**, *10*, 2945. [CrossRef]

10. Gomez-Tames, J.; Laakso, I.; Hirata, A. Review on biophysical modelling and simulation studies for transcranial magnetic stimulation. *Phys. Med. Biol.* **2020**, *65*, 24TR03. [CrossRef]
11. Colella, M.; Paffi, A.; De Santis, V.; Apollonio, F.; Liberti, M. Effect of skin conductivity on the electric field induced by transcranial stimulation techniques in different head models. *Phys. Med. Biol.* **2021**, *66*, 035010. [CrossRef] [PubMed]
12. Laakso, I.; Hirata, A. Fast multigrid-based computation of the induced electric field for transcranial magnetic stimulation. *Phys. Med. Biol.* **2012**, *57*, 7753–7765. [CrossRef] [PubMed]
13. Paffi, A.; Camera, F.; Carducci, F.; Rubino, G.; Tampieri, P.; Liberti, M.; Apollonio, F. A Computational Model for Real-Time Calculation of Electric Field due to Transcranial Magnetic Stimulation in Clinics. *Int. J. Antennas Propag.* **2015**, *2015*, 1–11. [CrossRef]
14. Cvetkovic, M.; Poljak, D.; Hauelsen, J. Analysis of Transcranial Magnetic Stimulation Based on the Surface Integral Equation Formulation. *IEEE Trans. Biomed. Eng.* **2015**, *62*, 1535–1545. [CrossRef] [PubMed]
15. Poljak, D.; Cvetkovic, M.; Bottauscio, O.; Hirata, A.; Laakso, I.; Neufeld, E.; Reboux, S.; Warren, C.; Giannopoulos, A.; Costen, F. On the Use of Conformal Models and Methods in Dosimetry for Nonuniform Field Exposure. *IEEE Trans. Electromagn. Compat.* **2018**, *60*, 328–337. [CrossRef]
16. Soldati, M.; Laakso, I. Computational errors of the induced electric field in voxelized and tetrahedral anatomical head models exposed to spatially uniform and localized magnetic fields. *Phys. Med. Biol.* **2020**, *65*, 015001. [CrossRef] [PubMed]
17. Rashed, E.A.; Gomez-Tames, J.; Hirata, A. Deep Learning-Based Development of Personalized Human Head Model With Non-Uniform Conductivity for Brain Stimulation. *IEEE Trans. Med. Imaging* **2020**, *39*, 2351–2362. [CrossRef] [PubMed]
18. Diao, Y.; Liu, L.; Deng, N.; Lyu, S.; Hirata, A. Tensor-conductance model for reducing the computational artifact in target tissue for low-frequency dosimetry. *Phys. Med. Biol.* **2023**, *68*, 205014. [CrossRef] [PubMed]
19. Saturnino, G.B.; Puonti, O.; Nielsen, J.D.; Antonenko, D.; Madsen, K.H.; Thielscher, A. SimNIBS 2.1: A Comprehensive Pipeline for Individualized Electric Field Modelling for Transcranial Brain Stimulation. In *Brain and Human Body Modeling: Computational Human Modeling at EMBC 2018*; Makarov, S., Horner, M., Noetscher, G., Eds.; Springer International Publishing: Cham, Switzerland, 2019; pp. 3–25. [CrossRef]
20. Stuchly, M.; Gandhi, O. Inter-laboratory comparison of numerical dosimetry for human exposure to 60 Hz electric and magnetic fields. *Bioelectromagnetics* **2000**, *21*, 167–174. [CrossRef]
21. Hirata, A.; Yamazaki, K.; Hamada, S.; Kamimura, Y.; Tarao, H.; Wake, K.; Suzuki, Y.; Hayashi, N.; Fujiwara, O. Intercomparison of induced fields in Japanese male model for ELF magnetic field exposures: Effect of different computational methods and codes. *Radiat. Prot. Dosim.* **2010**, *138*, 237–244. [CrossRef]
22. Aga, K.; Hirata, A.; Laakso, I.; Tarao, H.; Diao, Y.; Ito, T.; Sekiba, Y.; Yamazaki, K. Intercomparison of *In Situ* Electric Fields Human Models Exposed Spatially Uniform Magnetic Fields. *IEEE Access* **2018**, *6*, 70964–70973. [CrossRef]
23. Diao, Y.; Rashed, E.A.; Giaccone, L.; Laakso, I.; Li, C.; Scorretti, R.; Sekiba, Y.; Yamazaki, K.; Hirata, A. Intercomparison of the Averaged Induced Electric Field in Learning-Based Human Head Models Exposed to Low-Frequency Magnetic Fields. *IEEE Access* **2023**, *11*, 38739–38752. [CrossRef]
24. Poljak, D.; Cvetković, M.; Peratta, A.; Peratta, C.; Dodig, H.; Hirata, A. On some integral approaches in electromagnetic dosimetry. In Proceedings of the Joint Annual Meeting of The Bioelectromagnetics Society and the European BioElectromagnetics Association (BioEM2016), Ghent, Belgium, 5–10 June 2016, pp. 289–295.
25. Bottauscio, O.; Chiampi, M.; Zilberti, L. Boundary Element Solution of Electromagnetic and Bioheat Equations for the Simulation of SAR and Temperature Increase in Biological Tissues. *IEEE Trans. Magn.* **2012**, *48*, 691–694. [CrossRef]
26. Bottauscio, O.; Chiampi, M.; Hand, J.; Zilberti, L. A GPU Computational Code for Eddy-Current Problems in Voxel-Based Anatomy. *IEEE Trans. Magn.* **2015**, *51*, 5100904. [CrossRef]
27. Gubernati, A.C.; Freschi, F.; Giaccone, L.; Scorretti, R. Analysis of Numerical Artifacts Using Tetrahedral Meshes in Low Frequency Numerical Dosimetry. *Appl. Sci.* **2022**, *12*, 6526. [CrossRef]
28. Drakaki, M.; Mathiesen, C.; Siebner, H.R.; Madsen, K.; Thielscher, A. Database of 25 validated coil models for electric field simulations for TMS. *Brain Stimul.* **2022**, *15*, 697–706. [CrossRef] [PubMed]
29. Madsen, K.H.; Drakaki, M.; Thielscher, A. Electric Field Models of Transcranial Magnetic Stimulation Coils with Arbitrary Geometries: Reconstruction from Incomplete Magnetic Field Measurements. *arXiv* **2021**, arXiv:2112.14548.
30. Laakso, I.; De Santis, V.; Cruciani, S.; Campi, T.; Feliziani, M. Modelling of induced electric fields based on incompletely known magnetic fields. *Phys. Med. Biol.* **2017**, *62*, 6567. [CrossRef] [PubMed]
31. De Santis, V.; Douglas, M.; Kuster, N.; Chen, X.L. Impact of the skin conductivity and displacement currents on LF numerical dosimetry. In Proceedings of the International Symposium on Electromagnetic Compatibility—EMC EUROPE, Rome, Italy, 7–21 September 2012; pp. 1–4. [CrossRef]
32. Barchanski, A.; Gerssem, H.D.; Gjonaj, E.; Weiland, T. Impact of the displacement current on low-frequency electromagnetic fields computed using high-resolution anatomy models. *Phys. Med. Biol.* **2005**, *50*, N243. [CrossRef]
33. Wagner, T.; Zahn, M.; Grodzinsky, A.; Pascual-Leone, A. Three-dimensional head model Simulation of transcranial magnetic stimulation. *IEEE Trans. Biomed. Eng.* **2004**, *51*, 1586–1598. [CrossRef]
34. Gabriel, C.; Peyman, A.; Grant, E.H. Electrical conductivity of tissue at frequencies below 1 MHz. *Phys. Med. Biol.* **2009**, *54*, 4863–4878. [CrossRef] [PubMed]

35. Laakso, I.; Hirata, A. Reducing the staircasing error in computational dosimetry of low-frequency electromagnetic fields. *Phys. Med. Biol.* **2012**, *57*, N25. [CrossRef]
36. De Santis, V.; Chen, X.L. On the issues related to compliance assessment of ICNIRP 2010 basic restrictions. *J. Radiol. Prot.* **2014**, *34*, N31–N39. [CrossRef] [PubMed]
37. Gomez-Tames, J.; Laakso, I.; Haba, Y.; Hirata, A.; Poljak, D.; Yamazaki, K. Computational Artifacts of the In Situ Electric Field in Anatomical Models Exposed to Low-Frequency Magnetic Field. *IEEE Trans. Electromagn. Compat.* **2018**, *60*, 589–597. [CrossRef]
38. Diao, Y.; Gomez-Tames, J.; Rashed, E.A.; Kavet, R.; Hirata, A. Spatial Averaging Schemes of In Situ Electric Field Low-Frequency Magnetic Field Exposures. *IEEE Access* **2019**, *7*, 184320–184331. [CrossRef]
39. Arduino, A.; Bottauscio, O.; Chiampi, M.; Giaccone, L.; Liorni, I.; Kuster, N.; Zilberti, L.; Zucca, M. Accuracy Assessment of Numerical Dosimetry for the Evaluation of Human Exposure to Electric Vehicle Inductive Charging Systems. *IEEE Trans. Electromagn. Compat.* **2020**, *62*, 1939–1950. [CrossRef]
40. Soldati, M.; Murakami, T.; Laakso, I. Inter-individual variations in electric fields induced in the brain by exposure to uniform magnetic fields at 50 Hz. *Phys. Med. Biol.* **2020**, *65*, 215006. [CrossRef]
41. ICNIRP 2010. Guidelines for Limiting Exposure to Time-Varying Electric and Magnetic Fields (1 Hz–100 kHz). *Health Phys.* **2010**, *99*, 818–836. [CrossRef]

Disclaimer/Publisher’s Note: The statements, opinions and data contained in all publications are solely those of the individual author(s) and contributor(s) and not of MDPI and/or the editor(s). MDPI and/or the editor(s) disclaim responsibility for any injury to people or property resulting from any ideas, methods, instructions or products referred to in the content.

Article

Pulsed Radiofrequency Electromagnetic Fields as Modulators of Inflammation and Wound Healing in Primary Dermal Fibroblasts of Ulcers

Erica Costantini ^{1,*}, Lisa Aielli ^{2,†}, Giulio Gualdi ¹, Manuela Baronio ³, Paola Monari ⁴, Paolo Amerio ¹ and Marcella Reale ²

¹ Department of Medicine and Aging Sciences, University “G. d’Annunzio”, 66100 Chieti, Italy; giulio.gualdi@unich.it (G.G.); paolo.amerio@unich.it (P.A.)

² Department of Innovative Technologies in Medicine and Dentistry, University “G. d’Annunzio”, 66100 Chieti, Italy; lisa.aielli@unich.it (L.A.); mreale@unich.it (M.R.)

³ Pediatrics Clinic and Institute for Molecular Medicine A. Novivelli, Department of Clinical and Experimental Sciences, University of Brescia and ASST-Spedali Civili of Brescia, 25123 Brescia, Italy; manuela.baronio@unibs.it

⁴ Department of Dermatology, Spedali Civili of Brescia, 25123 Brescia, Italy; paola.monari@libero.it

* Correspondence: erica.costantini@unich.it

† These authors contributed equally to this work.

Abstract: Venous leg ulcers are one of the most common nonhealing conditions and represent an important clinical problem. The application of pulsed radiofrequency electromagnetic fields (PRF-EMFs), already applied for pain, inflammation, and new tissue formation, can represent a promising approach for venous leg ulcer amelioration. This study aims to evaluate the effect of PRF-EMF exposure on the inflammatory, antioxidant, cell proliferation, and wound healing characteristics of human primary dermal fibroblasts collected from venous leg ulcer patients. The cells’ proliferative and migratory abilities were evaluated by means of a BrdU assay and scratch assay, respectively. The inflammatory response was investigated through TNF α , TGF β , COX2, IL6, and IL1 β gene expression analysis and PGE2 and IL1 β production, while the antioxidant activity was tested by measuring GSH, GSSG, tGSH, and GR levels. This study emphasizes the ability of PRF-EMFs to modulate the TGF β , COX2, IL6, IL1 β , and TNF α gene expression in exposed ulcers. Moreover, it confirms the improvement of the proliferative index and wound healing ability presented by PRF-EMFs. In conclusion, exposure to PRF-EMFs can represent a strategy to help tissue repair, regulating mediators involved in the wound healing process.

Keywords: pulsed radiofrequency electromagnetic field; wound healing; dermal fibroblasts; inflammation

1. Introduction

Chronic wounds have an important impact on global health [1]. Leg venous ulcers (VLU) account for 60 to 80% of leg ulcers, which are described as the most frequent type of chronic skin wound [2]. The alteration of the wound healing process in these ulcers may persist for weeks or years and can become chronic, leading to the establishment of nonhealing wounds and to the development of complications such as cardiovascular diseases, diabetes, and bacterial infection, thus leading to the worsening of the patient’s quality of life [3,4].

Wound healing (WH) goes through several overlapping and consecutive phases, including hemostasis, inflammation, new tissue formation, and tissue remodeling, in a well-coordinated process, with the active involvement of platelets, immune cells (neutrophils and macrophages) and fibroblasts [5]. Fibroblasts display a prominent role in the wound healing process, contributing to the creation of a new extracellular matrix (ECM) and the deposition of collagen structures, as well as removing denatured proteins

and matrix-associated materials not needed for the healing, thanks to the production of proteinases to support the migration and activity of immune cells, vascular cells, and organ-specific cells [6]. Furthermore, fibroblasts produce various cytokines and growth factors that can promote or suppress inflammation, depending on the stage of healing and the specific signals from the surrounding cells. Fibroblasts may play a key role in inflammatory signaling pathway regulation, managing the interplay between inflammatory cells, inflammatory cytokines and growth factors in several pathophysiological processes [7,8].

Nonhealing wounds display a reduced cellular proliferation and unbalanced production of inflammatory cytokines, such as interleukin (IL1), (IL6), and tumor necrosis factor (TNF) α , as well as of growth factors, such as transforming growth factor (TGF) β , platelet-derived growth factor (PDGF), epidermal growth factor (EGF), basic fibroblast growth factor (bFGF), and matrix metalloproteinases (MMPs) [9].

Oxidative damage is another feature in nonhealing wounds; this process can prolong microenvironmental homeostasis disruption [10].

All of the mentioned conditions cooperate to determine the pathological nonhealing in VLU and represent the targets of the therapeutical approach.

Currently, the standard therapy for VLU is local wound management, including debridement, dressing techniques, compression therapy [11], and biofilm and bacterial overgrowth control [12]. In non-responsive cases, the standard therapy is associated with advanced treatments. The advanced WH technologies act on tissue, inflammation/infection, moisture, and edge/epithelialization, referred to using the acronym "TIME". The most used techniques are negative pressure wound therapy, stem-cell therapy, the application of 3D hydrogel dressings, and oxygen therapy, alongside other remedies to better support the repair process [3,13].

Numerous clinical and in vitro studies have shown that electromagnetic therapy (EMT), including electromagnetic fields (EMFs), extremely low-frequency electromagnetic fields (ELF-EMFs) and pulsed radiofrequency radiation (PRF), could be a notable option in the treatment of different medical conditions.

To date, the clinical efficacy of PRF-EMFs has been observed in bone [14], joint, muscle, and soft tissue injuries, leading to a reduction in pain [15,16].

The pulsed signal generated by PRF-EMFs allows heat to dissipate, preventing excessive heat buildup, and exerts biological effects without causing important structural alterations. PRF-EMFs can induce biological changes such as the enhancement of endogenous bioelectrical currents [2,17], with Ca²⁺ efflux changes and the modulation of pathways involved in inflammatory responses [18–20].

Although specific intensities and frequencies are applied to help in the treatment of some health conditions, it is difficult to develop standardized treatment protocols due to the high variability of physical parameters and clinical variables, including the frequency and duration of therapy [14,21].

Despite the advanced knowledge and the widespread therapeutic application of these techniques, the complete mechanism of EMT, and above all of PRF-EMFs, is unclear.

Herein, we aimed to evaluate the mechanisms underlying the effect of a commercial medical device (generating a PRF-EMF) on cell proliferation and migration, the expression of tissue repair mediators and the production of antioxidant molecule in primary human dermal fibroblasts (HDFs) collected from patients affected by VLU.

2. Materials and Methods

2.1. Patients and Tissue Samples

Eleven patients (36.6% female and 63.4% male, mean age = 55 \pm 13) were enrolled from the Department of Dermatology, Spedali civili di Brescia, Brescia, Italy. Patients affected by stable VLU, unresponsive to traditional dressings, were selected for the study. The exclusion criteria included the presence of infective, arterial, inflammatory or diabetic diseases. Patients were treated according to the "Nested graft" technique, which involves the acquisition of numerous punch biopsies from the uninvolved skin and seeding in

pits made with other punch biopsies at the edge of venous ulcers of the leg of each patient [22,23]. The skin samples derived from the ulcer's edge (destined to be thrown away) constituted the study sample, while punches from healthy skin constituted the internal sample control. Informed consent was obtained from all patients, in accordance with the 1964 Declaration of Helsinki and its subsequent amendments. This study was approved by the internal local ethics committee and approved and supported by Scientific Committee of Sidemast (Società Italiana Dermatologia e Malattie Sessualmente Trasmesse).

2.2. Cell Culture

Immediately after collection, the biopsy samples were placed in trypsin at a ratio of 1:3 with Dulbecco's phosphate-balanced solution (DPBS) (Merk, St. Louis, MO, USA) for the exclusion of epidermis and adipose tissue residues. Biopsies were cut into fragments of about 2×1 mm (length by width), washed in DPBS and placed in 35 mm culture plates in the presence of Dulbecco's modified Eagle medium (DMEM, Merk, St. Louis, MO, USA) supplemented with 10% fetal bovine serum (FBS) (Merk, St. Louis, MO, USA) and 0.5% penicillin-streptomycin (Merk, St. Louis, MO, USA), and then were incubated at 37 °C in a humid atmosphere with 5% CO₂. The culture medium was replaced every 3 days. After about 2 weeks, each biopsy section spontaneously released fibroblasts that began to proliferate.

Once the cells started growing, skin fibroblasts were synchronized by being placed in 0.1% serum for 48 h before being trypsinized and plated in the presence of complete medium (DMEM with 10% FBS).

In order to avoid any effect deriving from the native environment, all skin fibroblasts were cultured under the same in vitro conditions for five passages. Ulcer fibroblasts (ulcer-HDFs), established in cultures from biopsies of the edge of chronic VLU, were tested and compared side by side in the same experiment with normal fibroblasts (normal-HDFs) grown from biopsies from normal skin. Conventional phase-contrast light microscopy (Leica DMI1, Wetzlar, Germany, obj. $\times 10$) was used daily to assess the morphological features of normal-HDFs and ulcer-HDFs throughout all growth phases.

2.3. Pulsed Radiofrequency Electromagnetic Field Device

Ulcer-HDF cultures were exposed to a PRF-EMF generated by a commercially available medical device provided by Tecnica Scientifica Service (TSS) Medical Srl, Turin, Italy. The device emits a PRF-EMF which induces a small constant electric charge over time for the purposes of its internal functioning; hence, its RF emissions are very low and do not cause interference with nearby electronic devices. The circuit that constitutes the PRF-EMF device is powered by a direct current provided by a CR2032 lithium battery with a nominal voltage of 3 V.

The same circuit converts the delivered square wave, emitted in packets of sinusoids, in PRF. The device's power is < 3 mW, and it does lead to an increase in local temperature. The PRF-EMF emits non-ionizing radiation at a carrier frequency of 27.1 MHz (37 ns) with a carrier RF modulated through a pulse at 600 Hz (1.66) and a duty cycle of 10%. The duration of a single pulse is 167 μ s. The load adapted to the antenna output is identical to the parallel between a 5 ohm resistor and a capacity of 150 pF. The PRF-EMF device also has the following specifications: height, 12 cm; antenna width, 5–6 cm; antenna material, copper wire; action depth, 5–7 cm; max thickness, 1 cm; electromagnetic compatibility level, Group 2 class A.

2.4. BrdU Assay

Normal-HDFs and ulcer-HDFs (3×10^3) were cultured in growth media (DMEM supplied with 10% FBS and 0.5% penicillin-streptomycin) in 96-well plates. After 24 h (~70% confluence), cell cycle synchronization was performed by means of overnight serum starvation (serum free culture). Once the cell culture preparation phase was concluded, fresh complete medium was added and the proliferation at different time points (3-6-24 and 48 h)

was determined by measuring bromodeoxyuridine (BrdU) incorporated into DNA, following BrdU Roche’s colorimetric protocol (Roche, Mannheim, Germany). BrdU incorporation was measured using the GloMax Multi-Detection System (Promega Corporation, Madison, WI, USA) at an absorbance of 450 nm. For ulcer-HDFs, a second culture plate was set up and exposed to the PRF-EMF for 6 h. Proliferation was assessed with BrdU, starting from the same concentration of cells (3×10^3) and at the same time points. All the experiments were performed in triplicate.

2.5. Wound Healing Assay and Image Acquisition

The wound healing assay was performed on normal-HDFs and ulcer-HDFs to test their damage repair capacity. A total of 1.6×10^5 cells/35 mm were plated, and after 48 h at 37 °C cells adhered and spread, obtaining a confluent monolayer. Cell cultures were scratched with a straight line across the center of the well with a p10 sterile pipette tip. After scratching, one wash with DPBS was performed to remove debris and fresh medium was added. Culture plates were then placed in the cell culture incubator for 24 h. The ulcer-HDFs were exposed, in a different set of culture plates, to a 6 h period of PRF-EMF.

Plates were observed using a phase-contrast microscope (Leica DMI1, Wetzlar, Germany), and the edges of the induced wound area (scratch) were documented, acquiring pictures with a digital camera (Leica DMI1, Wetzlar, Germany,) at 0 h, 6 h, and 24 h to evaluate the fibroblasts migration. The images were processed using the NIH ImageJ software version 1.54 h [24] to calculate the wound area dimensions. The data were obtained from triplicate experiments.

2.6. Gene Expression Profiling

Total RNA was isolated using QIAzol reagent (Qiagen, Hilden, Germany) and reverse transcribed with the QuantiTec Reverse Transcription kit (Qiagen, Hilden, Germany) according to the manufacturer’s instructions. Real-time qPCR was performed using GoTaq® qPCR Master Mix (Promega, Milan, Italy) and a Bio-Rad Real-Time PCR instrument (CFX Real-Time PCR Bio-Rad, Hercules, CA, USA) with the following cycling conditions: 95 °C for 10 min, followed by 40 cycles of denaturation at 95 °C for 10 s, annealing at 60 °C for 10 s, and extension at 72 °C for 20 s. The primer sequences used for qPCR are provided in Table 1. qPCR results were analyzed using Bio-Rad system software (CFX Manager). The $2^{-\Delta\Delta Ct}$ method was used to detect the relative expression of TNF α , TGF β , cyclooxygenase (COX)2, IL6 and IL1 β , using RPS18 to normalize the gene expression levels. Relative quantification cycle (Ct) values were reported as fold changes in expression. Experiments were performed in triplicate and the data were averaged.

Table 1. Primer pair sequences used in the study.

Gene	Forward Primer Sequence (5'–3')	Reverse Primer Sequence (5'–3')	Amplicon Length
TNF α	CCTTCCTGATCGTGCCAG	GCTTGAGGGTTTGCTACAAC	184 bp
TGF β	AACAATTCCTGGCGATACCTC	GTAGTGAACCCGTTGATGTCC	197 bp
COX2	GACAGTCCACCAACTTACAATG	GGCAATCATCAGGCACAGG	105 bp
IL6	GTACATCCTCGACGGCAGC	ACCTCAAACCTCCAAAAGACCAG	198 bp
IL1 β	TGAGGATGACTTGTTCTTTGAAG	GTGGTGGTCCGAGATTCCG	115 bp
RPS18	CTTGCCATCACTGCCATTAAG	TCCATCCTTTACATCCTTCTGTGTC	199 bp

2.7. ELISA Assay

The concentration of IL1 β and prostaglandin (PG)E2 was assessed in the supernatant of normal-HDFs, ulcer-HDFs, and PRF-EMF-exposed ulcer-HDFs using the Enzyme-Linked ImmunoSorbent Assay (ELISA). Specifically, after each experimental protocol, the cell culture supernatant was collected and stored at –80 °C for subsequent evaluation. Before assessing the IL1 β and PGE2 levels, samples were centrifugated at $10,000 \times g$ for 5 min to eliminate cell debris and they were then plated following the manufacturer’s instructions. Relative absorbance was measured at 450 nm using the GloMax Multi-Detection

System (Promega Corporation, Madison, WI, USA). Cytokine concentration was calculated using a standard reference curve. The intra- and inter-assay reproducibility was >90%. The specificity and the sensitivity of the cytokine were defined according to the manufacturer's guidelines.

2.8. Antioxidant Mediators Quantification

The amount of total GSH (tGSH), oxidized GSH (GSSG), and free GSH (GSH) in the cell culture supernatant was quantified using a colorimetric detection kit for Glutathione (Arbor Assays, Ann Arbor, MI, USA), while for glutathione reductase (GR), a fluorescent activity kit was used (Arbor Assays, Ann Arbor, MI, USA). GSH was calculated by subtracting GSSG from the total fraction, where the oxidized data were obtained using 2-vinylpyridine to block the free fraction in the samples. Experiments for each different condition (normal-HDFs, ulcer-HDFs, and exposed ulcer-HDFs) were conducted in duplicate.

2.9. Statistics

GraphPad Prism (v.6.0; GraphPad Software, La Jolla, CA, USA) was used for statistical analysis of the data. All results were expressed as mean \pm SD. For repeated measures, one-way ANOVA was performed to compare differences between groups. The differences between the normal-HDFs, ulcer-HDFs, and exposed ulcer-HDFs were measured by means of Tukey post hoc comparison or by Student's *t*-test for unpaired data. Significant differences were established at $p < 0.05$.

3. Results

3.1. Cell Morphology

Using light microscopy in the routine monitoring of cell cultures, differences in morphology and growth rate between normal-HDFs and ulcer-HDFs were highlighted. In normal-HDFs, the increased number of cells was readily apparent when cultures were viewed under a light microscope. Cells appear with a normal morphology, being compact with a spindle shape and well-defined nuclear morphologic features. Meanwhile, the ulcer-HDFs appear larger with a polygonal shape, including some lipid droplets and granular cytoplasmic structures, with nonuniform nuclear morphologic features such as segmented nucleoli. Furthermore, starting from the same density of plated cells, and observing the cultures after 6 and 24 h, cells are differently distributed in the well. Indeed, a reduction in the growth rate of ulcer-HDFs after only 6 h was observed, in accordance with the literature data [25,26]. After 24 h, differences in concentration, density, size, arrangement and orientation of ulcer-HDFs were still detectable with respect to normal-HDFs (Figure 1).

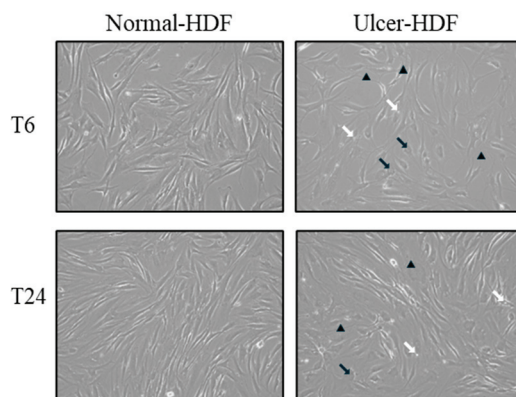


Figure 1. Light microscopy displaying the cellular morphology and confluency of normal-HDFs and ulcer-HDFs. Micrographs are representative images from independent experiments performed for each

sample and in duplicate. Images of normal-HDFs and ulcer-HDFs were captured after 6 h and after 24 h of cell incubation. Total magnification = $10\times$. Lipid droplets are indicated by white arrows, granular cytoplasmic structures are indicated by black arrows, and segmented nucleoli are indicated by black arrowheads.

3.2. BrdU Assay

The ability of normal-HDFs and ulcer-HDFs in cell proliferation was assessed by means of the BrdU uptake assay, which is a marker for cell proliferation due to it being rapidly taken up and accumulated by dividing cells since it is not metabolizable. Our results show that, starting from the same cell concentration (3×10^3), normal-HDFs have an increased proliferation rate compared to ulcer-HDFs. The proliferation rate is significantly enhanced for all measured time points (3, 6, 24 and 48 h), with a rapid increase in BrdU accumulation in normal-HDFs immediately after 3 h and with a steady increase at 6 and 24 h.

Otherwise, in ulcer-HDFs, a slow incorporation of BrdU is observed, with an increase after 6 h (ratio = 1.7 vs. 0 h) and an additional increase at 24 h (ratio = 1.9 vs. 0 h) in comparison with the basal levels. For both normal- and ulcer-HDFs after 48 h, there is a slight reduction in cell proliferation (Figure 2). These data underline that cells isolated from the ulcer area show a slower replicative capacity and a longer time to become confluent when compared with the healthy skin fibroblasts.

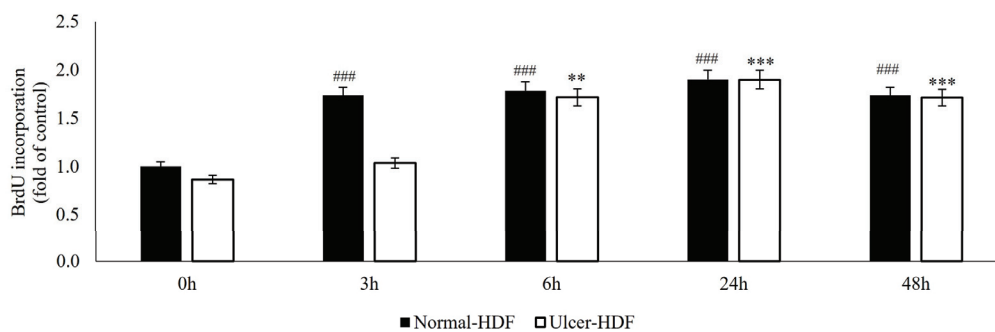


Figure 2. BrdU uptake of normal- and ulcer-HDFs evaluated by the BrdU assay. All experiments were performed in triplicate and the results are presented as fold of the control (normal-HDFs). Statistical significances: ### $p > 0.001$ for time comparison in the normal-HDF group vs. normal-HDF at 0 h; ** $p > 0.01$ and *** $p > 0.001$ for comparison in the ulcer-HDF group vs. ulcer-HDF at 0 h.

Recently, several studies [5,27–29] have suggested that the application of a PRF-EMF modulates fibroblasts' capability to regulate tissue homeostasis. To investigate the ability of a PRF-EMF to reduce the proliferative gap between ulcer-HDFs and normal-HDFs, the ulcer-HDFs of each patient were seeded at a concentration of 3×10^3 in 96-well plates and exposed for 6 h to the PRF-EMF. After 3, 6, 24 and 48 h, BrdU uptake and the proliferation rate were determined. A growth curve with the ratio between the different time points and the 0 h levels of BrdU for each condition is reported in Figure 3. Our results show that ulcer-HDFs' proliferation rate is significantly lower than that of normal-HDFs, while the exposure of ulcer-HDFs to a PRF-EMF determines an early improvement in proliferation at 3 h compared to the normal-HDFs. This improvement is maintained for the other time points (Figure 3).

3.3. Scratch Wound Assay

To evaluate cell migration and the regeneration of the cell monolayer, the most used *in vitro* model is the mechanical damage model ("scratch wound assay"). The ability of normal-HDFs, ulcer-HDFs and exposed ulcer-HDFs to migrate into the damaged area was evaluated. Immediately (0 h), 6 h, and 24 h after the scratch, pictures were acquired and processed with the ImageJ software to calculate the size of the damaged area. The size of the initial scratch was calculated and assumed as 100% of the cell-free area for each sample

and condition. After 6 h, in normal-HDFs, the cell-free area was 68.6%, and after 24 h, it was only 8.2%. In accordance with the decreased proliferation, the reduction in the cell-free area in scratched ulcer-HDFs is lower than that in normal-HDFs, with the cell-free area being 75.1% after 6 h and 10.4% after 24 h, compared with 100% after 0 h (Figure 4).

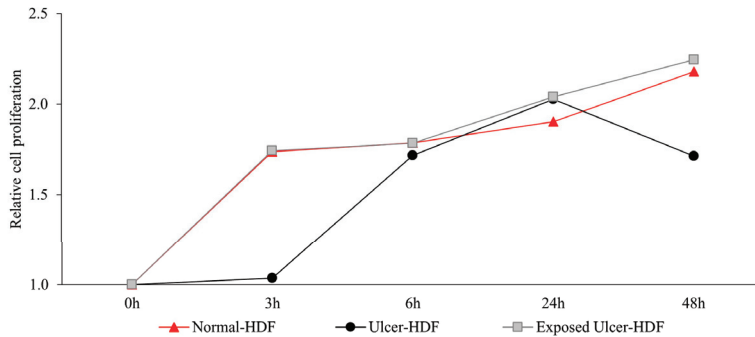


Figure 3. Relative cell proliferation ability in ulcer-HDFs after 6 h of PRF-EMF exposure compared to normal- and ulcer-HDFs without exposure, measured using the BrdU proliferation assay. Relative cell proliferation was calculated as the ratio between each time point and 0 h. All experiments were performed at least three times.

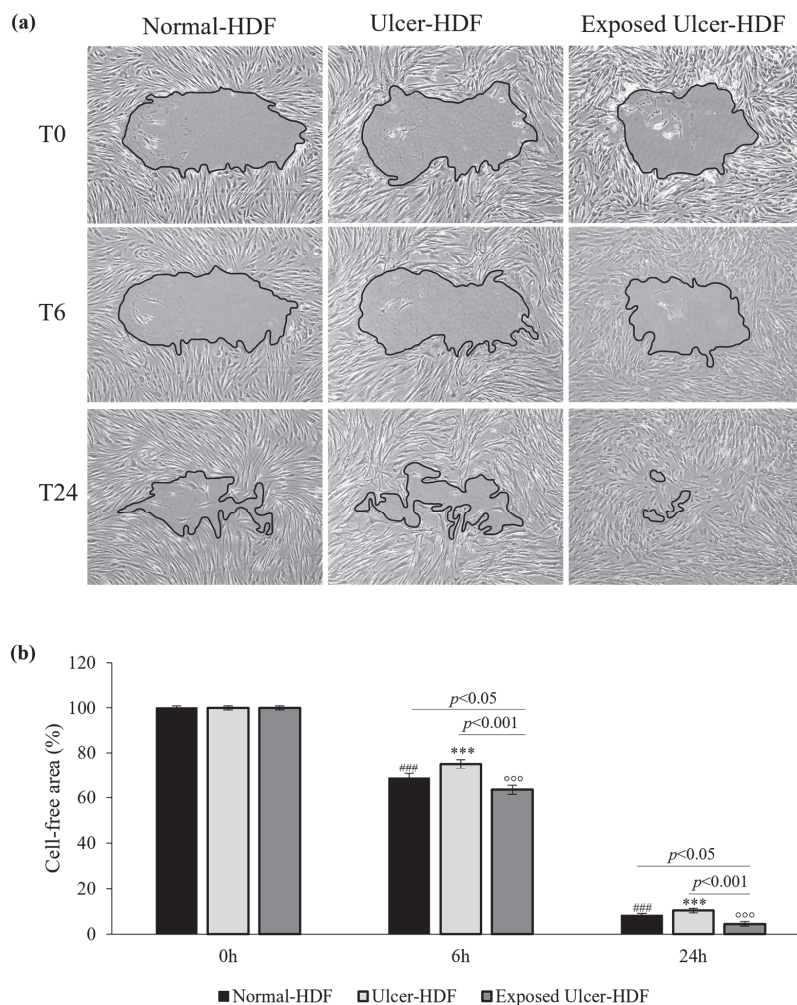


Figure 4. (a) Light microscopic images of normal-HDF, ulcer-HDF, and exposed ulcer-HDF scratched cells. Images with 10× magnification were captured at 0 h, immediately after the wound creation, at

6 h post wound, and at 24 h post wound. A Leica DMI1 microscope with a digital camera was used to capture images, and the cell-free area was measured using NIH ImageJ software version 1.54 h. (b) Graph of the percentage of cell-free area of the scratched HDFs. One-way ANOVA statistical significance: ### $p < 0.001$ for the comparison with normal-HDFs at 0 h; *** $p < 0.001$ for the comparison with ulcer-HDFs at 0 h; °°° $p < 0.001$ for the comparison with exposed ulcer-HDFs at 0 h. Differences between different samples were considered significant at $p < 0.05$.

To evaluate if PRF-EMF exposure can affect ulcer-HDFs' migration for wound closure, cells were scratched and exposed to the PRF-EMF for 6 h. Observing the exposed ulcer-HDFs after 6 h, the cell-free area was 63.5%, compared to 100% at 0 h, with significant differences compared to unexposed ulcer-HDFs (cell-free area of 75.1%; $p < 0.001$) and normal-HDFs (cell-free area of 68.6%; $p < 0.05$) at the same time. Furthermore, 24 h after the scratch in all of the evaluated HDF samples and conditions, a considerable improvement in the regenerative capacity was observed, with a significant reduction in cell-free area in PRF-EMF-exposed ulcer-HDFs with respect to both the normal- ($p < 0.05$) and ulcer-HDFs ($p < 0.001$) (Figure 4b).

3.4. Gene Expression

Considering the broad role of inflammatory cytokines in the regulation of the WH process, we evaluated the expression of COX2 and pro-inflammatory cytokines, namely IL1 β , IL6, TGF β , and TNF α , that are important for cell proliferation and the synthesis of the ECM, both in normal-HDFs and ulcer-HDFs. At the end of incubation (24 h), the gene expression of mediators in ulcer-HDFs in comparison with normal-HDFs was significantly higher, in accordance with the persistence of the inflammatory phase in chronic ulcers (Figure 5). Thus, in this study, we evaluated the effect of the exposure to a PRF-EMF on ulcer-HDFs, observing a significant increase in the expression levels of IL1 β , IL6, COX2, and TGF β with respect to unexposed normal-HDFs and ulcer-HDFs.

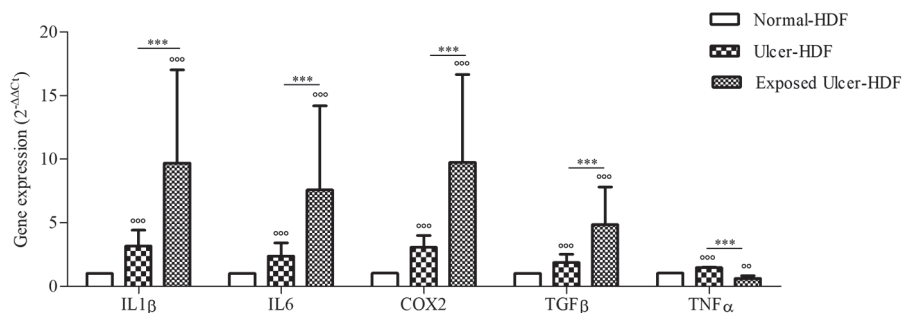


Figure 5. Gene expression of IL1 β , IL6, COX2, TGF β , and TNF α in ulcer-HDFs and exposed ulcer-HDFs compared to normal-HDFs, assumed as 1. Changes in gene expression were determined by means of qPCR and evaluated via the $2^{-\Delta\Delta C_t}$ method. Data are reported as the mean and 95% CI. °°° $p < 0.001$ and °° $p < 0.01$ for the comparison with normal-HDFs; *** $p < 0.001$ in PRF-EMF-exposed ulcer-HDFs compared with ulcer-HDFs.

3.5. PGE2 and IL1 β Levels

The levels of production of PGE2 and IL1 β were evaluated in scratched normal-HDF, ulcer-HDF, and exposed ulcer-HDF supernatants to underline the differences between the cell lines. PGE2, which constitutes the major PGE in human skin [30,31], and IL1 β , which is a master cytokine for cell recruitment and activation [32], can be produced by many cell types, such as epithelial cells, fibroblasts, and keratinocytes, as well as inflammatory cells. The production of PGE2 and IL1 β increases significantly in the presence of damage and influences cell growth and differentiation processes. Indeed, in our data, we observed increased levels of PGE2 in ulcer-HDFs with respect to normal-HDFs, although this was not significant. When ulcer-HDFs are exposed to a PRF-EMF, in accordance with the results of Cheng et al. [33], we observed a higher increase level of PGE2 with respect to normal-HDFs.

The levels of IL1 β show the same trend, with a slight increase in ulcer-HDFs and a more significant increase in exposed ulcer-HDFs with respect to normal-HDFs, in accordance with the increased cell proliferation and early scratch healing progression (Figure 6).

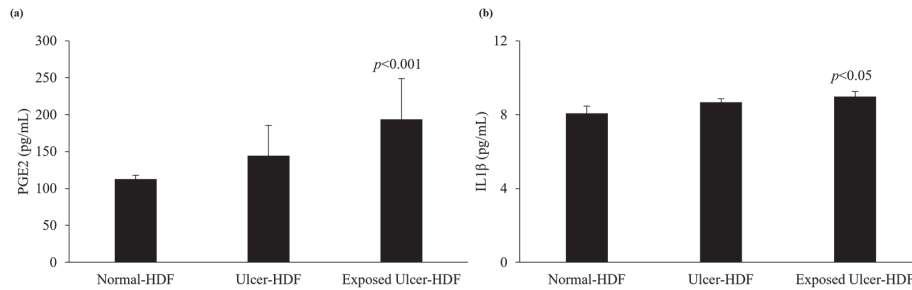


Figure 6. Analysis of levels of (a) PGE2 and (b) IL1 β in normal-HDF, ulcer-HDF, and exposed ulcer-HDF supernatants. Values represent the mean \pm SD of three independent experiments. Statistical significance for $p < 0.05$ with respect to normal-HDFs.

3.6. Antioxidant Activity

Oxidative stress, due to an imbalance in the pro-oxidant–antioxidant homeostasis, plays an important role in the nonhealing of wounds. When a higher load of reactive oxygen species (ROS), caused by the abnormal generation of or deficiencies in the antioxidant defenses, persists over a long time, continuous damage and chronic nonhealing wounds are detected. We focused our study on the evaluation of antioxidant mediators, measuring tGSH, GSSG, and GSH, as well as the activity of GR, an enzyme responsible for catalyzing the reduction of GSSG to GSH. Our results show that in comparison with normal-HDFs, in ulcer-HDFs, there are no significant differences in GR activity (0.18 mU/mL in normal-HDFs and 0.19 mU/mL in ulcer-HDFs) or in GSSG levels (0.22 μ M and 0.25 μ M in normal- and ulcer-HDFs, respectively), while tGSH and GSH levels are significantly reduced ($p < 0.001$), in accordance with the impaired fibroblast proliferation and migration driven by the production of ROS, the lack of antioxidant defenses, and the excessive oxidative stress.

After the PRF-EMF exposure of ulcer-HDFs, the levels of the antioxidant molecules are comparable to those in ulcer-HDFs (Figure 7).

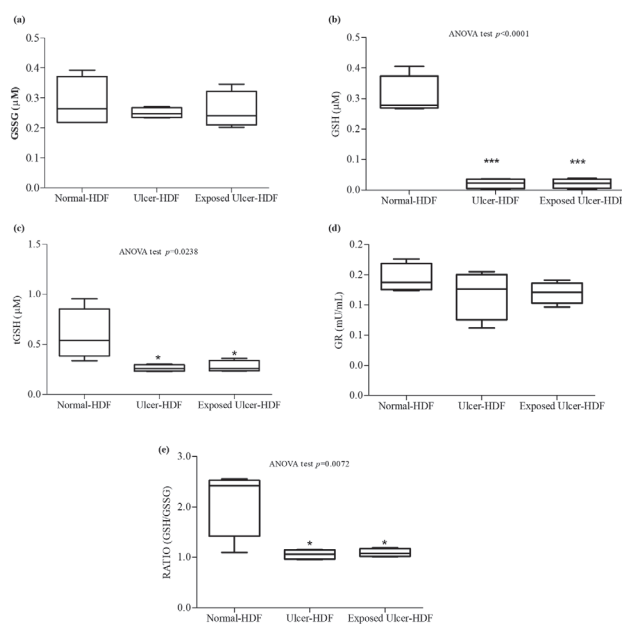


Figure 7. Antioxidant activity. (a) Oxidized glutathione (GSSG); (b) free glutathione (GSH); (c) total glutathione (tGSH); (d) glutathione reductase (GR); (e) ratio of GSH/GSSG concentrations in the

supernatant of wounded normal-HDFs, ulcer-HDFs, and exposed ulcer-HDFs. Whisker plot represents the distribution of numeric data values with the minimum and maximum. Significant differences were detected at * $p < 0.05$ and *** $p < 0.001$ with respect to normal-HDFs.

Therefore, since the ratio between GSH and GSSG can represent an important indicator of cell health [34], we calculated the ratio and pointed out that in both ulcer-HDFs and exposed ulcer-HDFs, there is a significant reduction compared to normal-HDFs. Thus, PRF-EMF exposure is unable to modify the antioxidant system.

4. Discussion

A complex crosstalk and a different cellular response are involved in the WH process, resulting in the overlap of dynamic phases (hemostasis, inflammation response, new tissue formation, and tissue remodeling). The alteration or deregulation of one or more of these phases may lead to chronic ulcers. Fibroblasts actively participate in WH and orchestrate all of the phases of tissue repair/regeneration process through interactions with other cell populations involved in the process [7]. In this study, we first assessed the differences between HDFs isolated from normal and ulcerative areas of patients affected by VLU, the most frequent form of chronic skin ulcers, and following this we evaluated the effect of a PRF-EMF on ulcer-HDFs' morphology, proliferation and gene expression, as well as WH modulation.

Significant differences were observed in the morphology and proliferation rate of ulcer-HDFs compared to normal-HDFs, with alterations in shape and a reduced growth time. These characteristics resemble those observed in senescent fibroblasts and confirm the findings of Wall et al., who demonstrated that fibroblasts from chronic nonhealing wounds display abnormal phenotypes, including decreased proliferation, early senescence, and altered patterns of cytokine release [35].

In the last few years, an increasing number of reports have evaluated the effects of ELF-EMFs on keratinocytes and immune cells involved in skin repair. ELF-EMFs act on the WH process through the modulation of inflammation, protease matrix rearrangement, neo-angiogenesis, senescence, stem-cell proliferation, and epithelialization. The exposure times, waveforms, frequencies, and amplitudes used in the different literature reports are very varied and the results obtained are often in contrast, highlighting that the biological effects of ELF-EMFs may vary with the EMF's physical characteristics and based on the type of target cell [28].

To evaluate the cell migration and regenerative capacity, we applied the widely used *in vitro* "scratch wound assay", inducing mechanical damage to confluent cell layers.

PRF-EMF exposure for 6 h led to a significant improvement in the proliferation ability of ulcer-HDFs subjected to the scratch wound assay, which promptly migrated to the wounded area and displayed accelerated wound closure.

The cell-free area caused by the scratch was covered at a proportion of 31.4% by normal-HDFs 6 h after the scratch, while ulcer-HDFs were capable of covering only 24.9% of the wound area. These differences were also maintained at 24 h, when ulcer-HDFs presented an 89% reduction in the cell-free area compared to the 92% reduction noted for the normal-HDFs, supporting the hypothesis regarding the altered proliferation/migration capabilities of ulcer-HDFs.

The pattern displayed by ulcer-HDFs in reaching a confluence layer was dissimilar from that of normal-HDFs. Ulcer-derived HDFs individually adhered to the dish and then randomly migrated, occasionally coming into contact with other cells. We hypothesize that the shape alteration of ulcer-HDFs weakens the cell-cell interaction and may be responsible for their reduced ability to cover the cell-free area.

Interestingly, after exposure to the PRF-EMF, the proliferative index of ulcer-HDFs increased significantly and better cell alignment and movement towards neighboring cells were evident, resulting in optimal wound closure.

The exposure to PRF-EMF prompts an earlier reduction in the scratch-induced cell-free area displayed by exposed ulcer-HDFs (11.6% coverage) compared to the unexposed ulcer-HDFs and even to normal-HDFs (5.1% coverage) ($p < 0.05$). This trend persisted after 24 h, showing that in PRF-EMF-exposed ulcer-derived HDFs, there is an increase in the repair ability.

In agreement with the literature [36,37], a more intense expression of COX2, IL1 β , IL6, TGF β , and TNF α was observed in ulcer-HDFs than in normal-HDFs.

These cytokines are involved not only in the inflammation phase but also in the epithelialization phase, promoting cell proliferation and migration, fibroblast differentiation, and the mobilization of resident stem/progenitor cells [38]. Our study demonstrated an increase in the levels of these cytokines in ulcer-HDFs after PRF-EMF exposure, which may explain the results regarding the increased migration in the scratch wound assay.

We suggest that in inefficient WH, such as in chronic wounds, the exposure to a PRF-EMF may help to restore the well-orchestrated interaction between cells and mediators, driving the progression of overlapping phases of inflammation, proliferation, and tissue remodeling.

Furthermore, we hypothesize that the increase in TGF β gene expression after PRF-EMF exposure can be responsible for fibroblast and mesenchymal cell activation, as well as the recruitment and activation of neutrophils and macrophages.

This could be important since it is known from the literature that in the early phase of WH perturbation, neutrophil recruitment may induce the alteration of monocyte infiltration timing with decreased IL1 β secretion, which in turn reduces keratinocyte migration and proliferation.

Changes in the macrophage phenotype during the healing process help in the transition from a pro-inflammatory to a pro-resolution state, promoting keratinocyte, fibroblast, and epithelial cell proliferation with the secretion of cytokines and growth factors [39].

Interestingly, our finding that that levels of IL1 β were significantly higher in the supernatant of exposed ulcer-HDFs with respect to unexposed ulcer-HDFs and normal-HDFs may explain the optimization of the wound closure assay, since evidence [38,40,41] has shown that IL1 β levels correlate with active immune cell infiltration following the exacerbation of inflammation, leading to the rebalancing of pro-inflammatory cytokines and aiding in the transition from the inflammatory to the proliferative phase in skin wounds.

Moreover, our study revealed that the overproduction of IL1 β correlates with the higher release of PGE2 in PRF-EMF-exposed cells, prompting an increase in cell proliferation [42] and TNF α gene expression inhibition [43,44].

In both unexposed and exposed scratched ulcer-HDFs, we observed decreased activity of antioxidants with respect to scratched normal-HDFs. These data agree with the role of unbalanced oxidant/antioxidant homeostasis, a reduction in GSH levels and alterations in the overall redox status in the worsening of the microenvironment in chronic wounds [45,46]. In our study, in exposed ulcer-HDFs, probably due to the system parameters of the PRF-EMF device, such as the frequency, pulse or intensity, significant modulation of antioxidant activity was observed [47,48].

5. Conclusions

The results of this study show that a PRF-EMF may affect ulcer-HDFs' cell proliferation and modulate the expression and production of cytokines, leading to an improvement in WH. Our results indicate that a PRF-EMF enhances ulcer-HDF activation, helping the WH by activating the robust migration of fibroblasts and by further stimulating the inflammatory response. The recruitment of other cells is necessary to continue the healing process, pushing forward all repair phases and stimulating and coordinating the essential functions of wound repair.

We acknowledge that the transition from two-dimensional (2D) monocultures of dominant cell types such as keratinocytes and fibroblasts to co-culture systems and to more

complex three-dimensional (3D) tissue models is needed to improve the transferability of our results.

The exploration of the mechanics and effects PRF-EMF exposure might help in the search for promising approaches for chronic WH treatment. The next goal would be to evaluate the effect of PRF-EMFs, alone and in addition to other standard therapies, in order to investigate additional effects and hypothesize the application of a PRF-EMF as a supportive therapy.

Author Contributions: Conceptualization, E.C. and M.R.; methodology, L.A., E.C., M.B. and P.M.; validation, P.A., G.G. and M.R.; formal analysis, P.A.; investigation, E.C., M.B. and P.M.; resources, M.B., P.M. and G.G.; data curation, E.C.; writing—original draft preparation, E.C., L.A. and M.R.; writing—review and editing, G.G.; supervision, P.A. and M.R.; project administration, M.R.; funding acquisition, M.R. All authors have read and agreed to the published version of the manuscript.

Funding: This research received no external funding.

Institutional Review Board Statement: The study was conducted in accordance with the Declaration of Helsinki.

Informed Consent Statement: Informed consent was obtained from all subjects involved in this study.

Data Availability Statement: Data are contained within the article.

Acknowledgments: We thank Tecnica Scientifica Service SRL, 10154 Turin, Italy (www.algo-care.com; info@algo-care.com, accessed on 3 April 2024) for providing us with the electromagnetic device.

Conflicts of Interest: The authors declare no conflict of interest.

References

- Nelzén, O. Prevalence of venous leg ulcer: The importance of the data collection method. *Phlebology* **2008**, *15*, 143–150.
- Mohamady, H.M.; Taha, M.M.; Aneis, Y.M.; Aldhahi, M.I.; Attalla, A.F. Effect of Combined Electromagnetic Field and Plantar Flexion Resistance Exercise on Wound Healing in Patients with Venous Leg Ulcers: A Randomized Controlled Trial. *Medicina* **2023**, *59*, 1157. [CrossRef] [PubMed]
- Sharma, A.; Sharma, D.; Zhao, F. Updates on Recent Clinical Assessment of Commercial Chronic Wound Care Products. *Adv. Healthc. Mater.* **2023**, *12*, e2300556. [CrossRef]
- Joaquim, F.L.; Silva, R.M.C.R.A.; Garcia-Caro, M.P.; Cruz-Quintana, F.; Pereira, E.R. Impact of venous ulcers on patients' quality of life: An integrative review. *Rev. Bras. Enferm.* **2018**, *71*, 2021–2029. [CrossRef] [PubMed]
- Gualdi, G.; Costantini, E.; Reale, M.; Amerio, P. Wound Repair and Extremely Low Frequency-Electromagnetic Field: Insight from In Vitro Study and Potential Clinical Application. *Int. J. Mol. Sci.* **2021**, *22*, 5037. [CrossRef] [PubMed]
- Bainbridge, P. Wound healing and the role of fibroblasts. *J. Wound Care* **2013**, *22*, 407–412. [CrossRef]
- Liu, Y.; Liu, Y.; He, W.; Mu, X.; Wu, X.; Deng, J.; Nie, X. Fibroblasts: Immunomodulatory factors in refractory diabetic wound healing. *Front. Immunol.* **2022**, *13*, 918223. [CrossRef] [PubMed]
- Raffetto, J.D. Inflammation in chronic venous ulcers. *Phlebology* **2013**, *28* (Suppl. S1), 61–67. [CrossRef]
- Zhao, R.; Liang, H.; Clarke, E.; Jackson, C.; Xue, M. Inflammation in Chronic Wounds. *Int. J. Mol. Sci.* **2016**, *17*, 2085. [CrossRef]
- Hong, W.X.; Hu, M.S.; Esquivel, M.; Liang, G.Y.; Rennert, R.C.; McArdle, A.; Paik, K.J.; Duscher, D.; Gurtner, G.C.; Lorenz, H.P.; et al. The Role of Hypoxia-Inducible Factor in Wound Healing. *Adv. Wound Care* **2014**, *3*, 390–399. [CrossRef]
- Franks, P.J.; Barker, J.; Collier, M.; Gethin, G.; Haesler, E.; Jawien, A.; Laeuchli, S.; Mosti, G.; Probst, S.; Weller, C. Management of Patients With Venous Leg Ulcers: Challenges and Current Best Practice. *J. Wound Care* **2016**, *25* (Suppl. S6), S1–S67. [CrossRef] [PubMed]
- Percival, S.L.; Thomas, J.G.; Williams, D.W. Biofilms and bacterial imbalances in chronic wounds: Anti-Koch. *Int. Wound J.* **2010**, *7*, 169–175. [CrossRef] [PubMed]
- Aleksandrowicz, H.; Owczarczyk-Saczonek, A.; Placek, W. Venous Leg Ulcers: Advanced Therapies and New Technologies. *Biomedicines* **2021**, *9*, 1569. [CrossRef] [PubMed]
- Flatscher, J.; Pavez Lorié, E.; Mittermayr, R.; Meznik, P.; Slezak, P.; Redl, H.; Slezak, C. Pulsed Electromagnetic Fields (PEMF)-Physiological Response and Its Potential in Trauma Treatment. *Int. J. Mol. Sci.* **2023**, *24*, 11239. [CrossRef] [PubMed]
- Lietz-Kijak, D.; Ardan, R. Physiotherapeutic Reduction of Orofacial Pain Using Extremely Low-Frequency Electromagnetic Field and Light-Emitting Diode Therapy-A Pilot Study. *Pain. Res. Manag.* **2022**, *2022*, 3115154. [CrossRef] [PubMed]
- Fernández-Guarino, M.; Bacci, S.; Pérez González, L.A.; Bermejo-Martínez, M.; Cecilia-Matilla, A.; Hernández-Bule, M.L. The Role of Physical Therapies in Wound Healing and Assisted Scarring. *Int. J. Mol. Sci.* **2023**, *24*, 7487. [CrossRef] [PubMed]
- Aziz, Z.; Cullum, N. Electromagnetic therapy for treating venous leg ulcers. *Cochrane Database Syst. Rev.* **2015**, *2015*, CD002933. [CrossRef] [PubMed]

18. Asci, H.; Savran, M.; Comlekci, S.; Sofu, M.M.; Erzurumlu, Y.; Ozmen, O.; Kaynak, M.; Sahin, M.E.; Taner, R.; Gecin, M. Combined Pulsed Magnetic Field and Radiofrequency Electromagnetic Field Enhances MMP-9, Collagen-4, VEGF Synthesis to Improve Wound Healing Via Hif-1 α /eNOS Pathway. *Aesthetic Plast. Surg.* **2023**, *47*, 2841–2852. [CrossRef]
19. Kubat, N.J.; Moffett, J.; Fray, L.M. Effect of pulsed electromagnetic field treatment on programmed resolution of inflammation pathway markers in human cells in culture. *J. Inflamm. Res.* **2015**, *8*, 59–69. [CrossRef]
20. Costantini, E.; Aielli, L.; Serra, F.; De Dominicis, L.; Falasca, K.; Di Giovanni, P.; Reale, M. Evaluation of Cell Migration and Cytokines Expression Changes under the Radiofrequency Electromagnetic Field on Wound Healing In Vitro Model. *Int. J. Mol. Sci.* **2022**, *23*, 2205. [CrossRef]
21. Peng, L.; Fu, C.; Xiong, F.; Zhang, Q.; Liang, Z.; Chen, L.; He, C.; Wei, Q. Effectiveness of Pulsed Electromagnetic Fields on Bone Healing: A Systematic Review and Meta-Analysis of Randomized Controlled Trials. *Bioelectromagnetics* **2020**, *41*, 323–337. [CrossRef] [PubMed]
22. Gualdi, G.; Monari, P.; Farisoglio, C.; Calzavara-Pinton, P. Nested graft in chronic wounds: A new solution for an old problem. *Int. Wound J.* **2011**, *8*, 127–131. [CrossRef]
23. Gualdi, G.; Crotti, S.; Monari, P.; Calzavara-Pinton, P.; Vitali, M.; Baronio, M.; Lougaris, V. The nested graft acts by inducing the process of de-senescence of the fibroblasts in chronic venous ulcers. *Int. Wound J.* **2016**, *13*, 1104–1110. [CrossRef] [PubMed]
24. Schneider, C.A.; Rasband, W.S.; Eliceiri, K.W. NIH Image to ImageJ: 25 years of image analysis. *Nat. Methods* **2012**, *9*, 671–675. [CrossRef]
25. Mendez, M.V.; Stanley, A.; Park, H.Y.; Shon, K.; Phillips, T.; Menzoian, J.O. Fibroblasts cultured from venous ulcers display cellular characteristics of senescence. *J. Vasc. Surg.* **1998**, *28*, 876–883. [CrossRef]
26. Rai, V.; Moellmer, R.; Agrawal, D.K. Role of fibroblast plasticity and heterogeneity in modulating angiogenesis and healing in the diabetic foot ulcer. *Mol. Biol. Rep.* **2023**, *50*, 1913–1929. [CrossRef]
27. Blyakhman, F.A.; Melnikov, G.Y.; Makarova, E.B.; Fadeyev, F.A.; Sedneva-Lugovets, D.V.; Shabadrov, P.A.; Volchkov, S.O.; Mekhdieva, K.R.; Safronov, A.P.; Fernández Armas, S.; et al. Effects of Constant Magnetic Field to the Proliferation Rate of Human Fibroblasts Grown onto Different Substrates: Tissue Culture Polystyrene, Polyacrylamide Hydrogel and Ferrogels γ -Fe₂O₃ Magnetic Nanoparticles. *Nanomaterials* **2020**, *10*, 1697. [CrossRef]
28. Costantini, E.; Sinjari, B.; D’Angelo, C.; Murmura, G.; Reale, M.; Caputi, S. Human Gingival Fibroblasts Exposed to Extremely Low-Frequency Electromagnetic Fields: In Vitro Model of Wound-Healing Improvement. *Int. J. Mol. Sci.* **2021**, *22*, 2108. [CrossRef]
29. Zafari, J.; Javani Jouni, F.; Abdolmaleki, P.; Jalali, A.; Khodayar, M.J. Investigation on the effect of static magnetic field up to 30 mT on viability percent, proliferation rate and IC₅₀ of HeLa and fibroblast cells. *Electromagn. Biol. Med.* **2015**, *34*, 216–220. [CrossRef] [PubMed]
30. Jonsson, C.E.; Anggård, E. Biosynthesis and metabolism of prostaglandin E₂ in human skin. *Scand. J. Clin. Lab. Invest.* **1972**, *29*, 289–296. [CrossRef]
31. Jouvenaz, G.H.; Nugteren, D.H.; Beerthuis, R.K.; van Dorp, D.A. A sensitive method for the determination of prostaglandins by gas chromatography with electron-capture detection. *Biochim. Biophys. Acta* **1970**, *202*, 231–234. [CrossRef] [PubMed]
32. Pyrillou, K.; Burzynski, L.C.; Clarke, M.C.H. Alternative Pathways of IL-1 Activation, and Its Role in Health and Disease. *Front. Immunol.* **2020**, *11*, 613170. [CrossRef] [PubMed]
33. Cheng, H.; Huang, H.; Guo, Z.; Chang, Y.; Li, Z. Role of prostaglandin E₂ in tissue repair and regeneration. *Theranostics* **2021**, *11*, 8836–8854. [CrossRef] [PubMed]
34. Owen, J.B.; Butterfield, D.A. Measurement of oxidized/reduced glutathione ratio. *Methods Mol. Biol.* **2010**, *648*, 269–277. [CrossRef]
35. Wall, I.B.; Moseley, R.; Baird, D.M.; Kipling, D.; Giles, P.; Laffafian, I.; Price, P.E.; Thomas, D.W.; Stephens, P. Fibroblast dysfunction is a key factor in the non-healing of chronic venous leg ulcers. *J. Investig. Dermatol.* **2008**, *128*, 2526–2540. [CrossRef]
36. Maddipati, K.R. Non-inflammatory Physiology of “Inflammatory” Mediators—Unalation, a New Paradigm. *Front. Immunol.* **2020**, *11*, 580117. [CrossRef]
37. Megha, K.B.; Joseph, X.; Akhil, V.; Mohanan, P.V. Cascade of immune mechanism and consequences of inflammatory disorders. *Phytomedicine* **2021**, *91*, 153712. [CrossRef]
38. Xiao, T.; Yan, Z.; Xiao, S.; Xia, Y. Proinflammatory cytokines regulate epidermal stem cells in wound epithelialization. *Stem Cell Res. Ther.* **2020**, *11*, 232. [CrossRef]
39. Larouche, J.; Sheoran, S.; Maruyama, K.; Martino, M.M. Immune Regulation of Skin Wound Healing: Mechanisms and Novel Therapeutic Targets. *Adv. Wound Care* **2018**, *7*, 209–231. [CrossRef]
40. Gan, M.S.; Yang, B.; Fang, D.L.; Wu, B.L. IL-1B can serve as a healing process and is a critical regulator of diabetic foot ulcer. *Ann. Transl. Med.* **2022**, *10*, 179. [CrossRef]
41. Lee, M.K.S.; Sreejit, G.; Nagareddy, P.R.; Murphy, A.J. Attack of the NETs! NETosis primes IL-1 β -mediated inflammation in diabetic foot ulcers. *Clin. Sci.* **2020**, *134*, 1399–1401. [CrossRef]
42. Pentland, A.P.; Needleman, P. Modulation of keratinocyte proliferation in vitro by endogenous prostaglandin synthesis. *J. Clin. Investig.* **1986**, *77*, 246–251. [CrossRef]
43. Uematsu, S.; Matsumoto, M.; Takeda, K.; Akira, S. Lipopolysaccharide-dependent prostaglandin E₂ production is regulated by the glutathione-dependent prostaglandin E₂ synthase gene induced by the Toll-like receptor 4/MyD88/NF-IL6 pathway. *J. Immunol.* **2002**, *168*, 5811–5816. [CrossRef]

44. Ganesh, K.; Das, A.; Dickerson, R.; Khanna, S.; Parinandi, N.L.; Gordillo, G.M.; Sen, C.K.; Roy, S. Prostaglandin E₂ induces oncostatin M expression in human chronic wound macrophages through Axl receptor tyrosine kinase pathway. *J. Immunol.* **2012**, *189*, 2563–2573. [CrossRef]
45. Mudge, B.P.; Harris, C.; Gilmont, R.R.; Adamson, B.S.; Rees, R.S. Role of glutathione redox dysfunction in diabetic wounds. *Wound Repair. Regen.* **2002**, *10*, 52–58. [CrossRef]
46. Latifa, K.; Sondess, S.; Hajer, G.; Manel, B.H.; Souhir, K.; Nadia, B.; Abir, J.; Salima, F.; Abdelhedi, M. Evaluation of physiological risk factors, oxidant-antioxidant imbalance, proteolytic and genetic variations of matrix metalloproteinase-9 in patients with pressure ulcer. *Sci. Rep.* **2016**, *6*, 29371. [CrossRef]
47. Calcabrini, C.; Mancini, U.; De Bellis, R.; Diaz, A.R.; Martinelli, M.; Cucchiari, L.; Sestili, P.; Stocchi, V.; Potenza, L. Effect of extremely low-frequency electromagnetic fields on antioxidant activity in the human keratinocyte cell line NCTC 2544. *Biotechnol. Appl. Biochem.* **2017**, *64*, 415–422. [CrossRef]
48. Martinelli, I.; Cinato, M.; Keita, S.; Marsal, D.; Antoszewski, V.; Tao, J.; Kunduzova, O. Cardiac Cell Exposure to Electromagnetic Fields: Focus on Oxidative Stress and Apoptosis. *Biomedicines* **2022**, *10*, 929. [CrossRef] [PubMed]

Disclaimer/Publisher’s Note: The statements, opinions and data contained in all publications are solely those of the individual author(s) and contributor(s) and not of MDPI and/or the editor(s). MDPI and/or the editor(s) disclaim responsibility for any injury to people or property resulting from any ideas, methods, instructions or products referred to in the content.

Optimized Conditions for Electrical Tissue Stimulation with Biphasic, Charge-Balanced Impulses

Zhengwu Sun¹, Payel Sen^{1,2}, Jules Hamers^{1,2}, Thomas Seidel³, Andreas Dendorfer^{1,2} and Petra Kameritsch^{1,*}

¹ Walter-Brendel-Centre of Experimental Medicine, LMU Klinikum, Ludwig-Maximilians-University, 81377 München, Germany; zhengwu.sun@med.uni-muenchen.de (Z.S.); payel.sen@med.uni-muenchen.de (P.S.); jules.hamers@med.uni-muenchen.de (J.H.); andreas.dendorfer@med.uni-muenchen.de (A.D.)

² DZHK (German Center for Cardiovascular Research), Partner Site Munich, Munich Heart Alliance (MHA), 80336 Munich, Germany

³ Institute of Cellular and Molecular Physiology, Friedrich-Alexander University Erlangen-Nürnberg, 91054 Erlangen, Germany; thomas.seidel@fau.de

* Correspondence: kameritsch@lmu.de; Tel.: +49-89-2180-76543

Abstract: The cultivation of excitable cells typically profits from continuous electrical stimulation, but electrochemical consequences are mostly harmful and must be minimized. The properties of the electrode materials and stimulation impulses are key. Here, we developed an easy method to analyze the electrochemical impact of biphasic, current-controlled impulses, applied via graphite electrodes, using phenol red as the redox indicator. We also tested the stimulation conditions for the long-term cultivation of myocardial tissue. The colorimetric assay was able to detect $\pm 0.2\%$ deviations in typical positive and negative pulse charges. Phenol red was best preserved (20% degradation over 24 h) by impulses of equivalent positive and negative charges (full charge balance), generated with either manual calibration, capacitive electrode coupling, or feedback regulation of electrode polarization. Feedback regulation established full charge balance at pre-pulse voltages of about 300 mV, but also provided the option to selectively compensate irreversible electrode reactions. Modifications to shape and timing did not affect the electrochemical effects of symmetric impulses. Charge-balanced stimulation maintained more than 80% of the contractility of porcine left ventricular myocardium after 10 days of culture, whereas disbalances of 2–4% provoked weakening and discoloration of the tissues. Active polarization regulation, in contrast to capacitive electrode coupling, reproduced the biological advantages of full charge balance.

Keywords: field stimulation; biphasic; charge balance; tissue culture; living myocardial slice

1. Introduction

The cultivation of excitable cells has become an important research tool. To maintain the physiological function of such cells *in vitro*, chronic and cell-specific electrical stimulation seems to be essential [1,2]. Stimulation is usually performed by an electrical field, applied through electrodes which are not in direct contact with the cells, but are submerged in the culture medium at some distance [3]. In this indirect configuration of field stimulation, electrical gradients, e.g., at the cell membrane, are a function of local conductivity and current density, implying a direct correlation of biological effectivity and stimulation current. An effective depolarization of excitable cells typically occurs at current densities in the range of 15 mA/cm² [1,4–6], and such currents require electrode

voltages well above the redox potential of many medium constituents [7]. Consequently, electrochemical reactions at the electrode surface cannot be avoided, but must be kept to a minimum since they degrade bioactive substances, produce reactive oxygen species, or shifts in pH [7–10]. This is particularly detrimental in cell culture applications, where electrodes and solutions cannot be changed frequently, and electrochemical reaction products accumulate over time [6,7]. One way to separate electrode reactions from the cultivated cells is the transmission of currents by a defined electrolyte solution, e.g., provided by an agar bridge [11], but such designs are not compatible with the requirements of tissue culture and would not be stable over long periods. Alternatively, stimulation modalities may be chosen that take advantage of the capacitive properties of some electrode materials. The capacitance arises from the charges at the electrode surface that are reversibly bound in an ionic bilayer or as partial redox-reactions at the electrode interface [12]. As a consequence of capacitance, stimulation currents can be generated apart from irreversible electrochemical (faradaic) reactions; however, reversibility of these reactions is only ensured if the charge applied to the electrode with an electrical impulse is removed subsequently. Shortening of the electrodes after each impulse can achieve this, but typically, discharging of the electrodes is performed actively by application of an inverted current. Technically, this is implemented by biphasic impulses, which are characterized by a leading impulse, followed by an equivalent current of inverted polarity.

Recent studies employed either mono- or biphasic impulses for the long-term stimulation of cardiac cells [13–16] but information about their electrochemical impact is missing. One comprehensive investigation reported a 15% fraction as the non-recovered charge of monophasic impulses [17]. This may be important, since this charge is fully absorbed by redox reactions, possibly affecting medium components and electrode materials. Consistently, a regular exchange of electrodes has been recommended [16]. In these studies, the potential to minimize the electrochemical impact of stimulation was limited by the fact that voltage-controlled impulses were applied exclusively. With this mode of stimulation, the electrical charge of a stimulation impulse is not usually considered, and therefore, its recoverable fraction is unknown. Importantly, the biological implications of electrochemical electrode reactions are mostly disregarded.

Obviously, uncertainty exists with regard to the electrical configuration and technical implementation of field stimulation ensuring the highest biocompatibility. As stated, stimulation impulses can be generated with constant voltage or current. Voltage control is more easily implemented, but the resistance of the stimulation circuit, particularly the electrode–solution interface, may change over time. This implies alterations in the biological activity of the impulses, which directly correlates to current density. In this regard, impulses with constant current provide better control and they are a requirement for the application of a defined charge to an electrode, including its removal in an equivalent, “balanced” way. The most appropriate strength of the discharging impulse has been discussed [12]. The leading impulse will not only generate capacitive, but also irreversible currents, and it is unclear whether only reversible or total charges should be antagonized by the discharging impulse. The first option will remove the reversible charge of the electrode and therefore may prevent delayed faradaic reactions, while the second option of “fully balanced” impulses will avoid any direct current [12].

Another approach to optimize the electrochemical compatibility of field stimulation takes into account the non-linear relationship between currents and the durations of impulses with equivalent biological activities. In general, stimulation voltage and current should be kept at low but sufficient levels to guarantee stimulation of the cells [18]. However, such conditions will favor long pulse durations of the discharging impulses which might increase the total charges at the electrodes. On the other hand, short impulses will

only be effective when applied with high overpotentials, and these might even produce new classes of reaction products because they exceed the redox potentials of additional culture medium ingredients. Even the frequently used symmetrical biphasic impulses may be subject to optimization, since they have been reported to exert less biological efficacy compared to monophasic impulses [18,19]. An inhibitory biological activity of the discharging pulse might be overcome by a low current and long duration of discharge, thus suggesting superior properties of asymmetric, biphasic stimulation impulses.

In the present study, the electrochemical compatibility of various configurations of field stimulation was evaluated. For the analytical part, it was assumed that faradaic reactions at the electrode surface can be quantified using phenol red as a redox-sensitive tracer. The stability of phenol red under continuous stimulation may therefore be considered as an indicator of high biological compliance with the electrical currents. Phenol red is typically used in cell culture to monitor the pH value [20]. However, in redox reactions, which can be independent of the pH value, phenol red is decolorized to transparency [21]. This characteristic can be used to measure the degradation rate of phenol red in the cell culture medium with a spectrometer which, in our case, reflects the activity of redox reactions caused by the stimulation impulses.

For the biological evaluation of various stimulation modalities, we chose their application for the long-term cultivation of myocardial tissue. It has been shown that the myocardial differentiation of stem cell-derived artificial myocardium, as well as the functional maintenance of adult myocardial tissue slices greatly profit from continuous electrical stimulation *in vitro* [22]. Bioreactors for the cultivation of such tissues have been designed to provide suitable biomechanical conditions, and to apply regular field stimulation [23]. In many cell culture applications, the electrical field is introduced by electrodes made of graphite, because this material is highly conductive, non-toxic, inert, and autoclavable [5]. In addition, particle-based graphite is cost-effective, and features high porosity which is associated with large specific capacitance [24]. Such electrodes were therefore used to evaluate various stimulation impulse configurations for the maintenance of living myocardial slice preparations obtained from porcine hearts. To improve the quality of long-term cultivation and stimulation of these heart slices and of bio-engineered tissues, our study pursued the following aims:

1. Development of a simple and sensitive method to quantify the electrochemical reactivity of biphasic stimulation impulses.
2. Determination of the impact of charge balance on the electrochemical properties of biphasic stimulation impulses.
3. Evaluation of capacitive electrode coupling and active impulse adaptation as the technical means to establish charge balance.
4. Evaluation of various pulse configurations with regard to the individual biological excitation efficacy and electrochemical compatibility.
5. Demonstration of the benefit of charge-balanced stimulation for the cultivation of adult pig myocardium.

2. Materials and Methods

2.1. Electrochemical Degradation of Phenol Red

A MyoDish tissue culture system designed for long term cultivation of heart slices was used in this study (InVitroSys GmbH, Gräfelfing, Germany). Each original culture chamber was filled with 2.4 mL PBS (DPBS (1×), titrated to pH 7.4, Gibco, Thermo Fisher Scientific, Waltham, MA, USA) containing 20 mg/L phenol red (Sigma-Aldrich, Merck, Darmstadt, Germany), and was incubated on the system's integrated rocker (60/min) for 10 h or 24 h at room temperature. Electrical stimulation was performed by the MyoDish

control unit, which generated constant current, biphasic impulses with arbitrary timing and PC-controlled scheduling. The initial phase of these impulses is addressed as “charging” or “stimulatory” phase, whereas the secondary phase is “discharging” the electrode capacitance. Stimulation pulses were applied at 4 Hz, using parameters well established for myocardial tissue culture (50 mA, 3 ms duration, followed by 1 ms interval and 3 ms current of inverted polarity). The stimulation frequency and duration were chosen to simulate the number of impulses applied over 3 days of slice culture at stimulation frequencies of 0.5 or 1 Hz. As such, the typical protocol for slice cultivation administered 129,600 to 259,200 impulses in between medium exchanges. To increase the sensitivity of the system, we increased the incubation time to 24 h in a set of experiments. Stimulation currents were introduced into the phenol red solution by $6 \times 8 \times 2 \text{ mm}^3$ graphite electrodes (type CG 1290, CGC Klein, Siegen, Germany) placed at 16 mm distance. After the indicated exposure to stimulation, the absorbance of the phenol red solution was determined at 430 nm with a microplate reader (SpectraMax iD3, Molecular Devices, San Jose, CA, USA). The equilibrium polarization of the electrodes was measured as the imprinted voltage present in the open-circuit condition prior to each stimulation impulse (pre-pulse voltage). This voltage was determined during the experiments with an oscilloscope (HM407, Hameg, Frankfurt, Germany). Modifications of stimulation parameters are described for the individual experiments.

2.2. Balance and Regulation of Stimulation Impulse Charges

The equivalence of the negative and positive charges of each stimulation impulse was tested with an electronic model of the electrolyte interface (Figure 1). Essentially, a capacitor was charged and discharged during the respective periods of the biphasic impulses and the equivalence of both charges was assumed if no voltage was detectable during the interval between the impulses. To compensate imprecise current regulation of the impulse source, charge balance was established by manual adjustment of the duration of the positive current of each impulse. In practice, the electrode model (Figure 1) was connected to a digital voltmeter (Votcraft VC170-1, Conrad, Munich, Germany) and to the impulse generator, which was set to standard conditions (3 ms charge and discharge, 1 ms pause, 50 mA). Pre-pulse potential was assessed as the voltage between the single negative readings provoked by the impulses (Figure 1). The duration of the positive impulse phase was stepwise shortened or prolonged (range $\pm 200 \mu\text{s}$) to drive the pre-pulse potential to more negative or positive values, respectively. The duration resulting in the lowest pre-pulse potential (range 0–5 mV) was accepted as the reference value of charge balance. Intentional disbalance was established by reduction or prolongation of the positive impulse phase (range -60 to $+120 \mu\text{s}$), and the relative disbalance of negative and positive charges was expressed as the deviation in its actual duration in relation to the reference value (range -2 to $+4\%$). As an alternative way to keep positive and negative charges equivalent, we tested the suppression of any direct current by introduction of a serial capacitor into the stimulation circuit. Active control over the electrochemical consequences of biphasic stimulation was pursued by feedback regulation of the discharge pulse duration, targeting at a defined value of the pre-pulse voltage. The feedback loop was implemented with a level-shifter circuit and the internal analog–digital converter of the microcontroller (MCU).

2.3. Culture and Analysis of Living Heart Slices

The preparation and cultivation of living myocardial slices followed the procedures described elsewhere [5]. In short, pig hearts were obtained at the Walter-Brendel-Centre after termination of unrelated experiments. Slices of $300 \mu\text{m}$ thickness were cut from $1 \text{ cm} \times 1 \text{ cm}$ transmural blocks of left ventricular myocardium using a vibratome (VT1200s,

Leica AG, Wetzlar, Germany). Slices were glued to plastic holders, trimmed and mounted in MyoDish cultivation chambers with a preload tension of 1 mN. Slices were cultivated in Medium 199 (Thermo Fisher Scientific, Waltham, MA, USA), supplemented with 1% penicillin-streptomycin (Sigma-Aldrich, Merck, Darmstadt, Germany), 1% insulin-transferrin-selenium-ethanolamine (Thermo Fisher Scientific, Waltham, MA, USA), and 20 nM cortisol (Sigma-Aldrich, Merck, Darmstadt, Germany) for 10 days with constant rocking (60 rpm), and electrical stimulation (30 bpm) featuring the impulse characteristics of interest. Forces developed by the myocardial slices were continuously monitored, and the contraction force of an individual slice was derived from the amplitude of each stimulated beat. Preservation of contractility over 10 days of cultivation is given as the contraction force at the end of this period normalized to the initial value (10 h after start of cultivation, initial force). The stimulation threshold of each slice was determined by an automated protocol (starting at 50/60/70/90/120 mA for 3/2/1/0.5/0.3 ms pulse durations, respectively) which stepwise (2 mA steps in the critical region) decreased the stimulation current in 10 s intervals. The lowest current that was sufficient to maintain regular beating was considered as the stimulation threshold.

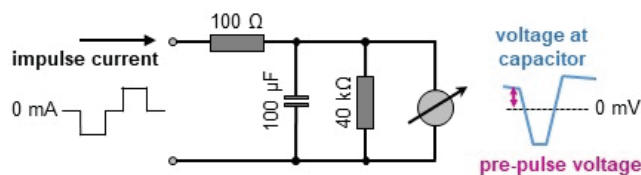


Figure 1. Test circuit for the manual calibration of biphasic pulses. Serial resistance and capacitance replicate electrode properties. A pre-pulse voltage of 0 V indicates equivalence of positive and negative pulse charges.

2.4. Statistics

One-way or two-way analysis of variance (ANOVA) was performed to test the raw data (Sigma Plot 12, Systat Software, San Jose, CA, USA). Tests were followed by comparisons versus the control (0% charge deviation) with Bonferroni's method. The method used and the number of samples are indicated in the figure legends. Mean values and standard error of the mean are given. At an error probability of less than 5% ($p < 0.05$), the effects were considered significant.

3. Results

3.1. Full Charge Balance of Biphasic Stimulation Minimizes the Degradation of the Redox-Indicator Phenol Red

Biphasic impulses were applied with either equivalent (balanced) charges of the positive and negative phases, or with modifications of the duration of the positive impulse in order to generate charge disbalance (Figure 2A). In the culture chambers containing either PBS with phenol red or heart slices in the culture medium, the impulses were applied via graphite electrodes embedded in the chamber (Figure 2B). Balanced biphasic impulses (charge disbalance 0%) degraded phenol red by about 10% within 10 h regardless of whether a negative (Figure 2C) or positive (Figure 2D) current was applied first. Disbalance of positive and negative impulse charges increased the redox degradation of phenol red. Deviations of $\pm 2\%$ applied at 4 Hz for 10 h led to an excessive medium decolorization and decrease in phenol red absorbance by approx. 60% (Figure 2C,D). Interestingly, a positive or negative excess of impulse charges did not promote phenol red degradation in an identical manner, thereby generating a non-symmetric relationship. Impulses starting with either negative or positive currents were less active in the degradation of phenol red, when their net charge was opposite to the polarity of the leading current (Figure 2C,D). Longer (24 h)

stimulation (Figure 2E) revealed that the method can detect as little as 0.2% imbalance in charges ($6 \mu\text{s}$ difference in impulse durations), and confirmed a peculiar drop in phenol red stability at a 0.2–0.27% excess in the positive charge, as was also observed in the previous experiment (Figure 2C).

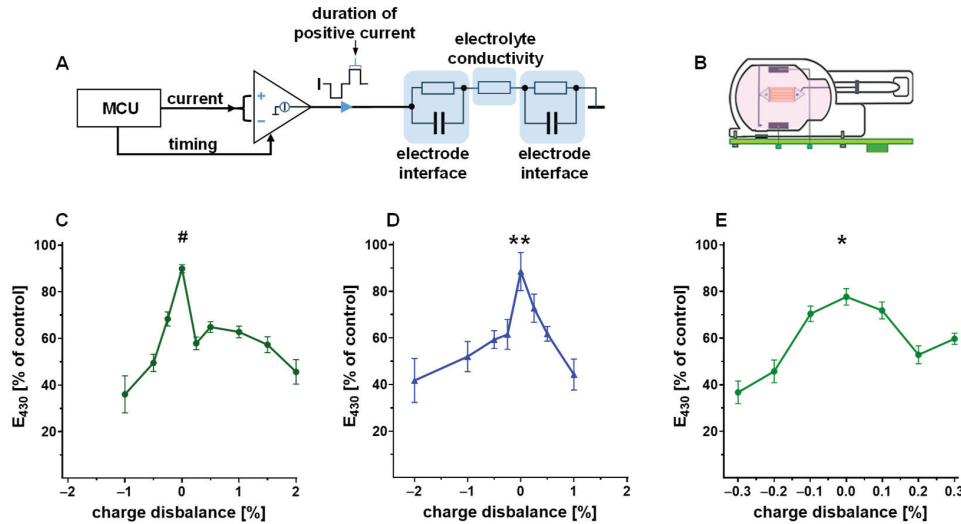


Figure 2. (A) Schematic of the impulse generator employing a microcontroller (MCU) and an adjustable current source. Highlighted in blue is the equivalent circuit of the Galvanic cell of the incubation chamber. (B) Design of the biomimetic chamber for tissue culture. The myocardial slice (red) is elastically mounted between the stimulation electrodes (grey rectangles). (C–E) Preservation of phenol red after stimulation for 10 h (C,D) or 24 h (E) with symmetric, biphasic impulses (4 Hz, 50 mA, 3 ms each phase). Impulses were generated with negative current first (C,E), or positive current first (D). Charge imbalance was set by shortening or prolonging the phase of positive impulse current. (C) # $p < 0.01$ vs. all conditions, ANOVA, Bonferroni correction, ($n = 3$ –11); (D) ** $p < 0.01$ vs. $\geq \pm 1\%$ imbalance, ANOVA, Bonferroni correction, ($n = 4$); (E) * $p < 0.01$ vs. $\geq \pm 0.2\%$ imbalance, ANOVA, Bonferroni correction, ($n = 7$ –10).

3.2. Capacitive Electrode Coupling Enforces Charge Balance and Improves the Electrochemical Compatibility of Stimulation

Biphasic impulses with a difference of up to -2% or $+2\%$ in the negative and positive charges led to a decolorization of phenol red up to 87% and 90% within 24 h, respectively (Figure 3B). Introduction of a serial capacitor into the stimulation circuit (Figure 3A) reduced phenol red degradation in all conditions tested, in a similar way as manual balancing of impulses (Figure 3B). The capacitor achieved the effect of charge balancing by accumulating the excess charge of any polarity until the impulse source could not deliver the requested charge due to its limitation in output voltage. The capacitor reduced the charge of the predominant polarity to the equivalent of the inverted impulse charge. Asymmetric stimulation with discharge prolongation (i.e., a decrease in current to one third, and an increase in duration by three-fold) had similar effects on electrochemical reactivity, as evidenced by the similarity of the minima and maxima of phenol red degradation, independent of the insertion of a capacitor (Figure 3C). A less pronounced formation of a plateau within a range of positive charge excess was the only notable difference from the symmetric impulse shape (Figure 3C).

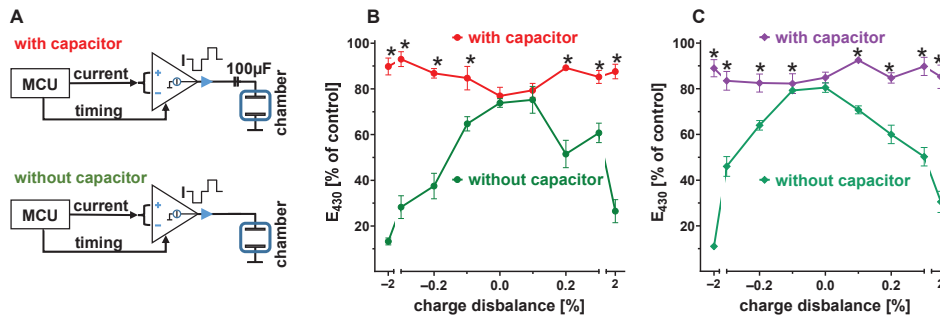


Figure 3. (A) Schematic of the pulse generator with direct or capacitive electrode coupling. (B,C) Preservation of phenol red after 24 h stimulation with biphasic impulses (4 Hz, negative current first) with or without a serial capacitor in the stimulation circuit. Impulses were either symmetric with 3 ms, 50 mA each phase (B), or asymmetric with a prolonged (9 ms) and attenuated (17 mA) secondary phase (C). * $p < 0.01$ vs. 0% direct coupling (without capacitor), two-way ANOVA, Bonferroni correction ((B) $n = 5-13$, (C) $n = 4-16$).

3.3. Electrode Polarization Enables Active Feedback Regulation of Impulse Charges

Any charge excess from repetitively applied biphasic impulses will accumulate on the electrodes until the resulting voltage will generate an equilibrium of net charge and faradaic (electrochemical) current. The voltage generated by the electrodes in an open-circuit condition can therefore be used as an indicator of charge balance. We measured the electrode voltage right before each biphasic stimulation impulse (pre-pulse voltage) under equilibrium conditions, i.e., at the end of phenol red degradation experiments. It was expected that any consistent charge excess from the stimulation impulses would shift the pre-pulse voltage to the respective polarity (Figure 4A). Indeed, there was a strict, positive correlation between both parameters, which revealed the generation of a 244 ± 55 mV baseline potential by fully charge-balanced impulses (Figure 4C). The relative recovery of phenol red confirmed this observation by demonstrating an optimum preservation in the range of pre-pulse voltages between +200 and +400 mV (Figure 4B). A pre-pulse voltage close to zero requires a charge imbalance of about -0.14% (Figure 4C), and it may be deduced from Figure 2D, that such a deviation would effectively promote phenol red degradation after 24 h.

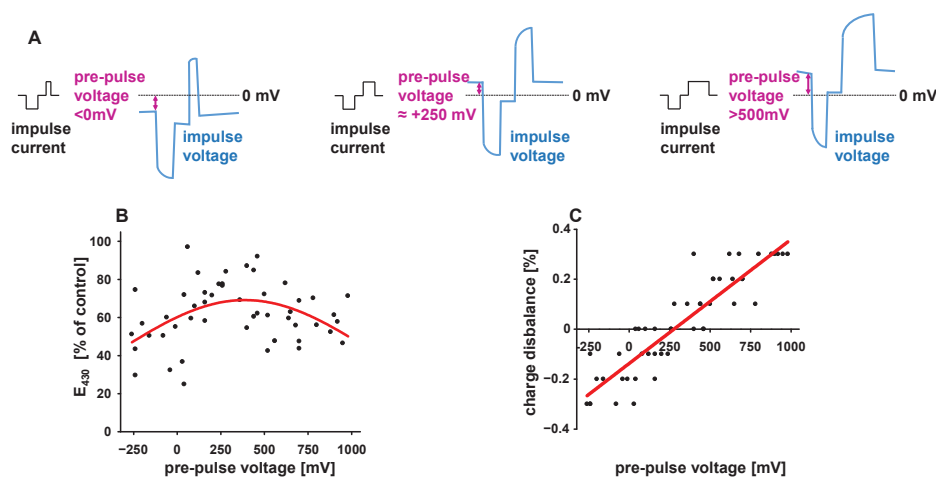


Figure 4. (A) Development of pre-pulse voltage of impulses with balanced (central graph) or disbalanced charges. (B) Preservation of phenol red and steady-state pre-pulse voltage after stimulation (24 h, 4 Hz, 50 mA, 3 ms, negative current first) with various states of disbalance. A non-linear fit based on a Gauss equation (red line) estimates best preservation at 390 mV. (C) Relationship of charge disbalance and pre-pulse voltage in the same experiment. Linear regression (red line) indicates a pre-pulse voltage of 244 mV for charge-balanced impulses ($n = 5-9$).

The strict correlation between pre-pulse voltage and charge balance inspired us to utilize the easily measurable voltage as the target value for active regulation of charge balance. With the interposition of a level shifter, the pre-pulse voltage was quantified by the analog–digital converter of the microcontroller. In response to these measurements, the duration of positive current was automatically modified to generate a defined pre-pulse voltage (Figure 5A). With this regulation, phenol red degradation was studied with pre-pulse voltages actively set within a wide range (Figure 5B). Preservation of phenol red by 80–90% was observed with pre-pulse voltages between 0 and +450 mV. The optimum preservation was equivalent to the stability of phenol red achieved with manually balanced impulses (Figure 2D).

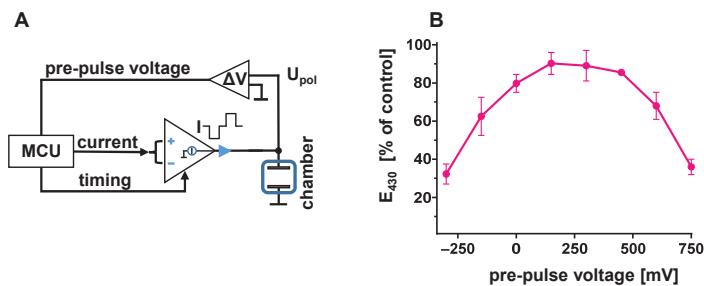


Figure 5. (A) Schematic of the active feedback regulation of pre-pulse voltage. The microcontroller (MCU) modified pulse charges in response to deviations from the pre-pulse target value. (B) Preservation of phenol red after 24 h stimulation (4 Hz, symmetric, 3 ms, 50 mA, negative current first) with pre-pulse voltage regulated to values of -300 to 750 mV. Best preservation was achieved with 150 mV pre-pulse voltage ($n = 4$).

3.4. Stimulation Efficacies of Various Impulse Configurations in Cultivated Pig Myocardium

To explore whether the biological efficacies of certain pulse configurations might be superior to those of standard symmetric, biphasic impulses, we determined their threshold intensities for the excitation of cultured myocardial slices. Thin slices of adult pig ventricular myocardium were cultured using the standard approach of the MyoDish cultivation system [5], with omission of beta-mercaptoethanol in the culture medium as the only modification. After 3–10 days of cultivation under standard stimulation (0.5 Hz, 50 mA, 3 ms biphasic balanced impulses), impulse shapes were modified, and stimulation was applied in a series of declining currents. The minimum current required to induce regular contractions of the heart slice was considered as the stimulation threshold. The stimulation threshold predicted for indefinite impulse durations is given here as the rheobase of the stimulation modality. For symmetrical impulses, the stimulation threshold (16.2 ± 0.2 mA for 3 ms, 65.2 ± 0.7 mA for 0.3 ms stimulus duration, $n = 20$) was lower, but very close to that of monophasic stimuli (18.9 ± 0.2 mA for 3 ms, 71.8 ± 0.9 mA for 0.3 ms stimulus duration, $n = 17$) (Figure 6A). Two-phase decay fitting revealed rheobase values of 14.5 mA and 16.5 mA for biphasic and monophasic impulses, respectively. Asymmetric impulses were generated with a three-fold extension of either the charge or the discharge duration and corresponding reductions in the pulse currents. Overall, their efficacies were comparable to those of symmetric impulses, indicated by rheobase values of 15.8 mA and 17.3 mA for impulses with prolonged charge or discharge durations, respectively. The overall charge of impulses was lowest using very short impulses, but, as the current required to induce stimulation was quite high in this setting, irreversible effects at the electrodes should be considered when choosing the stimulation duration for long term experiments (Figure 7B).

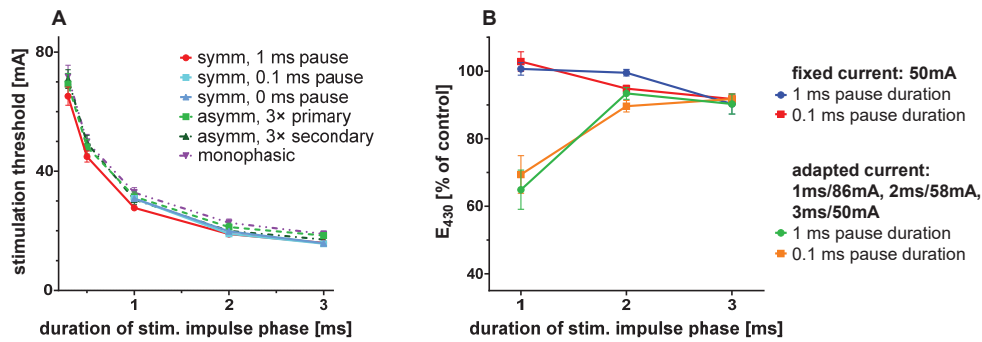


Figure 6. (A) Stimulation thresholds of impulses with various durations and shapes (symm: identical charge and discharge durations, asymm: asymmetric pulses with prolongation of duration and reduction in current by factors of 3 of either the first (3× primary) or the second (3× secondary) phase. The secondary phase was initiated after a 1 ms pause duration, if not indicated differently (n = 12–20). (B) Preservation of phenol red after 24 h stimulation (4 Hz, symmetric, negative current first) with pulse currents either set to 50 mA, or adapted to achieve biological efficacies equivalent to the 3 ms, 50 mA condition. Experiments were performed with either 1 ms or 0.1 ms pause intervals between negative and positive impulse phases (n = 5–11).

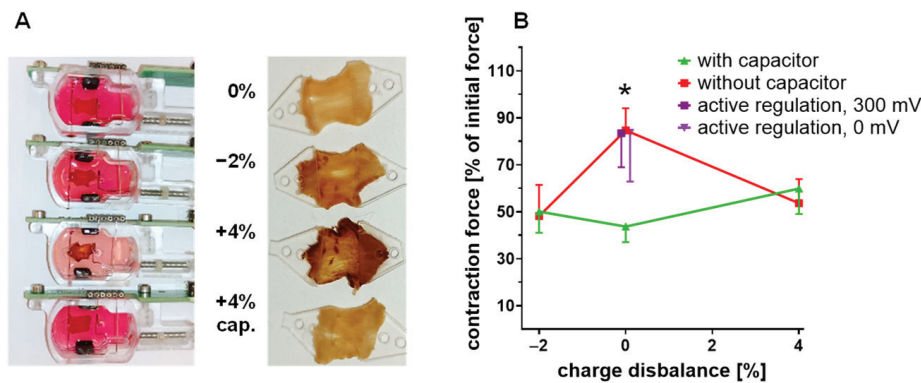


Figure 7. Effects of long-term stimulation on myocardial slices in tissue culture. (A) Typical presentation of tissue slices and cultivation medium in original biomimetic chambers after 10 days of cultivation, applying stimulation (0.5 Hz, symmetric, 3 ms, 50 mA, negative current first) with disbalanced (−2%, +4%) or balanced (0%) impulses, and direct or capacitive (cap.) electrode coupling. (B) Contraction forces at the end of the same experiment, as related to the initial (10 h cultivation) force of each slice. Stimulation conditions with active regulation of the pre-pulse voltages to 0 or 300 mV were included in this experiment (n = 9–19, * p < 0.05 vs. all conditions except active regulation, two-way ANOVA, Bonferroni’s correction).

3.5. Electrochemical Compatibility of Symmetric Biphasic Impulses with Various Pulse Timings

Electrode reactions were quantified in terms of phenol red degradation over 24 h. Stimulation with balanced symmetrical impulses of 50 mA current produced more intense decolorization of phenol red with increasing pulse durations, which directly corresponded to pulse charges (Figure 6B). A reduction in the interval between negative and positive currents from 1 ms to 0.1 ms did not change this relationship significantly (Figure 6B). The reversibility of charge accumulation and faradaic reactions during the leading impulse did not seem to change within such millisecond time ranges. Short (<3 ms) impulses were also applied with increased currents to compensate for their reduced efficacy, according to the established relationship of both parameters (Figure 6A). In this condition, the high overpotential (86 mA) of the 1 ms pulse durations greatly accelerated phenol red breakdown. In summary, biphasic symmetric impulses with 2 or 3 ms pulse and 1 ms pause durations seemed to have the best ratio of effectivity and chemical reactivity of all pulse configurations investigated.

3.6. Electrochemical Damage in Continuously Stimulated Cultured Myocardium

Slices of porcine myocardium were constantly stimulated with balanced or disbalanced biphasic stimuli for 10 days (50 mA, 0.5 Hz, 3 ms charge and discharge with 1 ms interval). The application of severely disbalanced stimuli (+4% charge excess) led to de-colorization of the phenol red during the intervals of medium exchange (2–3 days) with no significant influence on medium pH (Figure 7A). The cultivated tissue also underwent stimulation-dependent chemical reactions, whose products accumulated over the 10 days of cultivation, and resulted in a general brownish coloration of the tissues. These changes slowly evolved during cultivation, and were clearly visible after 10 days of stimulation with either –2% or +4% charge disbalance (Figure 7A). Neither discoloration of the medium, nor brownish coloration of the tissue was observed after stimulation with charge-balanced impulses. Integration of a capacitor into the stimulation line prevented the color changes in the slices and medium even at a disbalance of 4% (Figure 7A). Under constant stimulation, the myocardial tissues contracted synchronously, and contraction force was continuously recorded by the cultivation system. Contractility was determined as the difference between diastolic and maximum systolic forces. The stable values of twitch force after 10 h of cultivation were taken as the reference for the contractility development of each slice. Contractile performance generally declined over the subsequent 10 days of cultivation, but was best preserved (>80%) when impulse charges were manually balanced, or pre-pulse voltage was adjusted to 0 or +300 mV (Figure 7B). The amplitude of contraction decreased significantly in slices treated with disbalanced stimuli (–2% or +4% deviation of net charge) and, surprisingly, charge balance by capacitive coupling did not prevent this. The capacitor in the stimulation line even deteriorated the compatibility of charge-balanced impulses.

4. Discussion

This study represents a practical approach to optimize the electrochemical compatibility of continuous, long-term field stimulation in a demanding *in vitro* environment, characterized by product accumulation and low anti-oxidative capacities. The general problem of electrochemical compliance arises from the fact that induction of electrical current in an aqueous electrolyte solution is based on either redox (faradaic) reactions or reversible ion accumulation at the electrode surface [10]. Depending on time and energies, electrode-associated redox reactions may be reversed, but the best way to prevent irreversible faradaic reactions is unclear. Here, we present an easy assay that quantifies the electrochemical compatibility of stimulation impulses using phenol red as a redox indicator, and we confirm that the application of an inverted charge in a second phase of each set of stimulation impulses is an effective way to maximize the reversible fraction of the electrode reactions. Our study indicates that the technical implementation of an impulse generator should aim for a well-controlled balance of positive and negative impulse charges, with a deviation in charges as small as 0.2% already being significant. Since charge control with this accuracy may be technically demanding, we also present a way to accomplish it by feedback regulation of electrode polarization. This technique also enables partial compensation of impulse charges, which may be beneficial when complex media are considered as electrolytes.

4.1. Principles of Pulsatile Field Stimulation and Charge Balance

Any current applied to an electrode will redistribute electron and ion densities at the electrode–electrolyte interface and generate an electrode potential. Static currents will raise this potential until potential-driven redox reactions will convert all electrical charges into ionic currents [12]. Biphasic stimulation with two equivalent pulses of opposing polarities provides the opportunity to minimize such irreversible electrochemical reactions by rapid

discharge of the electrode capacitance and reversal of intermediate redox reactions [12]. Such discharge current can be enabled by shortening two working electrodes after termination of a monopolar impulse, but in this case, the full removal of all reversible charges will only occur at high levels of electrode polarization which will promote irreversible faradaic reactions [12]. Under such conditions, unrecoverable fractions of impulse charges as high as 15% have been reported [17]. Acceleration of electrode discharge by an inverted current subsequent to the leading impulse will reduce electrode polarization, but may provoke irreversible reactions by itself, when its inverse charge exceeds the reversible part of the leading current. Technically, this can be avoided by proper limitation of the discharging current [12].

Our study clearly indicates that full balance of positive and negative charges minimizes the electrochemical breakdown of phenol red (Figure 2B). However, the difference between the full and the reversible charge of the leading impulse is small. Charge disbalances less than 0.2% will double the degradation of phenol red compared to the balanced condition (Figure 2E). The net charge applied with this disbalance will therefore be equivalent to the faradaic loss of charges in the fully balanced condition. In this case, 99.8% of the initially applied charge will be retrieved by the discharging impulse. Consequently, discharging the electrodes to the full extent of the leading phase of the impulses (full charge balance) will leave a charge excess on each of the electrodes thereby generating an inverted polarization. This will reduce the overpotential of the leading current of the next stimulation impulse, which seems to be favorable in terms of phenol red stability even at higher degrees of charge excess, as can be concluded from the asymmetric dependency of phenol red degradation on the polarity of charge disbalance (Figure 2B,C). Equilibrium conditions are reached when each electrode has developed a baseline polarization that renders the faradaic reactions of the stimulation impulses equivalent to those within the pulse intervals. Essentially, two conditions must be considered for the irreversible part of faradaic reactions: a high redox potential during the usually short stimulatory phase of the biphasic impulse, and subsequently, a lower potential during the long interval between the impulses. Both phases may affect the degradation of various substrates differentially, according to their susceptibility to oxidation or reduction, as discussed below.

4.2. Electrode Reactions of Phenol Red and Electrolyte Constituents

For biological applications, the chemical nature of the electrode reactions is crucial. The effective potential at the electrode interface exceeds the redox potential of phenol red, but the respective reactions of this substrate cannot constitute a major fraction of the irreversible electrode currents. In our experiments, a total charge of $4 \text{ Hz} \times 0.003 \text{ s} \times 0.05 \text{ A} \times 86,400 \text{ s} = 103.7 \text{ C}$ is applied over 24 h, of which $0.2\% = 0.21 \text{ C}$, corresponding to $1.3 \times 10^{18} e^-$, are consumed by irreversible electrochemical reactions. This by far exceeds the $50.4 \times 10^{-6} \text{ mol/L} \times 0.0024 \text{ L} \times 6.02 \times 10^{23} \text{ parts/mol} \times 20\% = 1.46 \times 10^{16}$ molecules of phenol red that are degraded within this period. Under the assumption that the oxidation number of phenol red changes by 1 or 2, we would expect that only 1.1–2.2% of the irreversible faradaic reactions involve phenol red. There are several options for the electrochemical modifications underlying phenol red decolorization. Phenol red may undergo irreversible oxidation and reduction processes with complicated conformation and energy dependencies [25]. Oxidation will induce electropolymerization of phenol red, thereby forming a poly(phenol red) modification of the electrode surface [26]. Reduction may occur at a redox potential of -0.9 V by a one-electron transfer generating a radical intermediate [27].

This potential is close to the “water window” of aqueous electrolytes beyond which H_2O hydrolysis (anodic generation of $\text{O}_2 + 4\text{H}^+$, cathodic generation of $\text{H}_2 + 2\text{OH}^-$)

will occur [28]. However, graphite as an electrode material permits a greater range of electrocatalytic potentials since it demands high overpotentials of -0.47 V and $+0.5$ V for H_2O hydrolysis [29]. Therefore, phenol red oxidation is unlikely to compete with H_2O hydrolysis, but with reactions of lower redox potentials. A dominant cathodic reaction is the reduction of dissolved oxygen ($\text{O}_2 + 4\text{H}^+ + 4\text{e}^- \rightarrow 2\text{H}_2\text{O}$) which starts at $+0.2$ V electrode potential, and may include the formation of hydrogen peroxide ($\text{O}_2 + 2\text{H}^+ + 2\text{e}^- \rightarrow \text{H}_2\text{O}_2$). Anodic processes may produce O_2 from H_2O , but at similar potentials, also reduce chlorine ($2\text{Cl}^- \rightarrow \text{Cl}_2 + 2\text{e}^-$) with the formation of hypochlorite as a secondary product ($\text{Cl}_2 + \text{H}_2\text{O} \rightarrow \text{HOCl} + \text{H}^+$) [28]. A further anodic reaction with potential significance involves the electrode material graphite. Carbon may be oxidized by an anodic reaction ($\text{C} + 2\text{H}_2\text{O} \rightarrow \text{CO}_2 + 4\text{H}^+ + 4\text{e}^-$) at a redox potential of $+0.2$ V [30]. The initial reactions of graphite, however, lead to a functionalization of the surface by generating C-OH, C=O, and CO_2H groups, and these will require an overpotential of 0.6 – 1 V until degradation of graphite actually occurs [31,32]. Such reactions have been studied in simplified saline systems, but an application in cell culture will involve salt solutions with a multitude of biological supplements. Many organic substrates like carbohydrates, amino acids, and lipids are easily oxidized, so that these reactions may be predominant, particularly at low anodic potentials [28]. Due to the highly reversible nature of stimulation, the total of all irreversible reactions at balanced conditions might generate redox equivalents of 50 μM concentration per day. This may be of little significance for highly abundant medium constituents, such as glucose; however, trace amounts of vitamins, hormones and peptides may be heavily affected.

The antioxidant capacities of biological tissues and media may also explain why detrimental effects in cultured tissues occurred only under extensive charge disbalance of stimuli and after prolonged exposure. We did not further investigate the nature of brownish tissue discoloration, because it can be considered as a clearly artefactual phenomenon. The discoloration may reflect the formation of oxidized lipids, carbohydrates and proteins, and if so, it is most likely explained by the accumulation of radicals in the medium, such as peroxides and hypochlorite. In order to attenuate oxidative stress, the addition of antioxidants to the culture medium is frequently recommended. For the cultivation of heart slices, the use of 50 μM mercaptoethanol has been shown to be protective [33,34], but it has been omitted in this study to avoid electrochemical interactions. The biological significance of such interactions is still unclear, and therefore the use of mercaptoethanol should be re-evaluated, whenever novel conditions of electrical stimulation are applied.

4.3. Technical Implementation of Charge Balance

A variety of technical designs were developed for the specific purpose of stimulating individual muscle cells or multicellular muscle tissues [2,5,17,34]. In many cases, stimulation with voltage-controlled impulses has been successfully applied [16,17]. We opted for impulses with defined currents, because of their more direct association with the biological effects of field stimulation, and in favor of the opportunity to control impulse charges. Technically, constant current sources are readily available, and versatile control of impulse timing can be conveniently implemented with a microcontroller. Our study shows that best avoidance of electrochemical reactions requires rigorous charge balance. Unfortunately, an accuracy of pulsed currents within a range of $\pm 0.1\%$ are at the limit of integrated power sources and current sensors, and the specifications of custom-made or commercial stimulators in this regard are scarce. In one reported case of a neuronal stimulator, a 0.13% error of charge delivery was achieved with a specifically designed integrated circuit [35]. In the present study, the integrated amplifier LT1970 (Linear Technology, Analog Devices, Wilmington, MA, USA) was used as an adjustable current source, which is specified to

$\pm 2\%$ accuracy of current regulation. The deviations were stable enough to be compensated manually, but they vary with the amplitude and timing of impulses, so that more general ways of charge balancing were sought.

In theory, suppression of direct current by a capacitor enforces full equivalence of positive and negative charges, with kinetic properties just depending on amplitudes and capacitance. The principle of capacitive coupling has been confirmed in our study, by the prevention of all phenol red degradation raised by disbalanced impulses (Figure 3B,C). In agreement with this observation, manually balanced impulses did not present overt alterations in shape after introduction of the capacitor. Nevertheless, the capacitor did not improve, and in the case of manually balanced impulses it even impaired, the biological compatibility with cultivated tissues (Figure 7B). The reasons for this discrepancy may be found in the non-ideal properties of real ceramic capacitors, which comprise current leakage, dielectric absorption, DC bias and serial impedance [36]. A detailed assessment of each of these peculiarities is beyond the scope of this investigation. In short, the first three of these effects should not be of major importance in our setting since they would not impact the qualities of primarily balanced impulses. A capacitor's serial impedance includes a parasitic inductance which might generate voltage spikes in response to rapid changes of current. A quantitative estimation suggests that typical values of 1 nH and 50 mA/ μ s would provoke an inductive voltage of 50 μ V for 1 μ s duration, which is negligible in comparison to the 5 V for 3 ms duration of a typical stimulation impulse [5]. Another peculiarity related to the working principle of the capacitor is the fact that it may constitute a voltage source during the intervals between the stimulation impulses. This should not be of any consequence, provided that the stimulation circuit is fully disconnected during the intervals. Electronic switches, however, are prone to leakage currents in the range of nA, which would be driven by the charge of the capacitor throughout the pulse intervals. Such weak currents may be ineffective for the reduction in phenol red, but might affect sensitive medium constituents, e.g., ascorbic acid. This selectivity would explain the discrepancy between phenol red degradation and tissue performance which arises in the case of capacitive coupling only (Figures 5B and 7B). A hypothetical baseline current would also be unidirectional and, as such, might provoke phenomena of bioelectricity. These comprise effects on cellular differentiation, proliferation, and migration, which may be provoked by very weak electrical fields [37,38]. Whether such phenomena might be relevant for the development of myocardial contractility in tissue culture needs to be determined in future studies.

Because of the ambiguities of capacitive electrode coupling, we tried to achieve charge balance by a feedback regulation using the electrode pre-pulse voltage as the regulation target. The approach relies on the strict relationship between impulse disbalance and pre-pulse potential (Figure 4C), and is able to maintain both phenol red and tissue performance as effectively as the manual adjustment of impulse charges (Figures 2C, 5B and 7B). Active charge balancing also provides the opportunity to compensate the irreversible loss of charges to different degrees. Appropriate adjustment, however, requires consideration of the nature and ideal magnitude of the pre-pulse voltage, which represents the added potentials of both electrodes (Figure 2A). Since the faradaic impedance is a function of polarity and potential, the latter may not be identical for the two electrodes. In the case of full charge balance, it can be stated that each impulse will place a charge excess with the polarity of the discharging current on each electrode, which will be compensated by irreversible currents during the pulse intervals. Consequently, each electrode retains an individual charge which will attenuate the electrochemical potential of the next stimulation impulse, since this will be of opposite polarity. This situation may be ideal for the prevention of reactions with high redox potentials and low diffusion limits, as presumably applies to

phenol red, but it may do so at the expense of slow reactions with low redox potentials, because the sum of irreversible reactions of both electrodes will be reproduced during the intervals between the impulses. This might predominantly affect the stability of chemically susceptible substances in low abundance. In contrast, impulse adjustment to 0 mV pre-pulse potential will distribute only the difference in irreversibly lost impulse charges to both electrodes, so that their potentials during the inter-impulse phase are minimized. This situation seems favorable for the preservation of the sensitive ingredients in the culture medium. However, the differences between full and partial charge balance are small, and continuous stimulation of myocardial slices for 10 days with either condition did not reveal any superiority (Figure 7B).

4.4. Optimization of Impulse Shapes and Currents

Another attempt to improve the compatibility of electrical stimulation was made by modification to the impulse waveforms. The tested configurations were based on the considerations that the second phase of the biphasic impulse may attenuate the efficacy of stimulation [19], or the pause between charge and discharge may unnecessarily enhance the faradaic activity of the stimulatory phase. Neither of these hypotheses could be confirmed. The effectiveness of biological stimulation was not modified by the magnitude, current, or delay in discharge (Figure 6A). Shortening impulse durations may even enhance phenol red degradation, when the associated reduction in biological efficacy was accounted for (Figure 6B). These observations reflect the kinetics of myocardial depolarization and the exponential increase in faradaic reactions at higher electrode potentials, and indicate that bioelectrical characteristics provide no options for further improvement in the standard impulse configuration (biphasic symmetric, 2–3 ms each phase with 1 ms interval).

5. Conclusions

This study demonstrates that charge control is an effective measure to improve the electrochemical compatibility of biphasic electrical impulses. While its advantages have been demonstrated for the culture of adult myocardial slices, they may also apply to the chronic treatment of excitable cells (neurons, skeletal muscle cells), and to the manipulation of potential-dependent cellular functions (smooth muscle, sensory or secretory cells) in general. The observed negative impact of capacitive electrode coupling requires further investigation, since this mode is commonly used for charge balancing in medical cardiac pacemakers. For the purpose of field stimulation, the regulation of pre-pulse potential is a suitable, and probably a preferable, way to achieve charge balance. The technique is easily implemented, and avoids the technical challenge of precise current control. Assessment of electrode voltages and currents may also yield information about the redox capacities of the culture medium, thus enabling the improved control of cell metabolism and culture conditions. Technical implementations and protocols for such analyses need to be validated in future studies.

Supplementary Materials: The data supporting our results can be downloaded at: <https://www.mdpi.com/article/10.3390/bioengineering12030234/s1>, Supplementary data.

Author Contributions: Conceptualization, Z.S., A.D. and P.K.; methodology, P.K.; software, T.S.; validation, P.K. and A.D.; investigation, Z.S., P.S., J.H. and P.K. writing—original draft preparation, Z.S., T.S., A.D. and P.K.; writing—review and editing, P.S., J.H., T.S., A.D. and P.K.; All authors have read and agreed to the published version of the manuscript.

Funding: This research received no external funding.

Institutional Review Board Statement: Ethical review and approval were waived for this study, because pig hearts were obtained from terminations of independent experiments, each of which having been reviewed and approved individually.

Informed Consent Statement: Not applicable.

Data Availability Statement: The original contributions presented in this study are included in the Supplementary Materials. Further inquiries can be directed to the corresponding author.

Acknowledgments: The authors express their gratitude to Wilhelm Klein (CGC Klein Carbon Graphite Consulting, Siegen, Germany) for valuable advice regarding the selection and processing of carbon electrode materials.

Conflicts of Interest: A.D. and T.S. are founders and shareholders of InVitroSys GmbH. Other authors declare no competing interests.

References

- Berger, H.J.; Prasad, S.K.; Davidoff, A.J.; Pimental, D.; Ellingsen, O.; Marsh, J.D.; Smith, T.W.; Kelly, R.A. Continual Electric Field Stimulation Preserves Contractile Function of Adult Ventricular Myocytes in Primary Culture. *Am. J. Physiol.* **1994**, *266*, H341–H349. [CrossRef] [PubMed]
- Meng, S.; Rouabhia, M.; Zhang, Z. Electrical Stimulation and Cellular Behaviors in Electric Field in Biomedical Research. *Materials* **2021**, *15*, 165. [CrossRef]
- Guette-Marquet, S.; Roques, C.; Bergel, A. Theoretical Analysis of the Electrochemical Systems Used for the Application of Direct Current/Voltage Stimuli on Cell Cultures. *Bioelectrochemistry* **2021**, *139*, 107737. [CrossRef] [PubMed]
- Cogan, S.F. Neural Stimulation and Recording Electrodes. *Annu. Rev. Biomed. Eng.* **2008**, *10*, 275–309. [CrossRef] [PubMed]
- Fischer, C.; Milting, H.; Fein, E.; Reiser, E.; Lu, K.; Seidel, T.; Schinner, C.; Schwarzmayr, T.; Schramm, R.; Tomasi, R.; et al. Long-Term Functional and Structural Preservation of Precision-Cut Human Myocardium under Continuous Electromechanical Stimulation in Vitro. *Nat. Commun.* **2019**, *10*, 117. [CrossRef] [PubMed]
- Poch, C.M.; Dendorfer, A.; Laugwitz, K.-L.; Moretti, A. Ex Vivo Culture and Contractile Force Measurements of Non-Human Primate Heart Slices. *Bio Protoc.* **2023**, *13*, e4750. [CrossRef]
- Weinberg, N.L.; Weinberg, H.R. Electrochemical Oxidation of Organic Compounds. *Chem. Rev.* **1968**, *68*, 449–523. [CrossRef]
- Afify, A.A.; Hassan, G.K.; Al-Hazmi, H.E.; Kamal, R.M.; Mohamed, R.M.; Drewnowski, J.; Majtacz, J.; Małkinia, J.; El-Gawad, H.A. Electrochemical Production of Sodium Hypochlorite from Salty Wastewater Using a Flow-by Porous Graphite Electrode. *Energies* **2023**, *16*, 4754. [CrossRef]
- Verzola, M.A.; Oliveira, K.S.G.C.; Ruotolo, L.A.M. Optimization of Electrochemical Degradation of Organics Considering the Simultaneous Effects of Electroactive Area and Mass Transfer on Current Modulation. *J. Environ. Chem. Eng.* **2022**, *10*, 107395. [CrossRef]
- Persat, A.; Suss, M.E.; Santiago, J.G. Basic Principles of Electrolyte Chemistry for Microfluidic Electrokinetics. Part II: Coupling between Ion Mobility, Electrolysis, and Acid-Base Equilibria. *Lab Chip* **2009**, *9*, 2454–2469. [CrossRef] [PubMed]
- Hassel, A.W.; Fushimi, K.; Seo, M. An Agar-Based Silver | silver Chloride Reference Electrode for Use in Micro-Electrochemistry. *Electrochem. Commun.* **1999**, *1*, 180–183. [CrossRef]
- Merrill, D.R.; Bikson, M.; Jefferys, J.G.R. Electrical Stimulation of Excitable Tissue: Design of Efficacious and Safe Protocols. *J. Neurosci. Methods* **2005**, *141*, 171–198. [CrossRef]
- Chiu, L.L.Y.; Iyer, R.K.; King, J.-P.; Radisic, M. Biphasic Electrical Field Stimulation Aids in Tissue Engineering of Multicell-Type Cardiac Organoids. *Tissue Eng. Part A* **2011**, *17*, 1465–1477. [CrossRef] [PubMed]
- Pietronave, S.; Zamperone, A.; Oltolina, F.; Colangelo, D.; Follenzi, A.; Novelli, E.; Diena, M.; Pavesi, A.; Consolo, F.; Fiore, G.B.; et al. Monophasic and Biphasic Electrical Stimulation Induces a Precardiac Differentiation in Progenitor Cells Isolated from Human Heart. *Stem Cells Dev.* **2014**, *23*, 888–898. [CrossRef] [PubMed]
- Gabetti, S.; Sileo, A.; Montrone, F.; Putame, G.; Audenino, A.L.; Marsano, A.; Massai, D. Versatile Electrical Stimulator for Cardiac Tissue Engineering—Investigation of Charge-Balanced Monophasic and Biphasic Electrical Stimulations. *Front. Bioeng. Biotechnol.* **2023**, *10*, 1031183. [CrossRef]
- Hirt, M.N.; Boeddinghaus, J.; Mitchell, A.; Schaaf, S.; Börnchen, C.; Müller, C.; Schulz, H.; Hubner, N.; Stenzig, J.; Stoehr, A.; et al. Functional Improvement and Maturation of Rat and Human Engineered Heart Tissue by Chronic Electrical Stimulation. *J. Mol. Cell. Cardiol.* **2014**, *74*, 151–161. [CrossRef] [PubMed]
- Tandon, N.; Marsano, A.; Maidhof, R.; Wan, L.; Park, H.; Vunjak-Novakovic, G. Optimization of Electrical Stimulation Parameters for Cardiac Tissue Engineering. *J. Tissue Eng. Regen. Med.* **2011**, *5*, e115–e125. [CrossRef]

18. Bassani, R.A.; Lima, K.A.; Gomes, P.A.P.; Oliveira, P.X.; Bassani, J.W.M. Combining Stimulus Direction and Waveform for Optimization of Threshold Stimulation of Isolated Ventricular Myocytes. *Physiol. Meas.* **2006**, *27*, 851–863. [CrossRef] [PubMed]
19. Plonsey, R.; Barr, R.C. *Bioelectricity: A Quantitative Approach*, 3rd ed.; 2007 Edition; Springer: Boston, MA, USA, 2007; ISBN 978-0-387-48864-6.
20. Rasouli, Z.; Abdollahi, H.; Maeder, M. Generalized Indicator-Based Determination of Solution pH. *Anal. Chim. Acta* **2020**, *1109*, 90–97. [CrossRef]
21. Sanromán, M.A.; Pazos, M.; Ricart, M.T.; Comeselle, C. Electrochemical Decolourisation of Structurally Different Dyes. *Chemosphere* **2004**, *57*, 233–239. [CrossRef]
22. Ismaili, D.; Schulz, C.; Horváth, A.; Koivumäki, J.T.; Mika, D.; Hansen, A.; Eschenhagen, T.; Christ, T. Human Induced Pluripotent Stem Cell-Derived Cardiomyocytes as an Electrophysiological Model: Opportunities and Challenges—The Hamburg Perspective. *Front. Physiol.* **2023**, *14*, 1132165. [CrossRef] [PubMed]
23. Tandon, N.; Cannizzaro, C.; Chao, P.-H.G.; Maidhof, R.; Marsano, A.; Au, H.T.H.; Radisic, M.; Vunjak-Novakovic, G. Electrical Stimulation Systems for Cardiac Tissue Engineering. *Nat. Protoc.* **2009**, *4*, 155–173. [CrossRef]
24. Spallacci, C.; Görlin, M.; Kumar, A.; D'Amario, L.; Cheah, M.H. Fabricating High-Purity Graphite Disk Electrodes as a Cost-Effective Alternative in Fundamental Electrochemistry Research. *Sci. Rep.* **2024**, *14*, 4258. [CrossRef]
25. Mchedlov-Petrosyan, N.O.; Kukhtik, V.I.; Bezugliy, V.D. Dissociation, Tautomerism and Electroreduction of Xanthene and Sulfonephthalein Dyes in N,N-Dimethylformamide and Other Solvents. *J. Phys. Org. Chem.* **2003**, *16*, 380–397. [CrossRef]
26. Hsieh, M.-T.; Whang, T.-J. Mechanistic Investigation on the Electropolymerization of Phenol Red by Cyclic Voltammetry and the Catalytic Reactions toward Acetaminophen and Dopamine Using Poly(Phenol Red)-Modified GCE. *J. Electroanal. Chem.* **2017**, *795*, 130–140. [CrossRef]
27. Senne, J.K.; Marple, L.W. Electrochemical Reduction of Phenol Red. *Anal. Chem.* **1970**, *42*, 1147–1150. [CrossRef]
28. Ehlich, J.; Vašíček, Č.; Dobeš, J.; Ruggiero, A.; Vejvodová, M.; Głowacki, E.D. Shattering the Water Window: Comprehensive Mapping of Faradaic Reactions on Bioelectronics Electrodes. *ACS Appl. Mater. Interfaces* **2024**, *16*, 53567–53576. [CrossRef] [PubMed]
29. Heard, D.M.; Lennox, A.J.J. Electrode Materials in Modern Organic Electrochemistry. *Angew. Chem. Int. Ed.* **2020**, *59*, 18866–18884. [CrossRef]
30. Wei, L.; Chen, Y. Degradation of Carbon Materials in Electrocatalysis. *Curr. Opin. Electrochem.* **2022**, *36*, 101159. [CrossRef]
31. Rueffer, M.; Bejan, D.; Bunce, N.J. Graphite: An Active or an Inactive Anode? *Electrochim. Acta* **2011**, *56*, 2246–2253. [CrossRef]
32. Yi, Y.; Weinberg, G.; Prenzel, M.; Greiner, M.; Heumann, S.; Becker, S.; Schlögl, R. Electrochemical Corrosion of a Glassy Carbon Electrode. *Catal. Today* **2017**, *295*, 32–40. [CrossRef]
33. Brandenburger, M.; Wenzel, J.; Bogdan, R.; Richardt, D.; Nguemo, F.; Reppel, M.; Hescheler, J.; Terlau, H.; Dendorfer, A. Organotypic Slice Culture from Human Adult Ventricular Myocardium. *Cardiovasc. Res.* **2012**, *93*, 50–59. [CrossRef]
34. Cao-Ehlker, X.; Fischer, C.; Lu, K.; Bruegmann, T.; Sasse, P.; Dendorfer, A.; Tomasi, R. Optimized Conditions for the Long-Term Maintenance of Precision-Cut Murine Myocardium in Biomimetic Tissue Culture. *Bioengineering* **2023**, *10*, 171. [CrossRef]
35. Li, X.; Zhong, S.; Morizio, J. 16-Channel Biphasic Current-Mode Programmable Charge Balanced Neural Stimulation. *BioMed. Eng. OnLine* **2017**, *16*, 104. [CrossRef]
36. Ceramic Capacitor. Wikipedia 2025. Available online: https://en.wikipedia.org/wiki/ceramic_capacitor (accessed on 1 January 2025).
37. Yamashita, M. Weak Electric Fields Serve as Guidance Cues That Direct Retinal Ganglion Cell Axons in Vitro. *Biochem. Biophys. Rep.* **2015**, *4*, 83–88. [CrossRef] [PubMed]
38. McCaig, C.D.; Rajnicek, A.M.; Song, B.; Zhao, M. Controlling Cell Behavior Electrically: Current Views and Future Potential. *Physiol. Rev.* **2005**, *85*, 943–978. [CrossRef] [PubMed]

Disclaimer/Publisher's Note: The statements, opinions and data contained in all publications are solely those of the individual author(s) and contributor(s) and not of MDPI and/or the editor(s). MDPI and/or the editor(s) disclaim responsibility for any injury to people or property resulting from any ideas, methods, instructions or products referred to in the content.

Article

Ultra-Low Intensity Post-Pulse Affects Cellular Responses Caused by Nanosecond Pulsed Electric Fields

Kamal Asadipour ^{1,2}, Carol Zhou ², Vincent Yi ³, Stephen J. Beebe ² and Shu Xiao ^{1,2,*}

¹ Department of Electrical and Computer Engineering, Old Dominion University, Norfolk, VA 23529, USA; kasad001@odu.edu

² Frank Reidy Research Center for Bioelectronics, Old Dominion University, Norfolk, VA 23529, USA; czhou@odu.edu (C.Z.); sbeebe@odu.edu (S.J.B.)

³ Ocean Lakes High School, Virginia Beach, VA 23454, USA; vincentyi98@gmail.com

* Correspondence: sxiao@odu.edu

Abstract: High-intensity nanosecond pulse electric fields (nsPEF) can preferentially induce various effects, most notably regulated cell death and tumor elimination. These effects have almost exclusively been shown to be associated with nsPEF waveforms defined by pulse duration, rise time, amplitude (electric field), and pulse number. Other factors, such as low-intensity post-pulse waveform, have been completely overlooked. In this study, we show that post-pulse waveforms can alter the cell responses produced by the primary pulse waveform and can even elicit unique cellular responses, despite the primary pulse waveform being nearly identical. We employed two commonly used pulse generator designs, namely the Blumlein line (BL) and the pulse forming line (PFL), both featuring nearly identical 100 ns pulse durations, to investigate various cellular effects. Although the primary pulse waveforms were nearly identical in electric field and frequency distribution, the post-pulses differed between the two designs. The BL's post-pulse was relatively long-lasting (~50 μ s) and had an opposite polarity to the main pulse, whereas the PFL's post-pulse was much shorter (~2 μ s) and had the same polarity as the main pulse. Both post-pulse amplitudes were less than 5% of the main pulse, but the different post-pulses caused distinctly different cellular responses. The thresholds for dissipation of the mitochondrial membrane potential, loss of viability, and increase in plasma membrane PI permeability all occurred at lower pulsing numbers for the PFL than the BL, while mitochondrial reactive oxygen species generation occurred at similar pulsing numbers for both pulser designs. The PFL decreased spare respiratory capacity (SRC), whereas the BL increased SRC. Only the PFL caused a biphasic effect on trans-plasma membrane electron transport (tPMET). These studies demonstrate, for the first time, that conditions resulting from low post-pulse intensity charging have a significant impact on cell responses and should be considered when comparing the results from similar pulse waveforms.

Keywords: nanosecond pulse; post-pulse; charging current; intracellular effects; spare respiratory capacity

1. Introduction

In recent years, there have been significant advancements in the field of bioelectronics, specifically in the study of nanosecond pulsed power technology and its effects on cellular responses [1–3]. Intense nanosecond pulses have been shown to induce diverse biological responses, such as membrane permeabilization [4], DNA damage, and activation of signaling pathways [5,6]. Nanosecond pulsed electric fields (nsPEFs) have emerged as a promising tool for various biomedical applications such as tissue treatment [7,8], atrium ablation for heart defibrillation [9,10], and immune response expression for cancer treatment [11–14].

Nevertheless, different research groups have used custom-designed and custom-manufactured pulse generators, resulting in varying pulse conditions [15–26]. This may

present a perplexing and challenging situation when comparing and interpreting results. Results of experiments involving intense nanosecond pulses typically report the electric field, pulse duration, and pulse number, but nuances in pulse waveforms such as rise time, pulse plateau, and fall time also exist [27,28]. Even the pulse plateau is not perfectly flat and can rise or fall to a certain degree between the rise time and fall time. However, these waveform characteristics are often not well-characterized and not reported. The pulse rise time and fall time, for example, has been shown to affect mitochondrial membrane potential and cell viability under the assumption that a pulse rising faster can reach the cell interior more effectively bypassing the capacitive barrier of a cell membrane compared to a pulse rising slower [27]. The phenomenon of nanosecond bipolar cancellation (NBC) occurs when an additional pulse of opposite polarity is applied, resulting in weaker responses than the unipolar pulse condition where no such cancellation occurs [29–31]. This difference in results can be explained by the disruption of cell membrane charging by the opposite current before any harm to the cell is done. However, this is only one possible hypothesis, and other mechanisms may also be valid. Although standardizing pulse parameters is difficult, it is becoming evident that the pulse waveform details should be considered when interpreting results that are generated in close conditions.

As such, there is also a possibility that the charging current of a pulse generator (in the form of a post-pulse) could affect biological responses, but it is often overlooked after the main pulse due to its low intensity. The post-pulse can have a magnitude no more than 10% of the main pulse and often does not show up on the oscilloscope because of the small scale, while the biological response is solely attributed to the main pulse.

Our study, for the first time, investigated the effect of these post-pulses on biological responses elicited by nanosecond pulses. We used two pulse generators based on transmission lines, namely a pulse forming line (PFL) and a Blumlein line (BL), to demonstrate the different post-pulse characteristics while maintaining nearly identical main pulse features. It is worth noting that PFL and BL remain robust pulsers for in-vitro applications that require high current, low impedance, and short pulse duration (≤ 100 ns), despite the growing utilization of solid-state pulse generators [32].

Understanding the interplay between nsPEFs and ultra-low intensity post-pulses is crucial for advancing the applications of pulse power technologies in diverse fields. These findings may have implications for improving therapeutic strategies such as atrium ablation for heart defibrillation and enhancing immune response expression for cancer treatment. Moreover, unraveling the underlying mechanisms can provide valuable insights into the fundamental principles governing cellular responses to pulsed electric fields. Our study highlights the importance of characterizing and reporting pulse waveforms to enhance the reproducibility and comparability of results across different research groups using different pulse generators.

2. Results

2.1. BL Had a Low-Intensity Post-Pulse Opposite to the Main Pulse, Contrary to PFL, despite Having the Same Main Pulse

The 100 ns pulses generated by PFL and BL are shown in Figure 1. These waveforms were obtained for the cuvettes with a resistance of approximately 10Ω , which was needed to match PFL and BL. Five voltages (1.5, 2, 3, 4, and 5 kV) and ten waveforms are shown, with each representing the average waveform over 30 pulses with standard errors ± 0.5 kV. For a given voltage, the rise time for PFL was slightly faster than BL, and the pulse duration for BL was slightly longer than that of PFL (< 10 ns, measured at the full width at half maximum). The peak voltages of BL were slightly larger than those of PFL (< 0.5 kV). The charges flowing through the load were calculated as the time integral of the voltage divided by the resistance, $\int \frac{V}{R} dt$, where $R = 10 \Omega$ (Figure 1c). The charge for BL was always slightly higher if not equal to that of PFL. Also shown in Figure 1d is the energy calculated by the integral of the power, $\int \frac{V^2}{R} dt$. As the voltage increased, the difference in energy deposited

in the load resistance between PFL and BL became larger. However, the energy for BL was always larger than that of PFL.

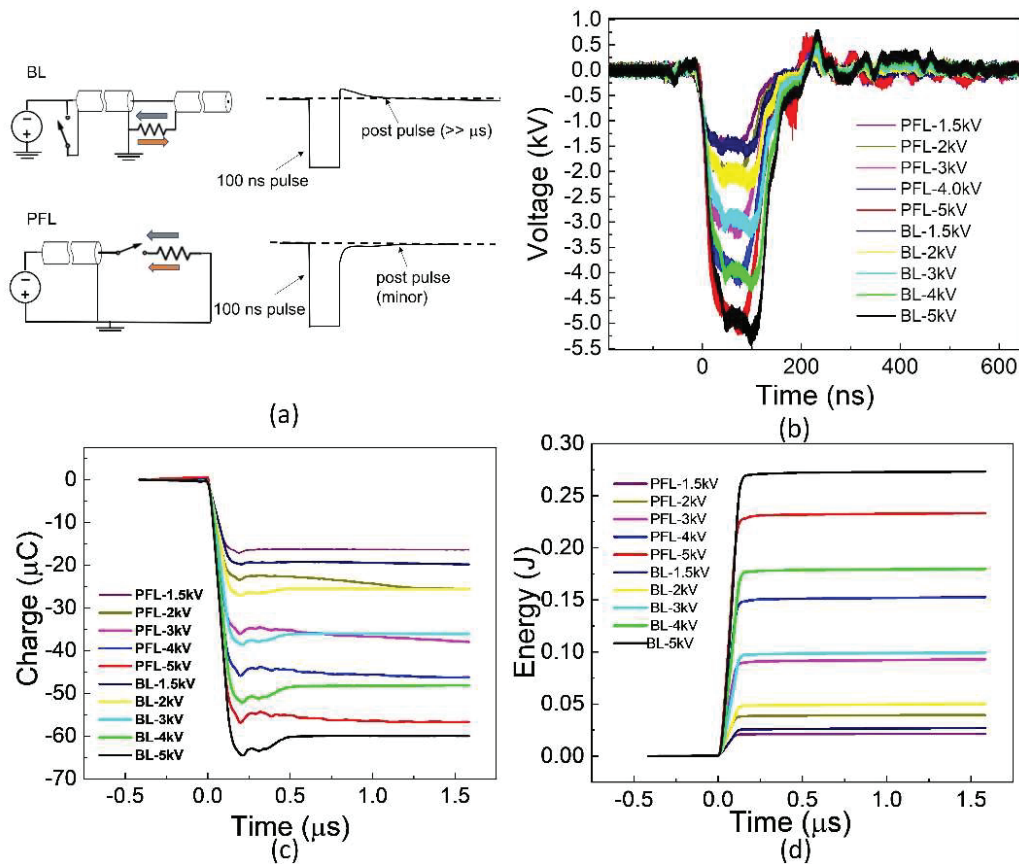


Figure 1. The waveforms were generated using two pulse generators: the Blumlein line (BL) and the pulse forming line (PFL). (a): The BL exhibits an opposite polarity post-pulse compared to the main pulse, whereas the PFL has a post-pulse with the same polarity. In the figure, the BL pulse is intentionally inverted to match the text, although it should be positive due to the negative charging power supply concerning the ground. The grey arrow: is pulse current; The orange arrow: post pulse current. (b): The waveforms display a voltage increase from -1.5 kV to -5 kV. Each waveform represents the average of 30 consecutive waveforms. (c): The charges delivered to the load are calculated by integrating the current over time. In this case, the load was a cuvette. (d): The energy deposited into the load.

To examine the difference in the spectrum of the PFL and BL pulses, Fourier transform (FT) was performed on the 4 kV data (both PFL and BL) over three time-intervals: the prepulse (-450 ns to -100 ns), the main pulse (-100 ns to 500 ns), and the post-pulse (500 ns to 1600 ns) (Figure 2a–d). In the prepulse interval, no signal was observed (Figure 2b). In the main pulse interval, the BL spectrum almost overlapped with that of the PFL, although it appeared slightly higher in the near DC frequency (Figure 2c). In the post-pulse interval, the PFL spectrum appeared higher than the BL one near the low frequencies (up to 2.5×10^7 Hz). Furthermore, the post-pulse difference between the PFL and BL waveforms for all voltages can be observed in Figure 3, obtained using STFT (short-time Fourier Transform). The PFL post-pulses consistently exhibited a more extended signal spread than the BL pulses, despite mostly being low intensity.

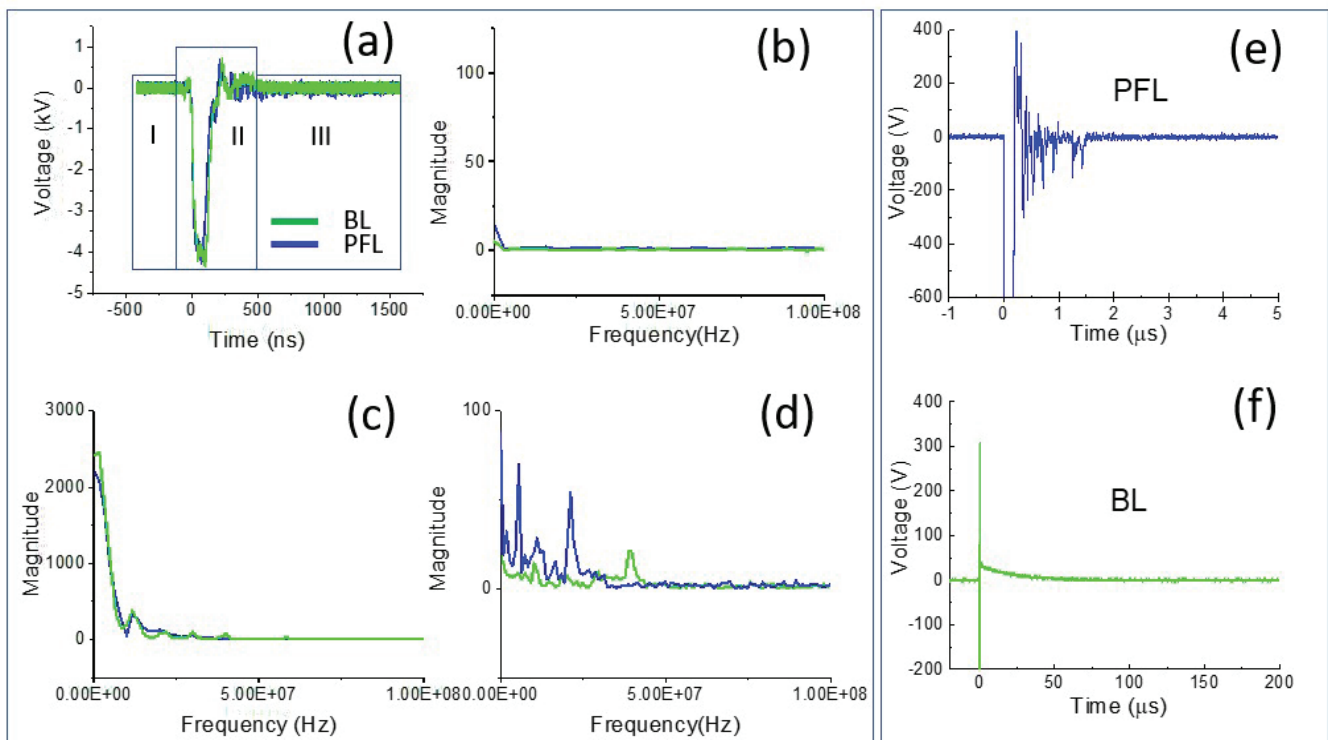


Figure 2. The pulse waveforms were analyzed in both the time and frequency domains. (a) The intervals of interest in the waveform, including the prepulse (−450 ns to −100 ns), main pulse (−100 ns to 500 ns), and post-pulse (500 ns to 1600 ns); the spectrum of the pulses was calculated for each interval using FFT: (b) the prepulse; (c) the main pulse; and (d) the post-pulse; (e,f) zoomed-in views of the post-pulses for both PFL and BL on a smaller voltage and longer time scale.

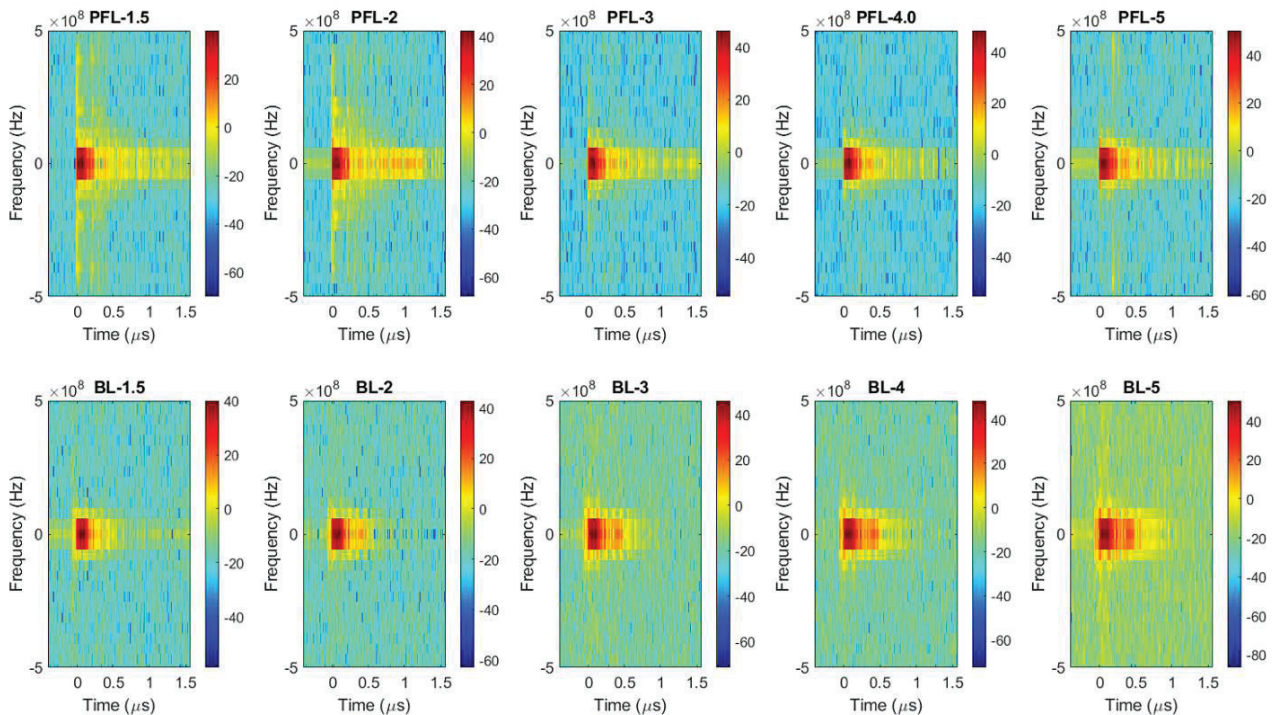


Figure 3. The spectrums of the pulses over time were calculated for the PFL and BL waveforms using STFT performed on the data shown in Figure 1b. **Top** row: the PFL voltages (−1.5 kV to −5 kV); **bottom** row: the BL voltages (−1.5 kV to −5 kV). The color bars show the magnitude of the spectrum.

Such a large difference led us to re-examine the post-pulse phases in the time domain, but this time at a much smaller voltage scale and longer time. Figure 2e,f show the post-pulses for both PFL and BL. The main pulses were both -4 kV but were truncated to highlight the difference. In the case of PFL, the post-pulse had the same polarity as the main pulse and lasted for less than $2 \mu\text{s}$. On the other hand, for the BL, the post-pulse was much longer ($50 \mu\text{s}$) but had the opposite polarity to the main pulse. It is worth noting that both BL and PFL's post-pulses consisted of two components: the charging voltage and a mismatched component resulting from the slight impedance mismatching between the transmission line and the cuvette. In terms of duration by excluding the mismatched component, the charging pulses extended much longer, although their magnitudes were small and decaying: the PFL's post-pulse was (5%) of the main pulse, whereas the BL's was (1–2%) of the main pulse.

2.2. PFL Pulses Extended the Duration of OMP and Posed Less Change on IMP than BL Pulses

Using a linear cell model consisting of resistances and capacitances representing the cell structure [33], potential drops across the outer membrane (OMP) and intracellular organelle membrane (IMP) were calculated for three scenarios: the clean pulse, the PFL pulse, and the BL pulse. During the 100 ns main pulse, there was no discernible change in the OMP among all pulse conditions. Moreover, the pulses in all cases resulted in approximately a threefold increase in the IMP compared to the OMP, indicating that nanosecond pulses generally bypass the outer membrane and penetrate to the cytoplasm for intracellular manipulation (Figure 4). After the main pulse (>100 ns), the IMPs reversed their polarity and swung in the opposite direction, with the magnitude being 13.3% of that during the main pulse for the CP and BL pulses. Conversely, the PFL post-pulse caused a smaller change in the IMP, reducing it to only 8% of its value during the main pulse. Additionally, the PL post-pulse sustained the OMP longer than the CP and BL pulses. The BL pulse dissipated the OMP rather rapidly ($<4 \mu\text{s}$) and led to a reversed OMP.

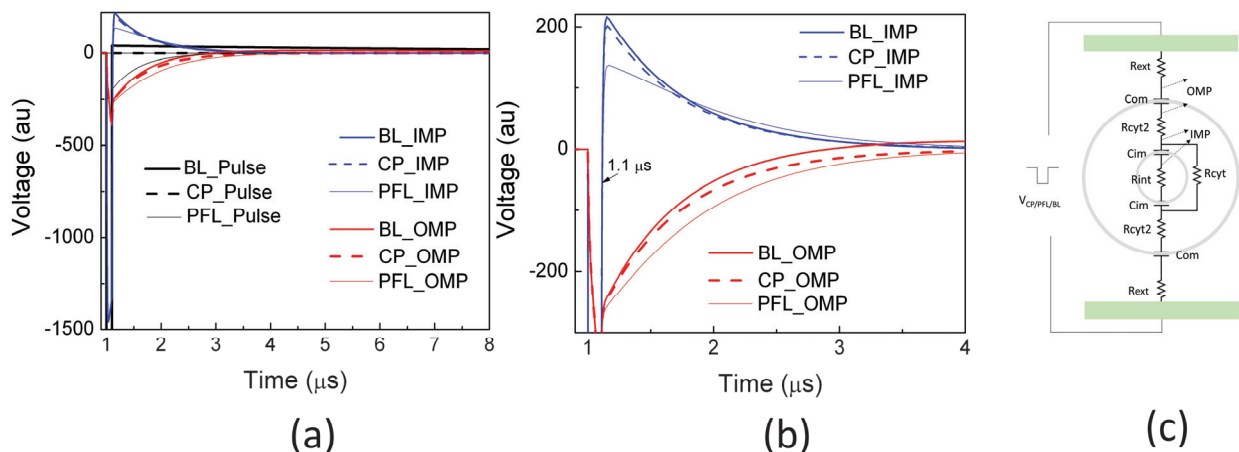


Figure 4. The potential drops were simulated using a linear equivalent cell model by applying a clean pulse (CP), a PFL pulse, and a BL pulse at $1 \mu\text{s}$. The potential between the outer membrane (OMP) and the potential between an intracellular organelle (e.g., mitochondrion) (IMP) are shown in (a) on a larger scale (both in voltage and time) and (b) on a smaller scale. (c) The equivalent cell model in Pspice (Version 9.1) along with the parameters ($R_{ext}= 1 \text{ k}\Omega$, $C_{om} = 100 \text{ pF}$, $R_{cyl2} = 100 \Omega$, $C_{im} = 10 \text{ pF}$, $R_{cyl} = 10 \text{ k}\Omega$) [33].

The ability of the BL post-pulse to reverse the OMP is significant due to its much longer duration (>100 ns), despite maintaining a low voltage. Generally, the PFL post-pulse, which shares the same polarity as the main pulse, prolongs the duration of the OMP, while the BL post-pulse shortens and even reverses the OMP. Moreover, the PFL post-pulse induces less change in the IMP compared to the BL post-pulse. These observations suggest that the PFL pulse can sustain membrane potential changes in both IMP and OMP for a

longer duration compared to the BL pulse, indicating its potential for greater effectiveness in inducing cellular responses. However, it should be noted that this model has limitations, as it assumes intact cell membranes and constant resistances without considering factors such as electroporation, cell shapes, orientations, etc. It thus provides a qualitative analysis that predicts the general trend of the potential changes resulting from electric pulses but does not reflect the absolute membrane potential changes.

2.3. Effects of PFL and BL Pulsers on Cellular Plasma Membrane Responses

Plasma membranes (PMs) are best known as physical barriers that define the cell and maintain ion transport across the membrane as a means of excitability and homeostatic maintenance. The PM also exhibits an electron transport (ET) mechanism carried out by plasma membrane redox systems (PMRSs). These ET systems transfer electrons from either intra- or extracellular donors to extracellular acceptors [34,35]. They regulate cellular redox homeostasis by maintaining the NAD(P)⁺/NAD(P)H ratios and attenuate oxidative stress acting as a compensatory mechanism during the stress, and aging process [36]. Given the known effects of electric fields to electroporate the PM, it was of interest to see if the PFL and BL pulsers had different effects on PM permeabilization as propidium iodide uptake and effects on trans plasma membrane electron transport (tPMET).

Figure 5 shows two distinct responses from the plasma membrane activity of the PMRS regulating tPMET rates and plasma membrane permeability to propidium iodide (PI) in response to the PFL and BL pulsers. The linear tPMET velocity rates were measured in the 10–35 min range, which serves to measure the tPMET activity of the PMRS in B16F10 cells after pulsing with the BL or PFL pulser. The PFL pulser showed biphasic tPMET rates across different ranges of nsPEF pulsing. Under lower pulsing conditions (≤ 5 pulses), nsPEFs increased tPMET rates above the control rates while there was no increase in PI influx. However, under higher pulsing conditions (≥ 10 pulses), tPMET rates decreased below the control rates as there were increases in PI influx coincident with the decrease in tPMET. The maximum dimension of the PI molecule is typically 1.4 nm. Therefore, the absence of PI uptake does not definitively prove that the cell membrane is completely electroporation pore-free, as nsPEFs have been observed to create smaller nanopores that can cause Ca²⁺ influx [37]. In contrast, the BL pulser at low pulsing conditions (≤ 5 pulses) showed the same level of tPMET activity as the control. However, as the pulse number was increased to ≥ 20 , a significant pulse number-dependent reduction in tPMET activity was observed coincident with a pulse number-dependent increase in PI influx. In general, for both the decrease in tPMET and the increase in PI influx, the PFL has a lower threshold or is more sensitive for determining these changes in cell responses. Thus, the PFL pulses can elicit a biphasic response, stimulating tPMET activity with a low number of pulses, but inhibiting it with a high number of pulses. In contrast, the BL pulses did not induce such a biphasic response and only inhibited tPMET.

2.4. PFL Has a Lower IC₅₀ for Cell Death Induction than BL

Figure 6a shows the effects on cell viability 24 h after PFL and BL pulsing (100 ns, 40 kV/cm) with different pulsing numbers. Viability was found to be dependent on the number of pulses, such that the PFL IC₅₀ value was 9 pulses and the BL IC₅₀ value was 14 pulses. For 100 ns and 40 kV/cm, the decrease in cell viability from 95% to 25% occurred between 5 and 15 pulses for the PFL pulser and between 10 and 20 pulses for the BL pulser.

Figure 6b considers the electric field decreases in cell viability with the 100 ns pulses at 10 pulses. For PFL pulses, cell viability began to decrease at a threshold of 30 kV/cm. On the other hand, a significant decrease in viability for BL pulses was observed only when the electric field was raised to 50 kV/cm, with a slight decrease noticeable at 40 kV/cm.

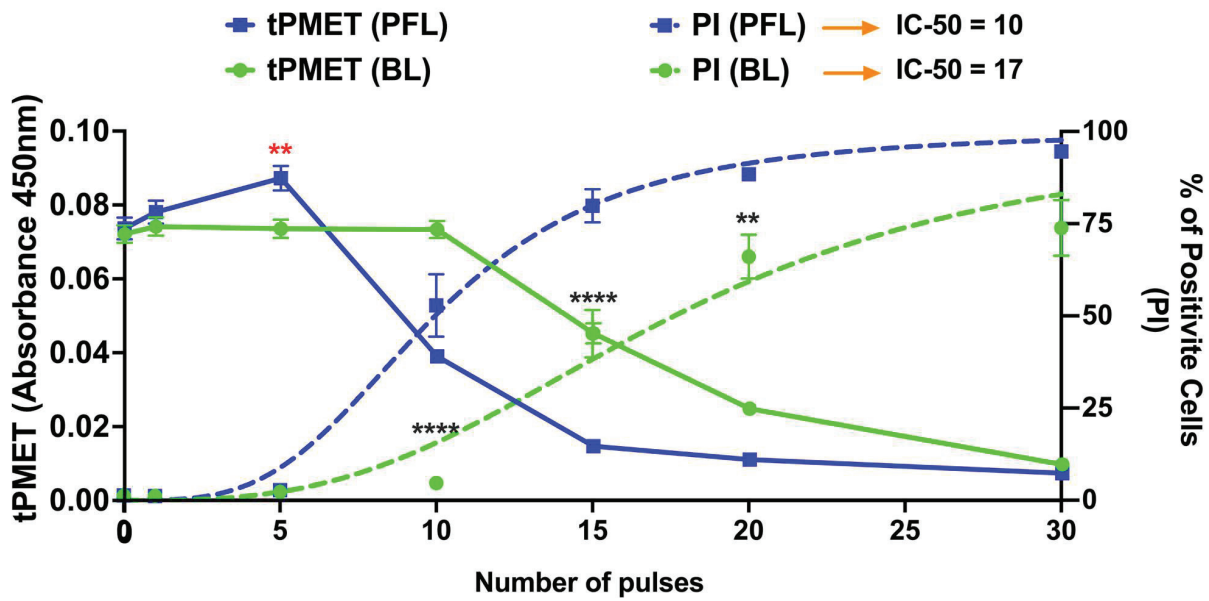


Figure 5. nsPEF effects of BL and PFL pulsers on tPMET and PI uptake. The tPMET rates defined as the rate of increase in WST-8 absorbance per min of reaction (left axis, solid lines), and PI fluorescence (Right axis, dotted lines) were determined by plate reader (10–35 min) and flow cytometry (5 min) respectively in a different assay. B16F10 cells were exposed to different pulsing numbers with BL or PFL (green and blue color code respectively) with a fixed electric field of 40 kV/cm. BL pulser showed the inhibitory effect on tPMET (significant decrease start at 20 pulses compared to control) while the PFL showed the biphasic effect on tPMET with a significant increase at fewer pulsing numbers (5 pulses, showed by red **) and then decrease for high pulsing number (significant decrease at 10 pulses). Significant differences were observed between these two pulsers in regard to an increase in PI uptake (at 10, 15, 20, and 30 Pulses), indicated by the (****). ($n = 3$) ** $p < 0.05$ and **** $p < 0.0001$.

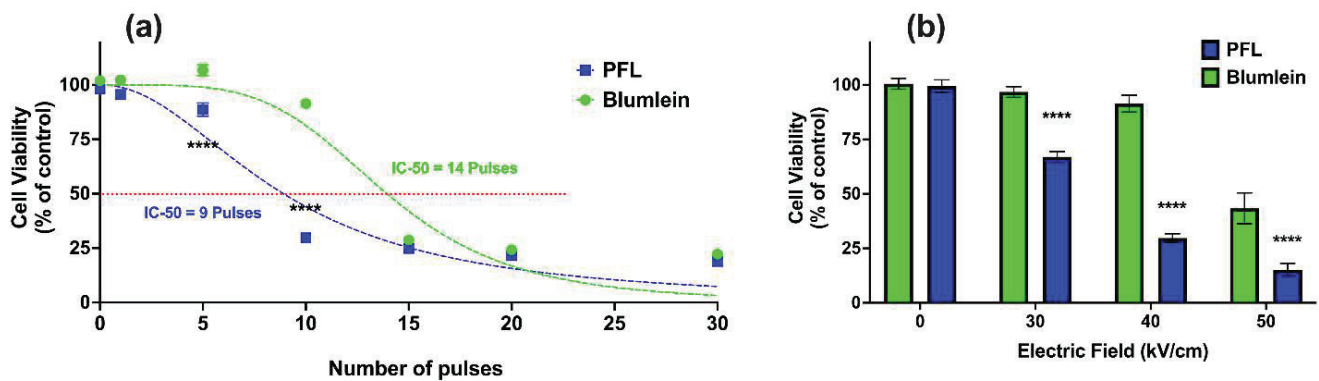


Figure 6. nsPEF effects of BL and PFL pulsers cell viability. Cell viability of B16F10 cells was determined using a plate reader after 24 h for (a) various pulsing numbers with a fixed electric field of 40 kV/cm, or (b) different electric fields (0, 30, 40, and 50 kV/cm) of 10 pulses, with BL (green) or PFL (blue) pulsers. In (a), significant differences were observed between these two pulsers, particularly at 5 and 10 pulses. In (b), the viability did not show a significant decrease compared to the control at 30 and 40 kV/cm with BL pulsing, whereas with PFL pulsing, a significant decrease in viability was observed (**** $p < 0.0001$).

2.5. Differential Loss of $\Delta\Psi_m$ with Increases in mROS Production with the PFL and the BL Pulsers

Figure 7 shows nsPEF-induced mitochondrial ROS (mROS) production determined by MitoSox (solid lines) and change in the $\Delta\Psi_m$ (dotted lines) as pulse numbers are increased at 40 kV/cm. In contrast to the differential loss of $\Delta\Psi_m$ as the PFL (blue lines) and BL pulse (green lines) numbers increased, there was no difference in the production of ROS between

the two pulsers. For the PFL, 75% of cells were mROS positive and only about 25% of cells had a loss in $\Delta\Psi_m$. In contrast, essentially all the cells were mROS positive before there is a significant loss in loss in BL $\Delta\Psi_m$. The losses in $\Delta\Psi_m$ were nearly parallel with 50% of cells showing a loss in $\Delta\Psi_m$ for the PFL and BL at about 12 pulses 20 pulses. Thus, the PFL was more sensitive than BL for loss of $\Delta\Psi_m$ but there were no differences between the two pulsers in pulse number for mROS production. The difference in the response thresholds of $\Delta\Psi_m$ and ROS indicates that the ROS mechanism is not directly linked to the $\Delta\Psi_m$ mechanism. This disparity in response solely attributable to the pulse condition is noteworthy.

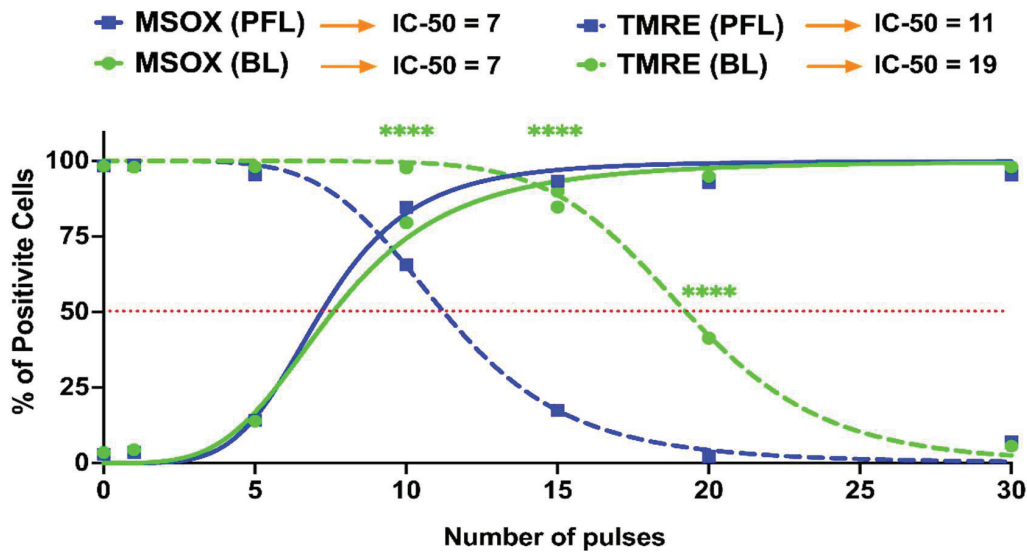


Figure 7. nsPEF effects of BL and PFL pulsers on the reactive oxygen species and mitochondria membrane potential at 20 min after pulsing. B16F10 cells were exposed to different pulsing numbers with BL or PFL (green and blue color code respectively) with a fixed electric field of 40 kV/cm. Dotted lines represent the TMRE and solid lines represent the MSOX. The IC-50 is mentioned at the top. Significant differences were observed between these two pulsers in regard to a decrease in mitochondrial membrane potential (at 10, 15, and 20 pulses), indicated by the (**** with $p < 0.0001$).

2.6. PFL but Not BL Caused a Decrease in Maximal OCR and Spare Respiratory Capacity (SRC)

Figure 8 shows the metabolic effects of PFL and BL nsPEFs on oxygen consumption rate (OCR) using the Seahorse. Cells were treated with nsPEFs and then incubated until they were attached, as required for analyses. A look at responses that were measured after 5 pulses within the first 30 min after pulsing indicates that there was no ROS production or loss of $\Delta\Psi_m$ (Figure 7), no PI uptake or no loss in tPMET (Figure 5), and no loss in viability after 24 h post pulse (Figure 6). However, for the PFL, there was an increase in tPMET. Seahorse results show that there was no significant decrease in basal OCR 15 h after nsPEFs with either pulser. However, after FCCP (uncoupling agent) treatment, the PFL treatment resulted in a significant decrease in maximal OCR and a decrease in spare respiratory capacity (SRC) determined by FCCP OCR minus basal OCR. BL pulses led to a slight but insignificant increase in SRC. The SRC reflects the mitochondria’s ability to fulfill additional energy requirements beyond the basal level in response to acute cellular stress. Thus, PFL pulsers show differences in responses to maximal OCR and SRC that are not present in the BL pulser and not present in basal conditions for either pulser occur 15 h after nsPEF treatment.

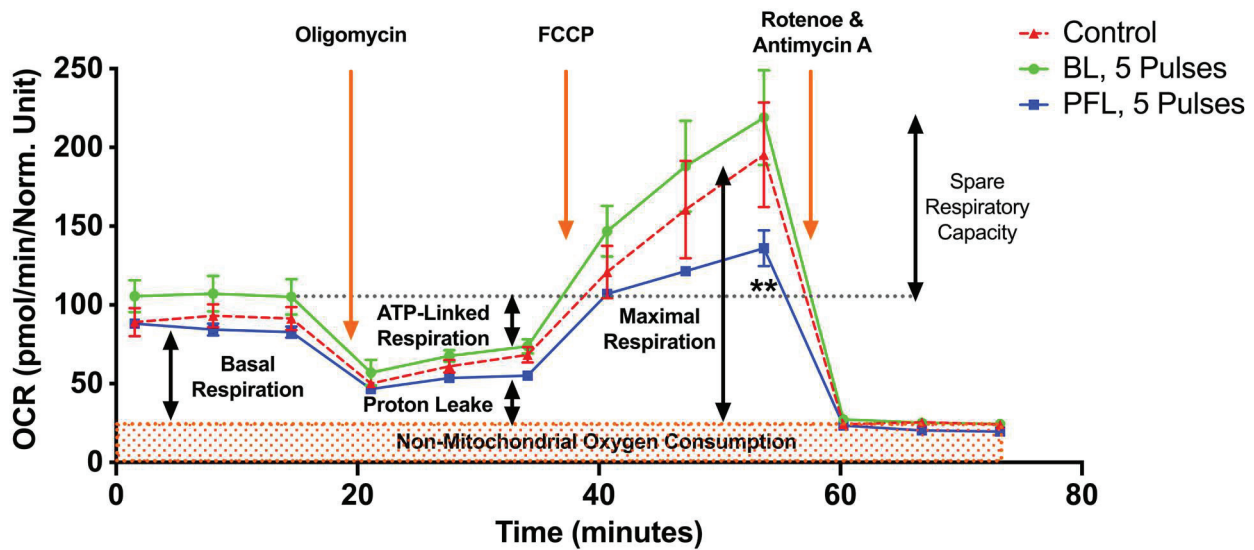


Figure 8. nsPEF effects of BL and PFL pulsers on mitochondrial oxidative metabolism in B16F10 melanoma cell lines. The oxygen consumption rate (OCR) of cells was measured 15 h after pulsing with 5 pulses. The x-axis represents time (up to 75 min), which aligns with the recommended test profile in the Seahorse assay for measuring mitochondrial respiration. The electric field was maintained at 40 kV/cm for both pulsers. The cells were maintained at 37 °C during the 15 h while they adhered. The different states of mitochondrial respiration are indicated: basal respiration (Basal), proton leak (respiration after oligomycin exposure), maximal respiratory capacity (respiration after FCCP, MRC), and non-mitochondrial respiration (after rotenone and antimycin A) (NM). * $p < 0.05$ compared to control. Cells treated with PFL pulses showed a lower SRC compared to the control group (** $p < 0.002$).

3. Discussion

These studies show that nanosecond pulses generated by commonly used pulse generators (PFL and BL) with the same pulse duration and essentially the same electric field and frequency distributions can result in different cell responses owing to distinct post-pulse waveforms determined by their dissimilar circuit topology. These subtle post-pulse waveform differences, which have been overlooked, can have a significant impact on functional outcomes. Specifically, the PFL post-pulse waveform was unipolar, while the BL pulse was bipolar. For instance, at 4 kV, the PFL pulse exhibited a small post-pulse waveform (5% of the main pulse, same polarity) lasting approximately 2 μ s. Conversely, the BL pulse had an even smaller post-pulse waveform (1–2% of the main pulse, opposite polarity) but lasted longer (~50 μ s). These post-pulses were a result of their electrical configurations being unique. In the PFL configuration, the load (cells in cuvette) was isolated from the charging circuit by a switch. After the switch closed, allowing the 100 ns pulse current flow, there was a brief charging current from the high voltage power supply. However, this current stopped quickly as the switch recovered and isolated the load from the charging circuit. The recovery process occurred on a scale of 2 μ s, much shorter than that of a conventional spark gap switch [18]. This could be attributed to the small energy involved (100 mJ) and the short pulse duration (100 ns), whereas a conventional spark gap switch can handle >10 J and conduct for >1 ms. In our case, the discharge mode might involve a streamer-arc channel without significant heating of the ambient air, allowing for a rapid switch recovery. On the other hand, in the BL configuration, the load was continuously connected to the BL and remained in the charging loop regardless of the switch state. A small charging current was present throughout the charging time until the BL was fully charged before the next pulse (Figure 1a).

The distinction in cell responses to PFL pulses and BL pulses, as summarized in Figure 9, can be attributed to the differences in their post-pulse condition. During the

main pulse interval, the frequency contents, charges, and energy of both types of pulses were almost identical, with some cases where the BL pulses exceeded the PFL pulses. However, in the post-pulse interval, compared to the BL post-pulses, the PFL post-pulses demonstrated a longer duration effect on the OMP and had a lesser impact on the IMP established by the main pulse, (Figure 4). Given that the MP created by the main pulse leads to membrane pore formation, Ca⁺⁺ influx, and other effects, it would be expected to elicit a stronger cell response for holding longer. Therefore, it is not surprising that the PFL pulses generally demonstrated greater potency than the BL pulses.

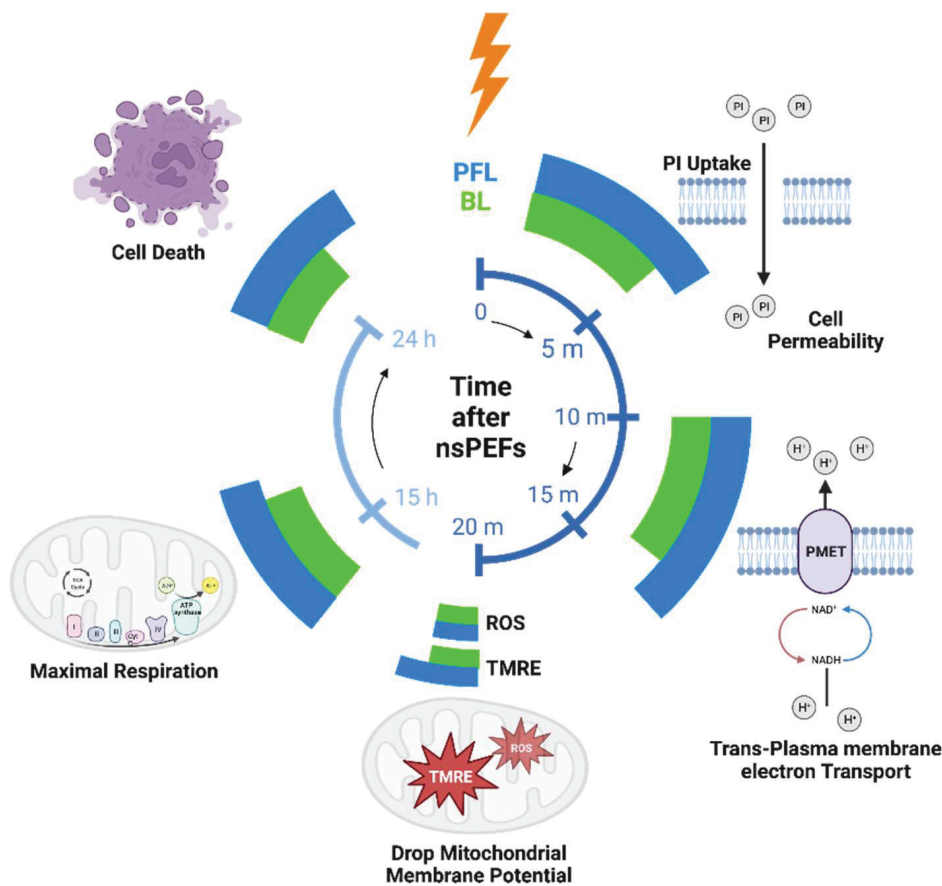


Figure 9. The timeline of the cell responses to PFL and BL pulses at different time intervals: 10–50 min, 15 h, and 24 h after pulsing. The magnitude of cell responses is represented by the extension of azimuthal angles (larger angle meaning larger response). Created with BioRender.com.

The main pulse waveforms of PFL and BL, which are nearly identical in charge and spectrum, can induce similar membrane and intracellular effects. For example, the charging of the cell's outer membrane can lead to an amplified electric field across it, resulting in pore formation and increased membrane permeability. However, the subsequent post-pulse current can modify the membrane potential by neutralizing the charges that have accumulated across the membrane. This effect is particularly pronounced in the case of BL pulses, which have an opposite post-pulse current. The charge of the main pulse was estimated as $-40 \mu\text{C}$ ($-4 \text{ kV} \times 100 \text{ ns}/10 \Omega$), which is close to the measured value of $-50 \mu\text{C}$ presented in Figure 1c. On the other hand, the charge flowing during the post-pulse can be calculated by integrating over the post-pulse waveform to be $75 \mu\text{C}$. This accounts for the same magnitude of the charge of the main pulse charge, which would have reduced the membrane charging established by the main pulse, and it would certainly cause a significant change in both the OMP and the IMP, as indicated in Figure 4. In contrast, in the case of PFL pulses, the post-pulse current does not significantly alter the membrane potentials initiated by the main pulse. However, it is possible that the potential could be

slightly larger due to the same polarity of the post-pulse, which serves to maintain the charging of the membranes.

However, in addition to plasma membrane electroporation as PI influx, nsPEFs also shows a unique electric field modulation of a well-known but seldomly discussed activity of the plasma membrane redox system (PMRS) function of tPMET, which plays a crucial role in safeguarding cells against intracellular oxidative stress, maintains redox balance, and regenerates NAD⁺ for glycolysis [36]. Notably, in contrast to the BL pulser showing only a decrease in nsPEF-induced tPMET, the effect of the PFL induced a biphasic effect with an increase in tPMET at lower electric field conditions before any PI influx appeared and an inhibition of tPMET at higher electric fields where PI influx demonstrated PM EP. So, the presence of PM pores was coincident with the loss of tPMET for both PFL and BL. Although coincidence is not an indication of the cause, it does raise the question of the relationship between nsPEF-induced PM permeabilization (pore formation) and tPMET. Nevertheless, the increase in tPMET appears to be independent of PI permeability. However, it is possible that molecules smaller than PI, such as Ca²⁺ could gain entry at lower nsPEF conditions through pores smaller than PI [27]. Overall, for effects on the PM, the PFL has a greater sensitivity or lower pulse number threshold for all three PM effects on the PI influx, gain and loss of tPMET activity.

Having seen these differences between the PFL and the BL pulsers, it was of interest to see the effects on cell viability. While effects depend on different factors, in all studies of nsPEFs no cell line or tumor type has shown resistances to nsPEF elimination. Two models have shown vaccine effects as vaccinations [13,38,39], meaning that tumor-free animals are resistant to regrowing the treated cancer again. In the viability studies, like that seen for the PM responses, the PFL had a lower IC₅₀ value for viability than the BL pulser, as shown by requiring fewer pulses and requiring a lower electric field. This is interesting because all the nsPEF pulsers in those studies were BL constructions. Although the construction of a PFL for studies is less practical than the BL construction because of half-charging voltage output, it would be interesting to determine if a PFL pulser would require lower electric fields or fewer pulses for tumor elimination and be more effective for inducing immunity and vaccination.

Having shown that nsPEFs cause a dissipation of the mitochondrial membrane potential ($\Delta\Psi_m$) [27], we were curious to determine what caused this loss of $\Delta\Psi_m$. One obvious possibility was that like nsPEF effects on the plasma membrane, they could also permeabilize the inner mitochondrial membrane (IMM). However, another way that the nsPEFs could cause a loss of the $\Delta\Psi_m$, is through opening the mitochondrial permeability transition pore (mPTP). When we saw that the nsPEF-induced loss of $\Delta\Psi_m$ was enhanced by Ca²⁺ [27], we considered that membrane permeabilization does not require Ca²⁺ and further that Ca²⁺ effects are essentially always mediated through a protein. Therefore, we hypothesized that nsPEF-induced loss of $\Delta\Psi_m$ was not due to permeabilization of the IMM but more likely due to opening the mPTP, a hypothesis yet to be proved. Although the identity of the mPTP has been controversial, it has recently been proposed that the mPTP is a dimer of the F0F1 ATP synthase [40,41] and that Ca²⁺ binding to F-ATP synthase β subunit triggers the mitochondrial permeability transition [42]. This is consistent with the role of Ca²⁺ to enhance the dissipation of the $\Delta\Psi_m$.

ROS is a well-known activator of the mPTP and disturbances in Ca²⁺ and oxidative stress are tightly coupled for opening the mPTP. nsPEF induces the production of ROS with no distinctions between the PFL and the BL pulsers. These observations that nsPEF-induced ROS and that the elevation of ROS was enhanced in the presence of Ca²⁺ have heightened our attention to determining the roles of nsPEF-induced ROS in mPTP opening. Although there is no established direct role of ROS in opening the mPTP, ROS has effects that indirectly influence opening the mPTP. Many factors determine the probability for opening the mPTP including Ca²⁺, $\Delta\Psi_m$, and the redox state of mitochondrial components, which can be influenced by ROS [43]. Many SH reagents were among the strongest stimulators of permeability transition, so it was proposed that thiol groups on some protein(s) played

roles in opening the mPTP [44]. It was proposed that the mPTP is modulated by the redox state of pyridine nucleotides and glutathione at two independent sites, one of which could be the adenine nucleotide translocase (ANT) [45]. Although the protein structure of the mPTP is still not defined, cyclophilin D (CypD) is a well-characterized regulator of the mPTP. CypD has also been shown to be redox regulated by forming an intramolecular disulfide with a conformational change playing a major role in cell necrosis by opening the mPTP acting as a redox-sensor protein in mitochondria [46].

In many of our studies, we have monitored the dissipation of the $\Delta\Psi_m$ in response to nsPEFs in the presence of Ca^{2+} and ROS indicators, and antioxidants to determine roles for Ca^{2+} and ROS in $\Delta\Psi_m$. Figure 7 is one of those studies using TMRE to determine changes in the $\Delta\Psi_m$ and MitoSox (MSOX) to monitor mitochondrial ROS (mROS) changes in response to the PFL and BL pulsers. Interestingly the results indicate that ROS plays different roles for the loss of $\Delta\Psi_m$ depending on the pulser. The pulse number-dependent increase in ROS is essentially the same with both pulsers showing a significant increase in mROS between 5 and 10 pulses and a maximum at 15 pulses. In contrast, the loss of $\Delta\Psi_m$ is different between the two pulsers.

Therefore, the relationships between mROS and loss of $\Delta\Psi_m$ are dissimilar between the two pulsers. What is similar between the two pulsers with the other cell responses is that compared to BL responses, PFL responses are more sensitive for dissipation of $\Delta\Psi_m$, loss of cell viability, PI permeability, activation of tPMET activity, and loss of tPMET activity. In contrast to all these cell responses, nsPEF-induced ROS production is the same for both PFL and BL pulsers. This suggests that the nsPEF-induced loss of $\Delta\Psi_m$ is relatively independent of the production of ROS.

In another approach for analyzing these pulsers on biological responses, we evaluated metabolic responses using the Seahorse to determine nsPEF effects on oxygen consumption rate (OCR) in control (sham-treated) and nsPEF-treated cells with 5 pulses from each of the PFL and BL pulsers. The 5-pulse condition did not cause any cell death, PI permeabilization, increase in ROS, loss of $\Delta\Psi_m$, or loss of tPMET activity with either pulser. However, the 5-pulse treatment did induce an increase in tPMET activity with the PFL but not the BL pulser. It should be noted that except for cell death, all these cell responses were determined within ≤ 30 min after treatment. Yet 15 h after treatment there were no significant differences in basal OCR with either pulser. With the increase in OCR after the addition of the FCCP uncoupling agent, the BL OCR was not significantly different than the control while the PFL treatment exhibited a significant decrease in OCR compared to the control and the BL response. The spare respiratory capacity (SRC) of the cells (FCCP minus basal OCR), was lightly increased with the BL pulser but significantly decreased in the PFL, which was due to the attenuated FCCP response and independent of the basal OCR. This suggests that there was a time-dependent deterioration of the status of the mitochondria presumably in response to cellular stress and the ability to fulfill additional energy requirements beyond the basal level in response to acute cellular stress. While there was not a significant increase in ROS in the 5-pulse condition, ROS likely increased during the 15 h time it took the nsPEF-treated cells to bind to the Seahorse plate for OCR analysis. Given that the increased ROS response was the same for both pulsers and only the response to the PFL showed a decreased SRC, any hypothesized increase in cellular ROS would be expected in the response to the PFL and not the BL. However, other stress response signaling pathways could have been activated that were not analyzed such as activation of the mitogen-activated protein kinase (MAPK) pathway and the nuclear factor kappa-light-chain-enhancer of activated NF- κ B pathway, which could also have been activated during the 15 h post nsPEF exposure to the PFL pulser [47]. These MAPK-NF κ B stress pathways could have caused a deterioration of mitochondrial SRC, but this would have occurred in the PFL but not the BL pulser. Given that the PFL induced more sensitive responses than the BL, this could have resulted in a selective response of these stress pathways from the PFL, like that for the increase in tPMET. However, these are speculations since we did not analyze these enzymatic stress responses. Nevertheless, the differences in the metabolic

response to the PFL and BL pulses provide another example of selectivity for a biological response from different nsPEF post-pulse waveforms.

We previously published a conformation that a fast or short pulse rise time of the primary pulse was an important feature for inducing intracellular effects [27]. We were not cognizant at that time about roles for a post pulse, yet both fast and slow rise time pulsers were based on PFL design. Those studies showed that faster rise times vs. slower rise times were more effects to dissipate the $\Delta\Psi_m$ and induce cell death while effects for Ca^{2+} or PI influx through the plasma membrane were not dependent on the pulse rise time. The present studies show yet a different way that nsPEF waveforms can have different and selective effects on cell responses. As indicated here, these different or selective effects have nothing to do with the primary pulse like the rise time studies just discussed but are related to the effects the post-pulse waveforms have on the primary pulse.

Regardless of the different primary pulse waveforms based on their rise times or the post-pulse waveforms based on dissimilar circuit topology, these results show that dissimilar nsPEF waveforms can have distinctive and possible selective biological outcomes that can determine cell fate. Given that nsPEFs produce ROS and ROS are endogenous signaling molecules, it is most likely that nsPEF waveforms at the lower pulse conditions will have a greater impact on physiological functions while higher pulse conditions will be more typical of pathological conditions or for regulated cell death mechanisms. It is also possible that these nsPEF waveforms will initiate other non-ROS cellular responses.

Furthermore, in Figure 8, the impact of 5 pulses on mitochondrial oxygen consumption is shown. The PFL pulser showed a significant decrease in spare respiratory capacity (SRC) by reducing maximal respiration without affecting the basal respiratory level. This observation indicates a disruption in the ETC and/or proton transport across the inner mitochondrial membrane [48]. These findings are consistent with the notion that glycolysis-derived pyruvate oxidation is involved in maintaining SRC levels, which supports the stimulating effect observed on tPMET (Figure 5). In contrast, the BL pulser led to high SRC levels, a characteristic often associated with cancer cells that are resistant to targeted agents. This can be attributed to the fact that the low pulse number (5 pulses) in this experiment was insufficient to cause significant pore formation and promote the loss of the $\Delta\Psi_m$.

There have been previous studies that involved the deliberate introduction of post-pulses to investigate cell responses. One phenomenon that has been observed is NBC [29,31,49], where a reversed-polarity nanosecond pulse can reduce the cell responses caused by a preceding ns pulse. The underlying mechanisms for NBC are still not fully understood and may involve assisted membrane discharge, a two-step process of charge transfer, an alternating reduction and oxidation mechanism, as well as cation diffusion reversal. These mechanisms are more pronounced when the second pulse is of similar magnitude as the first pulse. In another study [50], a double pulse strategy has been used for electroporation, where a high voltage short pulse is used for electroporation and a low voltage long pulse facilitates drug delivery through electrophoresis. Bipolar pulses with high frequency characteristics have also been employed for irreversible electroporation (HFIRE) [51,52], with the reversed polarity pulses used to suppress or remove muscle twitching by exploiting different time constants between electroporation and muscle excitation [53]. In these studies, the post-pulse to main pulse ratios were much larger compared to our study. For example, in BPC, the best cancellation efficiency was observed when the reversed pulse magnitude was 50% of the first pulse. In HFIRE, the first pulse was delivered at a higher amplitude than subsequent pulses, but it was common for the second pulse to be equal to the first phase. In the double pulse strategy, the second pulse was also 10% to 100% of the first pulse. In our study, the magnitude of the post-pulse was less than 5% of the main pulse and determined by dissimilar circuit topology differing between the two designs, yet it still resulted in disparate cell responses. This suggests that a mechanism like electrophoresis may be involved in cells responding to the post-pulse. Further investigation into the mechanisms, specifically in the realms of electrokinetics and bioelectrochemistry, may help elucidate the underlying processes that have often been overlooked in pulse engineering.

4. Conclusions

In the studies here, two different 100 ns pulses generators were used providing 100 ns pulse durations and electric fields of 40 kV/cm primary pulses with similar voltage and frequency wave distributions. One was a PFL with a post-pulse waveform having the same polarity as the primary pulse and the other was a BL pulses with a post-pulse waveform having an opposite polarity as the primary pulse. The cell responses obtained from these distinct pulse generators were determined from their post-pulse waveforms, not their primary waveforms.

Cells exhibited greater sensitivity to the PFL than the BL pulser with lower pulse numbers or electric field intensities for inducing cell membrane permeability, dissipation of $\Delta\Psi_m$, a decrease in mitochondrial SRC, a biphasic effect on tPMET, and eventual cell death. This biphasic behavior holds significant implications for enhancing the efficacy of ablation procedures and potentially facilitating cellular differentiation in cancer therapy, ultimately leading to the prospect of in-situ vaccination. Interestingly, both pulse types demonstrate a similar dependence on pulse number in terms of ROS production. Despite the post-pulse having a magnitude of less than 5% of the main pulse and lasting for a longer duration (50 μ s), its low intensity is still expected to decrease the membrane potential caused by the main pulse. To the best of our knowledge, this is the first time that charging current, which is reflected as a post-pulse, has been reported to have such a significant effect on cellular response. This work highlights the importance of considering the charging characteristics in pulse generator design and when comparing cell responses under similar pulse conditions.

5. Material and Methods

5.1. Experimental Conditions and Protocols

Pulse generators and Cell Exposure System

Two pulse generators were utilized in the experiments. The first generator employed a PFL comprised of five 50 Ω cables (RG-8) to generate 100 ns pulses. The second generator utilized a BL constructed with ten 50 Ω cables (RG-58), also producing 100 ns pulses (see details in Chaps. 15 & 16 in [1]). For both pulse generators, the lengths of the cables were determined based on a propagation length of 5 ns/m. Under ideally matched conditions, both loads required a resistance of 10 Ω . The switches for these generators were atmospheric pressure spark gaps. These spark gaps consisted of polished, plane-plane brass electrodes and would self-close once the voltage exceeded the breakdown threshold. During the experiment, the breakdown voltages of the two pulse generators were regulated by adjusting the gap distances of the corresponding spark switches. Both generators were powered by the same high voltage supply (Glassman, series EH, 60 kV). No extra charging resistor was employed throughout the experiments. The pulse repetition rate was set at 1 Hz, controlled by the current setting on the power supply. Standard electroporation cuvettes with a 1-mm gap distance were used for the experiments. The solution contained within the cuvettes resulted in a resistance that was close to 10 Ω , eliminating the need for additional resistance for impedance matching. The pulse waveforms were measured with a custom-made, calibrated, high precision resistor divider (1000:1).

5.2. Cell Culture

The murine melanoma cell line B16F10 (ATCC[®] CRL-6475TM) was used in this study. The cells were grown in a humidified incubator at 37 °C with 5% CO₂ in the Dulbecco's Modified Eagle Medium (DMEM) produced by ATCC (30-2002), supplemented with 10% fetal bovine serum (FBS) (ATCC, 30-2020) and 1% of penicillin-streptomycin (Sigma-Aldrich). B16F10 cells were harvested with 0.25% (*w/v*) Trypsin- 0.1% EDTA solution (Corning, MT25053CI). The cells were passaged no more than 20 times. Initial cell counts and viability were determined using a 0.4% trypan blue exclusion viability assay (Corning, 25900CI). Cells with greater than 95% viability were washed with PBS, centrifuged at 300 RCF for 5 min at room temperature, and resuspended at a concentration of 1×10^5 cells/ 100 μ L for nsPEF treatments. In all experiments, cell suspensions were added to 100 μ L cuvettes

(1-mm gap sterile electroporation cuvette, BioSmith, U-72001) and treated with a BL or PFL pulser in the culture medium with the conductivity of 1.18 S/m.

5.3. tPMET Rate Determination

The Cell Counting Kit-8 (CCK-8/WST-8-reducing NADH oxidoreductase activity, Dojindo, CK04-11) was used here to measure the trans-PM electron transport (t-PMET) of the plasma membrane redox system (PMRS). The quantification of the final electron acceptor (WST-8 reduction) was based on the change in absorption at 450 nm per minute of incubation. Cell suspensions with a concentration of 4×10^5 cells/100 μ L were added to cuvettes for treatment with different pulsers and varying numbers of pulses. Following the nsPEF treatment, the CCK-8 reagent was added (at a 1:1 volume ratio) and mixed immediately, and the cells were transferred to 384-well plates (Greiner Bio-One CELLSTAR plate, with cover, from VWR, 50051816) with 30 μ L per well. Microplate readers (Spectra Max i3) were used to measure the absorbance at 450 nm at 37 °C for 0–90 min. The tPMET rates were determined based on linear time courses between 10 and 35 min, as specified in the statistics analysis section.

5.4. Cell Viability Analysis

The Cell Counting Kit 8 (CCK-8, Dojindo, Kumamoto, Japan) was used to measure cell viability. B16F10 cells were grown to 80% confluency, and then the cell concentration was adjusted to 1×10^6 cells/mL for nsPEF treatment. Following the pulsing, 15,000 cells were seeded into 96-well plates (Corning Incorporated, Corning, NY, USA). The cells were cultured for 24 h, after which 10 μ L of CCK-8 solution (1:10 *v/v*) was added to each well. Following an additional 1.5 h incubation, the optical density was measured at an absorbent of 450 nm using a microplate reader (ELx800; BioTek Instruments, Inc., VT, USA). The OD value was divided by the control value to calculate the relative cell survival rate (background values were subtracted).

5.5. Flow Cytometry

$\Delta\Psi_m$ was detected using tetramethylrhodamine ethyl ester, perchlorate (TMRE; Immunochemistry Technologies LLC, Bloomington, MN, USA). B16F10 cells were harvested, counted, and resuspended following the previously described method. The samples were then treated with the BL and PFL pulsers, and TMRE was added to the cells at a concentration of 0.3 μ M. The cells were incubated for 20 min, protected from light. Cells were not subjected to pre-incubation prior to pulsing, as we observed that this could adversely impact cell viability [54]. The optimal approach is to introduce the dye immediately after pulsing and incubate it for precisely 20 min.

The same procedure was employed to detect ROS using MitoSOX-Red (MSOX; Invitrogen, Molecular Probes, Inc., Eugene, OR, USA), albeit with a final concentration of 2 μ M. Red fluorescence from TMRE and ROS was detected in separate experiments using the PE channel on a Miltenyi MacsQuant Analyzer 10 flow cytometer, as both molecules share the same excitation/emission characteristics.

To detect cell permeabilization, cells were exposed to nsPEFs, and Propidium Iodide (PI; Invitrogen, P3566) was added to a final concentration of 10 μ g/mL immediately after pulsing. Cells were then analyzed by flow cytometry 10 min after nsPEF treatment using the FITC channel [27]. Untreated and/or unstained samples were used as negative controls for treatment and fluorescence, respectively, in all experimental groups. Data analysis was conducted using FlowJo™ Software (Windows) Version 10 (Ashland, OR: Becton, Dickinson, and Company; 2019).

5.6. Seahorse Assay

The OCR (oxygen consumption rate) was measured using an XF HS Mini Analyzer (Seahorse Bioscience). Following the pulsing treatment, B16F10 cells were seeded into XFp cell culture 8-well mini plates in duplicate at a density of 3×10^3 cells/well. The

cells were then cultured under standard conditions for 15 h. Before measurement, the medium was replaced with Seahorse XF Assay Media (Agilent, Santa Clara, CA, USA) with a pH of 7.4. The assay media was supplemented with 10-mM glucose, 2-mM L-glutamine, and 1-mM pyruvate. For the mitochondrial stress test, the following inhibitors were used at the indicated final concentrations: 1.5- μ M oligomycin, 1- μ M FCCP, and 0.5- μ M rotenone-antimycin A. Two wells without cells were included to assess non-cellular oxygen consumption, and the value of non-cellular oxygen consumption was subtracted from the cellular OCR value. After completing the experiment, the OCR data were normalized to the number of cells.

5.7. Statistics Analysis

The tPMET data obtained from the 10–30-min time period was subjected to linear regression analysis using GraphPad Prism version 9 (GraphPad Software, San Diego, CA, USA). Statistical analyses comparing the tPMET rates of the samples to the control were conducted using one-way ANOVA. For the Seahorse data obtained from the XF HS Mini, analysis and normalization of the number of cells were performed using Agilent Seahorse Wave Desktop software (Agilent Technologies, USA). Flow cytometry analysis was carried out using FlowJo™ Software Version 10 (Ashland, OR: Becton, Dickinson, and Company; 2019). All experiments were conducted at least three times, and the data were expressed as Mean \pm Standard Error of the Mean (S.E.M.). Statistical analyses such as one-way or two-way ANOVA were performed using GraphPad Prism, with a significance level of $p < 0.05$.

Author Contributions: experimental design, S.X., K.A. and S.J.B.; manuscript writing, S.X., K.A., and S.J.B.; data analysis, S.X., K.A., S.J.B., and V.Y.; experiment, K.A., C.Z., and S.X.. All authors have read and agreed to the published version of the manuscript.

Funding: This project was in part funded by the US AFOSR (Air Force Office of Scientific Research) MURI project “Nanoelectropulse-induced Electromechanical Signaling and Control of Biological Systems,” (project number: FA9550-15-1-0517).

Institutional Review Board Statement: Not applicable.

Informed Consent Statement: Not applicable.

Data Availability Statement: The data presented in this study are available on request from the corresponding author.

Acknowledgments: All authors have reviewed and approved the final version of this paper and have given their consent for its publication.

Conflicts of Interest: The authors declare no conflict of interest.

References

1. Beebe, S.J.; Joshi, R.; Schoenbach, K.H.; Xiao, S. *Ultrashort Electric Pulse Effects in Biology and Medicine*; Springer: Singapore, 2021. [CrossRef]
2. Joshi, R.P.; Garner, A.L.; Sundararajan, R. Review of Developments in Bioelectrics as an Application of Pulsed Power Technology. *IEEE Trans. Plasma Sci.* **2023**, *51*, 1682–1717. [CrossRef]
3. Batista Napotnik, T.; Polajžer, T.; Miklavčič, D. Cell death due to electroporation—A review. *Bioelectrochemistry* **2021**, *141*, 107871. [CrossRef]
4. Pakhomov, A.G.; Kolb, J.F.; White, J.A.; Joshi, R.P.; Xiao, S.; Schoenbach, K.H. Long-lasting plasma membrane permeabilization in mammalian cells by nanosecond pulsed electric field (nsPEF). *Bioelectromagn. J. Bioelectromagn. Soc. Soc. Phys. Regul. Biol. Med. Eur. Bioelectromagn. Assoc.* **2007**, *28*, 655–663. [CrossRef]
5. Beebe, S.J.; Schoenbach, K.H. Nanosecond Pulsed Electric Fields: A New Stimulus to Activate Intracellular Signaling. *J. Biomed. Biotechnol.* **2005**, *2005*, 297–300. [CrossRef]
6. Casciati, A.; Tanori, M.; Gianlorenzi, I.; Rampazzo, E.; Persano, L.; Viola, G.; Cani, A.; Bresolin, S.; Marino, C.; Mancuso, M.; et al. Effects of Ultra-Short Pulsed Electric Field Exposure on Glioblastoma Cells. *Int. J. Mol. Sci.* **2022**, *23*, 3001. [CrossRef]
7. Beebe, S.; Fox, P.; Rec, L.; Somers, K.; Stark, R.; Schoenbach, K. Nanosecond pulsed electric field (nsPEF) effects on cells and tissues: Apoptosis induction and tumor growth inhibition. *IEEE Trans. Plasma Sci.* **2002**, *30*, 286–292. [CrossRef]

8. McDaniel, A.; Freimark, B.; Navarro, C.; Von Rothstein, K.; Gonzalez, D.; Linder, K.; Nuccitelli, R. Nano-pulse stimulation™ therapy (NPS™) is superior to cryoablation in clearing murine melanoma tumors. *Front. Oncol.* **2023**, *12*, 948472. [CrossRef]
9. Xie, F.; Varghese, F.; Pakhomov, A.G.; Semenov, I.; Xiao, S.; Philpott, J.; Zemlin, C. Ablation of Myocardial Tissue with Nanosecond Pulsed Electric Fields. *PLoS ONE* **2015**, *10*, e0144833. [CrossRef]
10. Zemlin, C.; Xie, F.; Xiao, S. Optimal Parameters for the Ablation of Myocardial Tissue with Pulsed Electric Fields. In Proceedings of the 2013 American Heart Association Scientific Sessions, Dallas, TX, USA, 16–20 November 2013.
11. Chen, R.; Sain, N.M.; Harlow, K.T.; Chen, Y.-J.; Shires, P.K.; Heller, R.; Beebe, S.J. A protective effect after clearance of orthotopic rat hepatocellular carcinoma by nanosecond pulsed electric fields. *Eur. J. Cancer* **2014**, *50*, 2705–2713. [CrossRef]
12. Nuccitelli, R.; Tran, K.; Lui, K.; Huynh, J.; Athos, B.; Kreis, M.; Nuccitelli, P.; De Fabo, E.C. Non-thermal Nanoelectroablation of UV-induced Murine Melanomas Stimulates an Immune Response. *Pigment. Cell Melanoma Res.* **2012**, *25*, 618–629. [CrossRef]
13. Guo, S.; Jing, Y.; Burcus, N.I.; Lassiter, B.P.; Tanaz, R.; Heller, R.; Beebe, S.J. Nano-pulse stimulation induces potent immune responses, eradicating local breast cancer while reducing distant metastases. *Int. J. Cancer* **2018**, *142*, 629–640. [CrossRef] [PubMed]
14. Guo, S.; Burcus, N.I.; Hornef, J.; Jing, Y.; Jiang, C.; Heller, R.; Beebe, S.J. Nano-Pulse Stimulation for the Treatment of Pancreatic Cancer and the Changes in Immune Profile. *Cancers* **2018**, *10*, 217. [CrossRef]
15. Romeo, S.; Sarti, M.; Scarfi, M.R.; Zeni, L. Modified Blumlein Pulse-Forming Networks for Bioelectrical Applications. *J. Membr. Biol.* **2010**, *236*, 55–60. [CrossRef]
16. Sun, Y.; Xiao, S.; White, J.A.; Kolb, J.F.; Stacey, M.; Schoenbach, K.H. Compact, nanosecond, high repetition rate, pulse generator for bioelectric studies. *IEEE Trans. Dielectr. Electr. Insul.* **2007**, *14*, 863–870. [CrossRef]
17. Kanaan, M.; El Amari, S.; Silve, A.; Merla, C.; Mir, L.M.; Couderc, V.; Arnaud-Cormos, D.; Leveque, P. Characterization of a 50-Ω Exposure Setup for High-Voltage Nanosecond Pulsed Electric Field Bioexperiments. *IEEE Trans. Biomed. Eng.* **2011**, *58*, 207–214. [CrossRef]
18. Xiao, S.; Zhou, C.; Yang, E.; Rajulapati, S.R. Nanosecond bipolar pulse generators for bioelectrics. *Bioelectrochemistry* **2018**, *123*, 77–87. [CrossRef]
19. Ma, J.; Yu, L.; Ren, L.; Liao, Y.; Dong, S.; Yao, C. High Voltage Nanosecond Pulse Generator based on Inductive Energy Storage with Adjustable Pulse Width. In Proceedings of the 2022 IEEE International Conference on High Voltage Engineering and Applications (ICHVE), Chongqing, China, 25–29 September 2022; pp. 1–4. [CrossRef]
20. Butkus, P.; Murauskas, A.; Tolvaišienė, S.; Novickij, V. Concepts and Capabilities of In-House Built Nanosecond Pulsed Electric Field (nsPEF) Generators for Electroporation: State of Art. *Appl. Sci.* **2020**, *10*, 4244. [CrossRef]
21. Merla, C.; El Amari, S.; Kanaan, M.; Liberti, M.; Apollonio, F.; Arnaud-Cormos, D.; Couderc, V.; Leveque, P. A 10-Ω High-Voltage Nanosecond Pulse Generator. *IEEE Trans. Microw. Theory Tech.* **2010**, *58*, 4079–4085. [CrossRef]
22. Kandratsyev, A.; Sabaleuski, U.; Redondo, L.; Pakhomov, A.G. Four Channel 6.5 kV, 65 A, 100 ns–100 μs Generator with Advanced Control of Pulse and Burst Protocols for Biomedical and Biotechnological Applications. *Appl. Sci.* **2021**, *11*, 11782. [CrossRef]
23. Garner, A.L.; Caiafa, A.; Jiang, Y.; Klopman, S.; Morton, C.; Torres, A.S.; Loveless, A.M.; Neculaes, V.B. Design, characterization and experimental validation of a compact, flexible pulsed power architecture for ex vivo platelet activation. *PLoS ONE* **2017**, *12*, e0181214. [CrossRef]
24. Urabe, G.; Sato, T.; Nakamura, G.; Kobashigawa, Y.; Morioka, H.; Katsuki, S. 1.2 MV/cm pulsed electric fields promote transthyretin aggregate degradation. *Sci. Rep.* **2020**, *10*, 12003. [CrossRef]
25. Yao, C.; Dong, S.; Zhao, Y.; Mi, Y.; Li, C. A Novel Configuration of Modular Bipolar Pulse Generator Topology Based on Marx Generator with Double Power Charging. *IEEE Trans. Plasma Sci.* **2016**, *44*, 1872–1878. [CrossRef]
26. Yao, C.; Zhang, X.; Guo, F.; Dong, S.; Mi, Y.; Sun, C. FPGA-Controlled All-Solid-State Nanosecond Pulse Generator for Biological Applications. *IEEE Trans. Plasma Sci.* **2012**, *40*, 2366–2372. [CrossRef]
27. Beebe, S.J.; Chen, Y.-J.; Sain, N.M.; Schoenbach, K.H.; Xiao, S. Transient Features in Nanosecond Pulsed Electric Fields Differentially Modulate Mitochondria and Viability. *PLoS ONE* **2012**, *7*, e51349. [CrossRef]
28. Novickij, V.; Rembiałkowska, N.; Szlaska, W.; Kulbacka, J. Does the shape of the electric pulse matter in electroporation? *Front. Oncol.* **2022**, *12*, 958128. [CrossRef]
29. Pakhomov, A.G.; Semenov, I.; Xiao, S.; Pakhomova, O.N.; Gregory, B.; Schoenbach, K.H.; Ullery, J.C.; Beier, H.T.; Rajulapati, S.R.; Ibey, B.L. Cancellation of cellular responses to nanoelectroporation by reversing the stimulus polarity. *Cell. Mol. Life Sci.* **2014**, *71*, 4431–4441. [CrossRef]
30. Bagalkot, T.R.; Leblanc, N.; Craviso, G.L. Stimulation or Cancellation of Ca²⁺ Influx by Bipolar Nanosecond Pulsed Electric Fields in Adrenal Chromaffin Cells Can Be Achieved by Tuning Pulse Waveform. *Sci. Rep.* **2019**, *9*, 1–13. [CrossRef] [PubMed]
31. Valdez, C.M.; Barnes, R.A.; Roth, C.C.; Moen, E.K.; Throckmorton, G.A.; Ibey, B.L. Asymmetrical bipolar nanosecond electric pulse widths modify bipolar cancellation. *Sci. Rep.* **2017**, *7*, 16372. [CrossRef] [PubMed]
32. Kolb, J.F.; Kono, S.; Schoenbach, K.H. Nanosecond pulsed electric field generators for the study of subcellular effects. *Bioelectromagnetics* **2006**, *27*, 172–187. [CrossRef]
33. Sözer, E.B.; Pakhomov, A.G.; Semenov, I.; Casciola, M.; Kim, V.; Vernier, P.T.; Zemlin, C.W. Analysis of electrostimulation and electroporation by high repetition rate bursts of nanosecond stimuli. *Bioelectrochemistry* **2021**, *140*, 107811. [CrossRef]
34. Berridge, M.; Tan, A. Trans-plasma membrane electron transport: A cellular assay for NADH-and NADPH-oxidase based on extracellular, superoxide-mediated reduction of the sulfonated tetrazolium salt WST-1. *Protoplasma* **1998**, *205*, 74–82. [CrossRef]

35. Herst, P.M.; Berridge, M.V. Plasma membrane electron transport: A new target for cancer drug development. *Curr. Mol. Med.* **2006**, *6*, 895–904. [CrossRef]
36. Ly, J.D.; Lawen, A. Transplasma membrane electron transport: Enzymes involved and biological function. *Redox Rep.* **2003**, *8*, 3–21. [CrossRef] [PubMed]
37. Pakhomov, A.G.; Bowman, A.M.; Ibey, B.L.; Andre, F.M.; Pakhomova, O.N.; Schoenbach, K.H. Lipid nanopores can form a stable, ion channel-like conduction pathway in cell membrane. *Biochem. Biophys. Res. Commun.* **2009**, *385*, 181–186. [CrossRef]
38. Beebe, S.J.; Lassiter, B.P.; Guo, S. Nanopulse Stimulation (NPS) Induces Tumor Ablation and Immunity in Orthotopic 4T1 Mouse Breast Cancer: A Review. *Cancers* **2018**, *10*, 97. [CrossRef] [PubMed]
39. Lassiter, B.P.; Guo, S.; Beebe, S.J. Nano-Pulse Stimulation Ablates Orthotopic Rat Hepatocellular Carcinoma and Induces Innate and Adaptive Memory Immune Mechanisms that Prevent Recurrence. *Cancers* **2018**, *10*, 69. [CrossRef]
40. Bernardi, P.; Rasola, A.; Forte, M.; Lippe, G.; Wang, D.Z.; Jones, A.W.; Wang, W.Z.; Wang, M.; Korthuis, R.J. The Mitochondrial Permeability Transition Pore: Channel Formation by F-ATP Synthase, Integration in Signal Transduction, and Role in Pathophysiology. *Physiol. Rev.* **2015**, *95*, 1111–1155. [CrossRef] [PubMed]
41. Bonora, M.; Pinton, P. The Mitochondrial Permeability Transition Pore and Cancer: Molecular Mechanisms Involved in Cell Death. *Front. Oncol.* **2014**, *4*, 302. [CrossRef]
42. Giorgio, V.; Burchell, V.; Schiavone, M.; Bassot, C.; Minervini, G.; Petronilli, V.; Argenton, F.; Forte, M.; Tosatto, S.; Lippe, G.; et al. Ca(2+) binding to F-ATP synthase β subunit triggers the mitochondrial permeability transition. *EMBO Rep.* **2017**, *18*, 1065–1076. [CrossRef]
43. Handy, D.; Loscalzo, J. Redox Regulation of Mitochondrial Function. *Antioxid. Redox Signal.* **2012**, *16*, 1323–1367. [CrossRef]
44. Zoratti, M.; Szabò, I. The mitochondrial permeability transition. *Biochim. Biophys. Acta* **1995**, *1241*, 139–176. [CrossRef] [PubMed]
45. Chernyak, B.V. Redox Regulation of the Mitochondrial Permeability Transition Pore. *Biosci. Rep.* **1997**, *17*, 293–302. [CrossRef] [PubMed]
46. Linard, D.; Kandlbinder, A.; Degand, H.; Morsomme, P.; Dietz, K.J.; Knoops, B. Redox characterization of human cyclophilin D: Identification of a new mammalian mitochondrial redox sensor? *Arch. Biochem. Biophys.* **2009**, *491*, 39–45. [CrossRef]
47. Liu, S.; Feng, G.; Wang, G.L.; Liu, G.J. p38MAPK inhibition attenuates LPS-induced acute lung injury involvement of NF-kappaB pathway. *Eur. J. Pharmacol.* **2008**, *584*, 159–165. [CrossRef] [PubMed]
48. Marchetti, P.; Fovez, Q.; Germain, N.; Khamari, R.; Kluza, J. Mitochondrial spare respiratory capacity: Mechanisms, regulation, and significance in non-transformed and cancer cells. *FASEB J.* **2020**, *34*, 13106–13124. [CrossRef]
49. Casciola, M.; Xiao, S.; Apollonio, F.; Paffi, A.; Liberti, M.; Muratori, C.; Pakhomov, A.G. Cancellation of nerve excitation by the reversal of nanosecond stimulus polarity and its relevance to the gating time of sodium channels. *Cell. Mol. Life Sci.* **2019**, *76*, 4539–4550. [CrossRef] [PubMed]
50. Sadik, M.M.; Yu, M.; Zheng, M.; Zahn, J.D.; Shan, J.W.; Shreiber, D.I.; Lin, H. Scaling Relationship and Optimization of Double-Pulse Electroporation. *Biophys. J.* **2014**, *106*, 801–812. [CrossRef]
51. Arena, C.B.; Sano, M.B.; Rylander, M.N.; Davalos, R.V. Theoretical Considerations of Tissue Electroporation With High-Frequency Bipolar Pulses. *IEEE Trans. Biomed. Eng.* **2010**, *58*, 1474–1482. [CrossRef]
52. Sano, M.B.; DeWitt, M.R.; Teeter, S.D.; Xing, L. Optimization of a single insertion electrode array for the creation of clinically relevant ablations using high-frequency irreversible electroporation. *Comput. Biol. Med.* **2018**, *95*, 107–117. [CrossRef]
53. Boye, C.; Christensen, K.; Asadipour, K.; DeClemente, S.; Francis, M.; Bulysheva, A. Gene electrotransfer of FGF2 enhances collagen scaffold biocompatibility. *Bioelectrochemistry* **2021**, *144*, 107980. [CrossRef]
54. Ford, W.E.; Ren, W.; Blackmore, P.F.; Schoenbach, K.H.; Beebe, S.J. Nanosecond pulsed electric fields stimulate apoptosis without release of pro-apoptotic factors from mitochondria in B16f10 melanoma. *Arch. Biochem. Biophys.* **2010**, *497*, 82–89. [CrossRef] [PubMed]

Disclaimer/Publisher’s Note: The statements, opinions and data contained in all publications are solely those of the individual author(s) and contributor(s) and not of MDPI and/or the editor(s). MDPI and/or the editor(s) disclaim responsibility for any injury to people or property resulting from any ideas, methods, instructions or products referred to in the content.

Review

Pulsing Addition to Modulated Electro-Hyperthermia

Andras Szasz

Department of Biotechnics, Hungarian University of Agriculture and Life Sciences, 2100 Gödöllő, Hungary; biotech@gek.szie.hu

Abstract: Numerous preclinical results have been verified, and clinical results have validated the advantages of modulated electro-hyperthermia (mEHT). This method uses the nonthermal effects of the electric field in addition to thermal energy absorption. Modulation helps with precisely targeting and immunogenically destroying malignant cells, which could have a vaccination-like abscopal effect. A new additional modulation (high-power pulsing) further develops the abilities of the mEHT. My objective is to present the advantages of pulsed treatment and how it fits into the mEHT therapy. Pulsed treatment increases the efficacy of destroying the selected tumor cells; it is active deeper in the body, at least tripling the penetration of the energy delivery. Due to the constant pulse amplitude, the dosing of the absorbed energy is more controllable. The induced blood flow for reoxygenation and drug delivery is high enough but not as high as increasing the risk of the dissemination of malignant cells. The short pulses have reduced surface absorption, making the treatment safer, and the increased power in the pulses allows the reduction of the treatment time needed to provide the necessary dose.

Keywords: hyperthermia; tumor; electric-field; thermal; energy; pulse; nonthermal; apoptosis; cell-selection

1. Introduction

Hyperthermia as a cancer cure is one of the early medical practices that originated from ancient medicine. The medical processes using heat remain a vital “household remedy”, even nowadays. Electromagnetic heating techniques replaced the ineffective ancient heat delivery. The application of electromagnetic effects presented unique possibilities and renewed the hyperthermia methodology. In modern therapeutic practices, using electromagnetic processes (mainly radiation) to heat the whole body or its local volume developed rapidly over a century ago. Various technical solutions for oncologic hyperthermia (HT) attract growing attention among oncology professionals.

The technical development of electromagnetic heating methods in the early 1900s revolutionized heat application for therapeutic gains, including malignancies. The curative processes with electromagnetic methods became available in the first quarter of the 19th century [1]. A French doctor, Arsene D’Arsonval, introduced a pure electromagnetic treatment called “Darsonvalization”. The absorbed electromagnetic energy resulted in heating. However, the physiological effects of heating (change in blood perfusion, thermal homeostatic regulations, risk of malignant dissemination, etc.) were initially neglected. The starting process was not free from extreme exaggerations. The German Electric Belt Agency went far, advertising that practitioners should reduce or even stop using drugs, advocating for electricity treatment alone [2].

The research on electromagnetic heating effects has revealed a complex interplay of factors. The temperature increase caused by electromagnetic energy absorption and the additional chemical changes (molecular excitations) induced by the electromagnetic field are key aspects. The thermal component is directly related to the square of the electric current, while the field component is proportional to that current. The bioelectromagnetic excitation alters the chemical bonds and the structure of compounds through direct electric forces, while some of the absorbed energy heats the target, raising its temperature. The

thermal effect alone can also trigger chemical reactions, and the field excitation enhances these effects. This understanding has paved the way for therapeutic practices that combine electromagnetic molecular, cellular, and tissue excitation with heating.

A further push on the development was the discovery of microwaves, which began clinical practice working similarly to microwave ovens. The thermal effect of electromagnetic energy absorption was much more straightforward to understand and was more accessible to study; therefore, separating the heating and exciting (thermal and nonthermal) effects became dominant (Figure 1). Our present approach creates synergy between the thermal and nonthermal components of the electromagnetic energy absorption processes.

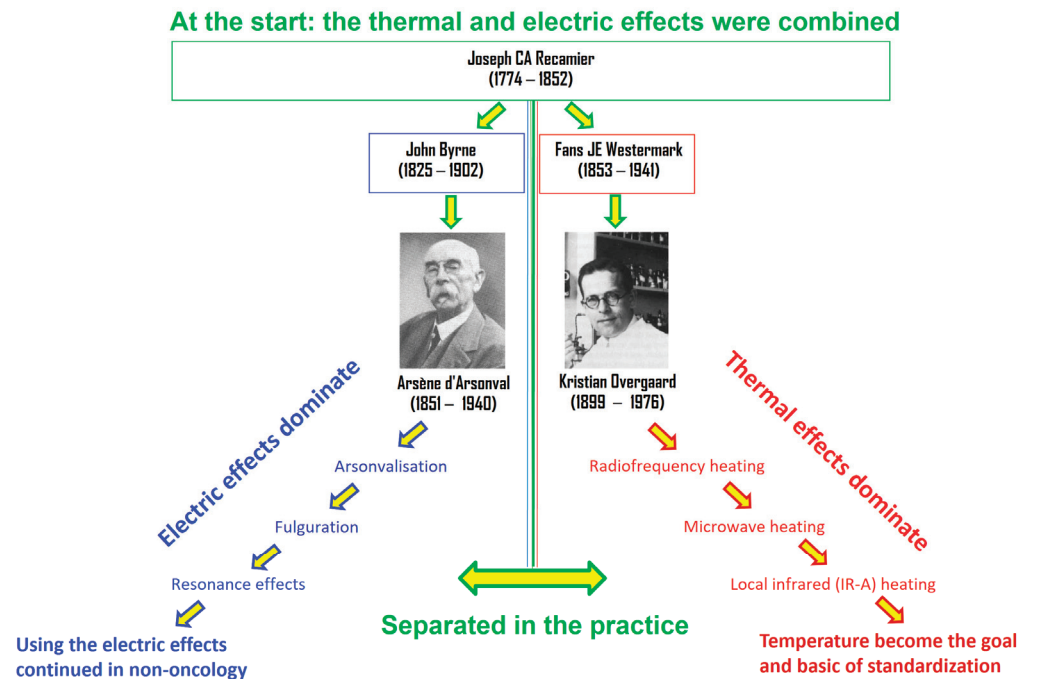


Figure 1. Arsene d’Arsonval (French) and Kristian Overgaard (Danish) are the leading doctors who divide the nonthermal field effects from heat, and the separation has widened over time.

The method’s long history has not benefited it and has increased skeptical opposition, with varying positive and negative results. Infancy is standard for all developing systems but is abnormal when it is unusually long. Hyperthermia is mature for broad acceptance.

The currently known and accepted oncological hyperthermia effects can be divided into three categories, according to Figure 2:

1. It destroys the tumor cells by absorbing energy;
2. It has immunogenic effect;
3. In the most frequent application, it sensitizes the conventional oncotherapies, like radiotherapy and chemotherapy.

Two primary electromagnetic therapies are applied in medicine: ionizing and nonionizing radiation. Ionizing radiation (e.g., radiotherapy) primarily has a nonthermal effect, breaking the DNA string with energy and causing more nonthermal radiative damage. At the same time, its thermal component is only tiny in most cases. The nonionizing radiation used in hyperthermia treatments is the opposite of the thermal/nonthermal ratio. It usually concentrates on the thermal component of the radiation, and the nonthermal component is a small part of conventional hyperthermia (Figure 3). The ratio of the thermal component effects looks at contrasts between the two methods, and direct cellular damage is also unlike. The direct cellular damage in the ionizing instance mostly breaks the DNA strands. At the same time, in nonionizing impact, the primary effect targets the cells as units, with concentration on the membrane damage at a temperature of about 42 °C. We discuss here

the non-ablative applications, where the nonionizing has less energy than necessary for a direct burn.

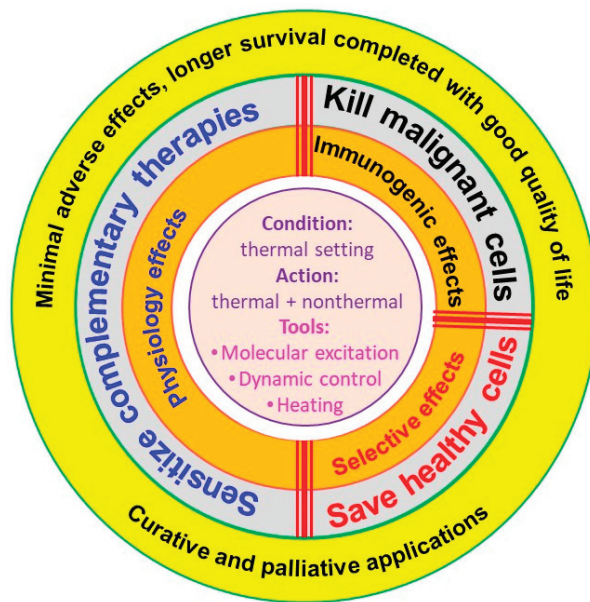


Figure 2. The hallmarks of hyperthermia’s effects in oncology. The main tasks are connected to complementary applications, where the thermal conditions promote the parallel administration of other therapies.

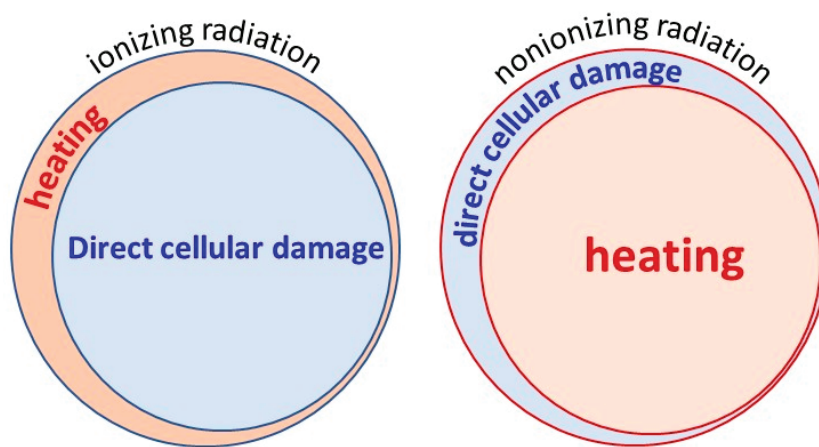


Figure 3. The treatments of electromagnetic radiation sharply differ in ionizing and nonionizing conditions.

2. Electrothermal Complexity

The electrothermal interactions are complex and can not be separated by thermal and nonthermal effects because their synergy does the job [3]. However, the ratio of these effects could be modified, forcing more nonthermal parts into the processes by the molecular excitation methods [4,5]. The primary selection mechanism uses the target’s extended electric and thermal heterogeneity, which can be utilized to select the molecular groups and excite the appropriate signal patterns [6]. The electric field gives the best opportunity for selection, which can technically be achieved with capacitive coupling [7]. Capacitive coupling with the intent of homogenous mass heating was applied on deep-seated [8] and superficial tumors [9]. Multiple clinical trials were performed for many metastatic stages. Soft-tissue [10] and Ewing sarcomas [11], pancreas cancer [12], breast cancer [13], liver tumors [14], rectal [15] and colorectal [16,17] malignancies, metastatic gastric tumors [18], urinary bladder lesions [19,20], esophageal [21–23], and head & neck tumors [24,25] all

have shown the feasibility of capacitive hyperthermia with remarkable results. Some studies were performed on non-small-cell lung cancer, too [26,27], but its efficacy was questioned [28]. Intraluminal capacitive application for the esophagus has also shown feasibility [21,29].

However, numerous challenges need solutions. The physiological thermal homeostasis, the thermal and electric inhomogeneity of the tumor, the complexity of the bioelectromagnetic processes, which are induced by the hyperthermia, the controllable dose, and the nearly exponential decay of the energy absorption, which overheats the surface, are all complications that need to be solved. The conventional dose is connected to the tumor's reached temperature, supporting isotherm homogeneity in the target. However, due to thermal and electric heterogeneity, the heating of biosystems is far from thermal equilibrium. Due to the physiological corrective feedback and the enormously inhomogeneous malignant target, fixing a homogeneous energy absorption in the tumor is impossible. The physiological feedback and thermodynamic processes destroy the possible homogeneous absorption part. The complex reality of living objects contradicts the macroscopic equilibrium. Moreover, the feedback processes deviate from the standard linearity of the specific absorption rate (SAR) and the temperature growth [30]. The isothermal expectation and the time-linearity in the heating process are only an illusion.

2.1. Temperature Development

The temperature development in the selected molecular group could be higher than their surroundings [31] and heat the area by the thermal convection of conduction, as is characteristically recognized in nanoparticle heating [32]. The extensively heated distance from the selectively heated small parts is small, less than 100 nm, and depends on how far it is from the artery, which cools it down. The heated molecular groups have relatively high temperatures due to the absorbed energy, and the larger volumes have gradually lower temperature averages (Figure 4). The concentrated energy absorption heats the transmembrane protein clusters (rafts), which heats the cell, but the average temperature will be less than in the raft. The cell heats the tumor, further lowering the average temperature. This thermal cascade makes it possible that the thermal effect, on average, remains safe and creates optimal conditions for the chemical reactions. Still, the micro-parts have enough energy to excite the necessary signal pathways.

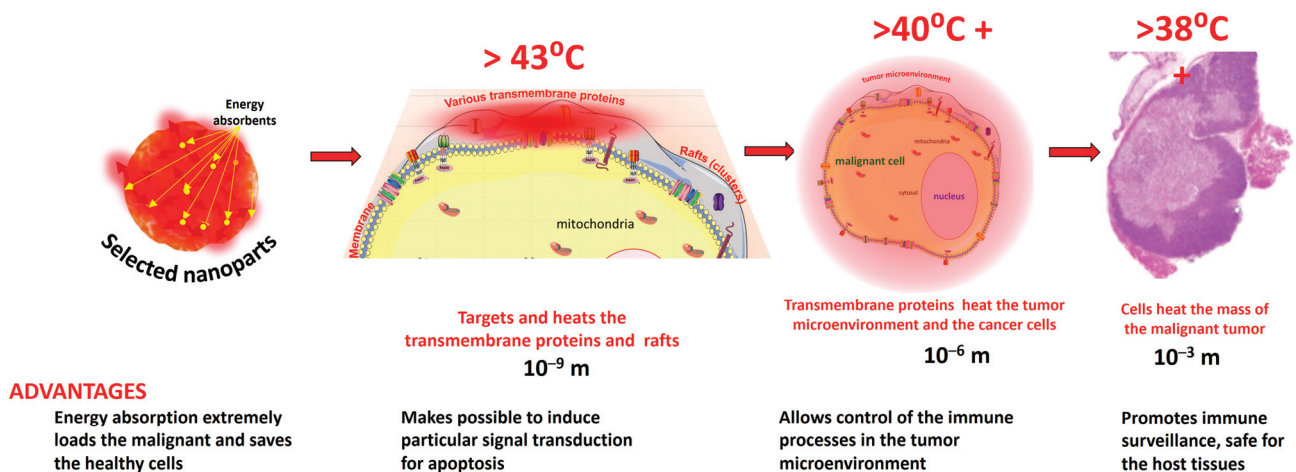


Figure 4. The thermal cascade of the averages for the heterogenic heating of the mEHT. The average sizes magnify about three orders of magnitudes in the different steps.

The heating by the small protein molecular groups (rafts) has limitations. When the energy is too large, the transmembrane proteins are dehydrated and decomposed, which does not serve the signal excitation demand. The selection no longer works, and the thermal component starts to overdominate the entire process.

2.2. Selection

The first selection step is based on the metabolic differences between cancer and healthy cells. The reprogrammed metabolism (Warburg effect) increases the ionic concentration in the tumor microenvironment, so the well-chosen RF current may prefer to flow through the tumor. The next selective factor finds the tumor cells, which will differ from their healthy counterpart because of their autonomy and the broken healthy network, which provides differentiation in the dielectric constant of the cell and offers a cellular selection. The selected malignant cells have transmembrane protein molecular clusters (membrane rafts) that are the target of the selection. These rafts are embedded in the well-insulating lipid membrane, so their relative conductivity is high, and they massively absorb the energy [31]. The energy absorption with the well-chosen modulation, delivered by the RF carrier frequency, induces signals leading the cell to immunogenic cell death (Figure 5).

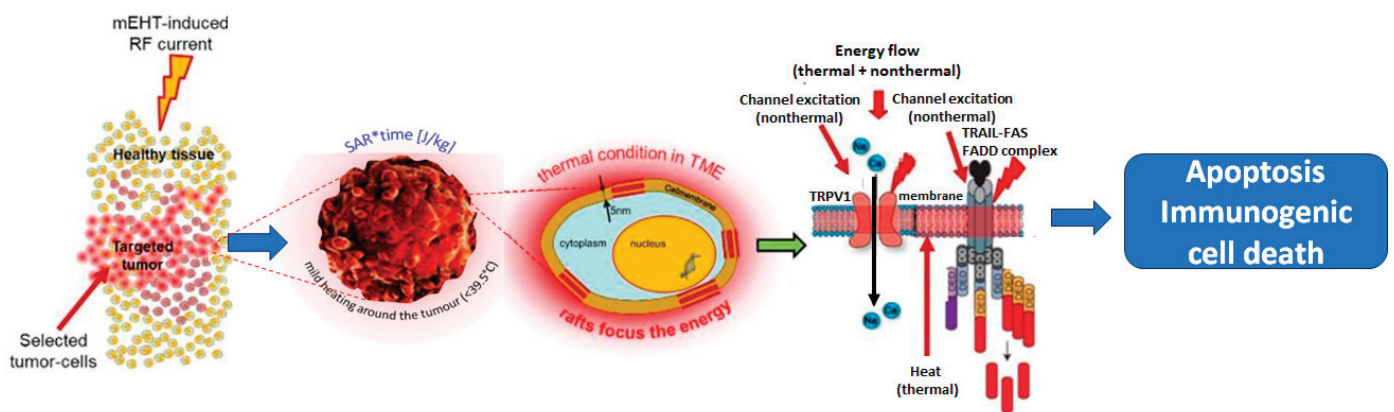


Figure 5. The cell is “gently” destroyed by the support of natural apoptotic signals, allowing the unhurt immunogenic information to be liberated during special apoptosis.

The impedance matching allows an energy-dose measure, ensuring that mainly the selected molecules absorb the energy. The specific absorption rate and temperature are connected at the physiological level by the blood flow (vasodilatation and vasocontraction changes) [30], which has no relevance when the heating is nanoscopic but has an increased modification of the energy intake by the homogenization of the temperature, leading to overdosing. Applied fractal modulation is also a novel technical innovation in impedance matching solutions [33], helping to produce immunogenic cell death (ICD) with its dynamic synchronization for homeostatic demands. The modulation with impedance-matching cellular selection completes the modulated electro-hyperthermia (mEHT) method [34,35]. The technical solution to optimize the ratio of the thermal and nonthermal components of the RF current needs a precise fit to the individual case, which changes with every treatment. The electronic solution is tuning the system to the measured impedance of the treated individual. The tuning seeks to form a touching situation as a purely metallic electrode would be fitted to the skin directly. This matching situation calculates the actual energy loss carefully, controls the reflected power, and matches the resonant compensation of the surface capacitor of the adipose tissue. The active impedance-guided capacitive solution (like mEHT) can use the bioelectromagnetic specialties of the malignant cells directly by RF current flow when it is matched to the optimized current. Cancer cells have an intensive metabolism to supply their proliferation [36]. The metabolic rate in most of the tumors is higher than their healthy counterpart (by at least 15% higher [37,38]), which selectively increases their temperature. The process has positive feedback because the growing temperature decreases the impedance of the tissue [39]. The high metabolic rate is used to identify the proliferation by positron-emission tomography (PET) [40,41]. The high nutrient/waste transport increases the ion concentration of the electrolytes in the surroundings of the malignant cell. The increased ionic concentration means a higher

microenvironment conductivity [42] in the tumor cells and lowers the resistivity of the whole tumor. It could distinguish between healthy and malignant situations [43]. Due to the lack of a healthy cellular network in malignancy, the extracellular matrix of malignant cells has high dielectric permittivity, which can be used for selection [44,45]. The permittivity and the conduction modify the total impedance in the microenvironment of the malignant cells [46], which allows their automatic selection, while the RF current flows in the direction of the low electric impedance. The RF current density (specially chosen frequency and modulation) will self-selectively flow toward the malignant cells, which is measurable by the MRI current density image [47,48]. This effect is entirely automatic and follows any movements of the cells in real-time, solving the challenge of focusing.

The amount of apoptosis could be regulated by the ratio of the heating (temperature grows) and keeping (temperature is stable) periods. In the heating-up period, the thermal effect grows, and the excitation (non-thermal effect) grows due to the better conditions of the molecular reaction rates. In the stable temperature period, the thermal and non-thermal factors are constant, and the absorbed energy replaces the heat loss in the system. It is observed that during the heating-up period by mEHT, the apoptosis rate is significantly higher than that of the temperature-keeping period [49]. Applied step-up heating uses this difference to improve apoptotic processes [50].

2.3. Nonthermal Effects

Living objects are profoundly heterogenic. This heterogeneity defines the nonthermal electromagnetic interactions and the final effect. Electromagnetism acts through the various molecular and cellular structures, making energy absorption by current flow, making the polarization effect for polar molecules, exciting electrons between two energy levels, arranging the structure (order/disorder transition), making connected or separated clusters (percolation), breaking the cellular membrane (electroporation), inducing electrophoresis, electroosmosis, and excitation of the membrane channels. These effects are well-oriented, while the thermal effect primarily increases the kinetic energy of the molecules, which move faster and vibrate more intensely. The more considerable thermal energy may change the molecular interactions or cause phase changes (Figure 6).

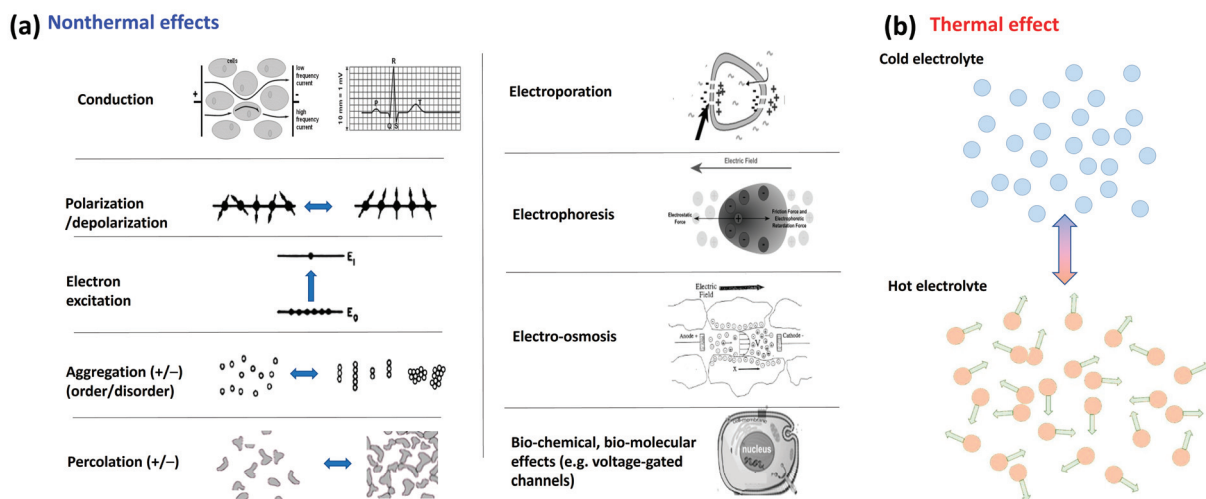


Figure 6. Nonthermal and thermal difference. (a) The nonthermal bioelectromagnetic effects vary widely in modifying energy absorption, allowing targeted manipulations of the chemical bonds in the body. (b) The thermal effects directly energize the target’s electrolyte components (ions, molecules, cells), significantly increasing their kinetic energy.

The applied RF electric field changes the cells’ polarization and has different current components caused by the target’s impedance (Figure 7). The target’s capacitive behavior declines a part of the current from the ohmic component, which is mainly responsible for thermal effects by its vectorial direction.

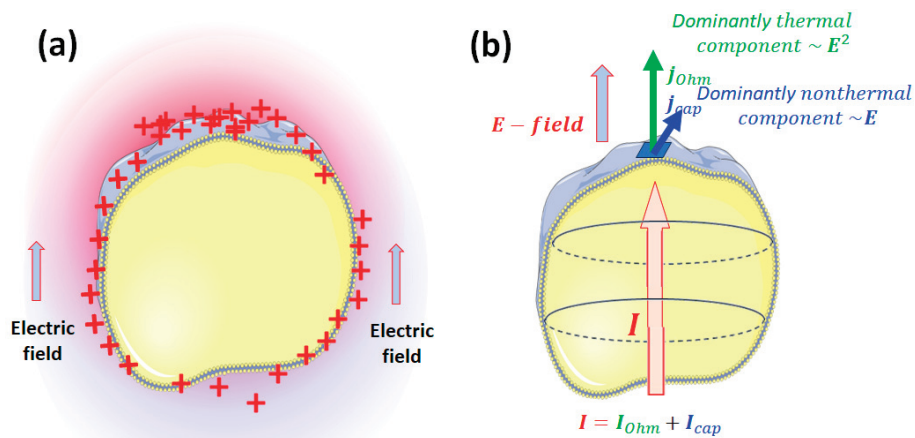


Figure 7. The effects of the external RF field. (a) The intense polarization effect of the external field repolarizes the cells, causing hyperpolarization and depolarization states on the membrane. (b) The complex current has two components flowing through capacitors (membrane lipid layers).

Many molecular and physiological processes are determined by the heterogeneous lipid domains serving as molecular sorting platforms [51]. The malignant cells have a denser lipid-raft population on their membranes than their healthy counterparts [52]. Consequently, membrane heterogeneity is crucial in malignant cells' selective energy absorption (Figure 8) and appears to be a synergy of thermal effects with nonthermal electricity.

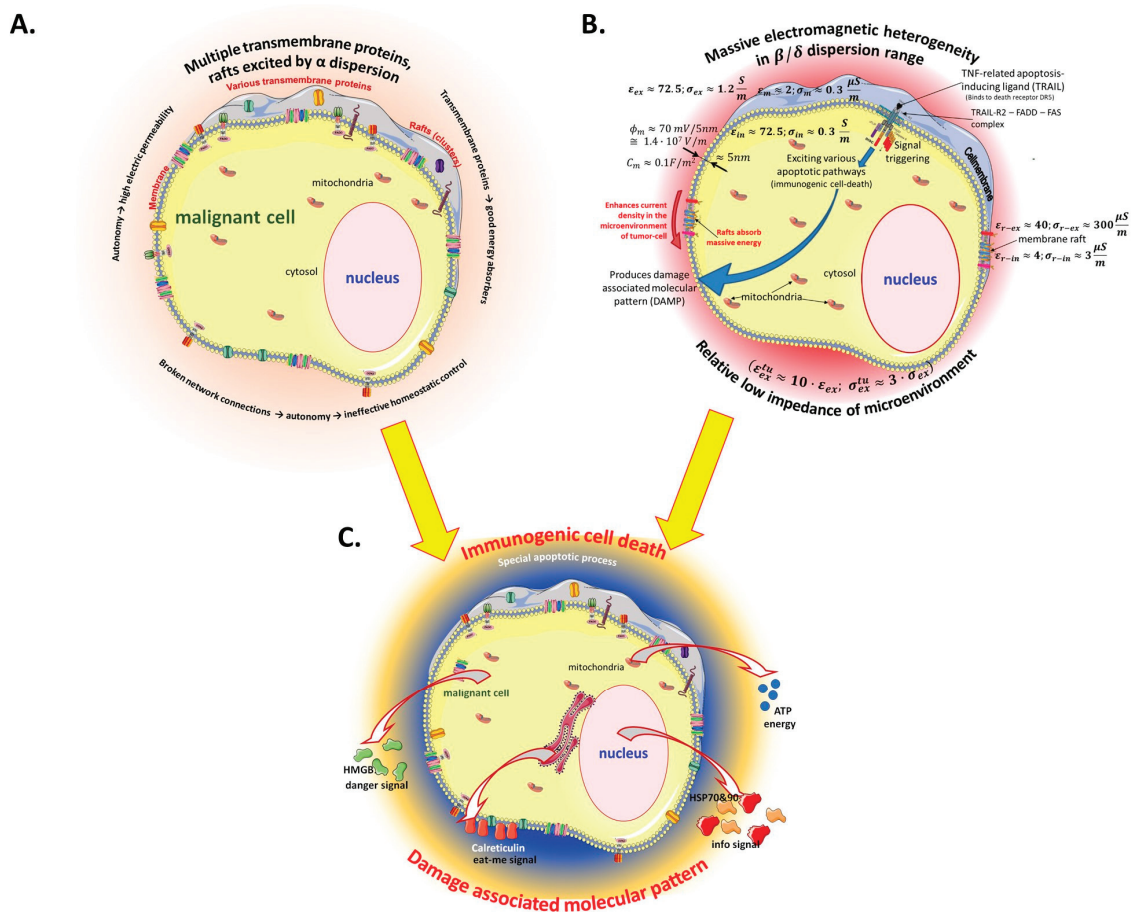


Figure 8. The electromagnetic heterogeneity of the selected tumor cell. (A) The transmembrane protein excitations are targeted by α -dispersion. (B) The electromagnetic heterogeneity is targeted by

particular RF frequency (C). The result is the damage associated with molecular patterns induced by immunogenic cell death. Abbreviations/references: ϵ_{ex} and σ_{ex} are the relative permittivity and conductivity of extracellular electrolytes in the microenvironment of a cell [53]; ϵ_{ex}^{tu} and σ_{ex}^{tu} are the relative permittivity and conductivity of extracellular electrolytes in the microenvironment of a tumor cell; ϵ_m and σ_m are the relative permittivity and conductivity of the cell membrane [54]; ϵ_{in} and σ_{in} are the relative permittivity and conductivity of intracellular electrolytes of a cell [52]; ϵ_{r-in} and σ_{r-in} are the relative permittivity and conductivity of the intracellular side of raft proteins [55,56]; ϵ_{r-ex} and σ_{r-ex} are the relative permittivity and conductivity of the extracellular side of raft proteins [57,58].

2.4. Thermal Homeostasis

The thermal processes have a complex nonlinear interaction with homeostatic regulation, which tries to keep thermal homeostasis. The hypothalamus receives thermal signals (primarily from TRP receptors) and acts to reduce the temperature. The principal effects are blood flow with vasodilation and sweating trying to cool using an evaporating process. The thermal regulation balances the incoming energy, which nonlinearly fluctuates in the equilibrium (Figure 9) of incoming energy [59]. The fluctuation has various physiological components, including the opposition sensory mechanisms [60] and the various relaxation times of the different processes. The basic relaxation times could be measured with NMR [61], and the complex processes by various physiological measurements [62,63].

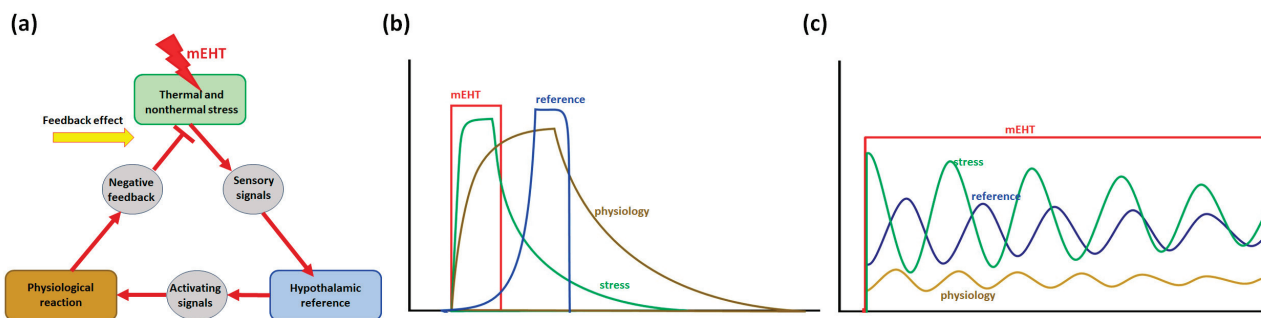


Figure 9. The temperature in the homeostatic range adapts to the new conditions, defining a new equilibrium state. (a) Thermal homeostasis has a negative feedback loop as the basis of regulation. (b) In a pulse of mEHT, the heat stress rises, and exponential decline returns to the baseline. The thermal reference (hypothalamus) and the physiological counter action (mainly the blood flow) have a time lag, acting later. (c) In continuing the mEHT impact, the stress, physiology, and reference point fluctuate decreasingly.

The temperature growth of local tissue in depth has a well-known character in time at constant absorbed power, defined by the specific absorption rate ($SAR = \frac{\text{Absorbed power [W]}}{\text{Mass of absorber [kg]}}$). The absorbed energy (E_{absorb}) heats the local target, increasing its temperature (T). The physiological feedback process has a condition-dependent delay. Still, thermal homeostasis tries to restore equilibrium after the reaction time with intensive heat exchange and electrolyte transport ($E_{transport}$), like blood and lymph. Some absorbed energy also heats the surroundings, initially nontargeted issues (E_{tissue}). Consequently, the energy which increases the temperature (E_T) is less than the incident E_{absorb} value. The absorbed energy grows the target temperature energy, but a part of the energy is used up for thermal homeostatic control (primarily the blood flow regulation) and heat conductivity to the neighboring tissues:

Considering the energy balance, the Pennes equation [64] describes the heating process:

$$\rho_h c \frac{\partial T}{\partial t} = \rho_h SAR - c_b \rho_b w_b (T) (\Delta T) - k_h \nabla^2 T + q_0 \rho 1.1^{(\Delta T)} \tag{1}$$

The terms in the Equation (1) are as follows: $\rho_h c \frac{\partial T}{\partial t}$ = Energy for the temperature grows, $\rho_h SAR$ = Energy for the in the target

Absorbed energy from outside incident power, $c_b \rho_b w_b(T)(\Delta T)$ = Energy loss by homeostatic regulation (blood, lymph transport), and $(k_h \nabla^2 T + q_0 \rho 1.1^{(\Delta T)})$

Energy loss by tissue environment.

The c , ρ , and w are the specific heat, density, and perfusion. The subscripts denote the healthy tissue (h) and the blood (b) values. When the Pennes equation is applied to the tumor, the subscript will be t . The w_b is the blood perfusion rate and T and t are the temperature and time, respectively. The analytical solution of this partial differential equation is a difficult task. The first approach uses the Green function [65,66] and the Green heat kernel function [67] and uses an analytical solution [68]. The point source Green function solution [69] can simulate the nanoparticle or thin needle with very local heating.

The differential equation can be well approached with differences when the time changes. The homeostatic control is slow enough and does not allow rapid changes, so the differences in the values can be used to approach the solution of the differential equations with enough accuracy, neglecting the minority effects in (1) at constant SAR. Introducing the temperature difference instead of the differential, $\Delta T = T - T_b$, we obtain the following:

$$\frac{\partial \Delta T}{\partial t} + \frac{1}{\tau} \Delta T = \frac{SAR}{c} \tag{2}$$

where $\tau_0 \cong \frac{1}{c_b w_b}$ is the relaxation time in the perfusion model according to the Pennes Equation (1). The solution to this difference-equation is as follows:

$$\Delta T = \frac{SAR}{c_b w_b} (1 - e^{-\frac{t}{\tau}}) \tag{3}$$

We must approximate the relaxation time in cancerous tissue. In rough approximations, the blood perfusion of the tumor is 0.833 kg/sm³ when the temperature is below 41 °C and 0.416 kg/sm³ when the temperature is above it [70]. Therefore, the following applies:

$$\begin{aligned} \tau_{<41} &\cong \frac{10^3}{0.833} = 1200 \text{ s} = 20 \text{ min}, \\ \tau_{>41} &\cong \frac{10^3}{0.416} = 40 \text{ min} \end{aligned} \tag{4}$$

However, the inflammatory reaction occurs in the surrounding tissues and not in the tumor itself, so the relaxation time in this constant perfusion model is as follows:

$$\tau_0 \cong \frac{10^3}{4} \cong 4.2 \text{ min} \tag{5}$$

It is the “wash-out” time of the heat perturbation in the tissue [71], depending on the blood flow of the studied tissue. This is the tissue relaxation after a heat shock by the blood-flow washout process. Healthy tissue is measured at ~ 4 – 7 min. The clinical standard average of SAR in the MHz range is 6 min [72], and we use it as a standard physiological average relaxation time, $\tau_{ave} = 6 \text{ min}$.

The time of thermal washout could be modified by changing the metabolic rate by lowering the temperature, and it will make the tail of the washout function longer in time. Consequently, a longer $t'_0 > t_0$ a value will be added to the simple exponential, which depends on the decreased metabolism by the cooling process. This additional effect will cause a time lag because of the actual physiological time of the metabolic reaction. Due to the physiological self-time, which is about the same as the thermal washout physiological time, is approximately 6 min.

Thermal homeostasis regulates the temperature of the tissue. The absorbed energy drives temperature growth, but the increased blood flow, as an energy sink, counteracts. Over time, thermal homeostasis fixes the temperature in the thermal equilibrium, forming a steady-state process. The temperature, in this case, becomes constant. The absorbed energy substitutes the losses by $E_{transport}$ and E_{tissue} , without changing the temperature (Figure 10).

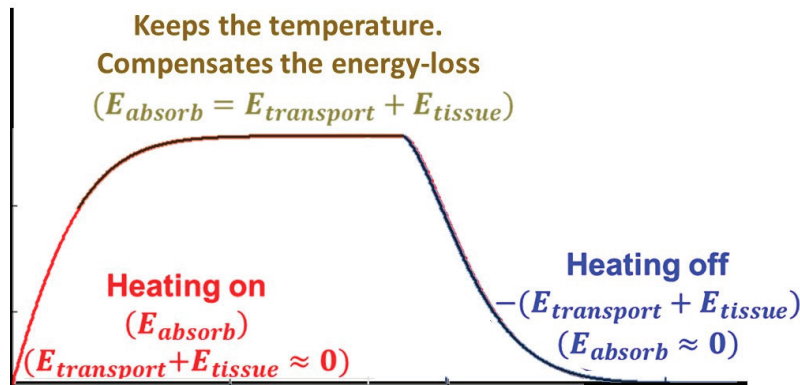


Figure 10. The phases of the temperature development while the absorption is on/off.

All these dynamic changes depend sharply on personal homeostatic regulations, the electrolyte transport in the targeted volume, and the incident power. The dynamism of the heat delivery may also profoundly change the heating process [69]. Due to the physiological changes (first due to the blood-stream variation), the linear dependence breaks (Figure 11). When the SAR value is moderate, thermal surveillance develops an equilibrium [73]. However, a higher SAR (rapid temperature gain) could cause overshooting, compensated only after an overshooting, but the SAR could be as much as the homeostatic regulation cannot fix the temperature. Notably, the tumors are usually hotter than their host due to the high proliferation and energy use, even in thermal equilibrium.

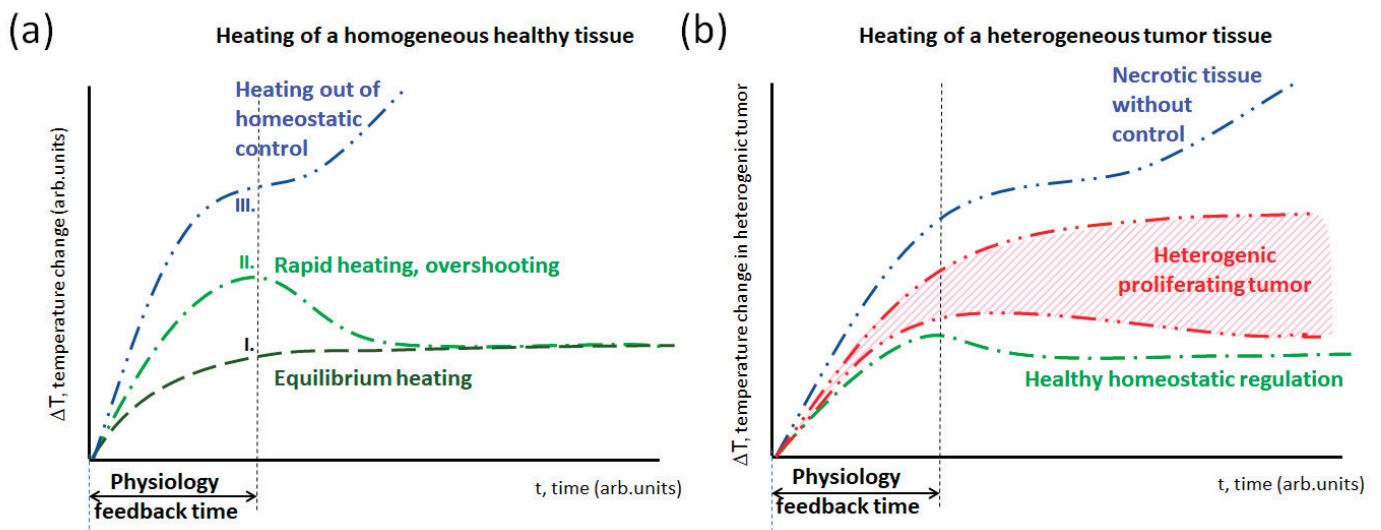


Figure 11. The incident heat could determine the different processes of the control process of thermal homeostasis. (a) (I) Is the simplest saturation, a steady state heating of a healthy tissue When the SAR is moderate, the temperature rise is relatively slow (this is the case in most regional treatments). (II) The SAR is high enough for sudden temperature changes, while the physiological thermal feedback

only reacts later and regulates the saturation value (this is the case in high-energy local treatments). (III) The SAR is huge; feedback is not able to moderate the temperature, and it toxically burns (this is the case in most ablation treatments). (b) The tumor is highly heterogenic, and the temperature develops differently in its parts [71,74]. The high proliferation rate of the tumor enhances the deviation from the healthy equilibrium. A significant volume of the tumor could be necrotic without control.

The blood delivers the drugs for chemotherapies and oxygen for radiotherapy, so its behaviors are essential. The timing of the deliveries and washing out the toxic species are important factors to consider. In hyperthermia applications, the thermal washout time is driven by the *BF* and differs from the nonthermal clearance of molecules (like radio-farmacons, tracers, blood-delivered molecules, drugs, particles, or cells) from the tissues. The main difference is in the mechanisms of diffusion, which are different for various blood-delivered particles or molecules and heat. The thermal washout is also a complex process mainly driven by the *BF*, but not determined by it alone. The investigations of the clearance of tracers clearly show that the clearance (wash-out) tightly depends on the *BF* but these parameters are not equal; instantaneous mixing with metabolic changes and diffusion breaks the unity. Also, the metabolic heat does not directly affect the clearance, while the thermal washout is directly modified by it.

A “similarity” could be observed in the washout of tracers [74], which is a rescaling of the time, showing a similar scaling behavior as we saw in the heat-up process. The washout scaling “similarity” is also present in the wash-in of the tracer [75]. An important observation in contrast material studies is that the enhancement of the contrast material decreases with the temperature growth while increasing with the thermal cooling coefficient [76]. The main message is the high variability of the *BF* with tumor entities, and the tumors have a massively heterogeneous *BF*, having a gradient from the center to the periphery.

Hyperthermia protocols usually apply step-up heating specialized to the patient’s sensing. The heat pain effectively limits the hyperthermia dose. The patient senses the process and thus guides the personalized homeostatic heating-up dosing. It is more patient-friendly, causing as little discomfort as possible because the patient’s homeostatic control is active. The central task is to provide the proper dose. The actual protocol for the treated patient must be optimized to the given conditions and curatively effective with a high standard for safety, limiting the applied dose. This concept is entirely different from the conventional hyperthermia goals because instead of trying to produce isothermal volumes (equal temperature in the tumor), it uses heterogenic heating, following the heterogeneity of the tissue itself. This far-from-equilibrium heating keeps the driving force between the heated membrane rafts and its environment, pumping the heat from these nanoclusters to the cell interior.

When the intended dose is too much, it has to be corrected via personal notes. On the other hand, when the protocol presets a low energy dose, higher energy can be applied until the patient indicates the personalized limit. Overheating is practically impossible because the skin’s surface has the highest thermal load, and heat sensing is also there. This personalized dose regulation is the main factor for safety and, together with this, for efficacy. In proper step-up heating, no continuous increase of the temperature is applied. The primary governing process is homeostasis, so the heating fits that equilibrium. A steady-state gradual heating is necessary. The physiological response time must be considered. This characteristic time is when the homeostatic equilibrium is re-established in the new conditions after a definite disturbance. The average wash-out time in humans is approx. five to seven minutes. Considering the transient “break” of six min, the step-up heating is shown in Figure 12. A detailed calculation shows the rise in temperature and its dependence on the power function in step-up heating [49,50].

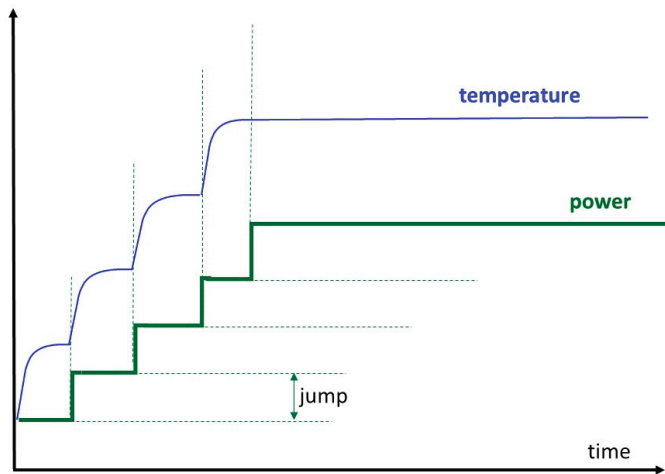


Figure 12. Step-up heating considers physiological adaptation. Step-up heating maintains the steps until homeostatic equilibrium. The provided cumulative energy could vary with the time intervals of the steps.

3. Semi-Adiabatic Synergy (SAR)

At the start of the heating, when the physiology does not impact ($E_{transport} = E_{tissue} = 0$), the complete E_T makes a temperature increase, so in this case, the following applies:

$$E_T = E_{absorb} = m_t \cdot c_t \cdot \Delta T \tag{6}$$

where m_t is the heated tumor mass, c_t is the specific heat of the tumor, and ΔT is the temperature increase. In a shorter time than the actual relaxation of the tissue, the thermal homeostasis does not modify the absorbed energy, and the SAR directly defines the temperature development. Using (6) in this initial stage as follows:

$$SAR = \frac{E_{absorb}}{m_t \cdot \Delta t} = \frac{m_t \cdot c_t \cdot \Delta T}{m_t \cdot \Delta t} = c_t \cdot \left(\frac{\Delta T}{\Delta t} \right) \tag{7}$$

This initial period is too short, causing a physiological reaction with blood perfusion. It is “semi-adiabatic”, and only the SAR acts for temperature development, neglecting the thermal homeostatic processes led by blood perfusion, but additionally keeps away from the growing metabolic rate, the change of the absorbed power due to the variation of electric and thermal parameters with the temperature, etc. All the absorbed energy appears like it would be a non-living target, so the thermal and nonthermal synergy appears. Due to this period not dealing with the homeostatic processes, the nonthermal effects occur more than in the further heating when the thermal control works. So, the nonthermal impact is dominantly active in this period Figure 13.

The temperature profile after this semi-adiabatic period declines with the slope of the temperature change and seeks thermal equilibrium without changing the temperature (Figure 14). This equilibrium temperature requests an energy dose, which replaces the lost energy by cooling.

The equilibrium process could be described with a stochastic explanation [49], approximating the different heat transfer parts. When thermal homeostasis stabilizes the temperature, the absorbed energy replaces that lost by heat conduction, convection, and radiation to keep the equilibrium. When the temperature development deviates from the slope, going stationary, another so-called constant perfusion rate model could be introduced. We seek to equilibrate the dominant factors that remain in the Pennes Equation (1) as follows:

$$\rho_h c_h \frac{\partial T}{\partial t} = \rho_h SAR - c_b \rho_b w_b(T) (\Delta T) \tag{8}$$

The solution of (8) is as follows:

$$\Delta T = \frac{\rho_h SAR}{c_b \rho_b w_b(T)} \left(1 - e^{-\left(\frac{t}{\tau_0}\right)} \right) \quad (9)$$

where

$$\tau_0 = \frac{c_h \rho_h}{c_b \rho_b w_b(T)} \cong \frac{1}{w_b(T)} \quad (10)$$

is the time constant of the constant perfusion model. Using realistic parameters, we obtain $\tau_{cp} \cong 6$ min. When t is large, the system reaches thermal equilibrium, and no further rise in the temperature is observed:

$$0 = \rho_h SAR - c_b \rho_b w_b(T) (\Delta T) \quad (11)$$

From (11), the equilibrium temperature is as follows:

$$T_{eq} \cong 1.4 \frac{SAR}{c_b \cdot w_b(T_{eq})} = 1.4 \frac{SAR}{perfusion} \quad (12)$$

When the power is switched off, the target cools down, determined by the wash-out time.

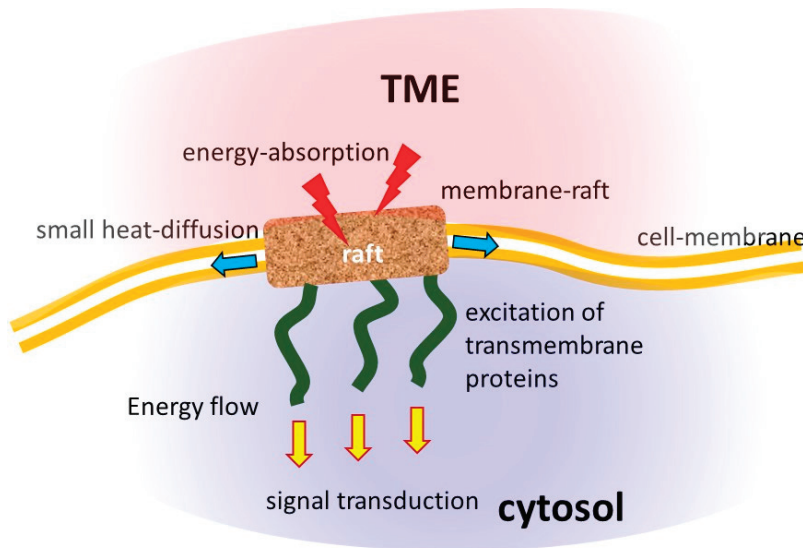


Figure 13. The semi-adiabatic heating of the raft structure. The energy absorption is focused on the rafts. They are embedded in a well-insulating lipid layer, which has bad heat conduction, increasing the time lag of the body’s reaction to the heating process.

The impedance matching covers the cooling process and stabilizes the homeostatic control in the subcutis layer under the electrodes. Significant differences appear in the doses during the heating period, showing an increase in the temperature until it reaches the stable thermal equilibrium. The emphasis on the thermal or nonthermal processes makes the principal difference between the two heating periods. The nonthermal period primarily depends on the heating technique, the position of the tumor, and the initial power density $\left[\frac{W}{cm^2} \right]$. The semi-adiabatic period in radiation is between 10 and 15 min [77], which is about 20% of the complete session time. However, some protocol modifications could change the ratio. Step-up heating typically increases relative nonthermal dominance because the power proceeds before the thermal regulation becomes active. Of course, the thermal and nonthermal effects are strongly synergistic and tightly interact (Figure 15).

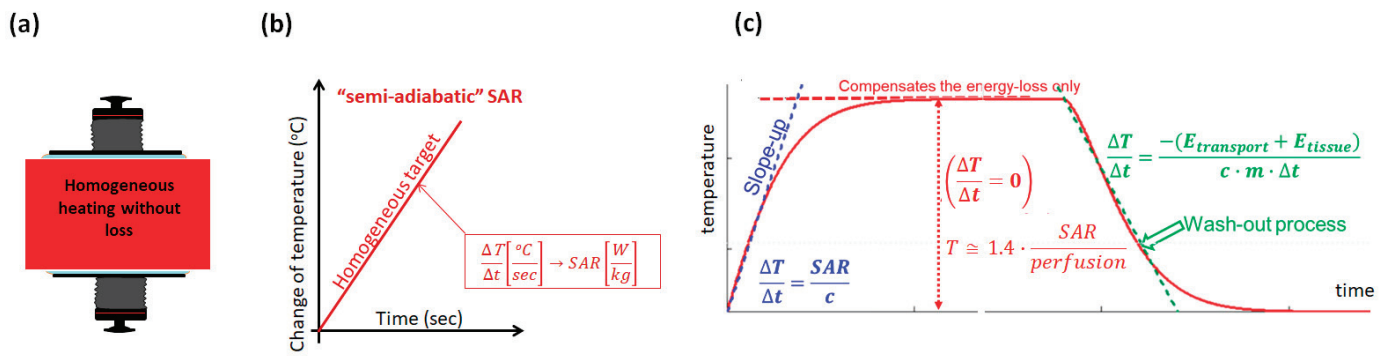


Figure 14. Heating process. (a) The target heated homogeneously. (b) The starting period heats only the target. It is semi-adiabatic. The physiological feedback has a conditional delay. (c) When the thermal regulation makes equilibrium, the temperature does not change, and the perfusion of the electrolyte transfer compensates for the incoming energy. When the power is switched off, the perfusion and tissue heat transfer defines the slope down (wash-out).

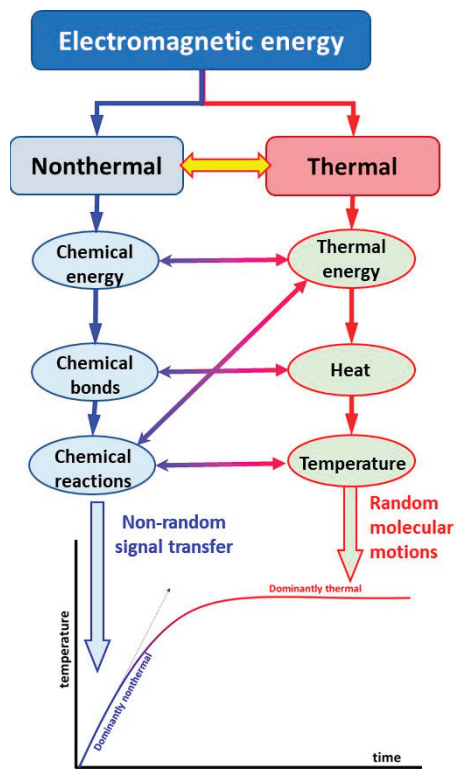


Figure 15. The thermal and nonthermal effects work in synergy. The nonthermal dominates the semi-adiabatic heating period, while the thermal dominates the equilibrium.

The length of the semi-adiabatic synergy (SAS) period depends on many factors. In addition to the leading thermal homeostasis, the heterogeneity of the target and the dynamism of the forced energy absorption define the length of the semi-adiabatic period (Figure 16). When the heating has no loss by various heat exchanges, the slope of the temperature change is linear. In heterogeneous heating, the small parts of the material absorb most of the energy, gradually heating the volume. In this case, a shorter period remains adiabatic, and the heat conduction actively spreads the energy. When the system has no other energy losses (well isolated), the temperature growth has no equilibrium. When the thermal homeostatic dynamism is active, the heat is gone quickly and forms an equilibrium.

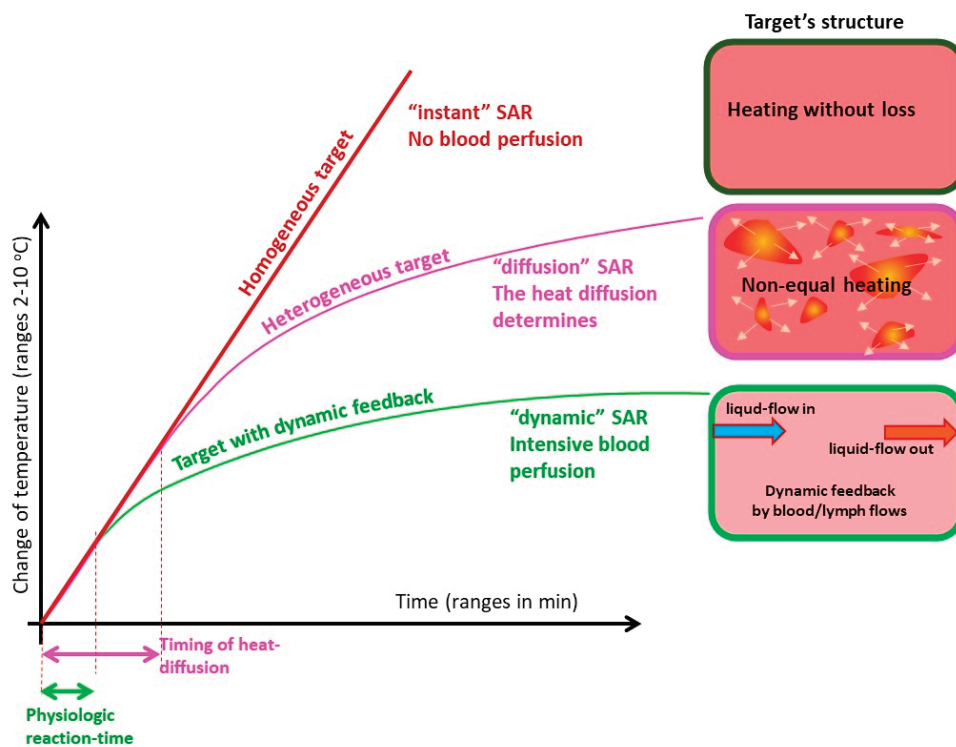


Figure 16. The temperature change strongly depends on the properties of the target. When there is no loss of heat, the target is a homogeneous material and thermally isolated (adiabatic heating); then, the temperature growth is linear, and no equilibrium exists. When only diffusion drives the temperature variation in heterogeneous material, the decline from the adiabatic slope starts, and the system seeks equilibrium at a high temperature. However, when the system has inside transports, the convective energy exchange is added to the conductive one, the radiation cools down the surface, and the dynamic equilibrium appears soon.

3.1. Semi-Adiabatic Synergy (SAS) Promotes Apoptosis

Two main categories (and many of their variants) cause cell death. Necrosis is the sudden rupture of the cell. The cytoplasm and the cellular organelles located freely in the extracellular matrix could cause inflammation or, in large quantities, could be toxic. Another major variant is apoptosis, where cell death is gentler. The cellular components became fragmented and could be embedded in lipid membranes for safe elimination. An extremely gentle fragmentation happens in immunogenic cell death when damage associated with a molecular pattern is released in an undestroyed form [78]. The unhurt molecules deliver information about the genetic structure of the cancer cell, which could be used to adapt the available dendritic cells for immune surveillance to overcome the evading capability of cancer [79,80]. The tumor-specific adaptive immune T cells (killer and helper cells) perform immune attacks on distant metastases to where the bloodstream delivers them [81], which was observed in human studies as well [82,83].

Nonthermal activity was widely studied [84,85], and its synergy with a thermal component of absorption is also studied [4,5]. The synergy of the thermal and nonthermal effects recognized in mEHT increases apoptosis compared to the only thermal conditions [86–88], which has been shown to be complementary to chemotherapy [89] and radiotherapy [90]. The effect of modulation as a purely nonthermal impact also increases apoptosis [91].

3.2. In Vitro Verification

In cell-line experimental conditions [49], it was proven that the increased temperature is proportional to the absorbed power (SAR) in semi-adiabatic states as shown in (7), while exponential declines from this linearity, as in (9), and equilibriums appear at constant temperature (12). The SAS conditions have nonthermal dominance. Apoptosis during

this linear changing period may be compared to the equilibrium to study the thermal and nonthermal impact difference on the cellular level [49]. The experiment measured apoptosis during the two definite periods of energy absorption. The regular mEHT of the adenocarcinoma human alveolar basal epithelial cell line, A549 treatment, was performed at 42 °C starting from 25 °C. The heating details were studied by divided periods, as shown in Figure 17:

1. Phase 1. heated the cells from the room temperature (25 °C) to the usual starting temperature of the in vitro experiments, the human body temperature (37 °C);
2. Phase 2. heated the cell culture from 37 °C to 42 °C, which is the equilibrium temperature of many standard hyperthermia treatments expecting the thermal impact;
3. Phase 3. kept the equilibrium 42 °C for 30 min;
4. Phase 4. continued the equilibrium heating at 42 °C for the next 30 min.

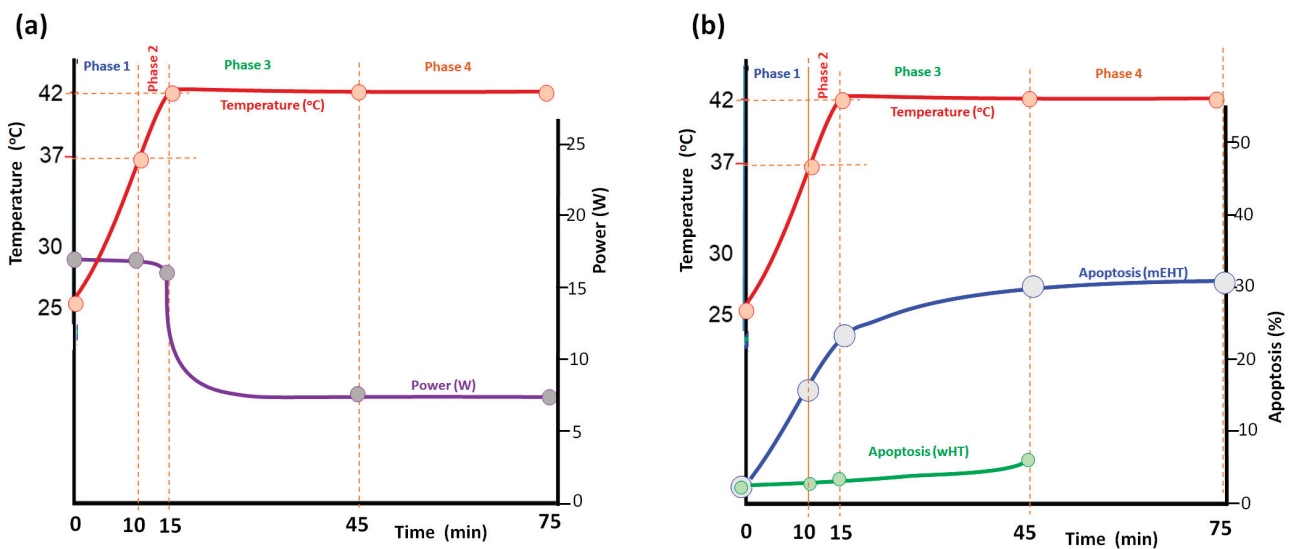


Figure 17. Analyzing the heating process in four phases: heat from 25 °C to 37 °C, from 37 °C to 42 °C, and keep the 42 °C for 30 and 60 min. (a) The power and temperature diagram: phase I and II 18 W, phase III and IV 7.5 W, and the absorbed energy in Phase I is 10.8 kJ, in Phase II 5.4 kJ in Phase III 13.5 kJ, and in Phase IV 13.5 kJ [49]. (b) The development of apoptosis in mEHT and wHT applications in the A549 cell line.

The SAS period was 15 min, (with 18 W power) the equilibrium period 30 min (7.5 W). In this case, the apoptosis (measured by Annexin V positive cells) was 31.18%. Remarkable apoptosis was measured in phases I and II, while in the longer phases III and IV, the apoptotic activity was low. Replacing the 1st phase with purely thermal water bath (WB) heating, apoptosis decreased to 22.6%, and when the 2nd phase was also replaced with WB, apoptosis decreased further to 7.2%, showing that the non-thermal effect in the heating up SAS period had produced the majority of apoptosis (Figure 18). Counting that the SAS had 18 W for 15 min (16.2 kJ), equilibrium needs only 7.5 W of power for 30 min (13.5 kJ). The energy-corrected expected apoptosis in the equilibrium period increased a little and became ~8.64%, but much smaller than the apoptosis in the SAS period. With the WB (42 °C) and the incubation (37 °C), applied for the same time when the mEHT treatment was performed, apoptosis was low at 2.61% and 2.42%, respectively.

Numerous control experiments were performed [49], substituting the various phases with WB or incubation; the results showed the same dominance of the SAS period in apoptotic production. When the treatment time in the equilibrium temperature (42 °C) was doubled (added Phase 4.), apoptosis grew significantly from 31.18% to 31.63%. However, when the equilibrium period cooled down the cell line to 37 °C for 5 min and up again to 42 °C in the next 5 min, apoptosis significantly increased to 51% altogether (Figure 19). In this experiment, the pulsing increased apoptosis to more than two times more than the

standard mEHT at the same time and same temperature. This remarkable result gave rise to the idea of the pulsed mEHT development.

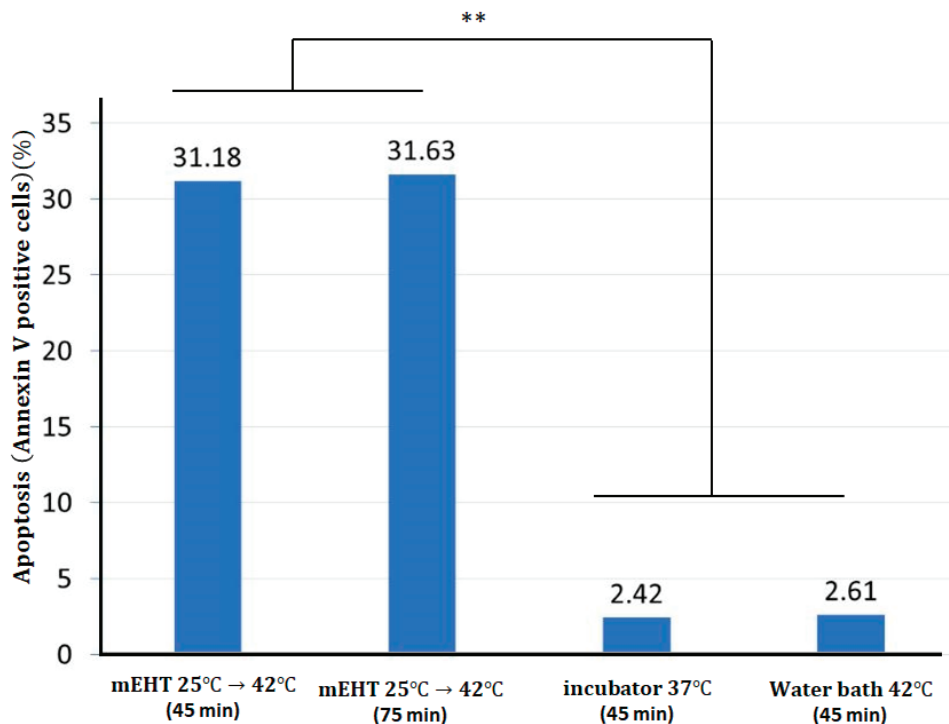


Figure 18. The apoptosis is high in the mEHT, keeping the treated adenocarcinoma human alveolar basal epithelial cell line, A549, at 42 °C, and statistically does not differ from the time of keeping the equilibrium (45 min or 75 min treatments), but the water bath with the same 42 °C has significantly less apoptosis in the same cell line and, at the same time [49]. This difference was observed by others, too [84,86]. It is noteworthy that the process in the incubator at 37 °C has statistically the same result as the water bath at 42 °C. Results are significant (**, $p < 0.005$).

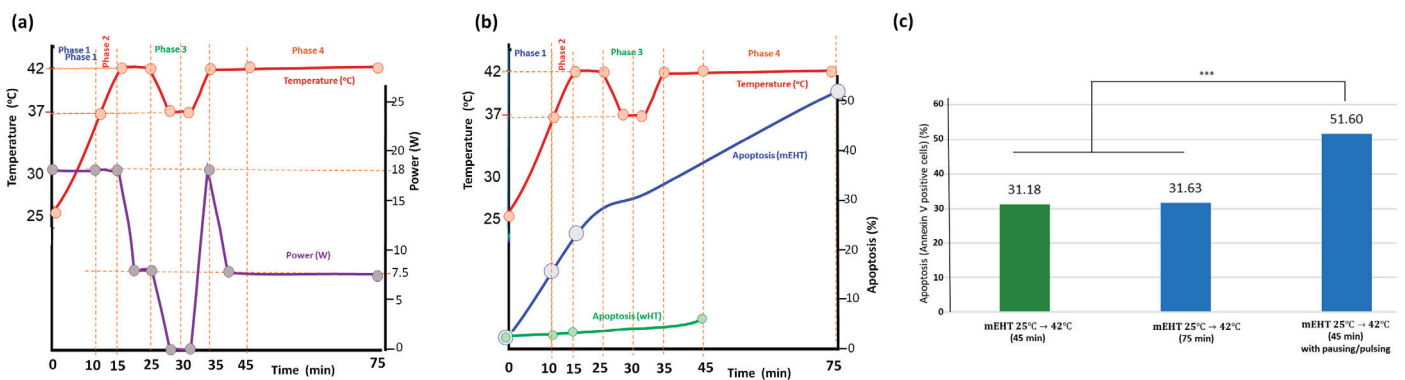


Figure 19. The interruption by pause/pulse power made a significant improvement in apoptosis. (a) the power impulse and the consequent temperature change in time. (b) The apoptosis development over time with mEHT and wHT is related to temperature. (c) Apoptosis in different treatment conditions. The difference between the continuous and pulsed treatment is highly significant (***, $p < 0.0005$).

The pulsing role in apoptosis well supports the importance of the semi-adiabatic heating period. At the same time, it proves the decisional role of the nonthermal effects on apoptosis. These experiences were verified in vivo.

3.3. In Vivo Verification

The in vivo rat model used immunocompetent animals [92]. An RG2 [D74] (ATCC®, CRL 2433™, Manassas, VA, USA) astrocytoma [93] was inoculated into the parietal lobe of syngeneic Fischer 344 rats. The inoculation was syngeneic, genetically sufficiently identical, and immunologically compatible to allow for transplantation. There were three groups (three animals in each): (1) sham, (2) continuous mEHT, and (3) periodically stopped, pulsed mEHT treatments. The pulsing periods were 6 min with a 0.5 duty cycle, using the homeostatic relaxation time shown in Figure 20. A gadolinium-based MRI contrast agent (MAGNEVIST®, 0.5 mmol/mL, 0.2 mL/kg bdw) was used to detect lesions associated with an altered blood-brain barrier, and the volume of the tumor was quantified at the 8th and 15th days after inoculations. The brain temperature was evaluated indirectly by measuring the temperature in the middle ear and using a correlation curve set up in an earlier experiment.

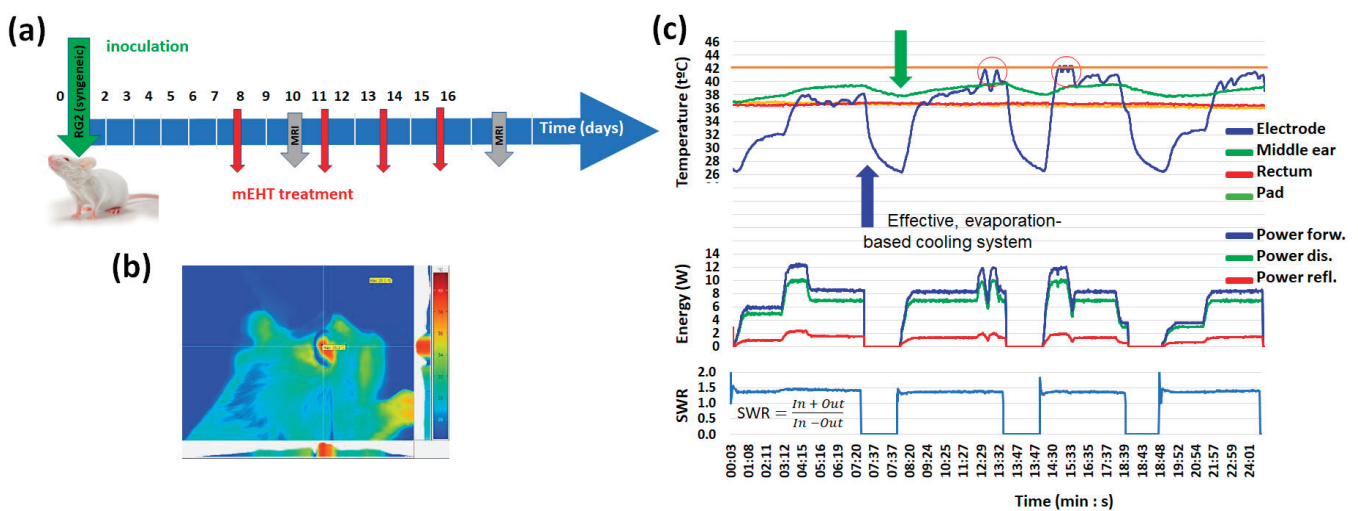


Figure 20. (a) The applied protocol. (b) Well-localized energy targeting on the head of the rat. (c) The parameters during the treatment [93].

The tumor growth rate between the 8th and 15th days after inoculations was, in the case of sham animals, 23.73 ± 12.15 , in the treated with classical mEHT protocol, 19.08 ± 0.49 , and in the treated with pulsing mEHT protocol, 6.83 ± 2.02 (Figure 21).

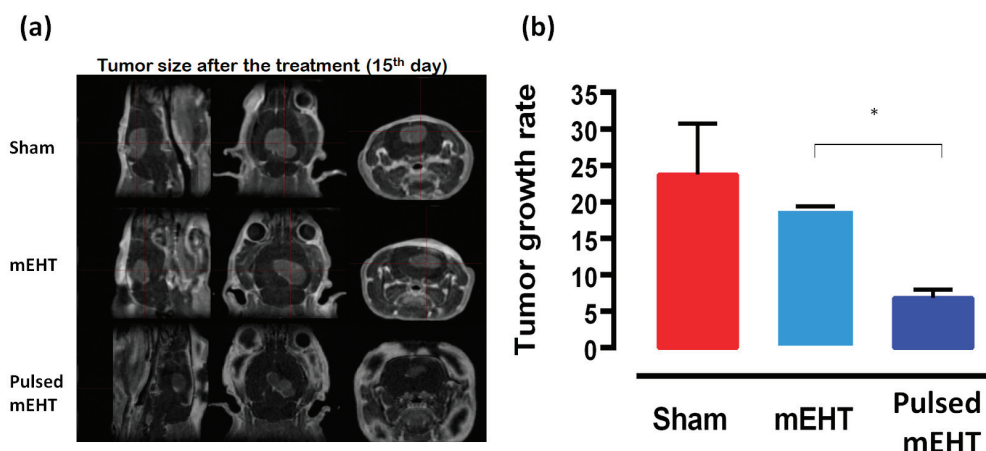


Figure 21. In vivo verification of the advantage of pulsed mEHT. (a) MRI imaging of the tumor 15th-day post-treatment with the Mediso nanoScan 1T small animal MRI system and a 3D image acquisition sequence MAGNEVIST®, 0.5 mmol/mL, 0.2 mL/kg body. (b) Tumor growth rate after the treatment (15th day) [92]. Results are significant (*, $p < 0.05$).

The immunohistochemical analysis shows the highest effects of the extracellular release of HSP70 in pulsed treatment. The extracellular HSP70 molecule has a decisional role [94] in tumor-specific immune reactions, delivering information for antigen-presenting and killer T cell priming [95,96]. The reduction of the Ki67 protein, which marks proliferation, shows the suppression of the malignant activity in the rat highest with pulsed mEHT, Figure 22.

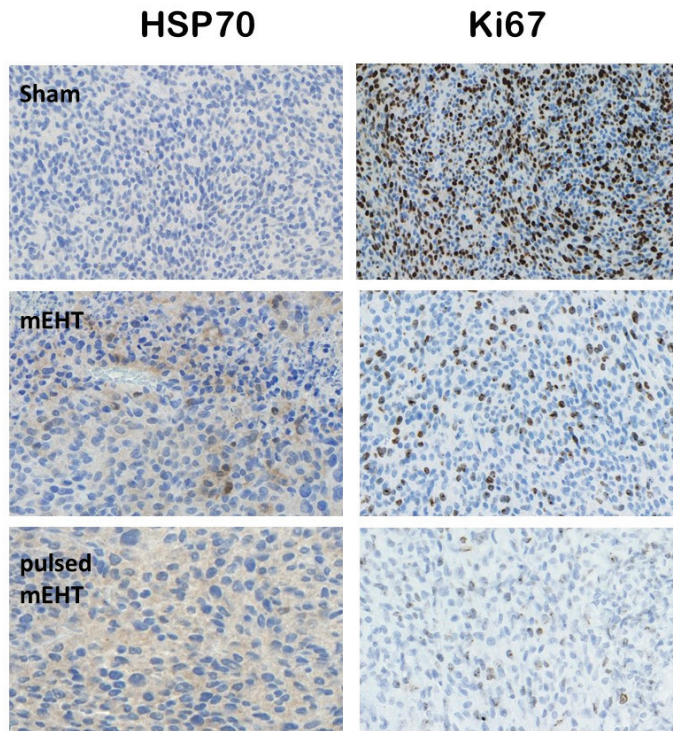


Figure 22. The increase of the extracellular HSP70 and the reduction of the Ki67 proliferation marker significantly increased in the pulsed experiment [92].

4. Pulsing Modulated Electro Hyperthermia

It is early knowledge that the blood flow and the speed of the heat delivery are connected. Rapid heating well differentiates the blood flow between the tumor and healthy host, while at slow heating, this difference tends to disappear [78], even when both were performed for 20 min at 43 °C. In an early experiment, a heating pulse (45 °C, 10 min) was used to treat experimental rhabdomyosarcoma BALL12 cells before continuous hyperthermia exposure for 3 h at 42.5 °C [97]. The starting pulse had a noticeable role in the results of the hyperthermia procedure. These observations emphasize the role of the semi-adiabatic heating period as one of the factors in the selection. Pulsed hyperthermia in cancer treatment refers to a technique where heat is applied to tumor tissue in short, controlled bursts rather than continuously. This approach can potentially enhance the effectiveness of cancer treatments while minimizing damage to healthy surrounding tissues. Pulsing is not a new heating technique. The precise temperature adjustment often uses pulsing for preciosity, like in the incubators [98]. Hyperthermia in cancer therapy also uses thermal cycling to enhance even the anticancer effect of natural compounds in pancreatic malignant cells [99], and it was also used in human treatment [100].

Continuous hyperthermia can also damage healthy tissues surrounding the tumor. Pulsed heating addresses this concern by delivering heat in cycles, having a heating phase (applied for a short duration and raising the temperature to the desired level), and following it with the resting phase (heating is stopped, allowing the tissue to cool down partially). This cycling provides for the following:

- Reduced risk of damage to healthy tissues: since healthy tissues cool down faster than tumors, they experience less heating during the resting phase;

- Potentially enhanced tumor damage: some tumor cells might be more susceptible to heat when exposed to pulsed heating than continuous heat;
- Improved treatment tolerability: patients may experience fewer side effects due to reduced overall heat exposure.

The nonthermal effects of pulsed electromagnetic fields have also been investigated [101] and are shown to have a harmful nonthermal effect when the pulsing power is high. Damage by the pulsing heat treatment is also displayed in skin layer experiments [102] and well applicable for the chemical and thermal activation of the TRPV3 vanillin receptor [103], which otherwise has a role in immunogenic effects in mEHT applications because the mechanism of these channels could be modified by electric field [5]. An essential application of the pulsed electric treatment makes the transient reversible opening of the blood-brain barrier (BBB) [104–106]. This non-invasive method could be applied to promote drug delivery to the brain, which the BBB blocks. The opening mechanism is connected to the impact on tight junctions even without thermal effect [107]. When the power has a periodic increase, the applied step-up heating is also a pulsed process with very low frequency. The pulsed electric field (PEF) heating has particular applications in pain management [108,109]. The oncological applications have just started and have a good perspective [110]. The pulses are short (most nanoseconds) [111]. Longer heating times (50 s) by magnetic pulses shows the usual heating pattern for breast cancer hyperthermia treatment [112] and for induced damage of the tumor microcirculation. Electrochemotherapy (ECT) is developing on this basis. Continuous ECT (galvanic treatment) is an old therapy [113], also developed in the early 1990s in Bad Aibling (Germany) [114]. The PEF application is quickly developing in electroporation [115]. While the “pulsing technique” is commonly used in hyperthermia treatments, capacitive hyperthermia specifically does not utilize this technique broadly.

The new mEHT with a pulsing technique is thermally assisted and provides all the advantages of continuous mEHT operation. The above-described selective mechanisms target the membrane rafts and the membrane microdomains, which have a role in intracellular signal excitation and regulation, as well as the ICD processes. The targeting of membrane rafts helps to develop novel complementary therapies to increase the sensitivity to chemotherapeutic compounds, opening the gate for drug penetration into the cell and reducing multidrug resistance [116]. The capacitive coupling could also give a unique advantage in modifying the membrane voltage [117] with a low electric field.

The personal sensing homeostatic step-up heating solves safety problems when the patient communicates about identifying any discomfort. The question naturally arises about the reliability of subjective sensing, but personal sensing is the best available method for monitoring the heating process. Personal sensing is typically used to drive many protocols active in today’s medical treatments. When the patient cannot tolerate the prescribed dose, it is lowered, trying to fit it to the personal tolerance level. There is no reliable personalized dosing without controlling the guidance of personal sensing. In pulsed heat treatment, immense power can be tolerated for the short pulsing time when the time between the two pulses is long enough to return the temperature to the tolerable zone, at least partially. In these conditions, personal sensing will be the average time of the power. The slow thermal and physiologic reaction to the rapid power absorption makes averaging possible. By applying heat in pulses, healthy tissue surrounding the targeted area has more time to cool between pulses, potentially minimizing damage and side effects. This can be especially beneficial for tumors located near sensitive organs or nerves.

4.1. The Pulsing Technique

The duty cycle is as follows:

$$D = \frac{\langle P \rangle}{P_p} = \frac{t_p}{t_r} \quad (13)$$

where $\langle P \rangle$ is the average, P_p is the pulsed power, t_p is the pulse width, and t_r is the repetition time. While the pulse “window is rectangular, the resulting heating pattern differs. It all depends on the thermal parameters of the targeted mass (Figure 23).

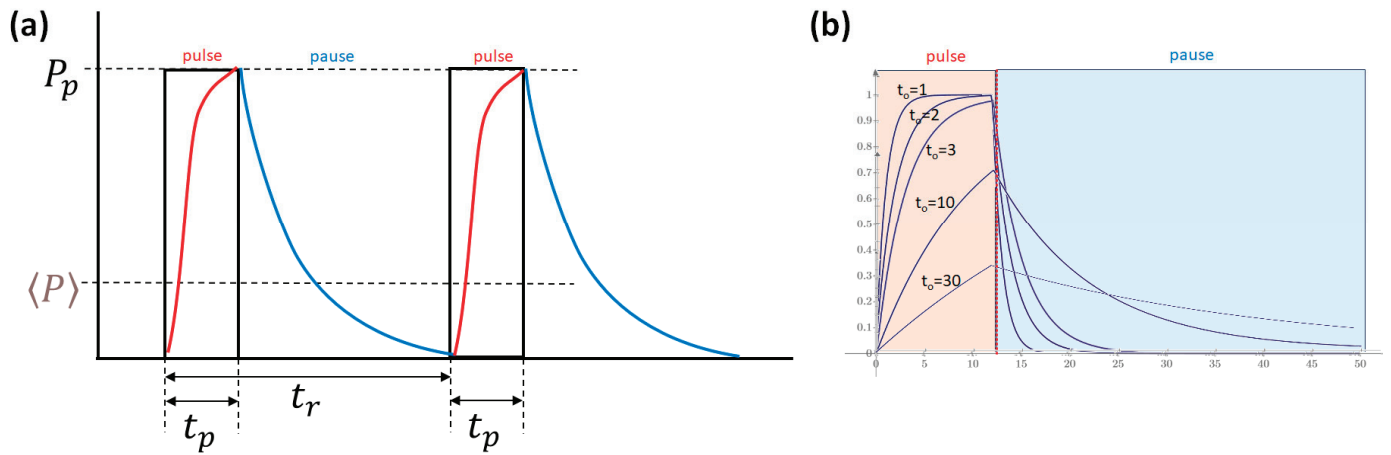


Figure 23. The electric pulsing and the thermal reaction differ. (a) The pulse heats the material, which is slower than the electric signal, and the end of the pulse starts a cooling process. (b) The thermal parameters of the target (t_0) define the relaxation time of heating–cooling phases. The change of t_0 may drastically change the thermal pulse at the same electric pulsing.

When the duty cycle is low, the average temperature is unchanged and remains on the baseline, having enough time to cool between the pulses. However, when the duty cycle grows, the cooling down period relatively shortens and could not be enough to reach the baseline again. In this case, the average temperature rises. The growing temperature follows roughly a cumulative Weibull function [49] $W = \exp\left(-\left(\frac{t}{t_0}\right)^n\right)$, where n is the shape parameter, and t_0 is the time parameter. Both depend on the target material (Figure 24).

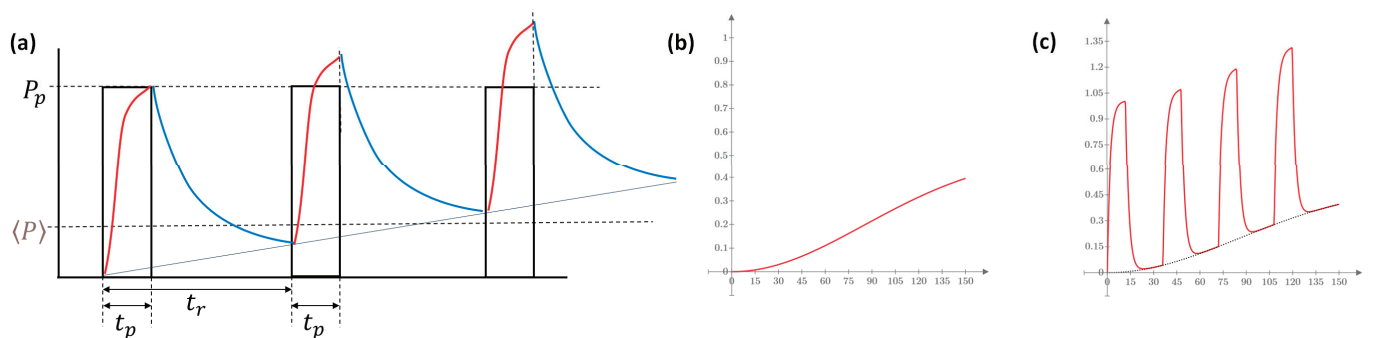


Figure 24. Effect of the duty cycle. (a) When the off-period of the pulsing is shorter than necessary for the thermal return to the baseline, the target cumulates the heat, and the overall average temperature grows. (b) The average temperature growth can usually be described with the Weibull function. (c) The pulsed heating process with Weibull heat-shape.

4.2. Advantages

The pulsing of mEHT has numerous advantages, as follows:

1. Enhanced Efficacy:
 - a. The active factor of the mEHT is the RF current, which selectively flows through the target. In pulsing conditions, the extreme power gives a proportionally sizeable current density, which causes an effect. Pulsed heating can be more

- effective at killing cancer cells than continuous heating at the same average temperature;
- b. The pulsing induces the semi-adiabatic start of temperature growth, which accounts for the most significant part of apoptosis and induces immunogenic processes;
 - c. In a low-duty cycle, increased blood flow to the tumor during the off pulses can bring in more oxygen and nutrients needed for the heat to damage the cells.
 - d. The high-power pulse may induce reversible electroporation, increasing synergic efficacy with complementary chemo and immune therapies;
 - e. Pulsed heating does not drastically influence homeostatic regulation as continuous heating does. So, the treatment and natural regulations are more effective in cooperative harmony;
 - f. Studies show that pulsed electric fields effectively relieve pain, improving patients' quality of life.
2. Control and Flexibility:
 - a. Pulsed heating allows for finer control over the temperature delivered to the target area. The pulse duration, frequency, and power can be adjusted to achieve the desired therapeutic effect while minimizing the heating of surrounding tissue;
 - b. The power in the pulses may be kept constant; only the duty cycle changes the average power, which determines the temperature. Like digital technologies, the continuous power (and constant energy absorption in a pulse) makes the dose more controllable;
 - c. The associated side effects are reduced due to the pulsed heating and its relatively long relaxing time with a low-duty cycle;
 - d. The synergy of the thermal and nonthermal electric absorption is more reliable;
 - e. Despite the large pulse power, skin and adipose burns are less likely because the subcutaneous blood flow is active, may quickly reduce the heat stress in the pausing period, the pulse is short to burn, and the low-duty cycle ensures the low average temperature on the surface, too.
 3. Potential Dose Reduction:
 - a. Due to potentially higher efficacy, pulsed heating might require lower overall heat doses than continuous heating, potentially reducing treatment time;
 - b. The specific benefits of pulsed heating may vary depending on the type of cancer, tumor size, location, and other factors.
 4. Technical advantages:
 - a. The reduced cooling facility makes designing a simpler and more efficient electrode system possible;
 - b. Forcing step-up heating is unnecessary; choosing the semi-adiabatic phase is automatic and self-adjusted;
 - c. The tuning is more accessible because the power (the pulse intensity) is constant during all the processes;
 - d. Having 200 W in continuous heating, the power is at a 36 cm depth (the heaviest patient) and is $\sim 15\%$ of the incident field, which is ~ 30 W. In the pulsed case, reaching the same temperature with 800 cap W pulses with 0.24 duty cycle (average power is also 200 cap W like it was in the continuous case), the power at 36 cm will be 120 W in pulses, which is a significant increase. I propose the idea that this method treats all depths in humans equally.

4.3. Limitations

While pulsed mEHT shows significant advantages in cancer treatment, there are still potential limitations and adverse effects. The severity of the possible adverse ef-

fects depends on various factors, such as individual health, treatment parameters, and tumor characteristics.

1. Local tissue damage: Although pulsed heating reduces overall heating time, localized areas within the treatment zone may still experience high temperatures, potentially leading to extended tissue damage. The selection mechanisms on the tumor localize it, so the host tissues are likely safe. Still, we may lose part of the immunogenic advantages by the necrotic way of tumor cell death;
2. Pain: The heating process can cause discomfort, and individual sensitivity varies. Some patients might experience more intense pain with pulsed heating than continuous heating, but the overall pain reduction after the treatment likely works for all;
3. Nerve effect: Depending on the location, pulsed mEHT could lead to local numbness, tingling, or other nerve-related issues, depending on the patient's state;
4. Systemic effects: Like any hyperthermia treatment, pulsed heating can cause systemic effects like thirstiness, fever, chills, fatigue, nausea, and vomiting. The severity of these effects depends on factors like individual health, treatment parameters, underlying medical conditions, and complementary medical applications;
5. Tumor-specific risks: The significantly high-power intensity in the pulses may cause rapid tumor lysis syndrome, which is toxic;
6. Unforeseen complications: As with any new medical technology, unforeseen complications are always possible. More research is needed to fully understand the long-term effects and potential rare side effects of pulsed mEHT. Open communication and regular monitoring during treatment are crucial to identify and promptly manage any adverse effects;
7. Technical challenge:
 - a. The pulsing power and temperature averages could differ depending on the tumor's thermal washout physiology, which patients may have differently.
 - b. The average power depends on the duty-cycle, so it does not serve as a dose in the mEHT as it was in continuous power. The dose could be only the integrative absorbed energy.
 - c. The pulsing can change the original $1/f$ modulation depending on its duty cycle.

5. Conclusions

The pulsed mEHT treatment gives additional advantages to the standard modulated electro-hyperthermia. This type of treatment provides promising improvements in terms of safety and efficacy. The additional impulse modulation (high-power pulsing) increases the mEHT efficacy. The increased penetration depth supports the treatment of deep-seated tumors for heavy patients, and the decreased thermal load on the skin and the adipose tissues increases the patient's safety and quality of life

Funding: This research was funded by Oncotherm GmbH, Troisdorf, Germany.

Conflicts of Interest: The author is a consultant of Oncotherm GmbH, Troisdorf, Germany.

References

1. Lurito, P.W. The message was electric. *IEEE Spectr.* **1984**, *21*, 84–96. [CrossRef]
2. Advertisement of German Electric Appliance Agency. In *Free Lance*; 1902; II, p. 18. Available online: <https://paperspast.natlib.govt.nz/newspapers/NZFL19020419.2.21.1> (accessed on 24 June 2024).
3. Andocs, G.; Renner, H.; Balogh, L.; Fonyad, L.; Jakab, C.; Szasz, A. Strong synergy of heat and modulated electro-magnetic field in tumor cell killing, Study of HT29 xenograft tumors in a nude mice model. *Strahlenther. Onkol.* **2009**, *185*, 120–126. [CrossRef] [PubMed]
4. Szasz, A. Thermal and nonthermal effects of radiofrequency on living state and applications as an adjuvant with radiation therapy. *J. Radiat. Cancer Res.* **2019**, *10*, 1–17. [CrossRef]
5. Szasz, A.M.; Lorant, G.; Szasz, A.; Szigeti, G. The immunogenic connection of thermal and nonthermal molecular effects in modulated electro-hyperthermia. *Open J. Biophys.* **2023**, *13*, 103–142. [CrossRef]

6. Szasz, A. Heterogeneous heat absorption is complementary to radiotherapy. *Cancers* **2022**, *14*, 901. [CrossRef] [PubMed]
7. Szasz, A. The capacitive coupling modalities for oncological hyperthermia. *Open J. Biophys.* **2021**, *11*, 252–313. [CrossRef]
8. Kakehi, M.; Ueda, K.; Mukojima, T.; Hiraoka, M.; Seto, O.; Akanuma, A.; Nakatsugawa, S. Multi-institutional Clinical Studies on hyperthermia combined with radiotherapy or chemotherapy or chemotherapy in advanced cancer of deep-seated organs. *Int. J. Hyperth.* **1990**, *6*, 719–740. [CrossRef]
9. Egawa, I.; Watanabe, S.; Ohno, Y.; Morita, K.; Tominaga, S.; Onoyama, Y.; Hashimoto, S. A randomized clinical trial of hyperthermia and radiation versus radiation alone for superficially located cancers. *J. Jap. Soc. Ther. Radiol. Oncol.* **1989**, *1*, 135–140.
10. Otsuka, T.; Yonezawa, M.; Kamiyama, F.; Matsushita, Y.; Matsui, N. Results of surgery and radio-hyperthermo-chemotherapy for patients with soft tissue sarcoma. *Int. J. Clin. Oncol.* **2001**, *6*, 253–258. [CrossRef]
11. Doi, O.; Kodama, K.; Tatsuta, M.; Higashiyama, M.; Aoki, Y.; Kuriyama, K.; Tateishi, R. Effectiveness of intrathoracic chemothermotherapy for malignant pleurisy due to Ewing's sarcoma: A case report. *Int. J. Hyperth.* **1990**, *6*, 947–963. [CrossRef]
12. Ishikawa, T.; Kokura, S.; Sakamoto, N.; Ando, T.; Imamoto, E.; Hattori, T.; Oyamada, H.; Yoshinami, N.; Sakamoto, M.; Kitagawa, K.; et al. Phase II trial of combined regional hyperthermia and Gemcitabine for locally advanced or metastatic pancreatic cancer. *Int. J. Hyperth.* **2012**, *28*, 597–604. [CrossRef] [PubMed]
13. Masunaga, S.; Hiraoka, M.; Takahashi, M.; Jo, S.; Akuta, K.; Nishimura, Y.; Nagata, Y.; Abe, M. Clinical results of thermoradiotherapy for locally advanced and/or recurrent breast cancer-comparison of results with radiotherapy alone. *Int. J. Hyperth.* **1990**, *6*, 487–497. [CrossRef] [PubMed]
14. Nagata, Y.; Hiraoka, M.; Nishimura, Y.; Masunaga, S.; Mitumori, M.; Okuno, Y.; Fujishiro, M.; Kanamori, S.; Horii, N.; Akuta, K.; et al. Clinical results of radiofrequency hyperthermia for malignant liver tumors. *Int. J. Radiat. Oncol. Biol. Phys.* **1997**, *38*, 359–365. [CrossRef]
15. Asao, T.; Sakurai, H.; Harashima, K.; Yamaguchi, S.; Tsutsumi, S.; Nonaka, T.; Shioya, M.; Nakano, T.; Kuwano, H. The synchronization of chemotherapy to circadian rhythms and irradiation in pre-operative chemoradiation therapy with hyperthermia for local advanced rectal cancer. *Int. J. Hyperth.* **2006**, *22*, 399–406. [CrossRef]
16. Nishimura, Y.; Hiraoka, M.; Akuta, K.; Jo, S.; Nagata, Y.; Masunaga, S.-I.; Takahashi, M.; Abe, M. Hyperthermia combined with radiation therapy for primarily unresectable and recurrent colorectal cancer. *Int. J. Radiat. Oncol. Biol. Phys.* **1992**, *23*, 759–768. [CrossRef] [PubMed]
17. Ohguri, T.; Imada, H.; Kato, F.; Yahara, K.; Morioka, T.; Nakano, K.; Korogi, Y. Radiotherapy with 8MHz radiofrequency-capacitive regional hyperthermia for pain relief of unresectable and recurrent colorectal cancer. *Int. J. Hyperth.* **2006**, *22*, 1–14. [CrossRef]
18. Mochiki, E.; Shioya, M.; Sakurai, H.; Andoh, H.; Ohno, T.; Aihara, R.; Asao, T.; Kuwano, H. Feasibility study of postoperative intraperitoneal hyperthermotherapy by radiofrequency capacitive heating system for advanced gastric cancer with peritoneal seeding. *Int. J. Hyperth.* **2007**, *23*, 493–500. [CrossRef]
19. Matsui, K.; Takebayashi, S.; Watai, K.; Kakehi, M.; Kubota, Y.; Yao, M.; Shuin, T. Combination radiotherapy of urinary bladder carcinoma with chemohyperthermia. *Int. J. Hyperth.* **1991**, *7*, 19–26. [CrossRef]
20. Arends, T.J.H.; Nativ, O.; Maffezzini, M.; de Cobelli, O.; Canepa, G.; Verweij, F.; Moskovitz, B.; van der Heijden, A.G.; Witjes, J.A. Results of a randomized chemohyperthermia with Mitomycin C versus Bacillus Calmette-Guérin for adjuvant treatment of patients with intermediate—And high-risk non-muscle-invasive bladder cancer. *Eur. Urol.* **2016**, *69*, 1046–1052. [CrossRef]
21. Sugimach, K.; Kuwano, H.; Ide, H.; Toge, T.; Saku, M.; Oshiumi, Y. Chemotherapy combined with or without hyperthermia for patients with oesophageal carcinoma: A prospective randomized trial. *Int. J. Hyperth.* **1994**, *10*, 485–493. [CrossRef]
22. Ohguri, T.; Imada, H.; Yahara, K.; Morioka, T.; Nakano, K.; Terashima, H.; Korogi, Y. Radiotherapy with 8-MHz radiofrequency-capacitive regional hyperthermia for stage III non-small cell lung cancer: The radiofrequency-output power correlates with the intraesophageal temperature and clinical outcomes. *Int. J. Radiat. Oncol. Biol. Phys.* **2009**, *1*, 128–135. [CrossRef] [PubMed]
23. Ohguri, T.; Imada, H.; Yahara, K.; Morioka, T.; Nakano, K.; Terashima, H.; Korogi, Y. Deep regional hyperthermia for the whole thoracic region using 8MHz radiofrequency-capacitive heating device: Relationship between the radiofrequency-output power and the intra-oesophageal temperature and predictive factors for a good heating in 59 patients. *Int. J. Hyperth.* **2011**, *27*, 20–26.
24. Huilgol, N.G.; Gupta, S.; Sridhar, C.R. Hyperthermia with radiation in the treatment of locally advanced head and neck cancer: A report of randomized trial. *J. Cancer Res. Ther.* **2010**, *6*, 492–496. [CrossRef]
25. Datta, N.R.; Bose, A.K.; Kapoor, H.K.; Gupta, S. Head and neck cancers: Results of thermoradiotherapy versus radiotherapy. *Int. J. Hyperth.* **1990**, *6*, 479–486. [CrossRef] [PubMed]
26. Ohguri, T.; Imada, H.; Narisada, H.; Yahara, K.; Morioka, T.; Nakano, K.; Miyaguni, Y.; Korogi, Y. Systemic chemotherapy using paclitaxel and carboplatin plus regional hyperthermia and hyperbaric oxygen treatment for non-small cell lung cancer with multiple pulmonary metastases: Preliminary results. *Int. J. Hyperth.* **2009**, *25*, 160–167. [CrossRef] [PubMed]
27. Kodama, K.; Doi, O.; Tatsuta, M.; Kuriyama, K.; Tateishi, R. Development of postoperative intrathoracic chemo-thermotherapy for lung cancer with objective of improving local cure. *Cancer* **1989**, *64*, 1422–1428. [CrossRef] [PubMed]
28. Mitsumori, M.; Zeng, Z.-F.; Oliynychenko, P.; Park, J.H.; Choi, B.I.; Tatsuzaki, H.; Tanaka, Y.; Hitaoka, M. Regional hyperthermia combined with radiotherapy for locally advanced non-small cell lung cancers: A multi-institutional prospective randomized trial of the International Atomic Energy Agency. *Int. J. Clin. Oncol.* **2007**, *12*, 192–198. [PubMed]
29. Kitamura, K.; Kuwano, H.; Watanabe, M.; Nozoe, T.; Yasuda, M.; Sumiyoshi, K.; Saku, M.; Sugimachi, K. Prospective randomized study of hyperthermia combined with chemoradiotherapy for esophageal carcinoma. *J. Surg Oncol.* **1995**, *60*, 55–58. [CrossRef]

30. Szasz, O.; Szigeti, G.; Szasz, A. Connections between the specific absorption rate and the local temperature. *Open J. Biophys.* **2016**, *6*, 53–74. [CrossRef]
31. Papp, E.; Vancsik, T.; Kiss, E.; Szasz, O. Energy absorption by the membrane rafts in the modulated electro-hyperthermia (mEHT). *Open J. Biophys.* **2017**, *7*, 216–229. [CrossRef]
32. Govorov, A.O.; Richardson, H.H. Generating heat with metal nanoparticles. *NanoToday* **2007**, *2*, 30–38. [CrossRef]
33. Szasz, O.; Andocs, G.; Meggyeshazi, N. Modulation effect in oncothermia. Hindawi Publishing Corporation. *Conf. Pap. Med.* **2013**, *2013*, 395678.
34. Szasz, O. Bioelectromagnetic paradigm of cancer treatment—Modulated electro-hyperthermia (mEHT). *Open J. Biophys.* **2019**, *9*, 98–109. [CrossRef]
35. Szasz, A. Bioelectromagnetic Paradigm of Cancer Treatment Oncothermia. In *Bioelectromagnetic and Subtle Energy Medicine*; Paul, J.R., Ed.; CRC Press: Boca Raton, FL, USA; Taylor & Francis Group: Oxford, UK, 2015; pp. 323–336.
36. Semenza, G.L. Tumor metabolism: Cancer cells give and take lactate. *J. Clin. Investig.* **2008**, *118*, 3835–3837. [CrossRef] [PubMed]
37. Stoy, R.D.; Foster, K.R.; Schwan, H.P. Dielectric properties of mammalian tissues from 0.1 to 100 MHz: A summary of recent data. *Phys. Med. Biol.* **1982**, *27*, 501–513. [CrossRef]
38. Foster, K.R.; Schepps, J.L. Dielectric properties of tumor and normal tissues at radio through microwave frequencies. *J. Microw. Power* **1981**, *16*, 107–119. [CrossRef] [PubMed]
39. Gershing, E. Monitoring temperature-induced changes in tissue during hyperthermia by impedance methods. In *Electrical Bioimpedance Methods*; Riu, P.J., Ed.; New York Academy of Sciences: New York, NY, USA, 1999; Volume 873, pp. 13–20.
40. Oehr, P.; Biersack, H.J.; Coleman, R.E. *PET and PET-CT in Oncology*; Springer: Berlin/Heidelberg, Germany, 2004.
41. Larson, S.M. Positron Emission Tomography-Based Molecular Imaging in Human Cancer: Exploring the Link between Hypoxia and Accelerated Glucose Metabolism. *Clin. Cancer Res.* **2004**, *10*, 2203–2204. [CrossRef]
42. Sha, L.; Ward, E.R.; Story, B. A review of dielectric properties of normal and malignant breast tissue. In Proceedings of the IEEE SoutheastCon 2002 (Cat. No.02CH37283), Columbia, SC, USA, 5–7 April 2002; pp. 457–462.
43. Blad, B.; Wendel, P.; Jonsson, M.; Lindstrom, K. An electrical impedance index to distinguish between normal and cancerous tissues. *J. Med. Eng. Technol.* **1999**, *23*, 57–62. [CrossRef]
44. Szentgyorgyi, A. *Electronic Biology and Cancer*; Marcel Dekker: New York, NY, USA, 1998.
45. Szentgyorgyi, A. *The Living State and Cancer*; Marcel Dekker: New York, NY, USA, 1978.
46. Szigeti, G.P.; Szasz, O.; Hegyi, G. Connections between Warburg’s and Szentgyorgyi’s Approach about the Causes of Cancer. *J. Neoplasms* **2017**, *1*, 1–13.
47. Joy, M.L.G. MR current density and conductivity imaging: The state of the Art, Engineering in Medicine and Biology. In Proceedings of the IEMBS 26th Annual International Conference of the IEEE, San Francisco, CA, USA, 1–5 September 2004; Volume 2, pp. 5315–5319.
48. Muftuler, L.T.; Hamamura, M.J.; Birgul, O.; Nalcioglu, O. In vivo MRI electrical impedance tomography (MREIT) of tumors. *Technol. Cancer Res. Treat.* **2006**, *5*, 381–387.
49. Kao, P.H.-J.; Chen, C.-H.; Tsang, Y.-W.; Lin, C.-S.; Chiang, H.-C.; Huang, C.-C.; Chi, M.-S.; Yang, K.-L.; Li, W.-T.; Kao, S.-J.; et al. Relationship between energy dosage and apoptotic cell death by modulated electro-hyperthermia. *Sci. Rep.* **2020**, *10*, 8936. [CrossRef] [PubMed]
50. Szasz, O.; Szasz, A. Approaching complexity: Hyperthermia dose and its possible measurement in oncology. *Open J. Biophys.* **2021**, *11*, 68–132. [CrossRef]
51. Lee, I.-H.; Imanaka, M.Y.; Modahl, E.H.; Torres-Ocampo, A.P. Lipid raft phase modulation by membrane-anchored proteins with inherent phase separation properties. *ACS Omega* **2019**, *4*, 6551–6559. [CrossRef]
52. Staunton, J.R.; Agus, D.B.; Alexander, J.F.; Arap, W.; Ashili, S.; Aslan, J.E.; Bonneau, R. The Physical Sciences—Oncology Centers Network; A physical sciences network characterization of non-tumorigenic and metastatic cells. *Sci. Rep.* **2008**, *3*, 1449.
53. Kotnik, T. Theoretical Evaluation of the Distributed Power Dissipation in Biological Cells Exposed to Electric Fields. *Bioelectromagnetics* **2000**, *21*, 385–394. [CrossRef] [PubMed]
54. Campello, E.M.B.; Zohdi, T.I. Design Evaluation of a Particle Bombardment System Used to Deliver Substances into Cells. *CMES* **2014**, *98*, 221–245.
55. Lee, B.W.; Faller, R.; Sum, A.K.; Vattulainen, I.; Patra, M.; Karttunen, M. Structural Effects of Small Molecules on Phospholipid Bilayers Investigated by Molecular Simulations. *Fluid Phase Equilibria* **2004**, *225*, 63–68. [CrossRef]
56. Guest, W.C.; Cashman, N.R.; Plotkin, S.S. A theory for the anisotropic and inhomogeneous dielectric properties of proteins. *Phys. Chem. Chem. Phys.* **2011**, *13*, 6286–6295. [CrossRef] [PubMed]
57. Heikelä, M.; Vattulainen, I.; Hyvönen, M.T. Atomistic simulation studies of cholesterol leaflets: Model for the core of lipoprotein particles. *J. Biophys.* **2006**, *90*, 2247–2257. [CrossRef]
58. Waxham, M.N. Molecular mobility in cells examined with optical methods. In *Protein Trafficking in Neurons*; Bean, A.J., Ed.; Academic Press: Houston, TX, USA, 2007; pp. 3–27.
59. Cloutier, M.; Wang, E. Dynamic modeling and analysis of cancer cellular network motifs. *Integr. Biol.* **2011**, *3*, 724–732. [CrossRef] [PubMed]

60. Hernandez-Nunez, L.; Chen, A.; Budelli, G.; Berck, M.E.; Richter, V.; Rist, A.; Thum, A.S.; Cardona, A.; Klein, M.; Garrity, P.; et al. Synchronous and opponent thermosensors use flexible cross-inhibition to orchestrate thermal homeostasis. *Sci. Adv.* **2021**, *7*, eabg6707. [CrossRef] [PubMed] [PubMed Central]
61. Mathur-DeVre, R. Biomedical implications of the relaxation behaviour of water related to NMR imaging. *Br. J. Radiol.* **1984**, *57*, 955–976. [CrossRef]
62. Benson, H. The relaxation response: Its subjective and objective historical precedents and physiology. *Trends Neurosci.* **1983**, *6*, 281–284. [CrossRef]
63. Li, X.; Sun, S.; Yao, J.; Sun, Z. Using Relaxation Time to characterize biological effects of different mutagens. *Sci. Rep.* **2020**, *10*, 13941. [CrossRef] [PubMed]
64. Pennes, H.H. Analysis of tissue and arterial blood temperatures in the resting human forearm. *J. Appl. Phys.* **1948**, *1*, 93–122. [CrossRef] [PubMed]
65. Deng, Z.-S.; Liu, J. Analytical solutions to 3-D bioheat transfer problems with or without phase change. In *Heat Transfer Phenomena and Applications*; Intech: London, UK, 2012; Chapter 8; pp. 205–242.
66. Deng, Z.-S.; Liu, J. Analytical study on bioheat transfer problems with spatial or transient heating on skin surface or inside biological bodies. *Trans. ASME* **2002**, *124*, 638–649.
67. Cundin, L.X.; Roach, W.P.; Millenbaugh, N. Empirical comparison of Pennes' Bio-Heat equation. *Proc. SPIE* **2009**, *7175*, 238–246.
68. Lakhssassi, A.; Kengne, E.; Semmaoui, H. Modified Pennes' equation modelling bio-heat transfer in living tissues: Analytical and numerical analysis. *Nat. Sci.* **2010**, *2*, 1375–1385.
69. Gao, B.; Langer, S.; Corry, P.M. Application of the time-dependent Green's function and Fourier transforms to the solution of the bioheat equation. *Int. J. Hyp.* **1995**, *11*, 267–285. [CrossRef]
70. Erdman, B.; Lang, J.; Seebaas, M. Optimisation of Temperature Distributions for Regional Hyperthermia Based on a Nonlinear Heat Transfer Model. *Ann. N. Y. Acad. Sci.* **1998**, *858*, 36–46. [CrossRef]
71. Hasegawa, T.; Gu, Y.-H.; Takahashi, T.; Hasegawa, T.; Yamamoto, I. Enhancement of hyperthermic effects using rapid heating. In *Thermotherapy for Neoplasia, Inflammation, and Pain*; Kosaka, M., Sugahara, T., Schmidt, K.L., Simon, E., Eds.; Springer: Tokyo, Japan; Berlin/Heidelberg, Germany, 2001; pp. 439–444.
72. *IEEE C95.1*; IEEE Standard for Safety Levels with Respect to Human Exposure to Radio Frequency Electromagnetic Fields, 3 kHz to 300 GHz. IEEE: Piscataway, NJ, USA, 2005.
73. Song, C.W.; Park, H.; Griffin, R.J. *Theoretical and Experimental Basis of Hyperthermia, Thermotherapy for Neoplasia, Inflammation, and Pain*; Kosaka, M., Sugahara, T., Schmidt, K.L., Simon, E., Eds.; Springer: Tokyo, Japan, 2001; pp. 394–407.
74. Bassingthwaighte, J.B. Physiology and theory of tracer washout techniques for the estimation of myocardial blood flow: Flow estimation from tracer washout. *Prog. Cardiovasc. Dis.* **1977**, *20*, 165–189. [CrossRef] [PubMed]
75. Bassingthwaighte, J.B.; Yipintosoi, T. Organ blood flow, wash-in, washout, and clearance of nutrients and metabolites. *Mayo Clin. Proc.* **1974**, *49*, 248–255. [PubMed]
76. Feldmann, H.J.; Molls, M.; Hoederath, A.; Krümpelmann, S.; Sack, H. Blood flow and steady state temperatures in deep-seated tumors and normal tissues. *Int. J. Radiat. Oncol. Biol. Phys.* **1992**, *23*, 1003–1008. [CrossRef] [PubMed]
77. Fatehi, D.; van der Zee, J.; Notenboom, A.; van Rhoon, G.C. Comparison of intratumor and intraluminal temperatures during loco-regional deep hyperthermia of pelvic tumors. *Strahlenther. Und Onkol.* **2007**, *183*, 479–486. [CrossRef] [PubMed]
78. Lee, S.Y.; Szasz, A. Immunogenic Effect of Modulated Electro-hyperthermia (mEHT) in Solid Tumors. In *Interdisciplinary Cancer Research*; Springer: Cham, Switzerland, 2022. [CrossRef]
79. Tsang, Y.-W.; Huang, C.-C.; Yang, K.-L.; Chi, M.-S.; Chiang, H.-C.; Wang, Y.-S.; Andocs, G.; Szasz, A.; Li, W.-T.; Chi, K.-H. Improving immunological tumor microenvironment using electro-hyperthermia followed by dendritic cell immunotherapy. *BMC Cancer* **2015**, *15*, 708. [CrossRef]
80. Qin, W.; Akutsu, Y.; Andocs, G.; Suganami, A.; Hu, X.; Yusup, G.; Komatsu-Akimoto, A.; Hoshino, I.; Hanari, N.; Mori, M.; et al. Modulated electro-hyperthermia enhances dendritic cell therapy through an abscopal effect in mice. *Oncol. Rep.* **2014**, *32*, 2373–2379. [CrossRef] [PubMed]
81. Vancsik, T.; Kovago, C.; Kiss, E.; Papp, E.; Forika, G.; Benyo, Z.; Meggyeshazi, N.; Krenacs, T. Modulated electro-hyperthermia induced loco-regional and systemic tumor destruction in colorectal cancer allografts. *J. Cancer* **2018**, *9*, 41–53. [CrossRef]
82. Minnaar, C.A.; Kotzen, J.A.; Ayeni, O.A.; Vangu, M.-D.-T.; Baeyens, A. Potentiation of the abscopal effect by modulated electro-hyperthermia in locally advanced cervical cancer patients. *Front. Oncol.* **2020**, *10*, 376. [CrossRef]
83. Chi, M.-S.; Mehta, M.P.; Yang, K.-L.; Lai, H.-C.; Lin, Y.-C.; Ko, H.-L.; Wang, Y.-S.; Liao, K.-W.; Chi, K.-H. Putative abscopal effect in three patients treated by combined radiotherapy and modulated electrohyperthermia. *Front. Oncol.* **2020**, *10*, 254. [CrossRef]
84. Wust, P.; Stein, U.; Ghadjar, P. Non-thermal membrane effects of electromagnetic fields and therapeutic applications in oncology. *Int. J. Hyperth.* **2021**, *38*, 715–731. [CrossRef]
85. Wust, P.; Kortüm, B.; Strauss, U.; Nadobny, J.; Zschaek, S.; Beck, M.; Stein, U.; Ghadjar, P. Non-thermal effects of radiofrequency electromagnetic fields. *Sci. Rep.* **2020**, *10*, 13488. [CrossRef]
86. Yang, K.-L.; Huang, C.-C.; Chi, M.-S.; Chiang, H.-C.; Wang, Y.-S.; Hsia, C.-C.; Andocs, G.; Wang, H.-E.; Chi, K.-H. In vitro comparison of conventional hyperthermia and modulated electro-hyperthermia. *Oncotarget* **2016**, *7*, 84082–84092. [CrossRef] [PubMed]

87. Cha, J.; Jeon, T.-W.; Lee, C.G.; Oh, S.T.; Yang, H.-B.; Choi, K.-J.; Seo, D.; Yun, I.; Baik, I.H.; Park, K.R.; et al. Electro-hyperthermia inhibits glioma tumorigenicity through the induction of E2F1-mediated apoptosis. *Int. J. Hyperth.* **2015**, *31*, 784–792. [CrossRef]
88. Andocs, G.; Rehman, M.U.; Zhao, Q.-L.; Tabuchi, Y.; Kanamori, M.; Kondo, T. Comparison of biological effects of modulated electro-hyperthermia and conventional heat treatment in human lymphoma U937 cell. *Cell Death Discov.* **2016**, *2*, 16039. [CrossRef] [PubMed]
89. Vancsik, T.; Forika, G.; Balogh, A.; Kiss, E.; Krenacs, T. Modulated electro-hyperthermia induced p53 driven apoptosis and cell cycle arrest additively support doxorubicin chemotherapy of colorectal cancer in vitro. *Cancer Med.* **2019**, *8*, 4292–4303. [CrossRef]
90. Forika, G.; Balogh, A.; Vancsik, T.; Zalatnai, A.; Petovari, G.; Benyo, Z.; Krenacs, T. Modulated electro-hyperthermia resolves radioresistance of Panc1 pancreas adenocarcinoma and promotes DNA damage and apoptosis in vitro. *Int. J. Mol. Sci.* **2020**, *21*, 5100. [CrossRef] [PubMed]
91. Wust, P.; Veltsista, P.D.; Oberacker, E.; Yavvari, P.; Walther, W.; Bengtsson, O.; Sterner-Kock, A.; Weinhart, M.; Heyd, F.; Grabowski, P.; et al. Radiofrequency electromagnetic fields cause non-temperature-induced physical and biological effects in cancer cells. *Cancers* **2022**, *14*, 5349. [CrossRef]
92. Portoro, I.; Danics, L.; Veres, D. Increased efficacy in treatment of glioma by a new modulated electro-hyperthermia (mEHT) protocol. *Oncothermia J.* **2018**, *24*, 344–356.
93. Aas, A.T.; Brun, A.; Blennow, C.; Stromblad, S.; Salford, L.G. The RG2 rat glioma model. *J. Neurooncol.* **1995**, *23*, 175–183. [CrossRef]
94. Danics, L.; Schvarcz, C.A.; Viana, P.; Vancsik, T.; Krenács, T.; Benyó, Z.; Kaucsár, T.; Hamar, P. Exhaustion of protective heat shock response induces significant tumor damage by apoptosis after modulated electro-hyperthermia treatment of triple negative breast cancer isografts in mice. *Cancers* **2020**, *12*, 2581. [CrossRef]
95. Minnaar, C.A.; Szasz, A. Forcing the antitumor effects of HSPs using a modulated electric field. *Cells* **2022**, *11*, 1838. [CrossRef] [PubMed]
96. Szasz, O. Local Treatment with Systemic Effect: Abscopal Outcome. In *Challenges and Solutions of Oncological Hyperthermia*; Szasz, A., Ed.; Cambridge Scholars: Cambridge, UK, 2020; Chapter 11; pp. 192–205.
97. Reinhold, H.S.; van den Berg-Blok, A. The influence of a heat pulse on the thermally induced damage to tumour microcirculation. *Eur. J. Cancer Clin. Oncol.* **1983**, *19*, 221–225. [CrossRef] [PubMed]
98. Tisa, T.A.; Nisha, Z.A.; Kiber, M.A. Design of an Enhanced Temperature Control System for Neonatal Incubator. *Bangladesh J. Med. Phys.* **2013**, *5*, 53–61. [CrossRef]
99. Lu, C.H.; Chen, W.T.; Hsieh, C.H.; Kuo, Y.Y.; Chao, C.Y. Thermal cycling-hyperthermia in combination with polyphenols, epigallocatechin gallate and chlorogenic acid, exerts synergistic anticancer effect against human pancreatic cancer PANC-1 cells. *PLoS ONE* **2019**, *14*, e0217676. [CrossRef] [PubMed]
100. Kim, K.S.; Hernandez, D.; Lee, S.Y. Time-multiplexed two-channel capacitive radiofrequency hyperthermia with nanoparticle mediation. *Biomed. Eng. Online* **2015**, *14*, 95. [CrossRef] [PubMed]
101. Yaghmazadeh, O. Pulsed high-power radio frequency energy can cause non-thermal harmful effects on the brain. *arXiv* **2023**, arXiv:2309.03479v1. [CrossRef] [PubMed] [PubMed Central]
102. Li, C.-Y.; Lin, S.-M.; Wan, Y.-Y. Prediction of Temperature Field and Thermal Damage of Multilayer Skin Tissues Subjected to Time-Varying Laser Heating and Fluid Cooling by a Semianalytical Method. *Math. Probl. Eng.* **2020**, *2020*, 5074280. [CrossRef]
103. Chung, M.-K.; Güler, A.D.; Caterina, M.J. Biphasic currents evoked by chemical or thermal activation of the heat-gated ion channel. *J. Biol. Chem.* **2005**, *280*, 15928–15941. [CrossRef] [PubMed]
104. Ding, G.R.; Li, K.C.; Wang, X.W.; Zhou, Y.C.; Qiu, L.B.; Tan, J.; Xu, S.L.; Guo, G.Z. Effect of electromagnetic pulse exposure on brain micro vascular permeability in rats. *Biomed. Environ. Sci.* **2009**, *22*, 265–268. [CrossRef]
105. Wang, Q. The study of dose-response relationship of pulsed electromagnetic radiation on rat blood-brain-barrier. *Chin. J. Dis. Control Prev.* **2003**, *7*, 401–404.
106. Li, K.; Zhang, K.; Xu, S.; Wang, X.; Zhou, Y.; Zhou, Y.; Gao, P.; Lin, J.; Ding, G.; Guo, G. EMP-induced BBB-disruption enhances drug delivery to glioma and increases treatment efficacy in rats. *Bioelectromagnetics* **2018**, *39*, 60–67. [CrossRef] [PubMed]
107. Wang, S.; Song, Z.; Yuan, Y.; Guo, G.; Kang, J. Effects of pulse parameters on the temperature distribution of a human head exposed to the electromagnetic pulse. *Sci Rep.* **2021**, *11*, 22938. [CrossRef] [PubMed] [PubMed Central]
108. Sorrell, R.G.; Muhlenfeld, J.; Moffett, J.; Stevens, G.; Kesten, S. Evaluation of pulsed electromagnetic field therapy for the treatment of chronic postoperative pain following lumbar surgery: A pilot, double-blind, randomized, sham-controlled clinical trial. *J. Pain Res.* **2018**, *11*, 1209–1222. [CrossRef] [PubMed]
109. Lisi, A.J.; Scheinowitz, M.; Saporito, R.; Onorato, A.A. Pulsed Electromagnetic Field Therapy Device for Non-Specific Low Back Pain: A Pilot Randomized Controlled Trial. *Pain Ther.* **2019**, *8*, 133–140. [CrossRef] [PubMed]
110. Guo, S.; Sersa, G.; Heller, R. Editorial: Pulsed electric field based technologies for oncology applications. *Front. Oncol.* **2023**, *13*, 1183900. [CrossRef] [PubMed] [PubMed Central]
111. Nuccitelli, R. Application of Pulsed Electric Fields to Cancer Therapy. *Bioelectricity* **2019**, *1*, 30–34. [CrossRef] [PubMed] [PubMed Central]
112. Cao, T.L.; Le, T.A.; Hadadian, Y.; Yoon, J. Theoretical Analysis for Using Pulsed Heating Power in Magnetic Hyperthermia Therapy of Breast Cancer. *Int. J. Mol. Sci.* **2021**, *22*, 8895. [CrossRef] [PubMed] [PubMed Central]

113. Mir, L.M.; Belehradek, M.; Domenge, C.; Orłowski, S.; Poddevin, B.; Belehradek, J., Jr.; Schwaab, G.; Luboinski, B.; Paoletti, C. Electrochemotherapy, a new antitumor treatment: First clinical trial. *Comptes Rendus L'Académie Des Sci. Ser. III* **1991**, *313*, 613–618.
114. Galvano- or Electrochemical Tumor Therapy (ECT). Available online: <https://www.klinik-st-georg.de/en/klinik-st-georg/st-george-hospital/therapies/galvano-or-electrochemical-tumor-therapy-ect/> (accessed on 15 February 2024).
115. Campana, L.G.; Daud, A.; Lancellotti, F.; Arroyo, J.P.; Davalos, R.V.; Di Prata, C.; Gehl, J. Pulsed Electric Fields in Oncology: A Snapshot of Current Clinical Practices and Research Directions from the 4th World Congress of Electroporation. *Cancers* **2023**, *15*, 3340. [CrossRef]
116. Preta, G. New Insights Into Targeting Membrane Lipids for Cancer Therapy. *Front. Cell Dev. Biol.* **2020**, *8*, 571237. [CrossRef]
117. Robinson, V.S.; Garner, A.L.; Loveless, A.M.; Neculaes, V.B. Calculated plasma membrane voltage induced by applying electric pulses using capacitive coupling. *Biomed. Phys. Eng. Express* **2017**, *3*, 025016. [CrossRef]

Disclaimer/Publisher's Note: The statements, opinions and data contained in all publications are solely those of the individual author(s) and contributor(s) and not of MDPI and/or the editor(s). MDPI and/or the editor(s) disclaim responsibility for any injury to people or property resulting from any ideas, methods, instructions or products referred to in the content.

Review

Augmentation of Deficient Bone Healing by Pulsed Electromagnetic Fields—From Mechanisms to Clinical Outcomes

Amr Kaadan ¹, Simona Salati ², Stefania Setti ² and Roy Aaron ^{1,*}

¹ Department of Orthopedic Surgery, Warren Alpert Medical School of Brown University, Providence, RI 02903, USA; amro_kaadan@alumni.brown.edu

² Medical Division, Igea S.p.A, 41012 Carpi, Italy; s.salati@igeamedical.com (S.S.); s.setti@igeamedical.com (S.S.)

* Correspondence: roy_aaron@brown.edu

Abstract: Pulsed Electromagnetic Fields (PEMF) are widely used, with excellent clinical outcomes. However, their mechanism of action has not yet been completely understood. The purpose of this review is to describe current observations on the mechanisms of PEMF, together with its clinical efficacy. Osteoblast responsiveness to PEMF is described on several scales, from the cell membrane to clinically relevant bone formation. PEMF has been shown to activate membrane adenosine receptors. The role of adenosine receptors in activating intracellular second messenger pathways, such as the canonical Wnt/ β -catenin pathway and the mitogen-activated protein kinases (MAPK) pathway, is described. The responsiveness of osteoblasts and the synthesis of structural and signaling proteins constitute the role of PEMFs in promoting osteogenesis and bone matrix synthesis, and they are described. Multiple studies, ranging from observational and randomized to meta-analyses that investigate the clinical efficacy of PEMF, are described. This review presents a favorable conclusion on the clinical effects of PEMF while unlocking the “black box” of PEMF’s mechanism of action, thus improving confidence in the clinical utility of PEMF in bone repair.

Keywords: pulsed electromagnetic field; bone repair; intracellular second messenger; adenosine receptor

1. Introduction

Pulsed electromagnetic fields (PEMF) are regarded as safe and efficacious treatments for fracture non-unions and bone defects. Despite excellent clinical outcomes, however, the mechanisms of PEMF stimulation of bone have, until recently, been incompletely understood, compromising confidence in clinical and physiological observations. Within recent years, the mechanisms of PEMF effects on osteoblasts and repairing bone have been elucidated, allowing an understanding of the biology of PEMF-augmented bone formation and repair [1,2]. This review describes cell recognition of PEMF through signal transduction of adenosine A_{2A} and A_3 cell membrane receptors [3,4] and traces intracellular signaling through pathways such as the WNT- β -catenin pathway [5]. PEMF effects on osteoblast responses of the synthesis of structural and signaling cytokines and the formation of bone matrix are described. Then, a compilation of the clinical results of PEMF treatment of fractures and non-unions through individual studies and meta-analyses is presented [6–8]. Understanding of PEMF membrane reception and of the intracellular pathways involved, culminating in the synthesis of extracellular matrix proteins and bone restoration, should enhance confidence in the clinical use of PEMF and the identification of clinical conditions likely to be favorably affected by PEMF exposure. This review describes mechanistic observations of PEMF on bone on several scales, from the cellular to the organismal and clinical levels.

2. Cell Reception of Pulsed Electromagnetic Fields—The Role of A_{2A} Adenosine Receptors in PEMF-Mediated Bone Healing

PEMFs have been known to stimulate bone healing for more than 40 years. The most commonly accepted hypothesis of the mechanism of action is that PEMFs act through the modulation of Ca²⁺ intracellular concentration and the action on membrane receptors. Early studies showed that PEMF exposure affects membrane-associated second messenger systems such as Ca²⁺, cAMP, or phosphatidylinositol metabolism and subsequent cellular responses. Cain et al. demonstrated that PEMFs inhibit the cAMP response to parathyroid hormone in bone cells [9]. Similarly, Cadossi et al. found that PEMF exposure enhances the response of human lymphocytes to phytohemagglutinin (PHA) by enhancing ligand-receptor migration and capping at the cell membrane [10]. In 1999, Ventura et al. showed that PEMF-induced nuclear PKC activation led to myocardial opioid gene expression [11].

Adenosine is an endogenous purine nucleoside involved in various physiopathological processes. Adenosine is primarily synthesized through the dephosphorylation of ATP, ADP, and AMP by two hydrolyzing enzymes: ectonucleoside triphosphate diphosphohydrolase (CD39) and ecto-5'-nucleotidase (CD73) [12]. Adenosine functions are mediated by its interactions with four G-protein coupled receptors (GPCRs): A₁, A_{2A}, A_{2B}, and A₃ ARs. Specifically, A₁ and A₃ adenosine receptors (ARs) are coupled to Gi proteins, which inhibit adenylate cyclase (AC), leading to a reduction in cAMP levels. cAMP is located on the intracellular side of the plasma membrane and is important for activating intracellular second-messenger systems. Conversely, A_{2A} and A_{2B} ARs are coupled to Gs proteins, and their activation leads to an increase in cAMP [12].

Under physiological conditions, adenosine is found in low concentrations in the extracellular environment; however, under stress conditions, such as bone loading, fracture, and repair, adenosine concentrations increase [13]. Activation of adenosine receptors has been reported to affect the differentiation and activity of osteoblasts and osteoclasts both in vitro and in vivo, suggesting a role for adenosine in bone healing and regeneration. In particular, activation of A_{2A} ARs has been reported to inhibit osteoclast differentiation through the activation of protein kinase A (PKA) and inhibition of nuclear factor κB (NFκB) nuclear translocation [14], while the selective A_{2A} receptor agonist CGS21680 has been shown to inhibit osteoclast function, by decreasing interleukin-1β (IL-1β) and tumor necrosis factor-α (TNF-α) secretion [15].

Gharibi et al. reported that A_{2A} ARs are expressed in rat MSCs, and their expression is upregulated during the later stages of osteoblastic differentiation, where they play a crucial role in osteoblast maturation and osteoblast phenotype maintenance [1]. Micro-computed tomography of the femur from A_{2A} knockout mice showed a significant decrease in the bone volume/trabecular bone volume ratio, decreased trabecular number, and increased trabecular space. Histological analysis showed an increased number of tartrate-resistant acid phosphatase (TRAP)-positive osteoclasts, and electron microscopy showed increased bone reabsorption [15]. Altogether, these results suggest that A_{2A} ARs regulate osteoclast formation and function in vitro and that deletion of these receptors leads to enhanced osteoclast formation and function in vivo, causing a decline in bone mineral density (BMD) [15].

In vivo, the selective agonist for A_{2A} ARs has been shown to reduce osteoclast-mediated bone resorption in a murine calvaria model of wear particle-induced bone resorption [9]. Micro-computed tomography of calvaria showed that CGS21680, a specific A_{2A} AR agonist, treatment reduced particle-induced bone pitting porosity and increased local bone volume compared to control mice [16]. Moreover, A_{2A} ARs stimulation suppressed inflammation, leading to reduced secretion of pro-inflammatory cytokines and molecules that stimulate osteoclast formation, such as macrophage-colony stimulating factor (M-CSF) and receptor activator of nuclear factor-κB (RANKL) [16].

A number of other studies have been supportive of the role of A_{2A} in bone formation. In a critical size defect model in murine calvaria, Mediero et al. showed that the treatment with the A_{2A} R selective agonist stimulated new bone formation similar to BMP-2 [17].

Zheng et al. reported that local implantation of fibrin gel containing an A_{2A} adenosine receptor agonist enhanced bone healing in rat fractures [18]. Recently, Larranaga-Vera et al. used a conjugate of CGS21680 to alendronate through a PEG-linker to treat osteoporotic mice and showed that mice treated with the A_{2A} AR agonist only exhibited both new bone formation and reduced bone loss [19]. Altogether, these findings suggest a role for A_{2A} ARs in regulating bone homeostasis and regeneration.

In 2002, Varani et al. identified adenosine receptors (ARs) as the primary targets of PEMF stimulation [20]. PEMF exposure significantly increased the density of A_{2A} and A₃ ARs on the cell membrane of chondrocytes, synoviocytes, and osteoblasts [20]. Notably, A₁ and A_{2B} receptors are not influenced by the same exposure conditions. Moreover, PEMFs synergize with a specific A_{2A} receptor agonist to elevate intracellular cyclic adenosine monophosphate (cAMP) levels, while an A_{2A} receptor antagonist blocks these effects, suggesting that PEMFs specifically act through A_{2A} adenosine receptors with a pharmacological-like mechanism. In vitro studies conducted in the human osteoblast cell line, hFOB 1.19, showed that PEMF exposure leads to increased expression of A_{2A} and A₃ ARs, resulting in an increase in cAMP production [21]. The specific A_{2A} agonist, CGS21680, significantly increases hFOB 1.19 cell proliferation, and PEMF treatment further enhances such cellular proliferation. Furthermore, the A_{2A} and A₃ receptor agonists, CGS21680 and Cl-IB-MECA, respectively, showed anti-inflammatory activity, decreasing the release of inflammatory cytokines and other mediators implicated in bone diseases [21]. This agonist activity inhibits the NF-κB pathway, a key regulator of matrix metalloproteinase (MMP) expression, alongside several inflammatory response genes [6]. However, these effects were blocked when the specific A_{2A} receptor antagonist was present, suggesting that PEMFs act through A_{2A} AR activation via a pharmacologic-like mechanism [20]. An experimental study using an A_{2A} agonist drug demonstrated that PEMF may also provide chondroprotective effects on articular cartilage [22].

Recently Kar et al. studied the role of A_{2A} and A₃ ARs in PEMF-mediated bone healing by means of gene disruption experiments. The results showed that A_{2A} and A₃ ARs could activate two complementary signaling pathways involved in PEMF-induced osteoblast differentiation, suggesting that A_{2A} and A₃ ARs facilitate PEMF action in the initial phases of osteoblast differentiation [4].

Taken together, these results suggest that PEMF-induced bone healing could be mediated at least in part through agonistic activity on A_{2A} ARs. Table 1 summarizes the main findings described in this section. The studies described highlight the significant role played by A_{2A} receptors in bone healing alongside the complementary role played by A₃ receptors in osteoblast differentiation. These studies show that PEMF activation can activate these receptors.

Table 1. Summary of Studies that Highlight the Role ARs Play in Bone Healing.

Authors	Adenosine Receptor	Results
Gharibi et al. [1]	A _{2A}	A _{2A} ARs play a crucial role in osteoblast maturation and osteoblast phenotype maintenance.
Varani et al. [20]	A _{2A} and A ₃	PEMF significantly increased A _{2A} and A ₃ ARs density, but not A ₁ and A _{2B} receptors.
Kar et al. [4]	A _{2A} and A ₃	A _{2A} and A ₃ ARs can activate pathways that enhance osteoblast differentiation through PEMF exposure.
Mediero et al. [17]	A _{2A}	Treatment with an A _{2A} receptor selective agonist stimulated new bone formation in a murine calvaria model, similar to BMP-2.

Table 1. Cont.

Authors	Adenosine Receptor	Results
Zheng et al. [18]	A _{2A}	Local implantation of fibrin gel containing an A _{2A} receptor agonist enhanced bone healing in rat fractures.
Larrañaga-Vera et al. [19]	A _{2A}	CGS21680 conjugate to alendronate promoted new bone formation and reduced bone loss in osteoporotic mice.

3. Intracellular Signaling and Nuclear Responses to Pulsed Electromagnetic Fields: From Membrane to Nucleus

Intracellular signaling pathways convert received stimuli into cell responses, some of which can be therapeutically advantageous through the reinforcement or repair of local structures [23,24]. This section will describe the intracellular signaling paths, primarily in osteoblasts, resulting in bone formation. Several pathways have been implicated as intracellular messengers of the PEMF signal to the cell-to-bone repair. However, the roles of some of the pathways are still debated and will be briefly discussed to provide a more complete picture.

3.1. Calcium/Calmodulin

Several *in vitro* and *in vivo* studies showed that PEMF exposure elicits dose–response effects on osteoblast proliferation and on the synthesis of structural and signaling extracellular matrix (ECM) components. An important signaling mechanism described for PEMF involves the release of intracellular Ca²⁺ from the endoplasmic reticulum [25]. The subsequent increase in intracellular Ca²⁺ concentration leads to the activation of the Ca²⁺/Calmodulin pathway, resulting in the upregulation of osteogenic genes, such as Transforming Growth Factor- β family genes (TGF- β 1, - β 2, - β 3), Bone Morphogenetic Protein 2 and 4 (BMP-2 and -4), Fibroblast Growth Factor (FGF)-2, Osteocalcin (BGP), and alkaline phosphatase (ALP) [26]. Activated PLA2 leads to an increase in prostaglandin E2 (PGE2), a potent stimulator of bone formation *in vivo* and *in vitro* [27,28].

The increase in intracellular calcium concentration induced by PEMFs has also been reported in hMSCs as an early event during the stimulation of osteogenic differentiation [29]. Currently, the exact mechanism connecting PEMFs, calcium, and osteogenesis remains unclear, likely due to the intricate processes that control calcium influx and the not yet fully understood roles of calcium flux and voltage-gated calcium channels in osteogenic differentiation [30].

3.2. Bone Morphogenic Protein

Additionally, PEMF stimulation has been reported to significantly increase the pro-osteogenic activity of members of the TGF- β gene family, including BMP-2 and BMP-4. Martini et al. confirmed the combined osteogenic activity of PEMFs and BMP-2 in human bone marrow MSCs (hBMSCs) [31–33] in the presence of low doses of BMP-2. Their findings indicate that the effects of PEMFs were linked to the upregulation of several BMP signaling components, including BMP-2, BMP-6, and BMP type I receptor, and to the activation of SMAD1/5/8, the main player in the canonical BMP signaling pathway [33].

3.3. MAPK/ERK and Wnt/ β -Catenin

Two major messaging systems that are activated by ARs and result in nuclear activation are the MAPK/ERK pathway and the canonical Wnt/ β -catenin pathway.

The mitogen-activated protein kinases (MAPK) pathway transmits extracellular signals, such as those activated by PEMF, to the nucleus by utilizing the three MAPK subunits, composed of serine/threonine kinases: extracellular-regulated kinases (ERKs), Jun N-terminal kinases (JNKs), and p38 [5]. This pathway allows cells to interpret external signals and plays a significant role in many pathophysiological processes, such as differentia-

tion and apoptosis, through the regulation of nuclear transcription factor activation [5]. The MAPK pathway is important for osteogenic differentiation, particularly through its interactions with the TGF- β /BMP gene family.

The canonical Wnt/ β -catenin pathway promotes MSC commitment to differentiation into the osteoblastic lineage while indirectly repressing osteoclast differentiation and, accordingly, bone resorption by increasing the secretion of osteoprotegerin [22]. The pathway is stimulated by PEMF and is a regulator of bone homeostasis. A review reported increased bone mass as a result of increased Wnt- β -catenin pathway activation and decreased bone mass as a result of Wnt- β -catenin inhibition [5]. Increases in cAMP, which are further increased by A_{2A} receptors, enhance transmembrane signaling and activate intracellular second-messenger systems such as MAPK and Wnt- β -catenin.

3.4. Other Relevant Pathways

Other intracellular signaling pathways of importance have been described as well. Miyamoto et al. described the effects of PEMF on osteoblasts as they related to cellular responses such as the mTOR pathway [2]. They found that intermittent PEMF stimulation may participate in accelerated cell proliferation to promote fracture healing [2]. Wang et al. reported activation by PEMF exposure of the sAC-cAMP-PKA-CREB signaling pathway, stimulating osteogenic differentiation and mineralization [34].

The osteogenic differentiation of bone marrow mesenchymal stromal cells (BMSCs) may be stimulated through PEMF-activation of the Notch signaling pathway [35]. Four Notch receptors have been identified in humans (Notch 1–4), allowing the Notch pathway to play a dimorphic role in bone turnover [36]. Notch signaling on osteoblasts is cell context-dependent and not strictly inhibitory or stimulatory. For example, increased bone formation can result from a restriction of Notch signaling in osteoblasts [36].

Collectively, these data highlight the important role these pathways play in fracture healing, alongside PEMF interactions with second messenger systems and the membrane. Table 2 summarizes the main findings described in this section.

Table 2. Important Pathways Activated by PEMF Exposure that Increase Bone Formation.

Pathway	Affected Molecules	Outcome
Ca ²⁺ /Calmodulin	TGF- β 1, - β 2, and - β 3, BMP-2 and -4, FGF-2, BGP, and ALP.	Upregulation of osteogenic genes leading to bone formation.
MAPK/ERK	ERKs, JNKs, p38, and the TGF- β /BMP gene family.	Osteogenic differentiation
Wnt/ β -catenin	β -catenin, Wnt, osteoprotegerin	MSC commitment to osteoblastic differentiation and repression of osteoclast differentiation
mTOR	mTOR	Promotion and acceleration of cell proliferation and fracture healing.
Notch	Notch 1–4	Bone turnover

4. Pulsed Electromagnetic Field Stimulation of Bone Matrix Synthesis: From Stem Cells to Bone

PEMF has been shown to enhance chondrogenic and osteogenic mesenchymal stem cell (MSC) differentiation, most likely through AR activation [37]. AR activation activates many second messenger pathways, which activate relevant genes within the nucleus, where relevant bone proteins are eventually synthesized.

Some MSC types can express an adipogenic, chondrogenic, or osteogenic phenotype distinguished through the synthesis of molecules such as collagen, proteoglycan, fibronectin, and CD44 [38]. A study found increased osteoblastic gene expression in response to specific PEMFs on human bone marrow-derived MSCs [39]. MSCs are involved in bone repair following an injury, such as a fracture, through endochondral ossification

and intramembranous ossification [40]. During endochondral ossification, MSCs differentiate into chondrocytes to create a cartilage model, which is then replaced by vasculature and osteoblasts, which synthesize osteoid and induce calcification into bone. During intramembranous ossification, cartilage is not first formed, and MSCs directly differentiate into osteoblasts instead [40]. In both types of bone formation, osteoblasts build bone by depositing osteoid (the organic bone matrix) during bone remodeling and repair. Bone formation occurs when osteoid is calcified with inorganic calcium hydroxyapatite [41].

Bone morphogenetic protein (BMP) and transforming growth factor β (TGF- β) are the primary stimulators of MSC differentiation into osteoblasts and chondrocytes. BMPs have multiple subtypes. A comprehensive analysis found that BMP-2, -6, and -9 were the most potent in the differentiation of MSCs into osteoblasts [42]. Interestingly, low BMP-2 levels are associated with MSC differentiation into adipocytes [43].

TGF- β is a potent chemotactic agent that stimulates MSC, pre-osteoblast, osteoblast, and chondrocyte proliferation. During the early stages of fracture healing, TGF- β is released by activated platelets to induce MSC migration and proliferation [44]. Taken together, both BMP and TGF- β are essential for normal fracture healing since they are critical for MSC differentiation into osteogenic cells. Figure 1 below summarizes the impact of several physical factors, including PEMF, on MSC differentiation.

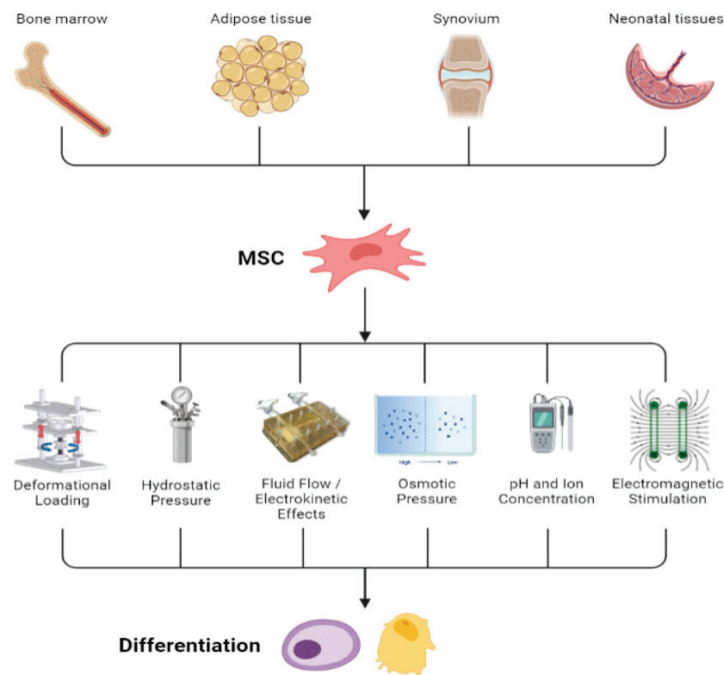


Figure 1. Sources of MSCs and physical factors that can stimulate MSC differentiation into osteogenic cells. Figure from Hung et al. [45].

With PEMF exposure, bone marrow-derived and other MSCs promote a more rapid onset of osteogenesis when compared to unexposed controls. This was identified through enhanced alkaline phosphatase, osteocalcin, BMP-2, and TGF- β measurements only during the early stages of differentiation [31,46].

Bone matrix synthesis is stimulated by PEMF through an increase in osteocalcin, alkaline phosphatase, and matrix mineralization in BMSCs and adipose stem cells (AMSCs), according to Ongaro et al. [32]. PEMF has also been shown to significantly enhance alkaline phosphatase production, an early osteogenesis marker, within seven days in “both basal and osteogenic cultures as compared to untreated controls” [39]. In an AMSC and osteoblast co-culture, Ehnert et al. demonstrated that PEMF increased osteogenic differentiation and proliferation [47]. Of particular importance, the Wnt- β -catenin pathway, which is stimulated by PEMF, increases the expression and activation of transcription factors, which,

in turn, stimulate the nucleus and protein synthesizing apparatus of subcellular organelles to synthesize the extracellular structural proteins that comprise osteoid.

Poh et al. showed that PEMF induced protein kinase B (Akt) and activation of the MAPK/ERK signaling cascade. This significantly upregulated osteocalcin, collagen type I, and alkaline phosphatase levels [48]. ARs activate MAPKs and, thus, provide an intracellular pathway for PEMF signaling. As a result of MAPK activation, PEMF upregulates ECM molecules, collagen type I, alkaline phosphatase, and osteocalcin [48]. Figure 2 describes how JNKs, a MAPK subunit, seem to be the most affected by PEMF exposure.

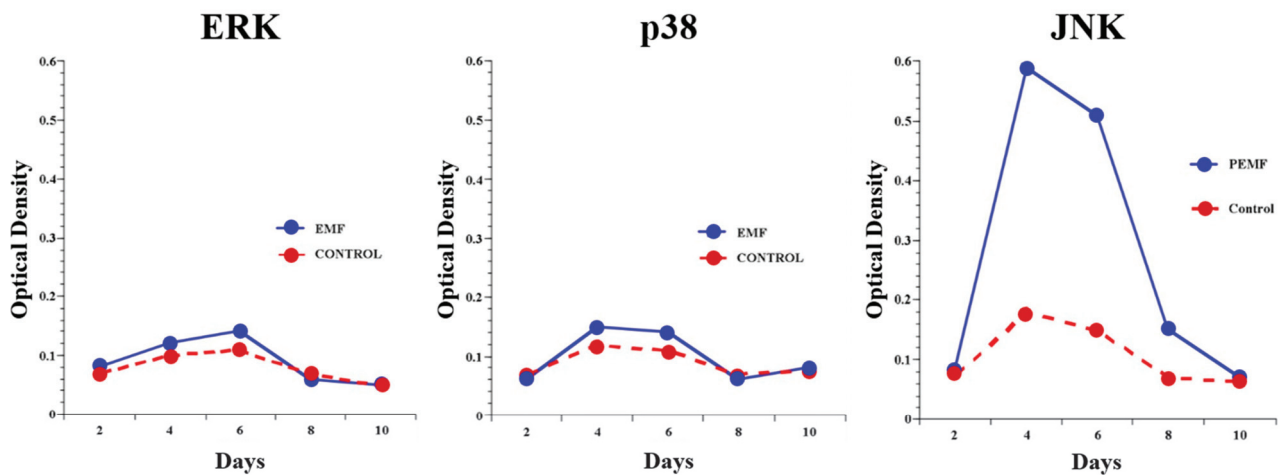


Figure 2. Effects of PEMF exposure on MAPK subunits. This is a western blot analysis of the three MAPK subunits, ERK, p38, and JNK, indicating that JNK is the only subunit affected by PEMF exposure. Figure from Littman [5].

One of the transcription factors activated by MAPKs is activating protein-1 (AP-1), which controls several cellular responses and regulates gene expression from external stimuli. Notably, AP-1 is a transcription factor for TGF- β , and it is enhanced by PEMF exposure. Electromobility shift assay (EMSA) of nuclear extracts has shown that, in experimental endochondral ossification, PEMF stimulation bound AP-1 at a significantly higher rate at all times compared to non-PEMF-stimulated endochondral bone formation, indicating increased transcriptional activity [5]. These results are described in Figure 3. As a consequence of nuclear activation by AP-1, a variety of structural and signaling proteins that are essential for successful bone healing are synthesized. These proteins include osteoprotegerin, osteocalcin, and collagen type I.

Immediately after a fracture occurs, a hematoma forms, where hematopoietic stem cells, such as MSCs, are recruited to the fracture site. Over a variable time period, depending on the fracture, inflammatory tissue and cartilage are formed, which are replaced by osteoid and, eventually, followed by bony callus formation and, finally, bone remodeling [49]. When fractures do not heal after nine months, without signs of healing for three months, they become known as fracture non-unions [50]. During fracture non-union, endochondral ossification occurs in a clinically insignificant degree, preventing the formation of calcifiable cartilage and eventual bone formation. Exposure to appropriately configured PEMF has been shown to stimulate endochondral ossification. In experimental endochondral ossification, radiolabeled sulfate incorporation into glycosaminoglycan demonstrated increased chondrogenesis. The chondroid matrix content was significantly increased and at an accelerated rate by PEMF (Figure 4a,b). Importantly, for the success of endochondral bone formation, chondrogenesis ceased on time, and the cartilage matrix was removed for calcification and bone formation [45].

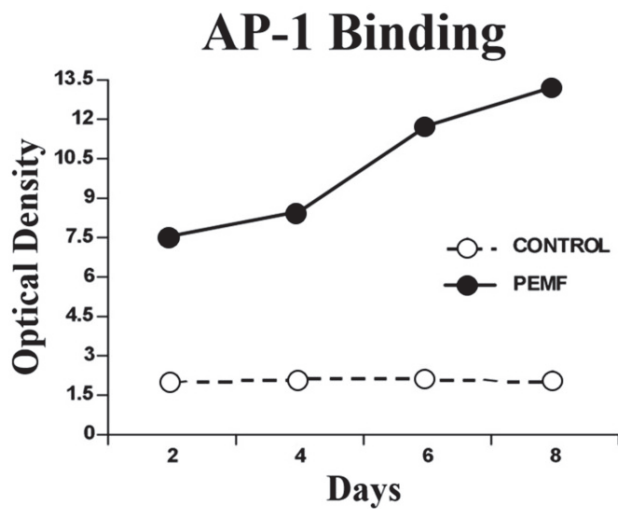


Figure 3. EMSA of nuclear extracts of ossicles demonstrating increased AP-1 binding as a result of PEMF stimulation. Figure from Littman [5].

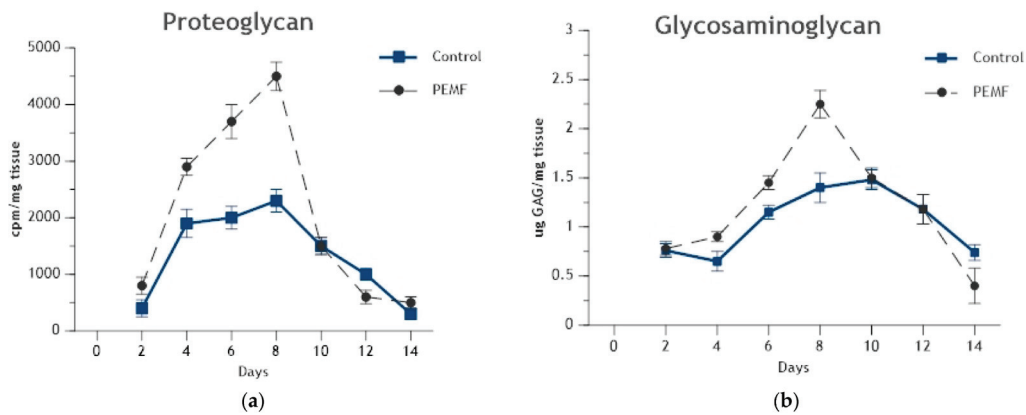


Figure 4. (a) In experimental endochondral ossification, PEMF stimulation produced a significant increase in proteoglycan synthesis on day 4 of stimulation, peaking at day 8 before dropping down to normal levels associated with calcification. (b) PEMF stimulation gradually increased glycosaminoglycan content between days 4 and 8 prior to calcification onset on day 10. Reprinted with permission from Ref. [45]. 2024, Oxford University Press.

Fassina et al. demonstrated in SAOS-1 human osteoblasts that PEMF improved cell proliferation and decorin, fibronectin, osteopontin, types I and III collagen, osteocalcin, and TGF- β [51]. Collectively, the data presented in this section show that PEMF stimulates a variety of structural and signaling molecules of importance to bone formation. Table 3 summarizes the main findings from this section.

Table 3. Summary of Key Studies Showing PEMFs’ Effects on Bone Matrix Synthesis.

Author	Affected Molecules	Outcome
Ongaro et al. [32]	Osteocalcin and alkaline phosphatase	PEMF enhances bone matrix synthesis and osteogenic differentiation in BMSCs and AMSCs.
Ehnert et al. [47]	Alkaline phosphatase	PEMF increased osteogenic differentiation and proliferation in AMSCs and osteoblasts.

Table 3. Cont.

Author	Affected Molecules	Outcome
Poh et al. [48]	Akt, osteocalcin, collagen type I, and alkaline phosphatase	PEMF activation upregulates ECM molecules and osteogenic markers via the MAPK pathway.
Fassina et al. [51]	Decorin, fibronectin, osteopontin, types I and III collagen, osteocalcin, and TGF- β	PEMF improved cell proliferation in SAOS-1 human osteoblasts.

5. Clinical Evidence for Enhanced Fracture Repair by Pulsed Electromagnetic Field Exposure

Bone fractures and non-union present significant challenges in orthopedic care, often leading to prolonged pain, disability, and increased healthcare costs, requiring interventions beyond traditional methods to promote healing. Traditional methods such as casting, surgical fixation, bone grafting, and pharmacological interventions are effective but can be limited by patient-specific factors, complications, or delayed healing. PEMF is a non-invasive treatment modality that has emerged as a promising adjunct therapy, offering a non-invasive approach to stimulate bone repair [52,53]. Recent reviews suggest that PEMF stimulation is both beneficial and cost-effective for specific orthopedic conditions, particularly when used alongside standard first-line treatments. When applied appropriately, PEMF stimulation enhances the success rates of fracture healing and is effective in preventing and treating non-unions [6,53–55]. PEMF stimulation is U.S. F.D.A. approved as a non-invasive method to promote bone healing and is widely used in both the U.S. and Europe.

Evidence for the clinical efficacy of PEMF in bone healing is provided by observational studies, controlled trials, and meta-analyses for both fresh fractures and non-unions.

5.1. Clinical Efficacy of PEMF in Fresh Fractures and Osteotomies

Del Buono et al. conducted a case-control study with 50 diaphyseal tibial fractures that underwent reduction and nailing fixation and were allocated to two groups: PEMF-stimulated and unstimulated controls [7]. The pain was significantly lower in the PEMF group at three months, with an average functional recovery of 4.1 months, while control patients took an average of 5.3 months ($p < 0.0001$). The PEMF group achieved fracture healing, assessed by X-ray, more quickly (12.3 ± 2.8 weeks) than the control group (16.5 ± 8.4 weeks, $p = 0.02$). PEMF reduced postoperative pain, analgesic use, and fracture healing time.

In 1986, Fontanesi et al. showed a clinically significant acceleration in healing time in 20 PEMF-stimulated patients (85.7 ± 18.1 days) compared to 20 unstimulated control patients (109.2 ± 30.7 days; $p < 0.005$) [56]. Borsalino et al. conducted a double-blind study of 32 patients (16 treatment and 16 control) who underwent femoral intertrochanteric osteotomy. The authors conducted a roentgenographic evaluation and callus density measurements. All patients were given a placebo control or active PEMF unit on the third day after osteotomy. PEMF exposure accelerated femoral osteotomy healing by increasing callus formation and trabecular bone bridging in the osteotomy area ($p < 0.01$). At 40 and 90 days after surgery, consolidation was described as significantly more advanced in the PEMF-treated group: $p < 0.05$ [57].

Mammi et al. investigated the effects of PEMF in 40 patients treated for degenerative knee arthrosis who underwent valgus tibial osteotomy. Patients were randomly assigned to either a placebo control group or a PEMF-stimulated group. The patients were then rated by osteotomy healing progress into four categories. Category one was the least advanced stage in healing, while category four was the most advanced. 72.2% of the PEMF-stimulated group were ranked categories three and four, while 73.6% of the placebo control group were ranked to categories one and two. PEMF exposure accelerated tibial osteotomy healing ($p < 0.04$) [58].

In both the Borsalino and Mammi studies, performance bias was minimized by having a standard operating protocol and a single operating surgeon in each [57,58]. The data from both studies were combined by Massari et al. Figure 5 highlights these findings.

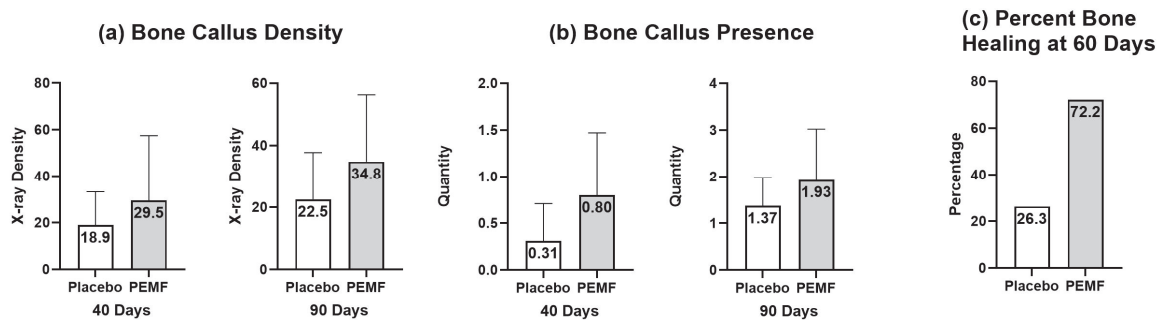


Figure 5. Adapted from Massari et al. [6]. Data are presented as mean \pm standard deviation. (a) represents increased bone callus density measurements at both 40 and 90 days with PEMF stimulation compared to placebo from Borsalino et al. (b) represents increased bone callus quantity measurements at both 40 and 90 days with PEMF stimulation compared to placebo. (c) represents an increased percentage of bone healing at 60 days with PEMF stimulation compared to the placebo from Mammi et al.

Sharrard et al. conducted an RCT assessing the impact of PEMF therapy on tibial shaft fracture, all of which were conservatively treated and had union delay between 16 and 32 weeks [59]. All patients were treated with plaster immobilization; however, 20 patients received active PEMF stimulation units, while 25 received placebo control units for 12 weeks. Radiographic assessments were conducted, and evaluation of the PEMF-stimulated group revealed radiological union in 5/20 fractures, progression toward union in another 5/20, and no progress in 10/20 cases. In the control group, only one fracture showed union, another showed progress, and 23/25 showed no progress. These results indicated a highly significant difference in favor of the active group ($p = 0.002$). The study concluded that PEMFs significantly promote healing in tibial fractures with delayed union.

Faldini et al. conducted an RCT of 77 patients with femoral neck fractures treated with screw fixation in which patients were randomized into a PEMF-stimulated group or a placebo control group. During follow-up at 15.7 months, fracture healing occurred in 15/16 (94%) of patients who were compliant with the active PEMF treatment (more than 6 h/day), compared to 11/16 (69%) in the placebo group. Pain levels were significantly lower in the compliant active group at all follow-up visits compared to the placebo group. In compliant patients, a reduced incidence of osteonecrosis was observed (37% vs. 78%, $p < 0.03$). This demonstrated that PEMF can increase healing rates of fresh femoral neck fractures [60].

In these six studies of the clinical efficacy of PEMF for fresh fractures and osteotomy, PEMF has been demonstrated to increase healing rates by accelerating the healing time and increasing the number of patients who were healed when compared to a placebo control group.

5.2. Clinical Efficacy of PEMF in Non-Unions

Marcer et al. completed a case series where a 73% healing rate was observed in 147 patients who underwent PEMF stimulation for 10 h/day after tibial, femoral, or humeral external fixation. On average, the time elapsed since the original fracture was 13.8 months, and an average of 3.3 operations were performed without successful union prior to PEMF-stimulated [61].

Traina et al. reported a controlled study of patients suffering from non-union fresh tibial fractures in which they found that 41 PEMF-stimulated patients had a shorter union time compared to 26 unstimulated control patients. In the control group, the average

healing time was 7.8 ± 3.5 months versus 5.7 ± 2.5 months in the stimulated group ($p < 0.01$); 69% of the control patients healed compared to healing in 88% of the PEMF-stimulated patients ($p < 0.03$) [62].

In a prospective comparative study, Cebrià et al. reported 57 patients who underwent intramedullary nailing for non-union of tibial pseudoarthrosis. Of those patients, 22 received PEMF stimulation in addition to the nailing [63]. Successful healing was observed in both groups. 20/22 (91%) in the PEMF-stimulated group compared to 29/35 (83%) in the surgery-only group. The average time to union, based on radiological evidence, was 3.3 months with PEMF and 4.9 months with the surgery-only group ($p \leq 0.05$). PEMFs proved beneficial in treating tibial non-union, and their non-invasive nature contributed to a higher rate of complication-free unions.

Shi et al. conducted an RCT that evaluated the effectiveness of early PEMF application compared to a placebo control group in the treatment of delayed union of long-bone fractures [64]. A total of 58 patients who presented with delayed union ranging from 16 weeks to 6 months were included. Of those patients, 31 received PEMF stimulation, and 27 were in the control group. Clinical and radiological assessments were conducted to evaluate the healing progress. PEMF treatment, administered for an average of 4.8 months, resulted in a 24/31 (77.4%) success rate. This was significantly higher than the control group, which had a success rate of 13/27 (48.1%) with an average treatment duration of 4.4 months ($p = 0.029$) [64]. Figure 6 presents an example of a delayed union of a tibial fracture treated with PEMF.

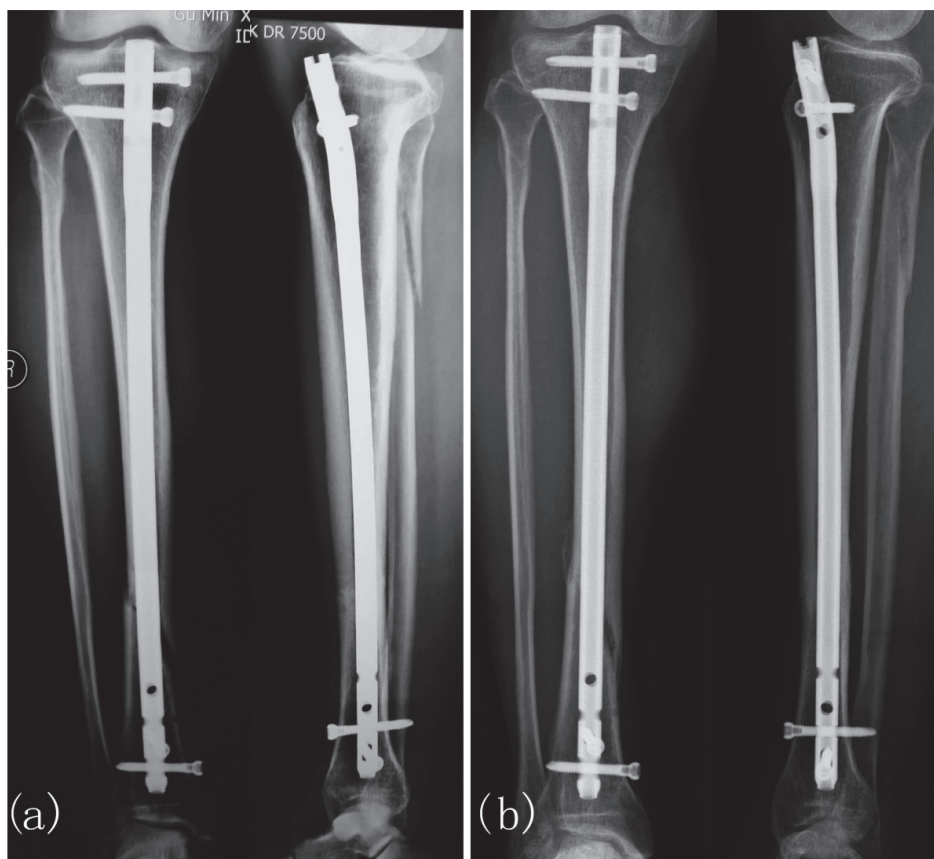


Figure 6. Delayed Union of Tibial Fracture in a 65-year-old Patient Treated with PEMF. (a) Delayed union present after closed reduction and intramedullary fixation 16 weeks post-op. PEMF treatment was initiated at this stage. (b) Fracture union observed at the 3-month treatment mark. Figure from Shi et al. [64].

Murray et al. found that a longer daily PEMF stimulation in 1382 patients with fracture non-unions was associated with a significant reduction in healing time. The group that

used PEMF for 9 h per day on average healed within 112 days. This was 76 days faster than the patients who used PEMF for 3 h or less per day, on average, which took them 188 days to heal ($p < 0.001$) [65].

In 2023, Factor et al. conducted an RCT that investigated a novel PEMF device in the treatment of distal radius fractures in comparison to a placebo group. PEMF treatment significantly demonstrated higher union rates (76%) than the placebo group (58%) at 4 weeks as assessed by CT imaging ($p = 0.02$). Additionally, time to cast removal was notably shorter in the PEMF group (33 ± 5.9 days) compared to the placebo group (39.8 ± 7.4 days) ($p = 0.002$) [57]. Additional observations suggested that early application of PEMF therapy during cast immobilization can improve pain, sensation, range of motion, and daily function in patients with distal radius fractures [66].

5.3. Clinical Efficacy of PEMF Described in Meta-Analyses

In recent years, there has been a surge in high-quality studies evaluating the effectiveness of PEMFs in fracture healing. These studies have focused on a range of fracture types and patient populations, providing more robust data on the clinical utility of PEMFs. Several meta-analyses have evaluated clinical studies conducted in recent years:

A 2011 meta-analysis by Schmidt-Rohlfing et al. examined the potential effects of electrical stimulation (ES) on bone healing. The meta-analysis included RCTs that focused on the primary endpoint of the 'rate of bone healing'. A total of 14 RCTs were identified, encompassing 915 patients. Nine of the 14 studies were suitable for inclusion in the meta-analysis, which yielded a cumulative odds ratio of 3.5 with a 95% confidence interval of 1.94–6.3. This systematic review demonstrated a positive effect of ES on bone healing time ($p < 0.0001$) [67].

In 2014, a meta-analysis of RCTs by Hannemann et al. investigated the use of PEMF or low-intensity pulsed ultrasound system (LIPUS) in treating acute fractures in adults. A total of 737 patients from 13 trials were included in the analysis. Analyzing the time to radiological union, the results were heterogeneous, with a significant benefit observed for PEMF in non-operatively treated fractures or fractures of the upper limb (mean difference [MD] = -26.65 , 95% CI = -50.38 to -2.91 , $p = 0.03$). No studies investigated PEMF stimulation in the lower limb. Additionally, significant evidence was found in accelerating the time to clinical union in acute diaphyseal fractures (MD = -18.27 , 95% CI = -34.59 to -1.95 , $p = 0.03$). However, no significant differences were found in time to clinical union in acute metaphyseal fractures (MD = 1.31 , 95% CI = 11.45 to 14.08 , $p = 0.84$) [68].

In 2020, a meta-analysis by Peng et al. aimed to assess the effect of PEMF on fracture healing. Twenty-two studies involving a total of 1468 participants met the inclusion criteria and were analyzed. The pooled results from 14 studies showed a healing rate of 79.7% in the PEMF group, compared to 64.3% in the control group. PEMF was associated with an increased healing rate (RR = 1.22; 95% confidence interval [CI] = 1.10–1.35; I² = 48) and accelerated healing time (SMD = -1.01 ; 95% CI = -2.01 to -0.00 ; I² = 90%) also based on inverse variance analysis [69].

Bhandari's group has presented an interesting progression of the evolution of thought on PEMF in three meta-analyses beginning in 2008. The evolving search patterns, outcome variables, and data observations throughout these meta-analyses are important to highlight because they influence the conclusions as to the efficacy of PEMF in bone repair.

The 2008 meta-analysis of RCTs sought to evaluate the effects of ES on long-bone fracture healing [70]. This particular meta-analysis utilized eligibility criteria, which included studies for which PEMF was not indicated, such as pseudoarthrosis and limb-lengthening procedures. The ES devices used in the studies varied considerably. Eight out of the 11 articles that met inclusion criteria utilized PEMF. Adding further heterogeneity, frequencies of PEMF varied widely from 15 to 75 Hz, and the electromagnetic force ranged from 0.0025 to 150 V. The trials used a wide range of daily treatment duration from 4 to 24 h per day over a treatment period ranging from 4 to 76 weeks. The clinical outcomes consisted of a heterogeneous group of markers such as tenderness, pain at specific time

points, osteonecrosis rates, arthroplasty needs, radiographic injury severity, pseudarthrosis, and re-displacement rates that compromised statistical assessment. Given the heterogeneity of included conditions and stimulation dosimetry and the wide range of clinical outcomes, there were no benefits for PEMF stimulation use. The authors' data observations on radiographic outcomes described four studies with a nonsignificant pooled relative risk of 1.76, favoring PEMF. The authors concluded that the impact of PEMF on fracture healing was uncertain and that the current evidence at the time was insufficient in supporting the benefit of PEMF in improving union rates in fresh fracture patients, osteotomy, delayed union, or non-union [70]. It must be noted that given the wide range of eligibility and inclusion criteria applied to the studies, alongside the variety of devices, frequencies, electromagnetic forces, and treatment durations, it is difficult to reach any conclusions.

Six years later, Bhandari's group conducted a second meta-analysis to indirectly compare low-intensity pulsed ultrasonography (LIPUS) with electrical stimulation (ESTIM) for fracture healing [71]. This time, the authors searched two Cochrane systematic reviews to identify relevant RCTs. A total of 15 eligible ESTIM trials were found. This restricted the inclusion criteria to trials that enrolled patients with more homogeneous and appropriate pathology, either a recent fresh fracture or delayed union or non-union. Of those trials, seven reported union rates as one of the outcomes. The patients were randomly assigned to an ESTIM group or a control group. The trials included were heterogeneous in the dose of ESTIM, especially exposure duration. They used a wide range of daily treatment duration from 4 to 24 h per day over a treatment period ranging from 4 to 26 weeks, with one trial's treatment period ending when the fracture completely healed. The primary outcome variable was the fracture union rate at 3, 6, and 12 months. The criterion for a successful outcome was four cortices of bridging bone. Low-quality evidence showed a nonsignificant benefit for ESTIM over standard care for non-union populations only at 3 months (RR 2.05, 95% CI = 0.99–4.24) but not for fresh fracture populations (RR 1.23, 95% CI = 0.91–1.66). The study concluded that ESTIM had no significant benefit over standard care in improving fracture union rates. It must be noted that none of the ESTIM trials reported functional outcomes [71].

Two years later, the same group conducted a third meta-analysis, this time investigating 12 studies that reported PEMF use as the therapy method [8]. The rest either used direct current or continuous current stimulation, which may work through different mechanisms. Considerable heterogeneity remained as the trials assessed patients undergoing various conditions, such as spinal fusion, fresh fracture treatment, delayed union/non-unions, or surgical osteotomy, in which the biology may be different. Observational or uncontrolled studies were excluded. Data extracted included interventions, reported outcomes and follow-up times, and loss to follow-up. The primary outcome variables were functional improvement, pain relief, and radiographic non-union. The data observations were different this time, showing a significant improvement in bone healing rates when ES was used in comparison to controls. For pain, the pooled estimate of ES effect showed a statistically significant difference in pain when compared to sham controls (MD on the 100 mm visual analogue scale = -7.67 mm, 95% CI = -13.92 to -1.43 ; $p = 0.02$; $I^2 = 0\%$). For function, the pooled estimate of the ES effect was not statistically significant (MD -0.88 , 95% CI = -6.63 to 4.87 , $p = 0.76$), though this was only based on two trials. For radiographic non-union, the pooled estimate of ES effect showed a reduction in the relative risk of non-union by 35% and the absolute risk by 15% (RR 0.65, 95% CI = 0.53 to 0.81, $p < 0.01$) when compared to sham controls. The authors concluded that ES may improve radiographic union rates and produce clinically significant, albeit modest, improvements in pain [8].

All three meta-analyses highlighted the need for more trials to establish the efficacy of electrical bone stimulators [8,70,71]. As Bhandari's group used more appropriate search criteria over time, which included but was not limited to trials that investigated conditions where PEMF is used clinically, the growing evidence supporting the safety and efficacy of PEMF in non-union populations is highlighted. Combined, the discussed clinical studies demonstrate the safety and effectiveness of PEMF in accelerating healing time and

increasing healing success of clinical fracture non-unions when the treated conditions and dosimetry were appropriate. Table 4 describes the most important findings from each subsection of this section. These studies show consistent positive outcomes by PEMF in clinical settings, improving bone healing rates and reducing pain.

Table 4. The Most Important Clinical Findings in Each Clinical Subsection.

Author	Study Type	Fracture Type	Outcome
Faldini et al. [60]	RCT	Fresh (femoral neck)	PEMF increased healing rates (94% vs. 69%) and reduced pain and osteonecrosis incidence in compliant patients.
Shi et al. [64]	RCT	Delayed union (long-bone)	PEMF treatment had a higher success rate (77.4% vs. 48.1%) compared to the control group ($p = 0.029$).
Aleem et al. [8]	Meta-analysis	Various	ES improved radiographic union rates (RR = 0.65) and reduced pain but had no significant functional improvement.

5.4. Potential PEMF Limitations

No therapy is 100% effective. Most studies show that PEMF is approximately 75% effective in the healing of fracture non-unions, as discussed in this section. Even though PEMF has been shown to be highly successful, it has limitations that should be mentioned. First, it cannot be used with people who have implanted electrical devices such as cardiac pacemakers and deep brain stimulators. Its teratogenic effects are unknown; therefore, pregnant women should avoid PEMF therapy until those effects are known.

Optimal dosimetry is not known in terms of amplitude, frequency, or duration of use, and the experimental matrix to determine optimum dosimetry is complex, involving frequency, amplitude, duration, magnetic field strength, and other factors. The dosimetry studies that do exist are generally within clinical parameters. We have found no reports of side effects such as burns or nerve/skin damage from PEMF when clinically appropriate doses have been used.

Another technique for bone repair stimulation is LIPUS, which has shown good clinical results. The 2014 meta-analysis by Bhandari’s group [71], which we discussed, compared LIPUS with ESTIM. The meta-analysis found that there was low-quality evidence suggesting a potential benefit of LIPUS compared to ESTIM in improving union rates at 6 months in fresh fracture populations. However, ESTIM demonstrated better results than standard care in improving union rates at 3 months for cases of delayed union or existing non-union. Another meta-analysis has shown that PEMF stimulation seems to reduce healing time, whereas LIPUS may be useful for fresh fractures [72].

5.5. Study Selection Criteria

This was a clinical review that generally followed PRISMA guidelines. As authors, we included two scientists who are experts in adenosine receptor activation by PEMF. Their expertise provided guidance to our study selection. The PI has extensive experience using PEMF for bone restoration and bone matrix restoration. For study selection, we searched PubMed, Undermind.ai, Google Scholar, and references from four meta-analyses included in the analysis of fracture efficacy. Since the intent of this paper was to show the progression of PEMF from the membrane to the organ, we had many search queries, including but not limited to membrane receptor activation, intracellular second messengers, synthesis of extracellular matrix molecules, and clinical bone healing. The inclusion criteria focused on studies that demonstrated strong evidence across a wide range, from basic science experiments to RCTs, and ensured the inclusion of more recent studies. This was

conducted to provide a more complete picture of the effects of PEMF. The exclusion criteria focused on disregarding studies without strong evidence and/or had a weak study design. The final outcome of our biblio search has been presented throughout this paper with an overarching and detailed account of how PEMF works and is supported by many studies.

6. Conclusions

PEMFs have emerged as a valuable non-invasive therapy for the treatment of fresh fractures, delayed union, and non-union, with a growing body of clinical data supporting their efficacy. Until recently, the mechanisms of PEMF stimulation on bones have not been completely understood. This review described current mechanistic observations, specifically through the effects of PEMF on ARs, notably A_{2A} and A_3 , then described various intracellular signaling pathways that may be stimulated by PEMF. Clinical studies, ranging from early trials to recent multicenter RCTs, consistently demonstrate that PEMFs improve healing rates, reduce time to union, and are particularly effective in cases of non-union where traditional methods have failed.

This review is unique because it presents biological pathways, starting from the cellular scale, followed by the tissue and organismal scale, provides a complete explanation of how PEMF works, and unlocks the “black box” that previously existed. The safety profile of PEMFs is favorable, with no adverse effects reported, and their non-invasive nature makes them an attractive option for patients, surgeons, and healthcare providers alike. Additionally, PEMFs have been shown to be cost-effective, reducing the need for surgical interventions and associated healthcare costs.

As the field continues to evolve, PEMFs are likely to become a standard adjunctive therapy in the management of fractures and non-union. With continued research and innovation, PEMFs have the potential to transform the landscape of orthopedic care, offering hope to patients with challenging bone healing conditions.

Author Contributions: Conceptualization, A.K. and R.A.; methodology, A.K. and R.A.; validation, A.K. and R.A.; investigation, A.K., S.S. (Simona Salati), S.S. (Stefania Setti) and R.A.; resources, S.S. (Simona Salati), S.S. (Stefania Setti) and R.A.; data curation, A.K., S.S. (Simona Salati), S.S. (Stefania Setti) and R.A.; writing—original draft preparation, A.K., S.S. (Simona Salati), S.S. (Stefania Setti) and R.A.; writing—review and editing, A.K., S.S. (Simona Salati), S.S. (Stefania Setti) and R.A.; visualization, A.K. and R.A.; supervision, A.K. and R.A.; project administration, A.K. and R.A.; funding acquisition, R.A. All authors have read and agreed to the published version of the manuscript.

Funding: This research was funded by an institutional research grant by the Miriam Hospital.

Institutional Review Board Statement: Not applicable.

Data Availability Statement: Not applicable.

Conflicts of Interest: Although the author Simona Salati and Stefania Setti were employed by the company Igea S.p.A, Amr Kaadan and Roy Aaron declare that the research was conducted in the absence of any commercial or financial relationships that could be construed as a potential conflict of interest. The company had no role in the design of the study; in the collection, analyses, or interpretation of data; in the writing of the manuscript, or in the decision to publish the results.

References

1. Gharibi, B.; Abraham, A.A.; Ham, J.; Evans, B.A. Adenosine Receptor Subtype Expression and Activation Influence the Differentiation of Mesenchymal Stem Cells to Osteoblasts and Adipocytes. *J. Bone Miner. Res.* **2011**, *26*, 2112–2124. [CrossRef] [PubMed]
2. Miyamoto, H.; Sawaji, Y.; Iwaki, T.; Masaoka, T.; Fukada, E.; Date, M.; Yamamoto, K. Intermittent pulsed electromagnetic field stimulation activates the mTOR pathway and stimulates the proliferation of osteoblast-like cells. *Bioelectromagnetics* **2019**, *40*, 412–421. [CrossRef] [PubMed]
3. Varani, K.; Gessi, S.; Merighi, S.; Iannotta, V.; Cattabriga, E.; Spisani, S.; Cadossi, R.; Borea, P.A. Effect of Low Frequency Electromagnetic Fields on A_{2A} Adenosine Receptors in Human Neutrophils. *Br. J. Pharmacol.* **2002**, *136*, 57–66. [CrossRef] [PubMed]

4. Kar, N.S.; Ferguson, D.; Zhang, N.; Waldorff, E.I.; Ryaby, J.T.; DiDonato, J.A. Pulsed-Electromagnetic-Field Induced Osteoblast Differentiation Requires Activation of Genes Downstream of Adenosine Receptors A_{2A} and A₃. *PLoS ONE* **2021**, *16*, e02470247659. [CrossRef]
5. Littman, J.; Aaron, R.K. Stimulation of Chondrogenesis in a Developmental Model of Endochondral Bone Formation by Pulsed Electromagnetic Fields. *Int. J. Mol. Sci.* **2023**, *24*, 3275. [CrossRef]
6. Massari, L.; Benazzo, F.; Falez, F.; Perugia, D.; Pietrogrande, L.; Setti, S.; Osti, R.; Vaienti, E.; Ruosi, C.; Cadossi, R. Biophysical Stimulation of Bone and Cartilage: State of the Art and Future Perspectives. *Int. Orthop.* **2019**, *43*, 539–551. [CrossRef]
7. Del Buono, A.; Zampogna, B.; Osti, L.; Fontanarosa, A.; Garofalo, R.; Papalia, R. Pulsed Electromagnetic Fields after Intramedullary Nailing of Tibial Fractures: A Case Control Study. *Int. Orthop. (SICOT)* **2021**, *45*, 2945–2950. [CrossRef]
8. Aleem, I.S.; Aleem, I.; Evaniew, N.; Busse, J.W.; Yaszemski, M.; Agarwal, A.; Einhorn, T.; Bhandari, M. Efficacy of Electrical Stimulators for Bone Healing: A Meta-Analysis of Randomized Sham-Controlled Trials. *Sci. Rep.* **2016**, *6*, 31724. [CrossRef]
9. Cain, C.D.; Adey, W.R.; Luben, R.A. Evidence That Pulsed Electromagnetic Fields Inhibit Coupling of Adenylate Cyclase by Parathyroid Hormone in Bone Cells. *J. Bone Min. Res.* **2009**, *2*, 437–441. [CrossRef]
10. Cadossi, R.; Bersani, F.; Cossarizza, A.; Zucchini, P.; Emilia, G.; Torelli, G.; Franceschi, C. Lymphocytes and Low-Frequency Electromagnetic Fields. *FASEB J.* **1992**, *6*, 2667–2674. [CrossRef]
11. Ventura, C. Elf-Pulsed Magnetic Fields Modulate Opioid Peptide Gene Expression in Myocardial Cells. *Cardiovasc. Res.* **2000**, *45*, 1054–1064. [CrossRef] [PubMed]
12. Borea, P.A.; Gessi, S.; Merighi, S.; Vincenzi, F.; Varani, K. Pharmacology of Adenosine Receptors: The State of the Art. *Physiol. Rev.* **2018**, *98*, 1591–1625. [CrossRef] [PubMed]
13. Hoebertz, A.; Arnett, T.R.; Burnstock, G. Regulation of Bone Resorption and Formation by Purines and Pyrimidines. *Trends Pharmacol. Sci.* **2003**, *24*, 290–297. [CrossRef]
14. Mediero, A.; Perez-Aso, M.; Cronstein, B.N. Activation of Adenosine A_{2A} Receptor Reduces Osteoclast Formation via PKA-and ERK1 /2-mediated Suppression of NF κ B Nuclear Translocation. *Br. J. Pharmacol.* **2013**, *169*, 1372–1388. [CrossRef]
15. Mediero, A.; Kara, F.M.; Wilder, T.; Cronstein, B.N. Adenosine A_{2A} Receptor Ligation Inhibits Osteoclast Formation. *Am. J. Pathol.* **2012**, *180*, 775–786. [CrossRef]
16. Mediero, A.; Frenkel, S.R.; Wilder, T.; He, W.; Mazumder, A.; Cronstein, B.N. Adenosine A_{2A} Receptor Activation Prevents Wear Particle-Induced Osteolysis. *Sci. Transl. Med.* **2012**, *4*, 135ra65. [CrossRef]
17. Mediero, A.; Wilder, T.; Perez-Aso, M.; Cronstein, B.N. Direct or Indirect Stimulation of Adenosine A_{2A} Receptors Enhances Bone Regeneration as Well as Bone Morphogenetic Protein-2. *FASEB J.* **2015**, *29*, 1577–1590. [CrossRef] [PubMed]
18. Zheng, X.; Wang, D. The Adenosine A_{2A} Receptor Agonist Accelerates Bone Healing and Adjusts Treg/Th17 Cell Balance through Interleukin 6. *BioMed Res. Int.* **2020**, *2020*, 2603873. [CrossRef]
19. Larrañaga-Vera, A.; Toti, K.S.; Flatow, J.S.; Haraczy, A.J.; Warnick, E.; Rao, H.; Gao, Z.-G.; Sussman, S.M.; Mediero, A.; Leucht, P.; et al. Novel Alendronate-CGS21680 Conjugate Reduces Bone Resorption and Induces New Bone Formation in Post-Menopausal Osteoporosis and Inflammatory Osteolysis Mouse Models. *Arthritis Res. Ther.* **2022**, *24*, 265. [CrossRef]
20. Varani, K.; Vincenzi, F.; Ravani, A.; Pasquini, S.; Merighi, S.; Gessi, S.; Setti, S.; Cadossi, M.; Borea, P.A.; Cadossi, R. Adenosine Receptors as a Biological Pathway for the Anti-Inflammatory and Beneficial Effects of Low Frequency Low Energy Pulsed Electromagnetic Fields. *Mediat. Inflamm.* **2017**, *2017*, 2740963. [CrossRef]
21. Vincenzi, F.; Targa, M.; Corciulo, C.; Gessi, S.; Merighi, S.; Setti, S.; Cadossi, R.; Goldring, M.B.; Borea, P.A.; Varani, K. Pulsed Electromagnetic Fields Increased the Anti-Inflammatory Effect of A_{2A} and A₃ Adenosine Receptors in Human T/C-28a2 Chondrocytes and hFOB 1.19 Osteoblasts. *PLoS ONE* **2013**, *8*, e65561. [CrossRef] [PubMed]
22. Cohen, S.B.; Gill, S.S.; Baer, G.S.; Leo, B.M.; Scheld, W.M.; Diduch, D.R. Reducing joint destruction due to septic arthritis using an adenosine_{2A} receptor agonist. *J. Orthop. Res.* **2004**, *22*, 427–435. [CrossRef] [PubMed]
23. Jaalouk, D.E.; Lammerding, J. Mechanotransduction gone awry. *Nat. Rev. Mol. Cell Biol.* **2009**, *10*, 63–73. [CrossRef]
24. Martino, F.; Perestrelo, A.R.; Vinarský, V.; Pagliari, S.; Forte, G. Cellular Mechanotransduction: From Tension to Function. *Front. Physiol.* **2018**, *9*, 824. [CrossRef] [PubMed]
25. Brighton, C.T.; Wang, W.; Seldes, R.; Zhang, G.; Pollack, S.R. Signal Transduction in Electrically Stimulated Bone Cells. *J. Bone Jt. Surg. Am.* **2001**, *83-A*, 1514–1523. [CrossRef] [PubMed]
26. Clark, C.C.; Wang, W.; Brighton, C.T. Up-Regulation of Expression of Selected Genes in Human Bone Cells with Specific Capacitively Coupled Electric Fields: Electrical Stimulation of Human Osteoblasts. *J. Orthop. Res.* **2014**, *32*, 894–903. [CrossRef]
27. Yang, R.S.; Liu, T.K.; Lin-Shiau, S.Y. Increased Bone Growth by Local Prostaglandin E₂ in Rats. *Calcif. Tissue Int.* **1993**, *52*, 57–61. [CrossRef]
28. Wu, X.; Zeng, L.-H.; Taniguchi, T.; Xie, Q.-M. Activation of PKA and Phosphorylation of Sodium-Dependent Vitamin C Transporter 2 by Prostaglandin E₂ Promote Osteoblast-like Differentiation in MC3T3-E1 Cells. *Cell Death Differ.* **2007**, *14*, 1792–1801. [CrossRef]
29. Petecchia, L.; Sbrana, F.; Utzeri, R.; Vercellino, M.; Usai, C.; Visai, L.; Vassalli, M.; Gavazzo, P. Electro-Magnetic Field Promotes Osteogenic Differentiation of BM-hMSCs through a Selective Action on Ca²⁺-Related Mechanisms. *Sci. Rep.* **2015**, *5*, 13856. [CrossRef]
30. Tan, Y.; Fei, D.; He, X.; Dai, J.; Xu, R.; Xu, X.; Wu, J.; Li, B. L-Type Voltage-Dependent Calcium Channels in Stem Cells and Tissue Engineering. *Cell Prolif.* **2019**, *52*, e12623. [CrossRef]

31. Schwartz, Z.; Simon, B.J.; Duran, M.A.; Barabino, G.; Chaudhri, R.; Boyan, B.D. Pulsed electromagnetic fields enhance BMP-2 dependent osteoblastic differentiation of human mesenchymal stem cells. *J. Orthop. Res.* **2008**, *26*, 1250–1255. [CrossRef]
32. Ongaro, A.; Pellati, A.; Bagheri, L.; Fortini, C.; Setti, S.; De Mattei, M. Pulsed electromagnetic fields stimulate osteogenic differentiation in human bone marrow and adipose tissue derived mesenchymal stem cells. *Bioelectromagnetics* **2014**, *35*, 426–436. [CrossRef] [PubMed]
33. Martini, F.; Pellati, A.; Mazzoni, E.; Salati, S.; Caruso, G.; Contartese, D.; De Mattei, M. Bone Morphogenetic Protein-2 Signaling in the Osteogenic Differentiation of Human Bone Marrow Mesenchymal Stem Cells Induced by Pulsed Electromagnetic Fields. *Int. J. Mol. Sci.* **2020**, *21*, 2104. [CrossRef] [PubMed]
34. Wang, Y.Y.; Pu, X.Y.; Shi, W.G.; Fang, Q.; Chen, X.; Xi, H.; Gao, Y.; Zhou, J.; Xian, C.J.; Chen, K. Pulsed electromagnetic fields promote bone formation by activating the sAC-cAMP-PKA-CREB signaling pathway. *J. Cell Physiol.* **2019**, *234*, 2807–2821. [CrossRef] [PubMed]
35. Bagheri, L.; Pellati, A.; Rizzo, P.; Aquila, G.; Massari, L.; De Mattei, M.; Ongaro, A. Notch pathway is active during osteogenic differentiation of human bone marrow mesenchymal stem cells induced by pulsed electromagnetic fields. *J. Tissue Eng. Regen. Med.* **2018**, *12*, 304–315. [CrossRef]
36. Ballhause, T.M.; Jiang, S.; Baranowsky, A.; Brandt, S.; Mertens, P.R.; Frosch, K.-H.; Yorgan, T.; Keller, J. Relevance of Notch Signaling for Bone Metabolism and Regeneration. *Int. J. Mol. Sci.* **2021**, *22*, 1325. [CrossRef]
37. Varani, K.; Vincenzi, F.; Pasquini, S.; Blo, I.; Salati, S.; Cadossi, M.; De Mattei, M. Pulsed Electromagnetic Field Stimulation in Osteogenesis and Chondrogenesis: Signaling Pathways and Therapeutic Implications. *Int. J. Mol. Sci.* **2021**, *22*, 809. [CrossRef]
38. Minguell, J.J.; Erices, A.; Conget, P. Mesenchymal Stem Cells. *Exp. Biol. Med.* **2001**, *226*, 507–520. [CrossRef]
39. Tsai, M.-T.; Li, W.-J.; Tuan, R.S.; Chang, W.H. Modulation of osteogenesis in human mesenchymal stem cells by specific pulsed electromagnetic field stimulation. *J. Orthop. Res.* **2009**, *27*, 1169–1174. [CrossRef]
40. Su, P.; Tian, Y.; Yang, C.; Ma, X.; Wang, X.; Pei, J.; Qian, A. Mesenchymal Stem Cell Migration during Bone Formation and Bone Diseases Therapy. *Int. J. Mol. Sci.* **2018**, *19*, 2343. [CrossRef]
41. Henry, J.P.; Bordoni, B. Histology, Osteoblasts. In *StatPearls [Internet]*; StatPearls Publishing: Treasure Island, FL, USA, January 2024. Available online: <https://www.ncbi.nlm.nih.gov/books/NBK557792/> (accessed on 25 November 2024).
42. Cheng, H.; Jiang, W.; Phillips, F.M.; Haydon, R.C.; Peng, Y.; Zhou, L.; Luu, H.H.; An, N.; Breyer, B.; Vanichakarn, P.; et al. Osteogenic activity of the fourteen types of human bone morphogenetic proteins (BMPs). *J. Bone Jt. Surg. Am.* **2003**, *85*, 1544–1552, Erratum in *J. Bone Jt. Surg. Am.* **2004**, *86-A*, 141. [CrossRef] [PubMed]
43. Dimitriou, R.; Tsiridis, E.; Giannoudis, P.V. Current concepts of molecular aspects of bone healing. *Injury* **2005**, *36*, 1392–1404. [CrossRef] [PubMed]
44. Pelissier, P.; Masquelet, A.C.; Bareille, R.; Pelissier, S.M.; Amedee, J. Induced membranes secrete growth factors including vascular and osteoinductive factors and could stimulate bone regeneration. *J. Orthop. Res.* **2004**, *22*, 73–79. [CrossRef]
45. Hung, C.T.; Racine-Avila, J.; Pellicore, M.J.; Aaron, R. Biophysical Modulation of Mesenchymal Stem Cell Differentiation in the Context of Skeletal Repair. *Int. J. Mol. Sci.* **2022**, *23*, 3919. [CrossRef]
46. Esposito, M.; Lucariello, A.; Riccio, I.; Riccio, V.; Esposito, V.; Riccardi, G. Differentiation of human osteoprogenitor cells increases after treatment with pulsed electromagnetic fields. *Vivo* **2012**, *26*, 299–304.
47. Ehnert, S.; van Griensven, M.; Unger, M.; Scheffler, H.; Falldorf, K.; Fentz, A.-K.; Seeliger, C.; Schröter, S.; Nussler, A.K.; Balmayor, E.R. Co-Culture with Human Osteoblasts and Exposure to Extremely Low Frequency Pulsed Electromagnetic Fields Improve Osteogenic Differentiation of Human Adipose-Derived Mesenchymal Stem Cells. *Int. J. Mol. Sci.* **2018**, *19*, 994. [CrossRef]
48. Poh, P.S.P.; Seeliger, C.; Unger, M.; Falldorf, K.; Balmayor, E.R.; van Griensven, M. Osteogenic Effect and Cell Signaling Activation of Extremely Low-Frequency Pulsed Electromagnetic Fields in Adipose-Derived Mesenchymal Stromal Cells. *Stem Cells Int.* **2018**, *2018*, 5402853. [CrossRef]
49. Sheen, J.R.; Mabrouk, A.; Garla, V.V. Fracture Healing Overview. In *StatPearls [Internet]*; StatPearls Publishing: Treasure Island, FL, USA, January 2024. Available online: <https://www.ncbi.nlm.nih.gov/books/NBK551678/> (accessed on 25 November 2024).
50. Stewart, S.K. Fracture Non-Union: A Review of Clinical Challenges and Future Research Needs. *Malays. Orthop. J.* **2019**, *13*, 1–10. [CrossRef]
51. Fassina, L.; Saino, E.; Sbarra, M.S.; Visai, L.; De Angelis, M.G.C.; Magenes, G.; Benazzo, F. In vitro electromagnetically stimulated SAOS-2 osteoblasts inside porous hydroxyapatite. *J. Biomed. Mater. Res. A* **2010**, *93*, 1272–1279. [CrossRef]
52. Cadossi, R.; Massari, L.; Racine-Avila, J.; Aaron, R.K. Pulsed Electromagnetic Field Stimulation of Bone Healing and Joint Preservation: Cellular Mechanisms of Skeletal Response. *JAAOS Glob. Res. Rev.* **2020**, *4*, e19.00155. [CrossRef]
53. Aaron, R.K.; Ciombor, D.; Wang, S.; Simon, B. Clinical Biophysics: The Promotion of Skeletal Repair by Physical Forces. *Ann. N. Y. Acad. Sci.* **2006**, *1068*, 513–531. [CrossRef] [PubMed]
54. Khalifeh, J.M.; Zohny, Z.; MacEwan, M.; Stephen, M.; Johnston, W.; Gamble, P.; Zeng, Y.; Yan, Y.; Ray, W.Z. Electrical Stimulation and Bone Healing: A Review of Current Technology and Clinical Applications. *IEEE Rev. Biomed. Eng.* **2018**, *11*, 217–232. [CrossRef] [PubMed]
55. Segina, D.; Ryaby, J. Osteogenesis Stimulator Devices Reduce Surgical Intervention, Opioid Utilization, and Overall Costs in Patients with Fracture Nonunions. *Orthop. Rev.* **2023**, *15*, 88398. [CrossRef]

56. Fontanesi, G.; Traina, G.C.; Giancetti, F.; Tartaglia, I.; Rotini, R.; Virgili, B.; Cadossi, R.; Ceccherelli, G.; Marino, A. Slow healing fractures: Can they be prevented? (Results of electrical stimulation in fibular osteotomies in rats and in diaphyseal fractures of the tibia in humans). *Ital. J. Orthop. Traumatol.* **1986**, *12*, 371–385.
57. Borsalino, G.; Bagnacani, M.; Bettati, E.; Fornaciari, F.; Rocchi, R.; Uluhogian, S.; Ceccherelli, G.; Cadossi, R.; Traina, G.C. Electrical stimulation of human femoral intertrochanteric osteotomies. Double-blind study. *Clin. Orthop. Relat. Res.* **1988**, *237*, 256–263. [CrossRef]
58. Mammi, G.I.; Rocchi, R.; Cadossi, R.; Massari, L.; Traina, G.C. The electrical stimulation of tibial osteotomies. Double-blind study. *Clin. Orthop. Relat. Res.* **1993**, *288*, 246–253. [CrossRef]
59. Sharrard, W.J. A double-blind trial of pulsed electromagnetic fields for delayed union of tibial fractures. *J. Bone Jt. Surg. Br.* **1990**, *72*, 347–355. [CrossRef]
60. Faldini, C.; Cadossi, M.; Luciani, D.; Betti, E.; Chiarello, E.; Giannini, S. Electromagnetic Bone Growth Stimulation in Patients with Femoral Neck Fractures Treated with Screws: Prospective Randomized Double-Blind Study. *Curr. Orthop. Pract.* **2010**, *21*, 282–287. [CrossRef]
61. Marcer, M.; Musatti, G.; Bassett, C.A. Results of pulsed electromagnetic fields (PEMFs) in ununited fractures after external skeletal fixation. *Clin. Orthop. Relat. Res.* **1984**, *190*, 260–265. [CrossRef]
62. Traina, G.C.; Fontanesi, G.; Costa, P.; Mammi, G.I.; Pisano, F.; Giancetti, F.; Adravanti, P. Effect of electromagnetic stimulation on patients suffering from non-union. A retrospective study with a control group. *J. Bioelectr.* **1991**, *10*, 101–117. [CrossRef]
63. Cebrián, J.L.; Gallego, P.; Francés, A.; Sánchez, P.; Manrique, E.; Marco, F.; López-Durán, L. Comparative study of the use of electromagnetic fields in patients with pseudoarthrosis of tibia treated by intramedullary nailing. *Int. Orthop.* **2010**, *34*, 437–440. [CrossRef] [PubMed]
64. Shi, H.; Xiong, J.; Chen, Y.; Wang, J.; Qiu, X.; Wang, Y.; Qiu, Y. Early Application of Pulsed Electromagnetic Field in the Treatment of Postoperative Delayed Union of Long-Bone Fractures: A Prospective Randomized Controlled Study. *BMC Musculoskelet. Disord.* **2013**, *14*, 35. [CrossRef]
65. Murray, H.; Pethica, B. A Follow-up Study of the in-Practice Results of Pulsed Electromagnetic Field Therapy in the Management of Nonunion Fractures. *Orthop. Res. Rev.* **2016**, *8*, 67–72. [CrossRef] [PubMed]
66. Factor, S.; Druckmann, I.; Atlan, F.; Rosenblatt, Y.; Tordjman, D.; Krespi, R.; Kazum, E.; Pritsch, T.; Eisenberg, G. The Effects of Novel Pulsed Electromagnetic Field Therapy Device on Acute Distal Radius Fractures: A Prospective, Double-Blind, Sham-Controlled, Randomized Pilot Study. *J. Clin. Med.* **2023**, *12*, 1866. [CrossRef] [PubMed]
67. Schmidt-Rohlfing, B.; Silny, J.; Gavenis, K.; Heussen, N. Elektromagnetische Felder, elektrischer Strom und Knochenheilung: Was ist gesichert? *Z. Orthop. Unfallchirurgie* **2011**, *149*, 265–270. [CrossRef]
68. Hannemann, P.F.W.; Mommers, E.H.H.; Schots, J.P.M.; Brink, P.R.G.; Poeze, M. The Effects of Low-Intensity Pulsed Ultrasound and Pulsed Electromagnetic Fields Bone Growth Stimulation in Acute Fractures: A Systematic Review and Meta-Analysis of Randomized Controlled Trials. *Arch. Orthop. Trauma. Surg.* **2014**, *134*, 1093–1106. [CrossRef]
69. Peng, L.; Fu, C.; Xiong, F.; Zhang, Q.; Liang, Z.; Chen, L.; He, C.; Wei, Q. Effectiveness of Pulsed Electromagnetic Fields on Bone Healing: A Systematic Review and Meta-Analysis of Randomized Controlled Trials. *Bioelectromagnetics* **2020**, *41*, 323–337. [CrossRef]
70. Mollon, B.; da Silva, V.; Busse, J.W.; Einhorn, T.A.; Bhandari, M. Electrical stimulation for long-bone fracture-healing: A meta-analysis of randomized controlled trials. *J. Bone Jt. Surg. Am.* **2008**, *90*, 2322–2330. [CrossRef]
71. Ebrahim, S.; Mollon, B.; Bance, S.; Busse, J.W.; Bhandari, M. Low-intensity pulsed ultrasonography versus electrical stimulation for fracture healing: A systematic review and network meta-analysis. *Can. J. Surg.* **2014**, *57*, E105–E118; Erratum in *Can. J. Surg.* **2014**, *57*, 297. [CrossRef]
72. Aifantis, I.D.; Mitsikostas, P.K. The role of biophysical enhancement (LIPUS, ESWT and PEMF's) in fracture healing. *J. Res. Pract. Musculoskelet. Syst.* **2021**, *5*, 110–115. [CrossRef]

Disclaimer/Publisher's Note: The statements, opinions and data contained in all publications are solely those of the individual author(s) and contributor(s) and not of MDPI and/or the editor(s). MDPI and/or the editor(s) disclaim responsibility for any injury to people or property resulting from any ideas, methods, instructions or products referred to in the content.

Article

Are Collagen Protons Visible with the Zero Echo Time (ZTE) Magnetic Resonance Imaging Sequence: A D₂O Exchange and Freeze-Drying Study

Tan Guo ^{1,2,†}, Dina Moazamian ^{2,†}, Arya A. Suprana ^{2,3}, Saeed Jerban ², Eric Y. Chang ^{2,4}, Yajun Ma ², Michael Carl ⁵, Min Chen ¹ and Jiang Du ^{2,3,4,*}

¹ Department of Radiology, Beijing Hospital, National Center of Gerontology, Institute of Geriatric Medicine, Chinese Academy of Medical Sciences, Beijing 100730, China; guotan369@hotmail.com (T.G.); cjr.chenmin@vip.163.com (M.C.)

² Department of Radiology, University of California San Diego, San Diego, CA 92037, USA; dmoazamian@health.ucsd.edu (D.M.); asuprana@ucsd.edu (A.A.S.); sjerban@health.ucsd.edu (S.J.); ericchangmd@gmail.com (E.Y.C.); yam013@health.ucsd.edu (Y.M.)

³ Department of Bioengineering, University of California San Diego, San Diego, CA 92092, USA

⁴ VA San Diego Healthcare System, San Diego, CA 92161, USA

⁵ GE Healthcare, San Diego, CA 92123, USA; michael.carl@gehealthcare.com

* Correspondence: jiangdu@health.ucsd.edu; Tel.: +1-(619)-471-0519; Fax: +1-(619) 471-0503

† These authors contributed equally to this work.

Abstract: It is known that ultrashort echo time (UTE) magnetic resonance imaging (MRI) sequences can detect signals from water protons but not collagen protons in short T₂ species such as cortical bone and tendons. However, whether collagen protons are visible with the zero echo time (ZTE) MRI sequence is still unclear. In this study, we investigated the potential of the ZTE MRI sequence on a clinical 3T scanner to directly image collagen protons via D₂O exchange and freeze-drying experiments. ZTE and UTE MRI sequences were employed to image fully hydrated bovine cortical bone ($n = 10$) and human patellar tendon ($n = 1$) specimens. Then, each specimen was kept in a 30 mL syringe filled with D₂O solution for two days. Fresh D₂O was flushed every 2 h to reach a more complete D₂O–H₂O exchange. Later, the samples were lyophilized for over 40 h and then sealed in tubes. Finally, the samples were brought to room temperature and visualized using the identical 3D ZTE and UTE sequences. All hydrated bone and tendon specimens showed high signals with ZTE and UTE sequences. However, all specimens showed zero signal after the D₂O exchange and freeze-drying procedures. Therefore, similar to UTE imaging, the signal source in ZTE imaging is water. The ZTE sequence cannot directly detect signals from collagen protons in bone and tendons.

Keywords: magnetic resonance imaging (MRI); ultrashort echo time (UTE); zero echo time (ZTE); D₂O–H₂O exchange; collagen

1. Introduction

Water and collagen are both important components of musculoskeletal (MSK) tissues, such as bone, tendons, and ligaments. Normal bone contains ~20% water by volume, while tendons and ligaments are made up of about two-thirds water [1,2]. The water content in MSK tissues can vary depending on age, sex, body weight, and other factors. On the other hand, collagen stands as the predominant protein present in the human body, forming the structural foundation of various connective tissues in the MSK system. It provides strength, elasticity, and support to bone, ligaments, tendons, and other MSK tissues [3]. For example,

collagen provides elasticity and the ability to absorb energy before bone fracture [4]. There is mounting evidence demonstrating that the role of collagen in these changes has been underappreciated [4–7]. Loss of collagen can reduce the energy needed to induce bone fracture (toughness), thereby increasing fracture risk [7]. While collagen has less effect on bone strength and stiffness than mineral, it profoundly affects bone fragility and is the primary toughening mechanism in bone [6,7]. Detection of changes in water and collagen in MSK tissues is clinically and scientifically significant.

Conventional magnetic resonance imaging (MRI) sequences can detect signals from water in soft tissues. However, water in tissues with high collagen content such as tendons, ligaments, and bone is typically “invisible” due to the strong dipole–dipole interaction, which significantly shortens the transverse relaxation time or apparent transverse relaxation time (T_2 or T_2^*), which refers to the time it takes for the transverse magnetization (magnetization in the plane perpendicular to the main magnetic field) to fall to approximately 37% of its initial value [8]. After radiofrequency (RF) excitation, their transverse magnetizations quickly decay to near zero before the receiving mode is enabled for Cartesian spatial encoding with conventional MRI. To achieve direct detection of water signals within tissues with short or ultrashort T_2 relaxation times (or the so-called short- T_2 tissues), it is critical to reduce the echo time (TE) to less than the tissue T_2^* s (T_2^* relaxation times in tissues) to allow enough time for spatial encoding before the transverse magnetization decays to near zero. Recently, a group of sequences with nominal TEs of 0.1 ms or less was developed for direct imaging of short- T_2 tissues [9–21]. These sequences include water- and fat-suppressed projection MR imaging (WASPI) [9], sweep imaging with Fourier transformation (SWIFT) imaging [10], hybrid acquisition-weighted stack of spirals (AWSOS) imaging [11], pointwise encoding time reduction with radial acquisition (PETRA) [12], ultrashort echo time (UTE) imaging [13–18], and zero echo time (ZTE) imaging [19–21]. UTE and ZTE sequences employ non-Cartesian spatial encoding to reduce TEs drastically to directly image the short- T_2 tissues with useful water signal levels and high spatial resolution.

While water signals in short- T_2 tissues can be directly detected with UTE and ZTE sequences, it is much more challenging to achieve direct detection of signals originating from collagen protons. The collagen molecule is structured as a triple helix comprising a three-stranded arrangement of an α -helix [22]. The collagen helix is maintained by a series of hydrogen bonds with additional support from stereo-electronic interactions and posttranslational modifications like hydroxylation and cross-linking [23]. As a result, collagen backbone protons have much-reduced mobility and thus extremely short T_2 relaxation times. A recent study by Ma et al. suggested that signals from collagen backbone protons in bone and tendons cannot be detected by two-dimensional (2D) radial UTE and 3D UTE cones sequences [24].

UTE sequences employ radial ramp sampling, where the k-space data are collected in a radial pattern, starting from the center and moving outwards quickly, allowing for much-reduced echo times. The ramp gradient leads to much longer effective TEs, thus slow sampling of the k-space center (the exact middle of the k-space) [25]. ZTE sequences sample the k-space center much faster, as the spatial encoding gradient has been fully ramped up during RF excitation and data acquisition [15]. Therefore, ZTE sequences are expected to provide shorter effective TEs and, thus, less spatial blurring for short- T_2 tissues. Several studies have claimed that ZTE-type sequences can detect signals from semisolids more efficiently than UTE sequences [9,19–21]. However, whether ZTE sequences can directly detect signals from collagen backbone protons is still unclear. This study aims to explore the feasibility of the 3D ZTE sequence in detecting signals from collagen backbone protons via H_2O – D_2O exchange and freeze-dry experiments of cortical bone and patellar tendon specimens on a clinical 3 Tesla whole-body scanner.

2. Materials and Methods

2.1. Sample Preparation

Ten bovine cortical bone samples sectioned in a rectangular shape (approximately $30 \times 10 \times 5 \text{ mm}^3$) and one cadaveric human patellar tendon sample (80 mm in length) were prepared for this study. The bone samples were sectioned from fresh femoral mid-shaft bovine specimens purchased from a local slaughterhouse using a low-speed diamond saw (Isomet 1000, Buehler, Lake Bluff, IL, USA) with continuous water irrigation. The patellar tendon sample was dissected from a cadaveric human knee specimen provided by the UCSD anatomy lab. Before MRI, all samples were fully hydrated by storing them in a phosphate-buffered saline (PBS) solution for 24 h.

2.2. Imaging Acquisition

All samples were imaged with 3D ZTE and UTE sequences on a 3T clinical MR scanner (GE Healthcare Technologies, Milwaukee, MI, USA). Figure 1 shows the ZTE and 3D radial UTE sequence diagrams. The ZTE sequence employed a short rectangular RF pulse (duration = 8 μs) for nonselective excitation, followed by 3D center-out radial sampling [15]. The 3D UTE sequence utilized a short rectangular pulse (duration = 32 μs) for nonselective excitation, followed by 3D radial ramp sampling with conical view ordering [14]. A 4-channel wrist coil was utilized for signal reception for both 3D ZTE and UTE imaging. For the 3D ZTE sequence, the following parameters were used: repetition time (TR) = 2.1 ms, flip angle (FA) = 4°, receiver bandwidth = 62.5 kHz, field of view (FOV) = 40 mm, slice thickness = 3 mm, number of slices = 52, acquisition matrix of $192 \times 192 \times 16$ for cortical bone and $256 \times 256 \times 16$ for patellar tendon. Similar sequence parameters were used for the 3D UTE sequence, with the exception of a longer TR of 10 ms and a higher flip angle of 10°. The 3D UTE sequence was also repeated with longer TEs of 1.1 ms, 2.2 ms, 3.3 ms, and 4.4 ms to investigate potential fat–water oscillations. The total scan time for each sequence was around 2 min. Table 1 summarizes the MRI parameters for both 3D ZTE and UTE sequences.

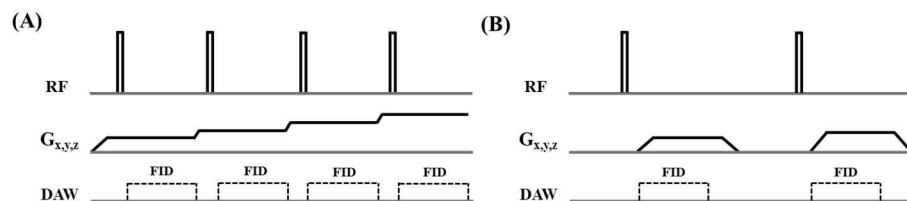


Figure 1. The 3D ZTE sequence utilizes a short rectangular RF pulse (duration = 8 μs , flip angle = 4°) for nonselective excitation, followed by 3D center-out radial sampling during fully ramped-up readout gradients (A). The 3D UTE sequence employs a short rectangular RF pulse (duration = 32 μs , flip angle = 10°) for nonselective excitation, followed by 3D center-out radial ramp sampling (B).

Table 1. MRI parameters of the 3D ZTE and UTE sequences.

Parameters	ZTE Sequence	UTE Sequence
Repetition Time (TR)	2.1 ms	10 ms
Echo Time (TE)	12 μs	28 μs
Flip Angle (FA)	4°	10°
Pulse Duration	8 μs	32 μs
Receiver Bandwidth		62.5 kHz
Field of View (FOV)		40 mm
Acquisition Matrix		Bone: $192 \times 192 \times 16$ Tendon: $256 \times 256 \times 16$
Slice Thickness		3 mm
Scan Time		2 minutes

2.3. Experimental Procedures

All samples were scanned twice, first when fully hydrated and next when water was completely removed by D₂O–H₂O exchange, followed by freeze-drying. All bone samples were put in a 30 mL syringe filled with D₂O solution (99.8% isotopic, Thermo Scientific Chemicals, 168 Third Avenue, Waltham, MA, USA) for exchange and kept in the refrigerator for two days (~4 °C). The tendon sample was placed in a separate syringe following the same process. Fresh D₂O was flushed for both syringes every 2 h to reach a more thorough D₂O–H₂O exchange. Then, the samples were lyophilized using a Labconco Lyph-Lock 4.5 L freeze-dry system (model 77510-00, Labconco Corp., Kansas City, MO, USA) for over 40 h. After freeze-drying, all bovine bone samples were stored in one sealed tube, while the human patellar tendon was kept in another sealed tubal container. Both tubes were brought to room temperature before being imaged again using the same protocols mentioned above. Figure 2 shows a flow diagram for the experimental procedure.

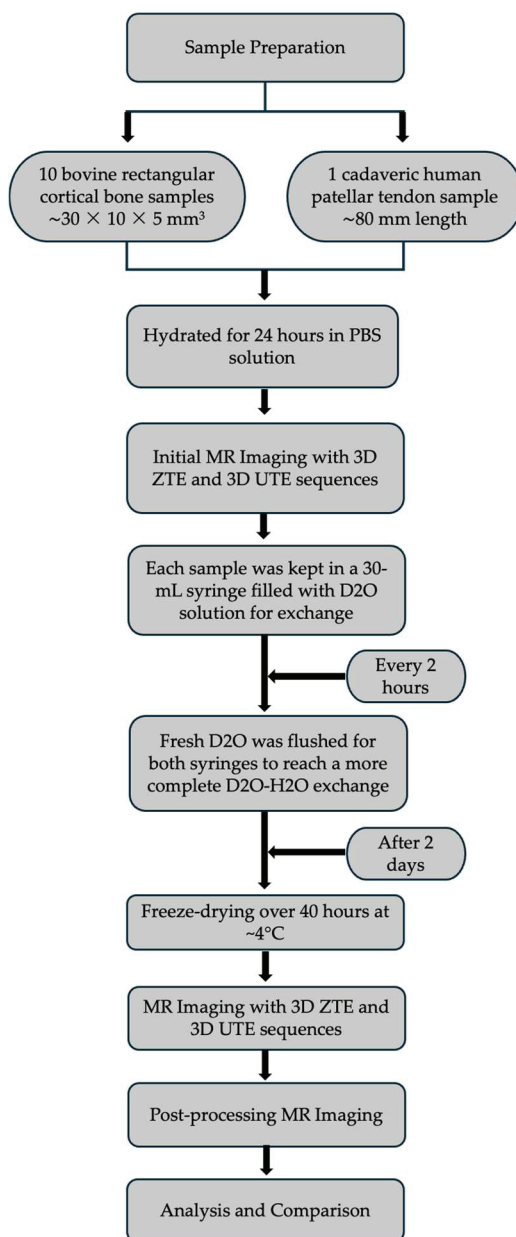


Figure 2. A flow diagram for the experimental procedure. PBS, phosphate-buffered saline.

2.4. Image Analysis

The signal-to-noise ratio (SNR) and contrast-to-noise ratio (CNR) were measured for cortical bone and patellar tendon samples, respectively. The SNR was calculated as the ratio of the mean signal intensity inside a user-drawn region of interest (ROI) to the standard deviation of the signal in ROI placed in the background. The CNR was calculated as the ratio of the signal difference between bone/tendon and background to the standard deviation of the background noise. The analysis was performed using the open-source software ImageJ (NIH, <https://imagej.net/ij>, accessed on 25 September 2024).

3. Results

3.1. Bovine Cortical Bone

Figure 3 shows the 3D ZTE and UTE imaging of bovine cortical bone samples before and after D₂O–H₂O exchange and freeze-drying. Both the ZTE and the UTE sequences depicted high signals from all hydrated bovine cortical bone samples, with average SNR values of 54.6 ± 3.1 for the ZTE images and 103.1 ± 9.8 for the UTE images. The CNR values were 46.2 ± 3.1 for the ZTE images and 98.4 ± 9.8 for the UTE images. The UTE images showed a higher signal because of the higher flip angle of 10°, which is 2.5 times higher than the flip angle of 4° used by the ZTE sequence. After D₂O–H₂O exchange and freeze-drying, pure noise was observed in the ZTE and UTE images. None of the bovine cortical bone samples were visible. The measured CNR values between the bone and the background air were 0.03 ± 1.11 for the ZTE images and 0.015 ± 0.082 for the UTE images, suggesting that the bone and background had the same signal level in both the ZTE and the UTE images. The sequential D₂O–H₂O exchange and freeze-drying procedures were expected to completely remove all water in the cortical bone. The pure noise images suggest that collagen backbone protons, which would stay in cortical bone after the D₂O–H₂O exchange and freeze-drying experiments, were invisible with the UTE and ZTE sequences.

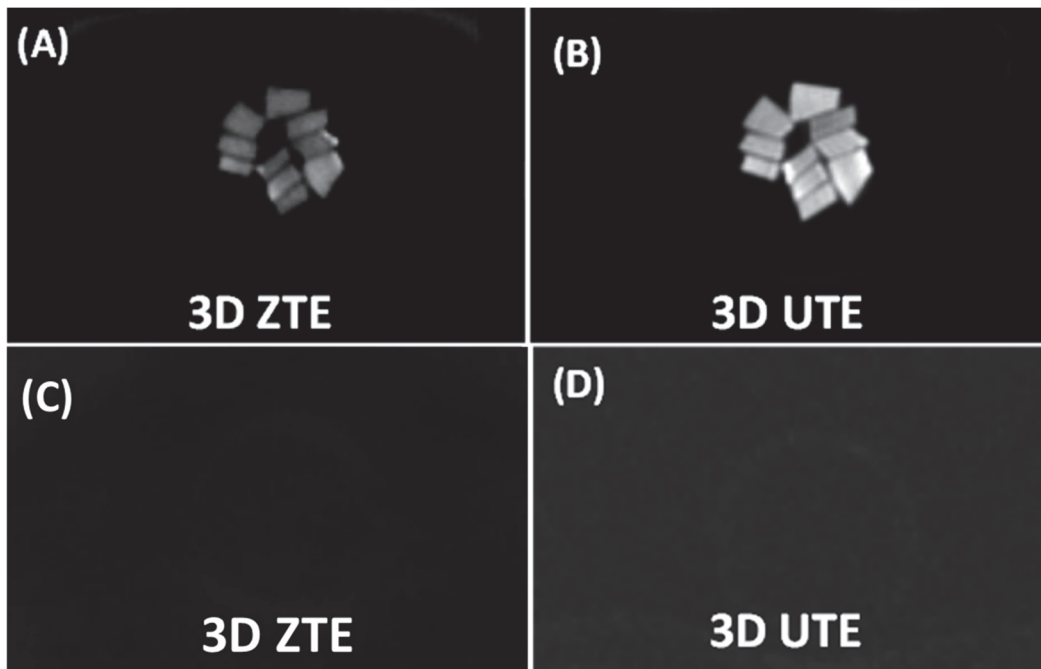


Figure 3. Fully hydrated bovine cortical bone samples were imaged with 3D ZTE (A) and UTE sequences (B), along with ZTE (C) and UTE (D) imaging of the same bone specimens after two days of repeated D₂O exchange followed by freeze-drying for over 40 h. Both the ZTE and the UTE sequences show high signals for the hydrated cortical bone samples but zero signals after the repeated D₂O exchange and freeze-drying procedure.

3.2. Human Patellar Tendon

Figure 4 shows ZTE and UTE imaging of a human patellar tendon sample before and after D₂O–H₂O exchange and freeze-drying. The ZTE and UTE sequences depicted high signals from the fully hydrated patellar tendon, with average SNR values of 77.0 ± 7.3 for the ZTE images and 108.3 ± 4.4 for the UTE images. The CNR values were 73.1 ± 7.0 for the ZTE images and 102.6 ± 4.2 for the UTE images. After D₂O–H₂O exchange and freeze-drying, only a thin bright line was observed in the margins of the patellar tendon sample. The measured CNR values between the central part of the patellar tendon and the background air were -0.09 ± 0.58 for the ZTE images and -0.7 ± 1.6 for the UTE images. The thin, bright line was from fat and showed typical fat/water in-phase and out-phase behaviors based on UTE imaging, with delayed TEs of 1.1 ms, 2.2 ms, 3.3 ms, and 4.4 ms. Collagen backbone protons in the patellar tendon, which were supposed to survive following the D₂O exchange and freeze drying, showed zero signal with the 3D ZTE and UTE sequences. Fat was also supposed to survive the D₂O exchange and freeze-drying process, and showed a high signal in both the ZTE and the UTE images. Therefore, the 3D ZTE sequence cannot directly detect signals from collagen backbone protons in tendons using clinical MR scanners.

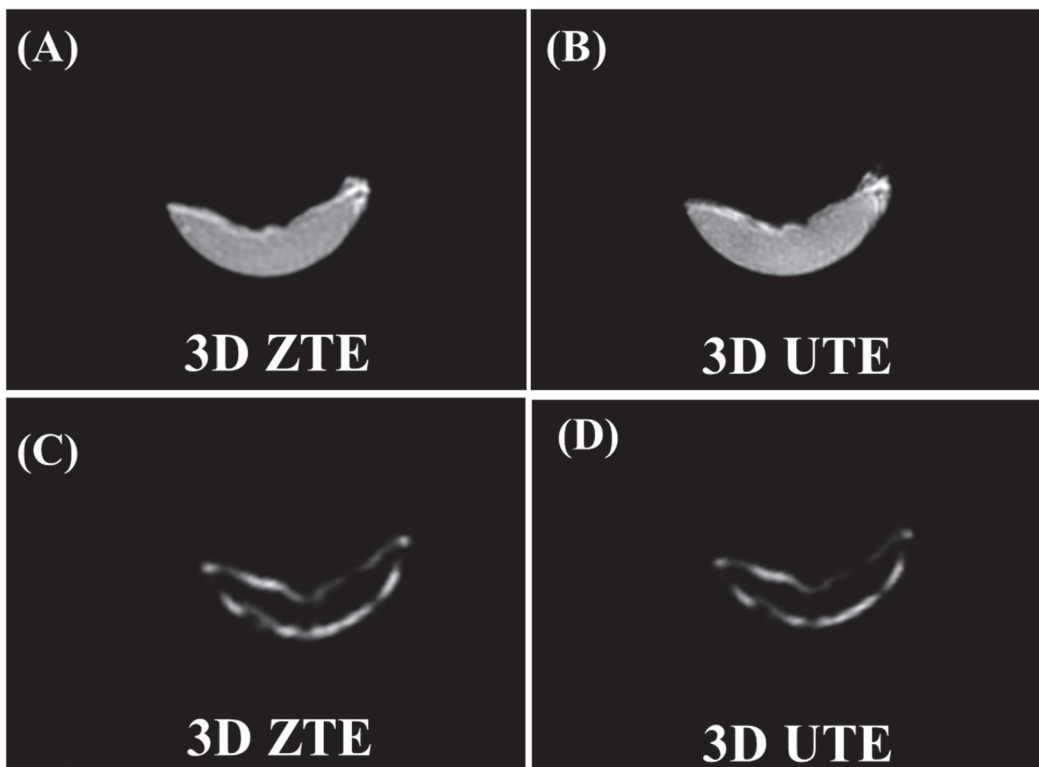


Figure 4. A fully hydrated cadaveric human patellar tendon sample was imaged with 3D ZTE (A) and UTE sequences (B), along with ZTE (C) and UTE (D) imaging of the same patellar tendon specimen after 2 days of repeated D₂O exchange followed by freeze-drying for over 40 h. The hydrated patellar tendon sample shows a high signal with both ZTE and UTE sequences. After the repeated D₂O exchange and freeze-drying procedure, only thin bright lines were observed, which showed typical fat/water in-phase and out-phase behaviors.

After D₂O–H₂O exchange and freeze-drying, pure noise was observed in the ZTE and UTE images, with SNR values of ~ 5 (close to the SNR values in background regions). Table 2 summarizes the SNR and CNR values of the ZTE and UTE imaging for both the bovine bone and the patellar tendon samples before and after the D₂O–H₂O exchange and freeze-drying procedure.

Table 2. Summarize the SNR and CNR values of the 3D ZTE and UTE images.

MRI Sequences	Tissue	Condition	SNR (Mean \pm SD)	CNR (Mean \pm SD)
ZTE	Bone	Hydrated	54.6 \pm 3.1	46.2 \pm 3.1
		D2O Exchange + Freeze-Dried	5.36 \pm 1.11	0.03 \pm 1.11
	Tendon	Hydrated	77.0 \pm 7.3	73.1 \pm 7.0
		D2O Exchange + Freeze-Dried	8.53 \pm 2.18	-0.09 \pm 0.58
UTE	Bone	Hydrated	103.1 \pm 9.8	98.4 \pm 9.8
		D2O Exchange + Freeze-Dried	5.64 \pm 0.08	0.015 \pm 0.082
	Tendon	Hydrated	108.3 \pm 4.4	102.6 \pm 4.2
		D2O Exchange + Freeze-Dried	4.95 \pm 0.60	-0.7 \pm 1.6

4. Discussion

Collagen-rich tissues such as cortical bone and tendons have very short T2 relaxation times. They are invisible with conventional MRI but detectable with ZTE and UTE sequences [26]. Understanding the signal origin is crucial to image interpretation, particularly in in vivo translation, where MRI possibly will substitute more invasive methods [15,16,24]. In this study, we demonstrated that water is the origin of the ZTE signal in bovine cortical bone and human patellar tendon samples on a clinical 3T scanner. The ZTE images show high signal intensity for fully hydrated bone and tendon samples. The lack of signal observed in the bone and tendon specimens after D₂O exchange and freeze-drying suggests that collagen backbone protons are not detectable using the ZTE sequence. This study is the first attempt to investigate the feasibility of directly imaging collagen backbone protons using the 3D ZTE technique.

The spatial encoding gradient is activated prior to the RF pulse excitation, leading to a theoretical TE of zero in ZTE imaging [19–21]. The acquisition starts after a short RF excitation with a delay set to accommodate the transmit/receive switching time. Utilizing a pulse generator that allows a minimization of the transmit/receive switching to 1 μ s, the actual TE time that ZTE can achieve is approximately 10 μ s. Data missed during the actual TE leads to a central gap in k-space, which has to be compensated by algebraic reconstruction [19], resampled with a Cartesian trajectory technique such as PETRA [12], or an additional acquisition with a set of low-frequency projections with lower gradient strength, such as WASPI [9]. To minimize the loss of data in the central k-space, the excitation pulse has to be kept very short (e.g., 8 μ s), leading to a low flip angle of typically less than 4°. The spatial encoding gradient is switched on after the RF excitation pulse in UTE imaging, allowing a high flip angle to be used. In this study, a low flip angle of 4° was used for ZTE imaging versus 10° for UTE imaging, which explains the higher SNR values for the bone and tendon samples in the UTE images over the ZTE images. Meanwhile, UTE employs radial ramp sampling, leading to a longer effective TE and, thus, more spatial blurring. ZTE uses a small step of changing gradients in three directions, allows acquisition with very low acoustic noise, and reduces eddy current problems, making ZTE imaging highly robust.

Results from this study are broadly consistent with results from a prior study by Ma et al., who reported that 2D and 3D UTE sequences could not directly image the collagen matrix [24]. UTE could detect bound water with an ultrashort T2* and free water with a slightly longer T2* in hydrated bone and tendon samples [24,26–28]. The D₂O exchange and freeze-drying procedures removed both bound water and free water, leaving collagen backbone protons being selectively detected by the UTE sequence. The signal void in the UTE images of the bone and tendon samples demonstrated that the UTE sequences could not directly detect any signal from collagen backbone protons.

However, a few prior studies reported contradictory results. For example, Wu et al. reported that WASPI could specifically suppress signals from water and fat within the bone, leaving only signals from the solid organic matrix like collagen being selectively imaged [9]. Cao et al. showed that the WASPI signal was highly correlated with the organic matrix density derived by gravimetric analysis ($R^2 = 0.98$) and by amino acid analysis ($R^2 = 0.95$) [29]. Another investigation by Siu et al. indicated that UTE sequences could detect signals from collagen protons at 7T [30]. The Siu experiments were performed in collagen solutions. Bi-exponential T_2^* fitting revealed a highly linear relationship ($R^2 = 0.99$) between the UTE collagen signal fraction and the measured collagen concentration in solutions. The authors concluded that the UTE signal originating from protons within the collagen molecule exhibited an average T_2^* relaxation time of 0.75 ± 0.05 ms and an average chemical shift of -3.56 ± 0.01 ppm in comparison to water at a magnetic field strength of 7T. They further concluded that collagen could be detected and quantified using UTE.

The major difference between our study and the Siu study is the different experimental conditions. In our study, intact bone and patellar tendon samples were directly imaged with ZTE and UTE sequences after D_2O exchange and freeze-drying. The Siu study used hydrolyzed type I and III collagen powder in solutions [30]. The hydrolyzed collagen solution could cleavage the structure of the collagen into small peptides, leading to the destruction of the 3D structure of the collagen molecules [31]. As a result, collagen backbone protons were in the rigid organic matrix and immobilized in our study, while the amorphous state of collagen provided much improved mobility in the Siu study, leading to a more prolonged T_2^* relaxation time. As the authors reported, collagen protons in the amorphous state had a relatively long T_2^* of 0.75 ms. In contrast, collagen backbone protons in the rigid matrix were expected to have much shorter T_2^* relaxation times. Bi-component analysis showed that tendons had two different water components, with T_2^* s of ~ 8 ms, which corresponds to free water, accounting for 75% of the total UTE signal, and ~ 0.6 ms, which corresponds to bound water, accounting for 25% of the total UTE signal [32]. Collagen backbone protons in tendons are expected to have a much shorter T_2^* than bound water. Therefore, collagen protons in the amorphous state should differ significantly from collagen backbone protons in intact collagen bundles in real tissues. This is also why magic angle spinning (MAS) is required to convert the very broad featureless NMR lines into much narrower line widths for high-resolution NMR spectroscopy of solid materials [33].

Another way to assess collagen backbone protons in bone and tendons is the UTE magnetization transfer (UTE-MT) imaging technique [34–38]. Two-pool modeling of UTE-MT data provides information about the water and macromolecular pools, including their pool sizes, exchange rates, and relaxation times. UTE-MT studies suggest that collagen backbone protons have extremely short T_2 s of 6–15 μ s [34–38]. The T_2 values are largely consistent with macromolecular proton T_2 s reported in the literature [39–41]. Our experimental results suggest that the 3D ZTE sequence cannot directly image species with T_2 s of ~ 10 μ s.

While collagen backbone protons in the bone and tendon samples were invisible with the 3D ZTE and UTE sequences, a large number of studies have reported that these sequences can directly detect signals from non-aqueous myelin protons in the white matter of the brain [16,17,20,42–45]. Horch et al. investigated the origins of the ultrashort T_2 proton NMR signals in myelinated nerves. They suggested that UTE sequences could be used to directly measure the ultrashort T_2 signals (50μ s $< T_2 < 1$ ms) as a new means of quantitative myelin mapping [16]. Wilhelm et al. examined UTE imaging of purified bovine myelin extract and rat thoracic spinal cord samples on a 9.4 T spectrometer (Bruker DMX 400). They found myelin T_2^* s varied between 8 μ s and 26 ms with $\sim 90\%$ of the myelin T_2^* less than 1 ms [17]. Weiger et al. investigated myelin imaging with a 3D ZTE-based

technique with hybrid filling (HYFI) on a 3T whole-body scanner and found 85% of the myelin signal had a $T2^*$ of $7.5 \mu\text{s}$ [20]. Sheth et al. studied UTE imaging of lyophilized bovine myelin powders and reported a $T2^*$ of $110\text{--}160 \mu\text{s}$ [43]. Ma et al. reported a novel 3D short TR adiabatic inversion recovery UTE (STAIR-UTE) technique for myelin mapping in vivo and reported a short $T2^*$ of $\sim 210 \mu\text{s}$ [44]. Shen et al. applied dual-echo UTE with a rosette k-space pattern to the brain and reported a $T2^*$ of $\sim 0.10 \pm 0.06 \text{ ms}$ and a fraction of $10.9\% \pm 1.9\%$ for myelin in white matter and a $T2^*$ of $0.09 \pm 0.12 \text{ ms}$ and a fraction of $5.7\% \pm 2.4\%$ for myelin in white matter [46]. The considerable variations in myelin $T2^*$ and fraction values suggest that more studies are needed to explore the signal sources in UTE and ZTE imaging of myelin. More studies are also necessary to explain why collagen backbone protons are invisible but myelin protons are visible. It is likely related to the increased mobility of non-aqueous protons in myelin over the more rigid collagen backbone protons in bone and tendons.

There are several limitations in this study. First, it is unclear whether the $\text{D}_2\text{O}\text{--}\text{H}_2\text{O}$ exchange and subsequent freeze-drying procedures would affect the collagen structure. Freeze-drying may result in slight protein denaturation and the disruption of water bridges, which are involved in stabilizing the structure [47]. However, the changes in collagen structure, if any, are likely small [23] and are unlikely to significantly affect the transverse relaxation times of collagen backbone protons. We expect the conclusion that ZTE cannot detect signals from collagen backbone protons still held in fresh bone, tendons, and other collagen-rich connective tissues in the MSK system. Second, repeated $\text{D}_2\text{O}\text{--}\text{H}_2\text{O}$ exchange and freeze-drying may lead to significant tissue degradation. Again, we expect that this degradation should not significantly affect the transverse relaxation times of collagen backbone protons. Therefore, the conclusion that collagen backbone protons are invisible with the ZTE sequence is still valid. Third, the $\text{D}_2\text{O}\text{--}\text{H}_2\text{O}$ exchange process removes all exchangeable protons, leaving unexchangeable protons in the collagen structure (e.g., $-\text{CH}_2-$, $-\text{CH}_3$) [48]. The pure noise images in ZTE imaging of bone and tendon samples post $\text{D}_2\text{O}\text{--}\text{H}_2\text{O}$ exchange and freeze drying could only demonstrate that the unexchangeable protons were invisible. There is no direct evidence that exchangeable protons in the collagen structure are invisible with the ZTE sequence. Fourth, the longitudinal and transverse relaxation times of collagen backbone protons are unknown. As far as we know, there are no papers reporting T_2 or T_2^* for collagen backbone protons in bone and tendons. The T_2 of $\sim 10 \mu\text{s}$ derived from MT modeling is indirect and might be inaccurate. It is difficult to explain why collagen backbone protons with $T_2^* \sim 10 \mu\text{s}$ are invisible with the ZTE sequence, but non-aqueous myelin protons with $T_2^* \sim 10 \mu\text{s}$ or less are visible with the ZTE sequence. Further research is necessary to enhance our understanding of this interesting topic. Finally, our preliminary results demonstrate that collagen backbone protons are invisible with UTE and ZTE sequences. We expect collagen backbone protons in bone and tendons to be invisible with other UTE-type sequences, including WASPI, SWIFT, AWSOS, and PETRA sequences.

5. Conclusions

The strong ZTE signal from fully hydrated bone and tendon samples but pure noise after D_2O exchange and freeze-drying suggest that collagen backbone protons are “invisible” with the ZTE sequence.

Author Contributions: Conceptualization, J.D. and T.G.; methodology, J.D., D.M., and A.A.S.; software, M.C. (Michael Carl); validation, D.M., A.A.S., and T.G.; formal analysis, D.M. and A.A.S.; investigation, D.M. and A.A.S.; resources, J.D., E.Y.C., Y.M., S.J., and M.C. (Min Chen); data curation, D.M., A.A.S., and J.D.; writing—original draft preparation, T.G., J.D., and D.M.; writing—review and editing, J.D., T.G., D.M., A.A.S., M.C. (Michael Carl), E.Y.C., Y.M., S.J., and M.C. (Min Chen);

visualization, T.G. and D.M.; supervision, J.D., E.Y.C., Y.M., S.J., and M.C. (Min Chen); project administration, A.A.S.; funding acquisition, J.D., E.Y.C., Y.M., and S.J. All authors have read and agreed to the published version of the manuscript.

Funding: The authors acknowledge grant support from the National Institutes of Health (NIH) (1R01 AR062581, 1R01 AR068987, R01AR075825, R01AR079484, RF1AG075717, and K01AR080257), the VA Clinical Science Research & Development Service (I01CX002211 and I01BX005952), and GE Healthcare.

Institutional Review Board Statement: The study was conducted in accordance with the Declaration of Helsinki, and the protocol was approved by the Ethics Committee of University of California, San Diego (Study #151622) on May 22, 2023. The animal study protocol was approved by the Veterans Affairs San Diego Healthcare System Institutional Animal Care and Use Committee (IACUC) (protocol code A22-023 and 9/21/22).

Informed Consent Statement: Informed consent was obtained from all subjects involved in the study.

Data Availability Statement: The original contributions presented in this study are included in the article. Further inquiries can be directed to the corresponding author(s).

Conflicts of Interest: The authors declare no conflicts of interest.

References

1. Granke, M.; Does, M.D.; Nyman, J.S. The role of water compartments in the material properties of cortical bone. *Calcif. Tissue Int.* **2015**, *97*, 292–307. [CrossRef]
2. Ristaniemi, A.; Tornaiainen, J.; Stenroth, L.; Finnila, M.A.J.; Paakkonen, T.; Toyras, J.; Korhonen, R.K. Comparison of water, hydroxy-proline, uronic acid and elastin contents of bovine knee ligaments and patellar tendon and their relationships with biomechanical properties. *J. Mech. Behav. Biomed. Mater.* **2020**, *104*, 103639. [CrossRef]
3. Di Lullo, G.A.; Sweeney, S.M.; Körkkö, J.; Ala-Kokko, L.; San Antonio, J.D. Mapping the Ligand-binding Sites and Disease-associated Mutations on the Most Abundant Protein in the Human, Type I Collagen. *J. Biol. Chem.* **2002**, *277*, 4223–4231. [CrossRef] [PubMed]
4. Viquet-Carrin, S.; Garnero, P.; Delmas, P.D. The role of collagen in bone strength. *Osteoporos. Int.* **2006**, *17*, 319–336. [CrossRef]
5. Ritchie, R.O.; Buehler, M.J.; Hansma, P. Plasticity and toughness in bone. *Phys. Today* **2009**, *62*, 41–47. [CrossRef]
6. Zioupos, P.; Currey, J.D.; Hamer, A.J. The role of collagen in the declining mechanical properties of aging human cortical bone. *J. Biomed. Mater. Res.* **1999**, *45*, 108–116. [CrossRef]
7. Burr, D.B. The contribution of the organic matrix to bone's material properties. *Bone* **2002**, *31*, 8–11. [CrossRef]
8. Ma, Y.; Jang, H.; Jerban, S.; Chang, E.Y.; Chung, C.B.; Bydder, G.M.; Du, J. Making the invisible visible—Ultrashort echo time magnetic resonance imaging: Technical developments and applications. *Appl. Phys. Rev.* **2022**, *9*, 041303. [CrossRef] [PubMed]
9. Wu, Y.; Chesler, D.A.; Glimcher, M.L.; Garrido, L.; Wang, J.; Jiang, H.J.; Ackerman, J.L. Multinuclear solid-state three-dimensional MRI of bone and synthetic calcium phosphates. *Proc. Natl. Acad. Sci. USA* **1999**, *96*, 1574–1578. [CrossRef] [PubMed]
10. Idiyatullin, D.; Corum, C.; Park, J.Y.; Garwood, M. Fast and quiet MRI using a swept radiofrequency. *J. Magn. Reson.* **2006**, *181*, 342–349. [CrossRef] [PubMed]
11. Qian, Y.; Williams, A.; Chu, C.R.; Boada, F.E. High-resolution ultrashort echo time (UTE) imaging on human knee with AWSOS sequence at 3.0 T. *J. Magn. Reson. Imaging* **2012**, *35*, 204–210. [CrossRef] [PubMed]
12. Grodzki, D.M.; Jakob, P.M.; Heismann, B. Ultrashort echo time imaging using pointwise encoding time reduction with radial acquisition (PETRA). *Magn. Reson. Med.* **2012**, *67*, 510–518. [CrossRef] [PubMed]
13. Robson, M.D.; Gatehouse, P.D.; Bydder, M.; Bydder, G.M. Magnetic resonance: An introduction to ultrashort TE (UTE) imaging. *J. Comput. Assist. Tomogr.* **2003**, *27*, 825–846. [CrossRef] [PubMed]
14. Du, J.; Carl, M.; Bydder, M.; Takahashi, A.; Chung, C.B.; Bydder, G.M. Qualitative and quantitative ultrashort echo time (UTE) imaging of cortical bone. *J. Magn. Reson.* **2010**, *207*, 304–311. [CrossRef] [PubMed]
15. Horch, R.A.; Nyman, J.S.; Gochberg, D.F.; Dortch, R.D.; Does, M.D. Characterization of ¹H NMR signal in human cortical bone for magnetic resonance imaging. *Magn. Reson. Med.* **2010**, *64*, 680–687. [CrossRef]
16. Horch, R.A.; Gore, J.C.; Does, M.D. Origins of the ultrashort T2 1H NMR signals in myelinated nerve: A direct measure of myelin content? *Magn. Reson. Med.* **2011**, *66*, 24–31. [CrossRef] [PubMed]
17. Wilhelm, M.J.; Ong, H.H.; Wehrli, S.L.; Li, C.; Tsai, P.H.; Hackney, D.B.; Wehrli, F.W. Direct magnetic resonance detection of myelin and prospects for quantitative imaging of myelin density. *Proc. Natl. Acad. Sci. USA* **2012**, *109*, 9605–9610. [CrossRef] [PubMed]

18. Carl, M.; Bydder, G.M.; Du, J. UTE imaging with simultaneous water and fat signal suppression using a time-efficient multi-spoke inversion recovery pulse sequence. *Magn. Reson. Med.* **2016**, *76*, 577–582. [CrossRef]
19. Weiger, M.; Pruessmann, K.P.; Hennel, F. MRI with zero echo time: Hard versus sweep pulse excitation. *Magn. Reson. Med.* **2011**, *66*, 379–389. [CrossRef] [PubMed]
20. Weiger, M.; Froidevaux, R.; Baadsvik, E.L.; Brunner, D.O.; Rosler, M.B.; Pruessmann, K.P. Advances in MRI of the myelin bilayer. *NeuroImage* **2020**, *217*, 116888. [CrossRef]
21. Weiger, M.; Pruessmann, K.P. Zero Echo Time (ZTE) MRI. In *MRI of Short- and Ultrashort-T2 Tissues Making the Invisible Visible*; Springer: Berlin/Heidelberg, Germany, 2024.
22. Fullerton, G.D.; Rahal, A. Collagen structure: The molecular source of the tendon magic angle effect. *J. Magn. Reson. Imaging* **2007**, *25*, 345–361. [CrossRef] [PubMed]
23. Shoulders, M.D.; Raines, R.T. Collagen structure and stability. *Annu. Rev. Biochem.* **2009**, *78*, 929–958. [CrossRef] [PubMed]
24. Ma, Y.J.; Chang, E.Y.; Bydder, G.M.; Du, J. Can ultrashort-TE (UTE) MRI sequences on a 3-T clinical scanner detect signal directly from collagen protons: Freeze-dry and D2 O exchange studies of cortical bone and Achilles tendon specimens. *NMR Biomed.* **2016**, *29*, 912–917. [CrossRef] [PubMed]
25. Rahmer, J.; Bornert, P.; Groen, J.; Bos, C. Three-dimensional radial ultrashort echo-time imaging with T2 adapted sampling. *Magn. Reson. Med.* **2006**, *55*, 1075–1082. [CrossRef] [PubMed]
26. Du, J.; Bydder, G.M. Qualitative and quantitative ultrashort-TE MRI of cortical bone. *NMR Biomed.* **2013**, *26*, 489–506. [CrossRef]
27. Biswas, R.; Bae, W.C.; Diaz, E.; Masuda, K.; Chung, C.B.; Bydder, G.M.; Du, J. Ultrashort echo time (UTE) imaging with bi-component analysis: Bound and free water evaluation of bovine cortical bone subject to sequential drying. *Bone* **2012**, *50*, 749–755. [CrossRef] [PubMed]
28. Du, J.; Diaz, E.; Carl, M.; Bae, W.; Chung, C.; Bydder, G.M. Ultrashort echo time imaging with bicomponent analysis. *Magn. Reson. Med.* **2012**, *67*, 645–649. [CrossRef]
29. Cao, H.; Ackerman, J.L.; Hrovat, M.I.; Graham, L.; Glimcher, M.J.; Wu, Y. Quantitative bone matrix density measurement by water- and fat-suppressed proton projection MRI (WASPI) with polymer calibration phantoms. *Magn. Reson. Med.* **2008**, *60*, 1433–1443. [CrossRef] [PubMed]
30. Siu, A.G.; Ramadeen, A.; Hu, X.D.; Morikawa, L.; Zhang, L.; Lau, J.Y.C.; Liu, G.; Pop, M.; Connelly, K.A.; Dorian, P.; et al. Characterization of the ultrashort-TE (UTE) MR collagen signal. *NMR Biomed.* **2015**, *28*, 1236–1244. [CrossRef] [PubMed]
31. Aliev, A.E. Solid-state NMR studies of collagen-based parchments and gelatin. *Biopolymers* **2005**, *77*, 230–245. [CrossRef] [PubMed]
32. Diaz, E.; Chung, C.B.; Bae, W.C.; Statum, S.; Znamirowski, R.; Bydder, G.M.; Du, J. Ultrashort echo time spectroscopic imaging (UTESI): An efficient method for quantifying bound and free water. *NMR Biomed.* **2012**, *25*, 161–168. [CrossRef] [PubMed]
33. Kaflik-Hachulska, A.; Samoson, A.; Kolodziejski, W. H-1 MAS and H-1 -> P-31 CP/MAS NMR study of human bone mineral. *Calcif. Tissue Int.* **2003**, *73*, 476–486. [CrossRef] [PubMed]
34. Ma, Y.; Carl, M.; Chang, E.Y.; Du, J. Quantitative magnetization transfer ultrashort echo time imaging using a time-efficient 3D multispoke cones sequence. *Magn. Reson. Med.* **2018**, *79*, 692–700. [CrossRef]
35. Jerban, S.; Ma, Y.; Wan, L.; Searleman, A.C.; Jang, H.; Sah, R.L.; Chang, E.Y.; Du, J. Collagen proton fraction from ultrashort echo time magnetization transfer (UTE-MT) MRI modeling correlates significantly with cortical bone porosity measured with micro-computed tomography (μ CT). *NMR Biomed.* **2019**, *32*, e4045. [CrossRef] [PubMed]
36. Jerban, S.; Ma, Y.J.; Nazaran, A.; Dorthe, E.W.; Cory, E.; Carl, M.; D’Lima, D.; Sah, R.L.; Chang, E.Y.; Du, J. Detecting stress injury (fatigue fracture) in fibular cortical bone using quantitative ultrashort echo time-magnetization transfer (UTE-MT): An ex vivo study. *NMR Biomed.* **2018**, *31*, e3994. [CrossRef]
37. Guo, T.; Ma, Y.J.; High, R.A.; Tang, Q.; Wong, J.H.; Byra, M.; Searleman, A.C.; To, S.C.; Wan, L.; Le, N.; et al. Assessment of an in vitro model of rotator cuff degeneration using quantitative magnetic resonance and ultrasound imaging with biochemical and histological correlation. *Eur. J. Radiol.* **2019**, *121*, 108706. [CrossRef] [PubMed]
38. Hodgson, R.J.; Evans, R.; Wright, P.; Grainger, A.J.; O’connor, P.J.; Helliwell, P.; McGonagle, D.; Emery, P.; Robson, M.D. Quantitative magnetization transfer ultrashort echo time imaging of the Achilles tendon. *Magn. Reson. Med.* **2011**, *65*, 1372–1376. [CrossRef] [PubMed]
39. Henkelman, R.M.; Huang, X.; Xiang, Q.-S.; Stanisz, G.J.; Swanson, S.D.; Bronskill, M.J. Quantitative interpretation of magnetization transfer. *Magn. Reson. Med.* **1993**, *29*, 759–766. [CrossRef]
40. Ramani, A.; Dalton, C.; Miller, D.H.; Tofts, P.S.; Barker, G.J. Precise estimate of fundamental in-vivo MT parameters in human brain in clinically feasible times. *Magn. Reson. Imaging* **2002**, *20*, 721–731. [CrossRef]
41. Sled, J.G.; Bruce Pike, G. Quantitative imaging of magnetization transfer exchange and relaxation properties in vivo using MRI. *Magn. Reson. Med.* **2001**, *46*, 923–931. [CrossRef]
42. Du, J.; Ma, G.; Li, S.; Carl, M.; Szevenenyi, N.; VandenBerg, S.; Corey-Bloom, J.; Bydder, G.M. Ultrashort TE echo time (UTE) magnetic resonance imaging of the short T2 components in white matter of the brain using a clinical 3T scanner. *NeuroImage* **2013**, *87C*, 32–41. [PubMed]

43. Sheth, V.; Shao, H.; Chen, J.; VandenBerg, S.; Corey-Bloom, J.; Bydder, G.M.; Du, J. Magnetic resonance imaging of myelin using ultrashort echo time (UTE) pulse sequence: Phantom, specimen, volunteers and multiple sclerosis patient studies. *NeuroImage* **2016**, *136*, 37–44. [CrossRef] [PubMed]
44. Ma, Y.; Jang, H.; Wei, Z.; Cai, Z.; Xue, Y.; Chang, E.Y.; Corey-Bloom, J.; Du, J. Robust human brain myelin imaging using a short TR adiabatic inversion recovery prepared ultrashort echo time (STAIR-UTE) Sequence. *Radiology* **2020**, *297*, 392–404. [CrossRef] [PubMed]
45. Fan, S.; Ma, Y.; Searleman, A.; Zhu, Y.; Bydder, G.M.; Du, J. Yet more evidence that myelin protons can be directly imaged with ultrashort echo time (UTE) sequences on a clinical 3T scanner: Bi-component T2* analysis of native and deuterated ovine brain specimens. *Magn. Reson. Med.* **2018**, *80*, 538–547. [CrossRef]
46. Shen, X.; Özen, A.C.; Sunjar, A.; Ilbey, S.; Sawiak, S.; Shi, R.; Chiew, M.; Emir, U. Ultra-short T2 components imaging of the whole brain using 3D dual-echo UTE MRI with rosette k-space pattern. *Magn. Reson. Med.* **2023**, *89*, 508–521. [CrossRef] [PubMed]
47. Roy, I.; Gupta, M.N. Freeze-drying of proteins: Some emerging concerns. *Biotechnol. Appl. Biochem.* **2004**, *39*, 165–177. [CrossRef] [PubMed]
48. Ong, H.H.; Wright, A.C.; Wehrli, F.W. Deuterium nuclear magnetic resonance unambiguously quantifies pore and collagen-bound water in cortical bone. *J. Bone Miner. Res.* **2012**, *27*, 2573–2581. [CrossRef]

Disclaimer/Publisher’s Note: The statements, opinions and data contained in all publications are solely those of the individual author(s) and contributor(s) and not of MDPI and/or the editor(s). MDPI and/or the editor(s) disclaim responsibility for any injury to people or property resulting from any ideas, methods, instructions or products referred to in the content.

Article

Uncertainty Quantification in SAR Induced by Ultra-High-Field MRI RF Coil via High-Dimensional Model Representation

Xi Wang ¹, Shao Ying Huang ² and Abdulkadir C. Yucel ^{1,*}

¹ School of Electrical and Electronic Engineering, Nanyang Technological University, Singapore 639798, Singapore; xi002@e.ntu.edu.sg

² Engineering Product Development Department, Singapore University of Technology and Design, Singapore 487372, Singapore; huangshaoying@sutd.edu.sg

* Correspondence: acyucel@ntu.edu.sg

Abstract: As magnetic field strength in Magnetic Resonance Imaging (MRI) technology increases, maintaining the specific absorption rate (SAR) within safe limits across human head tissues becomes challenging due to the formation of standing waves at a shortened wavelength. Compounding this challenge is the uncertainty in the dielectric properties of head tissues, which notably affects the SAR induced by the radiofrequency (RF) coils in an ultra-high-field (UHF) MRI system. To this end, this study introduces a computational framework to quantify the impacts of uncertainties in head tissues' dielectric properties on the induced SAR. The framework employs a surrogate model-assisted Monte Carlo (MC) technique, efficiently generating surrogate models of MRI observables (electric fields and SAR) and utilizing them to compute SAR statistics. Particularly, the framework leverages a high-dimensional model representation technique, which constructs the surrogate models of the MRI observables via univariate and bivariate component functions, approximated through generalized polynomial chaos expansions. The numerical results demonstrate the efficiency of the proposed technique, requiring significantly fewer deterministic simulations compared with traditional MC methods and other surrogate model-assisted MC techniques utilizing machine learning algorithms, all while maintaining high accuracy in SAR statistics. Specifically, the proposed framework constructs surrogate models of a local SAR with an average relative error of 0.28% using 289 simulations, outperforming the machine learning-based surrogate modeling techniques considered in this study. Furthermore, the SAR statistics obtained by the proposed framework reveal fluctuations of up to 30% in SAR values within specific head regions. These findings highlight the critical importance of considering dielectric property uncertainties to ensure MRI safety, particularly in 7 T MRI systems.

Keywords: generalized polynomial chaos (gPC); high-dimensional model representation (HDMR); magnetic resonance imaging (MRI); MRI safety; sensitivity analysis; surrogate model; ultra-high-field (UHF) MRI; uncertainty quantification

1. Introduction

Magnetic Resonance Imaging (MRI) stands as a cornerstone in medical diagnostics, offering unparalleled detail in imaging soft tissues without the risks associated with ionizing radiation [1,2]. During MRI scans, subjects are exposed to strong magnetic fields and radiofrequency (RF) pulses. These RF pulses cause hydrogen atoms in the body to resonate, emitting fields captured by the RF coil to produce high-resolution images of tissues and organs [2]. However, this process results in energy deposition in the body, quantified via the specific absorption rate (SAR), which measures the RF energy absorbed per unit mass during the scans [3]. High SAR values indicate elevated tissue temperatures, potentially causing tissue damage and burns. Consequently, ensuring SAR levels remain within safe limits is paramount for subject safety during an MRI scan [4]. Nonetheless, this task becomes challenging with the increasing frequency of the RF pulses in the

latest ultra-high-field (UHF) MRI systems, where standing waves form at a shortened wavelength [5,6].

The UHF MRI systems, particularly those operating at 7 T, have become available for clinical applications. The first 7 T MRI system was introduced to the market in 2017 [7,8]. As of 2023, over 100 7 T MRI systems are in operation globally [9]. These machines utilize a stronger magnetic field than their predecessors, offering enhanced image clarity and resolution but presenting new challenges in assessing SAR values and safety considerations. The increased magnetic field corresponds to an increased frequency of RF pulses, resulting in non-uniform electric fields (E-fields) and SAR distributions within the body [7,8]. Given these advancements, understanding the SAR distributions in the context of 7 T MRI systems has become important. Furthermore, the variability in SAR distributions is influenced by various factors beyond just the non-uniformity of E-fields. Among these factors, the dielectric properties of the tissues have a significant impact on the amount of RF energy absorbed [5,6,10]. Values of the dielectric properties, permittivity and conductivity, are not fixed but exhibit $\pm 20\%$ variability around their nominal values due to the change in physiological parameters, e.g., oxygen levels [11–16], reflecting the natural heterogeneity found within biological tissues. Such variability (or uncertainty) in dielectric properties can directly lead to variations in SAR values, which significantly impact image quality and patient safety. These variations in the SAR can introduce artifacts and reduce image clarity, thus compromising diagnostic accuracy and potentially necessitating repeat scans [17]. Additionally, such variations may cause tissue heating and thermal injuries in patients. This variability can also introduce significant discrepancies between the actual and computed E-field and SAR distributions [18,19]. Therefore, to lower such discrepancies and ensure the SAR values comply with high-tier SAR limit standards [20,21], there is a need for computational frameworks that can accurately quantify and assess the impact of uncertainties in tissue dielectric properties on the induced SAR values.

Current tools for computing SAR distributions rely on deterministic electromagnetic (EM) simulators [22,23]. However, these simulators do not account for the effects of uncertainties in tissue dielectric properties while generating the simulation results. In addressing this need, the traditional Monte Carlo (MC) methods [24,25] can be applied in conjunction with these simulators. The traditional MC methods require the execution of the deterministic simulator for numerous randomly selected realizations of tissue dielectric properties, yielding statistical measures, such as the mean and standard deviation, of the SAR. Despite their straightforward implementation, MC methods are inefficient as they require a large number of deterministic simulations, each of which is computationally expensive for EM characterization in MRI scenarios [24]. To overcome these challenges, surrogate model-assisted MC presents itself as a viable alternative [26]. This approach leverages surrogate models to approximate the outcomes of deterministic simulators, thereby significantly reducing the computational burden associated with traditional MC methods [26]. By integrating surrogate models, the surrogate model-assisted MC method retains the versatility of traditional MC approaches while acquiring statistics more efficiently.

Previously, researchers have successfully utilized surrogate modeling techniques and surrogate model-assisted MC methods to quantify the effects of uncertainties in various bioelectromagnetic problems, including transcranial magnetic stimulation (TMS), transcranial direct current stimulation (tDCS), and cellphone radiation safety assessment studies. For TMS, non-intrusive generalized polynomial chaos (gPC) [19] and high-dimensional model representation (HDMR) techniques [18] have been applied in uncertainty quantification. Similarly, in tDCS, various techniques, including the non-intrusive stochastic collocation method (SCM) [27] and gPC [19], have been implemented to achieve the same objective. Furthermore, both gPC and SCM [28,29] have been employed to quantify the uncertainties in the SAR induced due to cellphone radiation. These applications have yielded promising results in terms of accuracy and efficiency, and shown the necessity and effectiveness of the surrogate model-assisted MC methods for uncertainty quantification in bioelectromagnetic problems. However, to our knowledge, no study has performed uncertainty quantifica-

tion in the SAR induced by UHF MRI RF coils and necessarily employed these surrogate model-assisted MC methods.

This paper proposes a surrogate model-assisted MC framework to quantify the effects of uncertain tissue dielectric properties on the SAR induced by UHF MRI RF coils. The framework initially generates surrogate models of E-fields by using the outcomes of a small number of deterministic simulations performed by MARIE [23], an open-source MRI EM analysis software. Then, the SAR's mean, standard deviation, and sensitivity indices are obtained via MC using the surrogate models instead of the deterministic EM simulator. Specifically, the proposed framework constructs surrogate models by leveraging the HDMR technique [30], combined with the gPC method, which requires significantly fewer deterministic simulations than the traditional MC method's brute-force application [30–32]. The HDMR technique allows approximation of the multivariate MRI observables (E-field and SAR) via univariate and bivariate component functions. Doing so effectively tackles the 'curse of dimensionality' arising during surrogate model generation of multivariate functions. While the technique iteratively includes the most significant component functions (of most influential tissue dielectric parameters) in the HDMR expansion, it approximates each component function via the gPC method [31,32].

The numerical results (in Section 3) show that the proposed HDMR-based technique demonstrated superior performance over other surrogate modeling methods, including random vector functional link (RVFL) [33,34], extreme learning machine (ELM) [35,36], single-layer neural network (NN) [36], Gaussian process (GP) [37], and least square-based gPC [38]. Among all these techniques, the HDMR required the minimum number of simulations while providing the statistics with the highest accuracy, thanks to its capability of selectively incorporating the most significant component functions (with combined effects of dielectric properties).

The contributions of this study are threefold:

- This is the first and foremost study performing uncertainty quantification of the SAR induced by UHF MRI RF coils. It demonstrates the significance of uncertainties in the dielectric properties of human head tissues, which can cause up to 30% fluctuations in SAR values within specific head regions, as demonstrated in the numerical results section.
- This study proposes an HDMR-based surrogate modeling technique, which emerges as the best among various tested surrogate modeling methods for approximating E-fields and SAR induced by UHF MRI RF coils. The technique obtains the surrogate models with a mean relative error of 0.28% by only 289 deterministic simulations, surpassing the accuracy and efficiency of other surrogate modeling methods, as shown in the numerical results section.
- Finally, this study conducts statistical and sensitivity analyses on SAR values. The statistical analysis presents theoretical maximum 1g-SAR and 10g-SAR values after incorporating the uncertainties in tissue dielectric properties, which underscores their importance in MRI safety assessment. Furthermore, the sensitivity analysis shows the uncertainties in which tissues' dielectric properties affect the SAR values more in certain regions of the brain.

The rest of this paper is organized as follows. Section 2 presents the preliminary concepts, the formulation of the proposed gPC-based HDMR technique, and the general information on the deterministic simulator MARIE used in this study. Section 3 provides numerical results and analysis, focusing on the accuracy and efficiency of the proposed framework and presenting statistical and sensitivity analyses. Finally, Section 4 presents the conclusion, summarizing the study's key findings.

2. Formulation and Methods

Please refer to Appendix A for the nomenclature, which lists mathematical terms used throughout the paper.

2.1. Preliminary Concepts

Throughout this study, the dielectric properties of six human head tissues are assumed to be uncertain. Specifically, these uncertain parameters are the relative permittivity, ϵ_r , and conductivity, σ , of white matter, grey matter, cerebrospinal fluid, bone, scalp, and eye humor, with nominal values provided in Table 1, such that there exist $N = 12$ uncertain parameters in total. The uncertain parameters are represented by random variables, x^k , $k = 1, 2, \dots, N$, each uniformly distributed over a finite 1-D random domain defined by the ranges $[a^k, b^k]$, as outlined in Table 1. These random variables, x^k , $k = 1, 2, \dots, N$, assumed to be mutually independent, are integrated into a 12-dimensional vector, denoted as $\mathbf{x} = [x^1, x^2, \dots, x^{N-1}, x^N] = [\epsilon_{r1}, \dots, \epsilon_{r6}, \sigma_1, \dots, \sigma_6]$, where each symbol and corresponding random variable in \mathbf{x} are provided in Table 1 [11–16]. Given the absence of prior knowledge regarding the distributions of input parameters, they are assumed to follow uniform distributions according to the principle of maximum entropy and vary $\pm 20\%$ around their nominal values [11–16,39,40]. Moreover, while this study primarily focuses on the uncertainties associated with tissue properties, any uncertain parameter deemed significant for SAR variation can be incorporated in \mathbf{x} .

Table 1. Variability in tissue dielectric properties.

Tissue	ϵ_r	Range	Symbol	RV	σ (S/m)	Range	Symbol	RV	ρ (kg/m ³)
White Matter	43.8	[35.04, 52.56]	ϵ_{r1}	x_1	0.413	[0.33, 0.50]	σ_1	x_7	1041
Grey Matter	60.0	[48.00, 72.00]	ϵ_{r2}	x_2	0.692	[0.55, 0.83]	σ_2	x_8	1045
CSF	72.7	[58.16, 87.24]	ϵ_{r3}	x_3	2.220	[1.78, 2.66]	σ_3	x_9	1007
Bone	13.4	[10.72, 16.08]	ϵ_{r4}	x_4	0.083	[0.07, 0.10]	σ_4	x_{10}	1908
Scalp	49.8	[39.84, 59.76]	ϵ_{r5}	x_5	0.641	[0.51, 0.77]	σ_5	x_{11}	1109
Eye Humor	69.0	[55.20, 82.80]	ϵ_{r6}	x_6	1.520	[1.22, 1.82]	σ_6	x_{12}	1005

Let $\mathbf{y} = F(\mathbf{x})$ denote a vector storing the observable values, and F represent a complex and nonlinear function evaluated by a deterministic simulator for a given input vector, \mathbf{x} . Specifically, in this study, the vector $\mathbf{y} = [y^1, \dots, y^{N_{\text{vox}}}]$, with a dimension of $N_{\text{vox}} = 889,850$, contains the values of MRI observables (E-fields or SAR) on the voxels, where N_{vox} is the number of voxels used to discretize the tissues in the voxelized head model. While the observables are selected as E-fields and SAR in this study, the framework is applicable to any MRI observable deemed important.

The traditional MC method [24,25] can be used to obtain the statistics of each entry of \mathbf{y} . To do that, N_{MC} number of random vectors, \mathbf{x}_n , $n = 1, 2, \dots, N_{\text{MC}}$, are uniformly selected within the ranges provided in Table 1. Then, for each random vector/realization, \mathbf{x}_n , a deterministic simulation is performed by a deterministic simulator (please refer to Section 2.4 for the deterministic simulator used in this study). The results of N_{MC} deterministic simulations, $\mathbf{y}_n = F(\mathbf{x}_n)$, $n = 1, 2, \dots, N_{\text{MC}}$, are then used to compute the mean and variance of observables as

$$E[\mathbf{y}] \approx \frac{1}{N_{\text{MC}}} \sum_{n=1}^{N_{\text{MC}}} \mathbf{y}_n \tag{1}$$

$$\text{Var}[\mathbf{y}] \approx \frac{1}{N_{\text{MC}}} \sum_{n=1}^{N_{\text{MC}}} \mathbf{y}_n^2 - (E[\mathbf{y}])^2 \tag{2}$$

where summation on the vectors is an element-wise sum, so that $E[\cdot]$ and $\text{Var}[\cdot]$ operators are considered to be acting on each entry of the vector \mathbf{y} separately. Clearly, the traditional MC method is straightforward to implement. However, it requires a large number of random realizations/deterministic simulations to obtain reasonably accurate statistics since the convergence rate for the accuracy of the mean is $1/\sqrt{N_{\text{MC}}}$ [25]. To this end, the brute-force application of the traditional MC is not computationally feasible for uncertainty

quantification of the SAR induced by UHF MRI RF coils since each deterministic simulation performed by MARIE [23] is computationally costly. In addition to computing mean and variance, the traditional MC can be used to assess each random variable’s impact on the observable. This sensitivity assessment can be performed via Sobol indices [41], which quantify the contributions of individual random variables to the output variance. The k^{th} random variable’s Sobol index, S_k , can be calculated via

$$S_k = \text{Var}_{x^k}[\mathbf{y}] / \text{Var}[\mathbf{y}] \tag{3}$$

Here, $\text{Var}_{x^k}[\cdot]$ is the variance of the observable with respect to the random variable x^k , which can be computed by performing MC by only considering the k^{th} random variable while fixing all remaining random variables to their corresponding nominal values in Table 1.

2.2. The HDMR Technique

The HDMR, a powerful surrogate modeling technique, approximates N -dimensional observables with lower dimensional component functions as

$$\mathbf{y} = F(\mathbf{x}) = \sum_{\mathbf{v} \subseteq \Omega} F_{\mathbf{v}}(\mathbf{x}^{\mathbf{v}}) \tag{4}$$

where $\Omega = \{1, 2, \dots, N\}$ represents the set of random variable indices, and \mathbf{v} denotes the subset of Ω with cardinality $|\mathbf{v}| \in \{0, 1, 2, \dots, N\}$. Therefore, $F_{\mathbf{v}}(\mathbf{x}^{\mathbf{v}})$ is called the $|\mathbf{v}|$ -th order component function with respect to a $|\mathbf{v}|$ -dimensional random input vector, $\mathbf{x}^{\mathbf{v}}$ [42]. Expanding HDMR in (4) yields

$$F(\mathbf{x}) = F_0 + \sum_i F_i(x^i) + \sum_{i < j} F_{ij}(x^i, x^j) + \dots + F_{\Omega}(x^1, \dots, x^N) \tag{5}$$

In (5), F_0 denotes the zeroth-order component function that remains a constant. $F_i(x^i)$ is the first-order component function modeling the influence of x^i on the observable. The second-order component function, $F_{ij}(x^i, x^j)$, delineates the combined impact of input random variables x^i and x^j , while the remaining terms in the expansion are the higher-order component functions. When expanded, the number of component functions in HDMR expansion scales with $\sum_{k=0}^N N! / ((N - k)!k!)$, which increase rapidly with increasing N . To this end, to reduce the substantial computational expenses associated with the component function generation, HDMR is often truncated at a low order in practice, while discarding higher-order terms [32]. In many practical problems, encompassing correlations up to the second order among input random variables is generally sufficient to accurately describe the input–output relationship [43]. Therefore, in this study, the HDMR expansion is retained at a maximum of second order as

$$F(\mathbf{x}) \approx F_0 + \sum_i F_i(x^i) + \sum_{i < j} F_{ij}(x^i, x^j) \tag{6}$$

This truncated expansion can be better explained via an example. Suppose y is a function of three random variables ($N = 3$) with indices $\Omega = \{1, 2, 3\}$. The component functions in the HDMR expansion of $y = F(\mathbf{x})$ up to $|\mathbf{v}| = 2$ can be shown as:

$$\begin{aligned}
 |\mathbf{v}| = 0, & \quad \mathbf{v} = \emptyset, & F_0 \\
 |\mathbf{v}| = 1, & \quad \mathbf{v} = \{1\}, & F_1(x^1) \\
 |\mathbf{v}| = 1, & \quad \mathbf{v} = \{2\}, & F_2(x^2) \\
 |\mathbf{v}| = 1, & \quad \mathbf{v} = \{3\}, & F_3(x^3) \\
 |\mathbf{v}| = 2, & \quad \mathbf{v} = \{1, 2\}, & F_{1,2}(x^1, x^2) \\
 |\mathbf{v}| = 2, & \quad \mathbf{v} = \{1, 3\}, & F_{1,3}(x^1, x^3) \\
 |\mathbf{v}| = 2, & \quad \mathbf{v} = \{2, 3\}, & F_{2,3}(x^2, x^3)
 \end{aligned} \tag{7}$$

which can yield

$$\begin{aligned}
 F(\mathbf{x}) \approx & F_0 + F_1(x^1) + F_2(x^2) + F_3(x^3) \\
 & + F_{1,2}(x^1, x^2) + F_{1,3}(x^1, x^3) + F_{2,3}(x^2, x^3)
 \end{aligned} \tag{8}$$

These component functions can be obtained by the CUT-HDMR strategy. In this strategy, the component functions are interpolated on the multidimensional cuts passing through a reference point. In particular, the first- and second-order component functions are interpolated on lines and planes passing through reference point $\bar{\mathbf{x}}$ [42]. Then, the contributions from the lower-order component functions, $F_{\mathbf{u}}(\mathbf{x}^{\mathbf{u}})$, with indices \mathbf{u} , which is the subset of the index set \mathbf{v} of the component function, $F_{\mathbf{v}}(\mathbf{x}^{\mathbf{v}})$, are subtracted. In other words, the component functions, $F_{\mathbf{v}}(\mathbf{x}^{\mathbf{v}})$, are obtained as

$$F_{\mathbf{v}}(\mathbf{x}^{\mathbf{v}}) = F(\mathbf{x})|_{\mathbf{x}=\bar{\mathbf{x}} \setminus \mathbf{x}^{\mathbf{v}}} - \sum_{\mathbf{u} \subset \mathbf{v}} F_{\mathbf{u}}(\mathbf{x}^{\mathbf{u}}) \tag{9}$$

where $\mathbf{x} = \bar{\mathbf{x}} \setminus \mathbf{x}^{\mathbf{v}}$ denotes the condition where random variables, whose indices do not belong to subset \mathbf{v} , are set to their respective values at the reference point $\bar{\mathbf{x}}$, typically set to the mean values of random variables. For the above example with $N = 3$, the component functions in (7) become

$$\begin{aligned}
 F_0 &= F(\bar{\mathbf{x}}) \\
 F_1(x^1) &= F(x^1, \bar{x}^2, \bar{x}^3) - F_0 \\
 F_2(x^2) &= F(\bar{x}^1, x^2, \bar{x}^3) - F_0 \\
 F_3(x^3) &= F(\bar{x}^1, \bar{x}^2, x^3) - F_0 \\
 F_{1,2}(x^1, x^2) &= F(x^1, x^2, \bar{x}^3) - F_0 - F_1 - F_2 \\
 F_{1,3}(x^1, x^3) &= F(x^1, \bar{x}^2, x^3) - F_0 - F_1 - F_3 \\
 F_{2,3}(x^2, x^3) &= F(\bar{x}^1, x^2, x^3) - F_0 - F_2 - F_3
 \end{aligned} \tag{10}$$

To construct the HDMR expansion, an iterative scheme is employed [32]. This scheme allows carefully selecting the component functions significantly contributing to the observable and omitting the insignificant ones. Thereby, the scheme requires a minimum number of component functions and minimal computational resources to construct the HDMR expansion. In particular, the iterative scheme starts from $|\mathbf{v}| = 0$ by computing the zeroth-order component function, F_0 , which is the observable value at $\bar{\mathbf{x}}$ [42]. Next, the scheme proceeds to the computation of $F_i(x^i)$ defined on the lines, intersecting $\bar{\mathbf{x}}$. After the computation of all first-order component functions, the scheme computes the weights associated with each random variable (dimension) via

$$\eta_i = \left| \frac{E[F_i(x^i)]}{F_0} \right| \tag{11}$$

These weights, $\eta_i, i = 1, \dots, N$, measure the sensitivity of a specific dimension of the input, \mathbf{x} , to the observable, \mathbf{y} , by comparing means of first-order component functions

$E[F_i(x^i)] = \int F_i(x^i)dx^i$ to the mean of $F(\bar{\mathbf{x}}) = F_0$. Therefore, when η_i exceeds a prescribed tolerance, ζ , the random variable of that specific dimension is considered to have substantial contribution on \mathbf{y} and is thus considered as “important” dimension. These indices are retained in set S for subsequent-level generation, ensuring only second-order functions satisfying $\mathbf{v} \subseteq S$ are incorporated when constructing HDMR. Figure 1a illustrates the flowchart of the construction of surrogate models using the HDMR technique.

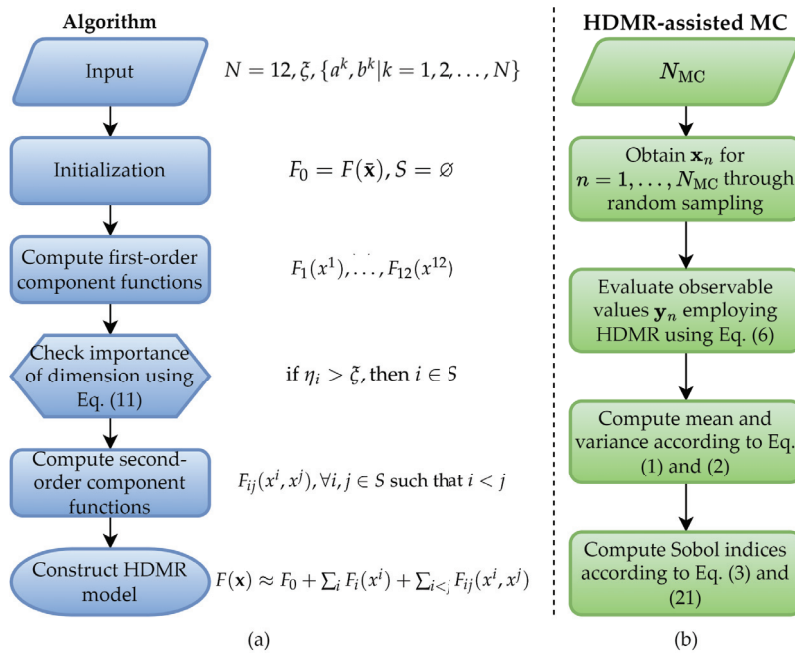


Figure 1. (a) Flowchart depicting the implementation of the truncated HDMR expansion applied in this study, with $N = 12$. (b) Flowchart of HDMR-assisted MC method.

For the above-given example (for $N = 3$), assume that the indices of important dimensions are found to be $S = \{2, 3\}$ after the computations of the zeroth- and first-order component functions and obtaining the weights $\eta_i, i = 1, 2, 3$. Thus, the component function with indices $\{2, 3\}$ is included in the expansion while the other second-order component functions with indices $\{1, 2\}$ and $\{1, 3\}$ will not be computed, since at least one of their corresponding first-order terms is considered to be insignificant, with η_i smaller than the tolerance, ζ . It should be noted that, after this construction, the indices of first-order component functions of insignificant dimensions are also included in set S since those first-order component functions are already computed. The component functions used to construct HDMR expansion are interpolated using the gPC expansion, explained next. After the HDMR model is constructed, statistics such as mean, variance, and sensitivity indices can be obtained, as shown in Figure 1b.

2.3. gPC Expansion

The fundamental principle of gPC involves determining the functional relationship between input vectors, \mathbf{x}^v , and the component functions, $F_v(\mathbf{x}^v)$. For simplicity in notation, let $\bar{\mathbf{x}} = \bar{\mathbf{x}} \setminus \mathbf{x}^v$ represent the scenario where the random variables with indices given in set \mathbf{v} are retained, while all remaining random variables with indices out of set \mathbf{v} are set to their mean values. To this end, $F(\bar{\mathbf{x}}) = F(\mathbf{x})|_{\mathbf{x}=\bar{\mathbf{x}} \setminus \mathbf{x}^v}$ is the part in (9) to be approximated via gPC as

$$F(\bar{\mathbf{x}}) \approx \sum_{n=0}^{N_p} \alpha_n \Phi_n(\bar{\mathbf{x}}) \tag{12}$$

where α_n are the coefficients to be calculated, and $N_p + 1$ is the total number of terms in gPC expansion, such that $N_p = (|\mathbf{v}| + p)! / (|\mathbf{v}|! p!) - 1$. Here, since the distribution

of random variables is assumed to be uniform, $\Phi_n(\tilde{\mathbf{x}})$ is selected as the product of 1D Legendre polynomials [44] as

$$\Phi_n(\tilde{\mathbf{x}}) = \prod_{k \in \mathbf{v}} \phi_{d_n^k}(x^k) \tag{13}$$

which denotes the joint polynomial basis functions of gPC, consisting of polynomials $\phi_k(x^k)$, which are individually defined for each random variable [44]. The multi-index d_n^k satisfies $\sum_{k \in \mathbf{v}} d_n^k \leq p$, such that the sum of degrees of all polynomials is constrained within a chosen degree, p . Also, when given degree p , all possibilities should be considered and incorporated when constructing (12). For example, for $\mathbf{v} = \{1, 3\}$, $|\mathbf{v}| = 2$, and $p = 2$, all possible polynomial bases are

$$\begin{aligned} \Phi_0(x^1, x^3) &= \phi_0(x^1)\phi_0(x^3) \\ \Phi_1(x^1, x^3) &= \phi_1(x^1)\phi_0(x^3) \\ \Phi_2(x^1, x^3) &= \phi_0(x^1)\phi_1(x^3) \\ \Phi_3(x^1, x^3) &= \phi_1(x^1)\phi_1(x^3) \\ \Phi_4(x^1, x^3) &= \phi_2(x^1)\phi_0(x^3) \\ \Phi_5(x^1, x^3) &= \phi_0(x^1)\phi_2(x^3) \end{aligned} \tag{14}$$

The coefficients α_n in (12) can be calculated by

$$\alpha_n = \int_{\Omega} F(\tilde{\mathbf{x}})\Phi_n(\tilde{\mathbf{x}})d\tilde{\mathbf{x}} \tag{15}$$

which is often difficult to compute analytically since analytical results of $F(\tilde{\mathbf{x}})$ are typically elusive for complex nonlinear systems. Thereby, the tensor-product Gauss–Legendre (GL) quadrature integration rule [44] is implemented to calculate gPC coefficients as

$$\alpha_n \approx \sum_{j=1}^{N_{GL}^{|\mathbf{v}|}} F(\tilde{\mathbf{x}}_j)\Phi_n(\tilde{\mathbf{x}}_j)w_j \tag{16}$$

Here, $\tilde{\mathbf{x}}_j$ and w_j are the collocation points and weights dictated by the GL quadrature rule, while the numbers of points and weights are $(N_{GL})^{|\mathbf{v}|}$, where the cardinality of \mathbf{v} , $|\mathbf{v}|$, is the power of the number of GL collocation points selected along each dimension, denoted by N_{GL} . Once these coefficients are computed, the component functions of HDMR can be approximated using the gPC method.

In short, the proposed methodology leverages the strengths of both techniques: HDMR’s ability to mitigate the curse of dimensionality and gPC’s capability to interpolate the component functions efficiently and accurately. Note that, while any univariate and bivariate interpolator could be employed, the application of gPC expansion on these subproblems demonstrates efficacy [42]. Furthermore, in determining the coefficients of each gPC expansion, the GL quadrature rule, delineated in (16), is applied. The observable values at collocation points of the GL quadrature are computed using a deterministic simulator, which is elaborated in the subsequent subsection. The number of required deterministic simulations corresponding to collocation points to construct HDMR can be calculated by:

$$N_{cp} = 1 + \sum_{\mathbf{v} \subseteq S} (N_{GL} - 1)^{|\mathbf{v}|} \tag{17}$$

where N_{cp} is the total number of collocation points and N_{GL} is kept fixed across all dimensions of univariate and bivariate component functions with indices, which are determined by the abovementioned iterative scheme and stored in the index set of S . In this study, we use odd-number GL quadrature rules, which share one collocation point (positioned at the reference point $\tilde{\mathbf{x}}$) for all component functions, while many collocation points of second-order component functions are already computed when interpolating the first-order component functions.

2.4. Deterministic Simulator MARIE [23]

To compute the component functions of HDMR expansion, the observable values on collocation points are computed via MARIE (MAGnetic Resonance Integral Equation suite) software [23], an open-source MATLAB-based simulator designed for fast EM analysis of MRI systems. The primary focus of MARIE is to offer comprehensive EM simulations in the context of the human body, targeting the determination of port parameters, E-field distribution, and key metrics like B1+, B1−, and local SAR. At its core, MARIE uses several integral equation methods. The inhomogeneous human body is voxelized and E-fields and currents inside the human body are solved using the volume integral equation technique. In parallel, the RF coils and shields, perfect electric conductors, are discretized by surface triangles, and the currents on them are computed using the surface integral equation technique. These techniques are carefully coupled, leveraging the volume–surface integral equation approach. Moreover, MARIE employs a fast iterative solution method for computational efficiency, incorporating a fast Fourier transform acceleration and special preconditioning technique for rapid iterative convergence. In this study, the observable values provided by MARIE are used to generate the surrogate models across voxels in the head model. The constructed surrogate models offer a computationally efficient representation for capturing the intricate relationships between the input random variables and the output MRI-induced E-field and SAR values in the head model.

3. Numerical Results and Discussion

This section demonstrates the proposed computational framework’s accuracy, efficiency, and applicability in obtaining the statistics of the UHF MRI RF coil-induced SAR on an MRI-derived head model. To construct the surrogate models, the tolerance for HDMR component function selection, ζ , is set to 10^{-2} , while the number of GL quadrature points along each dimension, N_{GL} , is set to 3, 5, or 7. As alluded in Section 2, the relative permittivities and conductivities of six types of head tissues are uniformly distributed in the ranges provided in Table 1, while the observables are the SAR values. To evaluate the accuracy of the surrogate models, the relative error of the observable on each voxel, err_i , $i = 1, \dots, N_{\text{vox}}$, is computed via

$$err_i = \frac{1}{N_{\text{test}}} \sum_{n=1}^{N_{\text{vox}}} \left| \frac{y_n^i - y_n^{i'}}{y_n^i} \right| \tag{18}$$

where $N_{\text{test}} = 100$ is the number of testing points, randomly selected according to the distributions shown in Table 1, while y_n^i and $y_n^{i'}$ represent the observable value on i^{th} voxel obtained by the deterministic simulator and surrogate model, respectively. Once the accuracy of each surrogate model of each voxel is assessed via its associated relative error, the overall accuracy of all surrogate models is evaluated via

$$err_{\text{max}} = \max_i \{err_i\}, \quad i = 1, 2, \dots, N_{\text{vox}}$$

$$err_{\text{ave}} = \frac{1}{N_{\text{vox}}} \sum_{i=1}^{N_{\text{vox}}} err_i \tag{19}$$

Here, the maximum relative error, err_{max} , gives insight into worst-case scenarios or outlier behavior, whereas the average relative error, err_{ave} , presents a more generalized view of the accuracy across the entire head model.

3.1. Numerical Settings

In the considered MRI scenario, a birdcage RF coil provided in MARIE [23] is used to stimulate a human head model, as depicted in Figure 2. This 32-port birdcage coil with a 140 mm radius operates at 298.06 MHz for 7 T MRI scans and is initially excited from the port 1 [Figure 2d]. Thereafter, ports 5, 9, and 13, demonstrated in Figure 2d, are also

activated to examine the accuracy of the constructed surrogate models, as discussed in subsequent subsections. The human head model is derived from an MR image selected from the OASIS2 dataset [45]. Initially, the MR image is transformed into a tetrahedral mesh using the headreco function [46] of SimNIBS [47]. This process yields a segmented head model with tissues, including white matter, grey matter, cerebrospinal fluid (CSF), bone, scalp, and eye humor. The conductivities and relative permittivities of these tissues are sequentially encapsulated in $\mathbf{x} = [\varepsilon_{r1}, \dots, \varepsilon_{r6}, \sigma_1, \dots, \sigma_6]$ and set randomly or according to the collocation point for each deterministic simulation. For compatibility with MARIE, the segmented head model is then converted to a voxel head model situated in a computational domain of $145 \times 145 \times 145$ with a voxel size of 1.6 mm, where 889,850 voxels occupy tissues. The head model is positioned at the center of the computational domain so that the head model coincides with the birdcage coil's center [Figure 2].

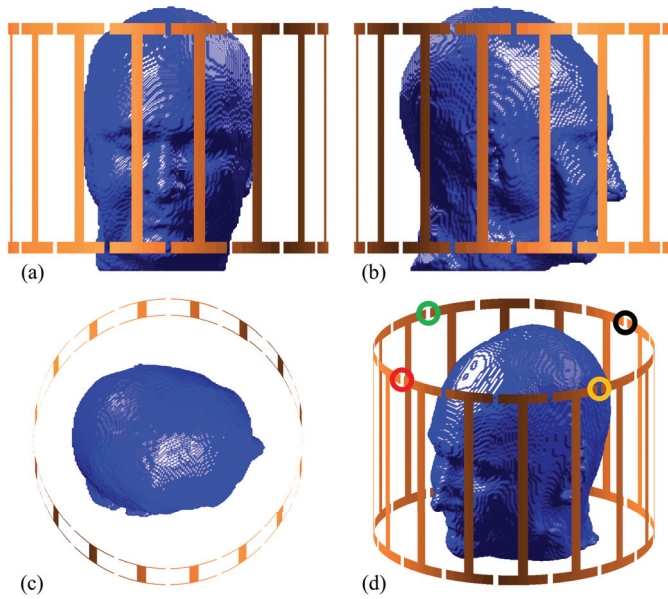


Figure 2. The MRI-derived head model in an MRI birdcage coil with the locations of activated ports highlighted. (a) Front view; (b) right side view; (c) top view; (d) port locations: port 1 (red), port 5 (green), port 9 (black), and port 13 (yellow).

3.2. Accuracy

The accuracy of the surrogate models generated by the proposed method is examined. To this end, the surrogate models of the SAR for all voxels in the head model are obtained by two approaches. In the first approach, called the *direct approach*, the input–output relation is directly formed between the input vector of the head tissues' dielectric properties, \mathbf{x} , and the output vector storing all SAR values on all 889,850 tissue voxels. In the second approach, called the *indirect approach*, the input vector remains unchanged, while the components of E-fields, $[E_x, E_y, E_z]$, are considered as the output and stored in an output vector of a size of 2,669,550; each entry of the vector is a complex number. In the indirect approach, after the construction of the surrogate models of E-fields, those are used to compute the SAR values on each tissue voxel i , SAR_i , via

$$SAR_i = (E_{x,i}^2 + E_{y,i}^2 + E_{z,i}^2) \cdot \sigma_i / \rho_i \quad (20)$$

where $[E_{x,i}, E_{y,i}, E_{z,i}]$ are the components of E-fields on each voxel i . The density, ρ_i , stands consistent for each tissue type throughout the study, as shown in Table 1. The accuracy of the surrogate models obtained using direct and indirect approaches is assessed using the SAR values as observables in (18) and (19). To test the accuracy with different parameters, first, the HDMR expansion is truncated right after the first component functions, and N_{GL} is set to 3, obtaining gPC coefficients in (16). Furthermore, to achieve better accuracy, the

number of component functions or GL points is increased in subsequent computations. This increase ensures a balanced approach between computational efficiency and the accuracy of the outcomes in the surrogate model assessments. Specifically, the number of GL points is augmented to 7 to improve approximation of component functions, or the HDMR is extended to encompass second-order component functions, which describe the combined effects between entries of the input vector. The results are shown in Table 2 for the direct approach and Table 3 for the indirect approach.

Table 2. Results of directly modeling SAR values.

Total Order of Component Functions	N_{GL}	N_{cp}	err_{max}	err_{ave}
1	3	25	34.36%	2.97%
1	5	49	33.80%	2.97%
1	7	73	33.74%	2.97%
2	3	289	14.28%	0.71%
2	5	1105	11.17%	0.51%

Table 3. Results of indirectly modeling SAR values through E-fields.

Total Order of Component Functions	N_{GL}	N_{cp}	err_{max}	err_{ave}
1	3	25	11.55%	1.46%
1	5	49	11.50%	1.48%
1	7	73	11.51%	1.47%
2	3	289	2.11%	0.28%
2	5	1105	1.65%	0.26%

A straightforward comparison between Tables 2 and 3 reveals that, generally, the results obtained through the indirect approach surpass those from the direct approach. This observation can be linked to the relationship between SAR values and the E-field, as shown in (20). The added complexity and interactions introduced by the squaring operations might necessitate a larger number of collocation points and the incorporation of higher-order terms to achieve a similar level of accuracy as that achieved when modeling indirectly.

Moreover, based on the data presented in the tables, it is noticeable that, when including solely the first-order component functions, there exists no direct correlation between an increment in the number of collocation points and the enhancement of accuracy in both scenarios. This suggests that the augmentation of collocation points does not significantly contribute to improving the accuracy of the surrogate modeling technique. Conversely, upon incorporating the second-order component functions, a notable enhancement in accuracy is observed, as evidenced by the substantial reduction in both mean and maximum relative errors. The optimal results are obtained in the second scenario, where the mean error is noted to be 0.26% and the maximum error is 1.65%, ensuring the confined error range for each voxel. In light of this, one should notice that the optimal accuracy in the study is attained in a scenario necessitating 1105 simulations. Considering the time-intensive nature of the deterministic simulations by MARIE, this approach might not be pragmatically viable. However, employing a mere 289 simulations yields results that, although slightly inferior to the 1105-simulation case in accuracy, offer a more feasible balance between accuracy and efficiency. Therefore, the subsequent analysis will be performed upon the 289-simulation case, utilizing a total order of 2 for component functions and three GL quadrature points along each dimension.

The distribution of voxel-based relative errors is shown in Figure 3. Indeed, most of the voxels exhibit an error of less than 1%, with only 0.339% of voxels surpassing this value. In Figure 4, selected slices are presented to highlight the accuracy of the proposed

method under the second scenario. The left column depicts the ground truth SAR values obtained from the deterministic simulator MARIE, while the middle column displays values approximated by the HDMR-generated surrogate models. The right column illustrates the logarithm of the relative difference. With a logarithmic error spanning 2 to 5 digits, these illustrations underscore the high accuracy achieved by the proposed method.

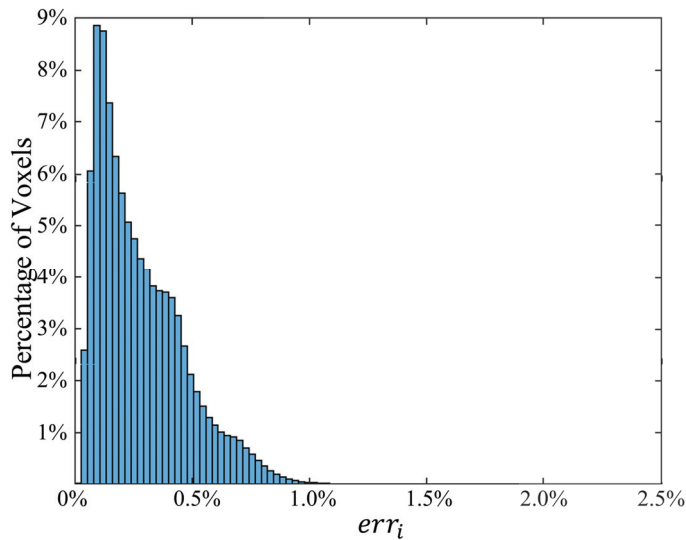


Figure 3. Relative error distributions for 889,850 tissue voxels. Derived from the second scenario where the total order for component functions is 2, with 3 GL quadrature points along each dimension.

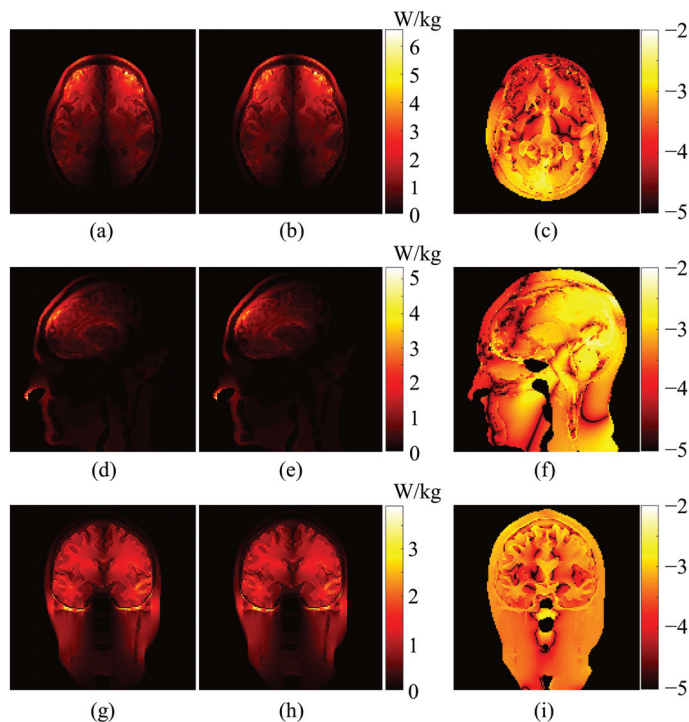


Figure 4. Comparison of the SAR on slices. The ground truth (Left), approximation via proposed framework (Mid), and the logarithm of the relative error between the ground truth and approximation (Right). (a) Ground truth of the axial slice. (b) Approximate SAR of the axial slice. (c) Logarithm of relative error between (a,b). (d) Ground truth of the sagittal slice. (e) Approximate SAR of the sagittal slice. (f) Logarithm of relative error between (d,e). (g) Ground truth of the coronal slice. (h) Approximate SAR of the coronal slice. (i) Logarithm of relative error between (g,h).

The accuracy of the HDMR technique is assessed by comparing it with other surrogate modeling techniques such as RVFL [33,34], ELM [34,35], single-layer NN [36], GP [37], and least square-based gPC [38]. Each of these techniques is applied within the framework of two scenarios (direct and indirect) and their performances are assessed in terms of SAR values utilizing the same error metrics. To ensure a fair comparison, a training set of 300 points is generated through Latin Hypercube Sampling; the testing set remains the same, with 100 testing points. The results are shown in Tables 4 and 5. Note that RVFL, ELM, and single-layer NN possess associated hyper-parameters. Therefore, multiple test cases are conducted to fine-tune these parameters, and the most optimal results are presented in the tables to ensure a fair and comprehensive comparison. As the tables illustrate, the proposed HDMR significantly outperforms all other surrogate modeling techniques.

Table 4. Results for other surrogate models of directly modeling SAR values.

Method	<i>err</i> _{max}	<i>err</i> _{ave}	Remarks
RVFL *	25.13%	3.35%	hidden nodes = 120
ELM *	27.00%	3.47%	hidden nodes = 120
Gaussian Process	85.64%	0.73%	/
Least Square PC	16.34%	0.77%	/
Single-layer NN *	≥ 100%	10.30%	nodes = 512
HDMR (proposed)	14.28%	0.71%	/

* For hyper-parameter tuning on RVFL and ELM, hidden nodes between 20 and 200 were tested, with an increment of 20 per step. Optimal results were observed at 120 for both ELM and RVFL. In the case of the single-layer neural network, tests were conducted evaluations spanning from 16 to 1024, progressing in powers of 2, with 512 yielding the optimal result. The optimal result is defined as the hyper-parameter that yields the lowest mean relative error on the testing set.

Table 5. Results for other surrogate models of indirectly modeling SAR values through E-fields.

Method	<i>err</i> _{max}	<i>err</i> _{ave}	Remarks
RVFL *	7.24%	1.27%	hidden nodes = 160
ELM *	7.90%	1.21%	hidden nodes = 140
Gaussian Process	16.41%	0.35%	/
Least Square PC	2.84%	0.41%	/
Single-layer NN *	45.85%	4.57%	nodes = 64
HDMR (proposed)	2.11%	0.28%	/

* For hyper-parameter tuning on RVFL and ELM, hidden nodes between 20 and 200 were tested, with an increment of 20 per step. Optimal results were observed at 160 and 140, respectively. In the case of the single-layer neural network, tests were conducted evaluations spanning from 16 to 128, progressing in powers of 2, with 64 yielding the optimal result. The optimal result is defined as the hyper-parameter that yields the lowest mean relative error on the testing set.

The proposed technique is further examined under various conditions by individually activating other ports (Port 5, Port 9, and Port 13), demonstrating the reliability of the approach. All results, obtained under the second ('indirect') scenario, incorporating a total of second-order component functions and three GL points, are presented in Table 6. One can see that the mean relative errors for all conditions exhibit a consistent behavior, fluctuating within a narrow range. This indicates a stable performance of the proposed method, irrespective of the port activated. However, while the mean relative error demonstrates satisfactory performances, reflecting the method's general effectiveness, the maximum relative error of port 9 is notably higher than that in all other conditions. The discrepancy in this case could be attributed to the spatial location of the voxels within an unexcited region. Given their substantial distance from the activation port, as shown in Figure 2d, the voxels near the nose region experienced less field excitation, resulting in comparatively

lower SAR values. Thus, inconsequential deviations in prediction within this region can result in amplified maximum relative errors, which is expected.

Table 6. Results for different activated ports using second-order component functions with three GL points.

Port No.	N_{GL}	N_{cp}	err_{max}	err_{ave}
Port 1	3	289	2.11%	0.28%
Port 5	3	289	2.08%	0.17%
Port 9	3	289	11.93%	0.31%
Port 13	3	289	3.82%	0.25%

3.3. Statistical Analysis

After establishing the accuracy of the proposed HDMR in the preceding section, it is important to assess the crucial statistical metrics obtained from the surrogate model. Employing the HDMR-assisted MC method with a sample size of 10,000 random points, the computed means and variances provide crucial insights into the performance and reliability of the proposed surrogate modeling technique. These statistical metrics are compared with the results derived from the traditional (brute-force) MC method, using simulations on MARIE with a sample size of 5000 randomly selected points. It is important to note that all points for the MC simulations are selected randomly, following the uniform distributions illustrated in Table 1. This comparative analysis is essential in corroborating the robustness and validity of the HDMR as a credible and efficient alternative to the traditional and computationally intensive MC methods for obtaining reliable statistical metrics. Figure 5 illustrates the convergence trends for the mean and variances of two selected voxels determined by the traditional MC method with increasing sample size. These metrics are juxtaposed and compared with the corresponding estimations from the proposed framework’s indirect approach. It becomes evident that the proposed method achieves a similar level of accuracy with a significantly lower number of deterministic simulations, underscoring its efficiency.

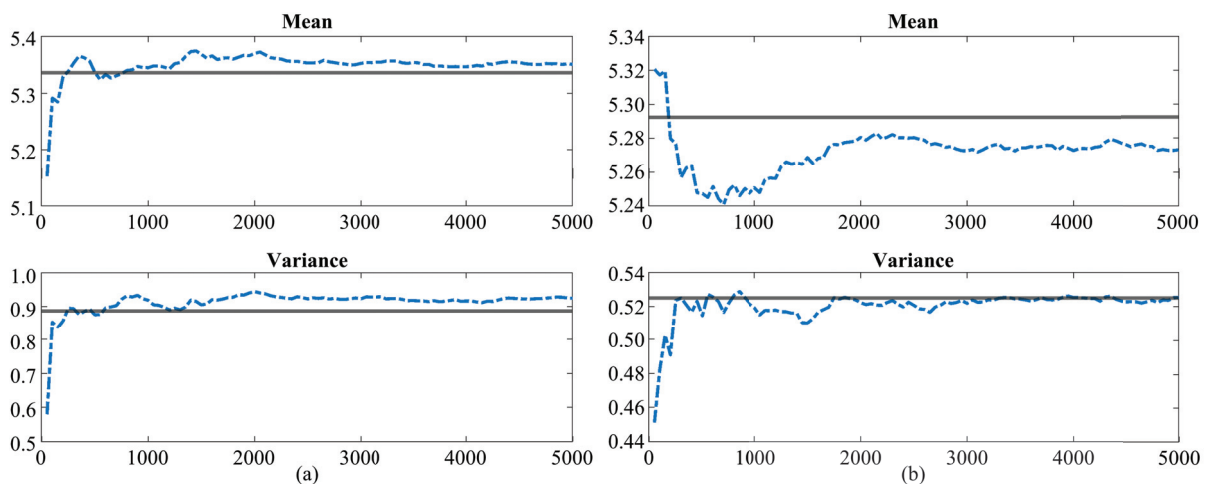


Figure 5. Convergence of mean (**top**) and variance (**bottom**) values for two different voxels, both computed using the 5000 point traditional MC method with increments of 50 random points/simulations. The black line represents the mean/variance values obtained via the HDMR-assisted MC method requiring 289 collocation points/simulations.

Furthermore, the maximum SAR values are also examined, given their paramount significance related to MRI safety regulations. This inquiry aims to discern the impacts of variations in tissue properties on the SAR values, which is vital for ensuring the safety of RF exposure. The nominal SAR values, obtained under nominal conditions of relative

permittivities and conductivities, serve as a benchmark for comparison. The SAR values are assumed to follow normal distributions, which allow the estimation of maximum SAR values, calculated as the mean plus three times the standard deviation. These mean and standard deviation values are computed using HDMR-assisted MC methods, based on a sample of 10,000 random points.

In keeping with regulatory standards, voxel SAR values undergo conversion to 1g-SAR and 10g-SAR using a standard method. This process involves averaging the SAR values in a progressively expanding region of tissue-containing voxels surrounding a central voxel. The expansion continues one voxel at a time until the specified tissue mass, either 1 g or 10 g, is achieved [48]. This procedure is executed using the algorithm detailed in [49]. The analysis of the maximum SAR further underscores the importance of the uncertainties of input parameters, which inevitably contribute to the variances observed in SAR value distributions.

Figure 6 presents a comparison between maximum and nominal 1g-SAR values. Note that only the top 5% of voxels with the highest values are selected for plotting to optimize visualization. Utilizing consistent colormaps, the voxels representing maximum values for the 1g-SAR exceed 6 W/kg, while those reflecting the nominal values for the same case are approximately 3.5 W/kg. For the 10g-SAR scenario, the maximum SAR values reach up to 4.5 W/kg, while voxels in the nominal values center around 2.5 W/kg.

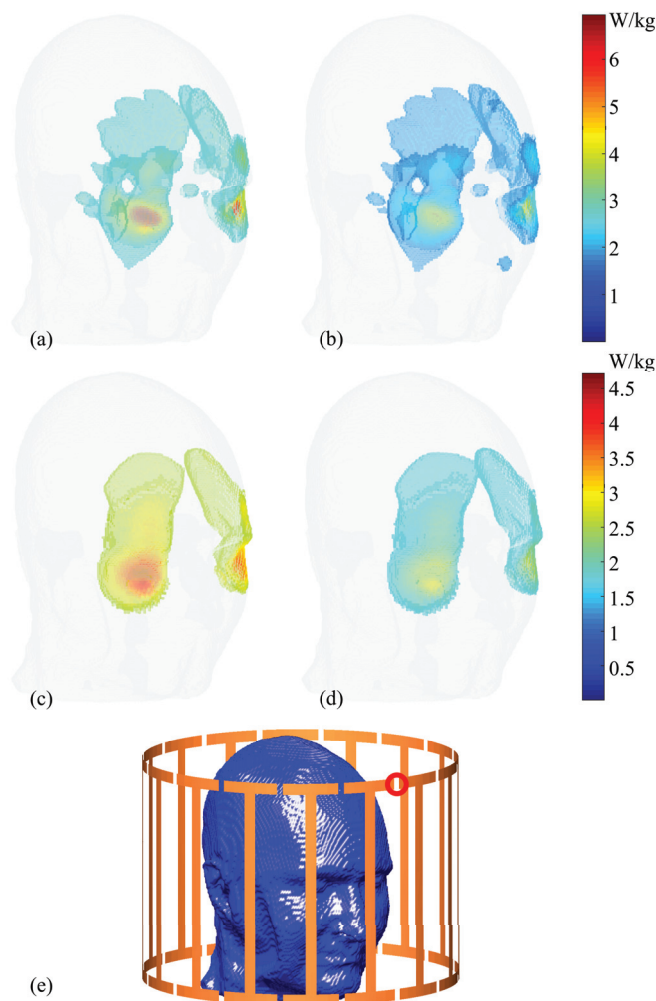


Figure 6. Comparison between maximum and nominal 1g-SAR and 10g-SAR distributions. For sub-figures (a–d), only the top 5% of voxels with highest SAR values are plotted. (a) Maximum 1g-SAR distributions. (b) Nominal 1g-SAR distributions. (c) Maximum 10g-SAR distributions. (d) Nominal 10g-SAR distributions. (e) Activation port location (circled in red).

Selected sagittal slices (Slice 72) of both 1g-SAR and 10g-SAR are depicted in Figure 7 for a comparative analysis between maximum and nominal SAR values, accompanied by their respective differences. For the 1g-SAR, there are noticeable increments of approximately 25% and 32% in the forehead and nose regions, respectively. Similarly, the 10g-SAR reveals an approximate 35% elevation in the forehead area.

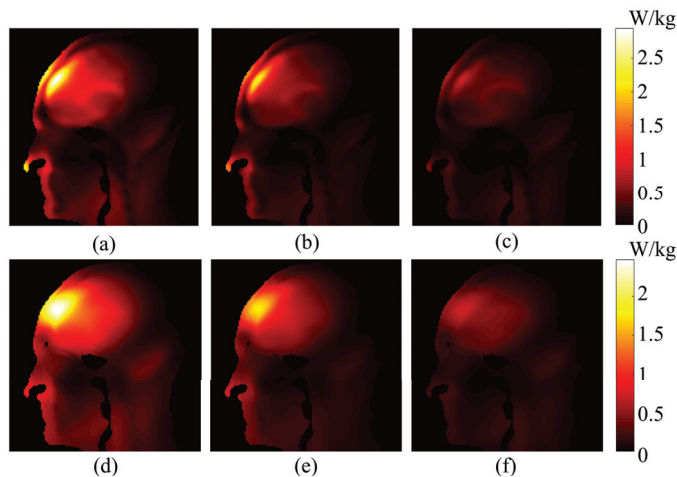


Figure 7. Comparison of sagittal slices between maximum and nominal SAR distributions, along with their differences. (a) Maximum 1g-SAR. (b) Nominal 1g-SAR. (c) Difference between (a,b). (d) Maximum 10g-SAR. (e) Nominal 10g-SAR. (f) Difference between (d,e).

3.4. Sobol Indices

For voxel i , its Sobol index with respect to \mathbf{v} , $S_{\mathbf{v},i}$, can be computed as in (3) and then classified based on the type of tissue it represents. The average Sobol indices for a given tissue type t , denoted by $S_{\mathbf{v}}^t$, is calculated by averaging $S_{\mathbf{v},i}$ across all voxels of the same tissue type, such that

$$S_{\mathbf{v}}^t = \frac{1}{N_t} \sum_{i=1}^{N_t} S_{\mathbf{v},i} \tag{21}$$

where N_t indicates total number of voxels of tissue type t .

Figure 8 displays the first-order Sobol indices of each tissue type t with respect to each input dimension. For most tissues, their own relative permittivity and conductivity have the greatest influence, followed closely by the relative permittivity and conductivity of neighboring tissue types. For the white matter, the primary influencers are its inherent relative permittivity and conductivity, with grey matter’s electrical properties coming next. In the case of grey matter, in addition to its own relative permittivity and conductivity, the relative permittivity of white matter and conductivity of the scalp also play significant roles. For CSF, while its own conductivity is the predominant contributor, other inputs also significantly influence the variances. This phenomenon can be attributed to the circumstance that CSF is a common neighbor to most tissues, resulting in its SAR values being impacted by the changes in the properties of adjacent tissues as well. This suggests a complex interaction between the CSF and its surrounding environment, emphasizing the necessity of incorporating second-order component functions in the HDMR framework. These functions are crucial for capturing the inputs’ combined effects, offering more accurate and detailed models. Sobol indices for bone and scalp tissues display similar patterns, with their respective relative permittivities and conductivities exerting the most impacts. The results for the eye require further analysis, given that the relative permittivity of the scalp appears to be the most influential dimension.

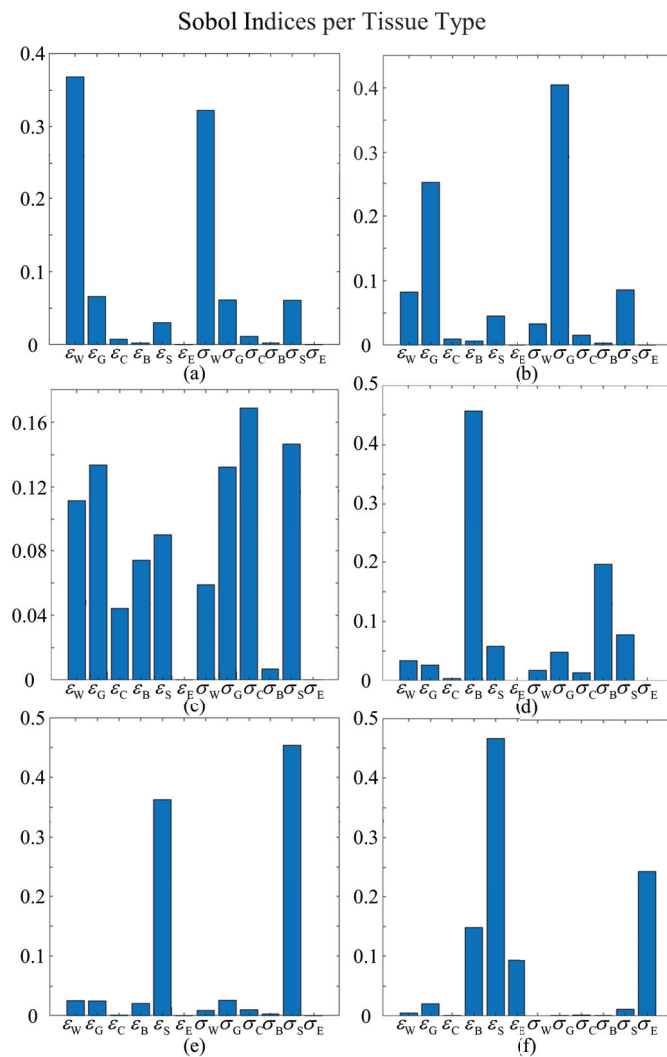


Figure 8. Averaged Sobol indices for each tissue type. The x-axis depicts input dimensions, where ϵ_r is relative permittivity and σ is conductivity; W, G, C, B, S, E represents white matter, grey matter, CSF, bone, scalp, and eye humor, respectively. Sub-figures show Sobol indices for (a) white matter, (b) grey matter, (c) CSF, (d) bone, (e) scalp, and (f) eye humor.

4. Conclusions

In this paper, a computational framework for uncertainty quantification of SAR and E-field values at voxel levels for MRI head scans at 7 T was proposed. This framework constructs the surrogate models for SAR distributions in head MRI scans utilizing the HDMR technique and then conducts statistical and sensitivity analyses on the observables. The application of the proposed framework to realistic head models demonstrated that the surrogate models are not only accurate in predicting SAR distributions but also significantly reduce the computational requirements compared with traditional MC methods. Subsequent statistical analysis revealed that 20% uncertainties in tissue dielectric properties could result in variations as substantial as 30% in the observed SAR values within certain regions. This highlights the importance of considering such uncertainties. The framework’s abilities to predict SAR distributions accurately and quantify the effects of variability in tissue properties underscore its potential as a valuable tool for supporting the analysis, design, and safety assessment of novel UHF MRI RF coils. Current research is focusing on the framework’s application with deep learning techniques for the SAR prediction on any provided head model [50]. The ultimate goal is to ensure the highest level of safety and efficacy in MRI procedures, particularly as the technology evolves and becomes more

complex. This paper’s contribution represents a fundamental advance, providing a robust tool for researchers and clinicians in the rapidly advancing field of UHF MRI technology.

Author Contributions: X.W.: data curation, formal analysis, investigation, software, validation, visualization, writing—original draft; S.Y.H.: formal analysis, visualization, writing—review & editing; A.C.Y.: conceptualization, formal analysis, methodology, project administration, resources, supervision, visualization, writing—review & editing. All authors have read and agreed to the published version of the manuscript.

Funding: This research received no external funding.

Data Availability Statement: Data are made available with a granted proposal upon reasonable request to the authors.

Conflicts of Interest: The authors declare no conflicts of interest.

Appendix A. Nomenclature

N	Dimension of the input vector, $N \in \mathbb{N}$
\mathbf{x}	Input vector, $\mathbf{x} \in \mathbb{R}^N$
x^k	k -th element of the input vector, where $k \in \{1, 2, \dots, N\}$
$[a^k, b^k]$	Range of x^k
\mathbf{y}	Observable vector
$F(\cdot)$	Deterministic simulator mapping \mathbf{x} to \mathbf{y}
N_{MC}	Number of MC simulations
\mathbf{x}_n	n -th input vector of the simulation
\mathbf{y}_n	n -th observable vector of the simulation
$E[\cdot]$	Expected value operator
$\text{Var}[\cdot]$	Variance operator
$\text{Var}_{x^k}[\cdot]$	Variance operator with respect to the random variable x^k
S_k	Sobol index for the k -th element of the input vector
Ω	The set of random variable indices, $\Omega = \{1, 2, \dots, N\}$
\mathbf{v}	Subset of Ω
$ \mathbf{v} $	Cardinality of \mathbf{v}
$\mathbf{x}^{\mathbf{v}}$	Selection of the input vector \mathbf{x} corresponding to the indices in \mathbf{v}
F_0	Zeroth-order component function of HDMR
$F_i(x^i)$	First-order component function of HDMR
$F_{ij}(x^i, x^j)$	Second-order component function of HDMR
$\bar{\mathbf{x}}$	Reference point in CUT-HDMR
$\tilde{\mathbf{x}} = \bar{\mathbf{x}} \setminus \mathbf{x}^{\mathbf{v}}$	Input vector whose random variables indexed by set \mathbf{v} are retained, and all others are set according to $\bar{\mathbf{x}}$
α	Coefficients of gPC expansion
$\Phi(\cdot)$	Product of 1D Legendre polynomials
$\phi(\cdot)$	1D Legendre polynomials
N_{GL}	Number of Gauss–Legendre quadrature points per dimension
N_{CP}	Number of total collocation points
N_{test}	Number of testing points
err_{max}	Maximum error among all tissue voxels
err_{ave}	Average error of all tissue voxels

References

1. Smith-Bindman, R.; Miglioretti, D.L.; Johnson, E.; Lee, C.; Feigelson, H.S.; Flynn, M.; Greenlee, R.T.; Kruger, R.L.; Hornbrook, M.C.; Roblin, D. Use of diagnostic imaging studies and associated radiation exposure for patients enrolled in large integrated health care systems, 1996–2010. *JAMA* **2012**, *307*, 2400–2409. [CrossRef] [PubMed]
2. Brown, R.W.; Cheng, Y.C.N.; Haacke, E.M.; Thompson, M.R.; Venkatesan, R. *Magnetic Resonance Imaging: Physical Principles and Sequence Design*; Wiley-Liss: New York, NY, USA, 2014.
3. Shellock, F.G. Radiofrequency energy-induced heating during MR procedures: A review. *J. Magn. Reson. Imaging* **2000**, *12*, 30–36. [CrossRef] [PubMed]

4. Shellock, F.G.; Crues, J.V. MR procedures: Biologic effects, safety, and patient care. *Radiology* **2004**, *232*, 635–652. [CrossRef] [PubMed]
5. Collins, C.M.; Wang, Z. Calculation of radiofrequency electromagnetic fields and their effects in MRI of human subjects. *Magn. Reson. Med.* **2011**, *65*, 1470–1482. [CrossRef] [PubMed]
6. Panych, L.P.; Madore, B. The physics of MRI safety. *J. Magn. Reson. Imaging* **2018**, *47*, 28–43. [CrossRef] [PubMed]
7. Ladd, M.E.; Bachert, P.; Meyerspeer, M.; Moser, E.; Nagel, A.M.; Norris, D.G.; Schmitter, S.; Speck, O.; Straub, S.; Zaiss, M. Pros and cons of ultra-high-field MRI/MRS for human application. *Prog. Nucl. Magn. Reson. Spectrosc.* **2018**, *109*, 1–50. [CrossRef] [PubMed]
8. Barisano, G.; Seppehrband, F.; Ma, S.; Jann, K.; Cabeen, R.; Wang, D.J.; Toga, A.W.; Law, M. Clinical 7 T MRI: Are we there yet? A review about magnetic resonance imaging at ultra-high field. *Br. J. Radiol.* **2019**, *92*, 20180492. [CrossRef] [PubMed]
9. Ladd, M.E.; Quick, H.H.; Speck, O.; Bock, M.; Doerfler, A.; Forsting, M.; Hennig, J.; Ittermann, B.; Möller, H.E.; Nagel, A.M. Germany's journey toward 14 Tesla human magnetic resonance. *Magn. Reson. Mater. Phys. Biol. Med.* **2023**, *36*, 191–210. [CrossRef]
10. Foster, K.R.; Glaser, R. Thermal mechanisms of interaction of radiofrequency energy with biological systems with relevance to exposure guidelines. *Health Phys.* **2007**, *92*, 609–620. [CrossRef] [PubMed]
11. Gabriel, C. Compilation of the dielectric properties of body tissues at RF and microwave frequencies. In *Report N.AL/OE-TR-1996-0037, Occupational and Environmental Health Directorate*; Radiofrequency Radiation Division, Brooks Air Force Base: San Antonio, TX, USA, 1996.
12. Gandhi, O.P.; Lazzi, G.; Furse, C.M. Electromagnetic absorption in the human head and neck for mobile telephones at 835 and 1900 MHz. *IEEE Trans. Microw. Theory Tech.* **1996**, *44*, 1884–1897. [CrossRef]
13. Peyman, A.; Holden, S.; Gabriel, C. Measurement of the dielectric properties of biological tissues in vivo at microwave frequencies. *Phys. Med. Biol.* **2009**, *54*, 4863–4878.
14. Smith, S.M. Stochastic Finite-Difference Time-Domain. Ph.D. Thesis, The University of Utah, Salt Lake City, UT, USA, 2011.
15. Masumnia-Bisheh, K.; Furse, C. Variability in Specific Absorption Rate From Variation in Tissue Properties. *IEEE J. Multiscale Multiphys. Comput. Tech.* **2022**, *7*, 304–311. [CrossRef]
16. Masumnia-Bisheh, K.; Ghaffari-Miab, M.; Zakeri, B. Evaluation of different approximations for correlation coefficients in stochastic FDTD to estimate SAR variance in a human head model. *IEEE Trans. Electromagn. Compat.* **2016**, *59*, 509–517. [CrossRef]
17. Machado-Rivas, F.; Jaimes, C.; Kirsch, J.E.; Gee, M.S. Image-quality optimization and artifact reduction in fetal magnetic resonance imaging. *Pediatr. Radiol.* **2020**, *50*, 1830–1838. [CrossRef] [PubMed]
18. Gomez, L.J.; Yucel, A.C.; Hernandez-Garcia, L.; Taylor, S.F.; Michielssen, E. Uncertainty quantification in transcranial magnetic stimulation via high-dimensional model representation. *IEEE Trans. Biomed. Eng.* **2014**, *62*, 361–372. [CrossRef] [PubMed]
19. Saturnino, G.B.; Thielscher, A.; Madsen, K.H.; Knösche, T.R.; Weise, K. A principled approach to conductivity uncertainty analysis in electric field calculations. *NeuroImage* **2019**, *188*, 821–834. [CrossRef] [PubMed]
20. International Electrotechnical Commission. *Medical Electrical Equipment-Part 2-33: Particular Requirements for the Basic Safety and Essential Performance of Magnetic Resonance Equipment for Medical Diagnosis*; IEC: Geneva, Switzerland, 2010.
21. *IEEE Std C95.1TM-2019*; IEEE Standard for Safety Levels with Respect to Human Exposure to Electric, Magnetic, and Electromagnetic Fields, 0 Hz to 300 GHz. IEEE: Piscataway, NJ, USA, 2019.
22. Kozlov, M.; Turner, R. A comparison of Ansoft HFSS and CST microwave studio simulation software for multi-channel coil design and SAR estimation at 7 T MRI. *PIERS Online* **2010**, *6*, 395–399. [CrossRef]
23. Polimeridis, A.G.; Villena, J.F.; Daniel, L.; White, J.K. Stable FFT-JVIE solvers for fast analysis of highly inhomogeneous dielectric objects. *J. Comput. Phys.* **2014**, *269*, 280–296. [CrossRef]
24. Rubinstein, R.Y.; Kroese, D.P. *Simulation and the Monte Carlo Method*; John Wiley & Sons: New York, NY, USA, 2007.
25. Robert, C.P.; Casella, G. *Introducing Monte Carlo Methods with R*; Springer: New York, NY, USA, 2010; Volume 18.
26. Forrester, A.; Sobester, A.; Keane, A. *Engineering Design via Surrogate Modelling: A Practical Guide*; John Wiley & Sons: Oxford, UK, 2008.
27. Šušnjara, A.; Verhnjak, O.; Poljak, D.; Cvetković, M.; Ravnik, J. Uncertainty quantification and sensitivity analysis of transcranial electric stimulation for 9-subdomain human head model. *Eng. Anal. Bound. Elem.* **2022**, *135*, 1–11. [CrossRef]
28. Wiart, J.; Conil, E.; Hadjem, A.; Jala, M.; Kersaudy, P.; Varsier, N. Handle variability in numerical exposure assessment: The challenge of the stochastic dosimetry. In *Proceedings of the 2013 7th European Conference on Antennas and Propagation (EuCAP)*, Gothenburg, Sweden, 8–12 April 2013; IEEE: Piscataway, NJ, USA, 2013; pp. 1979–1981.
29. Cheng, X.; Monebhurrun, V. Application of different methods to quantify uncertainty in specific absorption rate calculation using a CAD-based mobile phone model. *IEEE Trans. Electromagn. Compat.* **2016**, *59*, 14–23. [CrossRef]
30. Rabitz, H.; Alis, O.F.; Shorter, J.; Shim, K. Efficient input-output model representations. *Comput. Phys. Commun.* **1999**, *117*, 11–20. [CrossRef]
31. Foo, J.; Karniadakis, G.E. Multi-element probabilistic collocation method in high dimensions. *J. Comput. Phys.* **2010**, *229*, 1536–1557. [CrossRef]
32. Ma, X.; Zabaras, N. An adaptive high-dimensional stochastic model representation technique for the solution of stochastic partial differential equations. *J. Comput. Phys.* **2010**, *229*, 3884–3915. [CrossRef]
33. Pao, Y.H.; Park, G.H.; Sobajic, D.J. Learning and generalization characteristics of the random vector functional-link net. *Neurocomputing* **1994**, *6*, 163–180. [CrossRef]

34. Zhang, L.; Suganthan, P.N. A comprehensive evaluation of random vector functional link networks. *Inf. Sci.* **2016**, *367*, 1094–1105. [CrossRef]
35. Huang, G.B.; Zhu, Q.Y.; Siew, C.K. Extreme learning machine: Theory and applications. *Neurocomputing* **2006**, *70*, 489–501. [CrossRef]
36. Knerr, S.; Personnaz, L.; Dreyfus, G. Single-layer learning revisited: A stepwise procedure for building and training a neural network. In *Neurocomputing: Algorithms, Architectures and Applications*; Springer: Berlin/Heidelberg, Germany, 1990; pp. 41–50.
37. Rasmussen, C.E.; Nickisch, H. Gaussian processes for machine learning (GPML) toolbox. *J. Mach. Learn. Res.* **2010**, *11*, 3011–3015.
38. Berveiller, M.; Sudret, B.; Lemaire, M. Stochastic finite element: A non intrusive approach by regression. *Eur. J. Comput. Mech.* **2006**, *15*, 81–92. [CrossRef]
39. Jaynes, E.T. Information theory and statistical mechanics. *Phys. Rev.* **1957**, *106*, 620. [CrossRef]
40. Jaynes, E.T. Information theory and statistical mechanics. II. *Phys. Rev.* **1957**, *108*, 171. [CrossRef]
41. Sobol, I.M. Global sensitivity indices for nonlinear mathematical models and their Monte Carlo estimates. *Math. Comput. Simulat.* **2001**, *55*, 271–280. [CrossRef]
42. Yucel, A.C.; Bagci, H.; Michielssen, E. An ME-PC enhanced HDMR method for efficient statistical analysis of multiconductor transmission line networks. *IEEE Trans. Compon. Packag. Manuf. Technol.* **2015**, *5*, 685–696. [CrossRef]
43. Chowdhury, R.; Adhikari, S. High dimensional model representation for stochastic finite element analysis. *Appl. Math. Model.* **2010**, *34*, 3917–3932. [CrossRef]
44. Xiu, D.; Karniadakis, G.E. The Wiener–Askey polynomial chaos for stochastic differential equations. *SIAM J. Sci. Comput.* **2002**, *24*, 619–644. [CrossRef]
45. Marcus, D.S.; Fotenos, A.F.; Csernansky, J.G.; Morris, J.C.; Buckner, R.L. Open Access Series of Imaging Studies: Longitudinal MRI Data in Nondemented and Demented Older Adults. *J. Cogn. Neurosci.* **2010**, *22*, 2677–2684. [CrossRef] [PubMed]
46. Nielsen, J.D.; Madsen, K.H.; Puonti, O.; Siebner, H.R.; Bauer, C.; Madsen, C.G.; Saturnino, G.B.; Thielscher, A. Automatic skull segmentation from MR images for realistic volume conductor models of the head: Assessment of the state-of-the-art. *NeuroImage* **2018**, *174*, 587–598. [CrossRef] [PubMed]
47. Saturnino, G.B.; Madsen, K.H.; Thielscher, A. Electric field simulations for transcranial brain stimulation using FEM: An efficient implementation and error analysis. *J. Neural Eng.* **2019**, *16*, 066032. [CrossRef] [PubMed]
48. Caputa, K.; Okoniewski, M.; Stuchly, M.A. An algorithm for computations of the power deposition in human tissue. *IEEE Antennas Propag. Mag.* **1999**, *41*, 102–107. [CrossRef]
49. Carluccio, G.; Erricolo, D.; Oh, S.; Collins, C.M. An approach to rapid calculation of temperature change in tissue using spatial filters to approximate effects of thermal conduction. *IEEE Trans. Biomed. Eng.* **2013**, *60*, 1735–1741. [CrossRef] [PubMed]
50. Wang, X.; Jia, X.; Huang, S.Y.; Yucel, A.C. Deep learning-based estimation of specific absorption rate induced by high-field MRI RF head coils. In Proceedings of the IEEE International Symposium on Antennas and Propagation and USNC-URSI Radio Science Meeting, Portland, OR, USA, 23–28 July 2023.

Disclaimer/Publisher’s Note: The statements, opinions and data contained in all publications are solely those of the individual author(s) and contributor(s) and not of MDPI and/or the editor(s). MDPI and/or the editor(s) disclaim responsibility for any injury to people or property resulting from any ideas, methods, instructions or products referred to in the content.

Article

Modeling of Magnetic Scaffolds as Drug Delivery Platforms for Tissue Engineering and Cancer Therapy

Matteo B. Lodi ^{1,2,†}, Eleonora M. A. Corda ^{1,†}, Francesco Desogus ³, Alessandro Fanti ^{1,2,*} and Giuseppe Mazzarella ^{1,2}

¹ Department of Electrical and Electronic Engineering, University of Cagliari, via Marengo 2, 09123 Cagliari, Italy; matteob.lodi@unica.it (M.B.L.); eleonorama.corda@unica.it (E.M.A.C.); mazzarella@unica.it (G.M.)

² Consorzio Nazionale Interuniversitario per le Telecomunicazioni (CNIT), Cagliari Research Unit, Department of Electrical and Electronic Engineering, University of Cagliari, via Marengo 2, 09123 Cagliari, Italy

³ Department of Mechanical, Chemical and Material Engineering, University of Cagliari, via Marengo 2, 09123 Cagliari, Italy; francesco.desogus@unica.it

* Correspondence: alessandro.fanti@unica.it

† These authors contributed equally to this work.

Abstract: Magnetic scaffolds (MagSs) are magneto-responsive devices obtained by the combination of traditional biomaterials (e.g., polymers, bioceramics, and bioglasses) and magnetic nanoparticles. This work analyzes the literature about MagSs used as drug delivery systems for tissue repair and cancer treatment. These devices can be used as innovative drugs and/or biomolecules delivery systems. Through the application of a static or dynamic stimulus, MagSs can trigger drug release in a controlled and remote way. However, most of MagSs used as drug delivery systems are not optimized and properly modeled, causing a local inhomogeneous distribution of the drug's concentration and burst release. Few physical–mathematical models have been presented to study and analyze different MagSs, with the lack of a systematic vision. In this work, we propose a modeling framework. We modeled the experimental data of drug release from different MagSs, under various magnetic field types, taken from the literature. The data were fitted to a modified Gompertz equation and to the Korsmeyer–Peppas model (KPM). The correlation coefficient (R^2) and the root mean square error (RMSE) were the figures of merit used to evaluate the fitting quality. It has been found that the Gompertz model can fit most of the drug delivery cases, with an average RMSE below 0.01 and $R^2 > 0.9$. This quantitative interpretation of existing experimental data can foster the design and use of MagSs for drug delivery applications.

Keywords: cancer therapy; drug delivery; electromagnetic fields; magnetic nanoparticles; magnetic scaffolds; tissue engineering

1. Introduction

Tissue engineering (TE) and cancer therapeutics (CThs) have been enabled by the development of biocompatible tissue-mimicking biomaterials (e.g., metals, biopolymers, and bioceramics). Bioactive materials, manufactured as tissue scaffolds, are designed to elicit specific biological responses, which are crucial for controlled healing and regeneration or therapy [1–3]. For 3D scaffolds, a sufficient porosity (50–80%, depending on the tissue site), as well as pore size distribution (1 μm –250 μm), must be guaranteed to ensure tissue growth, adequate biomolecule signaling, cellular homing, and vascularization [4,5]. Kim et al. [6] developed a porous polycaprolactone (PCL) scaffold for bone tissue incorporating cuttlefish bone-derived hydroxyapatite (Hap) powder to demonstrate that, in vitro, the porosity influences the proliferation and differentiation by creating an adequate biomechanical microenvironment for tissue regeneration. However, some strategies for scaffold

designs do not meet TE goals [7–9]. Therefore, new solutions and alternative strategies to control cell–biomaterial interactions have been considered.

Biomaterial scaffolds have been explored as devices and platforms for controlled drug delivery (DD) aimed at manipulating tissue repair and/or therapeutic outcomes [10,11]. Several physical methods in a biomaterial to exert a therapeutic action are available [12,13]. For TE applications, biomaterials for DD have the aim of providing growth factors (GFs) around the implant region to control and manipulate tissue repair, acting on cell migration, proliferation, differentiation, or, for cancer therapy (CT), exerting an anti-proliferative action [2,8,12,14]. Initially, scaffold DD systems for TE relied on mechanisms, such as molecular diffusion, material degradation, or cell migration, which are poorly controllable [14]. This new approach allows us to recreate and mimic the *in vivo* release profiles of factors produced during natural tissue morphogenesis or repair. For instance, GFs, such as platelet-derived growth factor (PDGF) embedded in implanted polymeric (e.g., PLGA and PLA) formulation or alginate hydrogels, were used for endothelial cell proliferation with applications in angiogenesis and wound healing [15]. Bone morphogenetic protein-2 (BMP-2) when combined with hydrogels or PLGA scaffolds is useful for modulating cell proliferation and tuning bone regeneration [15]. The release of drugs and GFs from biomaterials is not exempt from shortcomings and limitations. Indeed, not all biomaterials with local DD exhibit a spatial and temporal controlled release and a sustained drug release behavior to ensure an optimum controlled therapy, thus avoiding side effects [16–18].

Therefore, bioengineers proposed to trigger and/or regulate the delivery of biological agents (e.g., drugs and cells) using external cues and physical stimuli, thus overcoming traditional DD limitations [19]. Potential candidates as therapeutic scaffolds used in DD applications, such as TE and CT, are called stimuli-responsive scaffolds [19,20]. Stimuli-responsive scaffolds are smart biomaterial implants that can respond to exogenous or endogenous physical and/or chemical changes [19–21]. Several active biomaterials, responsive to external stimuli, were proposed in the literature, such as the temperature-responsive injectable hydrogel scaffold [12] and pH-sensitive scaffold [10]. Furthermore, various physical fields and energy forms (e.g., mechanical, electric, piezoelectricity, etc.) were analyzed for controlled delivery with improved safety and efficiency, while enabling new therapies [22–25]. Despite the disruptive potential of stimuli-responsive biomaterials, some limitations and challenges must be underlined. Indeed, forms of energy, such mechanical, thermal, and ultrasound energy, are not specific, reach limited penetration depths, or, instead, lead to complex technological implementations [19–26].

In the framework of stimuli-responsive scaffolds, electromagnetic (EM) energy can play a key pivotal role, overcoming DD limitations. Indeed, the EM spectrum, especially ranging from very low frequencies (i.e., few Hz) to radiofrequency (herein, hundreds of kHz), can be used to control the response of scaffolds and trigger specific effects and actions on cells and tissues for both TE and CT remotely, noninvasively, and precisely [27–29]. Electric field-responsive scaffolds have been proposed [29], but they cannot be easy to reach if implanted in deep body sites. On the other hand, magnetic fields (MFs) are preferred for some biomedical applications since they have a higher penetration depth and high specificity. Therefore, the possibility of manufacturing a biomaterial able to respond to the magnetic field was investigated, too [30–33]. A magnetic implant can be achieved by incorporating specialized magnetic biomaterials in a nano-formulation into the biomaterial matrix (see Figure 1), thus conferring magnetic properties to the structure, which can then be controlled spatiotemporally and remotely [30–33].

Magnetic nanoparticles (MNPs) are particles (<200 nm in size) composed of magnetic elements, such as iron (Fe), nickel (Ni), cobalt (Co), or their oxides (e.g., magnetite, maghemite, etc.) [34]. Zn- and Mn-substituted magnetite MNPs hold therapeutic potential against colorectal cancers [35,36]. If MNPs are embedded in biomaterials such as bioceramics or biopolymers, thus creating a so-called magnetic scaffold (MagS), theragnostic and multifunctional abilities are provided to scaffolds, creating new usage and applications. By varying the magnetic field strength in space or time, it is possible to control the physical,

structural, and mechanical properties of these magneto-responsive scaffolds. Therefore, MagSs can be used for TE, DD, or CT [37]. MagSs can be activated (i) by static or very low-frequency MF-triggering mechanical forces and deformations, or (ii) by alternate MFs for magnetothermal conversion.

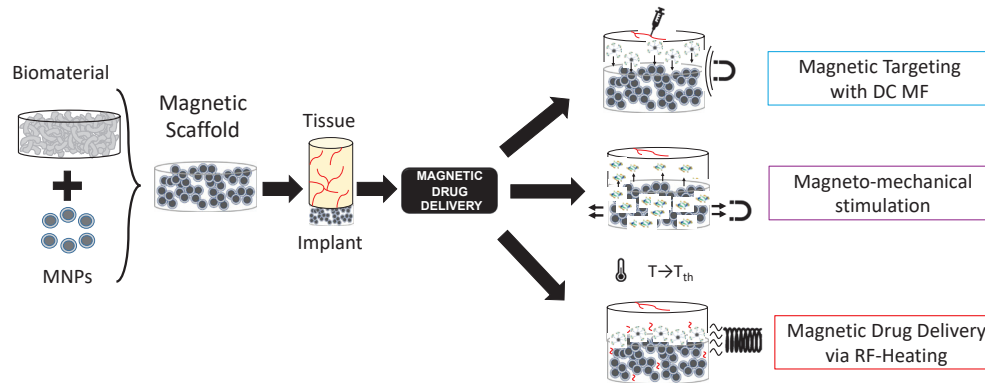


Figure 1. Graphical representation of the concept of magnetic scaffolds as the combination of magnetic nanoparticles and biomaterials, and their use for drug delivery applications.

In regard to TE, MagSs act as mechano-transducers modifying local Ca^{2+} fluxes. In [38], magnetic Hap scaffolds were cultured *in vitro* with pre-osteoblast and osteoblast cells (i.e., ROS 17/2.8 and MC3T3-E1, respectively) with and without an exterior static MF (~ 15 kA/m), finding that proliferation and differentiation were influenced. MagSs have been evaluated for cardiac tissue: a functional cardiac patch of microporous alginate scaffold impregnated with MNPs and the application of a 5 Hz external MF stimulation has been studied in [39]. The study of PCL/gelatin 3D magnetic nanofibrous constructs comprising MNPs has been carried out in [40].

On the other hand, MagSs can be used as therapeutic agents by exploiting the highly efficient magnetothermal conversion that MNPs embedded in a biomaterial matrix experience, if an RF MF is applied [37]. The dissipated heat can be exploited to administer hyperthermia at local and interstitial levels against solid cancers, such as bone or ductal tumors [37].

The intrinsic multifunctional nature of MagSs, in particular, the mechano-transducer and magnetothermal conversion features, have been exploited to implement an innovative DD platform for GFs or drug administration, as shown in Figure 1, as epitomized by the magnetic sponge loaded with docetaxel (DTX), whose release is triggered by static MF-induced (~ 50 – 350 mT) reversible mechanical deformations [41]. Exploiting a similar mechanism, in [42], hollow-fiber alginate/iron oxide nanoparticle scaffolds were prepared by 3D printing, and the MF-mediated delivery of encapsulated drugs (e.g., doxorubicin—DOX), protein, and mesenchymal stem cells was tested *in vitro* and *in vivo*. On the other hand, in [43,44], composite ethylcellulose membrane scaffolds with embedded thermosensitive poly(*n*-isopropyl acrylamide) (polyNIPAM)-based nanogels and MNPs exposed to 220–260 kHz, 0–20 mT MF proved to be able to increase membrane permeability as the dissipated magnetic heating increased the membrane temperature.

Recently, in [44], we dealt for the first time with the mathematical modeling of the magnetic drug delivery of growth factors to evaluate the effectiveness of MagSs as an *in situ* attraction platform for MNPs carrying GFs to control the bone regeneration process. The proposed DD strategy is a combination of different administration strategies mediated by different MF types (see Figure 1). Indeed, simulations to evaluate how a static MF can be used to force and drive MNPs+GFs to the MagSs were performed. Then, the *in silico* study of how RF MFs can be used to trigger GF release led to the findings that the quality of regenerated bone tissue can be improved using MagSs.

From this introductory discussion, it is possible to infer that MagSs have high potential for DD. Indeed, MagSs can overcome the significant common problems for traditional

biomaterials used for DD applications, such as burst release, heterogeneity in the release phase of the bioactive agent, inhomogeneous spatial distribution, control long-term release, reduce the leakage of drugs or GFs, avoiding side effects, or the impossibility of re-loading the biomaterial [10,11,25,44]. However, from the above discussion, it can be observed clearly that there are several types of MagSs, while presenting different and fuzzy features, as well as being characterized by various DD mechanisms. This work is motivated by the need for an engineering and quantitative rationale that can drive and lead their design and use for TE and DD applications. Traditionally, DD and biomaterials for DD find strong bases in mathematical modeling and kinetics models. For MagSs, it must be noted and highlighted that very few or no models were developed to interpret their response as DD platforms. Therefore, in this work, for the first time, we focus on the physical and mathematical modeling of MagSs as innovative structures for delivering bioactive agents, in the pursuit of achieving targeted, prolonged, and stimulus-responsive release. The aim is to provide a solid framework to empower and further develop the MagS design and DD applications. To this aim, in Section 2, we performed a literature analysis to select the most relevant cases study of MagSs used as DD platforms. Then, as explained in Section 3, the experimental data from DD experiments were digitized and fitted to kinetic models. Then, in Section 4, the results are presented, and the release and kinetic parameters are linked and analyzed with respect to the intrinsic magnetic features of MagSs, and an extensive critical discussion is provided too. In Section 5, the conclusions are reported.

2. Related Works and Cases Study

2.1. Methodology for the Literature Analysis

A literature search aimed at identifying all relevant articles was based on the selection of works to identify some cases studies of MagS DD applications. The search strategy, including all identified keywords, index terms, and abstract, has been adapted for each included database and/or information source. Studies published in the English language from January 2009 to 2024 were included. The databases used in the research included Wiley, National Institutes of Health (NIH), Scopus, PubMed, Science Direct, and IEEEExplore. We focused our attention on different aspects, namely, the biomaterial matrix; the type of MNPs (e.g., magnetic features and size); MagS manufacturing; the type of DD strategies triggered, modulated, and controlled by an external magnetic field (e.g., static, dynamic, magneto-thermal conversion, etc.); and, finally, if experimental tests were performed and for which DD applications they were proposed. In this respect, we critically and thoroughly analyzed these literature sources and carefully identified the knowledge gaps to propose a quantitative framework to study MagSs for DD.

2.2. Literature Analysis

The conducted literature research led to the identification of some different, specific articles for MagSs and DD applications [41–53]. The results of our literature analysis are reported in Table 1.

The selected articles offer a comprehensive overview of the different methodologies and approaches used in MagSs for targeted DD, especially in the context of TE and CT. From works [41–53], as can be seen from Table 1, the preferred biomaterial matrix formulation, which is a fundamental factor for achieving mechanical and biocompatibility properties, is polymeric, allowing the easy manufacturing of magnetic nanocomposite and drug- or biomolecule-loaded scaffolds.

We hypothesize that, for MagSs, the selection of the magnetic nanoparticles to embed or the magnetic phase to synthesize is crucial. MNPs can have a different magnetism. They can be ferrimagnetic or ferromagnetic (for diameters in the range of 25–50 nm to 100 nm), i.e., they can be intrinsically magnetic and possess a permanent magnetic moment [34,45]. On the other hand, MNPs (diameter below 25 nm) can respond to an externally applied magnetic field being superparamagnetic (SPM). In any case, MNPs' magnetism play an important role in enhancing DD efficiency. In Table 1, we can see that ferromagnetic and

SPM particles are used. Ferromagnetic particles have been used in [41]. On the other hand, SPM MNPs are preferred. For instance, in [46], a 3D-printed mesoporous bioactive glass (MBG)-PCL scaffold with SPM magnetite nanoparticles was proposed for TE and DD for CT applications. MBG possesses a more optimal surface area, nanopore volume, controlled drug delivery properties, and in vivo biocompatibility, and this makes the structure more suitable and effective for the specific applications studied. The particularity of Fe₃O₄/MBG/PCL composite scaffolds has been accentuated by the MNPs' presence that made these structures able to respond to the external magnetic field. The release of 20 mL of DOX was evaluated after the application of an alternating MF of 18 mT with an amplitude of 409 kHz for 30 min. In [47], the formulation of multilayer magnetic gelatin membrane scaffolds blended with Fe₃O₄ SPM MNPs was proposed. Gelatin MagSs are supposed to be used as in situ attraction sites for magnetized DD agents carrying GFs or drugs. However, SPM MNPs can also be used to perform DD based on the magneto-thermal mechanism. Chemical routes for doping bio-ceramics and producing in situ MNPs lead to an interesting sub-class of MagSs. For instance, in [48], magnetic hybrid composites made of (Fe²⁺/Fe³⁺)-doped Hap nanocrystals nucleated on self-assembling collagen fibers were prepared using a biologically inspired mineralization process. DOX was adsorbed onto Hap and released through the application of pulsed electromagnetic fields (PEMFs). These MagSs were tested as DD agents against osteosarcoma cancers [47,48]. In [49], a magnetic mesoporous glass formulation for a Fe₃O₄/CaO/SiO₂/P₂O₅ system is proposed. A dynamic MF with a strength value of 1.47 kA/m and frequency of 232 kHz was used to trigger, via magneto-thermal conversion, the in vitro release of 20 ml of gentamicin, thus proving the potential of this MagS for the regeneration of a critical-size bone defect [50]. The versatility of MagSs as DD platforms is limitless. Indeed, in [51], a macroporous ferrogel is manufactured by incorporating ferrite SPM MNPs and mitoxantrone (300 g); plasmid DNA and chemokines (SDF 1- α) were released under the action of a dynamic MF (38 A/m, 120 cycles (on/off), for 2 min). In this framework, new studies dealing with MagSs as DD systems are being published [52–55] and the interest of the scientific community is very high in this topic.

Table 1. Literature analysis of MagSs for DD.

Work	Biomaterial	MNPs	Manufacturing	Mechanism	Drug/GFs	DD App.
[41]	PDMS	Ferromagnetic carbonyl iron	Incorporation	Static MF Mechanical deformation	MB, DTX	CT
[42]	Alginate	Fe ₃ O ₄	Blending	Static MF Mechanical deformation	BSA, DOX	CT
[43,44]	poly(N-isopropylacrylamide)	Fe ₃ O ₄	Dissolution Evaporation	Dynamic MF Magneto-thermal	-	TE, CT
[46]	MBG-PCL	Fe ₃ O ₄	3D printing	Dynamic MF Magneto-thermal	DOX	TE, CT
[47]	Gelatin	Fe ₃ O ₄	Blending	Static MF Mechanical deformation	-	TE
[48]	Hap	Fe ₂ O ₃ Fe ₃ O ₄	Chemical doping	Pulsed MF Mechanical deformation	DOX	CT
[50]	MBG	Fe ₃ O ₄	Chemical doping	Dynamic MF Magneto-thermal	Gentamicin	TE
[51]	Alginate	Fe ₃ O ₄	Blending	Dynamic MF	Mitoxantrone plasmid DNA chemokine	TE
[52]	Bioactive glass	Fe ₃ O ₄	3D printing	Passive release	Mitomycin C	TE

2.3. Knowledge Gaps and Goals

From the above discussion and from Table 1, we can underline that key differences exist in MagS manufacturing. Depending on the combination of the biomaterial, MNPs and considering the intended DD applications, various mechanism of drug release are possible.

As can be observed in Table 1, several combinations of MNPs and biomaterials, different manufacturing approaches have been proposed, but the role of formulation in DD has been poorly investigated. A rationale or set of rules for driving the selection of biomaterials and MNPs is missing, as well as to identify the best manufacturing approach. This is further complicated by the fact that the magnetic response of MagSs, given that the MNPs interact with the complex material structure, cannot be easily interpreted a priori. Furthermore, the different release mechanisms obey different physical laws, where the MagSs' magnetic features play a pivotal role that has been poorly modeled and understood, to date. Therefore, despite the fact that the production techniques of these nano-systems have been carefully studied and tested with a proof of concept to test the release, there is a lack of theoretical or computational models to study, interpret, and design MagSs. The proposal and verification of such models are necessary to deal with MagS designs, treatment planning, and the investigation of the biological effects. In this work, we identified the difficulty to find an appropriate model suitable for modeling MagSs as DD agents. However, mathematical modeling has been widely employed in pharmacokinetics and DD, also for magnetic nano-formulations, such as in [56,57]. Furthermore, very few MagS-related studies reported the drug concentration profile as a function of release time [41–53]. Thus, in this work, for the first time, we will focus on works [41,43,44,46,48–51], since suitable, clear, and exhaustive experimental data for testing MagSs as DD platforms for TE and CT have been provided. These data have been studied and used to identify suitable models to apply the results to the understanding of the physical phenomena, mechanisms, and formulations underlying the interaction between the MF and MagSs for DD.

3. Model and Methodology

3.1. Data Retrieval

The data from studies [41,43,44,46,48–51] were digitized using the online software “PlotDigitizer” [58]. We retrieved the concentration of released drug for each time for all the data found in these literature references. For pre-processing, the data were normalized. The post-processing of the obtained data and subsequent comparison of the various candidate models were performed using the “Curve Fitting Toolbox” from MATLAB 2023a (The MathWorks Inc., Boston, MA, USA).

3.2. Modeling

A remark is in order. The aim of this work is the modeling of MagSs as DD agents, linking drug release to the EM properties. To this aim, the available models from pharmacokinetics and DD were used. Therefore, in the following section, we will describe the well-known pharmacokinetic models used to describe the mechanisms governing the release of bioactive agents. A comprehensive overview of DD models is provided in [59–63]. Given the availability of different models, several fittings were performed to identify the kinetic model that best fitted the studied data to describe the DD modalities from several MagSs [41,43,44,46,48–51] based on the available experimental data. In this work, we will focus on Gompertz and Korsmeyer–Peppas (KPM) models, proving that they are flexible and generally applicable [59–63].

3.2.1. Gompertz Model

A modified Gompertz model allows studying the dissolution profile of a pharmaceutical dosage [59–61]:

$$X(t) = e^{-\alpha e^{\beta \log t}}, \quad (1)$$

where $X(t)$ represents the percentage dissolved at a normalized time, t . Special attention should be given to the two coefficients: the first parameter, α , determines the proportion of the undissolved drug or molecule. This parameter is defined as a scale or position parameter [59–61]. On the other hand, β is a shape parameter and it determines the dissolution rate [59–61]. The Gompertz model is highly useful for determining the comparison between different in vitro drug release profiles, which, however, must exhibit good solubility and an intermediate release rate [61].

3.2.2. Korsmeyer–Peppas Model

The KPM is a semi-empirical, comprehensive equation that simulates drug release from several delivery systems, primarily for polymeric systems. The KPM is expressed as follows [56,57,59–63]:

$$X(t) = k_{KP}t^n \tag{2}$$

In Equation (2), k_{KP} represents the constant of proportionality (in s^{-1}), and n is the release rate index as a drug release indicator of the mechanism. The constant rate and release exponent are known to depend on dosage form geometry, as well as on the dominating process (e.g., diffusion), but also on other factors governing diffusion and relaxation rates [61]. The KPM, if the polymer relaxation process is the slowest step [61], results in a zero-order drug release kinetics, so that $n = 1$ [61]. Thus, the KPM can be suited for several MagS DD cases.

3.2.3. Fitting Quality

For the identification of the candidate equation most suited to the model, the MagS DD data trend was performed by comparing two figures of merit, namely the correlation coefficient (R^2), or so-called coefficient of determination, and the root mean square error (*RMSE*). The correlation coefficient is computed as [64]:

$$R^2 = 1 - \frac{\sum_{n=1}^N (y_i - \hat{y}_n)^2}{\sum_{n=1}^N (y_i - \bar{y})^2} \tag{3}$$

In Equation (3), $\hat{y}_1, \hat{y}_2, \dots, \hat{y}_n$ are the n -th predicted values, while y_1, y_2, \dots, y_n are the n -th observed values being $\bar{y} = \frac{1}{N} \sum_{n=1}^N y_n$. In Equation (3), the numerator is the sum of squares of errors generated by the model under consideration, while the denominator indicates the average of the sum of squares of errors generated by the reference model. Since $R^2 \in [0, 1]$, the best mathematical model will be selected for $R^2 \rightarrow 1$, as it is the most suitable and confirms the drug release kinetics.

Alongside the correlation coefficient, the *RMSE* is one of the most vital indicators for verifying the validity of a given mathematical model, as it measures the difference between the values predicted by the predictive model and the actual values [64]:

$$RMSE = \sqrt{\frac{1}{N} \sum_{n=1}^N |y_n - \bar{y}|^2} \tag{4}$$

The variable retains its usual meaning. As previously mentioned, it provides an estimate of the accuracy of the predictive model: the lower the value of the *RMSE*, the better the model. Consequently, the model that produces a better approximation and representation of the starting data is characterized by having the lowest *RMSE* value.

Therefore, we based our study on the simultaneous estimation and evaluation of these two figures of merit, aiming to find the kinetic model that best approximated the data of MagSs for DD. The expression of the theoretical equation to describe the release kinetics has been plotted to derive the predicted data values and graph them together with the initial ones, with the subsequent calculation of the previously described error metrics. The validity of the mathematical model, where validity means the ability to approximate as much as

possible the release kinetics of the drug contained by the scaffold under examination, has been evaluated.

4. Results and Discussion

We selected three different types of MagSs [41–44,46,49–51] as cases of study to find a suitable DD model. These MagSs are interesting since they present different biomaterial-MNP combinations and different types of drug or biomolecule loadings that have been tested as potential candidates for the magnetic DD strategy for TE and/or CT, relying on different release mechanisms, under the application of static or alternate magnetic fields, with different intensities and frequencies. Therefore, given the limited availability of the experimental data for MagSs for DD, we will model their response and establish, for the first time, a quantitative basis for their design and use. By solving the various kinetic models, the fitting model parameters, along with the error metrics, were evaluated. The fitting model parameters were correlated and linked to MagS properties (i.e., the saturation magnetization, M_S , and volume fraction of MNPs, ϕ_m), and to extrinsic magnetic DD parameters. The results have been interpreted and critically analyzed.

The data from the magnetic microsyringe from [41] (taken from Figure 4 pag. 4; Figure 6 pag. 6 from [41]), are presented in Figure 2. The figures of merit to evaluate the fitting quality and select the most suited kinetic model are provided in Table 2. The fitting results are presented in Figure 2. The best fitting model is the KPM model. In [41], methylene blue (MB) and DTX were considered as the drugs to be released. The cumulative release is studied in the case of a non-magnetic scenario and for a static MF applied to the MagSs. For the MB, few differences (~10%) are found between the two cases (17.81 μg vs. 19.97 μg) [41]. It must be reported that the authors tested different MF strengths, and a non-linear quadratic ($X(|\mathbf{B}|) = 18.6 \left[\frac{\%}{\text{mT}^2} \right] \cdot x^2 + 3.76 \left[\frac{\%}{\text{mT}} \right] \cdot x - 1.7101 [\%]$, $R^2 = 0.98$) trend of the maximum-released drug concentration as a function of the strength of the magnetic flux density vector (\mathbf{B} , in mT) can be derived from the data from [41]. The authors did not report the exact values of M_S and ϕ_m ; therefore, it is not possible to directly relate the DD data to the material properties. However, the magnetic force exerted on the MagSs by the action of the external \mathbf{B} field is $F \propto M_S \nabla B$ [65,66]; thus, by increasing the field strength, the gradient increases and so the force increases too. Therefore, if the DD mechanism is dictated by the mechanical deformation, a higher M_S can ensure a faster and more sustained release. However, the drug molecule can affect the release kinetics and the MagS features can impact on its release too. The most relevant case is DTX release. From the fitting coefficients reported in Table 3, and the actual docetaxel release [41] (data from pag. 6, Figure 6 from [41]), whose profiles are presented in Figure 2b, it can be noticed that the magnetically triggered and controlled release results in a larger proportionality constant (~two fold) and in a super transport condition ($n > 0.89$) [59–61]. From these quantitative findings, the boost of the release resulting from the MF action mediated by the magnetic biomaterial is evident.

In [42], magnetic alginate scaffolds were considered. The data shown in Figure 3 are taken from Figure 6, pag. 43 from ref. [42]. A 40–60% difference can be observed in the cumulative release of BSA and DOX between the non-magnetic and magnetic cases. This difference can be explained by the fact that the mechanical deformation induced by the magnetic force exerted by the external MF causes a faster diffusion. To explain the drug release, for this MagS, the Gompertz model is most suited, as can be seen from the results reported in Table 4 (on average, $R^2 = 0.95$ vs. $R^2 = 0.82$, $RMSE = 0.03$ vs. $RMSE = 0.05$). From the fitting coefficients reported in Table 5, we can observe a ~70% lower fraction of undissolved drugs and ~2–3-fold-higher dissolution rates for the magnetically mediated drug release of BSA and DOX.

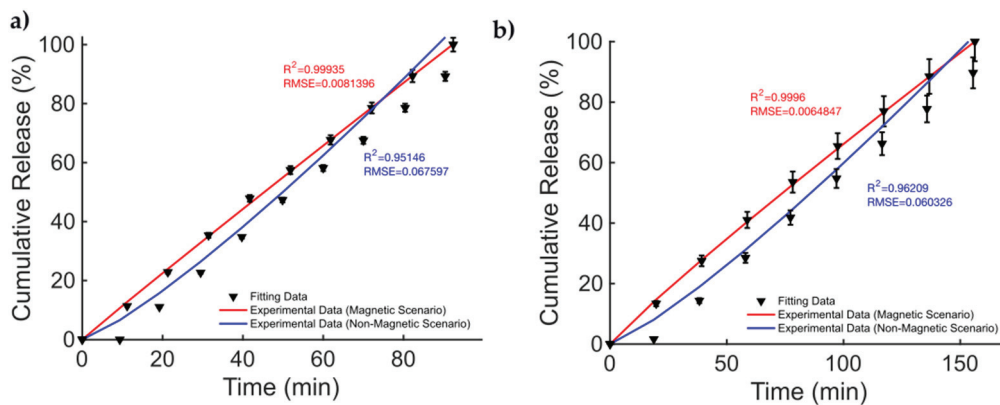


Figure 2. Release profile data for methylene blue in the cases of (a) non-magnetic and magnetic materials. Docetaxel release over time (b) for a non-magnetic membrane and in the presence of an external MF.

Table 2. Comparison of fitting quality for the Gompertz and KP models for magnetic microsputters.

	Gompertz Model		KPM	
	R^2	RMSE	R^2	RMSE
DTX (magnetic scenario)	0.9410	0.0888	0.9996	0.0069
DTX (non-magnetic scenario)	0.9636	0.0747	0.9934	0.0318
MB (magnetic scenario)	0.9423	0.0857	0.9994	0.0091
MB (non-magnetic scenario)	0.9631	0.0738	0.9931	0.0319

Table 3. Fitting coefficients for the two models for the drug released from magnetic microsputters.

	Gompertz Model		KPM	
	α	β	k_{KP} (1/min)	n
DTX (magnetic scenario)	624.75	-1.64	0.0093	0.9261
DTX (non-magnetic scenario)	4.6357×10^3	-2.04	0.0024	1.1984
MB (magnetic scenario)	316.05	-1.67	0.0121	0.9758
MB (non-magnetic scenario)	1.71×10^3	-2.07	0.0044	1.2102

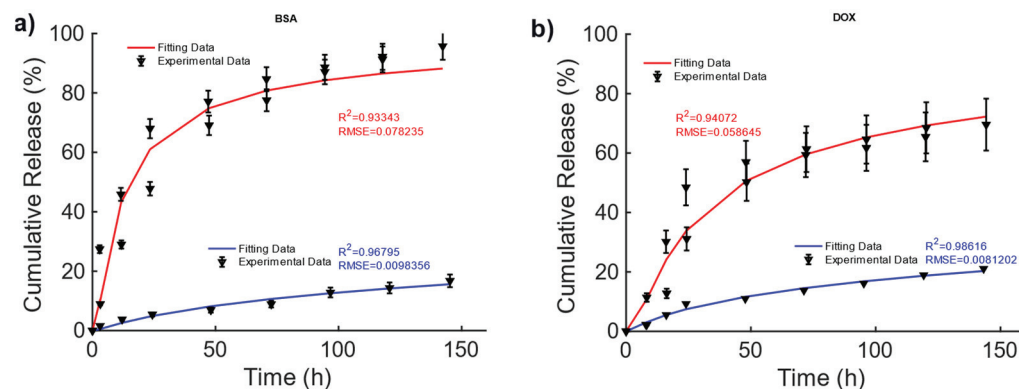


Figure 3. Cumulative release of (a) BSA and (b) DOX from hollow alginate non-magnetic (blue curve) and magnetic scaffolds (red) under the actions of a magnetic field being turned on and off.

Table 4. Comparison of fitting quality for the Gompertz and KP models for alginate SPIO scaffolds.

	Gompertz Model		KPM	
	R^2	RMSE	R^2	RMSE
BSA (magnetic scenario)	0.9334	0.0836	0.9398	0.0795
BSA (non-magnetic scenario)	0.9679	0.0112	0.9863	0.0073
DOX (magnetic scenario)	0.9407	0.0627	0.8780	0.0899
DOX (non-magnetic scenario)	0.9862	0.0092	0.9849	0.0096

Table 5. Fitting coefficients for the two models for the drug release alginate SPIO scaffolds.

	Gompertz Model		KPM	
	α	β	k_{KP} (1/h)	n
BSA (magnetic scenario)	5.3917	−0.7583	0.1667	0.3641
BSA (non-magnetic scenario)	7.1249	−0.2701	0.0055	0.6796
DOX (magnetic scenario)	9.2091	−0.6727	0.0698	0.4827
BSA (non-magnetic scenario)	6.1927	−0.2733	0.0112	0.5897

These findings are partially corroborated by the KPM coefficients, since in Table 5, larger time constants were observed, in the presence of a quasi-Fickian release in magnetic cases. Therefore, the MF can act on the release kinetic, modifying its features.

The data from [43], Figure 3A, pag. 1398, for the poly(N-isopropylacrylamide) embedding 25% wt. of Fe₃O₄ MNPs developed for DD for TE and CT under dynamic MF excitation were considered and are reported in Figure 4. For this MagS, the release is triggered by an alternate-current (AC) magnetic-flux density field working at 220–260 kHz and with strengths of some mT [43,44]. The best model is the KPM, and its fitting coefficients are presented in Table 6. Few details are available for the magnetic properties of this MagS. However, in the presence of super transport, the AC MF (H , in A/m) causes heat dissipation for the MNPs embedded in the MagS. The magnetic energy is converted into power per unit volume according to the law $Q_m = \pi f \mu_0 |H|^2 \chi''$, χ'' being the out-of-phase component of the complex magnetic susceptibility of the MNPs that ultimately depends on ϕ_m and M_s [45]. The magnetic energy converted in heat lead for the possibility of breaking chemical bonds causes phase changes or, as in this case, increases the permeability of membranes due to the increase in the system’s temperature [43–45].

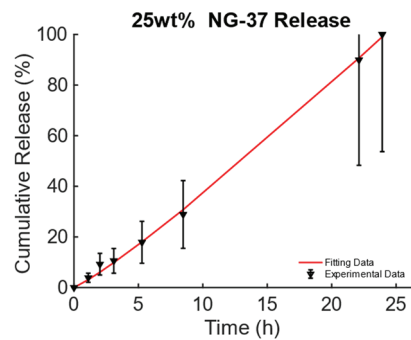


Figure 4. Cumulative release from magnetic poly(N-isopropylacrylamide) embedding 25% wt. of Fe₃O₄ MNPs triggered by magneto-thermal conversion using a dynamic MF.

Table 6. Comparison of fitting quality for the Gompertz and KP models for alginate SPIO scaffolds and associated derived coefficients.

Gompertz Model		KPM	
R^2	RMSE	R^2	RMSE
0.9532	0.0925	0.9985	0.0163
α	β	k_{KP} (1/h)	n
118.9692	-2.2373	0.0277	1.1266

With this knowledge, the release from the MBG-PCL 3D-printed scaffolds loaded with Fe_3O_4 MNPs under dynamic MF exposure could be better interpreted [46]. Indeed, the magneto-thermal conversion triggers a high DOX release useful for CT applications. In [46], (see Figure 5, pag. 7950 from [46]), the experimentally measured curves of drug release over time present a general sigmoidal trend, as shown in Figure 5. In [46], different MagS compositions have been tested, so information about how ϕ_m and M_s relate to kinetic parameters can be modeled for the first time. In Figure 5a, the data and the results from the fitting are shown. The best model fitting the release data for the bare MBG/PCL and the magnetic MBG/PCL scaffolds is the Gompertz model, as can be inferred from Table 7. By observing the retrieved coefficients for the Gompertz model (Table 8), a pattern can be identified. It can be noticed that a nonlinear relationship between the percentage of released drug at the final time ($t = 250$ h) and M_s can be identified (Figure 5b). It must be reported that the increase in the volumetric content of MNPs in the biomaterials leads to a slight modification of and increase in MagS porosity [41–53]. However, despite the porosity changes, we hypothesize that the differences in the DD mechanism are mediated by the interactions between the MF and the MagS. In other words, we assume that the released value is therefore a function of MagS features, considering that the MF parameters were fixed [49]. Therefore, α and β parameters, representing, respectively, the undissolved proportion and the dissolution rate, must be linked to MagS saturation magnetization. As it can be observed in Figure 5c, the α parameter is characterized by an approximately constant trend for all MagS compositions, hence being independent from the fraction of MNPs contained in the biomaterial (ϕ_m). On the other hand, observing β in Figure 5c, it is possible to infer that the dissolution rate depends on M_s in a linear way ($\beta = -0.015 \cdot M_s - 0.38$, $R^2 = 0.97$).

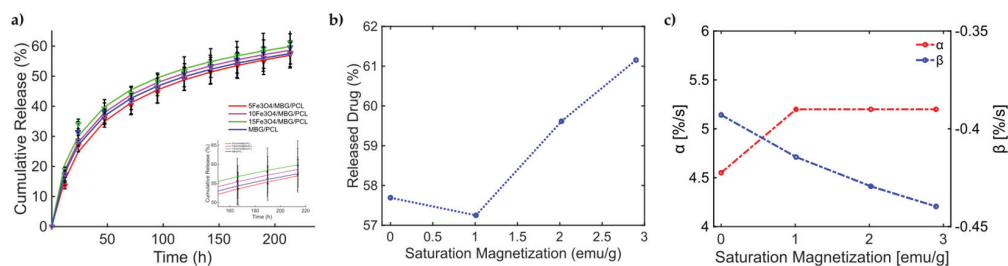


Figure 5. (a) Cumulative release from different MBG/PCL scaffolds with loadings from 5% to 15% of Fe_3O_4 MNPs [51]. (b) Released drug as a function of MagS saturation magnetization. (c) Variation in the undissolved proportion and the dissolution rate as a function of MagS saturation magnetization.

These findings represent a relevant quantitative result of this work, as they allow us to understand how, through the MF-MagS interaction, the release kinetics can greatly improve. Moreover, the finding poses an interesting challenge to material science, i.e., the investigation of mathematical and physical phenomena that rule the interaction between MagSs and MFs. To further support the conclusions reported in the above discussion, another mesoporous calcium–iron-based MagS was studied in [50].

Table 7. Comparison of fitting quality for the Gompertz and KP models for Fe₃O₄ MBG/PCL scaffolds.

	Gompertz Model		KPM	
	R ²	RMSE	R ²	RMSE
MBG/PCL	0.9986	0.0072	0.981	0.0265
5Fe ₃ O ₄ /MBG/PCL	0.9967	0.0112	0.9824	0.0257
10Fe ₃ O ₄ /MBG/PCL	0.9904	0.0183	0.9869	0.0225
15Fe ₃ O ₄ /MBG/PCL	0.9986	0.0273	0.9868	0.0228

Table 8. Fitting coefficients for the two models for the drug release for Fe₃O₄ MBG/PCL scaffolds.

	Gompertz Model		KPM	
	α	β	k _{KP} (1/h)	n
MBG/PCL	4.551	−0.3929	0.0824	0.3709
5Fe ₃ O ₄ /MBG/PCL	5.1993	−0.4144	0.0769	0.3804
10Fe ₃ O ₄ /MBG/PCL	5.1993	−0.4294	0.0946	0.3474
15Fe ₃ O ₄ /MBG/PCL	5.1993	−0.4397	0.1079	0.3263

This chemically doped MagS releases gentamicin under the action of 1.47 kA/m, 232 kHz MF [50]. The release curves from Figure 11, pag. 1287 ref. [50] are reported in Figure 6a. It is possible to observe that the MagS can release ~10% more drugs after 40–60 h than its nonmagnetic counterpart. From Table 9, it can be seen that both the modified Gompertz model (Equation (1)) and the KPM are suited to model kinetics. The release constant for the two cases has a 6% difference, and the transport process is diffusion-dominated ($n \leq 0.45$), leading to similar undissolved proportions across the two cases, whilst a 13% difference in the value of the dissolution rate coefficient is obtained, as shown in Figure 6b.

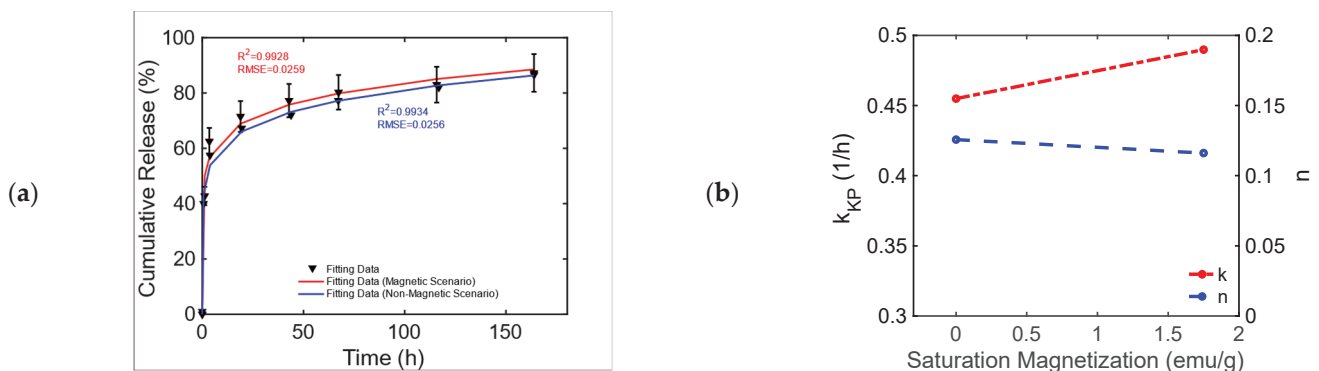


Figure 6. (a) Cumulative release from a bare and an iron-doped mesoporous bioglass triggered by an RF MF [50]. (b) Variation in the KPM parameters as a function of MagS saturation magnetization.

Finally, we focused on the investigation of a relevant case in which MagSs allowed drug transport by an external MF for triggering and controlling the release of very different drugs and biomolecules. In [49], nanoporous ferrogels were loaded with agents of three very different molecular weights and of diverse types [51] (see Figure 3, pag. 69 in [51]). Thus, the controlled release, mediated by the MF, has been evaluated, even under different drug functions or bioactive agent loadings. As first, the release of mitoxantrone for therapeutic purposes was performed in the presence and absence of MFs (Figure 7a). It can be noticed that, in the magnetic scenario, an increased release of ~40% is observed. The Gompertz model is the best fit (see Table 10). A faster release kinetic and dissolution

rate (~3 time) are observed, as well as a modification of the release mechanism (i.e., from non-Fickian to super transport) for the two cases can be noticed (see Table 11). Then, the releases of plasmid DNA condensed with polyethylene diamine (with a molecular weight of ~106) and chemokine SDF-1 α (with a molecular weight of ~8000) [51] from the MagS were modeled. It must be noticed that, in this case, the stimulation has been changed from 2 h intervals to 30 min, with magnetic stimulation achieved through 120 on/off cycles lasting 2 min, so that the highly macroporous structure was reversibly deformed, with subsequent release [51]. According to Figure 7b,c and the results from Table 10, the Gompertz equation faithfully simulates the envelope of the release kinetics of the loaded drug and of the other agents, with a high molecular weight. It is worth noting that the release of the chemokine is not sufficient and relatively low values are reached (Figure 7b). However, by relying on the findings shown in Figure 7c, considering the perspective of using MagSs as platforms for TE and CT, an ~8% release of plasmid DNA, in several hundreds of minutes, can be achieved from the MagSs using the external MF. The limited DNA release falls under a non-Fick mechanism that deserves further study, but could be optimized by relying on MagS properties and external MF parameters.

Table 9. Fitting results for the bare and iron-doped mesoporous bioglasses triggered by an RF MF.

	Gompertz Model		KPM	
	R^2	RMSE	R^2	RMSE
15Ca	0.9934	0.0256	0.983	0.041
10Fe5Ca	0.9928	0.0259	0.995	0.0216
	α	β	k_{KP} (1/h)	n
15Ca	0.8318	-0.3276	0.4898	0.1161
10Fe5Ca	0.8313	-0.2834	0.4549	0.1257

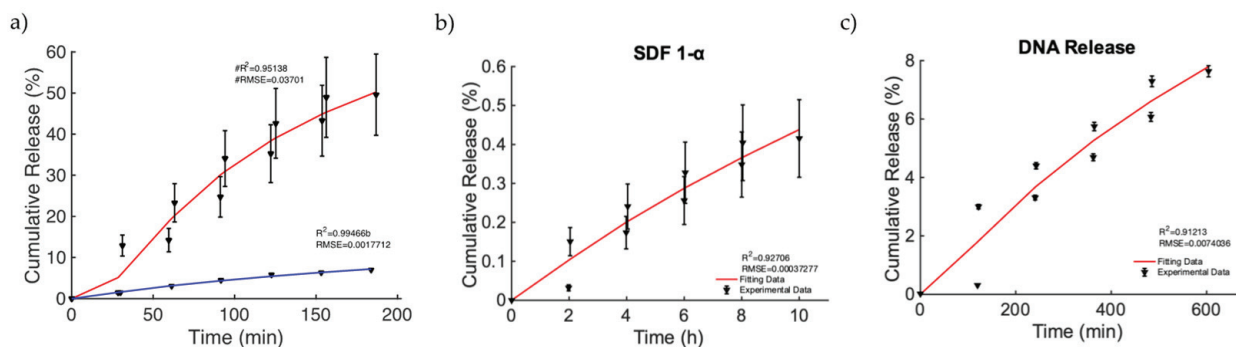


Figure 7. (a) Release of mitoxantrone for the non-magnetic (blue curve) and magnetic scenarios (red curve). (b) Release of chemokine SDF-1 α from a ferrogel MagS. (c) Release of DNA material over time from the MagS.

For the sake of clarity, in Table 12, we provide a complete summary of the best models fitting the drug release data from works [41,43,44,46,49–51]. It can be observed that, generally, the KPM is the most suitable theoretical framework to interpret drug release from MagSs, either for a DD triggered by static or alternate magnetic fields. We can further notice that the MagS composition and manufacturing approach cannot be easily related to drug delivery performances and to the best model; therefore, future studies to elucidate this point are needed.

Table 10. Comparison of fitting quality for the Gompertz and KP models for the active alginate MagS tested for the release of mitoxantrone, peptide, and DNA.

	Gompertz Model		KPM	
	R^2	RMSE	R^2	RMSE
Mitoxantrone (non-magnetic)	0.9944	0.0022	0.9882	0.0031
Mitoxantrone (magnetic)	0.9515	0.0405	0.9392	0.0454
SDF 1- α	0.927	0.0004	0.9101	0.0005
DNA	0.9121	0.0083	0.9066	0.0085

Table 11. Fitting coefficients for the Gompertz and KP models for the active alginate MagS tested for the release of mitoxantrone, peptide, and DNA.

	Gompertz Model		KPM	
	α	β	k_{KP}	n
Mitoxantrone (non-magnetic)	9.6482	-0.2491	0.0013 1/min	0.7664
Mitoxantrone (magnetic)	40.1393	-0.7774	0.0043 1/min	0.9231
SDF 1- α	7.6068	-0.1464	0.0008 1/h	0.7305
DNA	15.4473	0.2812	0.0003 1/min	0.8578

Table 12. Summary of the best model fitting the drug release data.

Ref.	[41]	[42]	[43,44]	[46]	[50]	[51]
Best model	KPM	Gompertz	KPM	Gompertz	Gompertz	Gompertz

5. Conclusions

This work dealt with the modeling of magnetic scaffolds that are magneto-responsive devices originating from the combination of traditional biomaterials and magnetic nanoparticles. MagSs can be used as platforms for magnetically triggered and controlled drug release for tissue engineering and cancer therapy. Therefore, static or dynamic external magnetic stimuli can be used to remotely control tissue repair or activate the release of drugs for tumor treatment. After having carefully analyzed the literature, we have identified that, despite several kinds of MagSs being manufactured, characterized, and tested, there is no quantitative framework to understand, interpret, or design magnetically triggered drug release. Furthermore, since most MagSs suffer from a local inhomogeneous distribution of drug concentration and burst release, models for their optimization are needed. By relying on experimental data from the literature, in this work, we proposed a modeling framework and a quantitative interpretation of different magnetic scaffolds. We found that, generally, the Gompertz model can better fit the drug release data, with a low error ($RMSE < 0.01$, $R^2 > 0.9$), for MagSs triggered by static or dynamic magnetic fields. We found that the intrinsic magnetic properties of MagSs are key features for selecting the most suited and effective drug release mechanism, as well as to tune the kinetics of release. It was observed that the undissolved proportion and the dissolution rate decrease as MagS saturation magnetization increases, whilst the time constant decreases. These findings can be useful to material scientists to design innovative MagSs for DD.

This work has the potential to be the quantitative basis for subsequent studies that aim at clarifying the physical phenomena and mechanisms underlying the interaction between magnetic fields and MagSs that determine the release of drugs or biomolecules for tissue engineering and/or cancer therapy. The proposed model can serve as a basis to design and plan experimental studies to further elucidate the mechanisms of DD mediated by MagSs. Therefore, future works must deal with the manufacturing, characterization, experimental tests, and modeling of MagSs for DD applications.

Author Contributions: Conceptualization, M.B.L.; methodology, all authors; software, E.M.A.C. and M.B.L.; validation, E.M.A.C. and M.B.L.; resources, F.D., A.F. and G.M.; data curation, E.M.A.C. and M.B.L.; writing—original draft preparation, E.M.A.C. and M.B.L.; writing—review and editing, all authors; visualization, E.M.A.C., M.B.L. and F.D.; supervision, M.B.L., F.D., A.F. and G.M. All authors have read and agreed to the published version of the manuscript.

Funding: The research leading to these results has received funding from the European Union–NextGenerationEU through the Italian Ministry of University and Research under PNRR–M4C2–I1.3 Project PE_00000019 “HEALITALIA” to Matteo Bruno Lodi and Alessandro Fanti, CUP F53C22000750006 University of Cagliari. The views and opinions expressed are those of the authors only and do not necessarily reflect those of the European Union or the European Commission. Neither the European Union nor the European Commission can be held responsible for them. This work was partially supported by the “Microwave Theranostics enhanced by Magnetic Scaffolds in the follow up of bone healing (MiTheMaS)” (CUP: F53D23000650001) project, funded by Bando PRIN 2022—Piano Nazionale di Ripresa e Resilienza a titolarità del Ministero dell’Università e della Ricerca, la misura M4C2–Investimento 1.1 “Fondo per il Programma Nazionale Ricerca (PNR) e progetti di Ricerca di Rilevante Interesse Nazionale (PRIN)”.

Institutional Review Board Statement: Not applicable.

Informed Consent Statement: Not applicable.

Data Availability Statement: Data will be available upon request.

Acknowledgments: The authors would like to sincerely thank Enrico Mattana for the valuable suggestions that helped to improve the quality of this manuscript.

Conflicts of Interest: The authors do not have any conflicts of interest to declare.

List of Abbreviations

Alternate Current	AC
Bovine Serum Albumin	BSA
Cancer Therapeutics	CTs
Drug Delivery	DD
Docetaxel	DTX
Doxorubicin	DOX
Electromagnetics	EMs
Graphene Acid–Gambogic Acid Polymer	GO-GA
Growth Factors	GFs
Hydroxyapatite	Hap
Korsemyer–Peppas	KP
Magnetic Fields	MFs
Magnetic Nanoparticles	MNPs
Magnetic Scaffolds	MagSs
Mesoporous Bioglass	MBG
Pulsed Electromagnetic Fields	PEMFs
Poly(Caprolactone)	PCL
Poly(Lactic Acid)	PLA
Poly(Lactic-co-Glycolic Acid)	PLGA
Poly(n-isopropyl Acrylamide)	polyNIPAm
Root Mean Square Error	RMSE
Superparamagnetic Iron Oxide Nanoparticles	SPIONs
Superparamagnetic	SPM
Tissue Engineering	TE
Tumor Microenvironment	TME

References

1. Gu, L.; Mooney, D.J. Biomaterials and emerging anticancer therapeutics: Engineering the microenvironment. *Nat. Rev. Cancer* **2016**, *16*, 56–66. [CrossRef] [PubMed]
2. Li, X.; Su, X. Multifunctional smart hydrogels: Potential in tissue engineering and cancer therapy. *J. Mater. Chem. B* **2018**, *6*, 4714–4730. [CrossRef] [PubMed]

3. de Sousa Victor, R.; Marcelo da Cunha Santos, A.; Viana de Sousa, B.; de Araújo Neves, G.; Navarro de Lima Santana, L.; Rodrigues Menezes, R. A review on Chitosan's uses as biomaterial: Tissue engineering, drug delivery systems and cancer treatment. *Materials* **2020**, *13*, 4995. [CrossRef] [PubMed]
4. Nour, S.; Baheiraei, N.; Imani, R.; Rabiee, N.; Khodaei, M.; Alizadeh, A.; Moazzeni, S.M. Bioactive materials: A comprehensive review on interactions with biological microenvironment based on the immune response. *J. Bionic Eng.* **2019**, *16*, 563–581. [CrossRef]
5. Roach, P.; Eglin, D.; Rohde, K.; Perry, C.C. Modern biomaterials: A review—Bulk properties and implications of surface modifications. *J. Mater. Sci. Mater. Med.* **2007**, *18*, 1263–1277. [CrossRef] [PubMed]
6. Kim, B.S.; Yang, S.S.; Lee, J. A polycaprolactone/cuttlefish bone-derived hydroxyapatite composite porous scaffold for bone tissue engineering. *J. Biomed. Mater. Res. Part B Appl. Biomater.* **2014**, *102*, 943–951. [CrossRef] [PubMed]
7. Winkler, T.; Sass, F.A.; Duda, G.N.; Schmidt-Bleek, K. A review of biomaterials in bone defect healing, remaining shortcomings and future opportunities for bone tissue engineering: The unsolved challenge. *Bone Jt. Res.* **2018**, *7*, 232–243. [CrossRef] [PubMed]
8. Williams, D.F. Challenges with the development of biomaterials for sustainable tissue engineering. *Front. Bioeng. Biotechnol.* **2019**, *7*, 127. [CrossRef] [PubMed]
9. Wang, L.; Guo, X.; Chen, J.; Zhen, Z.; Cao, B.; Wan, W.; Dou, Y.; Pan, H.; Xu, F.; Zhang, Z.; et al. Key considerations on the development of biodegradable biomaterials for clinical translation of medical devices: With cartilage repair products as an example. *Bioact. Mater.* **2022**, *9*, 332–342. [CrossRef] [PubMed]
10. Rambhia, K.J.; Ma, P.X. Controlled drug release for tissue engineering. *J. Control. Release* **2015**, *219*, 119–128. [CrossRef] [PubMed]
11. Mansour, A.; Romani, M.; Acharya, A.B.; Rahman, B.; Verron, E.; Badran, Z. Drug delivery systems in regenerative medicine: An updated review. *Pharmaceutics* **2023**, *15*, 695. [CrossRef] [PubMed]
12. Whitaker, M.J.; Quirk, R.A.; Howdle, S.M.; Shakesheff, K.M. Growth factor release from tissue engineering scaffolds. *J. Pharm. Pharmacol.* **2001**, *53*, 1427–1437. [CrossRef] [PubMed]
13. Yang, Y.; Zeng, W.; Huang, P.; Zeng, X.; Mei, L. Smart materials for drug delivery and cancer therapy. *View* **2021**, *2*, 20200042. [CrossRef]
14. Paltanea, G.; Manescu, V.; Antoniac, I.; Antoniac, A.; Nemoianu, I.V.; Robu, A.; Dura, H. A review of biomimetic and biodegradable magnetic scaffolds for bone tissue engineering and oncology. *Int. J. Mol. Sci.* **2023**, *24*, 4312. [CrossRef] [PubMed]
15. Calori, I.R.; Braga, G.; de Jesus, P.D.C.C.; Bi, H.; Tedesco, A.C. Polymer scaffolds as drug delivery systems. *Eur. Polym. J.* **2020**, *129*, 109621. [CrossRef]
16. Fenton, O.S.; Olafson, K.N.; Pillai, P.S.; Mitchell, M.J.; Langer, R. Advances in biomaterials for drug delivery. *Adv. Mater.* **2018**, *30*, 1705328. [CrossRef] [PubMed]
17. Adepu, S.; Ramakrishna, S. Controlled drug delivery systems: Current status and future directions. *Molecules* **2021**, *26*, 5905. [CrossRef] [PubMed]
18. Castellanos, I.M.S.; Balteanu, B.; Singh, T.; Zderic, V. Therapeutic modulation of calcium dynamics using ultrasound and other energy-based techniques. *IEEE Rev. Biomed. Eng.* **2016**, *9*, 177–191. [CrossRef] [PubMed]
19. Municoy, S.; Alvarez Echazu, M.I.; Antezana, P.E.; Galdopórpóra, J.M.; Olivetti, C.; Mebert, A.M.; Foglia, M.L.; Tuttolomondo, M.V.; Alvarez, G.S.; Hardy, J.G.; et al. Stimuli-responsive materials for tissue engineering and drug delivery. *Int. J. Mol. Sci.* **2020**, *21*, 4724. [CrossRef] [PubMed]
20. Bai, G.; Yuan, P.; Cai, B.; Qiu, X.; Jin, R.; Liu, S.; Li, Y.; Chen, X. Stimuli-responsive scaffold for breast cancer treatment combining accurate photothermal therapy and adipose tissue regeneration. *Adv. Funct. Mater.* **2019**, *29*, 1904401. [CrossRef]
21. Lakshmanan, S.; Gupta, G.K.; Avci, P.; Chandran, R.; Sadasivam, M.; Jorge, A.E.S.; Hamblin, M.R. Physical energy for drug delivery; poration, concentration and activation. *Adv. Drug Deliv. Rev.* **2014**, *71*, 98–114. [CrossRef] [PubMed]
22. Cicuéndez, M.; Doadrio, J.C.; Hernández, A.; Portolés, M.T.; Izquierdo-Barba, I.; Vallet-Regí, M. Multifunctional pH sensitive 3D scaffolds for treatment and prevention of bone infection. *Acta Biomater.* **2018**, *65*, 450–461. [CrossRef] [PubMed]
23. McCoy, C.P.; Brady, C.; Cowley, J.F.; McGlinchey, S.M.; McGoldrick, N.; Kinnear, D.J.; Andrews, G.P.; Jones, D.S. Triggered drug delivery from biomaterials. *Expert Opin. Drug Deliv.* **2016**, *7*, 605–616. [CrossRef] [PubMed]
24. Shah, A.; Malik, M.S.; Khan, G.S.; Nosheen, E.; Iftikhar, F.J.; Khan, F.A.; Shukla, S.S.; Akhter, M.S.; Kraatz, H.B.; Aminabhavi, T.M. Stimuli-responsive peptide-based biomaterials as drug delivery systems. *Chem. Eng. J.* **2018**, *353*, 559–583. [CrossRef]
25. Badeau, B.A.; DeForest, C.A. Programming stimuli-responsive behavior into biomaterials. *Annu. Rev. Biomed. Eng.* **2019**, *21*, 241–265. [CrossRef] [PubMed]
26. Moncion, A.; Lin, M.; Kripfgans, O.D.; Franceschi, R.T.; Putnam, A.J.; Fabiilli, M.L. Sequential payload release from acoustically-responsive scaffolds using focused ultrasound. *Ultrasound Med. Biol.* **2018**, *44*, 2323–2335. [CrossRef] [PubMed]
27. Wang, P.; Sun, J.; Lou, Z.; Fan, F.; Hu, K.; Sun, Y.; Gu, N. Assembly-Induced Thermogenesis of Gold Nanoparticles in the Presence of Alternating Magnetic Field for Controllable Drug Release of Hydrogel. *Adv. Mater.* **2016**, *28*, 10801–10808. [CrossRef] [PubMed]
28. Nardoni, M.; Della Valle, E.; Liberti, M.; Relucanti, M.; Casadei, M.A.; Paolicelli, P.; Apollonio, F.; Petralito, S. Can pulsed electromagnetic fields trigger on-demand drug release from high-tm magnetoliposomes? *Nanomaterials* **2018**, *8*, 196. [CrossRef]
29. Mirvakili, S.M.; Langer, R. Wireless on-demand drug delivery. *Nat. Electron.* **2021**, *4*, 464–477. [CrossRef]
30. Behrens, S. Preparation of functional magnetic nanocomposites and hybrid materials: Recent progress and future directions. *Nanoscale* **2011**, *3*, 877–892. [CrossRef]

31. Farzin, A.; Fathi, M.; Emadi, R. Multifunctional magnetic nanostructured hardystonite scaffold for hyperthermia, drug delivery and tissue engineering applications. *Mater. Sci. Eng. C* **2017**, *70*, 21–31. [CrossRef] [PubMed]
32. Liu, X.L.; Chen, S.; Zhang, H.; Zhou, J.; Fan, H.M.; Liang, X.J. Magnetic nanomaterials for advanced regenerative medicine: The promise and challenges. *Adv. Mater.* **2019**, *31*, 1804922. [CrossRef] [PubMed]
33. Miola, M.; Pakzad, Y.; Banijamali, S.; Kargozar, S.; Vitale-Brovarone, C.; Yazdanpanah, A.; Bretcanu, O.; Ramedani, A.; Vernè, E.; Mozafari, M. Glass-ceramics for cancer treatment: So close, or yet so far? *Acta Biomater.* **2019**, *83*, 55–70. [CrossRef] [PubMed]
34. Cardoso, V.F.; Francesko, A.; Ribeiro, C.; Bañobre-López, M.; Martins, P.; Lanceros-Mendez, S. Advances in magnetic nanoparticles for biomedical applications. *Adv. Healthc. Mater.* **2018**, *7*, 1700845. [CrossRef] [PubMed]
35. Singh, A.; Kumar, P.; Pathak, S.; Jain, K.; Garg, P.; Pant, M.; Mahapatro, A.K.; Rath, D.; Wang, L.; Kim, S.K.; et al. A threefold increase in SAR performance for magnetic hyperthermia by compositional tuning in zinc-substituted iron oxide superparamagnetic nanoparticles with superior biocompatibility. *J. Alloys Compd.* **2023**, *968*, 171868. [CrossRef]
36. Singh, A.; Kumar, P.; Pathak, S.; Jain, K.; Garg, P.; Pant, M.; Mahapatro, A.K.; Singh, R.K.; Rajput, P.; Kim, S.K.; et al. Tailored nanoparticles for magnetic hyperthermia: Highly stable aqueous dispersion of Mn-substituted magnetite superparamagnetic nanoparticles by double surfactant coating for improved heating efficiency. *J. Alloys Compd.* **2024**, *976*, 172999. [CrossRef]
37. Lodi, M.B.; Curreli, N.; Zappia, S.; Pilia, L.; Casula, M.F.; Fiorito, S.; Catapano, I.; Desogus, F.; Pellegrino, T.; Kriegel, I.; et al. Influence of magnetic scaffold loading patterns on their hyperthermic potential against bone tumors. *IEEE Trans. Biomed. Eng.* **2021**, *69*, 2029–2040. [CrossRef] [PubMed]
38. Zeng, X.B.; Hu, H.; Xie, L.Q.; Lan, F.; Jiang, W.; Wu, Y.; Gu, Z.W. Magnetic responsive hydroxyapatite composite scaffolds construction for bone defect repair. *Int. J. Nanomed.* **2012**, *7*, 3365–3378. [CrossRef] [PubMed]
39. Sapir, Y.; Polyak, B.; Cohen, S. Cardiac tissue engineering in magnetically actuated scaffolds. *Nanotechnology* **2013**, *25*, 014009. [CrossRef] [PubMed]
40. Bakhtiary, N.; Pezeshki-Modaress, M.; Najmoddin, N. Wet-electrospinning of nanofibrous magnetic composite 3-D scaffolds for enhanced stem cells neural differentiation. *Chem. Eng. Sci.* **2022**, *264*, 118144. [CrossRef]
41. Shademani, A.; Zhang, H.; Jackson, J.K.; Chiao, M. Active regulation of on-demand drug delivery by magnetically triggerable microspouters. *Adv. Funct. Mater.* **2017**, *27*, 1604558. [CrossRef]
42. Wang, Z.; Liu, C.; Chen, B.; Luo, Y. Magnetically-driven drug and cell on demand release system using 3D printed alginate based hollow fiber scaffolds. *Int. J. Biol. Macromol.* **2021**, *168*, 38–45. [CrossRef] [PubMed]
43. Hoare, T.; Santamaria, J.; Goya, G.F.; Irusta, S.; Lin, D.; Lau, S.; Padera, R.; Langer, R.; Kohane, D.S. A magnetically triggered composite membrane for on-demand drug delivery. *Nano Lett.* **2009**, *9*, 3651. [CrossRef]
44. Hoare, T.; Timko, B.P.; Santamaria, J.; Goya, G.F.; Irusta, S.; Lau, S.; Stefanescu, C.F.; Lin, D.; Langer, R.; Kohane, D.S. Magnetically Triggered Nanocomposite Membranes: A Versatile Platform for Triggered Drug Release. *Nano Lett.* **2011**, *11*, 1395. [CrossRef] [PubMed]
45. Lodi, M.B.; Fanti, A.; Vargiu, A.; Bozzi, M.; Mazzarella, G. A multiphysics model for bone repair using magnetic scaffolds for targeted drug delivery. *IEEE J. Multiscale Multiphysics Comput. Tech.* **2021**, *6*, 201–213. [CrossRef]
46. Zhang, J.; Zhao, S.; Zhu, M.; Zhu, Y.; Zhang, Y.; Liu, Z.; Zhang, C. 3D-printed magnetic Fe₃O₄/MBG/PCL composite scaffolds with multifunctionality of bone regeneration, local anticancer drug delivery and hyperthermia. *J. Mater. Chem. B* **2014**, *2*, 7583–7595. [CrossRef]
47. Samal, S.K.; Goranov, V.; Dash, M.; Russo, A.; Shelyakova, T.; Graziosi, P.; Lungaro, L.; Riminucci, A.; Uhlarz, M.; Banobre-Lopez, M.; et al. Multilayered magnetic gelatin membrane scaffolds. *ACS Appl. Mater. Interfaces* **2015**, *7*, 23098–23109. [CrossRef] [PubMed]
48. Iafisco, M.; Drouet, C.; Adamiano, A.; Pascaud, P.; Montesi, M.; Panseri, S.; Sarda, S.; Tampieri, A. Superparamagnetic iron-doped nanocrystalline apatite as a delivery system for doxorubicin. *J. Mater. Chem. B* **2016**, *4*, 57–70. [CrossRef] [PubMed]
49. Oliveira, T.M.; Berti, F.C.; Gasoto, S.C.; Schneider, B., Jr.; Stimamiglio, M.A.; Berti, L.F. Calcium phosphate-based bioceramics in the treatment of osteosarcoma: Drug delivery composites and magnetic hyperthermia agents. *Front. Med. Technol.* **2021**, *3*, 700266. [CrossRef] [PubMed]
50. Zhu, Y.; Shang, F.; Li, B.; Dong, Y.; Liu, Y.; Lohe, M.R.; Hanagata, N.; Kaskel, S. Magnetic mesoporous bioactive glass scaffolds: Preparation, physicochemistry and biological properties. *J. Mater. Chem. B* **2013**, *1*, 1279–1288. [CrossRef] [PubMed]
51. Zhao, X.; Kim, J.; Cezar, C.A.; Huebsch, N.; Lee, K.; Bouhadir, K.; Mooney, D.J. Active scaffolds for on-demand drug and cell delivery. *Proc. Natl. Acad. Sci. USA* **2011**, *108*, 67–72. [CrossRef] [PubMed]
52. Vishwakarma, A.; Sinha, N. Additive Manufacturing of Iron Carbide Incorporated Bioactive Glass Scaffolds for Bone Tissue Engineering and Drug Delivery Applications. *ACS Appl. Bio Mater.* **2024**, *7*, 892–908. [CrossRef]
53. Qi, M.; Ma, R.; Pham-Huy, C.; Hu, Y.; He, H.; Xiao, D. Controllable and Versatile Solvothermal Synthesis Strategy of Magnetic Carbon Nanocomposites as a Scaffold for Magnetic Targeted Drug Delivery. *Available at SSRN* **2024**, 4768280. [CrossRef]
54. Katti, P.D.; Katti, S.K. Functionalized magnetic nanosystems for drug delivery applications. *Funct. Magn. Nanosyst. Diagn. Tools Devices* **2024**, 381–412. [CrossRef]
55. Cardellini, J.; Surpi, A.; Muzzi, B.; Pacciani, V.; Innocenti, C.; Sangregorio, C.; Dediu, V.A.; Montis, C.; Berti, D. Magnetic-Plasmonic Nanoscale Liposomes with Tunable Optical and Magnetic Properties for Combined Multimodal Imaging and Drug Delivery. *ACS Appl. Nano Mater.* **2024**, *7*, 3668–3678. [CrossRef]

56. Sulttan, S.; Rohani, S. Controlled drug release of smart magnetic self-assembled micelle, kinetics and transport mechanisms. *J. Pharm. Sci.* **2022**, *111*, 2378–2388. [CrossRef] [PubMed]
57. Shin, B.Y.; Cha, B.G.; Jeong, J.H.; Kim, J. Injectable macroporous ferrogel microbeads with a high structural stability for magnetically actuated drug delivery. *ACS Appl. Mater. Interfaces* **2017**, *9*, 31372–31380. [CrossRef] [PubMed]
58. Rohatgi, A. WebPlotDigitizer User Manual Version 3.4. 2014; pp. 1–18. Available online: <https://apps.automeris.io/wpd4/> (accessed on 5 June 2024).
59. Ramteke, K.H.; Dighe, P.A.; Kharat, A.R.; Patil, S.V. Mathematical models of drug dissolution: A review. *Sch. Acad. J. Pharm.* **2014**, *3*, 388–396.
60. Easton, D.M. Gompertz pharmacokinetic model for drug disposition. *Pharm. Res.* **2002**, *19*, 463–469. [CrossRef] [PubMed]
61. Al Sawaftah, N.; Paul, V.; Awad, N.; Hussein, G.A. Modeling of Anti-Cancer Drug Release Kinetics from Liposomes and Micelles: A Review. *IEEE Trans. NanoBioscience* **2021**, *20*, 565–576. [CrossRef] [PubMed]
62. Askarizadeh, M.; Esfandiari, N.; Honarvar, B.; Sajadian, S.A.; Azdarpour, A. Kinetic modeling to explain the release of medicine from drug delivery systems. *ChemBioEng Rev.* **2023**, *10*, 1006–1049. [CrossRef]
63. Wang, J.; Guo, X. The Gompertz model and its applications in microbial growth and bioproduction kinetics: Past, present and future. *Biotechnol. Adv.* **2024**, *72*, 108335. [CrossRef] [PubMed]
64. Chicco, D.; Warrens, M.J.; Jurman, G. The coefficient of determination R-squared is more informative than SMAPE, MAE, MAPE, MSE and RMSE in regression analysis evaluation. *PeerJ Comput. Sci.* **2021**, *7*, e623. [CrossRef] [PubMed]
65. Mousavi, S.J.; Doweidar, M.H. Numerical modeling of cell differentiation and proliferation in force-induced substrates via encapsulated magnetic nanoparticles. *Comput. Methods Programs Biomed.* **2016**, *130*, 106–117. [CrossRef] [PubMed]
66. Czichy, C.; Kilian, D.; Wang, T.C.; Günther, S.; Lode, A.; Gelinsky, M.; Odenbach, S. CyMAD bioreactor: A cyclic magnetic actuation device for magnetically mediated mechanical stimulation of 3D bioprinted hydrogel scaffolds. *J. Mech. Behav. Biomed. Mater.* **2022**, *131*, 105253. [CrossRef] [PubMed]

Disclaimer/Publisher’s Note: The statements, opinions and data contained in all publications are solely those of the individual author(s) and contributor(s) and not of MDPI and/or the editor(s). MDPI and/or the editor(s) disclaim responsibility for any injury to people or property resulting from any ideas, methods, instructions or products referred to in the content.

Article

Rapid, Point-of-Care Microwave Lysis and Electrochemical Detection of *Clostridioides difficile* Directly from Stool Samples

Lovleen Tina Joshi ^{1,*}, Emmanuel Brousseau ², Trefor Morris ³, Jonathan Lees ², Adrian Porch ² and Les Baillie ⁴

¹ Faculty of Health, University of Plymouth, Plymouth PL4 8AA, UK

² School of Engineering, Cardiff University, Cardiff CF24 3AA, UK; brousseau@cardiff.ac.uk (E.B.); leesj2@cardiff.ac.uk (J.L.); porcha@cardiff.ac.uk (A.P.)

³ Anaerobe Reference Laboratory, Public Health Wales, University Hospital of Wales, Cardiff CF14 4XW, UK; trefor.morris@wales.nhs.uk

⁴ School of Pharmacy & Pharmaceutical Sciences, Cardiff University, Cardiff CF10 3NB, UK; bailliel@cardiff.ac.uk

* Correspondence: tina.joshi@plymouth.ac.uk

Abstract: The rapid detection of the spore form of *Clostridioides difficile* has remained a challenge for clinicians. To address this, we have developed a novel, precise, microwave-enhanced approach for near-spontaneous release of DNA from *C. difficile* spores via a bespoke microwave lysis platform. *C. difficile* spores were microwave-irradiated for 5 s in a pulsed microwave electric field at 2.45 GHz to lyse the spore and bacteria in each sample, which was then added to a screen-printed electrode and electrochemical DNA biosensor assay system to identify presence of the pathogen's two toxin genes. The microwave lysis method released both single-stranded and double-stranded genome DNA from the bacterium at quantifiable concentrations between 0.02 µg/mL to 250 µg/mL allowing for subsequent downstream detection in the biosensor. The electrochemical bench-top system comprises of oligonucleotide probes specific to conserved regions within *tcdA* and *tcdB* toxin genes of *C. difficile* and was able to detect 800 spores of *C. difficile* within 300 µL of unprocessed human stool samples in under 10 min. These results demonstrate the feasibility of using a solid-state power generated, pulsed microwave electric field to lyse and release DNA from human stool infected with *C. difficile* spores. This rapid microwave lysis method enhanced the rapidity of subsequent electrochemical detection in the development of a rapid point-of-care biosensor platform for *C. difficile*.

Keywords: microwaves; lysis; DNA detection; *Clostridioides difficile*; spores; electrochemistry; bio-engineering; point-of-care; biosensors

1. Introduction

Clostridioides difficile is an anaerobic spore-forming pathogen implicated as the primary cause of antibiotic-associated diarrhea, and healthcare-acquired infections (HCAs), globally [1]. Its spores are implicated in long-term survival, biocide, and heat resistance resulting in transmission of the pathogen [2,3]. *C. difficile* Infection (CDI) causes ~29,000 deaths per year in the USA and 8382 deaths per year in Europe, with current data showing an increased incidence of CDI after the COVID-19 pandemic [4,5].

Patients usually acquire CDI when spores are transmitted via the fecal to oral route in healthcare environments, either through direct or indirect contact with contaminated areas or an infected patient [6]. Once spores have been ingested, they germinate into vegetative bacteria in response to bile salts present in the colon, and toxigenic strains secrete two clostridial toxins, Toxin A (TcdA) and Toxin B (TcdB), and a Binary toxin [7]. The production of these toxins can contribute to patient symptoms ranging from diarrhea to pseudomembranous colitis and toxin megacolon [8].

Diagnostic laboratories regularly employ algorithms to detect toxigenic *C. difficile* in symptomatic hospitalized patients. This usually involves rapid immunogenic screening

for the presence of the glutamate dehydrogenase antigen (GDH) on *C. difficile* vegetative bacteria, in conjunction with an enzyme immunoassay (EIA) to detect the presence of TcdA and TcdB [9,10]. These algorithms have yet to be standardized globally; therefore, the performances of differing diagnostic test algorithms are directly compared to the gold standard cell culture neutralization assay (CCTA) in studies, often generating conflicting results and high operation costs [11,12]. While these algorithms improve patient diagnosis, they also increase the time taken to detect the pathogen, meaning results are often not available for hours. After sampling, the specimen must be transported to and tested in the laboratory. Therefore, results from potentially toxigenic samples may be compromised due to the degradation of toxins within the stool sample, affecting the reliability of results [13]. This, coupled with increased evidence of antimicrobial resistance in clinical isolates of the pathogen, highlights the importance of rapidly diagnosing CDI patients to reduce pathogen transmission, and deliver rapid antibiotic therapy. Therefore, a point-of-care (PoC) diagnostic test with a rapid (in under 10 min) result would increase the speed of patient diagnosis and assist in the implementation of infection control procedures.

To address this unmet need, we are developing a simple PoC test capable of operation with minimal training at the patient's bedside or within a doctor's appointment. This aims to support real-time clinical diagnosis of patients with suspected CDI prior to administration of an antibiotic, hence assisting appropriate antibiotic stewardship and prescribing [14]. We have designed a compact lysis platform that uses bespoke targeted microwave irradiation to lyse *C. difficile* spores and bacteria to release DNA which is then detected within an electrochemical biosensor assay platform. Our previous 2014 study [7] used a conventional kitchen microwave oven (operating at 2.45 GHz) to release DNA using a gold "bow tie" lysis slide, with a microwave-accelerated metal-enhanced fluorescence (MAMEF) assay technology for subsequent detection of DNA from *C. difficile* bacteria and spores, which was operated using large table-top laser platforms [7]. While the MAMEF and gold tie microwave method demonstrated high sensitivity and DNA release, neither was suitable for miniaturization or portable diagnostic PoC applications. The bespoke microwave system used in this study leverages solid-state power generation, with pulsed capability and full control over the microwave electric field to support bacterial cell and spore lysis [15].

Microwaves are a type of electromagnetic radiation with free-space wavelengths ranging from 1 m to 1 mm, with the frequency ranging between 300 MHz and 300 GHz, respectively. The microwave frequency employed in this study is centered around 2.45 GHz, which lies within the Industrial Scientific and Medical (ISM) radio band, which is reserved for such purposes [16,17]. Electromagnetic fields at a frequency of 2.45 GHz penetrate aqueous samples up to a few cm deep, and so enable uniform volumetric heating [15,18] in a targeted and highly efficient manner. This is especially so when compared with traditional conductive heating methods, whereby the resulting heating rate is highly dependent on the thermal resistance imposed by the nature of the boundaries between the material components [19].

The use of microwaves in biomedical applications has become more common in recent years, a relevant example being the microwave-accelerated metal-enhanced fluorescence (MAMEF) detection method for DNA [7,20]. The underlying principle of the MAMEF technology is the selective heating of the water molecules via microwave power, while the metallic surface is not heated. This generates a temperature gradient between the cold metal and the warm aqueous surface, facilitating mass transport of DNA to the surface where it is recognized [7,17,20,21]. Microwaves have also been used in a Polymerase Chain Reaction (PCR) microfluidics based-system, where researchers have used a tuned microwave cavity to heat and cool DNA (as usually performed by a thermocycler) to amplify DNA [22].

This study describes the use of a bespoke, single-mode microwave-resonant cavity with solid-state electronics to deliver constant (100% duty cycle) and pulsed microwaves at a range of duty cycles to the sample (Figure 1) [15]. The cavity allows for targeted and directed microwaves at a peak absorbed power of 30 W rms milli-Watts to penetrate the

sample, which in this instance is used to break open bacteria and spores of *C. difficile* to release DNA within 5 s [15]. The electrochemical platform uses previously designed [7] oligonucleotide DNA probes specific to the *tcdA* and *tcdB* genes of toxigenic *C. difficile* to detect its presence within human stool samples. Initially, the microwaved target DNA is captured by an anchor DNA probe linked to biotin that is attached to the surface of the sensor, which is impregnated with streptavidin, via a biotin/streptavidin link. A second reporter DNA probe, which has horse radish peroxidase (HRP) added, generates an electrochemical potential when bound to the three-piece DNA complex, producing a measurable voltametric signal. Herein we describe the rapid detection of *C. difficile* within stool from infected patients within 10 min, using the combined approach of microwave lysis and electrochemical detection. This study examines the utility of using microwave power to release DNA for subsequent detection within an electrochemical DNA biosensor platform in the development of a PoC device.

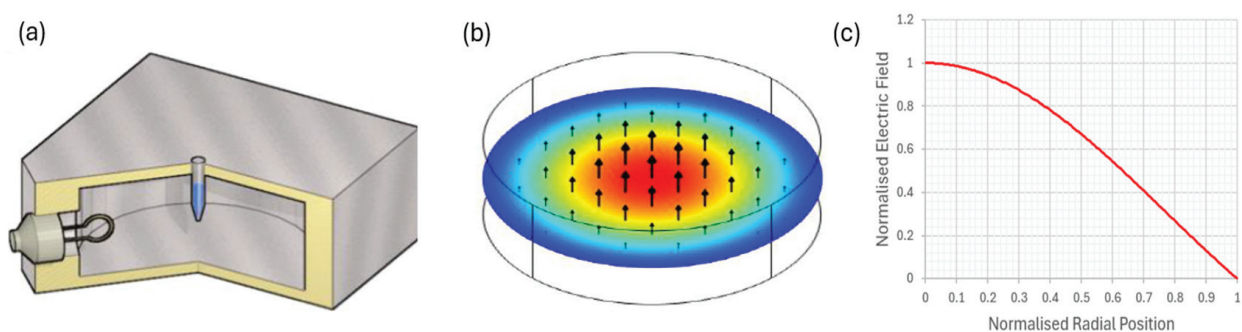


Figure 1. (a) A cylindrical aluminum cavity operating in its TM010 mode, designed to deliver 2.45 GHz of precise microwave radiation to the bacterial sample. An adjustable coupling loop is used to match the cavity to the microwave source to ensure maximum power delivery to the sample. (b) The normalized electric field distribution in the TM010 mode; the sample tube is placed in the region of the high microwave electric field, near the axis of the cavity, with the field parallel to the axis of the tube. (c) The well-known Bessel function form $J_0(2.405x)$ for the radial dependence of electric field magnitude.

2. Materials and Methods

2.1. Bacterial Strains and Growth Conditions

The clinical isolates of *C. difficile* used in this study were toxigenic clinical isolate DS1813 PCR Ribotype (RT) 027 (B1NAP1/027) containing *tcdA* and *tcdB* genes within its genome, and a non-toxigenic DS1684 PCR RT 010 with no toxin genes (or pathogenicity locus) within its genome. Strains were obtained from the National Anaerobic Reference Unit (Cardiff, Wales, UK). Unless otherwise stated, all organisms were stored as spores at 4 °C. Brain heart infusion (BHI) agar and broth (Oxoid Ltd., Basingstoke, UK) supplemented with 0.1% sodium taurocholate was used as a culture medium. The anaerobic incubation methods used were as previously published [3]. Clinical fecal samples submitted to Public Health Wales for diagnostic analysis were cultured on non-selective Fastidious Anaerobic Agar (FAA) and were residual, anonymous, discarded diagnostic material. These did not require ethical approval or consent in the United Kingdom.

2.2. Genomic DNA Extraction from *C. difficile* Using Chelex 100®

Genomic DNA (gDNA) was extracted from *C. difficile* as described previously [23]. Briefly, a single colony of *C. difficile* was harvested from a 24-h anaerobic culture on an FAA plate, and suspended in 5% (*w/v*) solution of Chelex-100 (Bio-Rad, Hemel Hempstead, UK). The solution was boiled for 12 min and cellular debris subsequently removed after centrifugation at $15,000 \times g$ for 10 min. The supernatant contained the gDNA.

2.3. Microwave Apparatus and Exposure Details

The microwave cavity used for the electric field exposure of *C. difficile* was of identical geometry to that reported elsewhere for the electromagnetic characterization of magnetite [24] and nano-diamond samples [25]. Briefly, the cylindrical cavity was machined from aluminum and had an internal diameter of 92 mm and an internal length of 40 mm, designed to have an unperturbed resonant frequency of the TM_{010} mode of 2.50 GHz (reduced to 2.45 GHz on dielectric loading by the sample). These dimensions ensured spectral separation of the TM_{010} mode from competing modes such as TE_{111} (at 4.2 GHz) and maintained a high quality (Q) factor of 8000 when the cavity was empty, both of which ensured maximum transfer of available microwave power. A bacterial sample within a 200 μ L Eppendorf tube (filled with an aqueous sample occupying a volume of 170 μ L) was found to reduce the Q factor to 200. Since the empty plastic Eppendorf tubes were measured in separate cavity experiments to have negligible microwave loss, ~98% of the microwave power delivered to the cavity was dissipated in the sample [18]. Microwaves were inductively coupled to the microwave magnetic field around the perimeter of the cavity via an adjustable coupling loop, made from a short-circuited N connector. This could be both rotated and moved in and out of the cavity to ensure fine control of the impedance matching at resonance. Coupling was adjusted to give a power reflection coefficient at a resonance of < -20 dB, so that at least 99% of the input power was absorbed by the cavity and its sample (about 98% of this absorbed by the sample).

A schematic of the microwave circuitry is shown in Figure 2. The solid-state microwave source (1—(Telemakus TEG27006, Telemakus, LLC, Folsom, CA, USA) provided a single-frequency microwave output at a power of 0 dBm (i.e., 1 mW rms). The RF switch (2—(Telemakus TES6000-30, Telemakus, LLC, Folsom, CA, USA) allowed the microwaves to be pulsed at duty cycles ranging from 0.3% to 100% (here we define a duty cycle to be the % ratio of the time the microwave power is on to the time it is off, as a percentage of the switched waveform cycle). The microwave power amplifier (3—(Mini-circuits ZHL-30W-262, Mini-Circuits, Brooklyn, NY, USA) had a maximum output power of approximately 30 Watts and a gain of approximately 50 dB over the system bandwidth of 2.0 to 2.5 GHz. The combination of the directional coupler (4—(Mini-circuits ZABDC20-322H, Mini-Circuits, Brooklyn, NY, USA) and the two precision power sensors (5—(Telemakus TED6000-50, Telemakus, LLC, Folsom, CA, USA) allowed simultaneous measurements of both the transmitted and reflected microwave powers of incident on and reflected from the sample-loaded cavity, respectively. The wideband power sensor (6—(Rhode & Schwarz NRP-Z81, Rohde & Schwarz USA, Inc., Columbia, MD, USA) had a maximum video bandwidth of 30 MHz and was capable of measuring pulses as small as 50 ns. The sensor was triggered to allow accurate measurement of the reflected power from the microwave pulses applied to the cavity and used to confirm that any change in reflection coefficient during the pulse cycle, due to sample heating, was minimal. All equipment was controlled by National Instruments LabVIEW 2015 software, which provided a user interface and also recorded the power readings from all of the power sensors. The maximum delivered power of 30 W rms gave a maximum local microwave electric field amplitude of approximately 15 kV/m within the sample. For continuous microwave exposure (i.e., at 100% duty cycle), this high electric field gives rise to an initial sample heating rate of over 40 °C/s and in practice, samples were found to boil in around 4 s. To ensure a high electric field yet negligible global sample heating, a low duty cycle of only a few percent was used in practice.

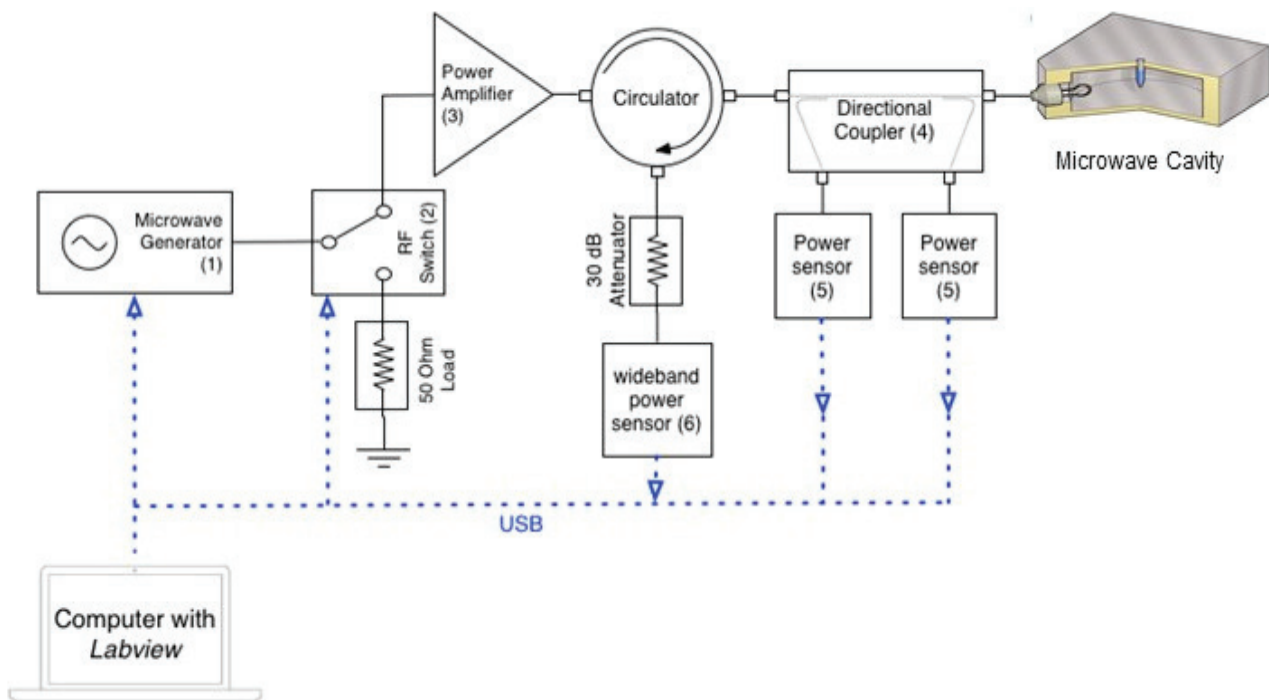


Figure 2. Microwave circuitry. The cavity is excited by a highly adaptable, solid-state microwave power delivery system (up to 30 W) comprising a low power source and high-power amplifier. The power sensors [5] are used to measure the incident and reflected power to ensure that maximum power transfer conditions can be attained. An additional, a wideband power sensor [6] allows the measurement of any reflected power for low duty cycles, during short pulses. The RF switch allows the microwaves to be pulsed at duty cycles ranging from 0.3% to 100% (Table S1).

In this study we utilized continuous microwaves (100% duty cycle), and pulsed microwaves at duty cycles of 1%, 10%, and 100% to examine DNA release from *C. difficile* spores suspended in varying matrices of sterile water and human feces.

The subject of the microwave dosage is a very important one. In Figure 1 we show the theoretical electric field associated with the TM₀₁₀ mode of the cylindrical cavity, normalized so that it takes the dimensionless value of 1 on-axis. This is the usual Bessel function dependence $J_0(x)$ and we placed samples on-axis, parallel to the axis, to maximize the effectiveness of the electric field and to minimize depolarization effects associated with the long, thin Eppendorf tubes. However, this was not the electric field within the sample to which the spores were exposed, which we estimate in magnitude below.

We did not want to boil the sample as this would have denatured the target DNA. At full 30 W continuous microwave power (CW) we estimated a heating rate of 40 °C/s for a sample of 170 µL of deionized water. This was measured by monitoring the reflected power from the cavity. As soon as the sample started to boil the bubbles of steam suddenly changed their effective permittivity and also the input match to the cavity, which introduced sudden and chaotic changes in the reflected power. Boiling occurred after 2.0 s for 30 W CW input power, giving the quoted heating rate based on a laboratory temperature of 20 °C. The sample volume of 170 µL corresponded to a heat capacity of approximately 0.7 J/°C and the dissipated power was then calculated to be approximately 28 W. This was consistent with the cavity and its aqueous sample load being impedance matched to the source, so that almost all the 30 W input power was dissipated as heat within the sample.

The most reliable way of estimating the electric field magnitude E within an aqueous sample within an Eppendorf tube (and hence representative of the absolute field to which the bacteria are exposed) is via an experiment using the power density equation, which

gives the power dissipated (in W) for a sample of volume V of loss factor (i.e., imaginary part of the permittivity ϵ_2 , dimensionless) as

$$P = \pi f \epsilon_2 \epsilon_0 E^2 V$$

Using this and the measured heating rate we estimate that $E \approx 16$ kV/m, assuming the well-known loss factor $\epsilon_2 \approx 10$ for water at 2.45 GHz.

Samples exposed to pulsed microwaves with low duty cycles do not boil but bacteria are still exposed to the 16 kV/m electric field when the microwaves are switched on. Even then we expected local heating, but in these instances, we measured no global increase in temperature of the sample by standard thermometry. Furthermore, an increase in sample temperature would increase the resonant frequency of the cavity and its sample in the TM010 mode, since the real part of the permittivity of water ϵ_1 decreases with increasing temperature; we measured no such change in frequency before and after exposure to pulsed microwaves. DNA release from bacterial spores is likely to be thermally driven, but in our experiments the heat was generated on a very local scale that did not measurably increase the global sample temperature. Each bacterial spore is a very complex structure in terms of its dielectric property, and any dielectric contrast is likely to produce a non-uniform local electric field; this will result in thermal hotspots (since the local heating rate is proportional to the square of the local electric field). We do not further explore the mechanism of DNA release in this paper, other than to note that the application of pulsed microwaves is an effective and rapid means of DNA release for the spores studied here. Its origin is likely to be highly localized heating, which is immeasurable without using a microscopic temperature probe.

2.4. Scanning Electron Microscopy Studies of *C. difficile*

Spores of *C. difficile* were microwaved at a peak power of 30 W rms milli-Watts at a range of microwave duty cycles: 100%, 10%, and 1% and analyzed using Scanning Electron Microscopy (SEM) to determine if morphological changes were present. (Supplementary Information Figure S1 shows SEM results for *C. difficile* spores exposed to duty cycles ranging from 0%, 0.3%, 1%, 3% 10%, 33%, and 100%. Table S1 shows microwave duty cycle information). After microwaving, 20 μ L spores of *C. difficile* strain DS1813 RT027 were inoculated onto a clean microscope slide and heat fixed [3]. Non-microwaved spores were used as a comparative control. Slides were sputter coated with metal using a gold palladium sputtering target (60% Au and 40% Pd from Testbourne Ltd., Basingstoke, UK) and argon as the sputtering gas. Images were taken on a scanning electron microscope (model XB1540 from Carl Zeiss, Jena, Germany) using an accelerating voltage of 5 kV. Forty spores per sample were viewed at magnifications of $\times 82,000$ and $\times 31,000$.

2.5. Measurement of DNA Released from Microwave Irradiated Samples

DNA quantification was performed using the Qubit 3.0 Fluorometer (Life Technologies, Renfrew, UK) as per the manufacturer's instructions before and after microwave exposure at 1%, 10%, and 100% DC. Specifically, we were interested in quantifying single-stranded DNA (ssDNA) release to support subsequent detection in the electrochemical biosensor assay. Each measurement was repeated in triplicate and DNA yields were measured in μ g/mL.

2.6. Electrochemical Nucleic Acid Detection of *tcdA* and *tcdB* Genes within DNA Released from Microwaved *C. difficile* in Water

DNA probes used to detect *tcdA* and *tcdB* genes of toxigenic *C. difficile* are as previously specified [7]. For utilization within the electrochemical DNA biosensor detection system, anchor DNA probes were labelled with biotin at the 5' region and the reporter probes were directly labelled at the 3' end with enzyme HRP. The anchor probe (40 μ M anchor probe) was bound to the surface of the silver-ink printed acetate sensor coated with 80 μ g/mL Streptavidin (Vantix, Cambridge, UK) via a biotin/streptavidin interaction. Subsequently;

50 μL target DNA lysed from *C. difficile* via microwaving was added to the anchor probe and then 40 μM reporter probe was added, forming a three-piece DNA assay complex on the biosensor [26]. The three-piece DNA assay complex (shown in Supplementary Materials Figure S2) was washed with potassium phosphate buffer (pH 7.8) to remove any unbound DNA, and an enzyme substrate was added to generate voltage proportional to the number of copies of the target gene within the sample. The electrochemical signal was generated by horseradish peroxidase (HRP), catalyzing the electro-reduction of hydrogen peroxide in the presence of a hydrogen donor, in this case o-phenylenediamine (OPD), resulting in the transfer of an electron from the sensor to the OPD substrate. Toxigenic strain DS1813 was used as the test strain, and non-toxigenic DS1684 was used as the negative control strain.

2.7. Electrochemical Nucleic Acid Detection of *tcdA* and *tcdB* Genes from Clinical Fecal Specimens

A panel of 50 blinded clinical fecal specimens submitted to Public Health Wales for diagnostic analysis (University Hospital Wales, Cardiff, UK) were tested for the presence of *tcdA* and *tcdB* genes. The blinded samples were previously tested for the presence of glutamate dehydrogenase and toxin A and toxin B using an Enzyme Immunoassay (EIA) with a limit of detection (LoD) of >0.8 ng/mL Toxin A and >2.5 ng/mL for Toxin B (Techlab, London, UK) [27] at the University Hospital of Wales' Public Health laboratories; of these, 10 samples were *C. difficile* negative and the remaining 40 were *C. difficile* positive. For the toxin assay, 50 μL of liquid stool sample was diluted to a volume of 200 μL . Public Health Wales also undertook selective agar culture to check each fecal sample for the presence of *C. difficile*.

To detect the presence of the pathogen in clinical samples using our microwave-enhanced method, 900 μL of loose stool was diluted with 100 μL Phosphate Buffered Saline (PBS) to enhance viscosity and was vortex mixed for 2 min. Then, 170 μL of that sample was microwaved at a peak power of 30 W rms milli-Watts at a duty cycle of 10% DC to release target DNA. Subsequently, 50 μL of the microwaved sample was added to the electrochemical reporter platform for detection purposes. Prior to, and post microwave exposure, the colony-forming counts (cfu) of *C. difficile* were enumerated to determine whether there was a reduction in recoverable *C. difficile* after microwave exposure [3]. Samples were diluted in Fastidious Anaerobic Broth (EO labs, York, UK) and enumeration was performed on Braziers CCEY Agar and incubated for 48 h under anaerobic conditions, as described previously [3].

2.8. Statistical Analysis

Data are expressed as means \pm SEM. Two-sample *t*-tests and One-way ANOVA tests were performed using Minitab 19 (Minitab Inc., State College, PA, USA).

3. Results

3.1. Microwave-Mediated Spore and Vegetative Cell Lysis

While relatively small amounts of mother cell-derived DNA will adhere to the surface of the spore, the majority of target DNA is sequestered within the spore itself. Our microwave-based lysis approach has been developed to break open the spore in a controlled manner to release the internal genomic DNA and increase the sensitivity of this assay. The microwave lysis method will also release gDNA from vegetative cells of *C. difficile* which can be detected downstream in the electrochemical assay. As in Figure 3B, exposure to constant microwaving at a peak power of 30 W rms milli-Watts at 100% DC caused major disruption to the spore structure. The magnitude of this damage increased with the level of microwave exposure (Figures 3A–D and S1, Table S1).

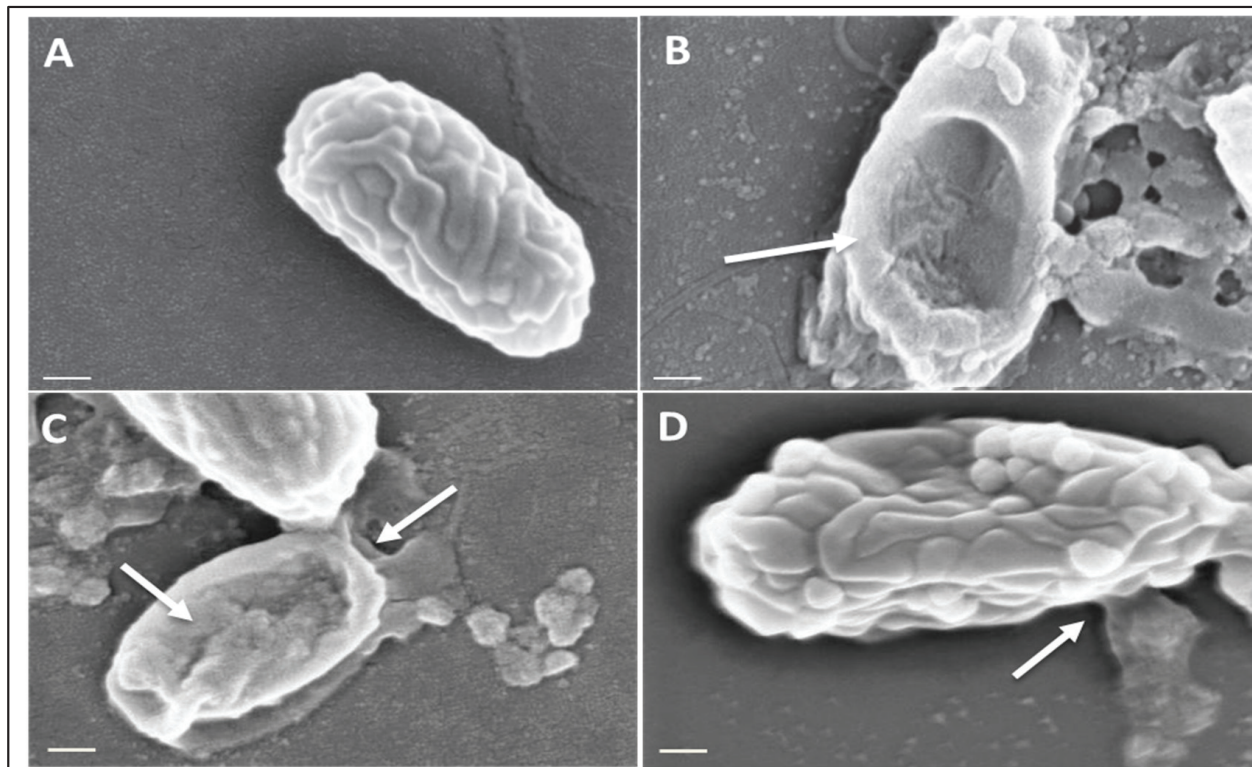


Figure 3. Scanning Electron Microscopy of *C. difficile* spores before and after microwaving. Spores of strain DS1813 were imaged under SEM before and after microwaving at a peak power of 30 W rms milli-Watts at 100%, 10%, and 1% duty cycles (DC) for 5 s. A total of 40 spores per sample were imaged per DC at $\times 82,000$ magnification, with the spores chosen here representative of spores consistently seen within the sample. White arrows indicate areas of lysis and morphological damage. (A) A control spore of DS1813 which was not exposed to microwaves. (B) DS1813 exposed to constant microwaves at 100% DC. Damage to the spore structure and debris is clearly visible on this spore. (C) DS1813 exposed to pulsed microwaves at 10% DC. Some damage to the spore structure is visible at its terminal end. (D) DS1813 exposed to pulsed microwaves at 1% DC. There is no visible damage to the spore structure. (Image scale bar = 200 nm).

3.2. The Release of Target DNA from Microwaved *C. difficile* Spores

In addition to characterizing the effect of microwave exposure on the physical structure of the spores, the effect of different microwave duty cycles on the release of double-stranded (ds) and single-stranded (ss) DNA was determined (Figure 4A,B). Quantification of ssDNA was particularly important as it is this form of DNA which is recognized by our pathogen-specific oligonucleotide DNA probes. Prior to microwave exposure we observed differences in the concentration of ss and ds DNA, with the single-stranded variant being the most concentrated. When the ratio of single- to double-stranded DNA was examined, the biggest relative difference was seen for DS1684 spores (ss/ds ratio 11,806) compared to DS1813 spores (3400) suggesting that DS1684 spores may carry more surface-associated extracellular DNA [26].

The quantity of ssDNA and dsDNA released from each spore type varied depending on the microwave duty cycle and level of microwave exposure. Treatment of DS1813 spores with pulsed microwave powers of 1% duty cycle (DC) and 10% DC resulted in a significant decrease in the concentration of ssDNA by 58% (Figure 2A; two-sample *t* test; $p = 0.017$) and 76% (two-sample *t* test; $p = 0.013$), respectively, when compared to spores prior to microwave exposure. In contrast, upon exposure to 100% DC, the concentration of ssDNA significantly increased by 59% (two-sample *t* test; $p = 0.007$) when also compared to control spores which were not exposed to microwaves. A one-way ANOVA established that there was a highly significant difference between the concentrations of ssDNA released when

spores were treated with varying microwave exposures for DS1813 ($p = 0.000$), and DS1684 ($p = 0.035$).

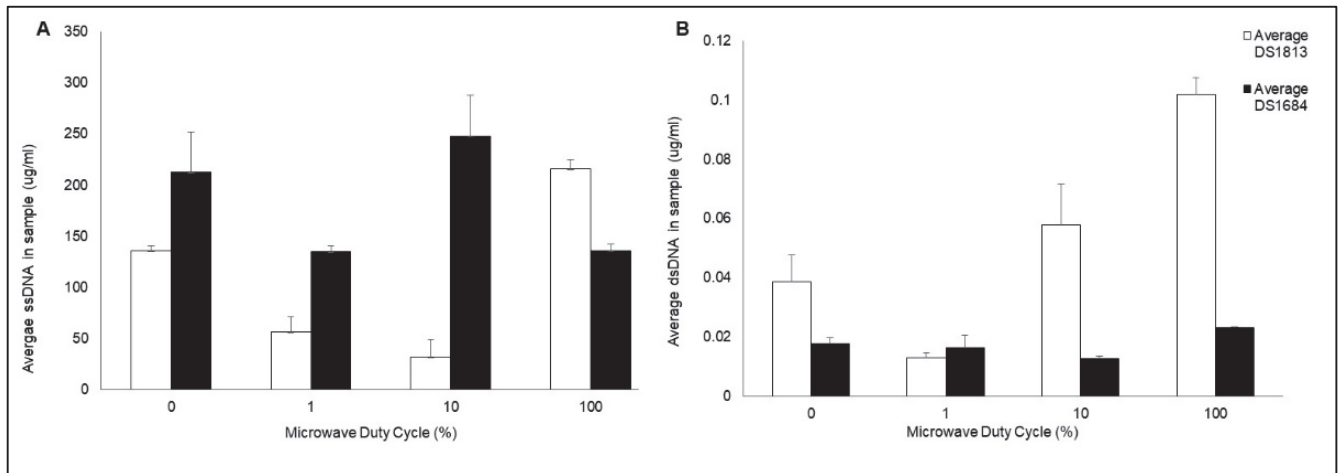


Figure 4. Quantification of double and single-stranded DNA released from microwaved *C. difficile* spores. Spores of toxigenic DS1813 and non-toxigenic DS1684 strains were microwaved a peak power of 30 W rms milli-Watts at a range of duty cycles (0%, 1%, 10%, 100%) for 5 s, each at a concentration of 1.67×10^7 spores/mL. The single-stranded (ss) and double-stranded (dsDNA) was quantified via Qubit Fluorometer 3.0. Each test was performed in triplicate ($n = 3$) (A) Concentration of ssDNA in samples of DS1813 and DS1684 (ug/mL). (B) Concentration of dsDNA in samples of DS1813 and DS1684 in ug/mL.

The concentration of dsDNA significantly decreased by 68% following exposure to 1% DC (two-sample t test; $p = 0.060$), in a similar fashion to the ssDNA levels. In contrast, the concentration of dsDNA released increased by 150% as the level of microwave exposure increased at 100% DC (Figure 2B; two-sample t test; $p = 0.014$). One-way ANOVA determined a significant difference between the concentrations of dsDNA released when spores were treated with varying microwave exposures for DS1813 ($p = 0.002$) and for DS1684 ($p = 0.042$). Microwave treatment of DS1684 spores (30 W rms milli-Watts) showed a different pattern of ss and dsDNA release than seen for DS1813. Following exposure with 1% DC an insignificant decrease in ssDNA concentration was observed (two-sample t test; $p = 0.108$) which was then followed by an increase at 10% DC (two-sample t test; $p = 0.461$) and at 100% DC (two-sample t test; $p = 0.110$). However, the release of dsDNA decreased from 0% DC through to 1% DC (two-sample t test; $p = 0.720$) and then increased at 100% DC (two-sample t test; $p = 0.057$) demonstrating that DS1684 spores differ in their response to microwaves when compared to DS1813.

3.3. Electrochemical Detection of *tcdA* and *tcdB* in Microwaved *C. difficile*

The specificity of the toxin-specific DNA probes following microwave treatment was determined using the VantixTM electrochemical reporter system (Figure S2) [27]. This reporter system generates a voltage signal which is proportional to the DNA concentration in the sample. Spores of toxigenic *C. difficile* DS1813 and the non-toxigenic control DS1684 (which lacks the toxin gene targets and pathogenicity locus) at a concentration of 1.33×10^4 spores/mL were exposed to 1%, 10%, and 100% DC of microwaves at a peak power of 30 W rms milli-Watts for 5 s. DNA released from spore lysis was then screened for the presence of toxin genes *tcdA* and *tcdB* using the VantixTM electrochemical reporter system.

As shown in Figure 5, exposure of DS1813 spores to 100% DC microwave power for 5 s gave the strongest signal (milliVolts) for both toxin-specific oligonucleotide probes. The signal increased as the microwave exposure increased. As expected, no measurable toxin-specific signal was observed for DS1684 spores under any of the test conditions (0 mV).

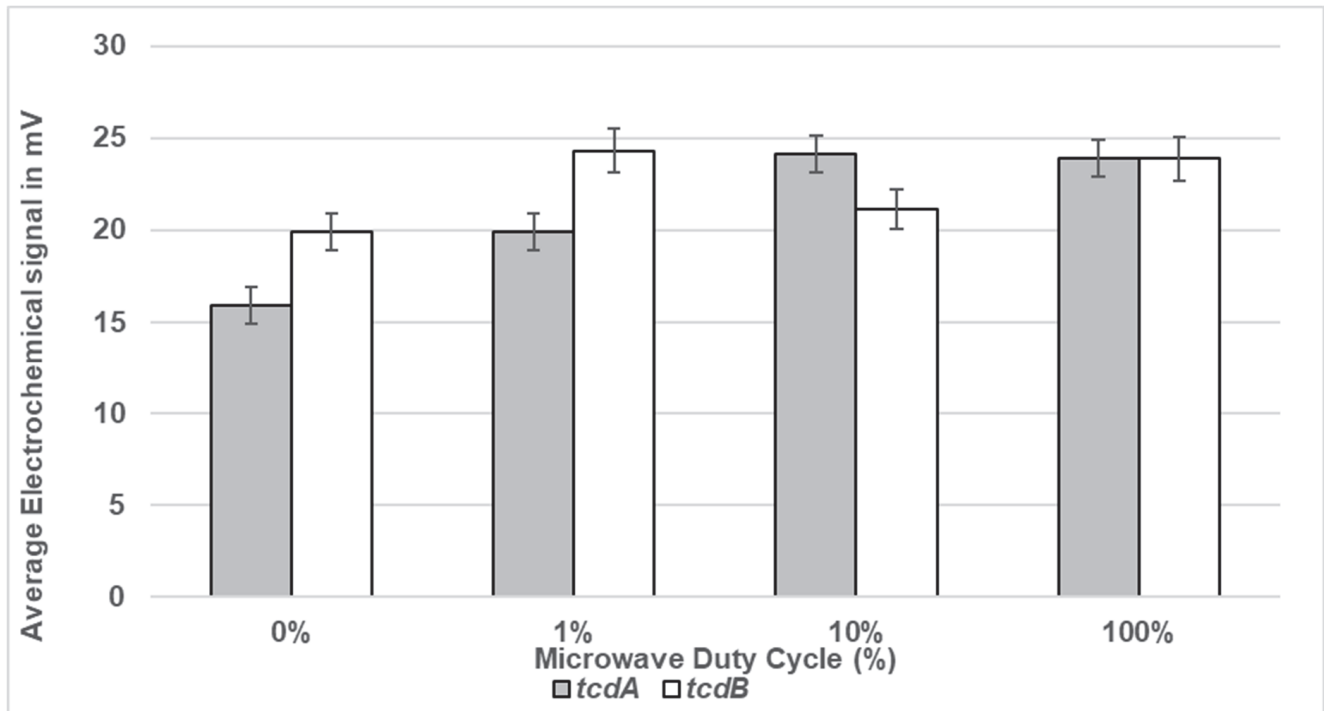


Figure 5. Electrochemical detection of toxigenic *C. difficile* spores suspended in sterile water following exposure to microwaves. Spores of toxigenic strain DS1813 and non-toxicogenic DS1684 at a set concentration of 1.33×10^4 spores/mL were exposed to duty cycles of 1%, 10%, and 100% for 5 s. Spores which were not microwaved were used at controls (0% DC). This equates to 665 spores within the 50 μ L of the assay sample. The microwaved spore samples were then introduced to the VantixTM electrochemical detection system and tested for the presence of toxin genes *tcdA* and *tcdB*. The results above show voltage signals measured from toxigenic DS1813. The results from the toxin-negative DS1684 strain did not generate a measurable signal (0 mV). Each result represents the mean of two independent tests ($n = 2$).

3.4. Determination of the Lower Limit of Electrochemical Detection in Sterile Water

The lower limit of detection (LoD) of the electrochemical detection assay was determined using a dose response. A range of spore concentrations suspended in sterile water were microwaved at a peak power of 30 W rms milli-Watts at 100% DC in sterile water and the lysed spores were then measured for LoD within the VantixTM electrochemical reporter system. The LoD for *tcdA* was 1×10^2 spores/mL which equated to five spores within a 50 μ L sample, whilst for *tcdB* the LoD was 1×10^3 spores/mL equating to 50 spores in a 50 μ L sample (Figure 6). As expected, no signal was detected at any of the DS1684 spore concentrations tested (0 mV).

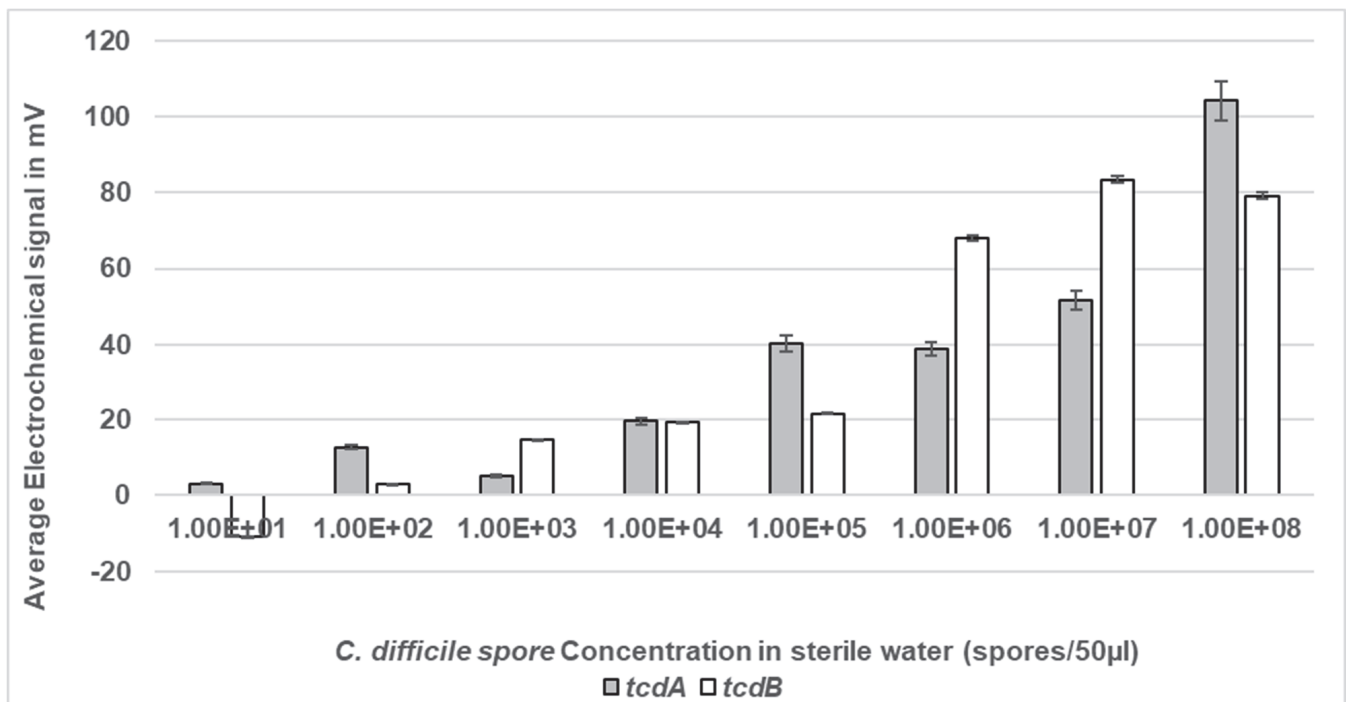


Figure 6. Electrochemical detection of *C. difficile* spores at a range of concentrations in sterile water. Spores of toxigenic strain DS1813 and non-toxicogenic DS1684 at concentrations ranging from 1×10^1 spores within a 50 µL sample to 1×10^8 spores within a 50 µL sample were exposed to microwaves at 100% DC for 5 s. The microwaved spore samples were then introduced to the Vantix™ electrochemical detection system and tested for the presence of both toxin genes *tcdA* and *tcdB*. No signal was detected for any of the DS1684 spore concentrations tested (0 mV). Each result represents the mean of two independent tests ($n = 2$).

3.5. Determination of the Lower Limit of Electrochemical Detection in Feces

The ability of the system to detect *C. difficile* spores in the presence of raw, unprocessed human stool was assessed (Figure 7). Feces is the usual matrix where *C. difficile* spores are present and the gut environment contains approximately 10^{12} per g bacteria [7]. The LoD of the assay was determined using a range of spore concentrations suspended in human feces from a healthy volunteer. All samples were microwaved at a peak power of 30 W rms milli-Watts at a new DC of 33% prior to detection of liberated DNA. Then, 33% DC was used to ensure limited thermal heating of the sample and to account for the change of medium from SDW to feces. The LoD for *tcdA* was 1×10^3 spores/mL which equated to 50 spores within a 50 µL sample, and for *tcdB* LoD was 1×10^2 spores/mL equating to five spores in a 50 µL sample (Figure 5). The detection signals increased as the spore concentration increased. As expected, no signal was detected at any of DS1684 spore concentrations tested (0 mV).

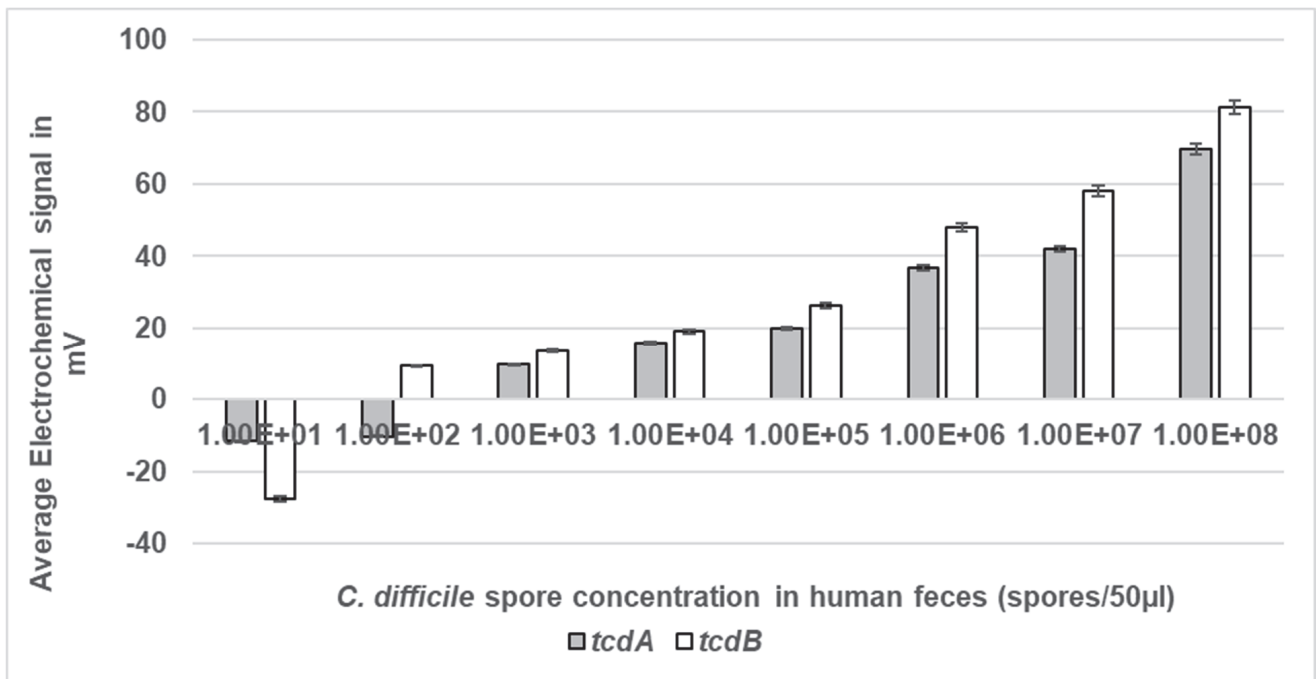


Figure 7. Electrochemical detection of *C. difficile* spores at a range of concentrations in human feces. Spores of toxigenic strain DS1813 and non-toxigenic DS1684 at concentrations ranging from 1×10^1 spores within a 50 µL sample to 1×10^8 spores within a 50 µL sample were exposed to microwaves at 100% DC for 5 s. The microwaved spore samples were then introduced to the Vantix™ electrochemical detection system and tested for the presence of both toxin genes *tcdA* and *tcdB*. No signal was detected for any of the DS1684 spore concentrations tested (0 mV). Each result represents the mean of two independent tests ($n = 2$).

3.6. Comparison of the Specificity and Sensitivity of the Microwave-Enhanced Electrochemical Detection Assay to a Toxin-Sensitive Enzyme Immunoassay (EIA)

The ability of the microwave-enhanced assay system to detect the presence of *C. difficile* *tcdA* and *tcdB* genes individually in clinical stool specimens was compared to that of the rapid Techlab *C. difficile* Tox A/B Quik Chek EIA assay [28]. The Techlab Tox A/B test is routinely used by the diagnostic service of Public Health Wales (PHW) to screen for the presence of *C. difficile*. A total of 50 discarded, anonymized human stool samples, which had been submitted to Public Health Wales to determine the presence *C. difficile*, were cultured and screened using both rapid assays (Figure 8). Of the 50 samples examined, 16 (32%) were culture-negative for *C. difficile* via selective agar testing. Of these samples, one gave a positive result with the Techlab assay and another separate sample gave a positive result using the microwave-enhanced electrochemical assay. These differences reflect that only a 50 µL fraction of the entire stool sample was agar cultured and that it is unlikely that spores would be homogeneously distributed throughout the whole stool sample during the sampling and would all germinate during the anaerobic agar culture process. When the samples were examined using the rapid assays, 32 of 34 culture-positive samples (94%) detected *C. difficile* using the microwave assay. In contrast, the EIA only detected the presence of *C. difficile* in 27 culture-positive samples (75%) (see Table 1).

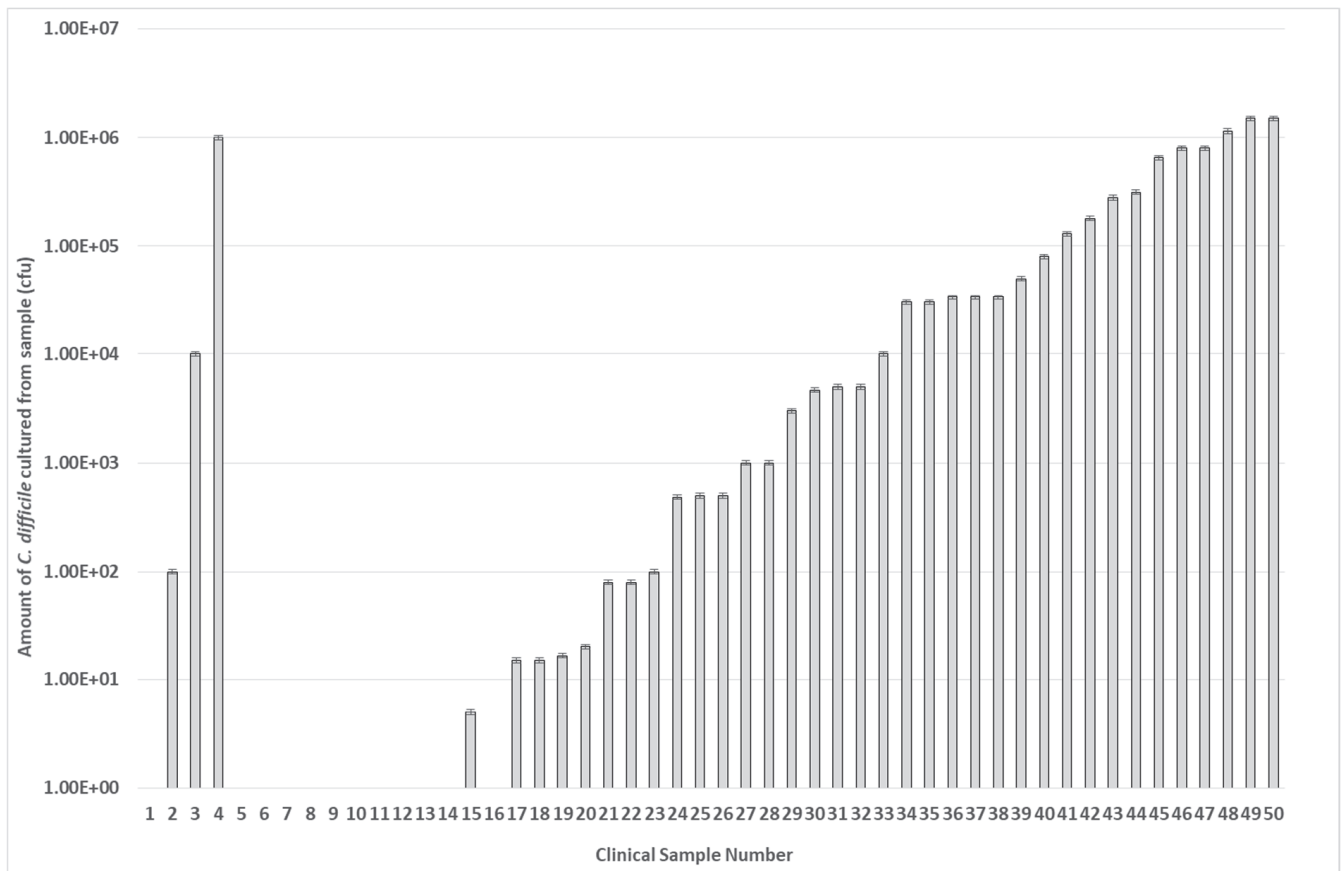


Figure 8. Presence of *C. difficile* in clinical stool samples. A total of 50 stool samples from patients at Public Health Wales were examined for the presence of *C. difficile* using selective agar culture. The data are arranged in order of bacterial number in each sample (cfu/mL). Samples 2, 3, & 4 are anomalous as these were deemed *C. difficile* negative by PHW. Each result represents the mean of two independent tests ($n = 2$).

Table 1. Comparison of Signals detected from Techlab *C. difficile* Tox A/B Quik Chek test against the MW-based assay. A total of 50 stool samples from patients at Public Health Wales were examined for the presence of *C. difficile* using the routine Techlab ELISA toxin assay and the MW based detection assay. The Clinical Sample Number is the same as Figure 8 and can be directly compared. The number (1) indicates positive detection of both *C. difficile* toxin genes (*tcdA*; *tcdB*) and (0) indicates negative detection of *C. difficile* toxin genes. Each result represents the mean of two independent tests ($n = 2$).

Clinical Sample Number	Techlab Tox A/B QuikChek	MW Based Assay
0	0	0
1	0	0
2	0	0
3	0	0
4	0	0
5	0	0
6	0	0
7	0	0
8	0	0
9	0	0

Table 1. *Cont.*

Clinical Sample Number	Techlab Tox A/B QuikChek	MW Based Assay
10	0	0
11	0	0
12	0	0
13	0	0
14	0	1
15	0	1
16	0	0
17	1	1
18	1	1
19	1	1
20	1	1
21	1	0
22	0	0
23	1	0
24	1	0
25	0	0
26	1	0
27	1	0
28	0	0
29	0	0
30	0	0
31	1	0
32	1	0
33	1	0
34	1	0
35	1	0
36	1	0
37	1	0
38	1	0
39	1	0
40	1	0
41	1	0
42	0	0
43	1	1
44	1	1
45	1	1
46	1	1
47	1	1
48	1	1
49	1	1
50	0	1

4. Discussion

In this study we describe a microwave-enhanced bacterial lysis method combined with an electrochemical sensor platform which uses oligonucleotide DNA probes for the rapid detection of *C. difficile* toxin genes in clinical stool specimens, without the need for DNA amplification. This builds on a previous study which utilized a conventional microwave oven to liberate DNA from bacteria, with utilization of the same *C. difficile* oligonucleotide DNA probes in a microwave-accelerated metal-enhanced fluorescence (MAMEF) reporter platform [7]. Results from the MAMEF study demonstrated the specificity and sensitivity of the designed oligonucleotide probes for detection of *C. difficile* toxin genes *tcdA* and *tcdB*.

The results from this small-scale pilot study (50 samples) show disruption of *C. difficile* spores using a 2.45 GHz electric field, leading to spore lysis and the release of target DNA within 5 s (Figure 3). Extraction of DNA from clinical samples is usually time consuming and requires lysis of the bacterium or spore [29]. We have overcome this by utilizing a bespoke microwave cavity able to precisely deliver electric fields at varying intensities to the clinical sample resulting in release of ssDNA which is able to bind to our oligonucleotide capture and reporter probes and be electrochemically detected directly, without any need for purification or DNA amplification (Figures 4–8 and S2) [7,15].

Variations in ss and ds DNA release were observed after using a range of microwave duty cycles (Figure 4A,B). This variation in lysis and overall DNA release may be attributed to the physical structure of the spores, which would influence the interactions of the microwave electric field with the spores inside the cavity [30–32]. It is also possible that the microwave electric field did not reach all spores within the test sample, which may be due to the natural properties of spore hydrophobicity/aggregation or changes in the generated convection current [33,34]. While we have determined that microwave irradiation does release DNA from the organism, the exact genomic mechanism of action of microwave lysis and DNA release has yet to be fully characterized and warrants further investigation.

Current Public Health England guidance for laboratory detection of *C. difficile* from clinical samples states that a combination of two-test algorithms should be used for screening, the first of which should be a Nucleic Acid Amplification Test (NAAT) or Glutamate dehydrogenase EIA followed by a sensitive toxin-EIA test, increasing the sensitivity and accuracy of CDI diagnosis [35–37]. NAATs are expensive to perform and require specialist laboratory equipment to yield results with rapid approved tests such as Cepheid Xpert™ still taking <1 h [38]. Current commercial NAATs include BD Gene Ohm, Cepheid Xpert, and the Cobas C diff PCR test from Roche, which only target the toxin B gene for amplification [39,40].

The ability of the microwave-based assay to detect the presence of both *C. difficile* genes *tcdA* and *tcdB* in clinical stool samples was compared to a commercially used toxin-sensitive EIA (Table 1). With this approach we have demonstrated that the microwave-enhanced assay was more sensitive in detecting culture-positive samples (94.1%) than the toxin sensitive EIA (75%) (Table 1). However, while this pilot study has shown that the microwave-enhanced assay is more sensitive than the commercial toxin-sensitive EIA, a larger clinical study is needed to determine sensitivity and specificity. A positive electrochemical detection result was obtained for sample 14 using the microwave assay when the sample was culture-negative. This could be a false positive result generated by the microwave assay as culture was unable to detect the organism [41]. The toxin-sensitive EIA was also unable to detect the presence of the toxins within the sample; correlating with the culture-negative result. However, the toxin-sensitive EIA only detects the presence of the toxins, not the genes, meaning there is a lack of sensitivity [42]; thus, there is a possibility that single copy numbers of *tcdA* and *tcdB* genes (located in the genome) may still be present within the sample through asymptomatic carriage. This possibility would need to be confirmed using a PCR test and the recommended algorithms [37].

This microwave-enhanced method detects the presence of both *tcdA* and *tcdB* genes and thus can also be used to detect asymptomatic carriage in patients—a useful screen when considering infection prevention and control of CDI. Other gold standard *C. difficile*

detection methods used in the UK such as toxin-sensitive EIA currently do not provide this level of discrimination. The method we describe has distinct advantages in reducing the test time from acquiring the samples to obtaining a definitive molecular result, which is useful in triage of CDI patients in hospitals and within community settings. There is an increasing appreciation of the importance of community-acquired CDI and the role of asymptomatic carriers in transmission [36]. A study, in a setting where 42% of CDI cases were community-onset, demonstrated that testing for asymptomatic carriers plus contact precautions reduced the number of new colonization and hospital-onset CDI cases by 40%–50% and 10%–25%, respectively [43].

These results demonstrate that microwaves can be used to rapidly liberate DNA from fecal samples and that subsequent electrochemical detection (using screen-printed electrodes) may be used to screen for patients with CDI. As the majority of CDI cases occur as a consequence of prescribing broad-spectrum antibiotics to asymptomatic carriers, an indication of the presence of toxigenic *C. difficile* in a patient upon hospital admission would enable clinicians to tailor their antibiotic treatment strategy appropriately, minimizing the development of active CDI. There is potential for the methodology to be adapted and optimized for the detection of other antimicrobial resistant pathogens in a range of human sample types. Thus, microwave-extraction of DNA combined with electrochemical biosensor detection of target DNA within 10 min represents a viable, rapid, and sensitive method for the detection of toxigenic *C. difficile* at point of care.

Supplementary Materials: The following supporting information can be downloaded at: <https://www.mdpi.com/article/10.3390/bioengineering11060632/s1>, Figure S1: Scanning Electron Microscopy studies. Spores were imaged under SEM before and after microwaving at a range of duty cycles between 100%–0.3%. 40 spores were imaged per DC at magnifications of $\times 82,000$ and $\times 31,000$. A–C show untreated (Control) *C. difficile* spores, D–F show spores treated with 100% Duty Cycle, G–I show spores treated with 33% Duty Cycle, J–L show spores treated with 10% Duty Cycle, M–O show spores treated with 3% Duty Cycle, P–R show spores treated with 1% Duty Cycle, S–U show spores treated with 0.3% Duty Cycle. Arrows indicate areas of spore damage. Table S1: Microwave pulsed duty cycles used in this study. The varying percentage duty cycles used when microwaving *C. difficile* spores is listed. The duty cycles range from 100% (continuous microwave power) to 0.3% pulsed microwaves. The time microwave power is on and off is shown in milliseconds. Spores were microwaved for 5 s in total, which is related to the total number of pulsed microwaves (N) in the table. Figure S2: Schematic demonstrating the three piece DNA assay and the chemical detection of HRP. This DNA assay was used to detect both toxin A and toxin B detection. The anchor probe is 17 nucleotides in length and anchored to the streptavidin sensor via addition of a biotin label. The reporter probe (22 nucleotides in length) was attached to an HRP at the 3' end. Once hybridisation and washing has occurred, the DNA sandwich complex is formed and the HRP can be detected.

Author Contributions: Conceptualization L.T.J., L.B., J.L. and A.P.; methodology, L.T.J., L.B., J.L. and A.P.; software J.L. and A.P.; validation, L.T.J., T.M. and E.B.; formal analysis, L.T.J.; investigation, L.T.J.; resources, L.T.J., E.B., T.M., L.B., J.L. and A.P.; data curation, L.T.J.; writing—original draft preparation, L.T.J.; writing—review and editing, L.T.J., L.B., J.L. and A.P.; project administration, L.T.J., L.B., T.M., J.L. and A.P.; funding acquisition, L.T.J., L.B., J.L. and A.P. All authors have read and agreed to the published version of the manuscript.

Funding: This research was funded by the Cardiff University EPSRC Impact Acceleration Account (IAA), and Cardiff University Wellcome Seedcorn Grant. The funders had no role in study design, data collection and interpretation, or the decision to submit the work for publication.

Institutional Review Board Statement: Ethical review and approval were waived for this study due to the fecal samples being discarded and anonymized waste.

Informed Consent Statement: Not applicable.

Data Availability Statement: The data are available within the article.

Acknowledgments: Authors wish to thank Public Health Wales and the Anaerobic Reference Unit, Cardiff, UK, for their kind collaboration. We also wish to thank Emmanuel Brousseau for their help with the Electron Microscopy work.

Conflicts of Interest: The authors declare no conflicts of interest.

References

- Guh, A.Y.; Mu, Y.; Winston, L.G.; Johnston, H.; Olson, D.; Farley, M.M.; Wilson, L.E.; Holzbauer, S.M.; Phipps, E.C.; Dumyati, G.K.; et al. Trends in US burden of *Clostridioides difficile* infection and outcomes. *N. Engl. J. Med.* **2020**, *382*, 1320–1330. [CrossRef]
- Czepiel, J.; Drózd, M.; Pituch, H.; Kuijper, E.J.; Perucki, W.; Mielimonka, A.; Goldman, S.; Wultańska, D.; Garlicki, A.; Biesiada, G. *Clostridium difficile* infection: Review. *Eur. J. Clin. Microbiol. Infect. Dis.* **2019**, *38*, 1211–1221. [CrossRef] [PubMed]
- Ahmed, H.; Joshi, L.T. *Clostridioides difficile* spores tolerate disinfection with sodium hypochlorite disinfectant and remain viable within surgical scrubs and gown fabrics. *Microbiology* **2023**, *169*, 001418. [CrossRef] [PubMed]
- Spigaglia, P. *Clostridioides difficile* infection (CDI) during the COVID-19 pandemic. *Anaerobe* **2022**, *74*, 102518. [CrossRef] [PubMed]
- Boyanova, L.; Dimitrov, G.; Gergova, R.; Hadzhiyski, P.; Markovska, R. *Clostridioides difficile* resistance to antibiotics, including post-COVID-19 data. *Expert Rev. Clin. Pharmacol.* **2023**, *16*, 925–938. [PubMed]
- Schäffler, H.; Breitrück, A. *Clostridium difficile*—From colonization to infection. *Front. Microbiol.* **2018**, *9*, 646. [CrossRef] [PubMed]
- Joshi, L.T.; Mali, B.L.; Geddes, C.D.; Baillie, L. Extraction and Sensitive Detection of Toxins A and B from the Human Pathogen *Clostridium difficile* in 40 Seconds Using Microwave-Accelerated Metal-Enhanced Fluorescence. *PLoS ONE* **2014**, *9*, e104334. [CrossRef] [PubMed]
- Barbut, F.; Petit, J. Epidemiology of *Clostridium difficile*-associated infections. *Clin. Microbiol. Infect.* **2001**, *7*, 405–410. [CrossRef] [PubMed]
- Lim, V.W.; Tomaru, T.; Chua, B.; Ma, Y.; Yanagihara, K. Budget Impact Analysis of Adopting a One-Step Nucleic Acid Amplification Testing (NAAT) Alone Diagnostic Pathway for *Clostridioides difficile* in Japan Compared to a Two-Step Algorithm with Glutamate Dehydrogenase/Toxin Followed by NAAT. *Diagnostics* **2023**, *13*, 1463. [CrossRef] [PubMed]
- UK Government. *Clostridioides Difficile: Guidance, Data and Analysis*. 2022. Available online: <https://www.gov.uk/government/collections/clostridium-difficile-guidance-data-and-analysis> (accessed on 15 January 2024).
- Pancholi, P.; Kelly, C.; Raczkowski, M.; Balada-Llasat, J.M. Detection of toxigenic *Clostridium difficile*: Comparison of the cell culture neutralization, Xpert C. *difficile*, Xpert C. *difficile*/Epi, and Illumigene C. *difficile* assays. *J. Clin. Microbiol.* **2012**, *50*, 1331–1335. [CrossRef] [PubMed]
- Elfassy, A.; Kalina, W.V.; French, R.; Nguyen, H.; Tan, C.; Sebastian, S.; Wilcox, M.H.; Davies, K.; Kutzler, M.A.; Jansen, K.U.; et al. Development and clinical validation of an automated cell cytotoxicity neutralization assay for detecting *Clostridioides difficile* toxins in clinically relevant stools samples. *Anaerobe* **2021**, *71*, 102415. [CrossRef] [PubMed]
- Tenover, F.C.; Baron, E.J.; Peterson, L.R.; Persing, D.H. Laboratory Diagnosis of *Clostridium difficile* Infection: Can Molecular Amplification Methods Move Us out of Uncertainty? *J. Mol. Diagn. JMD* **2011**, *13*, 573–582. [CrossRef] [PubMed]
- O’Neill, J. Review on Antimicrobial Resistance. Antimicrobial Resistance: Tackling a Crisis for the Health and Wealth of Nations. 2014. Available online: https://amr-review.org/sites/default/files/AMR%20Review%20Paper%20-%20Tackling%20a%20crisis%20for%20the%20health%20and%20wealth%20of%20nations_1.pdf (accessed on 16 January 2024).
- Imtiaz, A.; Lees, J.; Choi, H.; Joshi, L.T. An Integrated Continuous Class-F⁻¹ Mode Power Amplifier Design Approach for Microwave Enhanced Portable Diagnostic Applications. *IEEE Trans. Microw. Theory Tech.* **2015**, *63*, 3007–3015. [CrossRef]
- International Telecommunication Union. 19 October 2009. 1.15. Industrial, Scientific and Medical (ISM) Applications (of Radio Frequency Energy). Available online: https://www.itu.int/dms_pubrec/itu-r/rec/sm/R-REC-SM.1056-1-200704-I!!PDF-E.pdf (accessed on 11 December 2023).
- Gartshore, A.; Kidd, M.; Joshi, L.T. Applications of Microwave Energy in Medicine. *Biosensors* **2021**, *11*, 96. [CrossRef]
- Morgan, A.J.; Naylon, J.; Gooding, S.; John, C.; Squires, O.; Lees, J.; Porch, A. Efficient microwave heating of microfluidic systems. *Sens. Actuators B Chem.* **2013**, *181*, 904–909. [CrossRef]
- Porch, A.; Slocombe, D.; Edwards, P.P. Microwave absorption in powders of small conducting particles for heating applications. *Phys. Chem. Chem. Phys.* **2013**, *15*, 2757–2763. [CrossRef] [PubMed]
- Tennant, S.M.; Zhang, Y.; Galen, J.E.; Geddes, C.D.; Levine, M.M. Ultra-fast and sensitive detection of non-typhoidal Salmonella using microwave-accelerated metal-enhanced fluorescence (“MAMEF”). *PLoS ONE* **2011**, *6*, e18700. [CrossRef] [PubMed]
- Zhang, Y.; Agreda, P.; Kelley, S.; Gaydos, C.; Geddes, C.D. Development of a microwave-accelerated metal-enhanced fluorescence 40 second, <100 cfu/mL point of care assay for the detection of *Chlamydia trachomatis*. *Biomed. Eng. IEEE Trans.* **2011**, *58*, 781–784. [CrossRef] [PubMed]
- Shaw, K.J.; Docker, P.T.; Yelland, J.V.; Dyer, C.E.; Greenman, J.; Greenway, G.M.; Haswell, S.J. Rapid PCR amplification using a microfluidic device with integrated microwave heating and air impingement cooling. *Lab Chip* **2010**, *10*, 1725–1728. [CrossRef] [PubMed]
- Stubbs, S.L.J.; Brazier, J.S.; O’Neill, G.L.; Duerden, B.I. PCR targeted to the 16S-23S rRNA gene intergenic spacer region of *Clostridium difficile* and construction of a library consisting of 116 different PCR ribotypes. *J. Clin. Microbiol.* **1999**, *37*, 461. [CrossRef] [PubMed]

24. Cuenca, J.A.; Thomas, E.; Mandal, S.; Williams, O.; Porch, A. Microwave determination of sp² carbon fraction in nanodiamond powders. *Carbon* **2015**, *81*, 174–178. [CrossRef]
25. Cuenca, J.A.; Bugler, K.; Taylor, S.; Morgan, D.; Williams, P.; Bauer, J.; Porch, A. Study of the magnetite to maghemite transition using microwave permittivity and permeability measurements. *J. Phys.—Condens. Matter* **2016**, *28*, 106002. [CrossRef]
26. Techlab. C. DIFFICILE TOX A/B. 2008. An ELISA for the Detection of *Clostridium difficile* Toxins A and B. [C. DIFFICILE TOX A/B II™-TECHLAB, Inc.]. Available online: <https://www.techlab.com/diagnostics/c-difficile/c-difficile-tox-ab-ii/> (accessed on 7 February 2024).
27. Purvis, D.R.; Sentsortec Ltd. Method of Electrochemical Analysis of an Analyte. U.S. Patent 8,163,163, 24 April 2012.
28. Dawson, L.F.; Peltier, J.; Hall, C.L.; Harrison, M.A.; Derakhshan, M.; Shaw, H.A.; Fairweather, N.F.; Wren, B.W. Extracellular DNA, cell surface proteins and c-di-GMP promote biofilm formation in *Clostridioides difficile*. *Sci. Rep.* **2021**, *11*, 3244. [CrossRef] [PubMed]
29. Metcalf, D.; Weese, J.S. Evaluation of commercial kits for extraction of DNA and RNA from *Clostridium difficile*. *Anaerobe* **2012**, *18*, 608–613. [CrossRef] [PubMed]
30. Keller, M.D.; Bellows, W.K.; Guillard, R.R. Microwave treatment for sterilization of phytoplankton culture media. *J. Exp. Mar. Biol. Ecol.* **1988**, *117*, 279–283. [CrossRef]
31. Kim, S.Y.; Shin, S.J.; Song, C.H.; Jo, E.K.; Kim, H.J.; Park, J.K. Destruction of *Bacillus licheniformis* spores by microwave irradiation. *J. Appl. Microbiol.* **2009**, *106*, 877–885. [CrossRef] [PubMed]
32. Ojha, S.C.; Chankhamhaengdecha, S.; Singhakaew, S.; Ounjai, P.; Janvilisri, T. Inactivation of *Clostridium difficile* spores by microwave irradiation. *Anaerobe* **2016**, *38*, 14–20. [CrossRef] [PubMed]
33. Ellison, B.; Gibson, C.; Grant, N.; Hyland, G.; Lloyd, D.; Magee, J.; Pooley, D.; Stewart, W.; MRBP RESEARCH Ltd. Apparatus and Method for Analysing a Biological Sample in Response to Microwave Radiation. U.S. Patent Application 10/484,378, 9 September 2004.
34. Joshi, L.T.; Phillips, D.S.; Williams, C.F.; Alyousef, A.; Baillie, L. Contribution of spores to the ability of *Clostridium difficile* to adhere to surfaces. *Appl. Environ. Microbiol.* **2012**, *78*, 7671–7679. [CrossRef] [PubMed]
35. Robotham, J.; Wilcox, M. Updated Guidance on the Diagnosis and Reporting of *Clostridium difficile*. Department of Health, PHE, UK. 2012. Available online: <https://www.gov.uk/government/publications/updated-guidance-on-the-diagnosis-and-reporting-of-clostridium-difficile> (accessed on 15 January 2024).
36. Fang, F.C.; Polage, C.R.; Wilcox, M.H. Point-counterpoint: What is the optimal approach for detection of *Clostridium difficile* infection? *J. Clin. Microbiol.* **2017**, *55*, 670–680. [CrossRef] [PubMed]
37. Goldenberg, S.D.; French, G.L. Diagnostic testing for *Clostridium difficile*: A comprehensive survey of laboratories in England. *J. Hosp. Infect.* **2011**, *79*, 4–7. [CrossRef] [PubMed]
38. Williamson, D.A.; Basu, I.; Freeman, J.; Swager, T.; Roberts, S.A. Improved detection of toxigenic *Clostridium difficile* using the Cepheid Xpert C. *difficile* assay and impact on C. *difficile* infection rates in a tertiary hospital: A double-edged sword. *Am. J. Infect. Control* **2013**, *41*, 270–272. [CrossRef] [PubMed]
39. Deshpande, A.; Pasupuleti, V.; Rolston, D.D.; Jain, A.; Deshpande, N.; Pant, C.; Hernandez, A.V. Diagnostic accuracy of real-time polymerase chain reaction in detection of *Clostridium difficile* in the stool samples of patients with suspected *Clostridium difficile* infection: A meta-analysis. *Clin. Infect. Dis.* **2011**, *53*, 81–90. [CrossRef] [PubMed]
40. Peterson, L.R.; Young, S.A.; Davis, T.E.; Wang, Z.X.; Duncan, J.; Noutsios, C.; Liesenfeld, O.; Osiecki, J.C.; Lewinski, M.A. Evaluation of the cobas[®] Cdiff test for the Detection of Toxigenic *Clostridium difficile* in Stool Samples. *J. Clin. Microbiol.* **2017**, *55*, 3426. [CrossRef] [PubMed]
41. Planche, T.; Aghaizu, A.; Holliman, R.; Riley, P.; Poloniecki, J.; Breathnach, A.; Krishna, S. Diagnosis of *Clostridium difficile* infection by toxin detection kits: A systematic review. *Lancet Infect. Dis.* **2008**, *8*, 777–784. [CrossRef] [PubMed]
42. Davies, K.A.; Berry, C.E.; Morris, K.A.; Smith, R.; Young, S.; Davis, T.E.; Fuller, D.D.; Buckner, R.J.; Wilcox, M.H. Comparison of the Vidas C. *difficile* GDH automated enzyme-linked fluorescence immunoassay (ELFA) with another commercial enzyme immunoassay (EIA)(Quik Chek-60), two selective media, and a PCR assay for *gluD* for detection of *Clostridium difficile* in fecal samples. *J. Clin. Microbiol.* **2015**, *53*, 1931–1934. [CrossRef] [PubMed]
43. Lanzas, C.; Dubberke, E.R. Effectiveness of screening hospital admissions to detect asymptomatic carriers of *Clostridium difficile*: A modeling evaluation. *Infect. Control Hosp. Epidemiol.* **2014**, *35*, 1043–1050. [CrossRef] [PubMed]

Disclaimer/Publisher’s Note: The statements, opinions and data contained in all publications are solely those of the individual author(s) and contributor(s) and not of MDPI and/or the editor(s). MDPI and/or the editor(s) disclaim responsibility for any injury to people or property resulting from any ideas, methods, instructions or products referred to in the content.

MDPI AG
Grosspeteranlage 5
4052 Basel
Switzerland
Tel.: +41 61 683 77 34

Bioengineering Editorial Office
E-mail: bioengineering@mdpi.com
www.mdpi.com/journal/bioengineering



Disclaimer/Publisher's Note: The title and front matter of this reprint are at the discretion of the Guest Editors. The publisher is not responsible for their content or any associated concerns. The statements, opinions and data contained in all individual articles are solely those of the individual Editors and contributors and not of MDPI. MDPI disclaims responsibility for any injury to people or property resulting from any ideas, methods, instructions or products referred to in the content.



Academic Open
Access Publishing

mdpi.com

ISBN 978-3-7258-4700-6